The Long-Baseline Neutrino Experiment

Exploring Fundamental Symmetries of the Universe

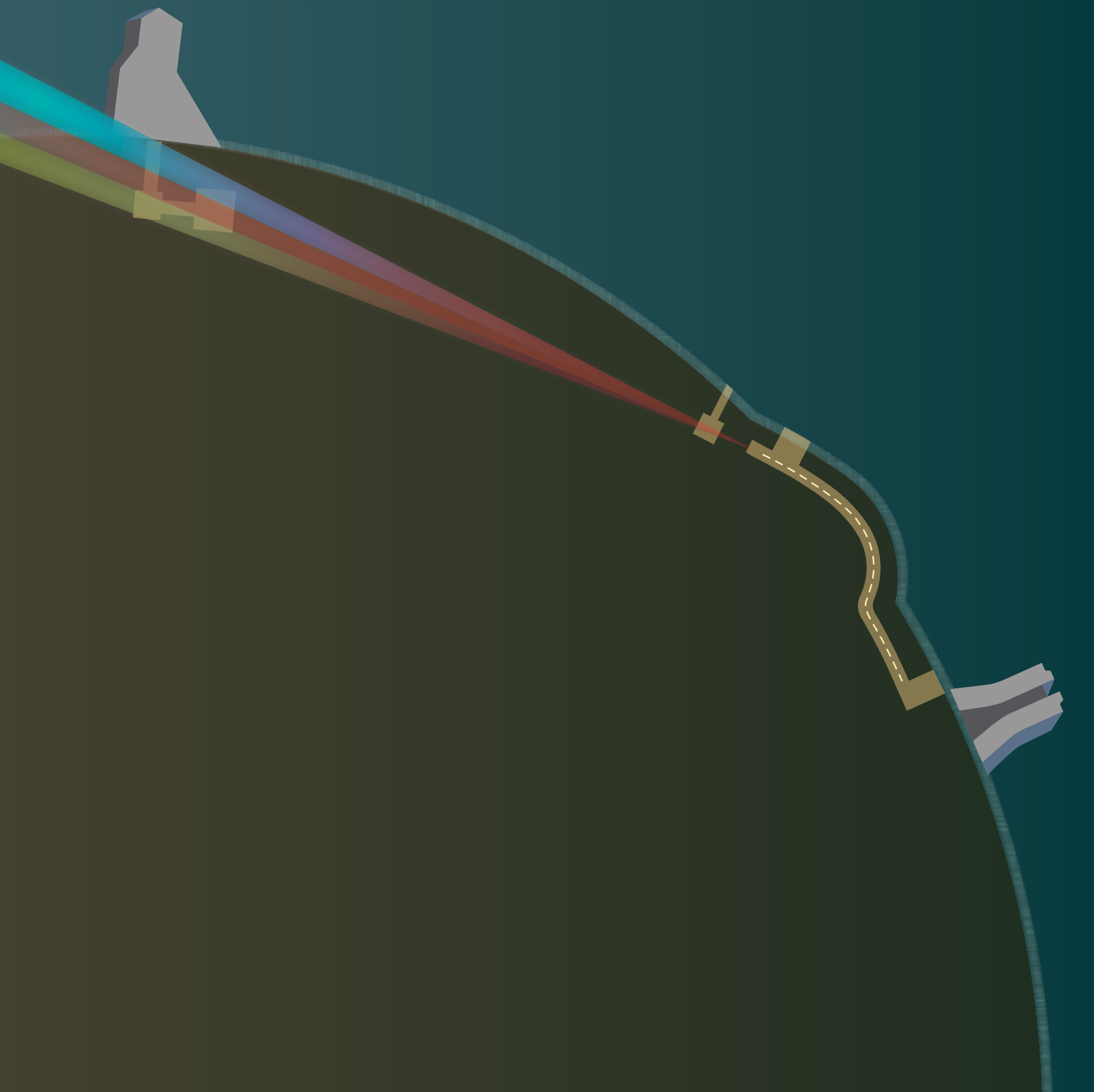

BNL-101354-2014-JA
FERMILAB-PUB-14-022
LA-UR-14-20881
arXiv:1307.7335

The Long-Baseline Neutrino Experiment

Exploring Fundamental Symmetries of the Universe

April 15, 2014

Cover design by Diana Brandonisio, Fermilab Visual Media Services

Typeset in LaTeX

The LBNE Collaboration

C. Adams[85], D. Adams[7], T. Akiri[23], T. Alion[67], K. Anderson[25], C. Andreopoulos[40], M. Andrews[25], I. Anghel[33], J. C. C. d. Anjos[14], M. Antonello[36], E. Arrieta-Diaz[46], M. Artuso[74], J. Asaadi[74], X. Bai[69], B. Baibussinov[56], M. Baird[32], B. Balantekin[84], B. Baller[25], B. Baptista[32], D. Barker[68], G. Barker[81], W. A. Barletta[45], G. Barr[55], L. Bartoszek[41], A. Bashyal[76], M. Bass[18], V. Bellini[13], P. A. Benetti[58], B. E. Berger[18], M. Bergevin[8], E. Berman[25], H. Berns[8], A. Bernstein[39], R. Bernstein[25], B. Bhandari[30], V. Bhatnagar[57], B. Bhuyan[31], J. Bian[49], M. Bishai[7], A. Blake[11], F. Blaszczyk[42], E. Blaufuss[44], B. Bleakley[71], E. Blucher[15], S. Blusk[74], V. Bocean[25], F. Boffelli[58], J. Boissevain[41], T. Bolton[35], M. Bonesini[48], S. Boyd[81], A. Brandt[76], R. Breedon[8], C. Bromberg[46], R. Brown[7], G. Brunetti[25], N. Buchanan[18], B. Bugg[75], J. Busenitz[2], E. Calligarich[58], L. Camilleri[19], G. Carminati[9], R. Carr[19], C. Castromonte[27], F. Cavanna[85], S. Centro[56], A. Chen[25], H. Chen[7], K. Chen[7], D. Cherdack[18], C. Chi[19], S. Childress[25], B. C. Choudhary[21], G. Christodoulou[40], C. Christofferson[69], E. Church[85], D. Cline[10], T. Coan[72], A. Cocco[51], J. Coelho[78], S. Coleman[17], J. M. Conrad[45], M. Convery[64], R. Corey[69], L. Corwin[69], J. Cranshaw[4], D. Cronin-Hennessy[49], A. Curioni[48], H. da Motta[14], T. Davenne[65], G. S. Davies[33], S. Dazeley[39], K. De[76], A. de Gouvea[53], J. K. de Jong[55], D. Demuth[49], C. Densham[65], M. Diwan[7], Z. Djurcic[4], R. Dolfini[58], J. Dolph[7], G. Drake[4], S. Dye[29], H. Dyuang[67], D. Edmunds[46], S. Elliott[41], M. Elnimr[2], S. Eno[44], S. Enomoto[82], C. O. Escobar[25], J. Evans[43], A. Falcone[58], L. Falk[73], A. Farbin[76], C. Farnese[56], A. Fava[56], J. Felde[44], S. Fernandes[2], F. Ferroni[58], F. Feyzi[84], L. Fields[53], A. Finch[37], M. Fitton[65], B. Fleming[85], J. Fowler[23], W. Fox[32], A. Friedland[41], S. Fuess[25], B. Fujikawa[38], H. Gallagher[78], R. Gandhi[28], G. Garvey[41], V. M. Gehman[38], G. d. Geronimo[7], D. Gibin[56], R. Gill[7], R. A. Gomes[27], M. C. Goodman[4], J. Goon[68], N. Graf[60], M. Graham[64], R. Gran[50], C. Grant[8], N. Grant[37], H. Greenlee[25], L. Greenler[84], S. Grullon[59], E. Guardincerri[41], V. Guarino[4], E. Guarnaccia[80], G. Guedes[24], R. Guenette[85], A. Guglielmi[56], M. M. Guzzo[12], A. T. Habig[50], R. W. Hackenburg[7], H. Hadavand[76], A. Hahn[25], M. Haigh[81], T. Haines[41], T. Handler[75], S. Hans[7], J. Hartnell[73], J. Harton[18], R. Hatcher[25], A. Hatzikoutelis[75], S. Hays[25], E. Hazen[6], M. Headley[70], A. Heavey[25], K. Heeger[85], J. Heise[70], R. Hellauer[44], J. Hewes[43], A. Himmel[23], M. Hogan[18], P. Holanda[12], A. Holin[79], G. Horton-Smith[35], J. Howell[25], P. Hurh[25], J. Huston[46], J. Hylen[25], R. Imlay[42], J. Insler[42], G. Introzzi[58], Z. Isvan[7], C. Jackson[76], J. Jacobsen[44], D. E. Jaffe[7], C. James[25], C. Jen[80], M. Johnson[25], R. Johnson[16], R. Johnson[17], S. Johnson[17], W. Johnston[18], J. Johnstone[25], B. J. Jones[45], H. Jostlein[25], T. Junk[25], R. Kadel[38], K. Kaess[50], G. Karagiorgi[19], J. Kaspar[82], T. Katori[45], B. Kayser[25], E. Kearns[6], P. Keener[59], E. Kemp[12], S. H. Kettell[7], M. Kirby[25], J. Klein[59], G. Koizumi[25], S. Kopp[77], L. Kormos[37], W. Kropp[9], V. A. Kudryavtsev[66], A. Kumar[57], J. Kumar[29], T. Kutter[42], F. La Zia[13], K. Lande[59], C. Lane[22], K. Lang[77], F. Lanni[7], R. Lanza[45], T. Latorre[59], J. Learned[29], D. Lee[41], K. Lee[10], Q. Li[25], S. Li[7], Y. Li[7], Z. Li[23], J. Libo[67], S. Linden[6], J. Ling[7], J. Link[80], L. Littenberg[7], H. Liu[30], Q. Liu[41], T. Liu[72], J. Losecco[54], W. Louis[41], B. Lundberg[25], T. Lundin[25], J. Lundy[76], A. A. Machado[26], C. Maesano[8], S. Magill[4], G. Mahler[7], D. Malon[4], S. Malys[52], F. Mammoliti[13], S. K. Mandal[21], A. Mann[78], P. Mantsch[25],

A. Marchionni[25], W. Marciano[7], C. Mariani[80], J. Maricic[29], A. Marino[17], M. Marshak[49], J. Marshall[11], S. Matsuno[29], C. Mauger[41], K. Mavrokoridis[40], N. Mayer[78], N. McCauley[40], E. McCluskey[25], K. McDonald[61], K. McFarland[63], D. McKee[35], R. McKeown[83], R. McTaggart[71], R. Mehdiyev[77], D. Mei[68], A. Menegolli[58], G. Meng[56], Y. Meng[10], D. Mertins[2], M. Messier[32], W. Metcalf[42], R. Milincic[29], W. Miller[49], G. Mills[41], S. R. Mishra[67], N. Mokhov[25], C. Montanari[58], D. Montanari[25], C. Moore[25], J. Morfin[25], B. Morgan[81], W. Morse[7], Z. Moss[45], C. A. Moura[1], S. Mufson[32], D. Muller[64], J. Musser[32], D. Naples[60], J. Napolitano[62], M. Newcomer[59], R. Nichol[79], T. Nicholls[65], E. Niner[32], B. Norris[25], J. Nowak[37], H. O'Keeffe[37], R. Oliveira[12], T. Olson[78], B. Page[46], S. Pakvasa[29], O. Palamara[85], J. Paley[4], V. Paolone[60], V. Papadimitriou[25], S. Park[76], Z. Parsa[7], K. Partyka[85], B. Paulos[84], Z. Pavlovic[41], S. Peeters[73], A. Perch[79], G. Perdue[63], J. D. Perkin[66], R. Petti[67], A. Petukhov[69], F. Pietropaolo[56], R. Plunkett[25], C. Polly[25], S. Pordes[25], M. Potekhin[7], R. Potenza[13], A. Prakash[45], O. Prokofiev[25], X. Qian[7], J. L. Raaf[25], V. Radeka[7], I. Rakhno[25], Y. Ramachers[81], R. Rameika[25], J. Ramsey[41], A. Rappoldi[58], G. Raselli[58], P. Ratoff[37], S. Ravindra[76], B. Rebel[25], J. Reichenbacher[2], D. Reitzner[25], S. Rescia[7], M. Richardson[66], K. Rielage[41], K. Riesselmann[25], M. Robinson[66], L. Rochester[64], M. Ronquest[41], M. Rosen[29], M. Rossella[58], C. Rubbia[26], R. Rucinski[25], S. Sahijpal[57], H. Sahoo[4], P. Sala[47], D. Salmiera[58], N. Samios[7], M. Sanchez[33], A. Scaramelli[47], H. Schellman[53], R. Schmitt[25], D. Schmitz[15], J. Schneps[78], K. Scholberg[23], E. Segreto[36], S. Seibert[59], L. Sexton-Kennedy[25], M. Shaevitz[19], P. Shanahan[25], R. Sharma[7], T. Shaw[25], N. Simos[7], V. Singh[5], G. Sinnis[41], W. Sippach[19], T. Skwarnicki[74], M. Smy[9], H. Sobel[9], M. Soderberg[74], J. Sondericker[7], W. Sondheim[41], A. Sousa[16], N. J. Spooner[66], M. Stancari[25], I. Stancu[2], D. Stefan[36], A. Stefanik[25], J. Stewart[7], S. Stone[74], J. Strait[25], M. Strait[15], S. Striganov[25], G. Sullivan[44], Y. Sun[29], L. Suter[4], A. Svenson[67], R. Svoboda[8], B. Szczerbinska[20], A. Szelc[85], M. Szydagis[8], S. Söldner-Rembold[43], R. Talaga[4], M. Tamsett[73], S. Tariq[25], R. Tayloe[32], C. Taylor[41], D. Taylor[70], A. Teymourian[10], H. Themann[7], M. Thiesse[66], J. Thomas[79], L. F. Thompson[66], M. Thomson[11], C. Thorn[7], M. Thorpe[65], X. Tian[67], D. Tiedt[69], W. Toki[18], N. Tolich[82], M. Torti[58], M. Toups[45], C. Touramanis[40], M. Tripathi[8], I. Tropin[25], Y. Tsai[64], C. Tull[38], M. Tzanov[42], J. Urheim[32], S. Usman[52], M. Vagins[34], G. A. Valdiviesso[3], R. Van Berg[59], R. Van de Water[41], P. Van Gemmeren[4], F. Varanini[56], G. Varner[29], K. Vaziri[25], G. Velev[25], S. Ventura[56], C. Vignoli[36], B. Viren[7], D. Wahl[84], A. Waldron[73], C. W. Walter[23], H. Wang[10], W. Wang[83], T.K. Warburton[66], D. Warner[18], R. Wasserman[18], B. Watson[76], A. Weber[55], W. Wei[68], D. Wells[69], M. Wetstein[15], A. White[76], H. White[41], L. Whitehead[30], D. Whittington[32], J. Willhite[70], R. J. Wilson[18], L. Winslow[10], K. Wood[67], E. Worcester[7], M. Worcester[7], T. Xin[33], K. Yarritu[41], J. Ye[72], M. Yeh[7], B. Yu[7], J. Yu[76], T. Yuan[17], A. Zani[58], G. P. Zeller[25], C. Zhang[7], C. Zhang[68], E. D. Zimmerman[17], and R. Zwaska[25]

[1]ABC Federal University, Santo André –SP, 09210-580, Brazil
[2]Univ. of Alabama (Tuscaloosa), Tuscaloosa, AL 35487-0324, USA
[3]Univ. Federal de Alfenas em Poços de Caldas, 11999, CEP 37715-900 Poços de Caldas-MG, Brazil
[4]Argonne National Lab., Argonne, IL 60439, USA
[5]Banaras Hindu University, Dept. of Physics, Varanasi UP 221005, India

[6]Boston University, Boston, MA 02215, USA
[7]Brookhaven National Lab., Upton, NY 11973-5000, USA
[8]Univ. of California (Davis), Davis, CA 95616, USA
[9]Univ. of California (Irvine), Irvine, CA 92697-4575, USA
[10]Univ. of California (Los Angeles), Los Angeles, CA 90095-1547, USA
[11]Univ. of Cambridge, JJ Thomson Avenue, Cambridge CB3 0HE, UK
[12]Univ. de Campinas, Av. Sérgio Buarque de Holanda, 777 CEP 13083-859 Campinas-SP, Brazil
[13]Univ. di Catania, Corso Italia, I-95129 Catania, Italy
[14]Centro Brasileiro de Pesquisas Físicas, Rio de Janeiro, BR-22290-180, Brazil
[15]Univ. of Chicago, Chicago, IL 60637-1434, USA
[16]Univ. of Cincinnati, Cincinnati, OH 45221-0011, USA
[17]Univ. of Colorado, Boulder, CO 80309, USA
[18]Colorado State University, Fort Collins, CO 80523, USA
[19]Columbia University, New York, NY 10027, USA
[20]Dakota State University, Madison, SD 57042, USA
[21]Univ. of Delhi, Department of Physics and Astrophysics, Delhi 110007, India
[22]Drexel University, Philadelphia, PA 19104, USA
[23]Duke University, Durham, NC 27706, USA
[24]Univ. Estadual de Feira de Santana, 44036-900, Feira de Santana-BA, Brazil
[25]Fermi National Accelerator Lab, Batavia, IL 60510-0500, USA
[26]INFN, Laboratori Nazionali del Gran Sasso, I-67010 Assergi, AQ, Italy
[27]Univ. Federal de Goias, Goiania, Goias, Brazil
[28]Harish-Chandra Research Institute, Jhunsi, Allahabad 211 019, India
[29]Univ. of Hawaii, Honolulu, HI 96822-2219, USA
[30]Univ. of Houston, Houston, TX 77204, USA
[31]Indian Institute of Technology Guwahati, Guwahati, 781 039, India
[32]Indiana University, Bloomington, IN 47405-7105, USA
[33]Iowa State University, Ames, IO 50011, USA
[34]Kavli IPMU, Univ. of Tokyo, Kashiwa Shi, Chiba 277-8568, Japan
[35]Kansas State University, Manhattan, KS 66506, USA
[36]Laboratori Nazionali del Gran Sasso, I-67010 Assergi, AQ, Italy
[37]Lancaster University, Bailrigg, Lancaster LA1 4YB, UK
[38]Lawrence Berkeley National Lab., Berkeley, CA 94720-8153, USA
[39]Lawrence Livermore National Lab., Livermore, CA 94551, USA
[40]Univ. of Liverpool, L69 7ZE, Liverpool, UK
[41]Los Alamos National Laboratory, Los Alamos, NM 87545, USA
[42]Louisiana State University, Baton Rouge, LA 70803-4001, USA
[43]Univ. of Manchester, Oxford Road, Manchester M13 9PL, UK
[44]Univ. of Maryland, College Park, MD 20742-4111, USA

[45]Massachusetts Institute of Technology, Cambridge, MA 02139-4307, USA
[46]Michigan State University, East Lansing, MI 48824, USA
[47]Univ. di Milano, INFN Sezione di Milano, I-20133 Milano, Italy
[48]Univ. of Milano and INFN Sezione di Milano Bicocca, Piazza della Scienza 3, 20126 Milano, Italy
[49]Univ. of Minnesota, Minneapolis, MN 55455, USA
[50]Univ. of Minnesota (Duluth), Duluth, MN 55812, USA
[51]Univ. di Napoli, Complesso Universitario di Monte S. Angelo, I-80126 Napoli, Italy
[52]National Geospatial-Intelligence Agency, Reston, VA 20191, USA
[53]Northwestern University, Evanston, Il 60208, USA
[54]Univ. of Notre Dame, Notre Dame, IN 46556-5670, USA
[55]Univ. of Oxford, Oxford, OX1 3RH, UK
[56]Univ. of Padova, Dip. Fisica e Astronomia G. Galilei and INFN Sezione di Padova, I-35131 Padova, Italy
[57]Panjab University, Chandigarh, 160014 U.T., India
[58]Univ. of Pavia, INFN Sezione di Pavia, I-27100 Pavia, Italy
[59]Univ. of Pennsylvania, Philadelphia, PA 19104-6396, USA
[60]Univ. of Pittsburgh, Pittsburgh, PA 15260, USA
[61]Princeton University, Princeton, New Jersey 08544-0708, USA
[62]Rensselaer Polytechnic Inst., Troy, NY 12180-3590, USA
[63]Univ. of Rochester, Rochester, NY 14627-0171, USA
[64]SLAC National Acceleratory Laboratory, Menlo Park, CA 94025, USA
[65]STFC Rutherford Appleton Laboratory, Harwell Oxford, Didcot OX11 0QX, UK
[66]Univ. of Sheffield, Sheffield, S3 7RH, UK
[67]Univ. of South Carolina, Columbia, SC 29208, USA
[68]Univ. of South Dakota, Vermillion, SD 57069, USA
[69]South Dakota School of Mines and Technology, Lead, SD 57754, USA
[70]South Dakota Science And Technology Authority, Lead, SD 57754, USA
[71]South Dakota State University, Brookings, SD 57007, USA
[72]Southern Methodist University, Dallas, TX 75275, USA
[73]Univ. of Sussex, Brighton, BN1 9RH, UK
[74]Syracuse University, Syracuse, NY 13244-1130, USA
[75]Univ. of Tennessee, Knoxville, TN, USA
[76]Univ. of Texas (Arlington), Arlington, TX 76019, USA
[77]Univ. of Texas (Austin), Austin, TX 78712-0264, USA
[78]Tufts University, Medford, MA 02155, USA
[79]University College London, London, WC1E 6BT, UK
[80]Virginia Tech., Blacksburg, VA 24061-0435, USA
[81]Univ. of Warwick, Coventry CV4 7AL, UK
[82]Univ. of Washington, Seattle, WA 98195-1560, USA
[83]College of William and Mary, Williamsburg, VA 23187-8795, USA

[84]Univ. of Wisconsin, Madison, WI 53706, USA
[85]Yale University, New Haven, CT 06520, USA

Abstract

The preponderance of matter over antimatter in the early Universe, the dynamics of the supernova bursts that produced the heavy elements necessary for life and whether protons eventually decay — these mysteries at the forefront of particle physics and astrophysics are key to understanding the early evolution of our Universe, its current state and its eventual fate. The Long-Baseline Neutrino Experiment (LBNE) represents an extensively developed plan for a world-class experiment dedicated to addressing these questions.

Experiments carried out over the past half century have revealed that neutrinos are found in three states, or *flavors*, and can transform from one flavor into another. These results indicate that each neutrino flavor state is a mixture of three different nonzero mass states, and to date offer the most compelling evidence for physics beyond the Standard Model. In a single experiment, LBNE will enable a broad exploration of the three-flavor model of neutrino physics with unprecedented detail. Chief among its potential discoveries is that of matter-antimatter asymmetries (through the mechanism of charge-parity violation) in neutrino flavor mixing — a step toward unraveling the mystery of matter generation in the early Universe. Independently, determination of the unknown neutrino mass ordering and precise measurement of neutrino mixing parameters by LBNE may reveal new fundamental symmetries of Nature.

Grand Unified Theories, which attempt to describe the unification of the known forces, predict rates for proton decay that cover a range directly accessible with the next generation of large underground detectors such as LBNE's. The experiment's sensitivity to key proton decay channels will offer unique opportunities for the ground-breaking discovery of this phenomenon.

Neutrinos emitted in the first few seconds of a core-collapse supernova carry with them the potential for great insight into the evolution of the Universe. LBNE's capability to collect and analyze this high-statistics neutrino signal from a supernova within our galaxy would provide a rare opportunity to peer inside a newly-formed neutron star and potentially witness the birth of a black hole.

To achieve its goals, LBNE is conceived around three central components: (1) a new, high-intensity neutrino source generated from a megawatt-class proton accelerator at Fermi National Accelerator Laboratory, (2) a fine-grained near neutrino detector installed just downstream of the source, and (3) a massive liquid argon time-projection chamber deployed as a far detector deep underground at the Sanford Underground Research Facility. This facility, located at the site of the former Homestake Mine in Lead, South Dakota, is $\sim$1,300 km from the neutrino source at Fermilab — a distance (baseline) that delivers optimal sensitivity to neutrino charge-parity symmetry violation and mass ordering effects. This ambitious yet cost-effective design incorporates scalability and flexibility and can accommodate a variety of upgrades and contributions.

With its exceptional combination of experimental configuration, technical capabilities, and potential for transformative discoveries, LBNE promises to be a vital facility for the field of particle physics worldwide, providing physicists from institutions around the globe with opportunities to collaborate in a twenty to thirty year program of exciting science.

Contents

List of Figures

List of Tables

How to Read this Document

The LBNE science document is intended to inform a diverse readership about the goals and capabilities of the LBNE experiment. Your approach to reading this document will depend upon your purpose as well as your level of knowledge about high energy and neutrino physics.

The colored boxes distributed throughout the document highlight the important take-away points. They are integral to the document, but to the extent possible, are written in language accessible to the nonscientist.

The three chapters Chapter 1 *Introduction and Executive Summary*, Chapter 3 *Project and Design* and Chapter 9 *Summary and Conclusion* together provide a comprehensive overview of LBNE's scientific objectives, its place in the landscape of neutrino physics experiments worldwide, the technologies it will incorporate and the capabilities it will possess. Much of the information in these chapters is accessible to the lay reader, but of course, the scientific concepts, goals and methods around which LBNE is designed are by their nature highly specialized, and the text in certain sections is correspondingly technical.

In Chapter 2 *The Science of LBNE*, the initial paragraphs in each section provide some introductory information, but in general this chapter assumes a working knowledge of high energy physics and, ideally, familiarity with neutrino physics.

The three chapters that delve into the areas corresponding to the scientific objectives of LBNE: Chapter 4 *Neutrino Mixing, Mass Hierarchy and CP Violation*, Chapter 5 *Nucleon Decay Motivated by Grand Unified Theories* and Chapter 6 *Core-Collapse Supernova Neutrinos*, assume a working knowledge of high energy physics and particle astrophysics. This is also true of Chapter 7 *Precision Measurements with a High-Intensity Neutrino Beam* and Chapter 8 *Additional Far Detector Physics Opportunities*, as well as the appendices.

Chapter 1 Introduction and Executive Summary

The Long-Baseline Neutrino Experiment (LBNE) will provide a unique, world-leading program for the exploration of key questions at the forefront of particle physics and astrophysics.

Chief among its potential discoveries is that of matter-antimatter symmetry violation in neutrino flavor mixing — a step toward unraveling the mystery of matter generation in the early Universe. Independently, determination of the neutrino mass ordering and precise measurement of neutrino mixing parameters by LBNE may reveal new fundamental symmetries of Nature.

To achieve its ambitious physics objectives as a world-class facility, LBNE has been conceived around three central components:

1. an intense, wide-band neutrino beam
2. a fine-grained *near* neutrino detector just downstream of the neutrino source
3. a massive liquid argon time-projection chamber (LArTPC) deployed as a *far* neutrino detector deep underground, 1,300 km downstream; this distance between the neutrino source and far detector — the *baseline* — is measured along the line of travel through the Earth

The neutrino beam and near detector will be installed at the Fermi National Accelerator Laboratory (Fermilab), in Batavia, Illinois. The far detector will be installed at the Sanford Underground Research Facility in Lead, South Dakota.

The location of its massive high-resolution far detector deep underground will enable LBNE to significantly expand the search for proton decay as predicted by Grand Unified Theories, as well as study the dynamics of core-collapse supernovae through observation of their neutrino bursts, should any occur in our galaxy during LBNE's operating lifetime.

The near neutrino detector will enable high-precision measurements of neutrino oscillations, thereby enhancing the sensitivity to matter-antimatter symmetry violations and will exploit the potential of high-intensity neutrino beams as probes of new physics.

With its extensively developed design and flexible configuration, LBNE provides a blueprint for an experimental program made even more relevant by recent neutrino mixing parameter measurements.

1.1 Overview

Although neutrinos are the most abundant of known matter particles (fermions) in the Universe, their properties are the least well understood. The very existence of neutrino mass constitutes evidence of physics beyond the Standard Model. Understanding the nature of neutrinos has consequently become an essential goal for particle physics.

Observations of oscillations of neutrinos from one type (flavor) to another in numerous recent experiments have provided evidence for neutrino flavor mixing and for small, but nonzero, neutrino masses. The framework characterizing these observations is similar to that describing corresponding phenomena in the quark sector, but with a very different pattern of mixing angle values. As in the quark case, this framework involves a phase parameter, $\delta_{\rm CP}$, that changes sign under combined charge conjugation and parity (CP) reversal operations and thus would lead to CP symmetry-violating asymmetries between the pattern of oscillations for neutrinos and antineutrinos. While groundbreaking on its own, the observation of such asymmetries would also provide an experimental underpinning for the basic idea of leptogenesis* as an explanation for the Baryon Asymmetry of the Universe (BAU).

Neutrino oscillation data so far tell us about differences in the squared masses of the neutrino mass states, and about the sign of the mass-squared difference between two of the states, but not about the difference of those with respect to the third, which may be heavier (*normal* ordering) or lighter (*inverted* ordering) than the other two. Resolving this neutrino mass hierarchy ambiguity, along with precise measurements of neutrino mixing angles, would have significant theoretical, cosmological and experimental implications. One important consequence of mass hierarchy determination, in particular, would be the impact on future experiments designed to determine whether — uniquely among the fundamental fermions — neutrinos are their own antiparticles, so-called *Majorana* particles. Though long suspected, this hypothesis that neutrinos are Majorana particles has yet to be either established or ruled out. Strong evidence for the *inverted* hierarchy would establish conditions required by the next generation of neutrinoless double-beta decay searches to settle this question even with a null result (no observation). Because the forward scattering of neutrinos in matter alters the oscillation pattern in a hierarchy-dependent way, the long baseline of LBNE — with the neutrinos traveling through the Earth's mantle — enables a decisive determination of the hierarchy, independent of the value of $\delta_{\rm CP}$.

Additionally, the high-precision determination of oscillation parameters such as mixing angles and squared-mass differences will provide insight into the differences between the quark and lepton mixing patterns, which is necessary for deciphering the flavor structure of physics in the Standard Model. Taken together, the above suite of measurements will thoroughly test the standard three-neutrino flavor paradigm that guides our current understanding, and will provide greatly extended

*Leptogenesis refers to the mechanisms that generated an asymmetry between leptons and antileptons in the early Universe, described in Section 2.2.1.

sensitivity to signatures for nonstandard neutrino interactions in matter.

The arena of non-accelerator physics using massive underground detectors such as the LBNE far detector is also ripe with discovery potential. The observation of nucleon decay would be a watershed event for the understanding of physics at high energy scales. Neutrinos from supernovae are expected to provide key insights into the physics of gravitational collapse, and may also reveal fundamental properties of the neutrino.

Among massive detectors designed for neutrino and nucleon decay physics, the LArTPC technology offers unmatched capabilities for position and energy resolution and for high-precision reconstruction of complex interaction topologies over a broad energy range. It also provides a compact, scalable approach for achieving the required sensitivity to the primary physics signatures to be explored by LBNE. As these capabilities are also important for non-accelerator neutrino physics, LBNE will complement the large, underground water Cherenkov and/or scintillator-based detectors that may be operating in parallel. LArTPC detectors are especially well-suited to proton decay modes such as the supersymmetry-favored $p \rightarrow K^{+}\overline{\nu}$ mode, uniquely providing detection efficiency and background rejection sufficient to enable a discovery with a single well-reconstructed event. With regard to supernova-neutrino detection, liquid argon detectors are primarily sensitive to the ν_e component of the flux, while $\overline{\nu}_e$ interactions dominate for water and scintillator-based detectors. Thus, LBNE will be sensitive to different features of the supernova-neutrino production process. Finally, the LArTPC technology opens up an avenue for precision studies of oscillation physics with atmospheric neutrinos, thereby augmenting the results of the beam-based measurements at the core of the experiment.

The highly capable near detector will measure the absolute flux and energy scales of all four neutrino species in the LBNE beam, as well as neutrino cross sections on argon, water, and other nuclear targets in the beam's energy range. These measurements are needed to attain the ultimately desired precision of the oscillation parameter measurements. Additionally, the near detector will enable a broad range of precision neutrino-interaction measurements, thereby adding a compelling scientific program of its own.

The unique combination in LBNE of a 1,300-km baseline, exceptional resolution, large target mass and deep underground location offers opportunity for discovery of entirely unanticipated phenomena. History shows that ambitious scientific endeavors with leading-edge instruments have often been rewarded with unexpected signatures of new physics.

LBNE is an extensively developed experiment whose execution will have substantial impact on the overall direction of high energy physics (HEP) in the U.S. The U.S. Department of Energy (DOE) has endorsed the science objectives of LBNE, envisioning the experiment as a phased program, and has given first stage (CD-1) approval with a budget of $867M toward the initial phase. The science scope of this and subsequent phases will depend on the level of investment by additional national and international partners.

This document outlines the LBNE physics program and how it may evolve in the context of long-term planning studies [1]. The physics reach of this program is summarized under scenarios that are consistent with short-, medium- and long-term considerations. The general conclusions regarding the scientific capabilities of LBNE in a phased program are twofold:

1. A full-scope LBNE will provide an exciting broad-based physics program with exceptional capabilities for all of the identified core physics objectives, and many additional ones.

2. A first phase with a LArTPC far detector of fiducial[†] mass 10 kt[‡] or greater will substantially advance the field of neutrino oscillation physics while laying the foundations for a broader physics program in a later phase.

Section 1.2 provides the context for development of LBNE as a phased program that maintains flexibility for enhancements in each of its stages through the contributions of additional partners. The physics reach of LBNE at various stages is summarized in Section 1.3.

[†]In neutrino experiments, not all neutrino interactions in the instrumented (active) volume of a detector are used for physics studies. Only interactions that are well contained within the instrumented volume are used. The smaller volume of detector that encompasses the neutrino interactions is known as the *fiducial volume* and the target mass contained within it is known as the *fiducial mass*. Unless otherwise noted, this document will use fiducial mass to characterize the far detector size.

[‡]The *kt* refers to a metric kiloton. A metric ton is equivalent to 1,000 kg.

1.2 Development of a World-Class Experiment

To achieve the transformative physics goals of LBNE in an era of highly constrained funding for basic research in the U.S., the conceptual design has evolved so as to provide a scalable, phased and global approach, while maintaining a U.S. leadership role as the host for a global facility. International partnerships are being actively pursued to both enhance and accelerate the LBNE Project.

LBNE's primary beamline is designed to operate initially with a beam power of 1.2 MW, upgradable to 2.3 MW. This beamline extracts protons with energies from 60 to 120 GeV from the Fermilab Main Injector. The protons collide with a target to generate a secondary beam of charged particles, which in turn decay to generate the neutrino beam.

The liquid argon TPC far detector technology combines fine-grained tracking with total absorption calorimetry. Installed 4,850 ft underground to minimize backgrounds, this detector will be a powerful tool for long-baseline neutrino oscillation physics and underground physics such as proton decay, supernova neutrinos and atmospheric neutrinos. The far detector design is scalable and flexible, allowing for a phased approach, with an initial fiducial mass of at least 10 kt and a final configuration of at least 34 kt.

A high-precision near detector is planned as a separate facility allowing maximal flexibility in phasing and deployment.

The concept of a high-intensity neutrino beam directed toward a distant, massive underground detector to simultaneously investigate the nature of the neutrino, proton decay and astrophysical sources of neutrinos has been under serious investigation since the late 1990s [2,3,4,5,6,7,8,9]. Since that time both the science goals and concepts for implementation have been the subject of intense study and review by distinguished panels. These panels include the National Academies Neutrino Facilities Assessment Committee in 2003 [10], the National Science and Technology Council Committee on Science in 2004 [11], the National Academies EPP2010 panel in 2006 [12], the HEPAP/NSAC Neutrino Scientific Assessment Group in 2007 [13], the HEPAP Particle Physics Project Prioritization Panel (P5) in 2008 [14], the National Academies ad hoc Committee to Assess the Science Proposed for DUSEL in 2011 [15], and most recently the HEPAP Facilities Subpanel in 2013 [16]. High-level studies performed in Europe and Asia have come to similar conclusions (e.g., [17]) about the merits and feasibility of such a program.

1.2.1 Long-Term Vision

LBNE as described in this document has been developed by a collaboration formally established in 2009, which currently comprises over 475 collaborators from over 80 institutions in six countries. In January 2010 the DOE formally recognized the LBNE science objectives with approval of the mission need statement (CD-0) [18]. This action established LBNE as a DOE project. Fermilab has recognized LBNE as a central component of its long-term future program.

The central role of LBNE within the U.S. particle physics program has been acknowledged in other documents prepared for the 2013 particle physics community planning exercise [1], including the Project X Physics Book [19] and the reports from Intensity Frontier working groups on neutrino physics [20] and baryon number violation [21].

The LBNE conceptual design reflects a flexible and cost-effective approach to next-generation neutrino physics experiments that maintains a world-leadership role for the U.S. over the long term. The full-scope LBNE includes a 34-kt fiducial mass (50-kt total) far detector located in a new experimental area to be excavated at the 4,850-ft level of the Sanford Underground Research Facility[§] in the former Homestake Mine, and a fine-grained near neutrino detector located on the Fermilab site. Simultaneous construction of a new neutrino beamline at Fermilab would permit operation with an initial beam power of 1.2 MW, enabled by upgrades to the front end of the accelerator complex carried out within the Proton Improvement Plan-II (PIP-II) program [22]. In anticipation of potential enhancements beyond PIP-II [23], the beamline is designed to support upgrades to accommodate a beam power of 2.3 MW. The 1,300-km baseline is in the optimal range for the neutrino oscillation program. The cosmic ray shielding provided by the deep underground site for the far detector enables the non-accelerator portion of the physics program, including proton decay searches, detailed studies of neutrino bursts from galactic supernovae, and precision analyses of atmospheric-neutrino samples.

The overall physics reach of LBNE is predominantly limited by detector mass. From the outset, a guiding principle of the far detector design has been scalability. The conceptual design for the full-scope detector, consisting of two identical 17-kt (25-kt total) TPC modules housed within separate vessels (cryostats), employs technology developed by the liquefied natural gas (LNG) storage and transport industry. The TPC modules themselves consist of arrays of modular anode and cathode plane assemblies (APAs and CPAs) that are suspended from rails affixed to the top of the cryostats. The APA/CPA dimensions are chosen for ease of transportation and installation. The modularity of the detectors allows flexibility in the geometry and phased construction of the LBNE far detector complex. Cost-effective designs for larger detector masses are readily obtained by increasing the vessel size and simply adding APA/CPA units, thereby also exploiting economies of scale and benefiting from an increased ratio of volume to surface area. Detector mass may also be increased through the addition of distinct detectors of the same or a different technology, either during initial

[§]Much larger detectors could also be accommodated at this facility.

construction or in a later phase.

1.2.2 Present Status of the LBNE Project

Since DOE CD-0 approval, a compete conceptual design for the full-scope LBNE has been developed, consisting of a 34-kt LArTPC far detector located 4,850 feet underground, a 1,300-km baseline, a highly capable near neutrino detector, and a multi-megawatt-capable neutrino beamline. This design has been thoroughly reviewed, and found to be sound, most recently at a Fermilab Director's CD-1 Readiness Review in March 2012 [24]. Since then, considerable effort has been devoted to understanding how the LBNE Project can be staged so as to accommodate anticipated budget conditions while maintaining compelling physics output at each stage [25]. This process led to a first-phase configuration that was reviewed by the DOE in October [26] and November 2012 [27], and that received CD-1 approval [28] in December 2012. This configuration [29,30,31,32,33,34] maintained the most important aspects of LBNE: the 1,300-km baseline to the Sanford Underground Research Facility, a large — of order tens of kilotons in fiducial mass — LArTPC far detector design, and a multi-megawatt-capable, wide-band neutrino/antineutrino beam. However, the far detector size was limited at CD-1 to 10 kt and placed at the surface under minimal overburden, and the near detector was deferred to a later phase.

The DOE CD-1 approval document [28] explicitly allows adjustment of the scope of the first phase of LBNE in advance of CD-2 if additional partners bring significant contributions to LBNE. *Using the CD-1 DOE funding as the foundation, the goal for the first phase of LBNE is a deep underground far detector of at least 10 kt, placed in a cavern that will accommodate up to a 34-kt detector, coupled with a 1.2-MW neutrino beamline, and a highly capable near detector.* This goal has been endorsed by the LBNE Collaboration, the LBNE Project, the Fermilab directorate, and the DOE Office of High Energy Physics. Since a large portion of the LBNE Project cost is in civil infrastructure, funding contributions from new partners could have considerable impact on the experimental facilities, and therefore the physics scope, in the first phase.

1.2.3 Global Partnerships

Global conditions are favorable for significant international partnerships in developing and building LBNE. As an example, the 2013 update [17] of the European Strategy for Particle Physics document places long-baseline neutrino physics among the highest-priority large-scale activities for Europe, recognizing that it requires "significant resources, sizeable collaborations and sustained commitment." It includes the primary recommendation of exploring "the possibility of major participation in leading long-baseline neutrino projects in the U.S. and Japan." As of March 2014 the LBNE Collaboration includes institutions from the U.S., Brazil, India, Italy, Japan and the United Kingdom. Discussions with a number of potential international partners are underway — some already at an advanced stage. A summary of recent progress in these discussions can be found in the

presentation of LBNE status to the U.S. Particle Physics Projects Prioritization Panel in November 2013 [35].

1.2.4 Context for Discussion of Physics Sensitivities

To reflect the physics reach of various phasing scenarios, this document presents many of the parameter sensitivities for the accelerator-based neutrino topics as functions of exposure, defined as the product of detector fiducial mass, beam power and run time. As needed, the capabilities of both a 10-kt first-phase configuration and the full 34-kt configuration are explicitly highlighted, each benchmarked for six to ten years of operations with a 1.2-MW beam power from the PIP-II accelerator upgrades at Fermilab. Since the U.S. program planning exercises currently under way look beyond the present decade, this document also presents the long-term physics impact of the full-scope LBNE operating with the 2.3-MW beam power available with further anticipated upgrades to the Fermilab accelerator complex.

1.3 The LBNE Physics Program

The technologies and configuration of the planned LBNE facilities offer excellent sensitivity to a range of physics processes:

- The muon-neutrino (ν_μ) beam produced at Fermilab with a peak flux at 2.5 GeV, coupled to the baseline of 1,300 km, will present near-optimal sensitivity to neutrino/antineutrino charge-parity (CP) symmetry violation effects.
- The long baseline of LBNE will ensure a large matter-induced asymmetry in the oscillations of neutrinos and antineutrinos, thus providing a clear, unambiguous determination of the mass ordering of the neutrino states.
- The near detector located just downstream of the neutrino beamline at Fermilab will enable high-precision long-baseline oscillation measurements as well as precise measurements and searches for new phenomena on its own using the high-intensity neutrino beam.
- The deep-underground LArTPC far detector will provide superior sensitivities to proton decay modes with kaons in the final states, modes that are favored by many Grand Unified and supersymmetric theoretical models.
- Liquid argon as a target material will provide unique sensitivity to the electron-neutrino (ν_e) component of the initial burst of neutrinos from a core-collapse supernova.
- The excellent energy and directional resolution of the LArTPC will allow novel physics studies with atmospheric neutrinos.

This section summarizes LBNE's potential for achieving its core physics objectives based on the current experimental landscape, scenarios for staging LBNE, and the technical capabilities of LBNE at each stage.

LBNE's capability to achieve the physics objectives described in this document has been subject to extensive review over a number of years. In addition to the various reviews of the LBNE Project described in Section 1.2, reviews that focused strongly on LBNE's science program include the DOE Office of Science Independent Review of Options for Underground Science in the spring of 2011 [36], the LBNE Science Capabilities Review (by an external panel commissioned by LBNE) [37] in the fall of 2011, and the LBNE Reconfiguration Review [25] in the summer of 2012.

1.3.1 Neutrino Mixing, Mass Hierarchy and CP Violation

Neutrino Mass Hierarchy: The 1,300-km baseline establishes one of LBNE's key strengths: sensitivity to the matter effect. This effect leads to a large discrete asymmetry in the $\nu_\mu \rightarrow \nu_e$ versus $\overline{\nu}_\mu \rightarrow \overline{\nu}_e$ oscillation probabilities, the sign of which depends on the mass hierarchy (MH). At 1,300 km this asymmetry is approximately $\pm 40\%$ in the region of the peak flux; this is larger than the maximal possible CP-violating asymmetry associated with $\delta_{\rm CP}$, meaning that both the MH and $\delta_{\rm CP}$ can be determined unambiguously with high confidence within the same experiment using the beam neutrinos.

In detail, the sensitivity of LBNE depends on the actual values of poorly known mixing parameters (mainly $\delta_{\rm CP}$ and $\sin^2\theta_{23}$), as well as the true value of the MH itself. The discrimination between the two MH hypotheses is characterized as a function of the *a priori* unknown true value of $\delta_{\rm CP}$ by considering the difference, denoted $\Delta\chi^2$, between the $-2\log\mathcal{L}$ values calculated for a data set with respect to these hypotheses, considering all possible values of $\delta_{\rm CP}$[¶]. In terms of this test statistic, the MH sensitivity of LBNE with 34 kt, and running three years each in ν and $\overline{\nu}$ modes in a 1.2-MW beam is illustrated in Figure 1.1 for the case of normal hierarchy for two different values of $\sin^2\theta_{23}$. Across the overwhelming majority of the parameter space for the mixing parameters that are not well known (mainly $\delta_{\rm CP}$ and $\sin^2\theta_{23}$), LBNE's determination of the MH will be definitive, but even for unfavorable combinations of the parameter values, a statistically ambiguous outcome is highly unlikely.

The least favorable scenario corresponds to a true value of $\delta_{\rm CP}$ in which the MH asymmetry is maximally offset by the leptonic CP asymmetry, and where, independently, $\sin^2\theta_{23}$ takes on a value at the low end of its experimentally allowed range. For this scenario, studies indicate that with a 34-kt LArTPC operating for six years in a 1.2-MW beam, LBNE on its own can (in a typical data set) distinguish between normal and inverted hierarchy with $|\Delta\chi^2| = \overline{|\Delta\chi^2|} = 25$. This corresponds to a $\geq 99.9996\%$ probability of determining the correct hierarchy. In $> 97.5\%$ of data sets, LBNE will measure $|\Delta\chi^2| > 9$ in this scenario, where measuring $|\Delta\chi^2| = 9$ with an expected value of 25 corresponds to a significance in excess of three Gaussian standard deviations.

Concurrent analysis of the corresponding atmospheric-neutrino samples in an underground detector will improve the precision with which the MH is resolved. It is important to note that for the initial stages of LBNE, a greatly improved level of precision in the determination of the MH can be achieved by incorporating constraints from NOνA and T2K data. With an initial 10-kt detector, for half the range of possible $\delta_{\rm CP}$ values, the expected significance exceeds $\overline{\Delta\chi^2} = 25$; again this corresponds to a $\geq 99.9996\%$ probability of determining the correct hierarchy. To put this in context, it is notable that even an extended NOνA program [38] at four times its nominal exposure

[¶]For the case of the MH determination, the usual association of this test statistic with a χ^2 distribution for one degree of freedom is incorrect; additionally the assumption of a Gaussian probability density implicit in this notation is not exact. The discussion in Chapter 4 provides a brief description of the statistical considerations.

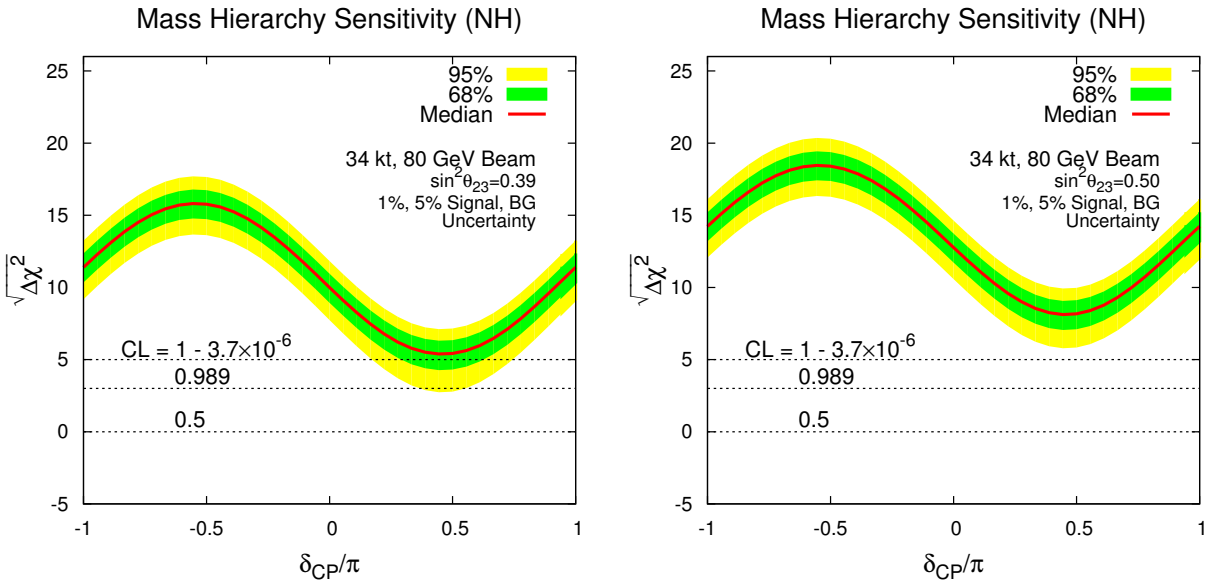

Figure 1.1: The square root of the mass hierarchy discrimination metric $\Delta\chi^2$ is plotted as a function of the unknown value of $\delta_{\rm CP}$ for the full-scope LBNE with 34 kt, 3+3 ($\nu + \overline{\nu}$) years of running in a 1.2-MW beam, assuming normal hierarchy. The plot on the left is for an assumed value of $\sin^2\theta_{23} = 0.39$ (based on global fits and assuming worst-case θ_{23} octant), while that on the right is for $\sin^2\theta_{23} = 0.5$ (maximal mixing). In each plot, the red curve represents the median experimental value expected ($\sqrt{\overline{\Delta\chi^2}}$), estimated using a data set absent statistical fluctuations, while the green and yellow bands represent the range of $\Delta\chi^2$ values expected in 68% and 95% of all possible experimental instances, respectively. For certain values of $\sqrt{\Delta\chi^2}$, horizontal lines are shown, indicating the corresponding confidence levels ($1-\alpha$ in the language of hypothesis testing) with which a typical experiment ($\beta = 0.5$) correctly determines the MH, computed according to a Bayesian statistical formulation (Section 4.3.1 for further discussion).

(of six years of operation at 700 kW), would have coverage at the $\overline{\Delta\chi^2} = 9$ level or better for only 40% of the $\delta_{\rm CP}$ range.

CP Violation and the Measurement of $\delta_{\rm CP}$: The LBNE program has two somewhat distinct objectives with regard to CP symmetry violation in the $\nu_\mu \to \nu_e$ oscillation channel. First, LBNE aims to make a precise determination of the value of $\delta_{\rm CP}$ within the context of the standard three-flavor mixing scenario described by the PMNS matrix (discussed in Section 2.2). Second, and perhaps more significantly, LBNE aims to observe a signal for leptonic CP violation, independent of the underlying nature of neutrino oscillation phenomenology. Within the standard three-flavor mixing scenario, such a signal will be observable, provided $\delta_{\rm CP}$ is not too close to either of the values for which there is no CP violation (zero and π). Together, the pursuit of these two goals provides a thorough test of the standard three-flavor scenario.

Figure 1.2 shows the expected 1σ resolution for $\delta_{\rm CP}$ as a function of exposure for a proton beam power of 1.2 MW. At this beam power, in a six-year run, a 10-kt far detector will be able to measure $\delta_{\rm CP}$ to $\pm\, 20^\circ - 30^\circ$ (depending on its value), independent of other experiments. A full-scope LBNE

operating with multi-megawatt beam power in a later phase, will achieve a precision better than $\pm 10^{\circ}$, comparable to the current precision on the CP phase in the CKM matrix in the quark sector.

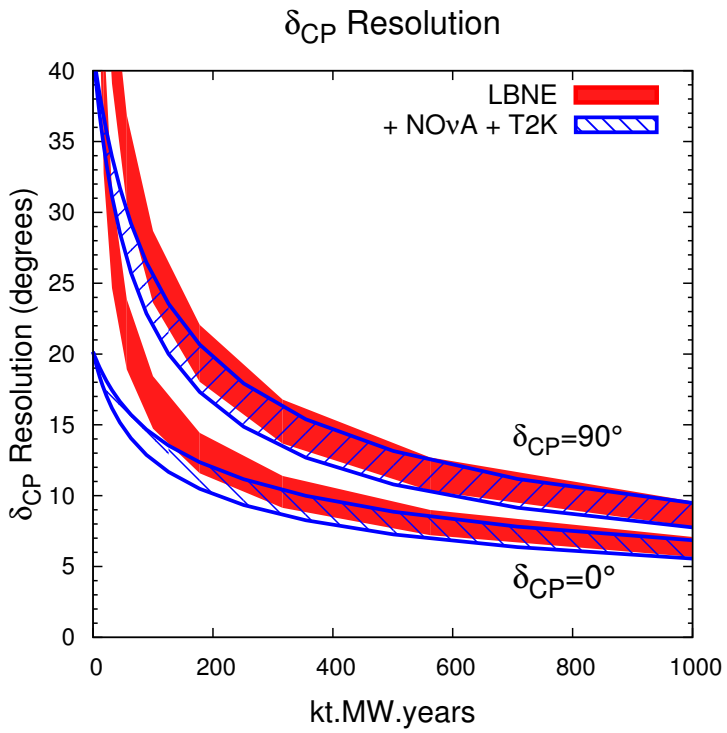

Figure 1.2: The expected 1σ resolution for $\delta_{\rm CP}$ as a function of exposure in detector mass (kiloton) $\times$ beam power (MW) $\times$ time (years). The red curve is the precision that could be obtained from LBNE alone, while the blue curve represents the combined precision from LBNE plus the T2K and NOνA experiments. The width of the bands represents variation with the range of beamline design parameters and proton energy values being considered.

LBNE with a 10-kt detector, in combination with T2K and NOνA, will determine leptonic CP violation with a precision of 3σ or greater for $\approx 40\%$ of $\delta_{\rm CP}$ values in a six-year run with 1.2-MW beam power. It is important to note that LBNE alone dominates the combined sensitivity and that T2K and NOνA have very limited sensitivity to CP violation on their own. To reach 5σ for an appreciable fraction of the range of $\delta_{\rm CP}$, the full-scope LBNE will be needed to control systematic errors while accumulating large enough samples in the far detector to reach this level of sensitivity. No experiment can provide coverage at 100%, since CP violation effects vanish as $\delta_{\rm CP} \to 0$ or π.

Determination of $\sin^2 2\theta_{23}$ and Octant Resolution: In long-baseline experiments with ν_μ beams, the magnitude of ν_μ disappearance and ν_e appearance signals is proportional to $\sin^2 2\theta_{23}$ and $\sin^2 \theta_{23}$, respectively, in the standard three-flavor mixing scenario. Current ν_μ disappearance data are consistent with maximal mixing, $\theta_{23} = 45^{\circ}$. To obtain the best sensitivity to both the magnitude of its deviation from 45° as well as its sign (θ_{23} octant), a combined analysis of the two channels is

needed [39]. As demonstrated in Chapter 4, a 10-kt LBNE detector will be able to resolve the θ_{23} octant at the 3σ level or better for θ_{23} values less than 40° or greater than 50°, provided $\delta_{\rm CP}$ is not too close to zero or π. A full-scope LBNE will measure θ_{23} with a precision of 1° or less, even for values within a few degrees of 45°.

1.3.2 Nucleon Decay Physics Motivated by Grand Unified Theories

The LBNE far detector will significantly extend lifetime sensitivity for specific nucleon decay modes by virtue of its high detection efficiency relative to water Cherenkov detectors and its low background rates. As an example, LBNE has enhanced capability for detecting the $p \rightarrow K^+\overline{\nu}$ channel, where lifetime predictions from supersymmetric models extend beyond, but remain close to, the current (preliminary) Super-Kamiokande limit of $\tau/B > 5.9 \times 10^{33}$ year (90% CL) from a 260-kt $\cdot$ year exposure [40][‖]. The signature for an isolated semi-monochromatic charged kaon in a LArTPC is distinctive, with multiple levels of redundancy. A 34-kt LBNE far detector deep underground will reach a limit of 3×10^{34} year after ten years of operation (Figure 1.3), and would see nine events with a background of 0.3 should τ/B be 1×10^{34} year, just beyond the current limit. Even a 10-kt detector (placed underground) would yield an intriguing signal of a few events after a ten-year exposure in this scenario.

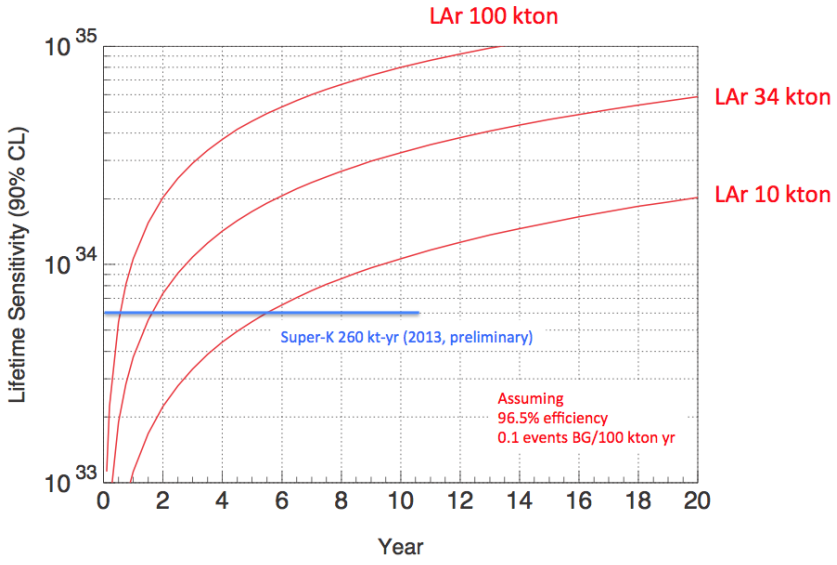

Figure 1.3: Sensitivity to the decay $p \rightarrow K^+\overline{\nu}$ as a function of time for underground liquid argon detectors with different masses.

[‖]The lifetime shown here is divided by the branching fraction for this decay mode, τ/B, and as such is a *partial lifetime*.

1.3.3 Supernova-Neutrino Physics and Astrophysics

The neutrinos from a core-collapse supernova are emitted in a burst of a few tens of seconds duration, with about half in the first second. Energies are in the range of a few tens of MeV, and the luminosity is divided roughly equally between the three known neutrino flavors. Currently, experiments worldwide are sensitive primarily to electron antineutrinos ($\overline{\nu}_e$), with detection through the inverse-beta decay process on free protons**, which dominates the interaction rate in water and liquid-scintillator detectors. Liquid argon has a unique sensitivity to the electron-neutrino (ν_e) component of the flux, via the absorption interaction on ^{40}Ar as follows:

$$\nu_e + {}^{40}\mathrm{Ar} \;\rightarrow\; e^- + {}^{40}\mathrm{K}^*$$

This interaction can be tagged via the coincidence of the emitted electron and the accompanying photon cascade from the ^{40}K* de-excitation. About 900 events would be expected in a 10-kt fiducial mass liquid argon detector for a supernova at a distance of 10 kpc. In the neutrino channel the oscillation features are in general more pronounced, since the ν_e spectrum is always significantly different from the ν_μ (ν_τ) spectra in the initial core-collapse stages, to a larger degree than is the case for the corresponding $\overline{\nu}_e$ spectrum. Detection of a large neutrino signal in LBNE would help provide critical information on key astrophysical phenomena such as

1. the neutronization burst
2. formation of a black hole
3. shock wave effects
4. shock instability oscillations
5. turbulence effects

1.3.4 Precision Measurements with a High-Intensity Neutrino Source and High-Resolution Near Detector

The near neutrino detector will provide precision measurements of neutrino interactions, which in the medium to long term are essential for controlling the systematic uncertainties in the long-baseline oscillation physics program. The near detector, which will include argon targets, will measure the absolute flux and energy-dependent shape of all four neutrino species, ν_μ, $\overline{\nu}_\mu$, ν_e and $\overline{\nu}_e$ to accurately predict for each species the far/near flux ratio as a function of energy. It will also measure the four-momenta of secondary hadrons, such as charged and neutral mesons, produced

**This refers to neutrino interactions with the nucleus of a hydrogen atom in H_2O in water detectors or in hydrocarbon chains in liquid scintillator detectors.

in the neutral and charged current interactions that constitute the dominant backgrounds to the oscillation signals.

With 240,000 (85,000) ν_μ ($\overline{\nu}_\mu$) charged current and 90,000 (35,000) neutral current interactions per ton per 1×10^{20} protons-on-target at 120 GeV in the ν ($\overline{\nu}$) beam, the near detector will also be the source of data for a rich program of neutrino-interaction physics in its own right. These numbers correspond to 10^7 neutrino interactions per year for the range of beam configurations and near detector designs under consideration. Measurement of fluxes, cross sections and particle production over a large energy range of 0.5 GeV to 50 GeV (which can also help constrain backgrounds to proton decay signals from atmospheric neutrinos) are the key elements of this program. Furthermore, since the near detector data will feature very large samples of events that are amenable to precision reconstruction and analysis, they can be exploited for sensitive studies of electroweak physics and nucleon structure, as well as for searches for new physics in unexplored regions (heavy sterile neutrinos, high-Δm^2 oscillations, light Dark Matter particles, and so on).

1.4 Summary

The LBNE physics program has been identified as a priority of the global HEP community for the coming decades. The facilities available in the U.S. are the best suited internationally to carry out this program and the substantially developed LBNE design is at the forefront of technical innovations in the field. Timely implementation of LBNE will significantly advance the global HEP program and assure continued intellectual leadership for the U.S. within this community.

This chapter has touched only briefly on the most prominent portion of the full suite of physics opportunities enabled by LBNE. The following chapters cover these in detail, as well as topics that were omitted here in the interest of brevity and focus. In Chapter 9 progress toward LBNE physics milestones is addressed, based on one potential scenario for the operation of successive stages of LBNE detector and PIP-II implementations, and the broad role of LBNE is discussed in the context of such scenarios. The present chapter concludes with a summary of its key points.

The primary science goals of LBNE are drivers for the advancement of particle physics. The questions being addressed are of wide-ranging consequence: the origin of flavor and the generation structure of the fermions (i.e., the existence of three families of quark and lepton flavors), the physical mechanism that provides the CP violation needed to generate the Baryon Asymmetry of the Universe, and the high energy physics that would lead to the instability of matter. Achieving these goals requires a dedicated, ambitious and long-term program. No other proposed long-baseline neutrino oscillation program with the scientific scope and sensitivity of LBNE is as advanced in terms of engineering development and project planning. A phased program with a far detector of

even modest size in the initial stage (e.g., 10 kt) will enable exciting physics in the intermediate term, including a definitive mass hierarchy determination and a measurement of the CP phase without ambiguities, while providing the fastest route toward achieving the full range of LBNE's science objectives. Should LBNE find that the CP phase is not zero or π, it will have found strong indications ($> 3\sigma$) of leptonic CP violation. Global interest is favorable for contributions from international partners to accelerate and enhance this program, including the LBNE first-phase scope.

Implementing the vision that has brought LBNE to this point will allow the U.S. to host this world-leading program, bringing together the world's neutrino community to explore key questions at the forefront of particle physics and astrophysics. Moreover, the excitement generated by both the technical challenges of mounting LBNE and the potential physics payoffs are widely shared — among the generation of scientists who have been paving the way for these innovations, as well as the young scientists for whom LBNE will provide numerous research opportunities over the next two decades.

Chapter 2 The Science of LBNE

The Standard Model of particle physics describes all of the known fundamental particles and the electroweak and strong forces that, in combination with gravity, govern today's Universe. The observation that neutrinos have mass is one demonstration that the Standard Model is incomplete. By exploring physics beyond the Standard Model, LBNE will address fundamental questions about the Universe:

What is the origin of the matter-antimatter asymmetry in the Universe? Immediately after the Big Bang, matter and antimatter were created equally, yet matter now dominates. By studying the properties of neutrino and antineutrino oscillations, LBNE is pursuing the most promising avenue for understanding this asymmetry.

What are the fundamental underlying symmetries of the Universe? Resolution by LBNE of the detailed mixing patterns and ordering of neutrino mass states, and comparisons to the corresponding phenomena in the quark sector, could reveal underlying symmetries that are as yet unknown.

Is there a Grand Unified Theory of the Universe? Experimental evidence hints that the physical forces observed today were unified into one force at the birth of the Universe. Grand Unified Theories (GUTs), which attempt to describe the unification of forces, predict that protons should decay, a process that has never been observed. LBNE will probe proton lifetimes predicted by a wide range of GUT models.

How do supernovae explode? The heavy elements that are the key components of life — such as carbon — were created in the super-hot cores of collapsing stars. LBNE's design will enable it to detect the neutrino burst from core-collapse supernovae. By measuring the time structure and energy spectrum of a neutrino burst, LBNE will be able to elucidate critical information about the dynamics of this special astrophysical phenomenon.

What more can LBNE discover about the Standard Model? The high intensity of the LBNE neutrino beam will provide a unique probe for precision tests of Standard Model processes as well as searches for new physics in unexplored regions.

LBNE has been designed to address a wide range of scientific topics using well-characterized, high-intensity, accelerator-based neutrino beams, a long baseline for neutrino oscillations, and a very large, deep-underground detector with excellent particle identification capabilities over a large

range of energies. While maximizing the reach for a core set of scientific objectives, its design — described in Chapter 3 — accommodates the flexibility to extend the scope of measurements as additional resources become available.

2.1 Scientific Objectives of LBNE

The scientific objectives of LBNE have been categorized into primary, secondary, and additional secondary objectives according to priorities developed and agreed upon by the LBNE community and accepted as part of the CD-0 (Mission Need) approval by the U.S. Department of Energy [41].

Primary objectives of LBNE, in priority order, are the following measurements:

1. precision measurements of the parameters that govern $\nu_\mu \rightarrow \nu_e$ oscillations; this includes precision measurement of the third mixing angle θ_{13}, measurement of the charge-parity (CP) violating phase $\delta_{\rm CP}$, and determination of the neutrino mass ordering (the sign of $\Delta m^2_{31} = m^2_3 - m^2_1$), the so-called *mass hierarchy*

2. precision measurements of the mixing angle θ_{23}, including the determination of the octant in which this angle lies, and the value of the mass difference, $|\Delta m^2_{32}|$, in $\nu_\mu \rightarrow \nu_{e,\mu}$ oscillations

3. search for proton decay, yielding significant improvement in the current limits on the partial lifetime of the proton (τ/BR) in one or more important candidate decay modes, e.g., $p \rightarrow K^+\overline{\nu}$

4. detection and measurement of the neutrino flux from a core-collapse supernova within our galaxy, should one occur during the lifetime of LBNE

In a phased approach to LBNE, the goal of the first phase is to maximize the effectiveness of the facility to achieve the first two objectives, above. The mass hierarchy determination and the precision determination of θ_{23} will most likely be complete in the first phase of LBNE; while the precision determination of CP violation will require the full-scope LBNE, an initial measurement of the CP phase parameter $\delta_{\rm CP}$ will be performed in earlier phases.

Secondary objectives, which may also be enabled by the facility designed to achieve the primary objectives, include:

1. other accelerator-based, neutrino oscillation measurements; these could include further sensitivity to Beyond Standard Model (BSM) physics such as nonstandard interactions

2. measurements of neutrino oscillation phenomena using atmospheric neutrinos

3. measurement of other astrophysical phenomena using medium-energy neutrinos

Additional secondary objectives, the achievement of which may require upgrades to the facility that is designed to achieve the primary physics objectives (e.g., deployment of additional detector mass or alternate detector technologies), include:

1. detection and measurement of the diffuse supernova-neutrino flux
2. measurements of neutrino oscillation phenomena and of solar physics using solar neutrinos
3. measurements of astrophysical and geophysical neutrinos of low energy

In addition, a rich set of science objectives enabled by a sophisticated near neutrino detector have been identified. A primary and a secondary objective, respectively, are:

1. measurements necessary to achieve the primary physics research objectives listed above
2. studies of neutrino interactions that may be enabled either by the facility designed to achieve the primary objectives or by future upgrades to the facility and detectors; these include precision studies of the weak interaction, studies of nuclear and nucleon structure, and searches for new physics

2.2 Neutrino Three-Flavor Mixing, CP Violation and the Mass Hierarchy

The Standard Model of particle physics (Figure 2.1) presents a remarkably accurate description of the elementary particles and their interactions. However, its limitations beg deeper questions about Nature. The unexplained patterns of quarks, leptons, flavors and generations imply that a more fundamental underlying theory must exist. LBNE plans to pursue a detailed study of neutrino mixing, resolve the neutrino mass ordering, and search for CP violation in the lepton sector by studying the oscillation patterns of high-intensity ν_μ and $\overline{\nu}_\mu$ beams measured over a long baseline.

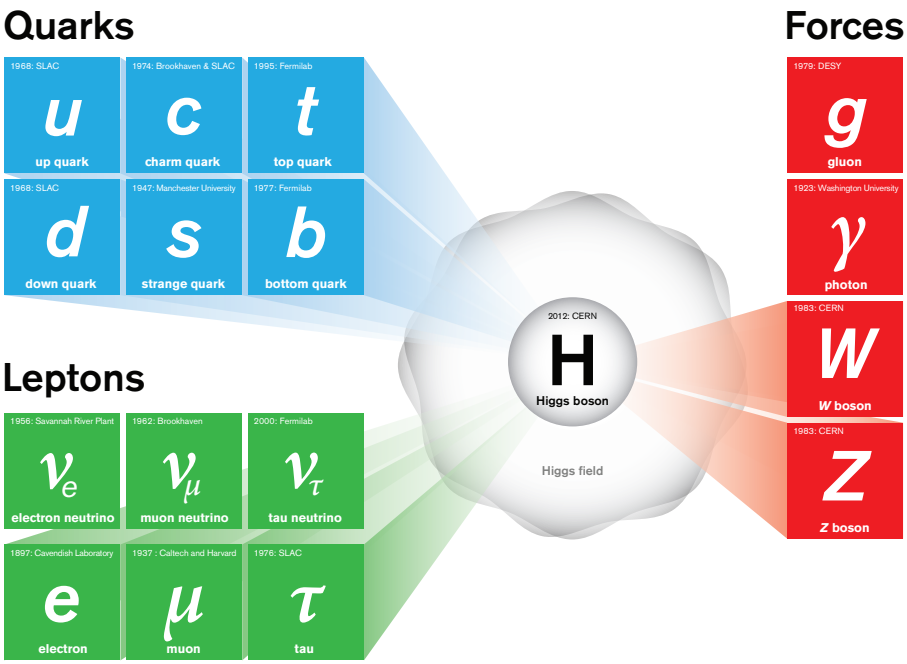

Figure 2.1: Known particles and forces in the Standard Model of particle physics. The quarks and leptons are arranged in pairs into three generations: $(u, d), (c, s), (t, b)$ and $(\nu_e, e), (\nu_\mu, \mu), (\nu_\tau, \tau)$, respectively. There are three known neutrino mass states ν_1, ν_2, ν_3 which are mixtures of the three neutrino flavors ν_e, ν_μ, ν_τ shown in this figure. The Standard Model includes the gluon (g), photon (γ) and $(W^\pm, Z^0)$ bosons that are the mediators of the strong, electromagnetic and weak interactions, respectively. The Higgs boson is a manifestation of the Higgs field that endows all the known particles with mass.

Results from the last decade, indicating that the three known types of neutrinos have nonzero mass, mix with one another and oscillate between generations, imply physics beyond the Standard Model [42]. Each of the three flavors of neutrinos, ν_e, ν_μ and ν_τ (Figure 2.1), is known to be a different mix of three mass eigenstates ν_1, ν_2 and ν_3 (Figure 2.2). In the Standard Model, the simple Higgs mechanism, which has now been confirmed by the observation of the Higgs boson [43,44], is responsible for both quark and lepton masses, mixing and charge-parity (CP) violation (the mechanism responsible for matter-antimatter asymmetries). However, the small size of neutrino masses and their relatively large mixing bears little resemblance to quark masses and mixing, suggesting that different physics — and possibly different mass scales — in the two sectors may be present, and motivating precision study of mixing and CP violation in the lepton sector.

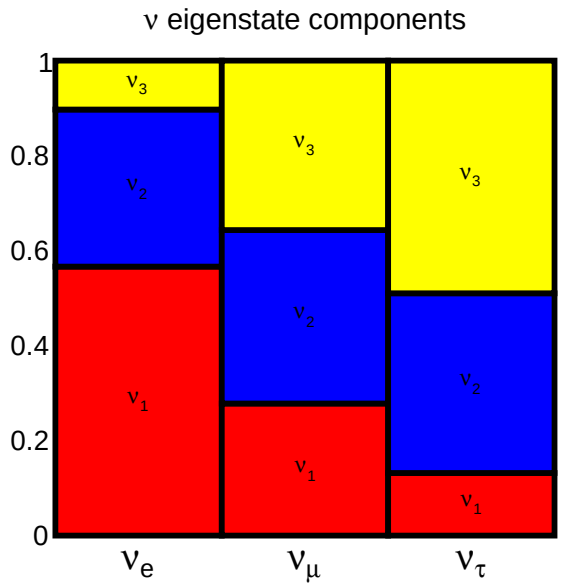

Figure 2.2: The neutrino mass eigenstate components of the known flavor eigenstates.

Neutrino oscillation arises from mixing between the flavor and mass eigenstates of neutrinos, corresponding to the weak and gravitational interactions, respectively. This three-flavor-mixing scenario can be described by a rotation between the weak-interaction eigenstate basis $(\nu_e,\ \nu_\mu,\ \nu_\tau)$ and the basis of states of definite mass $(\nu_1,\ \nu_2,\ \nu_3)$. In direct correspondence with mixing in the quark sector, the transformations between basis states is expressed in the form of a complex unitary matrix, known as the PMNS matrix :

$$\begin{pmatrix} \nu_e \\ \nu_\mu \\ \nu_\tau \end{pmatrix} = \underbrace{\begin{pmatrix} U_{e1} & U_{e2} & U_{e3} \\ U_{\mu 1} & U_{\mu 2} & U_{\mu 3} \\ U_{\tau 1} & U_{\tau 2} & U_{\tau 3} \end{pmatrix}}_{U_{\mathrm{PMNS}}} \begin{pmatrix} \nu_1 \\ \nu_2 \\ \nu_3 \end{pmatrix}. \tag{2.1}$$

The PMNS matrix in full generality depends on just three mixing angles and a CP-violating phase. The mixing angles and phase are designated as $(\theta_{12}, \theta_{23}, \theta_{13})$ and $\delta_{\rm CP}$. This matrix can be parameterized as the product of three two-flavor mixing matrices as follows, where $c_{\alpha\beta} = \cos\theta_{\alpha\beta}$ and $s_{\alpha\beta} = \sin\theta_{\alpha\beta}$:

$$U_{\rm PMNS} = \underbrace{\begin{pmatrix} 1 & 0 & 0 \\ 0 & c_{23} & s_{23} \\ 0 & -s_{23} & c_{23} \end{pmatrix}}_{\rm I} \underbrace{\begin{pmatrix} c_{13} & 0 & e^{i\delta_{\rm CP}} s_{13} \\ 0 & 1 & 0 \\ -e^{i\delta_{\rm CP}} s_{13} & 0 & c_{13} \end{pmatrix}}_{\rm II} \underbrace{\begin{pmatrix} c_{12} & s_{12} & 0 \\ -s_{12} & c_{12} & 0 \\ 0 & 0 & 1 \end{pmatrix}}_{\rm III} \tag{2.2}$$

The parameters of the PMNS matrix determine the probability amplitudes of the neutrino oscillation phenomena that arise from mixing.

The relationship between the three mixing angles θ_{12}, θ_{23}, and θ_{13} and the mixing between the neutrino flavor and mass states can be described as follows [45]:

$$\tan^2\theta_{12} \;:\; \frac{\text{amount of } \nu_{\rm e} \text{ in } \nu_2}{\text{amount of } \nu_{\rm e} \text{ in } \nu_1} \tag{2.3}$$

$$\tan^2\theta_{23} \;:\; \text{ratio of } \nu_\mu \text{ to } \nu_\tau \text{ in } \nu_3 \tag{2.4}$$

$$\sin^2\theta_{13} \;:\; \text{amount of } \nu_{\rm e} \text{ in } \nu_3 \tag{2.5}$$

The frequency of neutrino oscillation among the weak-interaction (flavor) eigenstates depends on the difference in the squares of the neutrino masses, $\Delta m^2_{ij} \equiv m^2_i - m^2_j$; a set of three neutrino mass states implies two independent mass-squared differences (Δm^2_{21} and Δm^2_{32}). The ordering of the mass states is known as the *neutrino mass hierarchy*. An ordering of $m_1 < m_2 < m_3$ is known as the *normal hierarchy* since it matches the ordering of the quarks in the Standard Model, whereas an ordering of $m_3 < m_1 < m_2$ is referred to as the *inverted hierarchy*.

Since each flavor eigenstate is a mixture of three mass eigenstates, there can be an overall phase difference between the quantum states, referred to as $\delta_{\rm CP}$. A nonzero value of this phase implies that neutrinos and antineutrinos oscillate differently — a phenomenon known as charge-parity (CP) violation. $\delta_{\rm CP}$ is therefore often referred to as the *CP phase* or the *CP-violating phase*.

The entire complement of neutrino experiments to date has measured five of the mixing parameters: the three angles θ_{12}, θ_{23} and (recently) θ_{13}, and the two mass differences Δm^2_{21} and Δm^2_{32}. The sign of Δm^2_{21} is known, but not that of Δm^2_{32}, which is the crux of the mass hierarchy ambiguity. The values of θ_{12} and θ_{23} are large, while θ_{13} is smaller [46]. The value of $\delta_{\rm CP}$ is unknown. The real values of the entries of the PMNS mixing matrix, which contains information on the strength of

flavor-changing weak decays in the lepton sector, can be expressed in approximate form as

$$|U_{\mathrm{PMNS}}| \sim \begin{pmatrix} 0.8 & 0.5 & 0.2 \\ 0.5 & 0.6 & 0.6 \\ 0.2 & 0.6 & 0.8 \end{pmatrix}. \tag{2.6}$$

The three-flavor-mixing scenario for neutrinos is now well established. However, the mixing parameters are not known to the same precision as are those in the corresponding quark sector, and several important quantities, including the value of δ_{CP} and the sign of the large mass splitting, are still undetermined. In addition, several recent anomalous experimental results count among their possible interpretations phenomena that do not fit this model [47,48,49,50].

The relationships between the values of the parameters in the neutrino and quark sectors suggest that mixing in the two sectors is qualitatively different. Illustrating this difference, the value of the entries of the CKM quark-mixing matrix (analogous to the PMNS matrix for neutrinos, and thus indicative of the strength of flavor-changing weak decays in the quark sector) can be expressed in approximate form as

$$|V_{\mathrm{CKM}}| \sim \begin{pmatrix} 1 & 0.2 & 0.004 \\ 0.2 & 1 & 0.04 \\ 0.008 & 0.04 & 1 \end{pmatrix} \tag{2.7}$$

and compared to the entries of the PMNS matrix given in Equation 2.6. As discussed in [51], the question of why the quark mixing angles are smaller than the lepton mixing angles is an important part of the "flavor problem."

Quoting the discussion in [20], "while the CKM matrix is almost proportional to the identity matrix plus hierarchically ordered off-diagonal elements, the PMNS matrix is far from diagonal and, with the possible exception of the U_{e3} element, all elements are $\mathcal{O}(1)$." One theoretical method often used to address this question involves the use of non-Abelian discrete subgroups of $SU(3)$ as flavor symmetries; the popularity of this method comes partially from the fact that these symmetries can give rise to the nearly *tri-bi-maximal** structure of the PMNS matrix. Whether employing these flavor symmetries or other methods, any theoretical principle that attempts to describe the fundamental symmetries implied by the observed organization of quark and neutrino mixing — such as those proposed in unification models — leads to testable predictions such as sum rules between CKM and PMNS parameters [20,42,51,53]. Data on the patterns of neutrino mixing are already proving crucial in the quest for a relationship between quarks and leptons and their seemingly arbitrary generation structure. Table 2.1 displays the comparison between quark and lepton mixing

*Tri-bi-maximal mixing refers to a form of the neutrino mixing matrix with effective bimaximal mixing of ν_μ and ν_τ at the atmospheric scale ($L/E \sim 500$ km/ GeV) and effective trimaximal mixing for ν_e with ν_μ and ν_τ at the solar scale ($L/E \sim 15{,}000$ km/ GeV) [52].

in terms of the fundamental parameters and the precision to which they are known[†], highlighting the limited precision of the neutrino-mixing parameter measurements.

Table 2.1: Best-fit values of the neutrino mixing parameters in the PMNS matrix (assumes normal hierarchy) from [54], their 1σ uncertainties and comparison to the analogous values in the CKM matrix [55]. ΔM^2 is defined as $m_3^2 - (m_1^2 + m_2^2)/2$.

Parameter	Value (neutrino PMNS matrix)	Value (quark CKM matrix)
$\boldsymbol{\theta_{12}}$	$34 \pm 1^\circ$	$13.04 \pm 0.05^\circ$
$\boldsymbol{\theta_{23}}$	$38 \pm 1^\circ$	$2.38 \pm 0.06^\circ$
$\boldsymbol{\theta_{13}}$	$8.9 \pm 0.5^\circ$	$0.201 \pm 0.011^\circ$
$\boldsymbol{\Delta m^2_{21}}$	$+(7.54 \pm 0.22) \times 10^{-5}$ eV^2	
$\boldsymbol{\lvert\Delta M^2\rvert}$	$(2.43^{+0.10}_{-0.06}) \times 10^{-3}$ eV^2	$m_3 >> m_2$
$\boldsymbol{\delta_{CP}}$	$-170 \pm 54^\circ$	$67 \pm 5^\circ$

Clearly much work remains in order to complete the standard three-flavor mixing picture, particularly with regard to θ_{23} (is it less than, greater than, or equal to 45°?), mass hierarchy (normal or inverted?) and $\delta_{\rm CP}$. Additionally, there is great value in obtaining a set of measurements for multiple parameters *from a single experiment*, so that correlations and systematic uncertainties can be handled properly. Such an experiment would also be well positioned to extensively test the standard picture of three-flavor mixing. LBNE is designed to be this experiment.

2.2.1 CP Violation in the Quark and Lepton Sectors

In the particular parameterization of the PMNS matrix shown in Equation 2.2, the middle factor, labeled 'II', describes the mixing between the ν_1 and ν_3 mass states, and depends on the CP-violating phase $\delta_{\rm CP}$. In the three-flavor model, leptonic CP violation in an oscillation mode occurs due to the interference of contributions from terms in this factor — some of which contain $\delta_{\rm CP}$ (i.e., involve the ν_1-ν_3 mixing directly) and some of which do not. The presence of nonzero CP-odd terms, e.g., Equation 2.15, (which requires $\delta_{\rm CP} \neq 0$ or π) in the interference patterns would result in an asymmetry in neutrino versus antineutrino oscillations. The magnitude of the CP-violating terms in the oscillation depends most directly on the size of the Jarlskog Invariant [56], a function that was introduced to provide a measure of CP violation independent of mixing-matrix parameterization. In terms of the three mixing angles and the (as yet unmeasured) CP-violating phase, the Jarlskog Invariant is:

$$J_{CP}^{\rm PMNS} \equiv \frac{1}{8} \sin 2\theta_{12} \sin 2\theta_{13} \sin 2\theta_{23} \cos\theta_{13} \sin\delta_{\rm CP}. \tag{2.8}$$

[†]A global fit [54] to existing results from current experiments sensitive to neutrino oscillation effects is the source for the PMNS matrix values.

The relatively large values of the mixing angles in the lepton sector imply that leptonic CP-violation effects may be quite large — depending on the value of the phase $\delta_{\rm CP}$, which is currently unknown. Experimentally, it is unconstrained at the 2σ level by the global fit [54]. Many theoretical models, examples of which include [57,58,59,60,61,62], provide predictions for $\delta_{\rm CP}$, but these predictions range over all possible values so do not yet provide any guidance.

Given the current best-fit values of the mixing angles [54] and assuming normal hierarchy,

$$J_{CP}^{\rm PMNS} \approx 0.03 \sin \delta_{\rm CP}. \tag{2.9}$$

This is in sharp contrast to the very small mixing in the quark sector, which leads to a very small value of the corresponding quark-sector Jarlskog Invariant [55],

$$J_{CP}^{\rm CKM} \approx 3 \times 10^{-5}, \tag{2.10}$$

despite the large value of $\delta_{CP}^{\rm CKM} \approx 70^\circ$.

To date, all observed CP-violating effects have occurred in experiments involving systems of quarks, in particular strange and b-mesons [55]. Furthermore, in spite of several decades of experimental searches for other sources of CP violation, all of these effects are explained by the CKM quark-mixing paradigm, and all are functions of the quark-sector CP phase parameter, $\delta_{\rm CP}^{\rm CKM}$. In cosmology, successful synthesis of the light elements after the Big Bang [63,64] (Big Bang Nucleosynthesis) requires that there be an imbalance in the number of baryons and antibaryons to one part in a billion when the Universe is a few minutes old [65]. CP violation in the quark sector has not, however, been able to explain the observed Baryon Asymmetry of the Universe (BAU), due to the small value of J_{CP}^{CKM}.

Baryogenesis [66] is a likely mechanism for generating the observed matter-antimatter asymmetry of our Universe. One way that it is elegantly achieved is by first having *leptogenesis* in the very early Universe. That mechanism can come about from the production and decay of very heavy right-handed neutrinos, if they are Majorana states (i.e. do not conserve lepton number[‡]), CP symmetry is violated in their decays (thus distinguishing particles and antiparticles) and the Universe is in non-equilibrium. Leptogenesis will lead to an early dominance of antileptons over leptons. When the cooling Universe reaches the electroweak phase transition, $T \sim 250\,$GeV, a baryon number excess is generated from the lepton asymmetry by a $B-L$[‡] conserving mechanism (analogous to proton decay in that it violates B and L separately but conserves $B-L$) already present in the Standard Model.

The heavy Majorana right-handed neutrino states that could give rise to leptogenesis in the very early Universe are also a natural consequence of the GUT-based *seesaw* mechanism [67] — the simplest and most natural explanation of the observed super-light neutrino mass scales. The seesaw

[‡]In the Standard Model, lepton number (L) and baryon number (B) are conserved quantum numbers. Leptons have $B=0$ and $L=1$ and antileptons have $L=-1$. A quark has $L=0$ and $B=1/3$ and an antiquark has $B=-1/3$.

mechanism is a theoretical attempt to reconcile the very small masses of neutrinos to the much larger masses of the other elementary particles in the Standard Model. The seesaw mechanism achieves this unification by assuming an unknown new physics scale that connects the observed low-energy neutrino masses with a higher mass scale that involves very heavy sterile neutrino states. The seesaw mechanism as generator of neutrino mass is in addition to the Higgs mechanism that is now known to be responsible for the generation of the quark, charged lepton, and vector boson masses.

The no-equilibrium leptogenesis ingredient is expected in a hot Big Bang scenario, but the Majorana nature of the heavy neutrinos and needed CP violation can only be indirectly inferred from light neutrino experiments by finding lepton number violation (validating their Majorana nature via neutrinoless double-beta decay) and observing CP violation in ordinary neutrino oscillations.

Recent theoretical advances have demonstrated that CP violation, necessary for the generation of the Baryon Asymmetry of the Universe at the GUT scale (baryogenesis), can be directly related to the low-energy CP violation in the lepton sector that could manifest in neutrino oscillations. As an example, the theoretical model described in [68] predicts that leptogenesis, the generation of the analogous lepton asymmetry, can be achieved if

$$|\sin\theta_{13}\sin\delta_{\rm CP}| \gtrsim 0.11 \tag{2.11}$$

This implies $|\sin\delta_{\rm CP}| \gtrsim 0.7$ given the latest global fit value of $|\sin\theta_{13}|$ [69].

The goal of establishing an experimental basis for assessing this possibility should rank very high on the list of programmatic priorities within particle physics, and can be effectively addressed by LBNE.

2.2.2 Observation of CP-Violating Effects in Neutrino Oscillation Experiments

Whereas the Standard Model allows for violation of charge-parity (CP) symmetries in weak interactions, CP transformations followed by time-reversal transformations (CPT) are invariant. Under CPT invariance, the probabilities of neutrino oscillation and antineutrino oscillation are equivalent, i.e., $P(\nu_l \to \nu_l) = P(\overline{\nu}_l \to \overline{\nu}_l)$ where $l = e,\ \mu,\ \tau$. Measurements of $\nu_l \to \nu_l$ oscillations in which the flavor of the neutrino before and after oscillations remains the same are referred to as *disappearance* or *survival* measurements. CPT invariance in neutrino oscillations was recently tested by measurements of $\nu_\mu \to \nu_\mu$ and $\overline{\nu}_\mu \to \overline{\nu}_\mu$ oscillations [70]; no evidence for CPT violation was found. Therefore, asymmetries in neutrino versus antineutrino oscillations arising from CP violation effects can only be accessed in *appearance* experiments, defined as oscillations of $\nu_l \to \nu_{l'}$, in which the flavor of the neutrino after oscillations has changed. Because of the intrinsic challenges

of producing and detecting ν_τ's, the oscillation modes $\nu_{\mu,e} \rightarrow \nu_{e,\mu}$ provide the most promising experimental signatures of leptonic CP violation.

For $\nu_{\mu,e} \rightarrow \nu_{e,\mu}$ oscillations that occur as the neutrinos propagate through matter, as in terrestrial long-baseline experiments, the coherent forward scattering of ν_e's on electrons in matter modifies the energy and path-length dependence of the vacuum oscillation probability in a way that depends on the magnitude *and* sign of Δm^2_{32}. This is the Mikheyev-Smirnov-Wolfenstein (MSW) effect [71,72] that has already been observed in solar-neutrino oscillation (disappearance) experiments [73,74,75,76]. The oscillation probability of $\nu_{\mu,e} \rightarrow \nu_{e,\mu}$ through matter, in a constant density approximation, keeping terms up to second order in $\alpha \equiv |\Delta m^2_{21}|/|\Delta m^2_{31}|$ and $\sin^2\theta_{13}$, is [77,55]:

$$P(\nu_\mu \rightarrow \nu_e) \cong P(\nu_e \rightarrow \nu_\mu) \cong P_0 + \underbrace{P_{\sin\delta}}_{\text{CP violating}} + P_{\cos\delta} + P_3 \tag{2.12}$$

where

$$P_0 = \sin^2\theta_{23}\frac{\sin^2 2\theta_{13}}{(A-1)^2}\sin^2[(A-1)\Delta], \tag{2.13}$$

$$P_3 = \alpha^2\cos^2\theta_{23}\frac{\sin^2 2\theta_{12}}{A^2}\sin^2(A\Delta), \tag{2.14}$$

$$P_{\sin\delta} = \alpha\frac{8J_{cp}}{A(1-A)}\sin\Delta\sin(A\Delta)\sin[(1-A)\Delta], \tag{2.15}$$

$$P_{\cos\delta} = \alpha\frac{8J_{cp}\cot\delta_{\rm CP}}{A(1-A)}\cos\Delta\sin(A\Delta)\sin[(1-A)\Delta], \tag{2.16}$$

and where

$$\Delta = \Delta m^2_{31}L/4E,\ and\ A = \sqrt{3}G_F N_e 2E/\Delta m^2_{31}.$$

In the above, the CP phase $\delta_{\rm CP}$ appears (via J_{cp}) in the expressions for $P_{\sin\delta}$ (the CP-odd term) which switches sign in going from $\nu_\mu \rightarrow \nu_e$ to the $\overline{\nu}_\mu \rightarrow \overline{\nu}_e$ channel, and $P_{\cos\delta}$ (the CP-conserving term) which does not. The matter effect also introduces a neutrino-antineutrino asymmetry, the origin of which is simply the presence of electrons and absence of positrons in the Earth.

Recall that in Equation 2.2, the CP phase appears in the PMNS matrix through the mixing of the ν_1 and ν_3 mass states. The physical characteristics of an appearance experiment are therefore determined by the baseline and neutrino energy at which the mixing between the ν_1 and ν_3 states is maximal, as follows:

$$\frac{L(\text{km})}{E_\nu(\text{GeV})} = (2n-1)\frac{\pi}{2}\frac{1}{1.27\times\Delta m^2_{31}(\text{eV}^2)} \tag{2.17}$$

$$\approx (2n-1)\times 510\ \text{km/GeV} \tag{2.18}$$

where $n = 1, 2, 3...$ denotes the oscillation nodes at which the appearance probability is maximal.

The dependences on E_ν of the oscillation probability for the LBNE baseline of L =1,300 km are plotted on the right in Figures 2.3 and 2.4. The colored curves demonstrate the variation in the ν_e appearance probability as a function of E_ν, for three different values of $\delta_{\rm CP}$.

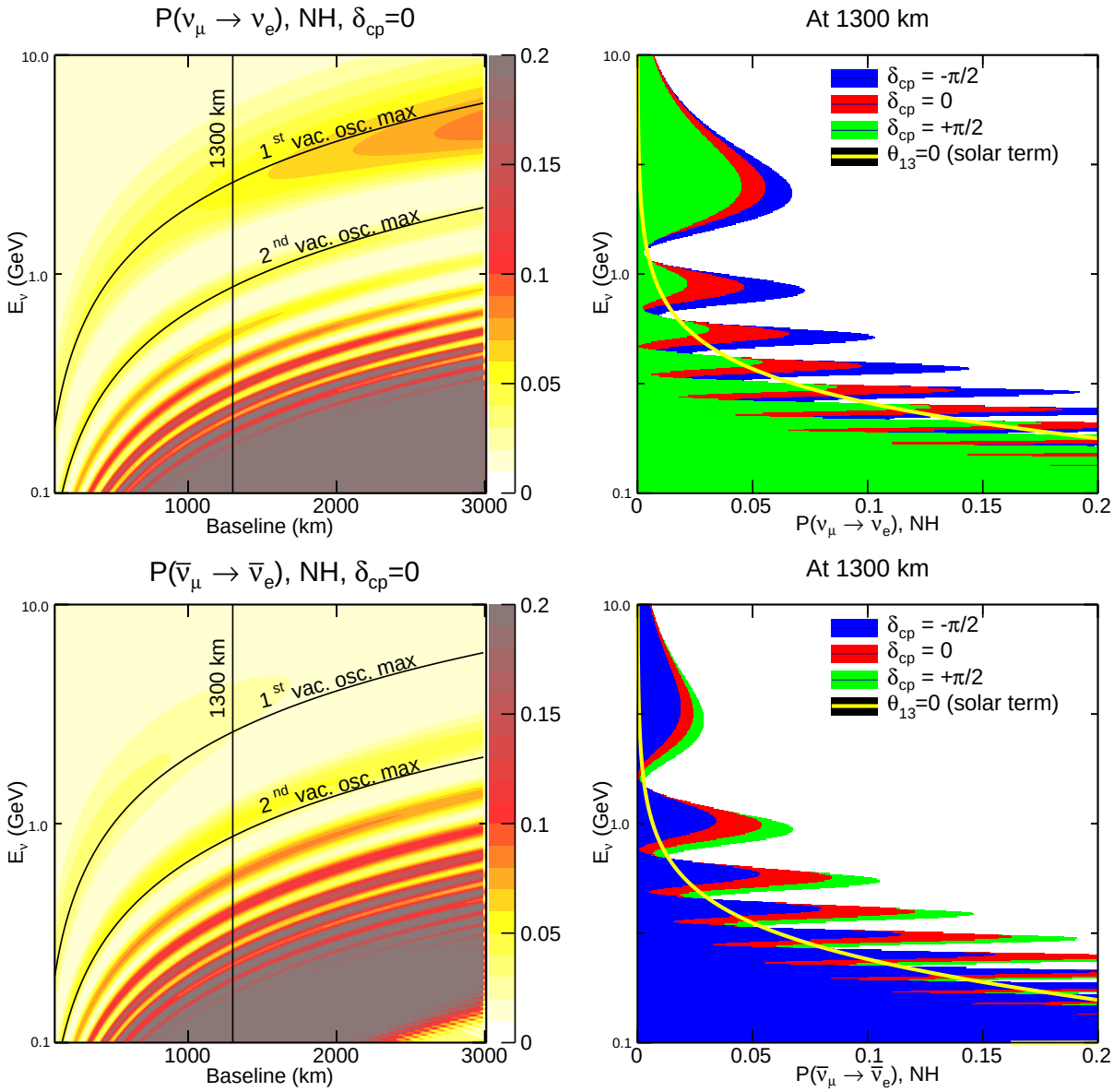

Figure 2.3: Neutrino oscillation probabilities as a function of energy and baseline, for different values of $\delta_{\rm CP}$, *normal hierarchy*. The oscillograms on the left show the $\nu_\mu \to \nu_e$ oscillation probabilities as a function of baseline and energy for *neutrinos* (top left) and *antineutrinos* (bottom left) with $\delta_{\rm CP} = 0$. The figures on the right show the projection of the oscillation probability on the neutrino energy axis at a baseline of 1,300 km for $\delta_{\rm CP} = 0$ (red), $\delta_{\rm CP} = +\pi/2$ (green), and $\delta_{\rm CP} = -\pi/2$ (blue) for neutrinos (top right) and antineutrinos (bottom right). The yellow curve is the ν_e appearance solely from the "solar term" due to ν_1 to ν_2 mixing as given by Equation 2.14.

The variation in the $\nu_\mu \to \nu_e$ oscillation probabilities with the value of $\delta_{\rm CP}$ indicates that it is experimentally possible to measure the value of $\delta_{\rm CP}$ at a fixed baseline using only the observed shape of the $\nu_\mu \to \nu_e$ *or* the $\overline{\nu}_\mu \to \overline{\nu}_e$ appearance signal measured over an energy range that encompasses at least one full oscillation interval. A measurement of the value of $\delta_{\rm CP} \neq 0$ or π, assuming that neutrino mixing follows the three-flavor model, would imply CP violation. The CP

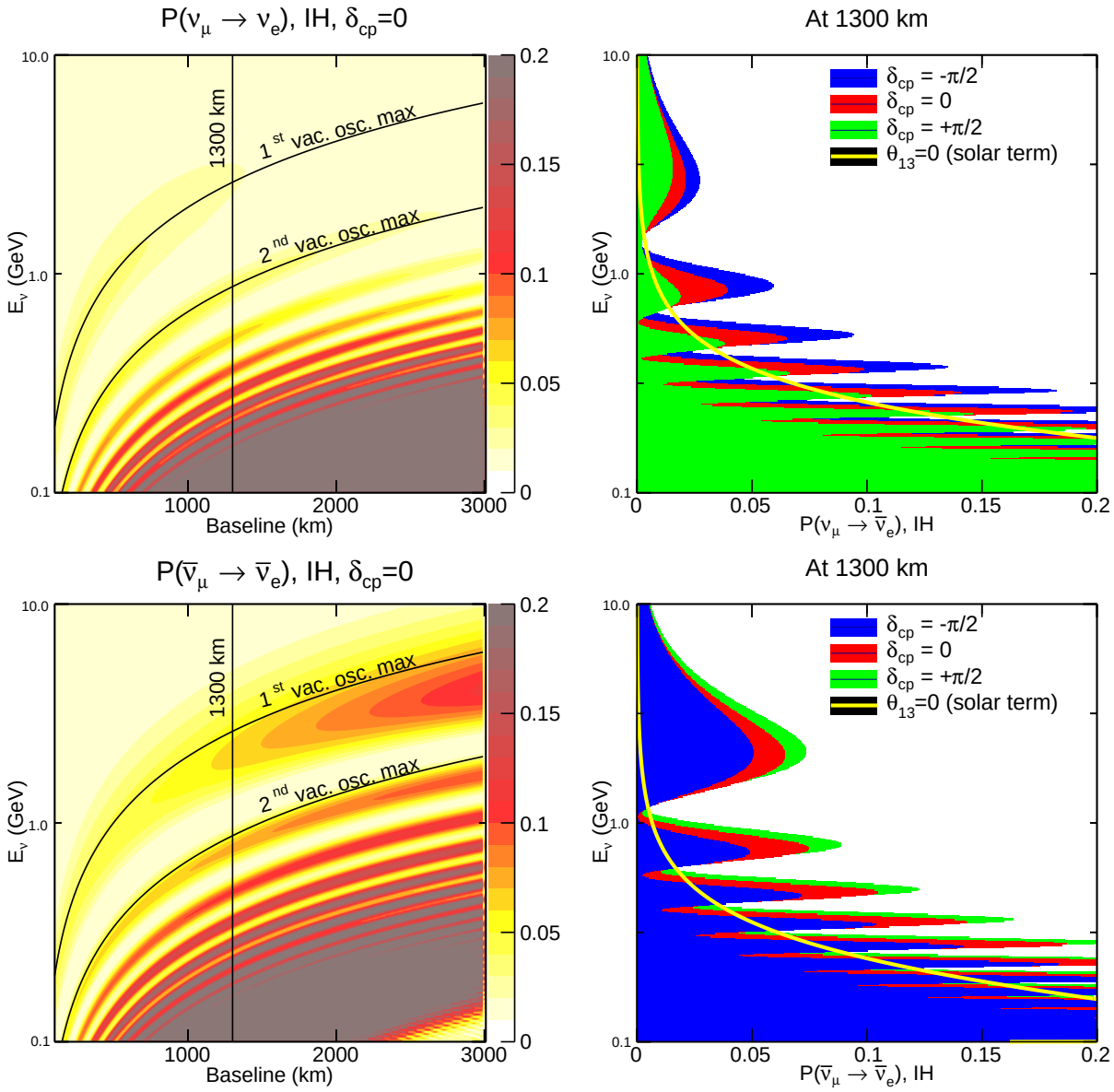

Figure 2.4: Neutrino oscillation probabilities as a function of energy and baseline, for different values of $\delta_{\rm CP}$, *inverted hierarchy*. The oscillograms on the left show the $\nu_\mu \to \nu_e$ oscillation probabilities as a function of baseline and energy for *neutrinos* (top left) and *antineutrinos* (bottom left) with $\delta_{\rm CP} = 0$. The figures on the right show the projection of the oscillation probability on the neutrino energy axis at a baseline of 1,300 km for $\delta_{\rm CP} = 0$ (red), $\delta_{\rm CP} = +\pi/2$ (green), and $\delta_{\rm CP} = -\pi/2$ (blue) for neutrinos (top right) and antineutrinos (bottom right).The yellow curve is the ν_e appearance solely from the "solar term" due to ν_1 to ν_2 mixing as given by Equation 2.14.

asymmetry, $\mathcal{A}_{CP}$, is defined as

$$\mathcal{A}_{CP} = \frac{P(\nu_\mu \to \nu_e) - P(\overline{\nu}_\mu \to \overline{\nu}_e)}{P(\nu_\mu \to \nu_e) + P(\overline{\nu}_\mu \to \overline{\nu}_e)}. \tag{2.19}$$

In the three-flavor model the asymmetry can be approximated to leading order in Δm^2_{21} as [78]:

$$\mathcal{A}_{CP} \sim \frac{\cos\theta_{23}\sin 2\theta_{12}\sin\delta_{\rm CP}}{\sin\theta_{23}\sin\theta_{13}}\left(\frac{\Delta m^2_{21}L}{4E_\nu}\right) + \text{matter effects} \tag{2.20}$$

Regardless of the value obtained for $\delta_{\rm CP}$, it is clear that the explicit observation of an asymmetry between $P(\nu_l \to \nu_{l'})$ and $P(\overline{\nu}_l \to \overline{\nu}_{l'})$ is sought to directly demonstrate the leptonic CP violation effect that a value of $\delta_{\rm CP}$ different from zero or π implies. For long-baseline experiments such as LBNE, where the neutrino beam propagates through the Earth's mantle, the leptonic CP-violation effects must be disentangled from the matter effects.

2.2.3 Probing the Neutrino Mass Hierarchy via the Matter Effect

The asymmetry induced by matter effects as neutrinos pass through the Earth arises from the change in sign of the factors proportional to Δm^2_{31} (namely A, Δ and α; Equations 2.12 to 2.16) in going from the normal to the inverted neutrino mass hierarchy. This sign change provides a means for determining the currently unknown mass hierarchy. The oscillation probabilities given in these approximate equations for $\nu_\mu \to \nu_e$ as a function of baseline in kilometers and energy in GeV are calculated numerically with an exact formalism [79] and shown in the oscillograms of Figure 2.3 and 2.4 for $\delta_{\rm CP} = 0$, for normal and inverted hierarchies, respectively. The oscillograms include the matter effect, assuming an Earth density and electron fraction described by [80]. These values are taken as a constant average over paths through regions of the Earth with continuous density change. Any baseline long enough to pass through a discontinuity is split into three or more segments each of constant average density and electron fraction. The solid black curves in the oscillograms indicate the location of the first and second oscillation maxima as given by Equation 2.18, assuming oscillations in a vacuum; matter effects will change the neutrino energy values at which the mixing between the ν_1 and ν_3 mass states is maximal.

The significant impact of the matter effect on the $\nu_\mu \to \nu_e$ and $\overline{\nu}_\mu \to \overline{\nu}_e$ oscillation probabilities at longer baselines (Figures 2.3 and 2.4) implies that ν_e appearance measurements over long distances through the Earth provide a powerful probe into the neutrino mass hierarchy question: is $m_1 > m_3$ or vice-versa?

The dependence of the matter effect on the mass hierarchy is illustrated in the oscillograms plotted on the left hand side of Figures 2.3 and 2.4, and can be characterized as follows:

- For normal hierarchy, $P(\nu_\mu \to \nu_e)$ is enhanced and $P(\overline{\nu}_\mu \to \overline{\nu}_e)$ is suppressed. The effect increases with baseline at a fixed L/E.
- For inverted hierarchy, $P(\nu_\mu \to \nu_e)$ is suppressed and $P(\overline{\nu}_\mu \to \overline{\nu}_e)$ is enhanced. The effect increases with baseline at a fixed L/E.

- The matter effect has the largest impact on the probability amplitude at the first oscillation maximum.
- The matter effect introduces a phase shift in the oscillation pattern, shifting it to a lower energy for a given baseline when the hierarchy changes from normal to inverted. The shift is approximately -100 MeV.

2.2.4 Disentangling CP-Violating and Matter Effects

In Figure 2.5, the asymmetries induced by matter and maximal CP violation (at $\delta_{\mathrm{CP}} = \pm\pi/2$) are shown separately as 2D oscillograms in baseline and neutrino energy. The matter effect induces an asymmetry in $P(\nu_l \rightarrow \nu_{l'})$ and $P(\overline{\nu}_l \rightarrow \overline{\nu}_{l'})$ that adds to the CP asymmetry. At longer baselines ($> 1000\,\mathrm{km}$), the matter asymmetry in the energy region of the first oscillation node is driven primarily by the change in the ν_e appearance amplitude. At shorter baselines ($\mathcal{O}(100\,\mathrm{km})$) the asymmetry is driven by the phase shift. The dependence of the asymmetry on baseline and energy, where the oscillation probabilities peak and the appearance signals are largest, can be approximated as follows:

$$\mathcal{A}_{cp} \propto L/E, \tag{2.21}$$

$$\mathcal{A}_{matter} \propto L \times E. \tag{2.22}$$

The phenomenology of $\nu_\mu \rightarrow \nu_e$ oscillations described in Section 2.2.2 implies that the experimental sensitivity to CP violation and the mass hierarchy from measurements of the total asymmetry between $P(\nu_l \rightarrow \nu_{l'})$ and $P(\overline{\nu}_l \rightarrow \overline{\nu}_{l'})$ requires the disambiguation of the asymmetry induced by the matter effect and that induced by CP violation. This is particularly true for experiments designed to access mixing between the ν_1 and ν_3 mass states using neutrino beams of $\mathcal{O}(1\,\mathrm{GeV})$. Such beams require baselines of at least several hundred kilometers, at which the matter asymmetries are significant. The currently known values of the oscillation parameters permit calculation of the magnitude of the matter asymmetry within an uncertainty of $< 10\%$; only the sign of the asymmetry, which depends on the sign of Δm^2_{31}, is unknown. Since the magnitude of the matter asymmetry is known, baselines at which the size of the matter asymmetry exceeds that of the maximal possible CP asymmetry are required in order to separate the two effects.

Figure 2.6 illustrates the ambiguities that can arise from the interference of the matter and CP asymmetries. The plots show the total asymmetry as a function of δ_{CP} at four baseline values (clockwise from top left): 290 km, 810 km, 2,300 km and 1,300 km. The curves in black and red illustrate the asymmetries at the first and second oscillation nodes, respectively. The solid lines represent normal hierarchy, and the dashed lines represent inverted hierarchy. The plots demonstrate that experimental measurements of the asymmetry (Equation 2.19) at the first oscillation node could yield ambiguous results for short baselines if the hierarchy is unknown. This occurs in regions of the $(L, E, \delta_{\mathrm{CP}})$ phase space where the matter and CP asymmetries cancel partially or

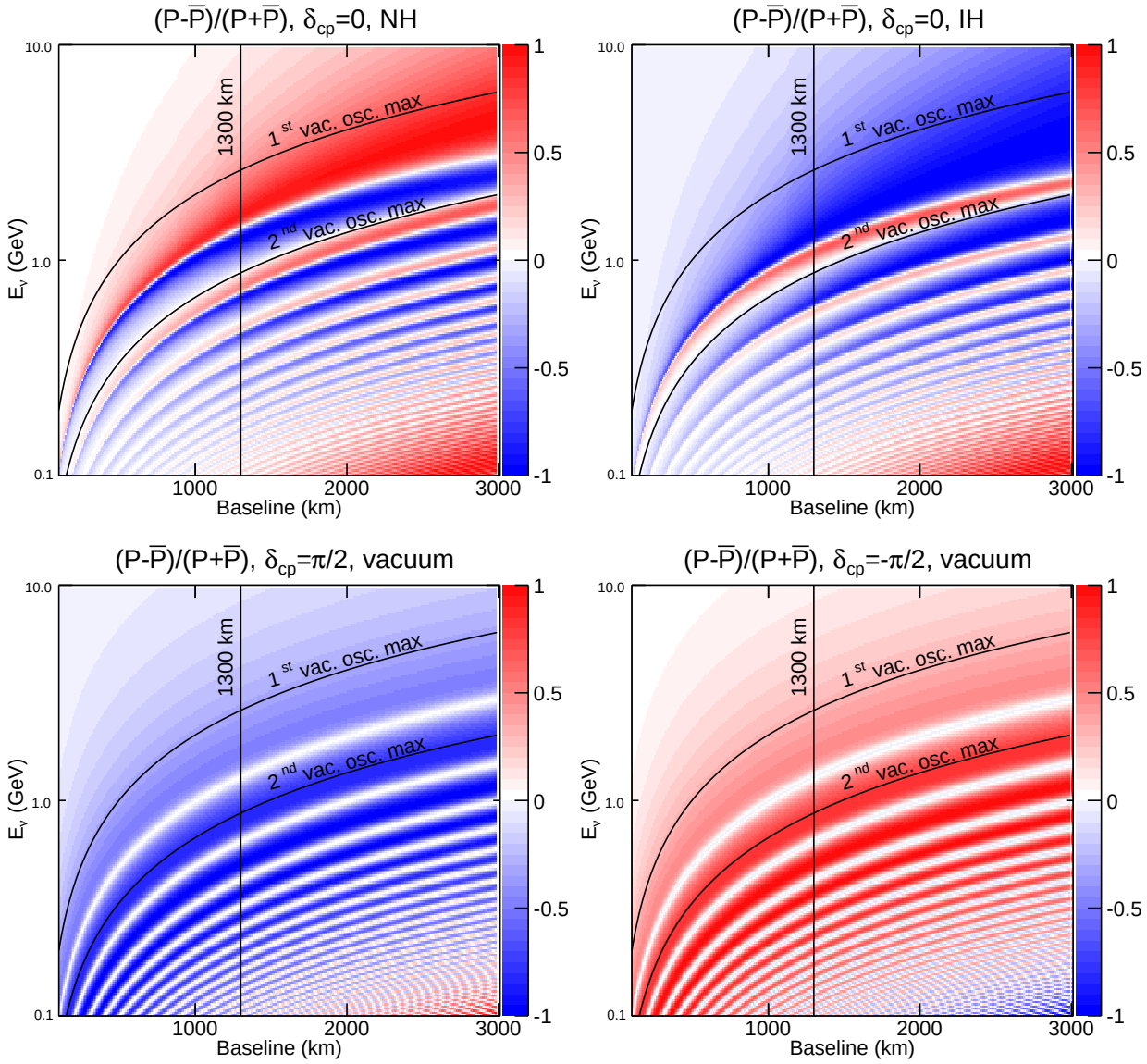

Figure 2.5: The $\nu/\overline{\nu}$ oscillation probability asymmetries as a function of baseline. The top two figures show the asymmetry induced by the matter effect only for normal (top left) and inverted (top right) hierarchies. The bottom figures show the asymmetry induced through the CP-violating phase $\delta_{\rm CP}$ in vacuum, for $\delta_{\rm CP} = +\pi/2$ (bottom left) and $\delta_{\rm CP} = -\pi/2$ (bottom right)

totally. For example, the green lines in Figure 2.6 indicate the asymmetry at the first node for maximal CP violation ($\delta_{\rm CP} = \pi/2$) with an inverted hierarchy. At a baseline of 290 km, the measured asymmetry at $\delta_{\rm CP} = \pi/2$ (inverted hierarchy) is degenerate with that at $\delta_{\rm CP} \sim 0$ (normal hierarchy) at the first node. Measurements of the asymmetry at different L/E or at different baselines can break the degeneracies (Equation 2.22). At very long baselines, for which the matter asymmetry exceeds the maximal CP asymmetry at the first oscillation node, there are no degeneracies and the mass hierarchy and CP asymmetries can be resolved within the same experiment. For the current

best-fit values of the oscillation parameters, the matter asymmetry exceeds the maximal possible CP asymmetry at baselines of $\geq$ 1,200 km.

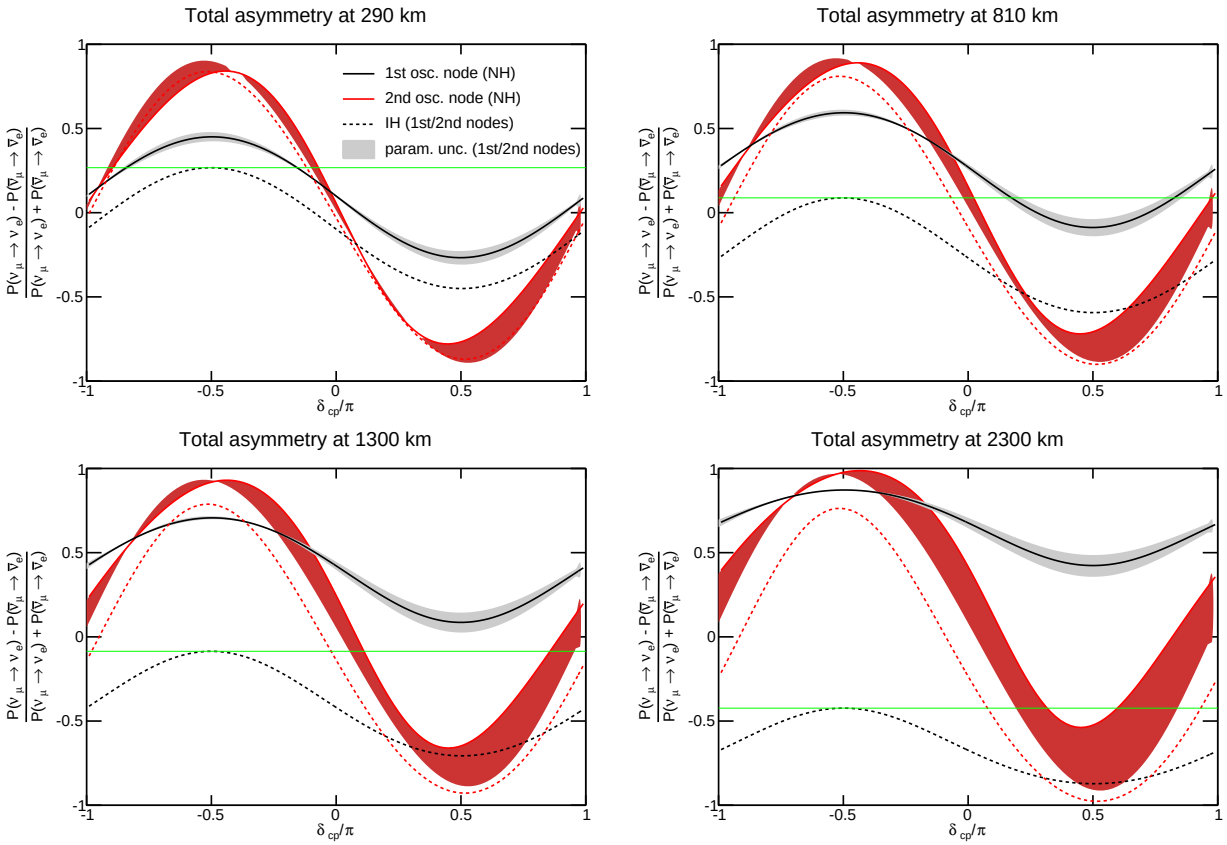

Figure 2.6: The $\nu/\overline{\nu}$ oscillation probability asymmetries versus δ_{CP} at the first two oscillation nodes. Clockwise from top left: 290 km, 810 km, 2,300 km and 1,300 km. The solid/dashed black line is the total asymmetry at the first oscillation node for normal/inverted hierarchy. The red lines indicate the asymmetries at the second node.

2.2.5 Optimization of the Oscillation Baseline for CPV and Mass Hierarchy

The simple arguments above suggest that a baseline $\geq$ 1,200 km is required to search for CP violation and determine the mass hierarchy simultaneously in a single long-baseline neutrino oscillation experiment. To understand the performance of a long-baseline experiment as a function of baseline using realistic neutrino beamline designs, a study of the sensitivities to CP violation and the mass hierarchy as a function of baseline was carried out using a neutrino beamline design optimized individually for each baseline. A 34-kt LArTPC neutrino detector at the far site was assumed since it has a high ν_e-identification efficiency that is flat over a large range of energies (Chapter 4). The beamline design was based on the NuMI beamline utilizing the 120-GeV, 1.2-MW proton beam from the Fermilab Main Injector and was fully simulated using GEANT3 [82]. Varying the distance between the target and the first horn allowed selection of a beam spectrum that covered the first

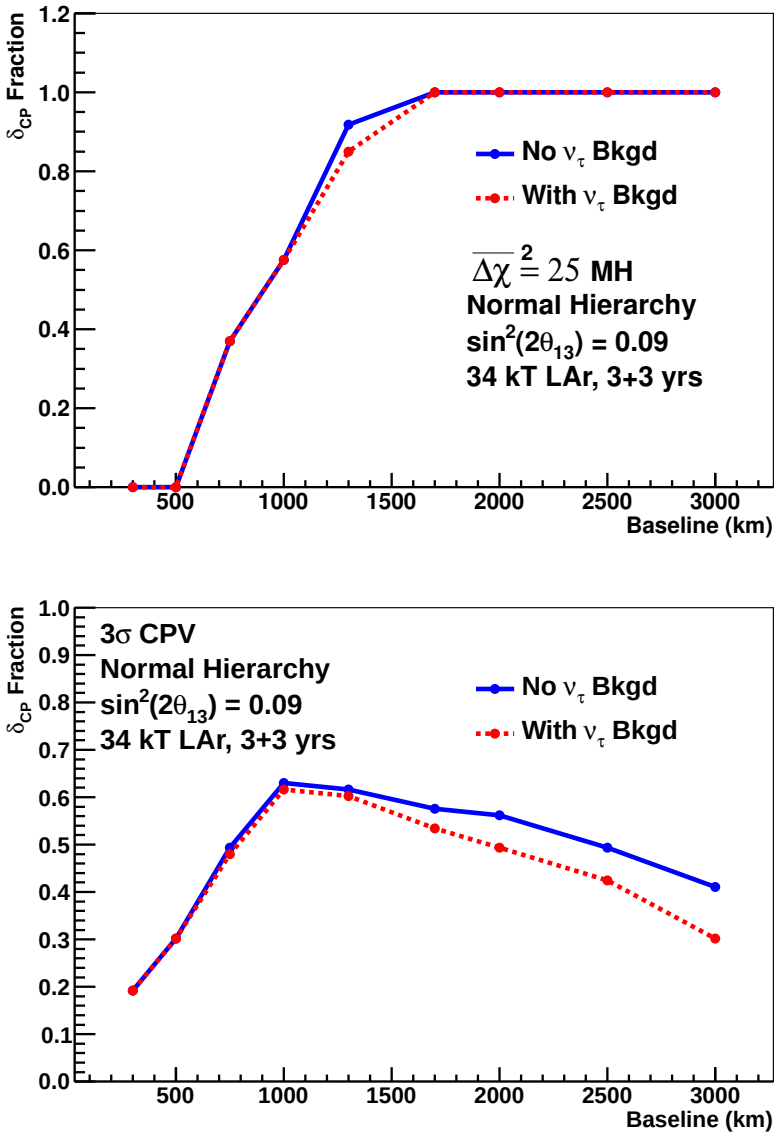

Figure 2.7: The fraction of $\delta_{\rm CP}$ values for which the mass hierarchy can be determined with an average $|\overline{\Delta\chi^2}| = 25$ or greater as a function of baseline (top) and the fraction of $\delta_{\rm CP}$ values which CP violation can be determined at the 3σ level or greater as a function of baseline (bottom). A NuMI based beam design with a 120-GeV beam was optimized for each baseline. Projections assume $\sin^2 2\theta_{13} = 0.09$ and a 34-kt LArTPC as the far detector [81]. An exposure of 3yrs+3yrs of neutrino+antineutrino running with 1.2-MW beam power is assumed.

oscillation node and part of the second. The design incorporated an evacuated decay pipe of 4-m diameter and a length that varied from 280 to 580 m. For baselines less than 1,000 m, the oscillation occurs at neutrino energies where on-axis beams produce too little flux. Therefore, off-axis beams — which produce narrow-band, low-energy neutrino fluxes — were simulated for these baselines, with the off-axis angle chosen to provide the most coverage of the first oscillation node. The re-

sults of this study [81] are summarized in Figure 2.7. The sensitivity to CP violation (bottom plot) assumes that the mass hierarchy is unknown. An updated study with more detail is available [83]. The baseline study indicates that with realistic experimental conditions, baselines between 1,000 and 1,300 km are near optimal for determination of CP violation. With baselines $>$ 1,500 km, the correct mass hierarchy could be determined with a probability greater than 99% for all values of $\delta_{\rm CP}$ with a large LArTPC far detector. However, at very long baselines, in one of the neutrino beam polarities (ν/$\overline{\nu}$ for inverted/normal hierarchy) the event rate suppression due to the matter effect becomes very large, making it difficult to observe an explicit CP-violation asymmetry.

2.2.6 Physics from Precision Measurements of Neutrino Mixing

Precision measurements of the neutrino mixing parameters in long-baseline oscillations not only reveal the neutrino mixing patterns in greater detail, but also serve as probes of new physics that manifests as perturbations in the oscillation patterns driven by three-flavor mixing.

The determination of whether there is maximal mixing between ν_μ and ν_τ — or a measurement of the deviation from maximal — is of great interest theoretically [59,84,85,86,87,88]. Models of quark-lepton universality propose that the quark and lepton mixing matrices (Equations 2.7 and 2.6, respectively) are given by

$$U^{\rm CKM} = 1 + \epsilon_{\rm Cabbibo} \text{ and} \tag{2.23}$$

$$U^{\rm PMNS} = T + \epsilon_{\rm Cabbibo}, \tag{2.24}$$

where T is determined by Majorana physics [89] and $\epsilon_{\rm Cabbibo}$ refers to small terms driven by the Cabbibo weak mixing angle ($\theta_C = \theta_{12}^{\rm CKM}$). In such models $\theta_{23} \sim \pi/4 + \Delta\theta$, where $\Delta\theta$ is of order the Cabbibo angle, θ_C, and $\theta_{13} \sim \theta_C/\sqrt{2}$. It is therefore important to determine experimentally both the value of $\sin^2\theta_{23}$ and the octant of θ_{23} if $\theta_{23} \neq 45°$.

Studying ν_μ disappearance probes $\sin^2 2\theta_{23}$ and $|\Delta m^2_{32}|$ with very high precision. Disappearance measurements can therefore determine whether ν_μ-ν_τ mixing is maximal or near maximal such that $\sin^2 2\theta_{23} = 1$, but they cannot resolve the octant of θ_{23} if ν_μ-ν_τ mixing is less than maximal. Combining the ν_μ disappearance signal with the ν_e appearance signal can help determine the θ_{23} octant and constrain some of the theoretical models of quark-lepton universality.

Direct unitarity tests, in which the individual components of the PMNS matrix are measured separately, are challenging due to limited experimentally available oscillation channels [90,91]. Application of the "proof by contradiction" principle offers another way to perform the unitarity tests. In these tests, the mixing angles are extracted from the data by assuming unitarity in the standard

three-flavor framework. If measurements of the same mixing angle by two different processes are inconsistent, then the standard three-flavor framework is insufficient and new physics beyond this framework is required. Observation of unitarity violation will constrain the phase space of possible new physics. In particular, the precision measurement of $\sin^2 2\theta_{13}$ provides the most promising unitarity test [91] for the PMNS matrix. It is important to note that several theoretical models of new physics, such as the existence of sterile neutrinos or nonstandard interactions, could lead to apparent deviations of the $\sin^2 2\theta_{13}$ value measured in ν_e appearance experiments from that measured in reactor ($\overline{\nu}_e$ disappearance) experiments.

Precision measurements of ν_μ and $\overline{\nu}_\mu$ survival over long baselines could reveal nonstandard physics driven by new interactions in matter. Examples of some of these effects and the experimental signatures in long-baseline oscillations are discussed in Chapter 4.

In addition, experiments with long enough baselines and sufficient neutrino flux at $E_\nu > 3$ GeV, coupled with high-resolution tracking detectors, as in the LBNE design, can also probe $\nu_\mu \rightarrow \nu_\tau$ appearance with higher precision than is currently possible using ν_τ charged-current interactions. The combination of $\nu_\mu \rightarrow \nu_\mu$, $\nu_\mu \rightarrow \nu_e$, and $\nu_\mu \rightarrow \nu_\tau$ can ultimately over-constrain the three-flavor model of neutrino oscillations both in neutrino and antineutrino modes.

2.2.7 Oscillation Physics with Atmospheric Neutrinos

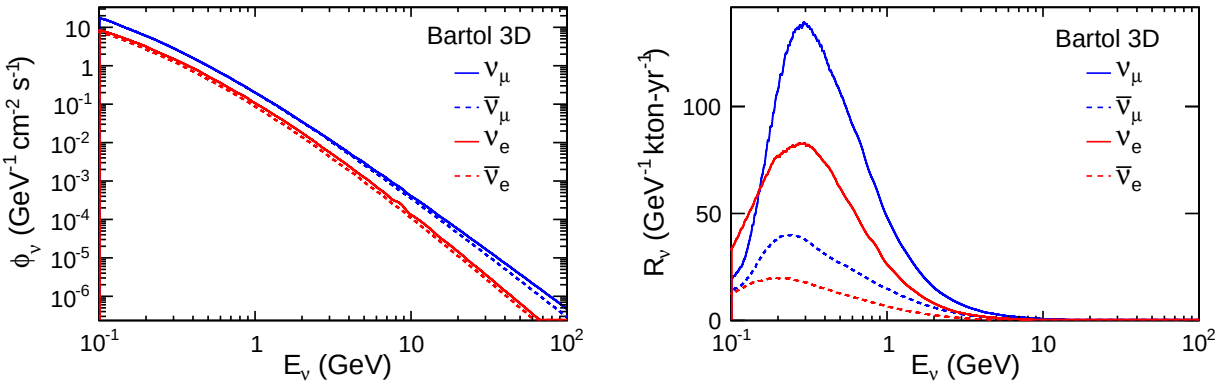

Figure 2.8: The atmospheric neutrino flux in neutrinos per second per square centimeter as a function of neutrino energy for different flavors (left). The atmospheric neutrino spectrum per GeV per kt per year for the different species (right).

Atmospheric neutrinos are unique among sources used to study oscillations; the flux contains neutrinos and antineutrinos of all flavors, matter effects play a significant role, both Δm^2 values contribute to the oscillation patterns, and the oscillation phenomenology occurs over several orders of magnitude in both energy (Figure 2.8) and path length. These characteristics make atmospheric neutrinos ideal for the study of oscillations and provide a laboratory suitable to search for exotic phenomena for which the dependence of the flavor-transition and survival probabilities on energy

and path length can be defined. The probabilities of atmospheric $\nu_\mu \to \nu_e$ and $\overline{\nu}_\mu \to \overline{\nu}_e$ oscillations for normal and inverted hierarchies are shown as a function of zenith angle in Figure 2.9.

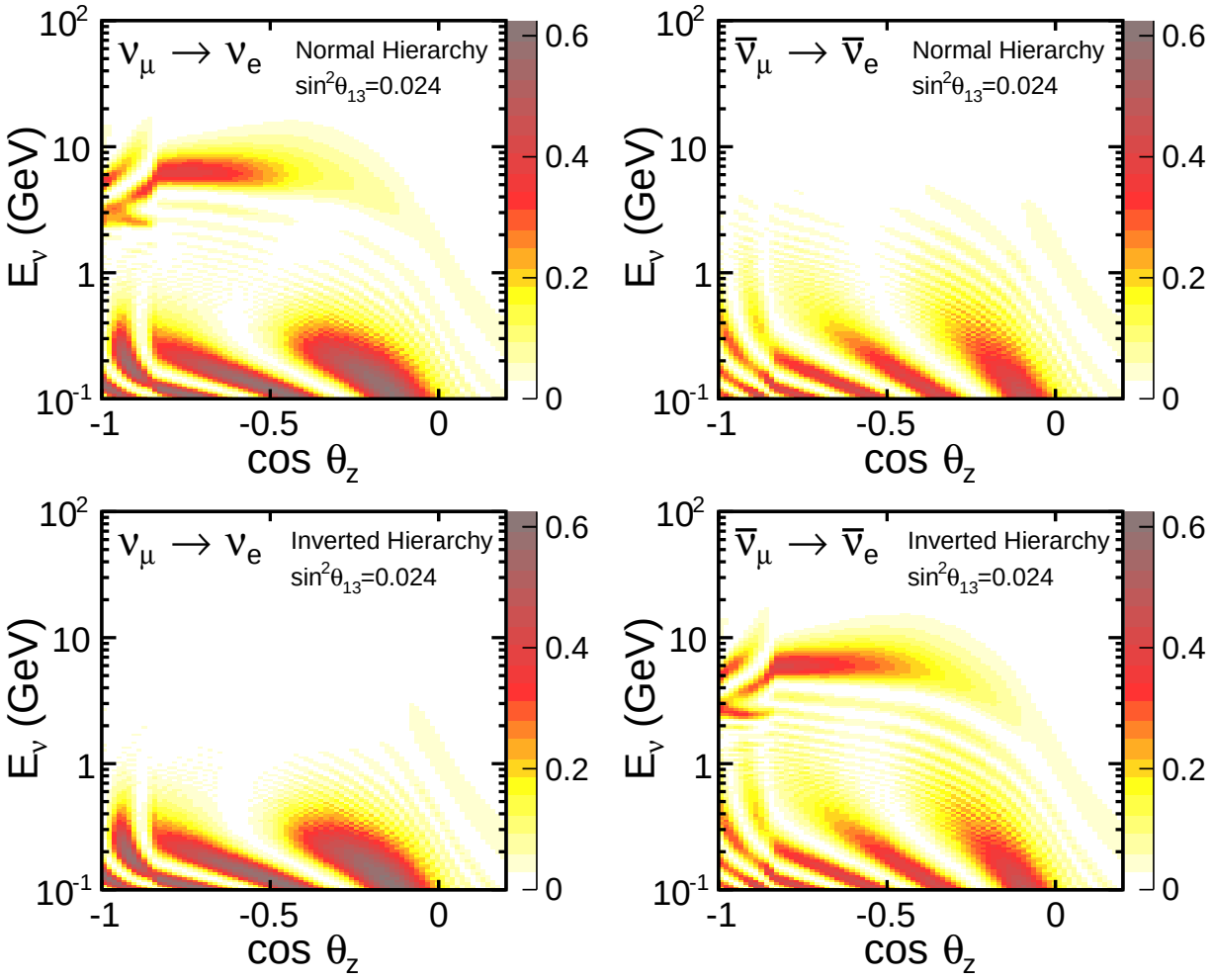

Figure 2.9: The probabilities of atmospheric $\nu_\mu \to \nu_e$ (left) and $\overline{\nu}_\mu \to \overline{\nu}_e$ (right) oscillations for normal (top) and inverted (bottom) hierarchies as a function of zenith angle.

Even with dedicated long-baseline experiments exploring the large mass splitting (Δm^2_{32}) for nearly a decade, atmospheric data continue to contribute substantially to our understanding of the neutrino sector. Broadly speaking:

- The data demonstrate *complementarity* with beam results via two- and three-flavor fits and the measurement of a ν_τ appearance signal consistent with expectations.
- The data serve to increase measurement *precision* through global fits, given that the sensitivity of atmospheric neutrinos to the mass hierarchy is largely independent of δ_{CP} and the octant of θ_{23}.

- *New physics* searches with atmospheric neutrinos have placed limits on CPT violation, non-standard interactions, mass-varying neutrinos and Lorentz-invariance violation.

Atmospheric neutrinos can continue to play these roles in the LBNE era given LBNE's deep-underground far detector. In particular, complementarity will be vital in a future where, worldwide, the number of high-precision, long-baseline beam/detector facilities is small. The physics potential of a large underground liquid argon detector for measuring atmospheric neutrinos is discussed in Section 4.6.

2.3 Nucleon Decay Physics Motivated by Grand Unified Theories

Searches for proton decay, bound-neutron decay and similar processes such as di-nucleon decay and neutron-antineutron oscillations test the apparent but unexplained conservation law of baryon number. These decays are already known to be rare based on decades of prior searches, all of which have produced negative results. If measurable event rates or even a single-candidate event were to be found, it would be sensible to presume that they occurred via unknown virtual processes based on physics beyond the Standard Model. The impact of demonstrating the existence of a baryon-number-violating process would be profound.

2.3.1 Theoretical Motivation from GUTs

The class of theories known as Grand Unified Theories (GUTs) make predictions about both baryon number violation and proton lifetime that may be within reach of the full-scope LBNE experiment. The theoretical motivation for the study of proton decay has a long and distinguished history [92,93,94] and has been reviewed many times [95,96,97]. Early GUTs provided the original motivation for proton decay searches in kiloton-scale detectors placed deep underground to limit backgrounds. The 22.5-kt Super–Kamiokande experiment extended the search for proton decay by more than an order of magnitude relative to the previous generation of experiments. Contemporary reviews [98,99,100] discuss the strict limits already set by Super–Kamiokande and the context of the proposed next generation of larger underground experiments such as Hyper-Kamiokande and LBNE.

Although no evidence for proton decay has been detected, the lifetime limits from the current generation of experiments already constrain the construction of many contemporary GUT models. In some cases, these lifetime limits are approaching the upper limits allowed by GUT models. This

situation points naturally toward continuing the search with new, larger detectors. These searches are motivated by a range of scientific issues:

- Conservation laws arise from underlying symmetries in Nature [101]. Conservation of baryon number is therefore unexplained since it corresponds to no known long-range force or symmetry.
- Baryon number non-conservation has cosmological consequences, such as a role in inflation and the matter-antimatter asymmetry of the Universe.
- Proton decay is predicted at some level by almost all GUTs.
- Some GUTs can accommodate neutrinos with nonzero mass and characteristics consistent with experimental observations.
- GUTs incorporate other previously unexplained features of the Standard Model such as the relationship between quark and lepton electric charges.
- The unification scale is suggested both experimentally and theoretically by the apparent convergence of the running coupling constants of the Standard Model. The unification scale is in excess of 10^{15} GeV.
- The unification scale is not accessible by any accelerator experiment; it can only be probed by virtual processes such as with proton decay.
- GUTs usually predict the relative branching fractions of different nucleon decay modes. Testing these predictions would, however, require a sizeable sample of proton decay events.
- The dominant proton decay mode of a GUT is often sufficient to roughly identify the likely characteristics of the GUT, such as gauge mediation or the involvement of supersymmetry.

The observation of even a single unambiguous proton decay event would corroborate the idea of unification and the signature of the decay would give strong guidance as to the nature of the underlying theory.

2.3.2 Proton Decay Modes

From the body of literature, two decay modes (shown in Figure 2.10) emerge that dominate the LBNE experimental design. The more well-known of the two, the decay mode of $p \rightarrow e^{+}\pi^{0}$, arises from gauge mediation. It is often predicted to have the higher branching fraction and is also demonstrably the more straightforward experimental signature for a water Cherenkov detector. In

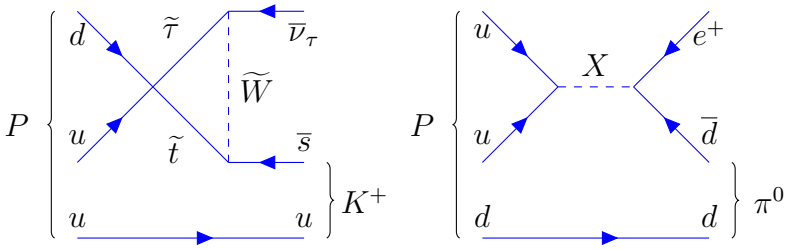

Figure 2.10: Feynman diagrams for proton decay modes from supersymmetric GUT, $p^+ \to K^+\overline{\nu}$ (left) and gauge-mediation GUT models, $p^+ \to e^+\pi^0$ (right).

this mode, the total mass of the proton is converted into the electromagnetic shower energy of the positron and two photons from π^0 decay, with a net momentum vector near zero.

The second key mode is $p \to K^+\overline{\nu}$. This mode is dominant in most supersymmetric GUTs, many of which also favor additional modes involving kaons in the final state. This decay mode with a charged kaon is uniquely interesting; since stopping kaons have a higher ionization density than other particles, a LArTPC could detect it with extremely high efficiency, as described in Chapter 5. In addition, many final states of K^+ decay would be fully reconstructable in a LArTPC.

There are many other allowed modes of proton or bound neutron into antilepton plus meson decay that conserve $B - L$[§], but none of these will influence the design of a next-generation experiment. The most stringent limits, besides those on $p \to e^+\pi^0$, include the lifetime limits on $p \to \mu^+\pi^0$ and $p \to e^+\eta$, both of which are greater than 4×10^{33} years [102]. Any experiment that will do well for $p \to e^+\pi^0$ will also do well for these decay modes. The decays $p \to \overline{\nu}\pi^+$ or $n \to \overline{\nu}\pi^0$ may have large theoretically predicted branching fractions, but they are experimentally difficult due to the sizeable backgrounds from atmospheric-neutrino interactions. The decay $p \to \mu^+K^0$ can be detected relatively efficiently by either water Cherenkov or LArTPC detectors.

A number of other possible modes exist, such as those that conserve $B+L$, that violate only baryon number, or that decay into only leptons. These possibilities are less well-motivated theoretically, as they do not appear in a wide range of models, and are therefore not considered here.

Figure 2.11 shows a comparison of experimental limits, dominated by recent results from Super–Kamiokande to the ranges of lifetimes predicted by an assortment of GUTs. At this time, the theory literature does not attempt to precisely predict lifetimes, concentrating instead on suggesting the dominant decay modes and relative branching ratios. The uncertainty in the lifetime predictions comes from details of the theory, such as masses and coupling constants of unknown heavy particles, as well as poorly known details of matrix elements for quarks within the nucleon.

It is apparent from Figure 2.11 that a continued search for proton decay is by no means assured

[§]In these models, the quantum number $B - L$ is expected to be conserved even though B and L are not individually conserved.

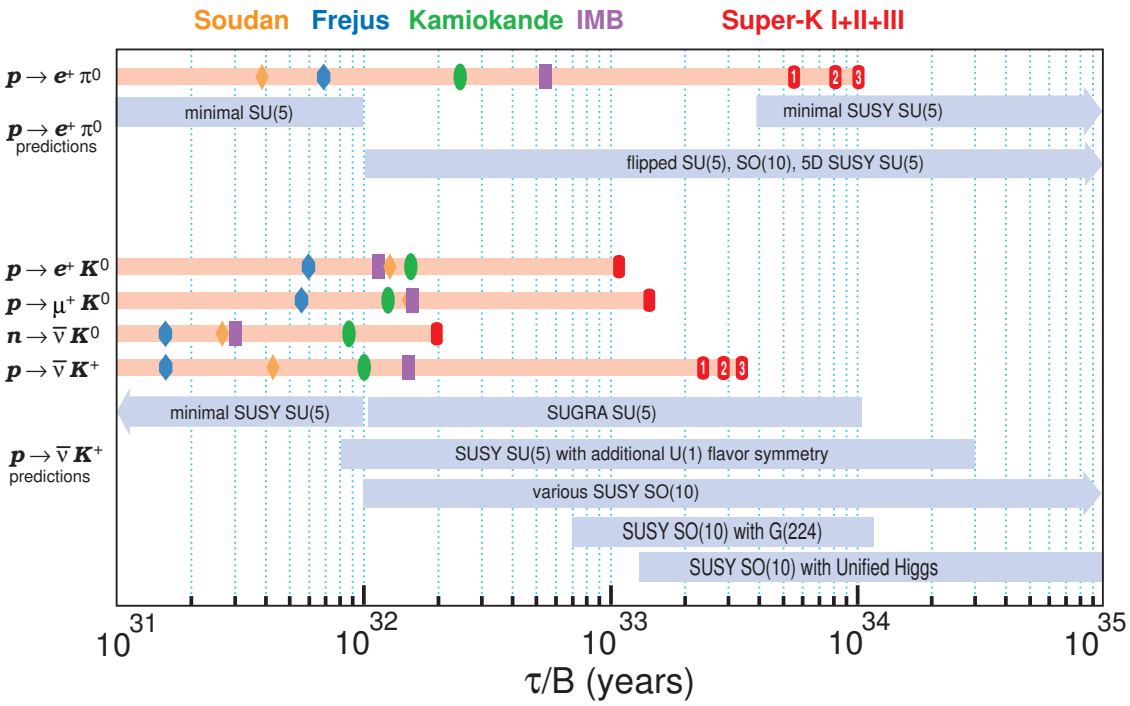

Figure 2.11: Proton decay lifetime limits [55,102] compared to lifetime ranges predicted by Grand Unified Theories. The upper section is for $p \rightarrow e^{+}\pi^{0}$, most commonly caused by gauge mediation. The lower section is for SUSY-motivated models, which commonly predict decay modes with kaons in the final state. The marker symbols indicate published experimental limits, as indicated by the sequence and colors on top of the figure.

of obtaining a positive result. With that caveat, an experiment with sensitivity to proton lifetimes between 10^{33} and 10^{35} years is searching in the right territory over virtually all GUTs; even if no proton decay is detected, stringent lifetime limits will provide strong constraints on such models. Minimal SU(5) was ruled out by the early work of IMB and Kamiokande and minimal SUSY SU(5) is considered to be ruled out by Super–Kamiokande. In most cases, another order of magnitude in improved limits will not rule out specific models but will constrain their allowed parameters; this could allow identification of models which must be fine-tuned in order to accommodate the data, and are thus less favored.

As Chapter 5 will show, the performance and scalability of the LArTPC technology opens up nucleon decay channels that are not as readily accessible in existing and proposed water Cherenkov detectors, providing LBNE with a unique and compelling opportunity for discovery.

2.4 Supernova-Neutrino Physics and Astrophysics

For over half a century, researchers have been grappling to understand the physics of the neutrino-driven core-collapse supernova. The interest in observing the core-collapse supernova explosion mechanism comes from the key role supernovae of this type have played in the history of the Universe. Without taking supernova feedback into account, for example, modern simulations of galaxy formation cannot reproduce the structure of our galactic disk. More poetically, the heavy elements that are the basis of life on Earth were synthesized inside stars and ejected by supernova explosions.

Neutrinos from a core-collapse supernova are emitted in a burst of a few tens of seconds duration, with about half emitted in the first second. They record the information about the physical processes in the center of the explosion during the first several seconds — as it is happening. Energies are in the few-tens-of-MeV range and luminosity is divided roughly equally between flavors. The basic model of core collapse was confirmed by the observation of neutrino events from SN1987A, a supernova in the Large Magellanic Cloud — outside the Milky Way — 50 kpc (kiloparsecs) away. Nineteen events were detected in two water Cherenkov detectors [103,104] and additional events were reported in a scintillator detector [105]. The neutrino signal from a core-collapse supernova in the Milky Way is expected to generate a high-statistics signal from which LBNE could extract a wealth of information [106,107].

The expected rate of core-collapse supernovae is two to three per century in the Milky Way [108,109]. In a 20-year experimental run, LBNE's probability of observing neutrinos from a core-collapse supernova in the Milky Way is about 40%. The detection of thousands of supernova-burst neutrinos from this event would dramatically expand the science reach of the experiment, allowing observation of the development of the explosion in the star's core and probing the equation-of-state of matter at nuclear densities. In addition, independent measurements of the neutrino mass hierarchy and the θ_{13} mixing angle are possible, as well as additional constraints on physics beyond the Standard Model.

Each of the topics that can be addressed by studying supernova-burst neutrinos represent important outstanding problems in modern physics, each worthy of a separate, dedicated experiment, and the neutrino physics and astrophysics communities would receive payback simultaneously. The opportunity of targeting these topics in a single experiment is very attractive, especially since it may come only at incremental cost to the LBNE Project.

The explosion mechanism is thought to have three distinct stages: the collapse of the iron core, with the formation of the shock and its breakout through the neutrinosphere; the accretion phase, in which the shock temporarily stalls at a radius of about 200 km while the material keeps raining in; and the cooling stage, in which the hot proto-neutron star loses its energy and trapped lepton

number, while the re-energized shock expands to push out the rest of the star. Each of these three stages is predicted to have a distinct signature in the neutrino signal. Thus, it should be possible to directly observe, for example, how long the shock is stalled. More exotic features of the collapse may be observable in the neutrino flux as well, such as possible transitions to quark matter or to a black hole. (An observation in conjunction with a gravitational wave detection would be especially interesting; e.g. [110,111].)

Over the last two decades, neutrino flavor oscillations have been firmly established in solar neutrinos and a variety of terrestrial sources. The physics of the oscillations in the supernova environment promises to be much richer than in any of the cases measured to date, for a variety of reasons:

- Neutrinos travel through the changing profile of the explosion with stochastic density fluctuations behind the expanding shock and, due to their coherent scattering off of each other, their flavor states are coupled.
- The oscillation patterns come out very differently for the normal and inverted mass hierarchies.
- The expanding shock and turbulence leave a unique imprint in the neutrino signal.
- Additional information on oscillation parameters, free of supernova model-dependence, will be available if matter effects due to the Earth can be observed in detectors at different locations around the world [112,113].
- The observation of this potentially copious source of neutrinos will also allow limits on coupling to axions, large extra dimensions, and other exotic physics (e.g., [114,115]).
- The oscillations of neutrinos and antineutrinos from a core-collapse supernova manifest very differently. In the neutrino channel, the oscillation features are in general more pronounced, since the initial spectra of ν_e and ν_μ (ν_τ) are always significantly different. It would be extremely valuable to detect both neutrino and antineutrino channels with high statistics.

Only about two dozen neutrinos were observed from SN1987A, which occurred in a nearby galaxy; in contrast, the currently proposed next-generation detectors would register thousands or tens of thousands of interactions from a core-collapse supernova in our galaxy. The type of observed interactions will depend on the detector technology: a water-Cherenkov detector is primarily sensitive to $\overline{\nu}_e$'s, whereas a LArTPC detector has excellent sensitivity to ν_e's. In each case, the high event rate implies that it should be possible to measure not only the time-integrated spectra, but also their second-by-second evolution. This is a key feature of the supernova-burst physics potential of the planned LBNE experiment.

Currently, experiments worldwide are sensitive primarily to $\overline{\nu}_e$'s, via inverse-beta decay on free protons, which dominates the interaction rate in water and liquid-scintillator detectors. Liquid argon exhibits a unique sensitivity to the ν_e component of the flux, via the absorption interaction on

^{40}Ar, $\nu_e + {}^{40}\mathrm{Ar} \rightarrow e^- + {}^{40}\mathrm{K}^*$. In principle, this interaction can be tagged via the coincidence of the electron and the $^{40}\mathrm{K}^*$ de-excitation gamma cascade. About 900 events would be expected in a 10-kt fiducial liquid argon detector for a core-collapse supernova at 10 kpc. The number of signal events scales with mass and the inverse square of distance, as shown in Figure 2.12. For a collapse

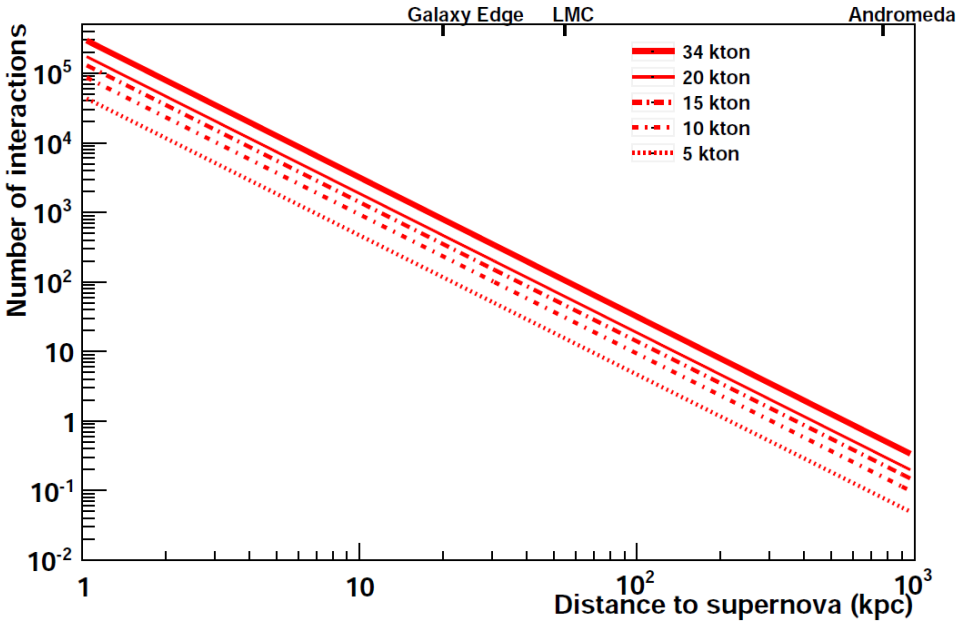

Figure 2.12: Number of supernova neutrino interactions in a liquid argon detector as a function of distance to the supernova for different detector masses. Core collapses are expected to occur a few times per century, at a most-likely distance from 10 kpc to 15 kpc.

in the Andromeda galaxy, massive detectors of hundreds of kilotons would be required to observe a handful of events. However, for supernovae within the Milky Way, even a relatively small 10-kt detector would gather a significant ν_e signal.

Because the neutrinos emerge promptly after core collapse, in contrast to the electromagnetic radiation which must beat its way out of the stellar envelope, an observation could provide a prompt supernova alert [116,117], allowing astronomers to find the supernova in early light turn-on stages, which could yield information about the progenitor (in turn, important for understanding oscillations). Further, observations and measurements by multiple, geographically separated detectors during a core collapse — of which several are expected to be online over the next few decades [106,118] — will enhance the potential science yield from such a rare and spectacular event [112].

Chapter 3 Project and Design

The LBNE Project was formed to design and construct the Long-Baseline Neutrino Experiment. The experiment will comprise a new, high-intensity neutrino source generated from a megawatt-class proton accelerator at Fermi National Accelerator Laboratory (Fermilab) directed at a large far detector at the Sanford Underground Research Facility in Lead, SD. A near detector will be located about 500 m downstream of the neutrino production target. LBNE is currently planned as a phased program, with increased scientific capabilities at each phase.

- The experimental facilities are designed to meet the primary scientific objectives of the experiment: (1) fully characterize neutrino oscillations, including measuring the value of the unknown CP-violating phase, δ_{CP}, and determining the ordering of the neutrino mass states, (2) significantly improve proton decay lifetime limits, and (3) measure the neutrino flux from potential core-collapse supernovae in our galaxy.
- The LBNE beamline, based on the existing *Neutrinos at the Main Injector* (NuMI) beamline design, is designed to deliver a wide-band, high-purity ν_μ beam with a peak flux at 2.5 GeV, which optimizes the oscillation physics potential at the 1,300-km baseline. The beamline will operate initially at 1.2 MW and will be upgradable to 2.3 MW utilizing a proton beam with energy tunable from 60 to 120 GeV.
- The full-scope LBNE far detector is a liquid argon time-projection chamber (LArTPC) of fiducial mass 34 kt.

  The TPC design is modular, allowing flexibility in the choice of initial detector size.
- The LBNE far detector will be located 4,850 feet underground, a depth favorable for LBNE's search for proton decay and detection of the neutrino flux from a core-collapse supernova.
- The high-precision near detector and its conventional facilities can be built as an independent project, at the same time as the far detector and beamline, or later.

3.1 LBNE and the U.S. Neutrino Physics Program

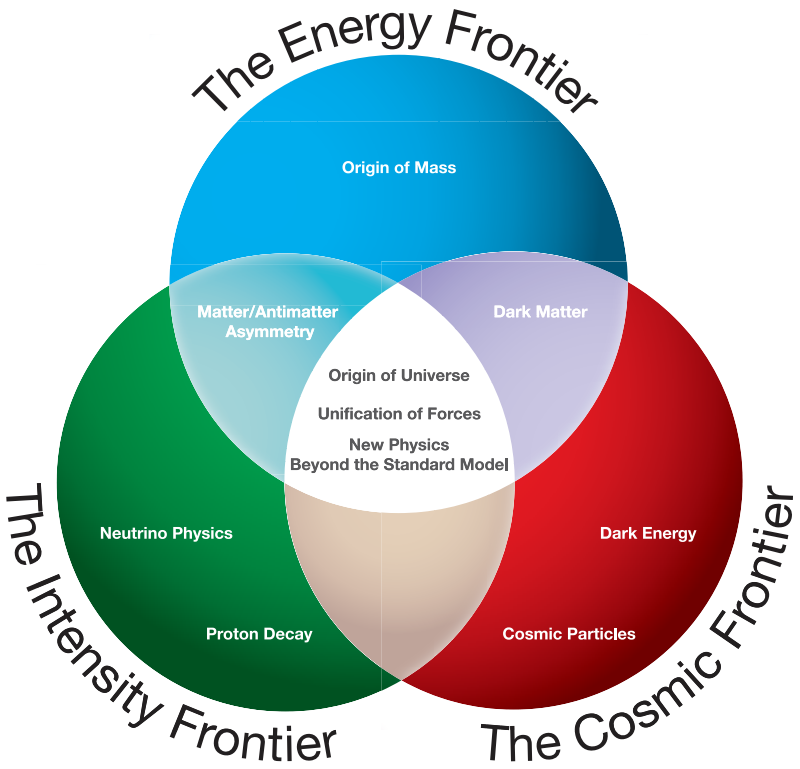

Figure 3.1: Three frontiers of research in particle physics form an interlocking framework that addresses fundamental questions about the laws of Nature and the cosmos. Each frontier, essential to the whole, has a unique approach to making discoveries [14].

In its 2008 report, the U.S. Particle Physics Project Prioritization Panel (P5)* recommended a world-class neutrino physics program as a core component of a U.S. particle physics program [14] that revolves around three research frontiers as shown in Figure 3.1. Included in the report is the long-term vision of a large far detector at the site of the former Homestake Mine in Lead, SD, and a high-intensity, wide-band neutrino source at Fermilab. At the time, the proposed Deep Underground Science and Engineering Laboratory (DUSEL) was planned to occupy the site of the former mine; it is now the Sanford Underground Research Facility.

*P5 is an advisory panel to the two main funding bodies for particle physics in the United States, the Department of Energy (DOE) and the National Science Foundation (NSF).

On January 8, 2010 the DOE approved the Mission Need [18] statement† for a new long-baseline neutrino experiment that would enable this world-class program and firmly establish the U.S. as the leader in neutrino science. The LBNE experiment is designed to meet this Mission Need.

With the facilities provided by the LBNE Project and the unique features of the experiment — in particular the long baseline of 1,300 km, the wide-band beam and the high-resolution, underground far detector — LBNE will conduct a broad scientific program addressing key physics questions concerning the nature of our Universe as described in Chapter 2. The focus of the long-baseline neutrino program will be the explicit demonstration of leptonic CP violation, if it exists, and the determination of the neutrino mass hierarchy.

The 1,300-km baseline has been determined to provide optimal sensitivity to CP violation and the measurement of δ_{CP}, and is long enough to enable an unambiguous determination of the neutrino mass hierarchy [83].

The focus of the non-beam scientific program will be to search for proton decay, to enable detailed studies of atmospheric neutrinos, and to detect and measure the neutrino flux from a supernova, should one occur within our galaxy.

It is currently planned to implement LBNE as a phased program, with increased scientific capabilities at each phase. The initial phase of LBNE will achieve significant advances with respect to its primary scientific objectives as compared to current experiments. The *goal* for the initial phase of LBNE is:

1. A new neutrino beamline at Fermilab driven by a 60 to 120 GeV proton beam with power of up to 1.2 MW.
2. A liquid argon time-projection chamber (LArTPC) detector of fiducial mass at least 10 kt located at the Sanford Underground Research Facility at a depth of 4,850 feet.
3. A high-precision near neutrino detector on the Fermilab site.

The cost for this initial phase (with a 10-kt far detector) is estimated to be 1.2B U.S.$ according to DOE standard project accounting.

In December of 2012, the DOE issued CD-1 (Conceptual Design phase) approval for a budget of 867M$ U.S. based on a reduced scope that excluded the near neutrino detector and the underground placement of the far detector. Domestic and international partners are being sought to enable construction of the full first-phase scope outlined above. Subsequent phases of LBNE are expected to include additional far detector mass and upgrades of the beam to $\geq$2.3-MW capability.

†A *Mission Need* statement initiates the process and provides initial funding toward developing the conceptual design of a DOE scientific project.

3.2 Near Site: Fermi National Accelerator Laboratory

Fermilab, located 40 miles west of Chicago, Illinois, is a DOE-funded laboratory dedicated to high energy physics. The laboratory builds and operates accelerators, detectors and other facilities that physicists from all over the world use to carry out forefront research.

Dramatic discoveries in high energy physics have revolutionized our understanding of the interactions of the particles and forces that determine the nature of matter in the Universe. Two major components of the Standard Model of Fundamental Particles and Forces were discovered at Fermilab: the bottom quark (May-June 1977) and the top quark (February 1995). In July 2000, Fermilab experimenters announced the first direct observation of the tau neutrino, thus filling the final slot in the lepton sector of the Standard Model. Run II of the Fermilab Tevatron Collider was inaugurated in March 2001. The Tevatron was the world's highest-energy particle accelerator and collider until the Large Hadron Collider at CERN came online in 2011.

While CERN now hosts the world's highest-energy particle collider, the Fermilab accelerator complex is being retooled to produce the world's highest-intensity beams of protons, muons and neutrinos. Scientists from around the world can exploit this capability to pursue cutting-edge research in the lepton sector of the Standard Model where strong hints of new physics have surfaced.

The beamline and near detector for LBNE will be constructed at Fermilab, referred to as the *Near Site*.

Fermi National Accelerator Laboratory, originally named the National Accelerator Laboratory, was commissioned by the U.S. Atomic Energy Commission, under a bill signed by President Lyndon B. Johnson on November 21, 1967. On May 11, 1974, the laboratory was renamed in honor of 1938 Nobel Prize winner Enrico Fermi, one of the preeminent physicists of the atomic age.

Today, the DOE operates national laboratories throughout the United States, including Fermilab. The DOE awarded to Fermi Research Alliance (FRA) the management and operating contract for Fermilab, effective January 1, 2007. The FRA is a tax-exempt, limited liability company (LLC) organized and operated for charitable, scientific and educational purposes under Section 501(c)(3) of the Internal Revenue Code. The two members of FRA are the University of Chicago and the Universities Research Association (URA). FRA has earned extensions to the Fermilab contract through Dec. 31, 2015.

At Fermilab, a robust scientific program pushes forward on the three interrelated scientific frontiers specified by the P5 panel in 2008 [14] and illustrated in Figure 3.1:

1. At the Energy Frontier, Fermilab scientists are significant contributors to the LHC and to the CMS experiment.

2. At the Intensity Frontier, Fermilab operates two neutrino beams that support a number of experiments. In the next few years several new neutrino and muon experiments will be coming online, of which LBNE will be the largest.

3. At the Cosmic Frontier, Fermilab runs and/or participates in several experiments, with instruments installed in North America, South America and Europe.

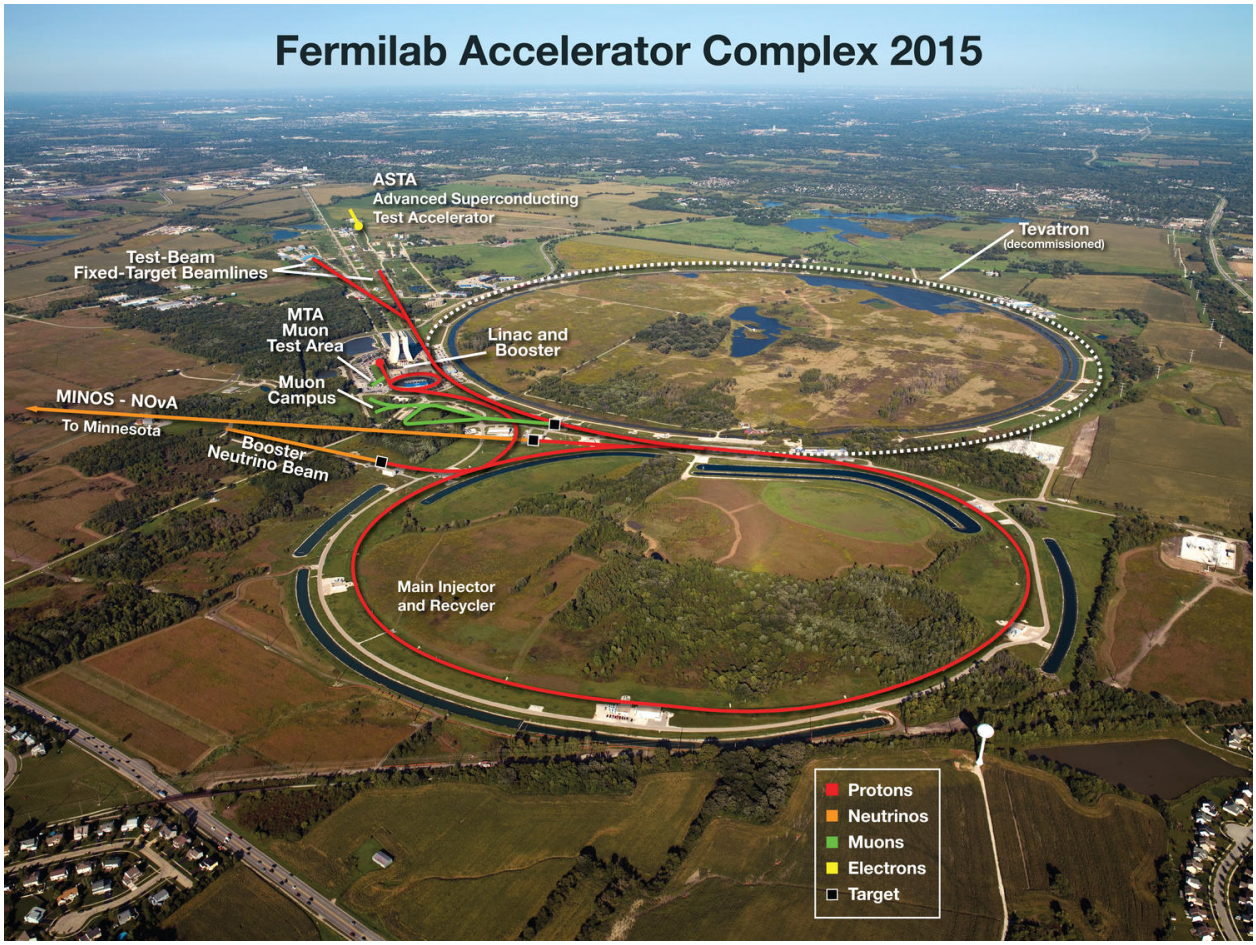

Figure 3.2: The accelerator chain at Fermi National Accelerator Laboratory. A 400-MeV linear accelerator (linac) feeds into the 15-Hz Booster, which produces an 8-GeV beam. The Booster beam is used for the Booster Neutrino Beamline experiments. The Booster feeds into the 120-GeV Main Injector. The Main Injector is the source for the NuMI beamline, which supplies a high-power, high-energy neutrino beam to the MINOS/MINOS+ and NOνA experiments.

The neutrino beams at Fermilab come from two of the lab's proton accelerators (Figure 3.2), the 8-GeV Booster, which feeds the *Booster Neutrino Beamline* (BNB), and the 120-GeV Main Injector (MI), which feeds the NuMI beamline. The LBNE beamline, described in Section 3.4, will utilize the MI beam.

NuMI, on which LBNE's beamline design is based, is a high-energy neutrino beam that has been operating since 2004. It was designed for steady 400-kW operation and achieved that goal by the end of the MINOS experimental run in 2012. As shown in Figure 3.3, the NuMI beamline was running with an average of 9×10^{18} protons per week ($\approx 2.7 \times 10^{20}$ protons-on-target per year) in mid 2012.

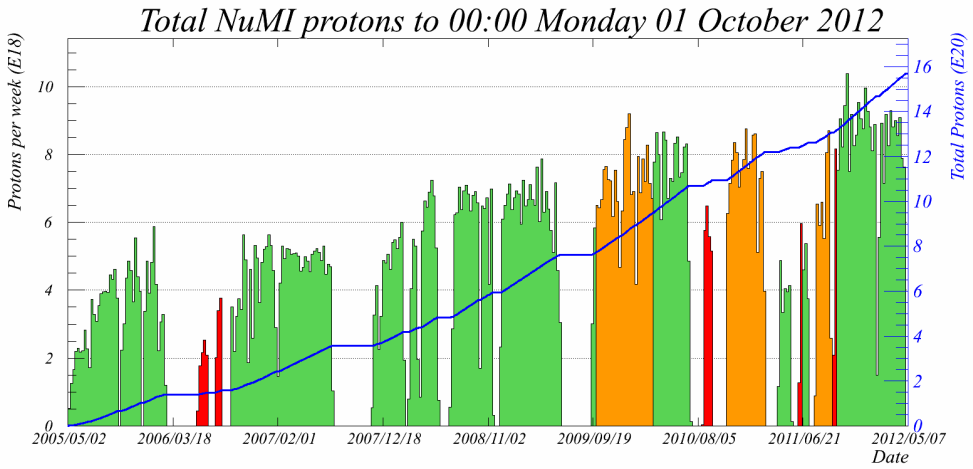

Figure 3.3: The NuMI beamline performance

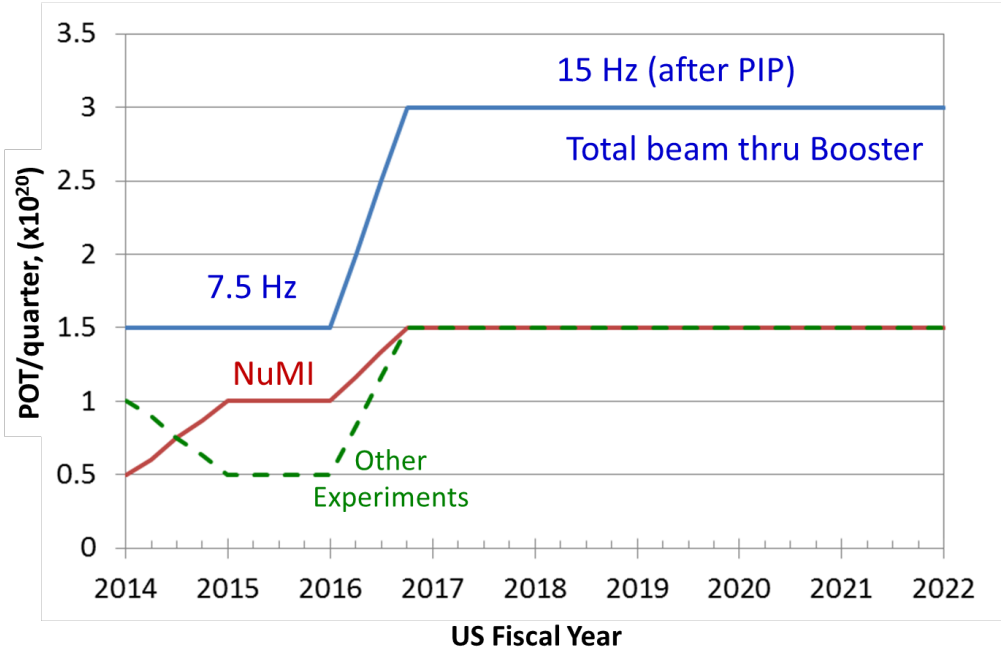

Figure 3.4: A possible ramp-up scenario for proton flux from Fermilab's proton source for the Intensity Frontier experiments.

Upgrades to the Recycler[‡] and MI as part of the NOνA Project, as well as the Proton Improvement Plan (PIP) that is currently underway, comprise a set of improvements to the existing Linac, Booster and MI aimed at supporting 15-Hz beam operations from the Booster (Figure 3.4).

In combination, the NOνA upgrades and the PIP create a capability of delivering 700 kW from the MI at 120 GeV ($\approx 6 \times 10^{20}$ proton-on-target per year) by 2016. The proton beam power expected to be available as a function of MI beam energy after completion of the PIP upgrades is shown in Figure 3.5.

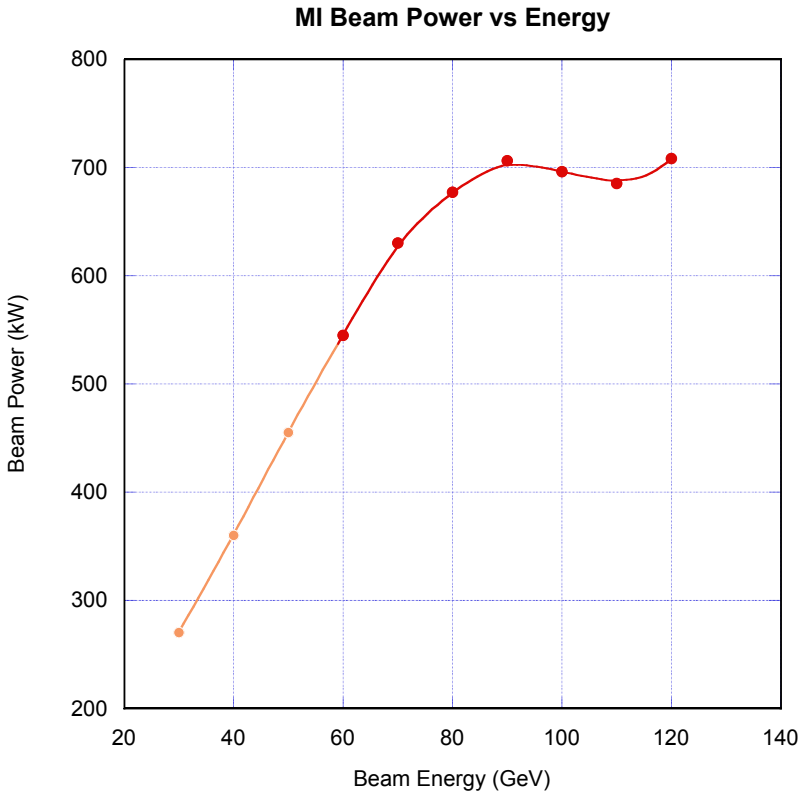

Figure 3.5: Proton beam power expected to be available as a function of MI beam energy after proton-improvement-plan (PIP) upgrades.

A conceptual plan for further upgrades to the Fermilab accelerator complex has been completed. Called the *Proton Improvement Plan-II* (PIP-II) [22], its goal is to increase the capabilities of the existing accelerator complex to support delivery of 1.2 MW of beam power to the LBNE production target at the initiation of operations, while simultaneously providing a platform for subsequent upgrades of the complex to multi-MW capability. The starting point of this plan is the *Project X Reference Design Report* [23].

[‡]The Recycler, a fixed 8-GeV kinetic energy storage ring located directly above the MI beamline, stores protons from the 8-GeV Booster during MI ramp up.

The primary bottleneck to providing increased beam power at Fermilab is the Fermilab Booster, limited by space-charge forces at injection. In the intermediate term the most cost-effective approach to removing this bottleneck is to increase the injection energy into the Booster. The PIP-II meets this goal via an 800-MeV superconducting linear accelerator (linac), operated at low duty factor, but constructed of accelerating modules that are capable of continuous-wave (CW) operations if provided with sufficient cryogenic cooling and appropriate RF power. This is expected to increase the beam intensity delivered from the Booster by 50% relative to current operations. Shortening the MI cycle time to 1.2 s yields a beam power of 1.2 MW at 120 GeV. The conceptual site layout of PIP-II is shown in Figure 3.6. Further possible upgrades beyond PIP-II would require replacing the 8-GeV Booster with a superconducting linac injecting into the MI at energies between 6 and 8 GeV as shown in Figure 3.6, eventually increasing the power from the MI to 2.0–2.3 MW at 60–120 GeV.

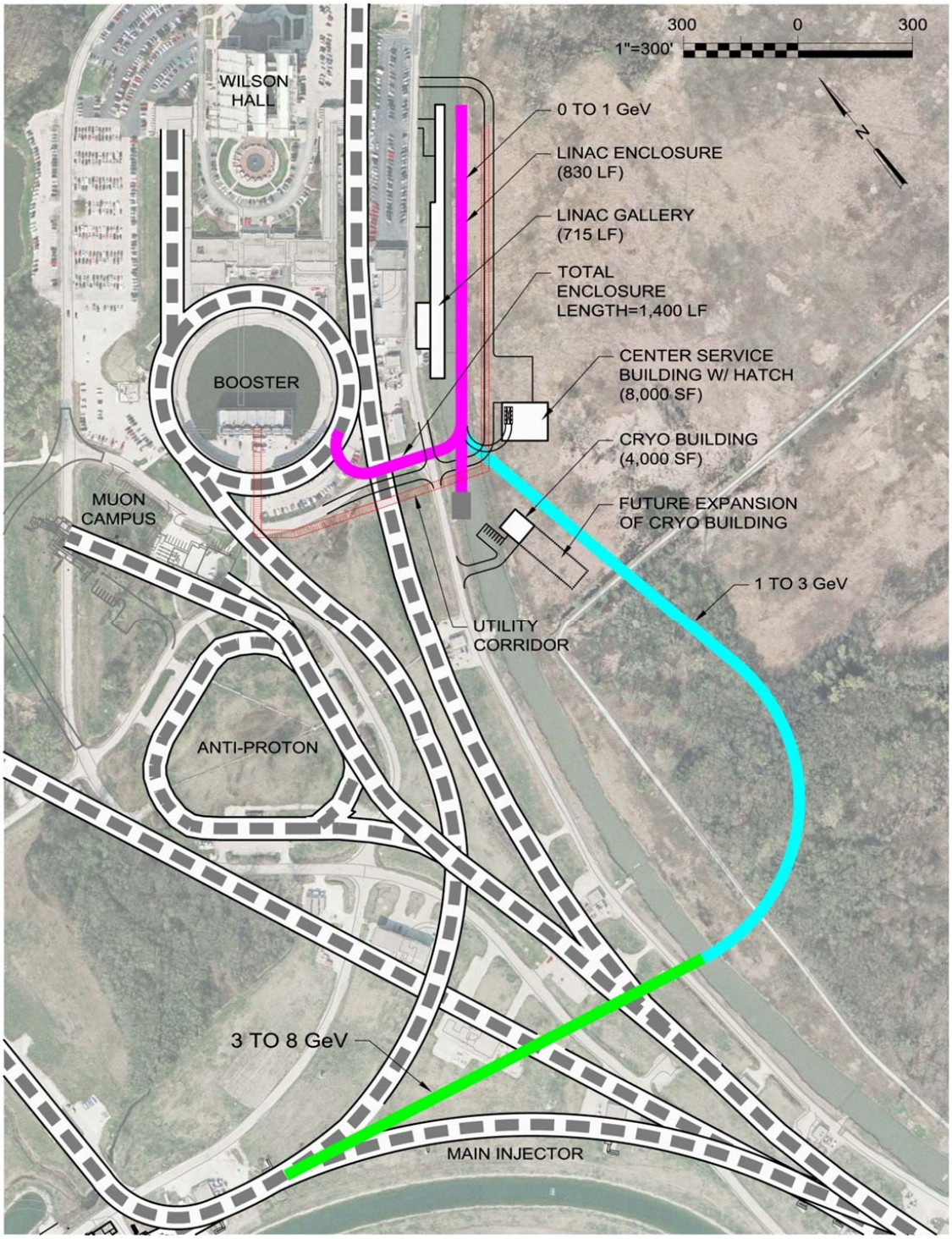

Figure 3.6: Site layout of PIP- II is shown as the magenta line which is the 800 MeV linac enclosure and transfer line. New construction includes the linac enclosure, transfer line enclosure, linac gallery, center service building, utility corridor, and cryo building. Dashed areas represent existing or planned underground enclosures. Further possible upgrades to the Fermilab complex beyond PIP- II are shown in the bottom half of the figure: cyan is a 1-3 GeV CW linac and transfer line, and green is a 3-8 GeV pulsed linac [22].

3.3 Far Site: Sanford Underground Research Facility

The Sanford Underground Research Facility [119] is a laboratory located on the site of the former Homestake gold mine in Lead, SD that is dedicated to underground science. This laboratory has been selected as the location of the far detector for LBNE, and is referred to as the *Far Site*.

Underground neutrino experiments in the former mine date back to 1967 when nuclear chemist Ray Davis installed a solar neutrino experiment 4,850 feet below the surface [120]. Ray Davis earned a share of the Nobel Prize for physics in 2002 for his experiment, which ran until 1993.

LBNE is envisioned as the next-generation, multi-decade neutrino experiment at this site seeking groundbreaking discoveries.

In 2006, Barrick Gold Corporation donated the Homestake Gold Mine site, located in Lead, South Dakota (Figure 3.7) to the State of South Dakota, following over 125 years of mining. Mining operations created over 600 km of tunnels and shafts in the facility, extending from the surface to over 8,000 feet below ground. The mining levels are distributed ∼150 feet apart and are referenced by their depth below the facility entrance, e.g., the level 4,850 feet below ground is referred to as the *4850L*. This former mine encompasses the deepest caverns in the western hemisphere, offering extensive drifts both vertically and laterally. A detailed vertical cross section of the 60 underground levels developed for mining is shown in Figure 3.8.

In 2004, the South Dakota state legislature created the South Dakota Science and Technology Authority (SDSTA) to foster scientific and technological investigations, experimentation and development in South Dakota. A six-member board of directors appointed by the governor of South Dakota directs the SDSTA. The SDSTA's first task was to reopen the former Homestake site to the 4,850-foot level for scientific research. At this site, the SDSTA now operates and maintains the Sanford Underground Research Facility through a contract managed and overseen by a dedicated operations office at Lawrence Berkeley National Laboratory as a deep-underground research laboratory. The Sanford Underground Research Facility property comprises 186 acres on the surface and 7,700 acres underground. The surface campus includes approximately 253,000 gross square feet of existing structures. A surface schematic of the campus is shown in Figure 3.9.

The state legislature has since committed more than $40 million in state funds to the development of the Sanford Underground Research Facility, and the state has also obtained a $10 million Community Development Block Grant to help rehabilitate the site. In addition, a $70 million donation from philanthropist T. Denny Sanford has been used to reopen the site for science and to establish the Sanford Center for Science Education. The initial concepts for the facility were developed with

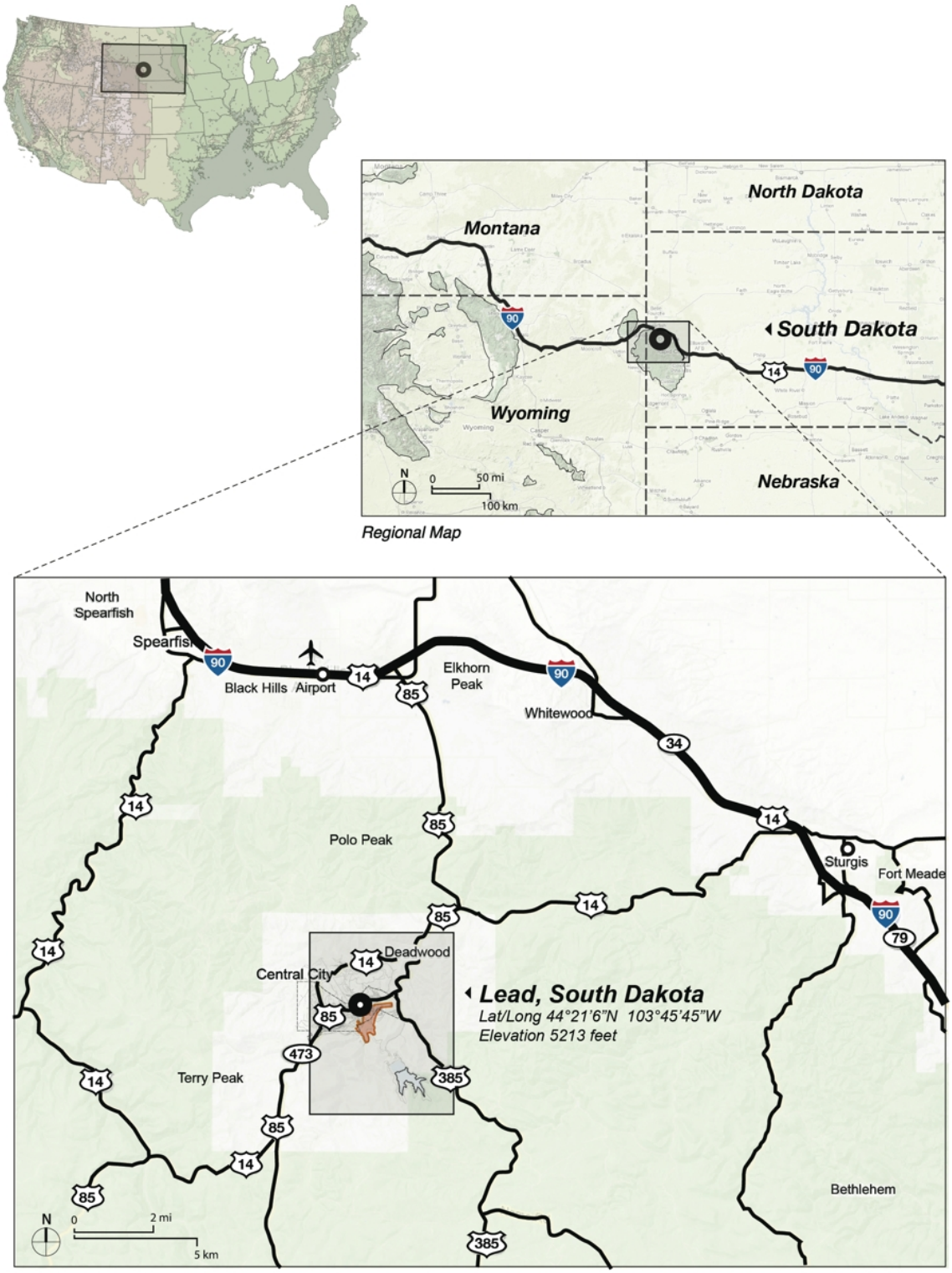

Figure 3.7: Location of the town of Lead, South Dakota - the site of the former Homestake Gold Mine.

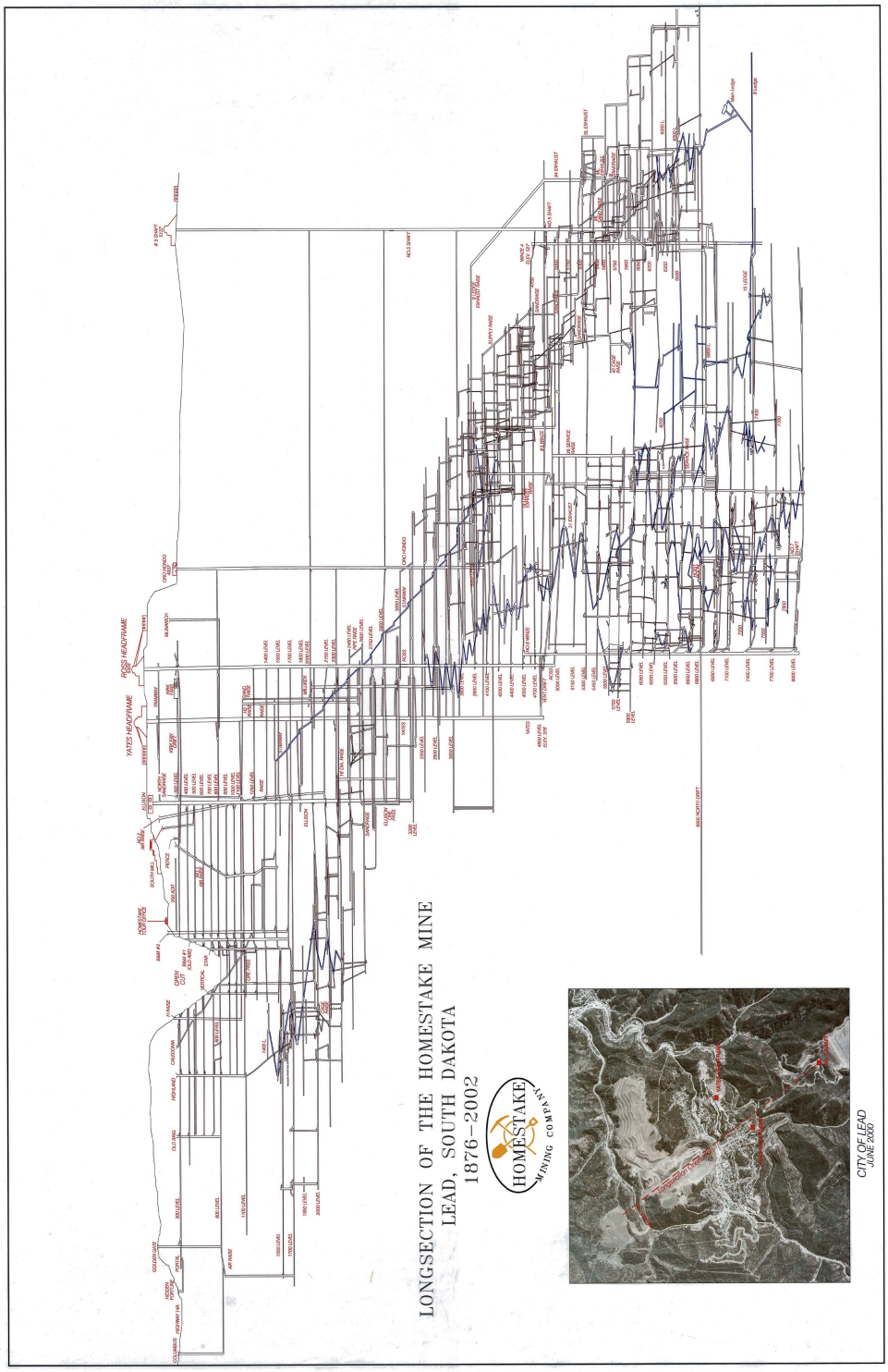

Figure 3.8: The long section of the former Homestake Gold Mine. This figure illustrates the 60 underground levels extending to depths greater than 8,000 feet. The location of cross section is indicated in the inset along a NW to SE plane. The projection extends for 5.2 km along this plane

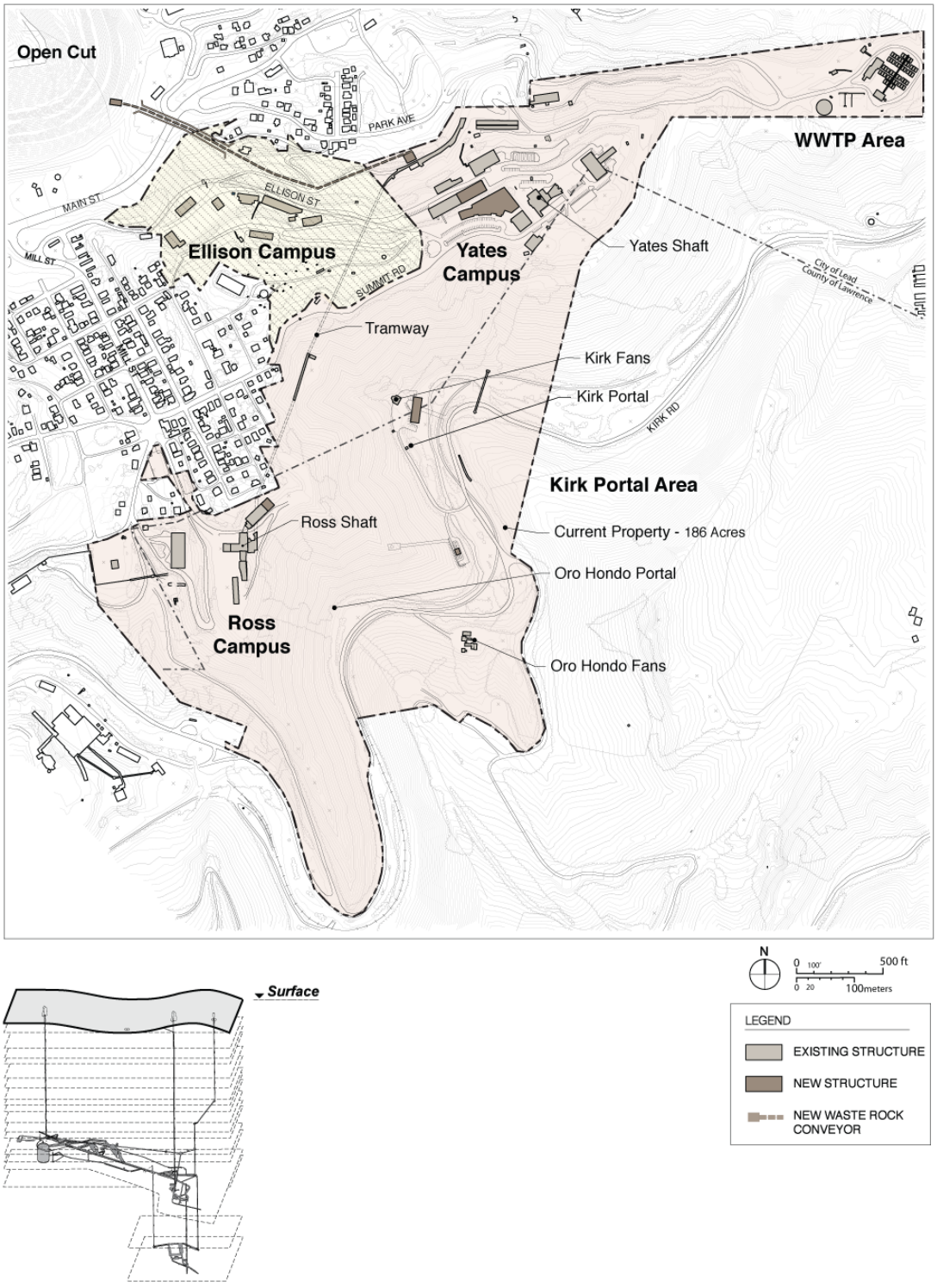

Figure 3.9: The surface and underground campuses of the Sanford Underground Research Facility. The 3D inset image illustrates the plans to develop the 4850L and 7400L. Most current experiments are at the 4850L.

the support of the U.S. National Science Foundation (NSF) as the primary site for the NSF's Deep Underground Science and Engineering Laboratory (DUSEL). With the National Science Board's decision to halt development of the NSF-supported underground laboratory, the DOE now supports the operation of the facility in addition to state and private funding. Both the NSF and the DOE support experiments at the site.

Access to the underground areas has been reestablished and the primary access rehabilitated and improved. The facility has been stabilized and the accumulated underground water has been pumped out below 5,680 ft. The area around the Davis cavern at the 4850L, named for the late Ray Davis, has been enlarged and adapted primarily for current and next-generation dark matter and neutrinoless double-beta decay experiments. This upgraded area of the 4850L is now called the Davis Campus. Additional science efforts are located throughout the facility, including an ultrapure detector development laboratory, geophysics and geological efforts, and a public outreach program. A 3D schematic highlighting the planned development of the 4850L is shown in Figure 3.10. The

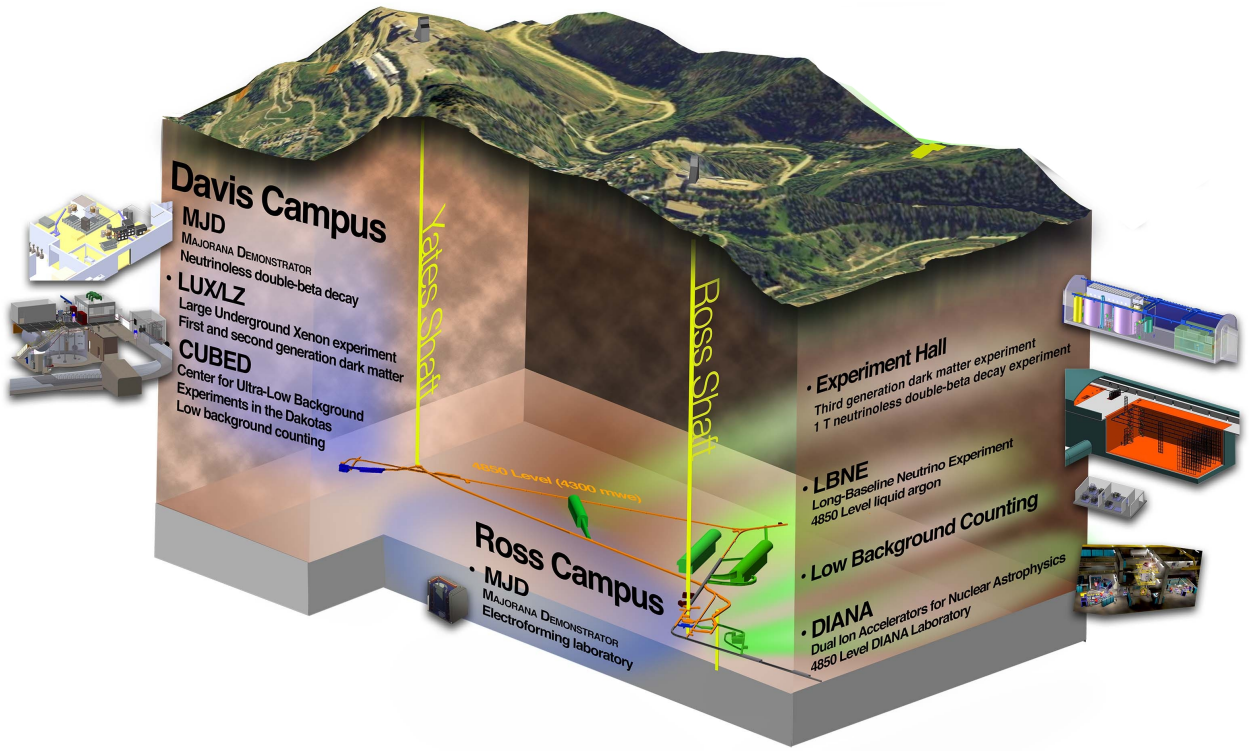

Figure 3.10: Layout of experiments at the 4,850-ft level in the Sanford Underground Research Facility

LBNE far detector will be located in new excavated spaces near the bottom of the Ross Shaft, about 1 km from the Davis Campus. The 4,850-ft depth makes it an extremely competitive location in terms of cosmic-ray background suppression for undertaking the nucleon decay and supernova neutrino studies that LBNE plans to address. Figure 3.11 shows the predicted cosmic-ray flux at this site [121] as compared to other underground laboratories worldwide.

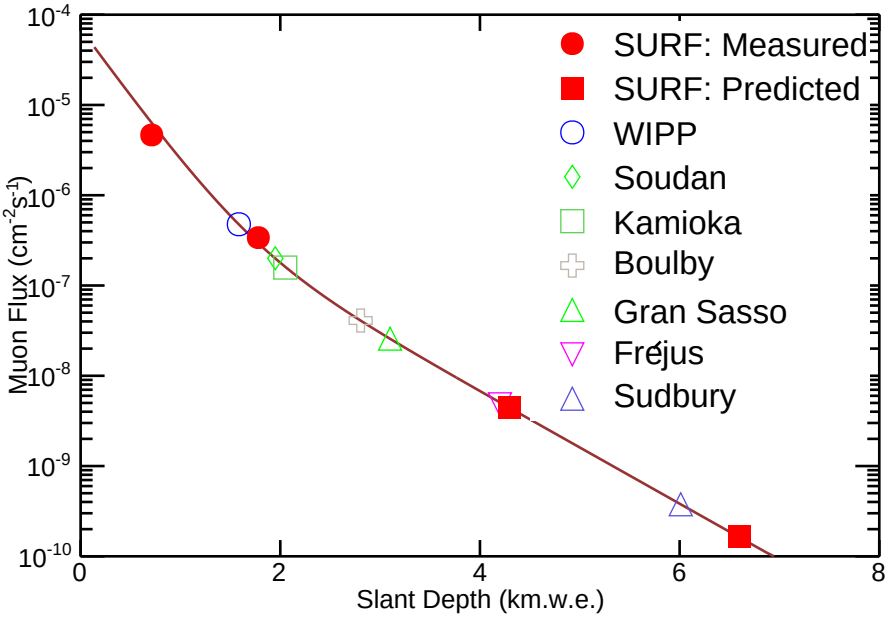

Figure 3.11: Predicted cosmic-ray flux as a function of depth. The predicted muon flux at the 4,850 ft and 8,000 ft levels of the Sanford Underground Research Facility (SURF) are show as red squares. Two measured depths in the facility are shown as red circles. Values for other underground laboratories are also shown [121]. The line shows a parameterized model of the muon flux.

Another advantage of the 4850L Sanford Underground Research Facility site for LBNE is the low level of rock radioactivity that could contribute backgrounds to the supernova burst neutrino signal and other low-energy physics searches. It was found that the U/Th/K radioactivity for the underground bedrocks at Homestake is in general very low when compared to common construction materials such as concrete and shotcrete; some samples are in the sub-ppm levels. However, samples from rhyolite intrusions, *a very small fraction of the total*, show a relatively high content of U, Th, and K more typical of the levels found in other laboratories, in particular those in granitic formations. Regions of potential rhyolite intrusions have been identified and documented as shown in Figure 3.12. In some cases local shielding significantly mitigates the impact of the rhyolite intrusions. Table 3.1 presents some of the assay results, obtained by direct gamma counting for rock samples from the mine, including those collected close to the 4850L [122]. The Large Underground Xenon (LUX) experiment is now operating in the cavern first excavated for Davis in the 1960s. LUX is the most sensitive detector yet to search for dark matter [123]. The Majorana Demonstrator experiment (MJD), also being installed in a newly excavated space adjacent to the original Davis cavern, will search for neutrinoless double-beta decay. Figure 3.13 shows four photographs of facilities and activities at the Sanford Underground Research Facility related to the LUX and MJD at the 4850L. The LBNE far detector will benefit from the common infrastructure being developed to house large experiments underground. The layout of the different proposed experiments at the 4850L, including the LBNE detector, is shown in Figure 3.10.

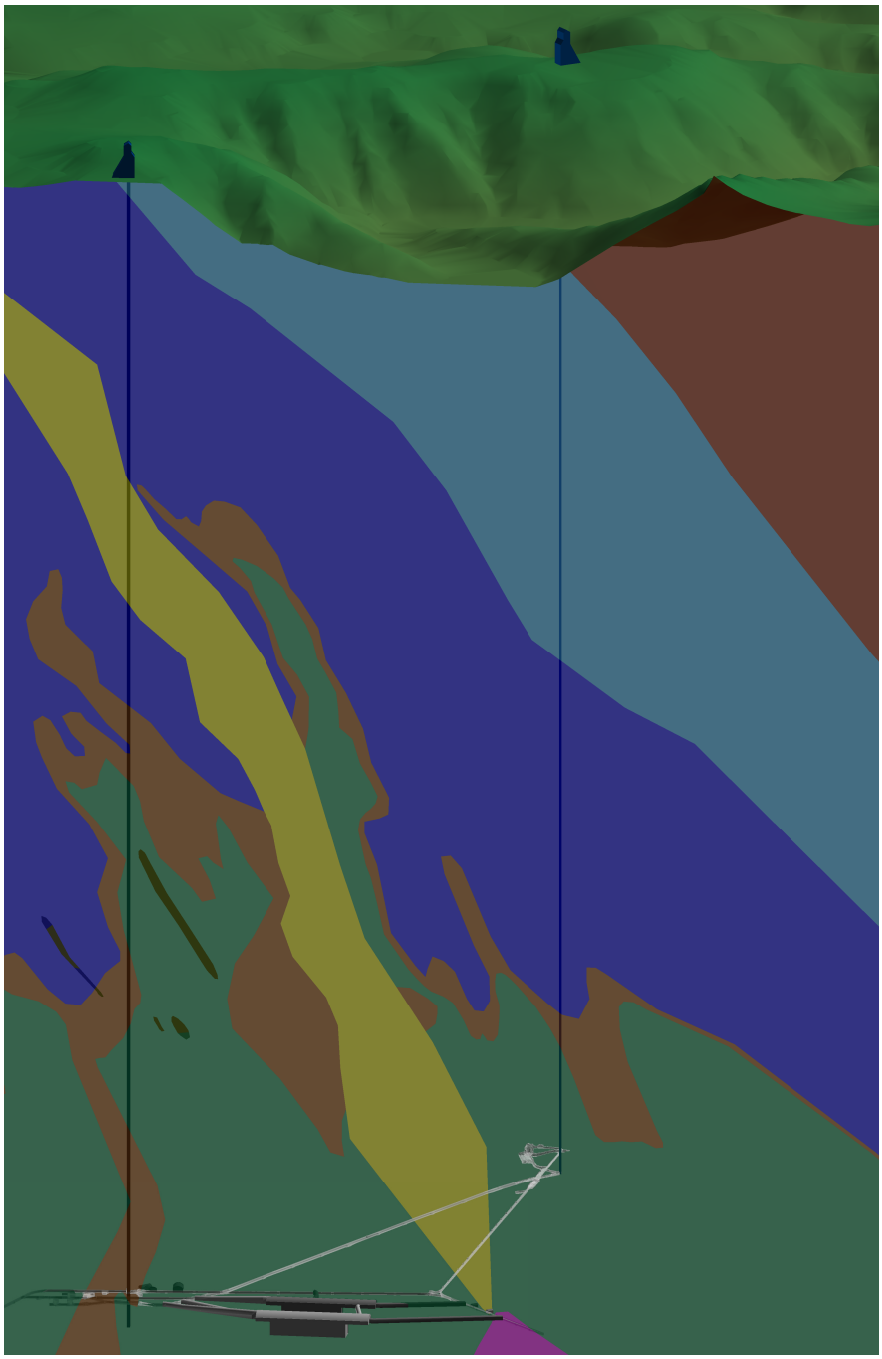

Figure 3.12: Geologic long section of Sanford Underground Research Facility showing the main rock formations. The dark green rock is the Poorman formation, and the yellow areas indicate a projected rhyolite swarm. The proposed location of two LBNE detector caverns are shown in the foreground.

In addition to LBNE, LUX and MJD, the Sanford Underground Research Facility science program for the coming five to ten years (Figure 3.14) consists of the expansion of the LUX dark matter search, the Center for Ultralow Background Experiments at Dakota (CUBED), and the geoscience installations. Long-term plans are being developed to host a nuclear astrophysics program

Table 3.1: Partial U/Th/K assay results for Sanford Underground Research Facility rock samples. Overall errors estimated to be ∼10-20%. Also shown are results for various construction materials (shotcrete/concrete).

	Uranium (ppm) Ave. [Range]	Thorium (ppm) Ave. [Range]	Potassium (%) Ave. [Range]
U/G Country Rock	0.22 [0.06-0.77]	0.33 [0.24-1.59]	0.96 [0.10-1.94]
Shotcrete	1.89 [1.74-2.23]	2.85 [2.00-3.46]	0.88 [0.41-1.27]
Concrete Blocks	2.16 [2.14-2.18]	3.20 [3.08-3.32]	1.23 [1.27-1.19]
Rhyolite Dike	8.75 [8.00-10.90]	10.86 [8.60-12.20]	4.17 [1.69-6.86]

Figure 3.13: Sanford Underground Research Facility: Administration building and Yates shaft headframe (top left); corridor at 4,850 ft (1,480 m) depth leading to clean rooms and experimental halls (top right); billet of radiopure electroformed copper for the MJD experiment being placed on a lathe in a clean room at 4,850 ft depth (bottom left); LUX experiment at 4,850 ft depth (bottom right).

involving underground particle accelerators (CASPAR and DIANA), and second- and third-generation dark matter experiments.

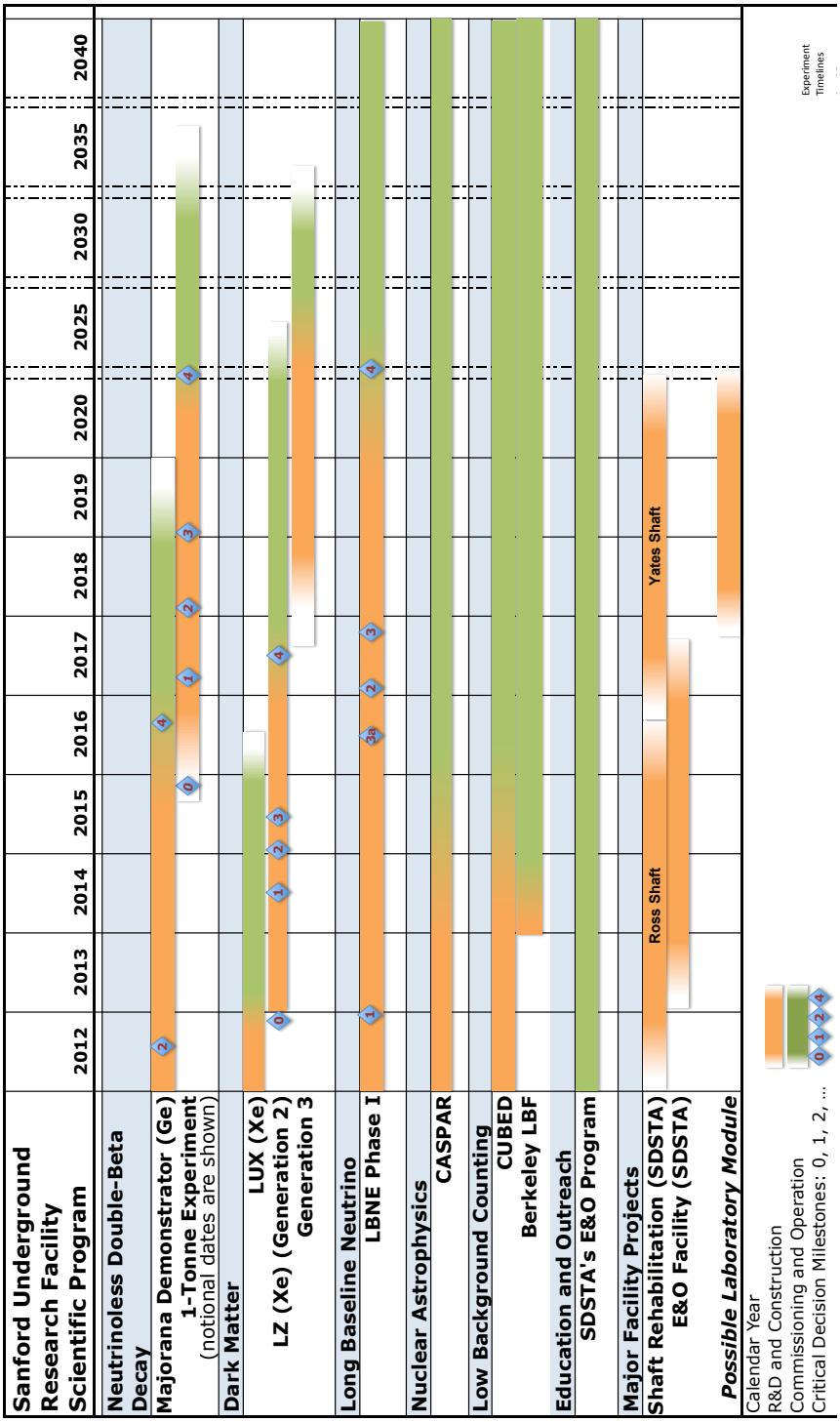

Figure 3.14: Timeline exploring the long-term potential of deep science experiments at the Sanford Underground Research Facility. Figure courtesy of Mike Headley, the Sanford Underground Research Facility.

3.4 Beamline

The LBNE neutrino beamline, located at Fermilab, utilizes a conventional horn-focused neutrino beam produced from pion decay-in-flight, based largely on the highly successful NuMI beamline design:

- The primary beam utilizes 60- to 120-GeV protons from the Main Injector accelerator. The primary beamline is embedded in an engineered earthen embankment — a novel construction concept to reduce costs and improve radiological controls.
- The beamline is designed to operate at 1.2 MW and to support an upgrade to 2.3-MW operation.
- The beamline will generate a wide-band, high-purity beam, selectable for muon neutrinos or muon antineutrinos. Its tunable energies from 60 to 120 GeV will be well matched to the 1,300-km neutrino oscillation baseline.

The LBNE beamline facility will aim a beam of neutrinos toward the LBNE far detector located 1,300 km away at the Sanford Underground Research Facility. The beamline facility, which will be fully contained within Fermilab property, will consist of a primary (proton) beamline, a neutrino beamline, and conventional facilities to support the technical components of the primary and neutrino beamlines [30]. The LBNE beamline reference design parameters approved at CD-1 are summarized in Table 3.2. Improvements to this design that have been made or are being considered are described in this section, including the important change to an initial beam power of 1.2 MW, enabled by the planned PIP-II. The beamline needed for the full-scope LBNE will be realized in the first phase of LBNE and will be upgradable to 2.3 MW.

The primary beam, composed of protons in the energy range of 60-120 GeV, will be extracted from the MI-10 straight section of the Main Injector using single-turn extraction. The beam will then be transported to the target area within a beam enclosure embedded in an engineered earthen embankment (hill). The primary-beam transport section is designed for very low losses. The embankment's dimensions are designed to be commensurate with the bending strength of the required dipole magnets so as to provide a net 5.8° downward vertical bend to the neutrino beam (Figures 3.15 and 3.16). The beamline is then buried by soil shielding that is placed at a stable angle of repose, resulting in the embankment final geometry.

For 120-GeV operation and with the MI upgrades implemented for the NOνA experiment [126], the fast, single-turn extraction will deliver 4.9×10^{13} protons to the LBNE target in a 10-μs pulse. With a 1.33-s cycle time, the beam power for NOνA is 700 kW. Additional accelerator upgrades planned as PIP-II [22] will increase the protons per cycle to 7.5×10^{13} and reduce the cycle

Table 3.2: Partial set of parameters for the elements of the LBNE Beamline reference design at CD-1 from Volume 2 of the CDR [30]. The reference design described a 700 kW beam; it has since been changed to 1.2 MW. For each parameter the third column lists the range that had been studied prior to CD-1. Distances between beam elements are given from the upstream face (the end facing the proton beam) with respect to the upstream (front) face of Horn 1.

Element	Parameter	Range studied	Reference design value (700 kW)
Proton Beam	energy	60 GeV to 120 GeV	120 GeV
	protons per pulse		4.9×10^{13}
	cycle time between pulses		1.33 s
	size at target $\sigma_{x,y}$	1 mm to 2 mm	1.3 mm
	duration		1.0×10^{-5} sec
	POT per year		6.5×10^{20}
Target	material	graphite, beryllium hybrid [124]	graphite
	length	$\geq$ 2 interaction lengths	966 mm
	profile	rectangular, round (r = 5 mm to 16 mm)	rectangular 7.4 mm x 15.4 mm
	dist. from Horn 1 (front)	0 cm to −250 cm	−35 cm to −285 cm
Focusing Horn 1 [125]	shape	cylindrical-parabolic, double-parabolic	double-parabolic (NuMI)
	length (focusing region)	2,500 mm to 3,500 mm	3,000 mm
	current	180 kA to 350 kA	200 kA
	minimum inner radius		9.0 mm
	maximum outer radius		174.6 mm
Focusing Horn 2	shape	double-parabolic	NuMI Horn 2
	length (focusing region)	3,000 mm to 4,000 mm	3,000 mm
	current	180 kA to 350 kA	200 kA
	minimum inner radius		39.0 mm
	maximum outer radius		395.4 mm
	dist. from Horn 1 (front)	4,000 mm to 10,000 mm	6,600 mm
Decay Pipe	length	200 m to 350 m	204 m
	radius	1.0 m to 3.0 m	2 m
	atmosphere	Air, He, vacuum	air at atm. pressure
	dist. from Horn 1 (front)	11 m to 23 m	17.3 m

time to 1.2 s, resulting in an initial beam power for LBNE of 1.2 MW. The LBNE beamline is designed to support additional beam power upgrades beyond PIP-II, discussed in Section 3.2, that can increase the beam power up to 2.3 MW. At 1.2-MW operation the accelerator and primary beamline complex are expected to deliver 11×10^{20} protons per year to the target.

Approximately 85% of the protons interact with the solid target, producing pions and kaons that subsequently get focused by a set of magnetic horns into a decay pipe where they decay into muons and neutrinos (Figure 3.17). The neutrinos form a wide-band, sign-selected neutrino or antineutrino

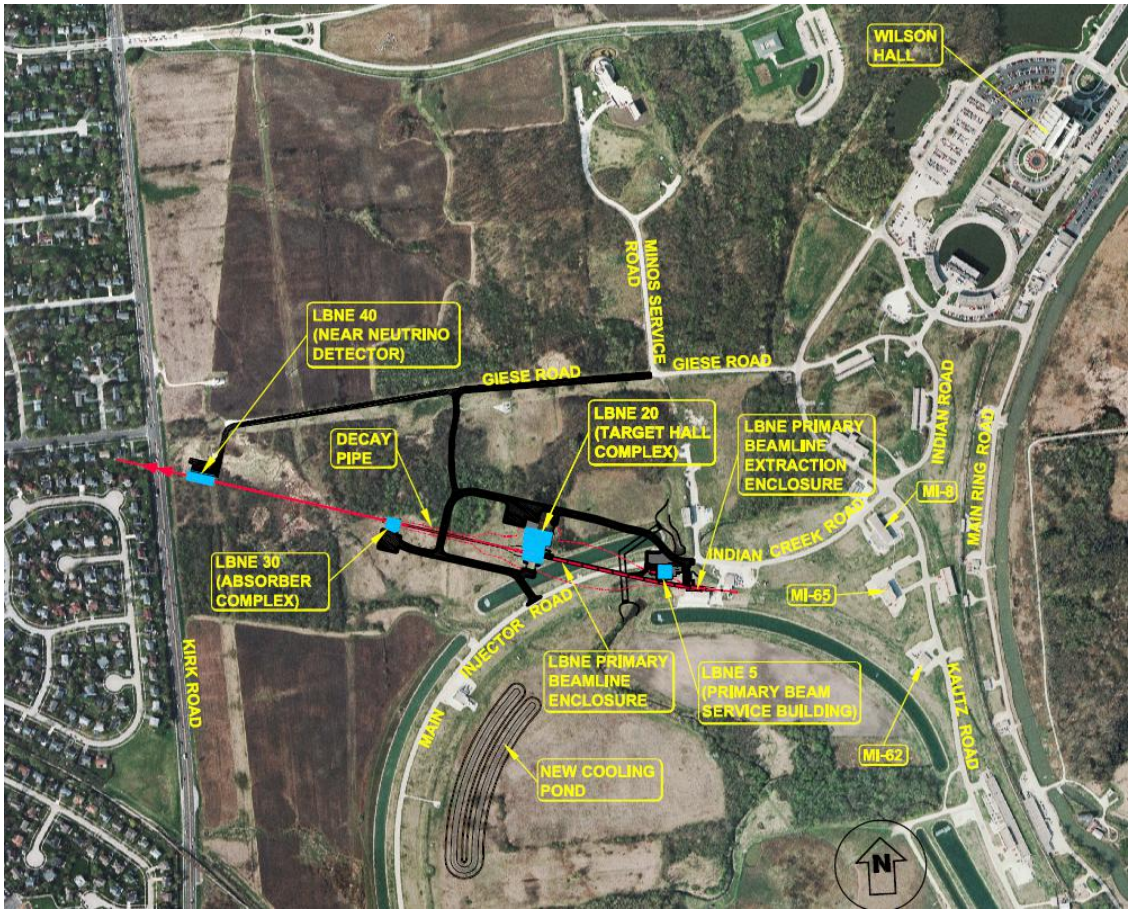

Figure 3.15: Plan view of the overall Near Site project layout showing locations for the LBNE Beamline extraction point from the MI, the primary beamline, target hall, decay pipe, absorber and near neutrino detector.

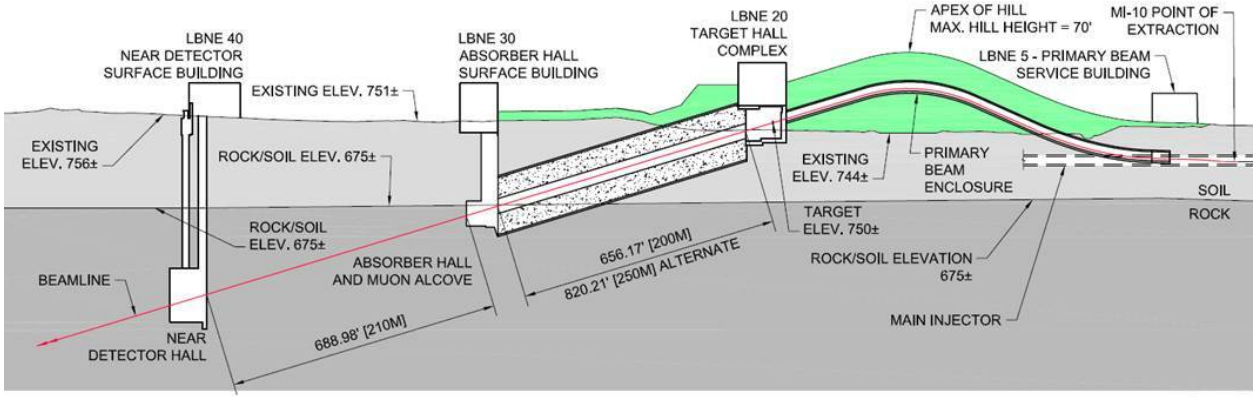

Figure 3.16: Longitudinal section of the LBNE Beamline facility. The beam enters from the right in the figure, the protons being extracted from the MI-10 extraction point at the Main Injector.

beam, designed to provide flux in the energy range of 0.5 to 5 GeV. This energy range will cover the first and second neutrino-oscillation maxima, which for a 1,300-km baseline are at approximately 2.5 and 0.8 GeV, respectively.

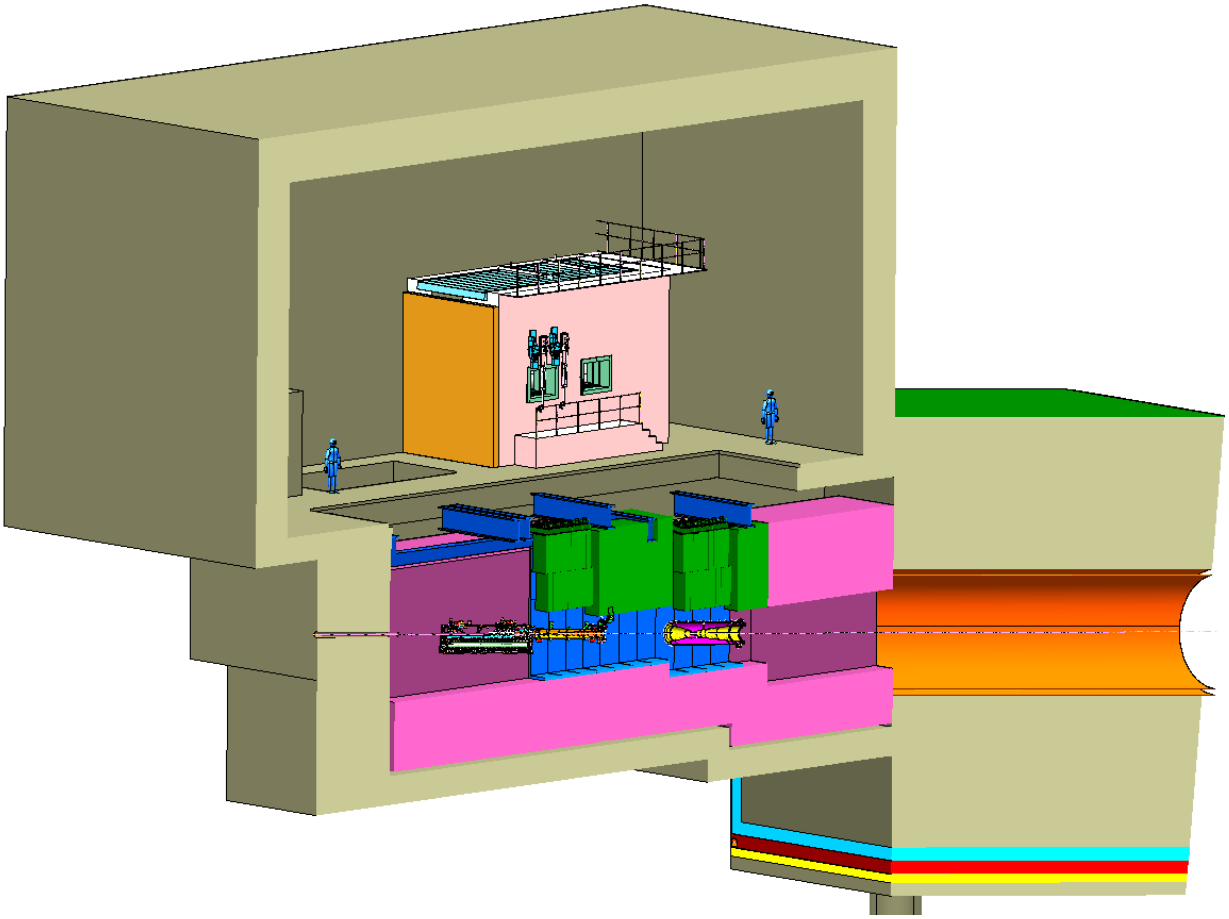

Figure 3.17: Schematic of the upstream portion of the LBNE neutrino beamline showing the major components of the neutrino beam. The target chase bulk steel shielding is shown in magenta. Inside the target chase from left to right (the direction of the beam) pointing downwards: the beam window, horn-protection baffle and target mounted on a carrier, the two toroidal focusing horns (the green custom shielding blocks are part of the horn support modules that are not shown) and the decay pipe (orange). Above the chase and to the right is the work cell for horn and target system repairs. The beige areas indicate concrete shielding.

The reference target design for LBNE is an upgraded version of the NuMI-LE (Low Energy) target that was used for eight years to deliver beam to the MINOS experiment. The target consists of 47 segments, each 2 cm long, of POCO graphite ZXF-5Q. Focusing of charged particles is achieved by two magnetic horns in series, the first of which partially surrounds the target. They are both NuMI/NOνA-design horns with double-paraboloid inner conductor profiles. The NuMI/NOνA-design horns currently operate at 185 kA to 200 kA. The horns have been evaluated and found to be operable with currents up to 230 kA but the striplines that supply the horn currents are still under evaluation. Additional development of the target and horns is required to adapt the existing designs

from the 700-kW beam power used by NOνA to 1.2 MW for LBNE. The horn current polarity can be changed to selectively focus positive or negative hadrons, thus producing high purity ($> 90\%$ in oscillation region) ν_μ or $\overline{\nu}_\mu$ beams. Each beam polarity will have a $< 10\%$ contamination of neutrinos of the "wrong sign" in the oscillation energy region ($\overline{\nu}$'s in the ν beam and vice-versa) from decays of wrong-sign hadrons that propagate down the center of the focusing horns — where there is no magnetic field — into the decay volume. In addition, a $\leq 1\%$ contamination of ν_e and $\overline{\nu}_e$ in the ν_e appearance signal region is produced by the decays of tertiary muons from pion decays, and decays of kaons. The neutrino flux components from the LBNE CD-1 beamline design produced using a full Geant4 simulation of both horn polarities are shown in Figure 3.18. The

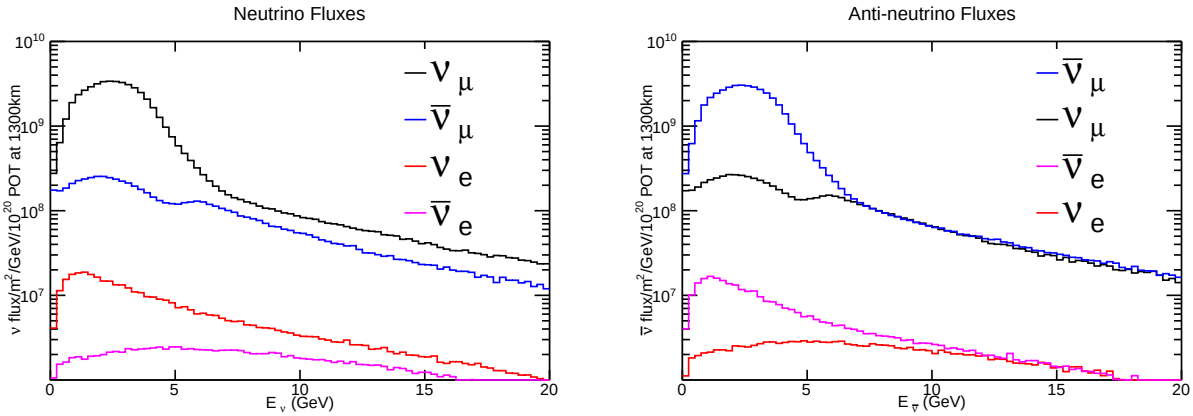

Figure 3.18: The neutrino beam fluxes (left) and antineutrino beam fluxes (right) produced by a Geant4 simulation of the LBNE beamline. The horn current assumed is 200 kA, the target is located 35 cm in front of horn 1, the decay pipe is air-filled, 4 m in diameter and 204 m in length.

beamline design provides a wide-band neutrino beam with a peak flux at 2.5 GeV, which matches the location of the first $\nu_\mu \rightarrow \nu_e$ oscillation maximum. The NuMI reference target design used for LBNE allows the target to be moved with respect to Horn 1. The location of the upstream face [§] of the target with respect to the upstream face of Horn 1 can be varied from -35 cm (default location) to -2.85 m, thus the LBNE beamline can produce a wide range of beam spectra. Three possible far-site beam spectra, produced by moving the target from -35 cm (low-energy) to -1.5 m (medium-energy) to -2.5 m (high energy) are shown in Figure 3.19.

The decay volume design for LBNE is a helium-filled, air-cooled pipe of circular cross section with a diameter of 4 m and length from 204 m to 250 m optimized such that decays of the pions and kaons result in neutrinos in the energy range useful for the experiment. A 250-m decay pipe is the maximum length that will allow the near neutrino detector complex to fit within the Fermilab site boundaries. At the end of the decay region, the absorber, a water-cooled structure of aluminum and steel, is designed to remove any residual hadronic particles; it must absorb a large fraction of the incident beam power of up to 2.3 MW. Instrumentation immediately upstream of the absorber

[§]The proton beam direction determines the upstream and downstream conventions. The upstream (front) face of Horn 1 is therefore the Horn 1 face closest to the proton beam window.

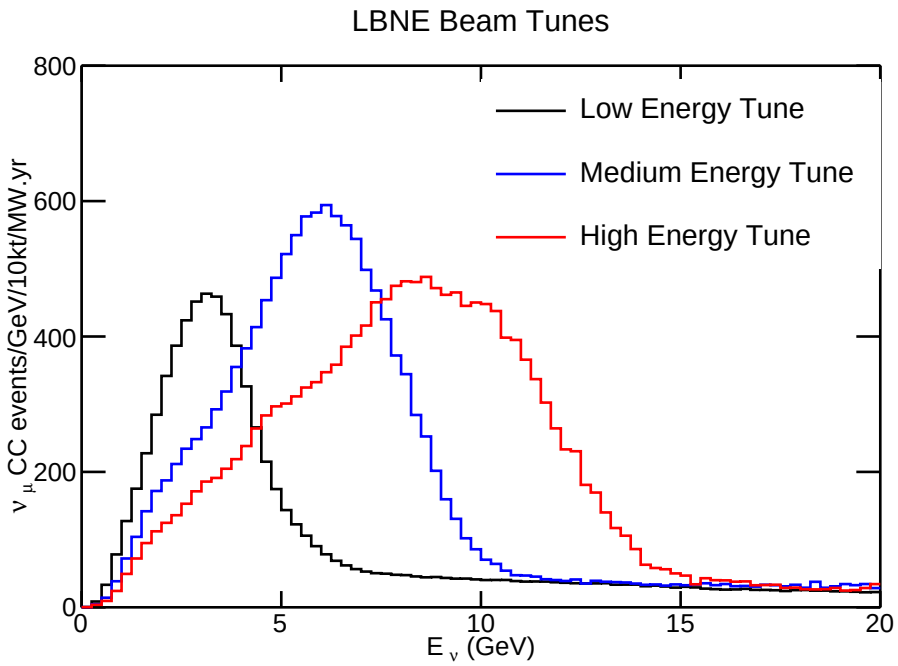

Figure 3.19: Event interaction rates at the LBNE far detector in the absence of oscillations and due to neutrinos produced by a 120 GeV proton beam for several target positions relative to Horn 1. The black curve shows the expected interaction spectrum for the low-energy tune (LE) where the upstream face of the target is located 35 cm upstream of Horn 1, the blue curve is a sample medium-energy (ME) tune with the target located 1.5 m upstream of Horn 1 and the red curve is the high-energy tune (HE) with the target located 2.5 m upstream of Horn 1. The horn current assumed is 200 kA, the decay pipe is air-filled, 4 m in diameter and 204 m in length.

measures the transverse distribution of the resultant hadronic showers to monitor the beam on a pulse-by-pulse basis.

An array of muon detectors in a small alcove immediately downstream of the absorber measures tertiary-beam muons and thereby indirectly provides information on the direction, profile and flux of the neutrino beam. This will be described in Section 3.5.

The beamline conventional facilities include the civil construction required to house the beamline components in their planned layout as shown in Figures 3.15 and 3.16. Following the beam from southeast to northwest, or roughly from right to left in Figure 3.15, the elements include the underground Extraction Enclosure, the Primary Beam Enclosure (inside the embankment) and its accompanying surface-based Service Building (LBNE 5), the Target Complex (LBNE 20) located in the embankment, the Decay Pipe, the underground Absorber Hall with the muon alcove, and its surface-based Service Building (LBNE 30). The embankment will need to be approximately 290 m long and 18 m above grade at its peak. The planned near neutrino detector facility is located as near as is feasible to the west site boundary of Fermilab, along the line-of-sight indicated in red in Figure 3.15.

The parameters of the beamline facility were determined taking into account several factors including the physics goals, the Monte Carlo modeling of the facility, spatial and radiological constraints and the experience gained by operating the NuMI facility at Fermilab. The relevant radiological concerns, prompt dose, residual dose, air activation and tritium production have been extensively modeled and the results implemented in the system design. The beamline facility design described above minimizes expensive underground construction and significantly enhances capability for ground-water radiological protection. In general, components of the LBNE beamline system that cannot be replaced or easily modified after substantial irradiation are being designed for 2.3-MW operation. Examples of such components are the shielding of the target chase and decay pipe, and the absorber with its associated shielding.

The following LBNE beamline design improvements beyond the CD-1 conceptual design are being assessed:

- An increase in the length of the decay pipe up to 250 m (the maximum length allowed by the existing Fermilab site boundaries), and also possibly an increase in its diameter up to 6 m. Increases to the decay pipe size would require additional cost of the order several tens of millions of dollars. Increasing the length of the decay pipe from 200 to 250 m increases the overall event rate in the oscillation region by 12%. Increases in the decay pipe diameter produce a 6% increase in the low-energy neutrino event rate as shown in Table 3.3.
- It has recently been decided to fill the decay pipe with helium instead of air. The total ν_μ event rate increases by about 11%, with a decrease in $\overline{\nu}$ contamination in the neutrino beam. Introducing helium in the decay pipe requires the design and construction of a decay pipe window.
- An increase in the horn current of the horns by a modest amount (from 200 kA to 230 kA); this is expected to increase the neutrino event rates by about 10-12% at the first oscillation maximum [127]. A Finite Element Analysis simulation and a cooling test of the horns are underway to evaluate this option.
- Use of an alternate material to the POCO graphite for the target to increase the target longevity. This would involve additional R&D effort and design work. A beryllium target, for example, could be made shorter, potentially improving the horn focusing.
- Development of more advanced horn designs that could boost the low-energy flux in the region of the second oscillation maximum. It should be noted that the target and horn systems can be modified or replaced even after operations have begun if improved designs enable higher beam flux.

Table 3.3 summarizes the impact of the beam design improvements after CD-1 and the additional costs required. Together, the changes are anticipated to result in an increase of $\sim 50\%$ in the ν_e

appearance signal rate at the far detector. A 30% increase in signal event rate at the far detector can be achieved for $<$ 10 M\$ without changing the CD-1 decay pipe size (4 m diameter $\times$ 204 m length) by changing from an air-filled to a helium-filled decay pipe. Increasing the decay pipe size to 6 m diameter $\times$ 250 m length would result in an additional 15% increase in flux but would cost an additional $\sim$ 47 M\$ — this includes the cost of a redesigned absorber.

Table 3.3: Impact of the beam improvements under study on the neutrino $\nu_\mu \rightarrow \nu_e$ CC appearance rates at the far detector in the range of the first and second oscillation maxima, shown as the ratio of appearance rates: the *improved* rate divided by the rate from the beam design described in the Conceptual Design Report.

Changes	0.5 to 2 GeV	2 to 5 GeV	Extra Cost
Horn current 200 kA $\rightarrow$ 230 kA	1.00	1.12	none
Proton beam 120 $\rightarrow$ 80 GeV at constant power	1.14	1.05	none
Target NuMI-style graphite $\rightarrow$ Be cylinder	1.10	1.00	$<$ 1 M\$
Decay pipe Air $\rightarrow$ He	1.07	1.11	$\sim$ 8 M\$
Decay pipe diameter 4 m $\rightarrow$ 6 m	1.06	1.02	$\sim$ 17 M\$
Decay pipe length 200 m $\rightarrow$ 250 m	1.04	1.12	$\sim$ 30 M\$
Total	**1.48**	**1.50**	

3.5 Near Detector

A high-resolution near neutrino detector located approximately 500 m downstream of the LBNE neutrino production target, as shown in Figure 3.16, is a key component of the full LBNE scientific program:

- The near neutrino detector will enable the LBNE experiment to achieve its primary scientific goals — in particular discovery-level sensitivity to CP violation and high-precision measurements of the neutrino oscillation parameters, including the unknown CP-violating phase, $\delta_{\rm CP}$.
- A rich program of LBNE physics measurements at the near detector will exploit the potential of high-intensity neutrino beams as probes of new physics.

To achieve the precision required to make a significant advancement in the measurement of neutrino oscillation parameters over current experiments and to reach the desired 5σ sensitivity to CP violation (discussed in Chapters 4 and 7), LBNE will need to measure the unoscillated flux spectrum, to a few percent, for all neutrino species in the beam: ν_μ, ν_e, $\overline{\nu}_\mu$ and $\overline{\nu}_e$. This requires a high-resolution, magnetized near neutrino detector with high efficiency for identifying and measuring

electrons and muons. To measure the small ν_e contamination in the beam with greater precision, the detector would need to be able to distinguish e^+ from e^-; this would require a low-density detector with a commensurately long physical radiation length. In addition, use of an argon target nucleus — similar to the far detector — would allow cancellation of systematic errors. A reference design has been developed for a near neutrino detector that will meet these requirements; in particular it will measure the neutrino event rates and cross sections on argon, water and other nuclear targets for both ν_e and ν_μ charged current (CC) and neutral current (NC) scattering events.

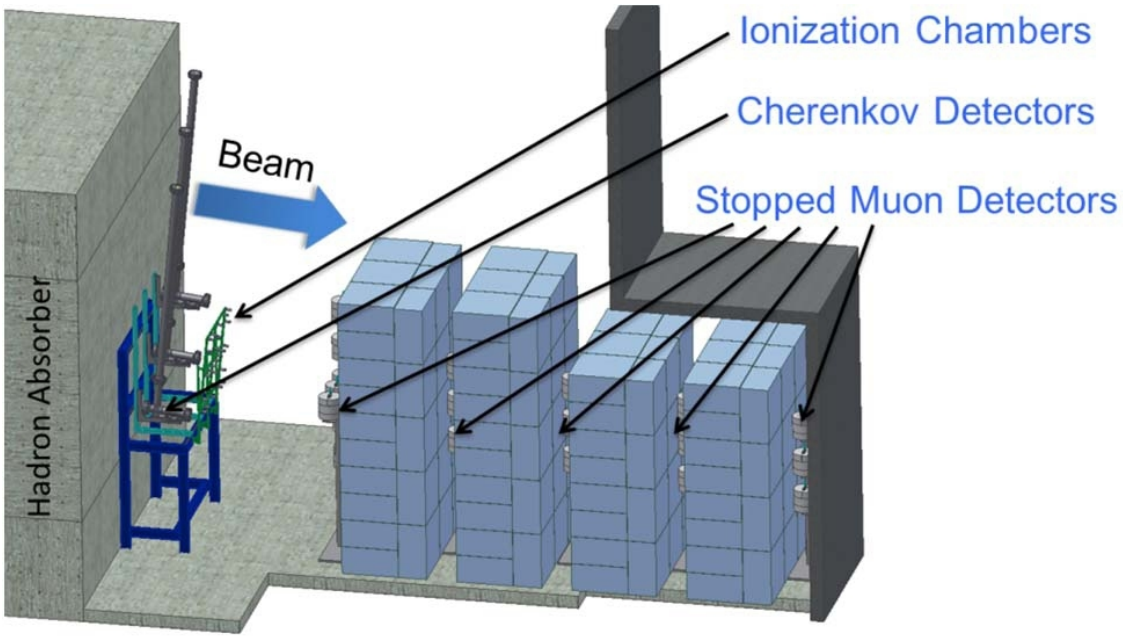

Figure 3.20: System of tertiary-beam muon detectors, located downstream of the LBNE beamline absorber, for monitoring the muon flux from the LBNE beamline.

In addition to the near neutrino detector, a sophisticated array of muon detectors will be placed just downstream of the absorber. The muon detectors, shown in Figure 3.20, detect mostly muons from the two-body decays of $\pi^{+(-)} \rightarrow \mu^{+(-)}\nu_\mu(\overline{\nu}_\mu)$ in the beamline, thus the measured muon and ν_μ flux distributions are highly correlated. The ionization chamber array will provide pulse-by-pulse monitoring of the beam profile and direction. The variable-threshold gas Cherenkov detectors will map the energy spectrum of the muons exiting the absorber on an on-going basis. The stopped muon detectors will sample the lowest-energy muons, which are known to correlate with the neutrino flux above 3 GeV — equivalent to about half the neutrino flux near the first oscillation maximum — and a decreasing fraction of it at lower energy. This system, together with the existing level of understanding of the similar NuMI beam and experience in previous neutrino oscillation experiments, will provide additional constraints on the understanding of the neutrino beam, and will thus support and complement the near neutrino detector measurements.

The reference design for the near neutrino detector is a fine-grained tracker [128], illustrated in Figure 3.21. It consists of a $3 \times 3 \times 7.04$ m^3 straw-tube tracking detector (STT) and electromagnetic

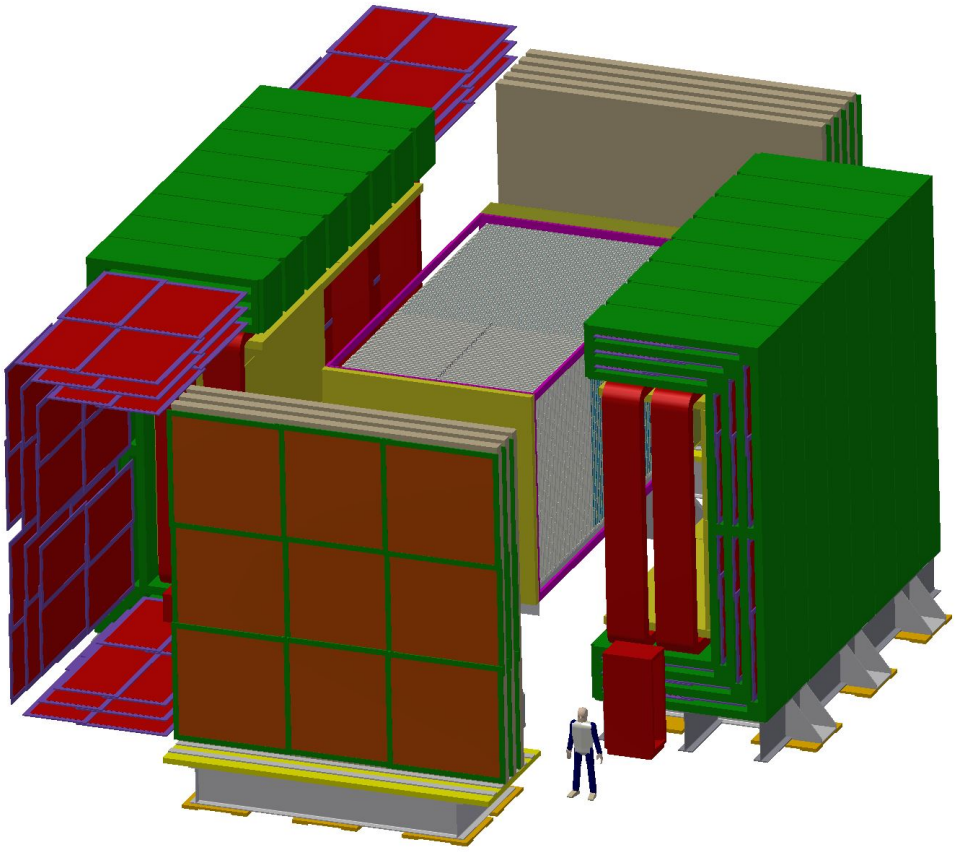

Figure 3.21: The LBNE near neutrino detector reference design with the dipole magnet open to show the straw-tube tracker (grey) and electromagnetic calorimeter (yellow). RPCs for muon identification (red squares) are embedded in the yoke steel and up- and downstream steel walls.

calorimeter inside of a 0.4-T dipole magnet, illustrated in Figure 3.22, and resistive plate chambers for muon identification (MuID) located in the steel of the magnet and also upstream and downstream of the tracker. High-pressure argon gas targets, as well as water and other nuclear targets, are embedded in the upstream part of the tracking volume. The nominal active volume of the STT corresponds to eight tons of mass. The STT is required to contain sufficient mass of argon gas in tubes (Al or composite material) to provide at least a factor of ten more statistics than expected in the far detector. Table 3.4 summarizes the performance for the fine-grained tracker's configuration, and Table 3.5 lists its parameters.

Figure 3.22 shows the locations of the electromagnetic calorimeter and MuID next to the magnet steel and magnet coils. The fine-grained tracker has excellent position and angular resolutions due to its low-density (~ 0.1 g/cm^3), high-precision STT. The low density and magnetic field allow it to distinguish e^+ from e^- on an event-by-event basis. The high resolution is important for determining the neutrino vertex and determining whether the neutrino interaction occurs in a water or argon target. Electrons are distinguished from hadrons using transition radiation.

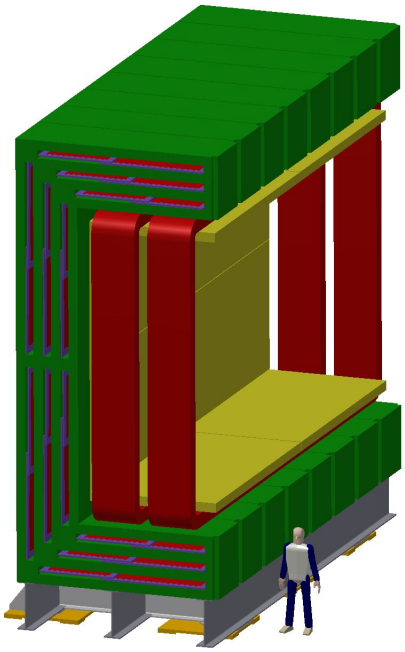

Figure 3.22: A schematic drawing of the ECAL (yellow modules) next to the magnet coils (red) and MuID (blue modules) interspersed in the magnet steel (green).

Table 3.4: Summary of the performance for the fine-grained tracker configuration

Performance Metric	Value
Vertex resolution	0.1 mm
Angular resolution	2 mrad
E_e resolution	5%
E_μ resolution	5%
$\nu_\mu/\overline{\nu}_\mu$ ID	Yes
$\nu_e/\overline{\nu}_e$ ID	Yes
NCπ^0/CCe rejection	0.1%
NCγ/CCe rejection	0.2%
NCμ/CCe rejection	0.01%

The design of the near neutrino detector is the subject of study by the LBNE Collaboration, and alternatives such as a magnetized liquid argon TPC will be investigated further. A detailed description of the fine-grained tracker can be found in [129], and descriptions of it and the alternative LArTPC design are presented in the March 2012 LBNE CDR (Volume 3 of [31]).

High-intensity neutrino beams can be used as probes of new physics and given the broad energy range of the LBNE beam, a diverse range of physics measurements is possible in the high-resolution near neutrino detector. These potentially wide-ranging physics measurements would complement other physics programs, such as those at Jefferson Laboratory, that are using proton,

Table 3.5: Parameters for the fine-grained tracker.

Parameter	Value
STT detector volume	$3 \times 3 \times 7.04$ m^3
STT detector mass	8 tons
Number of straws in STT	123,904
Inner magnetic volume	$4.5 \times 4.5 \times 8.0$ m^3
Targets	1.27-cm thick argon ($\sim$ 50 kg), water and others
Transition radiation radiators	2.5 cm thick
ECAL X_0	10 barrel, 10 backward, 18 forward
Number of scintillator bars in ECAL	32,320
Dipole magnet	2.4-MW power; 60-cm steel thickness
Magnetic field and uniformity	0.4 T; $< 2\%$ variation over inner volume
MuID configuration	32 RPC planes interspersed between 20-cm thick layers of steel

electron or ion beams from colliders and fixed-target facilities. A detailed discussion of the physics capabilities of a high-resolution near detector is presented in Chapter 7 and in [129].

3.6 Far Detector

The full-scope LBNE far detector is a liquid argon time-projection chamber of fiducial mass 34 kt located at the 4,850-ft level of the Sanford Underground Research Facility. The LArTPC technology allows for high-precision identification of neutrino flavors, offers excellent sensitivity to proton decay modes with kaons in the final state and provides unique sensitivity to electron neutrinos from a core-collapse supernova. The full detector size and its location at a depth of 4,850 feet will enable LBNE to meet the primary scientific goals — in particular, to find evidence for CP violation over a large range of δ_{CP} values, and to significantly advance proton-decay lifetime limits. Conceptual designs of the 34-kt underground detector are well developed.

The liquid argon TPC technology chosen for LBNE combines fine-grained tracking with total absorption calorimetry to provide a detailed view of particle interactions, making it a powerful tool for neutrino physics and underground physics such as proton decay and supernova-neutrino observation. It provides millimeter-scale resolution in 3D for all charged particles. Particle types can be identified both by their dE/dx and by track patterns, e.g., the decays of stopping particles. The modest radiation length (14 cm) is sufficiently short to identify and contain electromagnetic showers from electrons and photons, but long enough to provide good e/γ separation by dE/dx (one

versus two minimum ionizing particles) at the beginning of the shower. In addition, photons can be distinguished from electrons emanating from an event vertex by the flight path before their first interaction. These characteristics allow the LArTPC to identify and reconstruct signal events with high efficiency while rejecting backgrounds to provide a high-purity data sample. The principal design parameters of the full-scope LBNE LArTPC far detector are given in Table 3.6.

Table 3.6: Principal design parameters of the full-scope LBNE LArTPC far detector from [32].

Parameter	Value
Total/Active/Fiducial Mass	50/40/34 kt
Number of Detector Modules (Cryostats)	2
Drift Cell Configuration within Module	3 wide × 2 high × 18 long drift cells
Drift Cell Dimensions	2 × 3.7 m wide (drift) × 7 m high × 2.5 m long
Detector Module Dimensions	22.4 m wide × 14 m high × 45.6 m long
Anode Wire Spacing	∼5 mm
Wire Planes (Orientation from vertical)	Grid (0°), Induction 1 (45°), Induction 2 (-45°) Collection (0°)
Drift Electric Field	500 V/cm
Maximum Drift Time	2.3 ms

Scalability has been a design consideration of critical importance for the LBNE Project, and for the far detector in particular, since the Project's inception in 2009. A 10-kt LArTPC far detector configuration has been identified as the minimal initial configuration of LBNE that can make significant advances toward the primary scientific goals of LBNE. Because of the scalability built into the LBNE design, other, more capable, configurations could be accomplished either in the initial phase with the identification of additional resources, or at a later stage.

Other important considerations for the construction of LBNE's large LArTPC far detector include:

1. cryogenic safety and the elimination of hazards associated with large cryogenic liquid volumes
2. attainment of stringent argon purity requirements with respect to electronegative contaminants (e.g., < 0.2 ppb O_2 concentration)
3. ease of transport and assembly of TPC mechanical systems
4. efficient deployment of high-sensitivity/low-noise electronics for readout of the ionization signal

The far detector complex for both the first-phase ($\geq$ 10-kt) and full 34-kt options will be outfitted with two separately instrumented detector vessels instead of a single, larger vessel — an approach

which has several benefits. First, this design enables each cryostat and TPC to be filled and commissioned while the other remains available for liquid storage, allowing for repairs to be made after the start of commissioning, should that be necessary. Secondly, it allows deployment of TPCs of different designs. This would enable, for example, international partners to contribute a detector of an alternate design, based on their own experience, or one that would emphasize a particular research interest.

The detector vessels will be constructed using technology standards from the liquefied natural gas (LNG) industry. With similar requirements and geometries, adaptation of industrial LNG cryostat design provides a high-performance, extensively tested approach to the challenge of liquid argon containment for LBNE. The cryostats in large LNG tanker ships are constructed using a thin (1–2 mm), polished, stainless steel inner membrane surrounded by thick foam passive insulation. With stainless steel as the only wetted surface, this is an inherently clean design, ideal for liquid argon detectors where high purity is essential.

The underground detector placement at the 4850L of the Sanford Underground Research Facility was studied in detail during the Conceptual Design Phase of LBNE and presented at the Fermilab Director's Independent Conceptual Design Review in March of 2012 [24]. Significant effort has been invested to minimize the (dominant) cost of the far site conventional facilities.

3.6.1 The 10-kt Detector Design

- The far detector for the initial phase of LBNE will have fiducial mass of *at least* 10 kt. This mass allows for high probability determination of the neutrino mass hierarchy and can provide evidence for CP violation, if this effect is large.
- The detector needs to be located deep underground to provide sensitivity for proton decay searches in the kaon modes and for measuring neutrinos from potential supernovae in the galaxy.
- A conceptual design for a 10-kt LArTPC has been developed, thoroughly reviewed and found to be sound.
- LBNE is working with international partners in an effort to deploy a more massive far detector in the initial phase.

A conceptual design for the initial 10-kt far detector for the first-phase LBNE Project has been developed that is easily scalable to larger detectors. Many of the detector elements, in particular the modular TPC design and readout electronics, utilize full-scale modules and designs that can easily be replicated in larger numbers to instrument a larger detector. This design consists of two

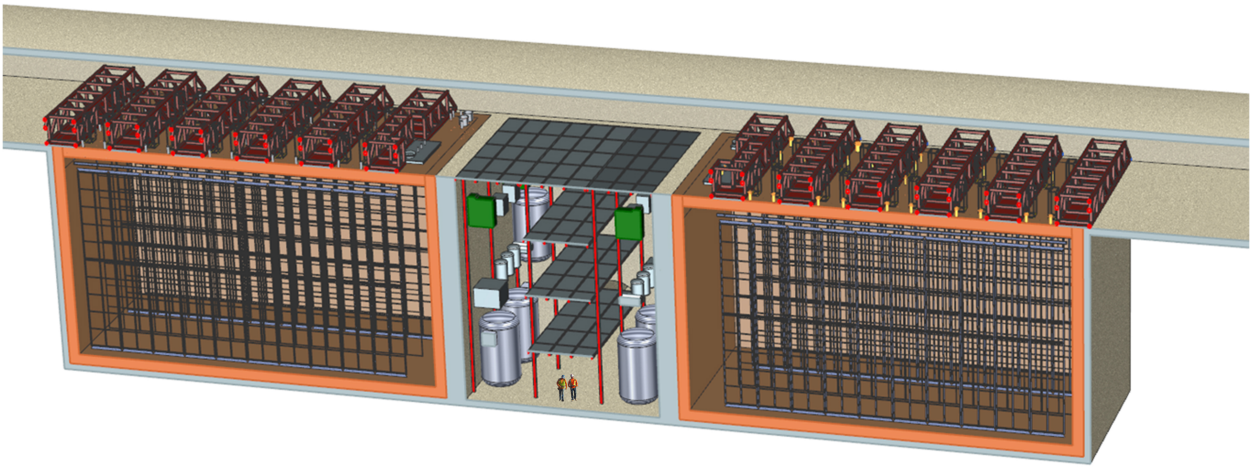

Figure 3.23: 3D view of the 10-kt far detector showing a lateral cross section of the two 5-kt fiducial-mass LArTPC vessels

9.4-kt liquid argon vessels [32], each designed to hold a 5-kt fiducial-mass LArTPC as shown in Figure 3.23.

The cryogenics systems for the 10-kt detector will consist of two 85-kW liquid nitrogen liquefaction plants, a liquid argon receiving station, a liquid argon circulation system with liquid purifiers, and a liquid argon re-condensing system. All the cryogenics systems are similar to large-scale systems found in industrial applications.

The LBNE TPC design for the 10-kt detector consists of three rows of cathode plane assemblies (CPAs) interspersed with two rows of anode plane assemblies (APAs), similar to the layout concept shown in Figure 3.24 bottom right, with readout electronics mounted directly on the APA frames (Figure 3.24, left). These elements run the length of a cryostat module, save for space at one end allocated to the cryogenics systems. A field cage for shaping the electric field covers the top, bottom, and ends of the detector. The spacing between the CPA and APA rows is 3.48 m and the cathode planes will be operated at 173 kV, establishing a drift field of 500 V/cm and a corresponding maximum drift time of 2.16 ms.

The APAs and CPAs are designed in a modular fashion as illustrated in Figure 3.24, top right. Each APA/CPA is constructed with a support frame 2.5 m long and 7 m high; these dimensions are chosen for ease of transportation to the detector site and installation within the cryostat. During installation, two APAs are connected end-to-end to form a 14 m tall, 2.5 m long unit, which is transported to its final position in the detector and suspended there using a rail system at the top of the detector. Pairs of CPAs are installed in a similar fashion. This system of 2.5 m long detector elements is easily scalable to any desired detector size. A total of 40 APAs and 60 CPAs per cryostat are needed for the 10-kt detector design, configured as two rows of APAs, ten APA pairs long.

Three sense wire planes (two *induction* planes and one *collection* plane) with wire pitches of 4.8

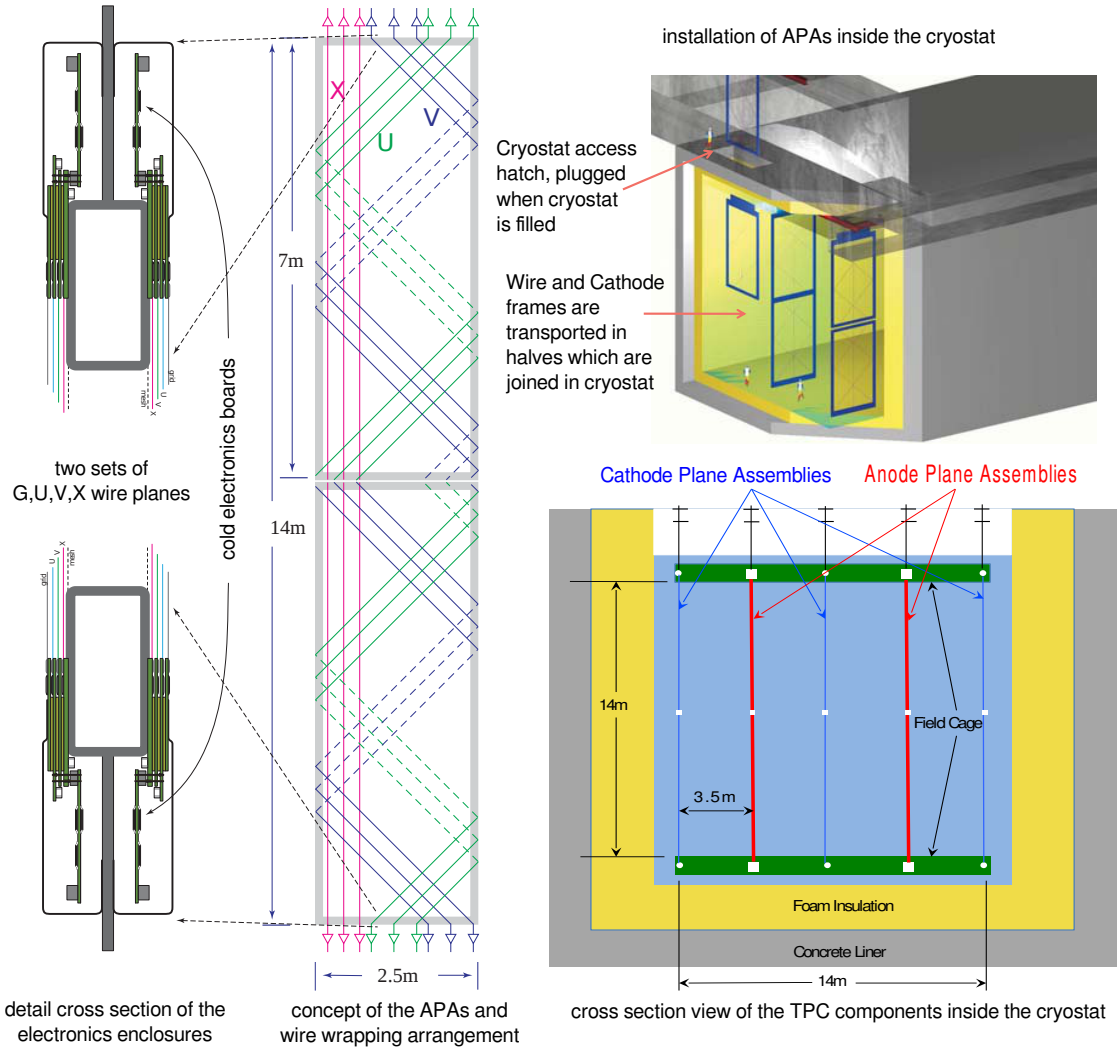

Figure 3.24: The LBNE TPC modular construction concept

mm are mounted on each side of an APA frame, for sensitivity to ionization signals originating within the TPC cell on either side. The wires on these planes are oriented vertically (collection) and at $\pm 45^\circ$ (induction)¶. The induction plane wires are wrapped around the APA frame, and are therefore sensitive to charge arriving from either side of the APA, depending on where the charge arrives along the length of the wires. This configuration allows placement of readout electronics at the top and bottom of each two-APA unit. (Cables from the bottom APA are routed up through the support frame, thereby eliminating any obstruction they would otherwise cause.) In this way, adjacent APA-pairs can be abutted so as to minimize the uninstrumented region in the gaps between them along the length of the detector.

¶The current design uses a 36° orientation to remove hit assignment ambiguities.

Low-noise, low-power CMOS (Complementary Metal Oxide Semiconductor) preamplifier and ADC ASICS (Application Specific Integrated Circuit) have been developed for deployment on circuit boards mounted directly on the APA frames. This scheme ensures good signal-to-noise performance, even allowing for some attenuation of long-drift ionization signals due to residual impurities in the argon. It also offers the possibility of digital signal processing, including multiplexing and zero suppression at the front end, thereby limiting the cable plant within the cryostat and the number of penetrations required, while also easing requirements on the downstream read-out/DAQ systems located outside the cryostat. The ASICS have been laid out following design rules developed explicitly for long-term operation at cryogenic temperatures.

In order to separate neutrino beam events from other interactions — particularly for proton decay and supernova neutrino signals — it is necessary to accurately determine the event time relative to the neutrino beam time window or an incoming cosmic muon. If the event time is known at the microsecond level then out-of-time cosmic-ray backgrounds for beam neutrinos can be rejected to the level of 10^{-5} (the beam spill duty factor). The slow ionization-electron drift velocity gives the TPC its 3D imaging capability, but an independent fast signal is required to localize events in time and in space along the drift direction. The excellent scintillation properties of liquid argon ($\mathcal{O}(10^4)$ photons per MeV of energy deposition) are exploited to address this issue. A photon detection system is planned for detection of the 128-nm scintillation light that, in turn, allows determination of the event timing. Several photon detector designs are under study. The most advanced design uses cast acrylic bars coated with wavelength shifter, and SiPMs (silicon photomultipliers) at the ends for read-out. These bars will be assembled into paddles of dimensions 10 cm by 2 m, and mounted on the APA frames, fitting within the 5-cm gap between the sets of wire planes located on both sides of the frames. Initial studies indicate a light yield of 0.1 to 0.5 photoelectrons per MeV.

3.6.2 The 34-kt Detector Design

One possible design of a 34-kt detector is two 17-kt modules placed end-to-end in a common cavern at the 4,850-ft level of the Sanford Underground Research Facility, as shown in Figure 3.25. This design was reviewed at the Fermilab Director's Independent Conceptual Design Review in March of 2012 [24].

Alternatively, the 34-kt detector can be realized by adding a roughly 24-kt detector of essentially the same design as the 10-kt detector, housed in a set of two cryostats, each holding 12 kt (20 kt total) of liquid argon. In this configuration the additional cryostats each have three APA rows (total 84 APAs) and four CPA rows (total 112 CPAs), making them wider than the 10-kt design described in Section 3.6.1. The APA-to-CPA row spacing is expanded to 3.77 m and the length of each is increased to 14 APA units long.The cryogenics system installed for the 10-kt design will simply be expanded from two to four 85-kW refrigerators to service both the 10-kt and the 24-kt detector. The 24-kt detector hall will be excavated parallel to the 10-kt detector hall as shown in Figure 3.26.

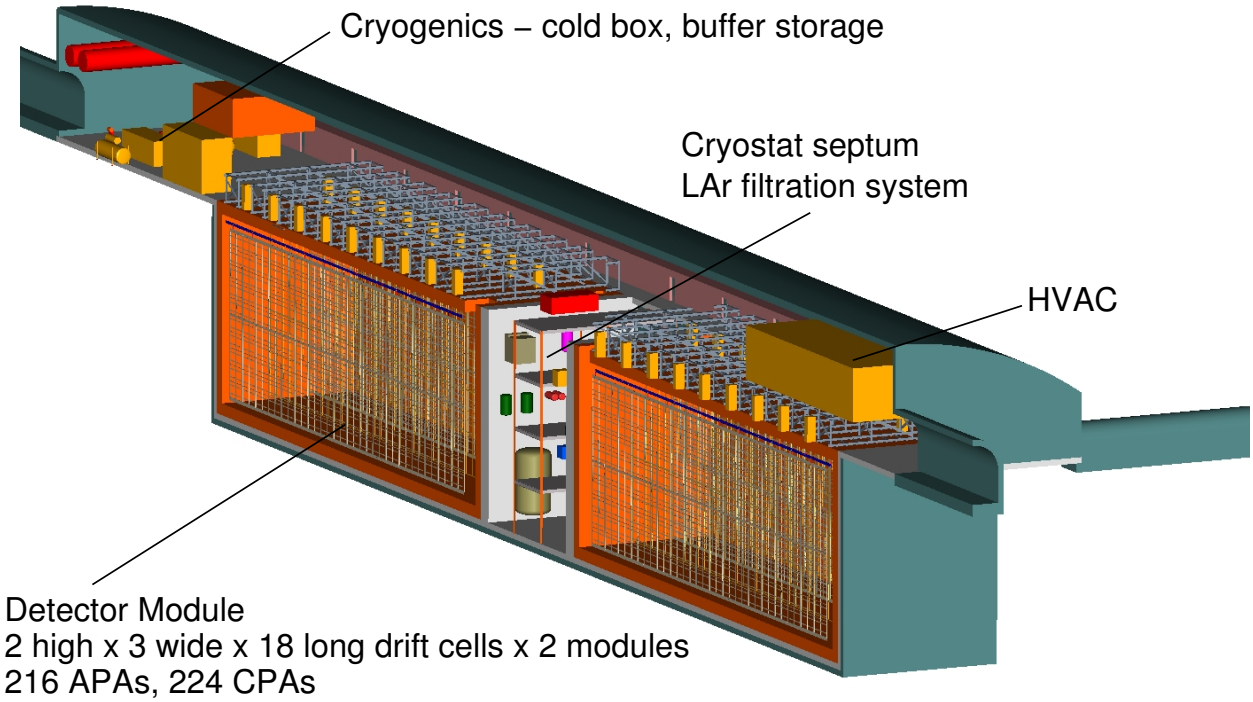

Figure 3.25: Schematic of a 34-kt LArTPC design. The detector comprises two 17-kt LArTPC vessels.

Given the modular design of the detector and the use of industrial technologies in the cryogenics system, there is a great deal of flexibility in possible contributions from new partners to expand the size of the detector. The details of any scope change would depend on the interests, capabilities and resources of the new partners.

A full geotechnical site investigation is underway to characterize the rock mass in which it is planned to site the LBNE far detector. Mapping of existing drifts in the vicinity of the proposed detector location has been completed and a core boring program was launched in early 2014. This investigation will explore the area with enough breadth to allow flexibility in siting and sizing detector modules in the future before design work begins. The proposed boring layouts are shown in Figure 3.27 overlaid with possible 34-kt and 70-kt modules to demonstrate the large capacity of this location.

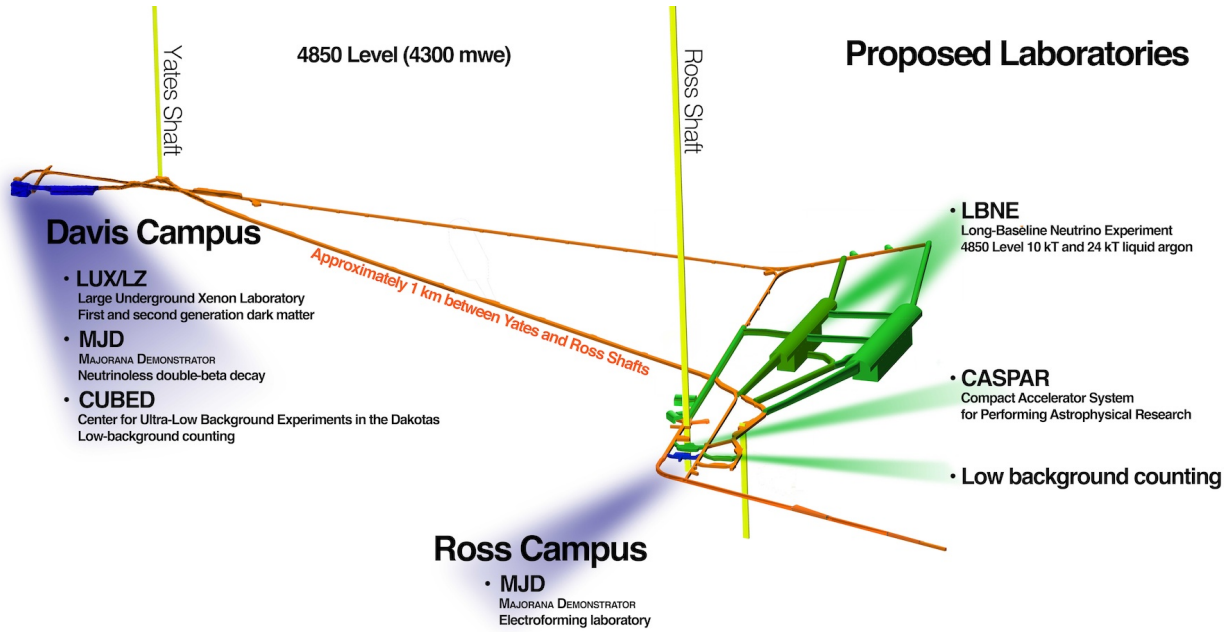

Figure 3.26: Layout of the 10-kt + 24-kt LArTPC detector halls at the 4,850-ft level of the Sanford Underground Research Facility.

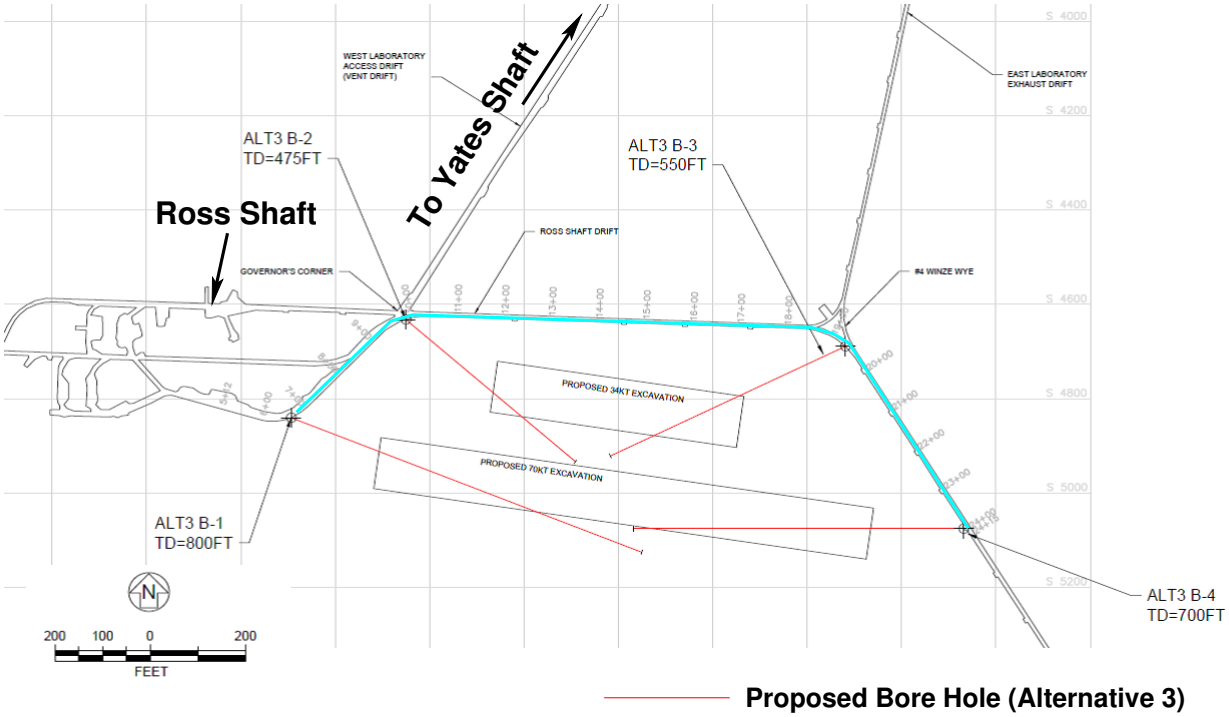

Figure 3.27: Geotechnical site investigation plan, showing the drifts that have been mapped (blue) and the planned core borings (red) overlaid on possible locations of caverns that would accommodate the 34-kt or larger (70-kt shown as an example) LArTPC detectors.

Chapter 4 Neutrino Mixing, Mass Hierarchy and CP Violation

LBNE is designed to address the science of neutrino oscillations with superior sensitivity to many mixing parameters in a single experiment, in particular,

1. precision measurements of the parameters that govern $\nu_\mu \rightarrow \nu_e$ and $\overline{\nu}_\mu \rightarrow \overline{\nu}_e$ oscillations; this includes precision measurement of the third mixing angle θ_{13}, measurement of the CP-violating phase $\delta_{\rm CP}$, and determination of the mass ordering (the sign of Δm^2_{32})
2. precision measurements of $\sin^2 2\theta_{23}$ and $|\Delta m^2_{32}|$ in the $\nu_\mu/\overline{\nu}_\mu$ disappearance channel
3. determination of the θ_{23} octant using combined precision measurements of the $\nu_e/\overline{\nu}_e$ appearance and $\nu_\mu/\overline{\nu}_\mu$ disappearance channels
4. search for nonstandard physics that can manifest itself as differences in higher-precision measurements of ν_μ and $\overline{\nu}_\mu$ oscillations over long baselines

4.1 Experimental Requirements Based on Oscillation Phenomenology

The experimental requirements for designing a neutrino oscillation experiment to simultaneously address neutrino CP violation and the mass hierarchy (MH) can be extrapolated as follows from the phenomenology summarized in Chapter 2:

1. *Phenomenology: An appearance experiment is necessary to extract the CP-violating effects.*

   Experimental requirements:

   - The experiment will probe oscillations of $\nu_{\mu,e} \rightarrow \nu_{e,\mu}$.
   - The experiment will identify ν_e and ν_μ with high efficiency and purity in order to tag (or otherwise know) the flavor of the neutrino before and after flavor transformations.
   - The experiment requires E_ν >100 MeV so that it will be possible to perform flavor-tagging of muon neutrinos using the lepton flavor produced in a charged current (CC) interaction ($\nu_\mu + N \rightarrow \mu N' X$).

2. *Phenomenology: In the three-flavor mixing model, the CP-violating Jarlskog invariant arises in the interference term $P_{\sin\delta}$ as given by Equation 2.15; the oscillation scale where the interference term is maximal is that determined by the mixing between the ν_1 and ν_3 states.*

   Experimental requirements:

   - The experimental baseline and corresponding neutrino energy are chosen according to Equation 2.18 such that L/E equals 510 km/GeV to maximize sensitivity to the CP-violating term in the neutrino flavor mixing.
   - Flavor-tagging of muon neutrinos that can be produced either at the source or after flavor-mixing requires $E_\nu > 100$ MeV; therefore, the experimental baselines over which to measure neutrino oscillations are $L > 50$ km*.

3. *Phenomenology: In the three-flavor model $\nu_{\mu,e} \to \nu_{e,\mu}$ oscillations depend on all parameters in the neutrino mixing matrix as well as on the mass differences, as shown in Equations 2.12 to 2.15.*

   Experimental requirements:

   - The precision with which $\delta_{\rm CP}$ can be determined — and the sensitivity to small CP-violating effects or CP violation outside the three-flavor model — requires precision determination of all the other mixing parameters, preferably in the same experiment. The experiment will be designed so as to minimize dependence on external measurements of the oscillation parameters.

4. *Phenomenology: Observation of CP violation requires the explicit observation of an asymmetry between $P(\nu \to \nu)$ and $P(\overline{\nu} \to \overline{\nu})$.*

   Experimental requirements:

   - The experiment will probe the oscillations of both neutrinos and antineutrinos in an unambiguous way.
   - The experiment will be capable of charge tagging in addition to flavor tagging. Charge tagging can be achieved at detection using the lepton charge and/or at production by selecting beams purely of neutrinos or antineutrinos.
   - The experiment will be capable of resolving degeneracies between matter and CP asymmetries in order to determine the MH. This can be achieved by using a baseline greater than 1,000 km or with measurements probing oscillations over a range of L/E values.

*Neutrino experiments using beams from pion decay-at-rest experiments such as DAEδALUS are exceptions since the $\overline{\nu}_\mu$ production spectrum is well known and only the $\overline{\nu}_e$ flavor after oscillations is tagged through inverse-beta decay. The neutrino energies are ~50 MeV below the CC muon-production threshold.

5. *Phenomenology: CP asymmetries are maximal at the secondary oscillation nodes.*

   Experimental requirements:

   - Coverage of the L/E scale of the secondary oscillation nodes improves experimental sensitivity to small values of $\delta_{\rm CP}$ by enabling measurements of the asymmetry at the secondary nodes where the CP asymmetries are much larger and where there is no degeneracy with the matter asymmetries. The experiment will be performed with a wide-band beam to provide sensitivity to the L/E scale of both the first and second oscillation nodes.
   - The experimental baseline will be >150 km, given that muon flavor tagging is required at either production or detection. The secondary oscillation nodes are located at scales set by Equation 2.18 where $n > 1$. The second oscillation maximum is located at scales given by $L/E \sim$1,500 km/GeV.

Based on the experimental requirements prescribed by the neutrino oscillation phenomenology detailed above, pursuit of the primary science objectives for LBNE dictates the need for a very large mass (10 kt to 100 kt) neutrino detector located at a distance greater than 1,000 km from the neutrino source. This large mass coupled with a powerful wide-band beam and long exposures is required to accumulate enough neutrino interactions — $\mathcal{O}$(1,000) events — to make precision measurements of the parameters that govern the subdominant $\nu_\mu \rightarrow \nu_e$ oscillations. At 1,300 km, the baseline chosen for LBNE, both the first and second oscillation nodes are at neutrino energies > 0.5 GeV, as shown in Figure 4.1. This places both neutrino oscillation nodes in a region that is well matched to the energy spectrum of the high-power conventional neutrino beams that can be obtained using the 60 GeV to 120 GeV Main Injector (MI) proton accelerator at Fermilab.

4.2 Simulation of Neutrino Oscillation Experiments

To evaluate the sensitivity of LBNE and to optimize the experiment design, it is important to accurately predict the neutrino flux produced by the neutrino beamline, the neutrino interaction rate at the far detector, and the far detector performance. This is achieved using Monte Carlo (MC) simulations and the GLoBES [130,131] package. The simulations and experimental assumptions that are used to evaluate the sensitivity of LBNE to neutrino mixing parameters, to the neutrino mass hierarchy (MH) and to CP violation are described in this section.

4.2.1 Expected Signal

The LBNE beamline design, described in Section 3.4, is simulated using Geant4 [132]. The simulated ν_μ spectrum (unoscillated flux $\times$ cross section) at 1,300 km obtained from the LBNE beamline using 80-GeV protons from the MI is shown as the black histogram in Figure 4.1. At this

baseline, there is no degeneracy between matter and CP asymmetries at the first oscillation node where the LBNE neutrino beam spectrum peaks. The wide coverage of the oscillation patterns enables the search for physics beyond the three-flavor model because new physics effects may interfere with the standard oscillations and induce a distortion in the oscillation patterns. As a next-generation neutrino oscillation experiment, LBNE aims to study in detail the spectral shape of neutrino mixing over the range of energies where the mixing effects are largest. This is crucial for advancing the science beyond the current generation of experiments, which depend primarily on rate asymmetries.

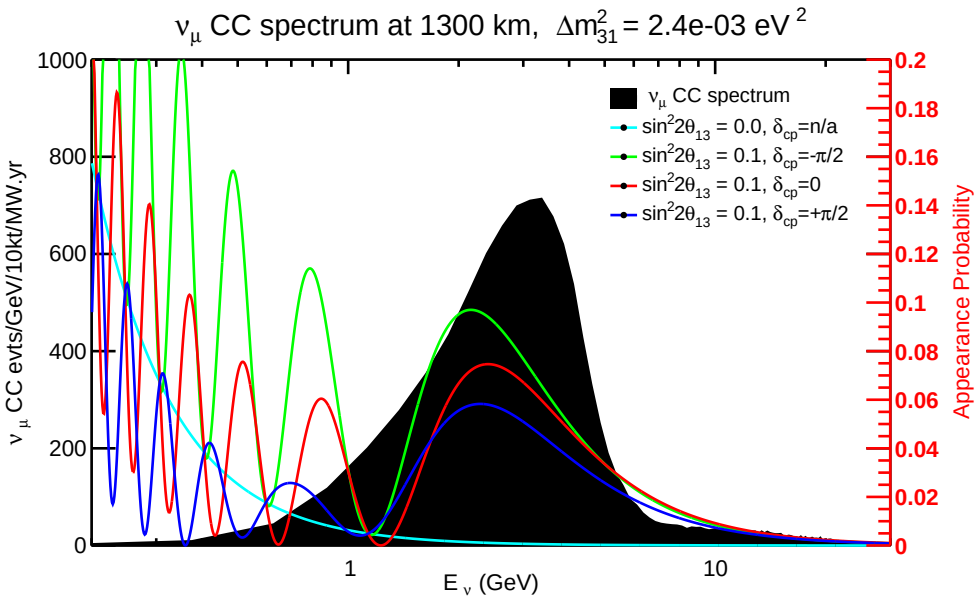

Figure 4.1: The simulated unoscillated spectrum of ν_μ events from the LBNE beam (black histogram) overlaid with the $\nu_\mu \rightarrow \nu_e$ oscillation probabilities (colored curves) for different values of δ_{CP} and normal hierarchy.

The LBNE reconfiguration study [25] determined that the far detector location at the Sanford Underground Research Facility provides an optimal baseline for precision measurement of neutrino oscillations using a conventional neutrino beam from Fermilab. The 1,300-km baseline optimizes sensitivity to CP violation and is long enough to resolve the MH with a high level of confidence, as shown in Figure 2.7.

Table 4.1 lists the beam neutrino interaction rates for all three known species of neutrinos as expected at the LBNE far detector. This table shows only the raw interaction rates using the neutrino flux from the Geant4 simulations of the LBNE beamline and the default interaction cross sections included in the GLoBeS package [130] with *no detector effects included*. A tunable LBNE beam spectrum, obtained by varying the distance between the target and the first focusing horn (Horn 1), is assumed. The higher-energy tunes are chosen to enhance the ν_τ appearance signal and improve the oscillation fits to the three-flavor paradigm. To estimate the NC event rates based on visible

Table 4.1: Raw ν oscillation event rates at the LBNE far site with $E_\nu < 10$ GeV. Assumes 1.8×10^7 seconds/year (Fermilab). *POT* is *protons-on-target*. Oscillation parameters used are: $\theta_{12} = 0.587$, $\theta_{13} = 0.156$, $\theta_{23} = 0.670$, $\Delta m^2_{21} = 7.54 \times 10^{-5}\,\text{eV}^2$, and $\Delta m^2_{31} = +2.47 \times 10^{-3}\,\text{eV}^2$ (normal hierarchy). The NC event rate is for events with visible energy > 0.5 GeV. For comparison, the rates at other neutrino oscillation experiments (current and proposed) are shown for similar exposure in mass and time. No detector effects are included.

Experiment *details*	**Baseline km**	ν_μ **unosc. CC**	ν_μ **osc. CC**	ν_e **beam CC**	ν_μ **NC**	$\nu_\mu \to \nu_\tau$ **CC**	$\nu_\mu \to \nu_e$ **CC** $\delta_{CP} = -\frac{\pi}{2}$,	**0,**	$\frac{\pi}{2}$
LBNE LE	1,300								
80 GeV, 1.2 MW									
1.5 × 10²¹ POT/year									
50 kt · year ν		12721	4339	108	3348	156	605	480	350
50 kt · year $\overline{\nu}$		4248	1392	34	1502	48	51	86	106
LBNE ME	1,300								
120 GeV, 1.2 MW									
1 × 10²¹ POT/year									
50 kt · year ν		19613	12317	72	5808	686	435	399	293
T2K	295								
30 GeV, 750 kW									
9 × 10²⁰ POT/year									
50 kt · year ν		2100	898	41	360	< 1	73	58	39
MINOS LE	735								
120 GeV, 700 kW									
6 × 10²⁰ POT/year									
50 kt · year ν		17574	11223	178	4806	115	345	326	232
50 kt · year $\overline{\nu}$		5607	3350	56	2017	32	58	85	88
NOvA ME	810								
120 GeV, 700 kW									
6 × 10²⁰ POT/year									
50 kt · year ν		4676	1460	74	1188	10	196	168	116
50 kt · year $\overline{\nu}$		1388	428	19	485	2	22	35	41
LBNO	2,300								
50 GeV ∼ 2 MW									
3 × 10²¹ POT/year									
50 kt · year ν		8553	2472	48	2454	570	534	426	336
50 kt · year $\overline{\nu}$		3066	828	15	1140	255	24	45	54
ν-Factory *details*		ν_μ **unosc. CC**	ν_μ **osc. CC**		ν_μ **NC**	$\nu_\mu \to \nu_\tau$ **CC**	$\nu_e \to \nu_\mu$ **CC** $\delta_{CP} = -\frac{\pi}{2}$,	**0,**	$\frac{\pi}{2}$
NuMAX I	1,300								
3 GeV, 1 MW									
0.94 × 10²⁰ μ/year									
50 kt · year μ^+		1039	339		484	28	71	97	117
50 kt · year μ^-		2743	904		945	89	24	19	12
NuMAX II	1,300								
3 GeV, 3 MW									
5.6 × 10²⁰ μ/year									
50 kt · year μ^+		6197	2018		2787	300	420	580	700
50 kt · year μ^-		16349	5390		5635	534	139	115	85

energies above 0.5 GeV, a true-to-visible energy smearing function based on output from the GENIE neutrino MC generator [133] is used. For comparison, the rates at current neutrino oscillation experiments such as T2K [134], MINOS [135] and NOνA [126] are shown for similar exposure in mass and time and using the same interaction cross sections. The raw interaction rates from other proposed neutrino oscillation experiments such as LBNO [136] and the NuMAX neutrino factory designs [137] are also shown[†]. It is important to note that the duty factors for the JPARC and CERN beams are $\sim 1/3$ and $\sim 1/2$ of NuMI/LBNE respectively. For LBNO, the event rates are obtained using the optimized beam from the HP-PS2 50-GeV synchrotron [138] with an exposure of 3×10^{21} POT/year. The LBNO duty cycle is assumed to be $\sim 10^7$ seconds/year, which corresponds to a beam power of 2 MW. Note that for Stage 1 and Stage 2 of the NuMAX neutrino factory proposal [137], Project X beams [23] at 3 GeV with 1 and 3 MW, respectively, are needed[‡] It is clear that the LBNE beam design and baseline produce high rates of ν_e appearance coupled with large rate asymmetries when CP-violating effects are included. For example, LBNE has significantly higher appearance rates with a Main Injector 1.2-MW beam when compared to Stage 1 of the NuMAX neutrino factory with a 1-MW beam from a 3-GeV linac. The ν_e appearance rates are very similar in LBNE and LBNO with normal hierarchy (NH), but the $\overline{\nu}_e$ appearance rates (NH) in LBNO are $\approx 1/2$ that of LBNE due to the suppression from the larger matter effect (longer baseline) in LBNO.

4.2.2 Detector Simulation using the GLoBES Package

For the sensitivity studies presented here, the GLoBES package [130,131] was used to simulate the detector response using simple smearing and using detector efficiency values based on results from ICARUS and earlier simulation efforts as documented in [29]. The values used in GLoBES are shown in Table 4.2.

Studies from ICARUS have estimated and measured single-particle energy resolutions in liquid argon. Below 50 MeV, the energy resolution of electrons is $11\%/\sqrt{E[\mathrm{MeV}]} + 2\%$. The energy resolution of an electromagnetic shower with energy in the range (50–5000) MeV is $33\%/\sqrt{E(\mathrm{MeV})} + 1\%$ [139] and that of hadronic showers is $\approx 30\%/\sqrt{E(\mathrm{GeV})}$. A significant fraction of the ν_e-CC signal in LBNE in the range of 1 GeV to 6 GeV comes from non-quasi-elastic CC interactions with a large component of the visible energy in the hadronic system. From recent simulations of neutrino interactions in this region it has been determined that $< E_{\mathrm{lepton}}/E_\nu > \approx 0.6$. For this reason, the total ν_e energy resolution for the neutrino oscillation sensitivity calculation is chosen to be $15\%/\sqrt{E(\mathrm{GeV})}$. In a non-magnetized LArTPC, the muon momentum can be obtained from measurements of range and multiple scattering. The muon momentum resolution for partially con-

[†]T2K uses a JPARC neutrino beam, MINOS and NOνA use the Fermilab NuMI neutrino beam and LBNO uses a CERN neutrino beam.

[‡]Project X has been superseded by PIP-II as of late 2013; PIP-II is briefly described in Section 3.4.

Table 4.2: Estimated range of the LArTPC detector performance parameters for the primary oscillation physics. Signal efficiencies, background levels, and resolutions are obtained from ICARUS and earlier simulation efforts (middle column) and the value chosen for the baseline LBNE neutrino oscillation sensitivity calculations (right column).

Parameter	Range of Values	Value Used for LBNE Sensitivities
	For ν_e-CC appearance studies	
ν_e-CC efficiency	70-95%	80%
ν_μ-NC misidentification rate	0.4-2.0%	1%
ν_μ-CC misidentification rate	0.5-2.0%	1%
Other background	0%	0%
Signal normalization error	1-5%	1-5%
Background normalization error	2-15%	5-15%
	For ν_μ-CC disappearance studies	
ν_μ-CC efficiency	80-95%	85%
ν_μ-NC misidentification rate	0.5–10%	1%
Other background	0%	0%
Signal normalization error	1-10%	5–10%
Background normalization error	2-20%	10-20%
	For ν-NC disappearance studies	
ν-NC efficiency	70-95%	90%
ν_μ-CC misidentification rate	2-10%	10%
ν_e-CC misidentification rate	1-10%	10%
Other background	0%	0%
Signal normalization error	1-5%	under study
Background normalization error	2-10%	under study
	Neutrino energy resolutions	
ν_e-CC energy resolution	$15\%/\sqrt{E(GeV)}$	$15\%/\sqrt{E(GeV)}$
ν_μ-CC energy resolution	$20\%/\sqrt{E(GeV)}$	$20\%/\sqrt{E(GeV)}$
E_{ν_e} scale uncertainty	under study	under study
E_{ν_μ} scale uncertainty	1-5%	2%

tained muons is found to be in the range $10-15\%$ [140,141] for muons in the 0.5 GeV to 3 GeV range. The ν_μ total energy resolution in LBNE is, therefore, assumed to be $20\%/\sqrt{E(\mathrm{GeV})}$; the resolution will be significantly better than this for the small subsample of events in which muons are fully contained by the detector.

Figures 4.2 and 4.3 show the predicted spectra of observed signal and background events in LBNE produced from the GLoBES implementation, including the effects of neutrino oscillation. Figure 4.2 shows the ν_μ and $\overline{\nu}_\mu$-CC sample and Figure 4.3 shows the ν_e and $\overline{\nu}_e$-CC appearance sample. Table 4.3 shows the expected LBNE signal and background event rates in ν_μ disappearance and ν_e

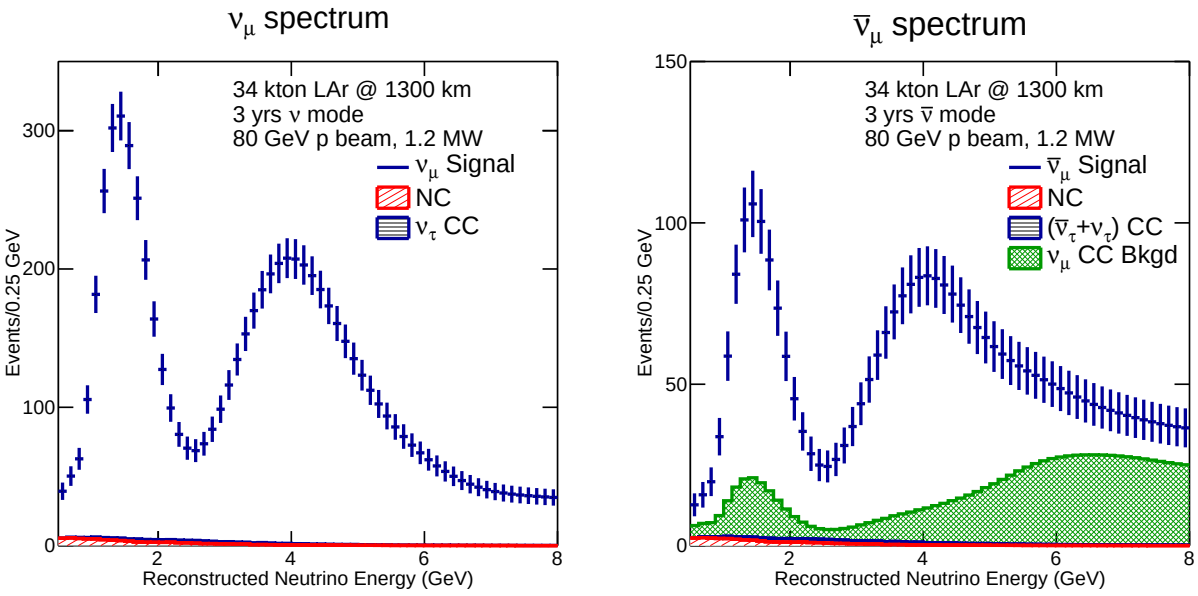

Figure 4.2: The expected reconstructed neutrino energy spectrum of ν_μ or $\overline{\nu}_\mu$ events in a 34-kt LArTPC for three years of neutrino (left) and antineutrino (right) running with a 1.2-MW beam.

Table 4.3: Expected number of neutrino oscillation signal and background events in the energy range 0.5 GeV to 8.0 GeV at the far detector after detector smearing and event selection. The calculation assumes $\sin^2(2\theta_{13}) = 0.09$ and $\delta_{\rm CP} = 0$. The event rates are given per 10-kt LArTPC and three years of running with the improved 80-GeV LBNE beam at 1.2 MW. For signal, the number of ν and $\overline{\nu}$ events are shown separately, while for the background estimates ν and $\overline{\nu}$ events are combined. The MH has negligible impact on ν_μ disappearance signals.

Beam	**Hierarchy**	**Signal Events**	**Background Events**				
		$\nu_x/\overline{\nu}_x$ **CC**	ν_μ **NC**	ν_μ **CC**	ν_e **Beam**	ν_τ **CC**	**Total**
			$\nu_\mu \rightarrow \nu_{x=\mu}$ **(disappearance)**				
Neutrino	-	2056/96	23	N/A	-	18	41
Antineutrino	-	280/655	10	N/A	-	10	20
			$\nu_\mu \rightarrow \nu_{x=e}$ **(appearance)**				
Neutrino	Normal	229/3	21	25	47	14	107
Neutrino	Inverted	101/5	21	25	49	17	112
Antineutrino	Normal	15/41	11	11	24	9	55
Antineutrino	Inverted	7/75	11	11	24	9	55

appearance modes for neutrinos and antineutrinos, for normal (NH) and inverted (IH) hierarchy. The rates are given per 10 kt of fiducial LArTPC mass.

The GLoBES implementation used in the sensitivity studies presented here appears to be in good agreement with more recent results from the Fast MC, described in Section A.3. Updated sensitivity and systematics studies are currently underway using the Fast MC for detector simulation, and customized GLoBES-based software for the oscillation fits and propagation of systematics. A full

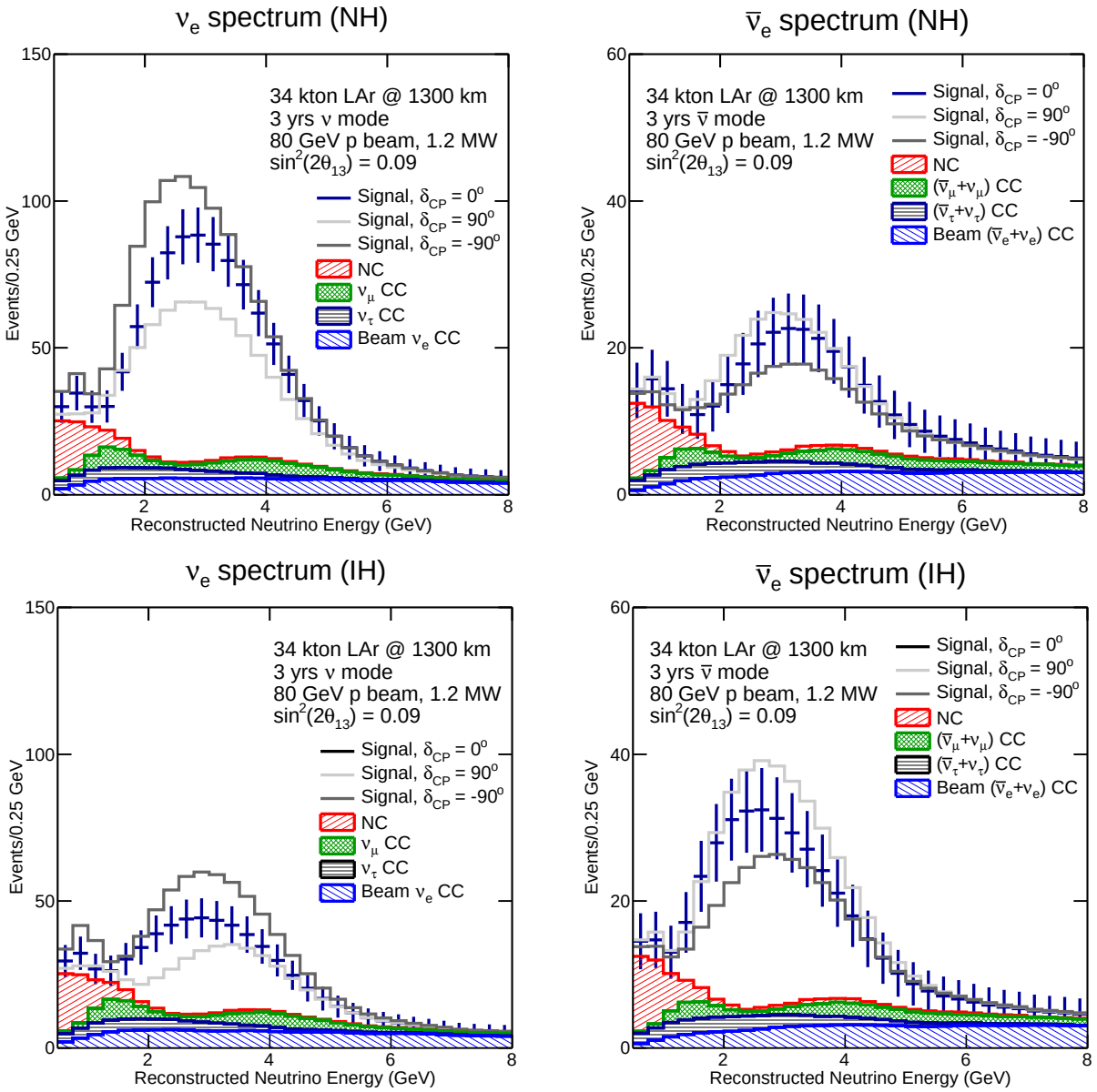

Figure 4.3: The expected reconstructed neutrino energy spectrum of ν_e or $\overline{\nu}_e$ oscillation events in a 34-kt LArTPC for three years of neutrino (left) and antineutrino (right) running with a 1.2-MW, 80-GeV beam assuming $\sin^2(2\theta_{13}) = 0.09$. The plots on the top are for normal hierarchy and the plots on the bottom are for inverted hierarchy.

MC simulation of the far detector and automated event reconstruction is being developed; this is also described in Appendix A.

4.3 Measurements of Mass Hierarchy and the CP-Violating Phase

The neutrino mass hierarchy (MH) and the value of the CP-violating phase, $\delta_{\rm CP}$, are currently unknown. Knowledge of the MH has significant theoretical, cosmological and experimental implications. A determination of the $\delta_{\rm CP}$ value to be neither zero (0) nor π would constitute the first observation of CP violation in the lepton sector.

The expected performance of a 10-kt LArTPC far detector 1,300 km downstream from a neutrino source is detailed in the LBNE Conceptual Design Report Volume 1 [29]. Estimated sensitivities to the determination of the MH and discovery of CP violation, presented both here and in the CDR, are calculated using the GLoBES package. The detector response assumed in these calculations is summarized in Table 4.2. The sensitivities are obtained by simultaneously fitting the $\nu_\mu \rightarrow \nu_\mu$, $\overline{\nu}_\mu \rightarrow \overline{\nu}_\mu$, $\nu_\mu \rightarrow \nu_e$, and $\overline{\nu}_\mu \rightarrow \overline{\nu}_e$ oscillated spectra, examples of which are shown in Figures 4.2 and 4.3. The ν_τ background is not used in the sensitivity calculations since it is expected that further analysis will reduce this background to negligible levels.

In these calculations, experimental sensitivity is quantified using $\Delta\chi^2$ parameters, which are determined by comparing the predicted spectra for various scenarios. These quantities are defined, differently for neutrino MH and CP-violation sensitivity, to be:

$$\Delta\chi^2_{MH} = |\chi^2_{MH^{test}=IH} - \chi^2_{MH^{test}=NH}|, \tag{4.1}$$

$$\Delta\chi^2_{CPV} = \min\left(\Delta\chi^2_{CP}(\delta^{test}_{\rm CP}=0), \Delta\chi^2_{CP}(\delta^{test}_{\rm CP}=\pi)\right), \text{ where} \tag{4.2}$$

$$\Delta\chi^2_{CP} = \chi^2_{\delta^{test}_{\rm CP}} - \chi^2_{\delta^{true}_{\rm CP}}. \tag{4.3}$$

These sensitivities are evaluated separately for true NH and IH. Since the true value of $\delta_{\rm CP}$ is unknown, a scan is performed over all possible values of $\delta^{true}_{\rm CP}$. The individual χ^2 values are calculated using

$$\chi^2(\mathbf{n}^{true}, \mathbf{n}^{test}, f) = 2\sum_i^{N_{reco}} (n_i^{true} ln \frac{n_i^{true}}{n_i^{test}(f)} + n_i^{test}(f) - n_i^{true}) + f^2, \tag{4.4}$$

where $\mathbf{n}$ are event rate vectors in N_{reco} bins of reconstructed energy and f represents a nuisance parameter to be profiled. Nuisance parameters include the values of mixing angles, mass splittings, and signal and background normalization. The nuisance parameters are constrained by Gaussian priors; in the case of the oscillation parameters, the Gaussian prior has standard deviation determined by taking 1/6 of the 3σ range allowed by the global fit [54].

With the exception of results reported in Section 4.3.1, where more information on the statistical interpretation of MH sensitivity is provided, the sensitivities presented here are for the *typical experiment* with no statistical fluctuations considered. In the absence of statistical fluctuations, the χ^2 value for the *true* spectra is identically zero. Statistical fluctuations are incorporated by

repeatedly varying the contents of each energy bin in each sample by drawing from a Poisson distribution with the expected number of events in that bin as the mean.

This section presents the sensitivities of various LBNE configurations to determination of the MH and CP violation. In particular, a 10-kt far detector and the full-scope 34-kt far detector are considered. In each case, the performance of LBNE with both the 120-GeV beamline design presented in the CDR [30] as well as the upgraded 80-GeV beam described in Section 3.4 is studied. In addition, the sensitivities at different possible stages of LBNE with increases to far detector mass and Main Injector beam upgrades are estimated.

Figure 4.4 summarizes the sensitivities for determining the MH and CP violation ($\delta_{\rm CP} \neq 0$ or π) as a function of the true value of $\delta_{\rm CP}$ with a 10-kt LArTPC. The red band shows the sensitivity that is achieved with an exposure of six years with equal exposures in ν and $\overline{\nu}$ mode in a 1.2-MW beam. The cyan band shows the sensitivity obtained by combining the 10-kt LBNE with T2K and NOνA, where the T2K exposure is 7.8×10^{21} POT in ν mode only and the NOνA exposure is six years (assuming 6×10^{20} POT per year) with equal exposures in ν and $\overline{\nu}$ mode. The bands indicate the sensitivity range corresponding to different levels of signal and background normalization uncertainties and different possible beam designs. The gray curves are the expected sensitivities for the combination of NOνA and T2K. The known mixing parameters are allowed to float in the fit, but are constrained (using a Gaussian prior) by the uncertainties from the 2012 global best fit [54]. The reactor mixing angle, $\sin^2 2\theta_{13}$, is constrained to be 0.094 ± 0.005. The uncertainty is equal to the size of the current systematic uncertainty from the Daya Bay Experiment [142] and is used as a conservative estimate of the precision that will be achieved by the current generation of reactor experiments. Figure 4.5 shows the sensitivities for determining the MH and CP violation as a function of the true value of $\delta_{\rm CP}$ after six years of running in the LBNE 34-kt configuration under the same assumptions.

The sensitivity bands in Figures 4.4 and 4.5 represent the variation in sensitivity as a function of the beam design and normalization uncertainties on the signal and background. The solid curve at the lower end of the red band represents the beamline design described in the LBNE CDR Volume 2 [30] for which there is no near detector. The dashed line above the solid curve represents the sensitivity with the beam design improvements currently under study as described in Section 3.4, still without a near detector. The dashed line at the upper end of the red band represents the case in which both the beam design improvements and a high-resolution, highly capable near detector are implemented. The key design goal of the LBNE near detector and beamline simulation software is to enable a prediction of the far detector unoscillated flux with a precision of $\leq 2\%$. Therefore, the total signal and background normalization uncertainties on the ν_μ disappearance signal are assumed to be 5% and 10%, respectively. The default ν_e appearance signal *uncorrelated* normalization uncertainties for the full-scope LBNE presented in this chapter are assumed to be 1%. The ν_e appearance background uncertainty is expected to be at least as good as the $\sim 5\%$ [143] achieved by the ν_e appearance search in the MINOS experiment.

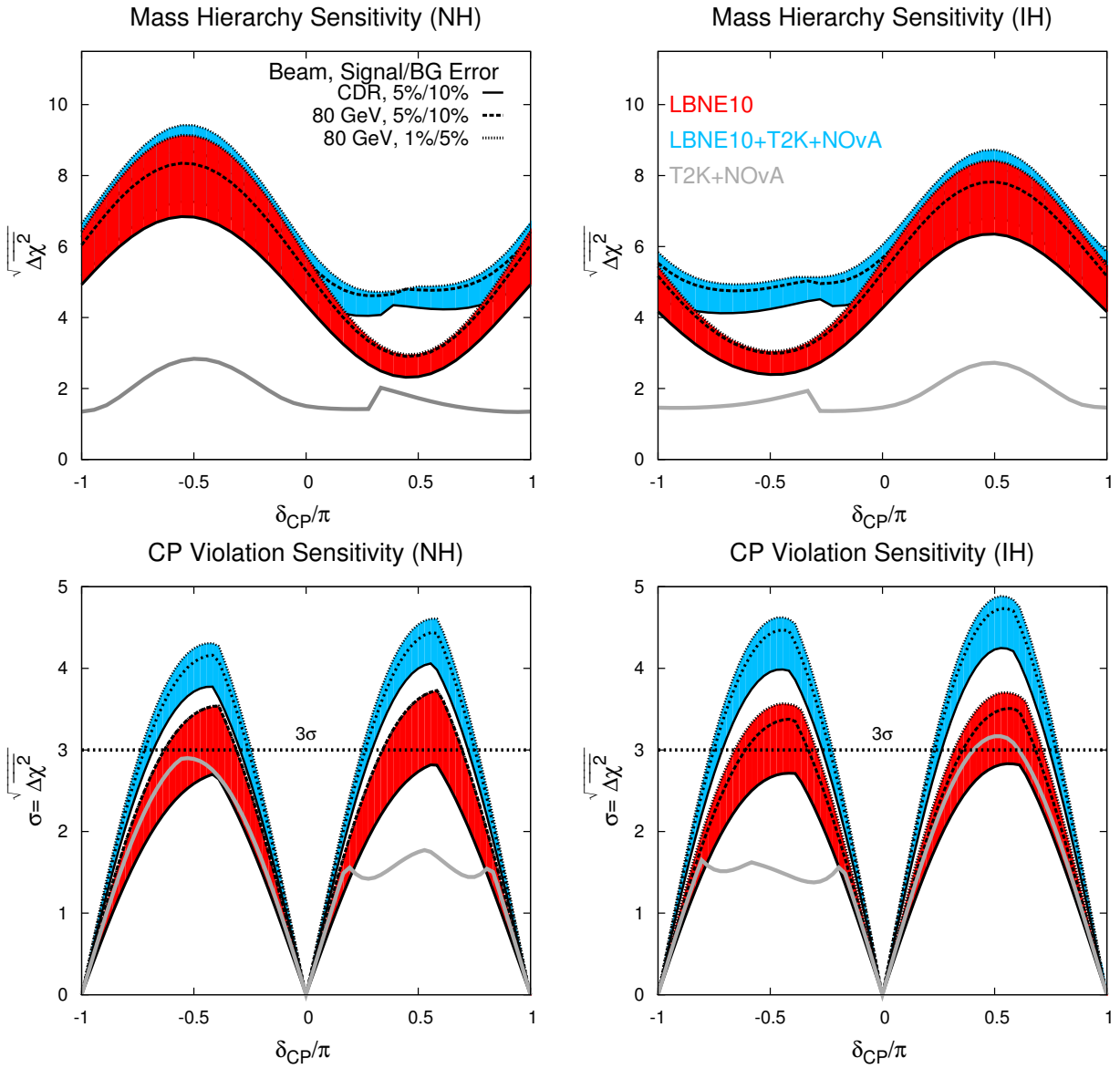

Figure 4.4: The significance with which the mass hierarchy (top) and CP violation ($\delta_{\rm CP} \neq 0$ or π, bottom) can be determined as a function of the value of $\delta_{\rm CP}$. The plots on the left are for normal hierarchy and the plots on the right are for inverted hierarchy. The red band shows the sensitivity that is achieved by a typical experiment with the LBNE 10-kt configuration alone, where the width of the band shows the range of sensitivities obtained by varying the beam design and the signal and background uncertainties as described in the text. The cyan band shows the sensitivity obtained by combining the 10-kt LBNE with T2K and NOνA, and the gray curves are the expected sensitivities for the combination of NOνA and T2K; the assumed exposures for each experiment are described in the text. For the CP-violation sensitivities, the MH is assumed to be unknown.

A detailed discussion of the systematics assumptions for LBNE is presented in Section 4.3.2. In the case that LBNE has no near neutrino detector, the uncertainties on signal and background are expected to be 5% and 10%, respectively, extrapolating from the performance and detailed knowledge of the NuMI beam on which the LBNE beamline is modeled, in situ measurements of

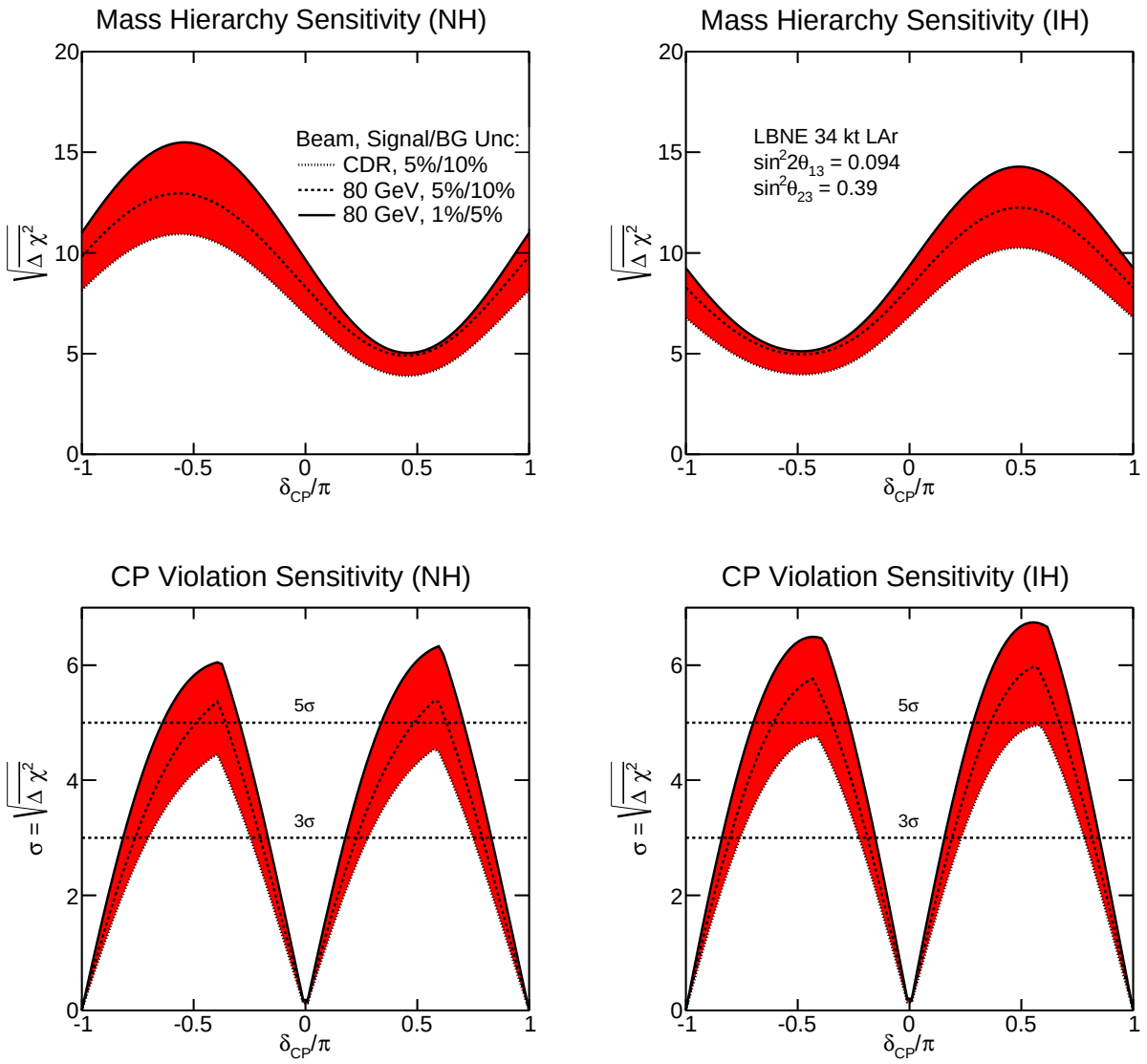

Figure 4.5: The significance with which the mass hierarchy (top) and CP violation ($\delta_{\rm CP} \neq 0$ or π, bottom) can be determined by a typical LBNE experiment with a 34-kt far detector as a function of the value of $\delta_{\rm CP}$. The plots on the left are for normal hierarchy and the plots on the right are for inverted hierarchy. The width of the red band shows the range of sensitivities that can be achieved by LBNE when varying the beam design and the signal and background uncertainties as described in the text.

the muon flux at the near site as described in [29], the expectation of improved hadron production measurements with the NA61 and MIPP experiments, and the experience of previous ν_e appearance experiments as summarized in Table 4.4.

Table 4.4: Summary of achieved systematic error performance in several select prior $\nu_\mu \to \nu_e$ oscillation experiments. These numbers were extracted from publications and may not correspond exactly to the description in the text. NBB/WBB indicates a narrow/wide band beam. *No ND* indicates there was no near detector, and *ND-FD* indicates a two (near-far) detector experiment with extrapolation of the expected background and signal from the near to the far detector. In the case of T2K, the quoted systematic (*) is actually the total uncertainty on the observed events, which are predominately signal.

Experiment	Year	ν_μ-NC/CC Events	ν_e-CC Events	Background Syst.Error	Comment
BNL E734 [144]	1985	235	418	20%	No ND
BNL E776(NBB) [145]	1989	10	9	20%	No ND
BNL E776 (WBB) [146]	1992	95	40	14%	No ND
NOMAD [147]	2003	$<$300	5500	$< 5\%$	No ND
MiniBooNE [148]	2008	460	380	9%	No ND
MiniBooNE [49]	2013	536	782	5%	SciBooNE
MINOS [143]	2013	111	36	4%	ND–FD
T2K [149]	2013	1.1	26	9%*	ND–FD

4.3.1 Interpretation of Mass Hierarchy Sensitivities

LBNE will be definitive in its ability to discriminate between normal and inverted mass hierarchy for the allowed range of unknown parameters such as $\delta_{\rm CP}$ and $\sin^2\theta_{23}$. To assess the sensitivity of LBNE to this physics, particularly for the case of less favorable parameter values, detailed understanding of statistical significance is essential.

At the true values of $\delta_{\rm CP}$ for which the mass hierarchy asymmetry is maximally offset by the leptonic CP asymmetry, LBNE's sensitivity to the mass hierarchy is at its minimum. Even in this case, with a 34-kt LArTPC operating for six years in a 1.2-MW beam, the $|\Delta\chi^2|$ value obtained in a typical data set will exceed 25, allowing LBNE on its own to rule out the incorrect mass ordering at a confidence level above $1-3.7\times10^{-6}$. Considering fluctuations, LBNE will measure, in $\geq 97.5\%$ of all possible data sets for this least favorable scenario, a value of $|\Delta\chi^2|$ equal to 9 or higher, which corresponds to a $\geq 99\%$ probability of ruling out the incorrect hierarchy hypothesis.

In the mass hierarchy (MH) determination, only two possible results are considered, as the true MH is either normal (NH) or inverted (IH). Reference [150] presents the statistical considerations of determining the sensitivity of an experiment to the MH, framed partly in the context of two separate but related questions:

1. *Given real experimental data, with what significance can the MH be determined?*

2. *When evaluating future experimental sensitivities, what is the probability that a particular experimental design will be able to determine the MH with a given significance?*

Once data are in hand, a number of techniques based either within Bayesian or frequentist statistics make it possible to determine the level of confidence at which one MH hypothesis or the other can be ruled out. In assessing the sensitivity of future experiments, it is common practice to generate a simulated data set (for an assumed true MH) that does not include statistical fluctuations. The expected sensitivity can be reported as $\overline{\Delta\chi^2}$, representative of the mean or the most likely value of $\Delta\chi^2$ that would be obtained in an ensemble of experiments for a particular true MH. With the exception of Figure 4.7, the sensitivity plots in this document have been generated using this method.

However, addressing the expected sensitivity of an experiment per the second question above requires consideration of the effect of statistical fluctuations and variations in systematics. If the experiment is repeated many times, a distribution of $\Delta\chi^2$ values will appear. Studies in [150] and elsewhere (e.g., [151]) show that the $\Delta\chi^2$ metric employed here *does not* follow the commonly expected χ^2 function for one degree of freedom, which has a mean of $\overline{\Delta\chi^2}$ and can be interpreted using a Gaussian distribution with a standard deviation of $\sqrt{|\overline{\Delta\chi^2}|}$. Rather, these studies show that when the observed counts in the experiment are large enough, the distribution of $\Delta\chi^2$ used here approximately follows a Gaussian distribution with a mean and standard deviation of $\overline{\Delta\chi^2}$ and $2\sqrt{|\overline{\Delta\chi^2}|}$, respectively [150].

Figure 4.6 shows the expected distribution of $\Delta\chi^2$ values in LBNE from toy Monte Carlo studies. The interpretation of pairs of distributions, such as those in the various panels of this figure, depends on the information being sought. For example, one is not necessarily interested simply in the fraction of experiments where $\Delta\chi^2$ has the "right" sign. (An experiment that obtains a small value of $\Delta\chi^2$, even with the "right" sign, would not be particularly constraining since there is no way *a priori* to know which is the right sign — this is what the experiment is attempting to measure.) It should also be noted that in general $|\overline{\Delta\chi^2_{\mathrm{MH=NH}}}|$, i.e., true NH, is not necessarily equal to $|\overline{\Delta\chi^2_{\mathrm{MH=IH}}}|$, i.e., true IH, nor do the corresponding distributions necessarily have the same shape. For some ranges in δ_{CP}, for example, the event rate in LBNE is sufficiently different for the two MH hypotheses that the corresponding distributions in $\Delta\chi^2$ are quite distinct.

The plots shown on the left in Figure 4.6 illustrate the case for a true value of $\delta_{\mathrm{CP}} = 0°$, where the $\Delta\chi^2$ distributions for NH and IH scenarios are similar. Shown on the right are the corresponding distributions for the case of $\delta_{\mathrm{CP}} = 90°$, where for NH the matter asymmetry is maximally offset by the CP asymmetry, leading to poorer MH discrimination. For the IH case, these effects go in the same direction, leading to better MH discrimination. The converse is the case for $\delta_{\mathrm{CP}} = -90°$. Since the true value of δ_{CP} is unknown (although a best-fit value and confidence interval

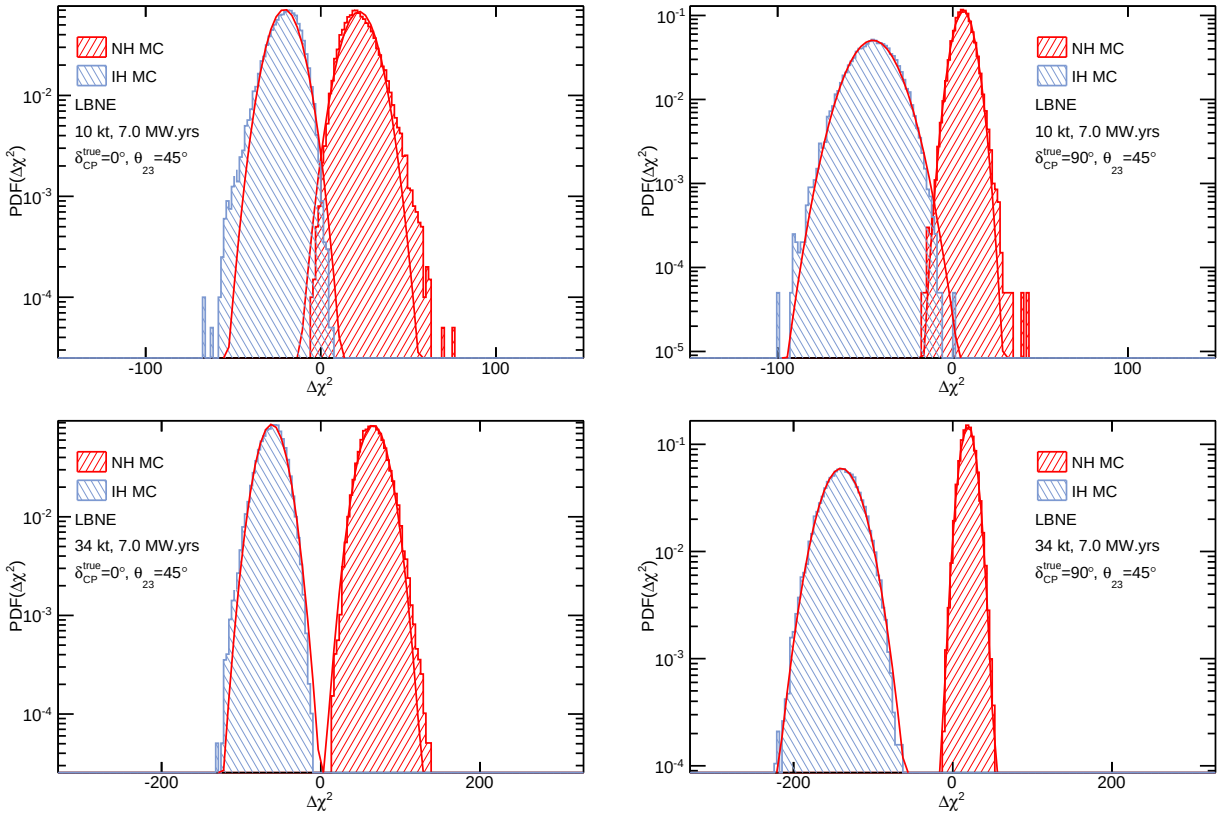

Figure 4.6: $\Delta\chi^2_{\mathrm{MH=NH}}$ (red) and $\Delta\chi^2_{\mathrm{MH=IH}}$ (blue) distributions for LBNE from Toy MC studies. The top set of figures are for a 10-kt detector operating six years in a 1.2-MW beam. The bottom set is for a 34-kt detector operating six years in a 1.2-MW beam. The figures on the left are for $\delta_{cp}^{true} = 0$ and the figures on the right are for $\delta_{cp}^{true} = 90°$. The value of δ_{CP} is unconstrained in the fit.

will emerge from the analysis of the data collected), comparison of a given value of $\Delta\chi^2$ with expected distributions for NH and IH cases for the *same* value of δ_{CP} does not in general provide the appropriate test. For simplicity, following [151], the discussion below focuses on the respective values of δ_{CP} for which the experiment will have poorest sensitivity for NH ($+90°$) and IH ($-90°$) scenarios.

Given the above introduction to the statistical fluctuation issues, it is natural to employ the statistical language of hypothesis testing in projecting LBNE's MH sensitivity. Specifically, α is defined as the desired Type-I error rate — that is, the probability of rejecting a particular hypothesis, e.g., NH, in the case where this is the true hypothesis. One can then ask what the corresponding Type-II error rate β would be, defined as the probability of accepting the hypothesis being tested (NH in this example), when in fact the alternate hypothesis (IH) is true. The pair of α and β would correspond to a particular value of $\overline{\Delta\chi^2}$ chosen (in advance of the experiment) as a criterion for deciding whether to rule out the NH (or IH). Historically, many experiments have characterized their anticipated sensitivity by reporting α for the case of $\beta = 0.5$, which is nothing more than that given by the median value of the test statistic (in this case, $\Delta\chi^2 = \overline{\Delta\chi^2}$) as described above.

Sometimes, the sensitivity is also reported as the square root of $\overline{\Delta\chi^2}$.

Due to the approximate symmetry of the MH ambiguity as a function of $\delta_{\rm CP}$ for the two MH scenarios and the desire to be able to reject exactly one of the two possible mass orderings [151], it is also natural to report a value of α for an experiment such that $\alpha = \beta$ [152,153,151]. In this way, it is possible to express just how *unlucky* an experiment can be while maintaining a corresponding sensitivity α. In the case of LBNE, a reasonable benchmark for comparison corresponds to $\overline{\Delta\chi^2} = 36$. For this case, specifying $\alpha = \beta$ yields $\alpha = 0.0013$, which means that the experiment will have a 0.13% probability of ruling out the true MH hypothesis and of accepting the wrong MH hypothesis.

As described above, and as is evident in the plots presented, such as those in Figures 4.4 and 4.5, the sensitivity of LBNE is strongly dependent on the true value of $\delta_{\rm CP}$; Figure 4.7 shows that it also depends on the true value of $\sin^2\theta_{23}$. While plotting the value of α (for some choice of β, such as $\beta = 0.5$ or $\beta = \alpha$) as a function of these parameters encapsulates the sensitivity, a visually helpful presentation is obtained by plotting the expected mean value, $\overline{\Delta\chi^2}$, as well as ranges of possible values corresponding to the expected distribution in $\Delta\chi^2$. Thus, Figure 4.7 shows the dependence of $\sqrt{|\overline{\Delta\chi^2}|}$ on the true value of $\delta_{\rm CP}$ for the typical LBNE data set, for two possible values of $\sin^2\theta_{23}$, as well as the corresponding expectation bands within which 68% (green) and 95% (yellow) of LBNE sensitivities will fall. These expectation bands give a semi-quantitative picture of the likely range of outcomes for the experiment.

The horizontal dashed lines on Figure 4.7 specify the confidence level of an experiment with a particular value of $\Delta\chi^2$ such that:

$$\mathrm{CL} = P(\text{favored MH}|\text{data}\,x)/(P(\text{favored MH}|\text{data}\,x) + P(\text{unfavored MH}|\text{data}\,x)), \quad (4.5)$$

following the convention in [150], where the notation $P(\mathrm{A}|\mathrm{B})$ represents the probability of A given condition B, and these probabilities are inferred from the corresponding likelihoods via Bayes' Theorem. Alternatively, the $\Delta\chi^2$ values shown in these plots can be approximately translated to sensitivities in terms of α, for whatever choice of β is desired, following, for example, the prescription described in [151].

As seen in Figure 4.7, a typical LBNE data set with a 34-kt detector can determine the MH with $|\overline{\Delta\chi^2}| \geq 25$ for all values of $\delta_{\rm CP}$ (for the left plot, where $\sin^2\theta_{23} = 0.39$). From a Bayesian analysis, the probability that an experiment measuring $|\Delta\chi^2| = 25$ has ruled out the true MH hypothesis is 3.7×10^{-6}, as indicated for the corresponding horizontal dashed line in the plots in this figure. When considering the effect of statistical fluctuations, for the same value of θ_{23}, about 97.5% of experiments will determine the MH with $|\Delta\chi^2| > 9$ for the least favorable value of $\delta_{\rm CP}$, where $|\Delta\chi^2| = 9$ corresponds to a CL of 98.9%.

For the bulk of the range of $\delta_{\rm CP}$, the sensitivity of LBNE is vastly better than for the least favorable value described above. Furthermore, newer data prefer values of θ_{23} closer to maximal [69], which

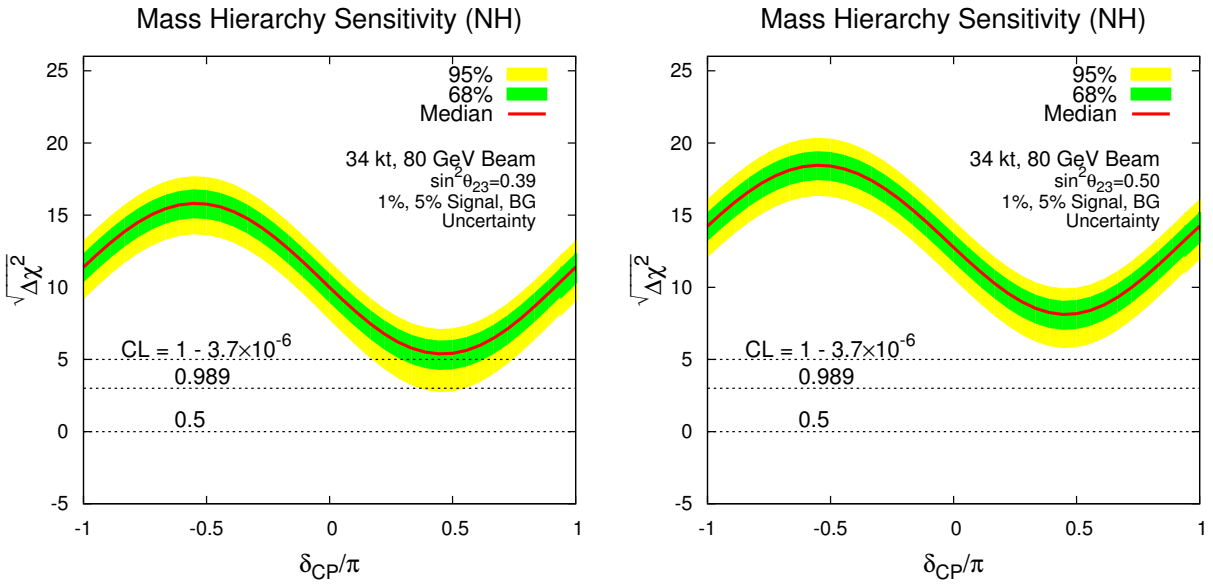

Figure 4.7: The square root of the mass hierarchy discrimination metric $\Delta\chi^2$ is plotted as a function of the unknown value of $\delta_{\rm CP}$ for the full-scope LBNE with 34 kt, 3+3 ($\nu + \overline{\nu}$) years of running in a 1.2-MW beam, for true NH. The red curve represents the most likely experimental value obtained, estimated using a data set absent statistical fluctuations, while the green and yellow bands represent the range of $\Delta\chi^2$ values expected in 68% and 95% of all possible experimental cases, respectively. The horizontal lines indicate the probability that an experiment with that value of $\Delta\chi^2$ correctly determines the MH, computed according to a Bayesian statistical formulation. The plot on the left assumes a value of $\sin^2\theta_{23} = 0.39$ [54], while that on the right assumes $\sin^2\theta_{23} = 0.5$ (maximal ν_μ-ν_τ mixing).

results in significantly enhanced LBNE MH sensitivity. As shown in the right-hand plot of Figure 4.7, if $\sin^2\theta_{23} = 0.5$, the expected MH sensitivity for the typical LBNE experiment at the least favorable $\delta_{\rm CP}$ point is $|\overline{\Delta\chi^2}| \approx 64$, which is significantly larger than the sensitivity of $|\overline{\Delta\chi^2}| \approx 25$ expected for the same value of $\delta_{\rm CP}$ if $\sin^2\theta_{23} = 0.39$. This suggests that a typical LBNE data set will determine the MH with $|\Delta\chi^2|$ well above the benchmark value of 36 mentioned above for even the least favorable values of $\delta_{\rm CP}$.

In addition to detailed LBNE-specific frequentist studies reported in [151], an LBNE-specific update (using both Bayesian and frequentist approaches) to the general statistical studies reported in [150] is in preparation.

4.3.2 Sensitivities and Systematics

The main systematic uncertainties in any experiment are determined by the analysis strategy employed and the performance of the detector. Figure 4.8 outlines the analysis strategy commonly employed to extract oscillation parameters in two-detector long-baseline neutrino oscillation experiments. The measured spectrum of ν_μ events in the near detector, $N_{\rm ND}^{data}(\nu_\mu)$ is extrapolated to the far detector and is used to predict both the ν_μ and ν_e appearance signals in the far detector, $N_{\rm FD}^{expected}(\nu_\mu)$ and $N_{\rm FD}^{expected}(\nu_e)$ respectively. The measured spectrum of ν_e candidates in the near

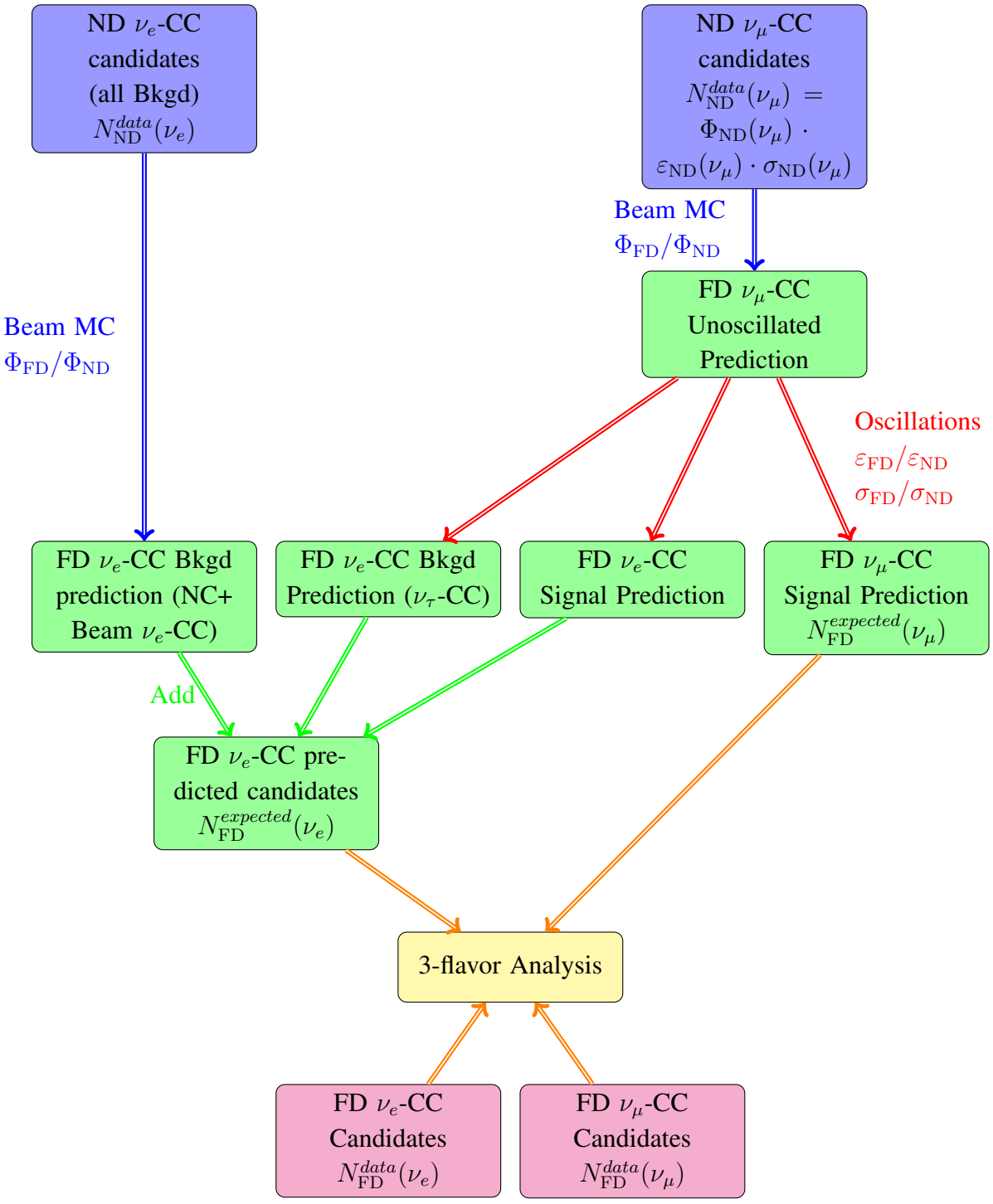

Figure 4.8: Flow chart of the ν_e appearance analysis method in a two-detector long-baseline experiment. Φ refers to the beam flux, ε refers to detector efficiencies and smearing, and σ refers to neutrino interaction modeling. The terms ND and FD refer to the near and far detector, respectively.

detector, $N_{\rm ND}^{data}(\nu_e)$, which comprises mostly the beam ν_e events and NC π^0 misidentified events, is used to predict the background to the ν_e appearance signal in the far detector. In LBNE, neutrino oscillation parameters will be extracted using a fit to four far detector data samples: ν_e, $\overline{\nu}_e$, ν_μ, and $\overline{\nu}_\mu$, which will allow for partial cancellation of uncertainties.

In the current generation of experiments, the measured spectrum of neutrino events in the near detector is a product of beam flux (Φ), detector efficiency and smearing (ε), and neutrino interaction dynamics (σ). To extrapolate the observed spectra in the near detector to the far detector, corrections have to be made for:

1. Differences in the beam flux in the near and far detectors, $\Phi_{\rm FD}/\Phi_{\rm ND}$: The near detector is much closer to the neutrino beamline and sees an extended source of neutrinos from the decay pipe as compared to the far detector, which observes a point source. A beam MC is used to correct for these differences. Uncertainties arise from inaccuracies in the simulation of the hadron production from the target, the focusing of the horns, the material in the beamline (which absorbs hadrons before they can decay), and the decay channel geometry.

2. Differences in near and far detector smearing and efficiencies, $\varepsilon_{\rm FD}/\varepsilon_{\rm ND}$: The largest uncertainties arise from the different event selection efficiencies in the near and far detectors and, in particular, the imperfect modeling of the energy scales of the near and far detectors. Identical near and far detectors allow most of these uncertainties to cancel in the extrapolation in the case of the ν_μ signal prediction. The ν_e signal prediction is extrapolated from $N_{\rm ND}^{data}(\nu_\mu)$; thus there are irreducible residual uncertainties arising from different criteria used to select ν_e and ν_μ candidate events and different detector response functions.

3. Differences in the interactions of neutrinos in the near and far detector, $\sigma_{\rm FD}/\sigma_{\rm ND}$: In the case in which both near and far detectors use the same target nucleus, the differences cancel for extrapolation of the ν_μ signal from the near to the far detector. When using the ν_μ signal in the near detector to predict the ν_e (and ν_τ) signals in the far detector, uncertainties arising from differences in ν_e (ν_τ) and ν_μ interactions, $\sigma_{\rm FD}(\nu_e)/\sigma_{\rm ND}(\nu_\mu)$, dominate. These uncertainties are limited by theoretical uncertainties and are typically smaller at higher energies.

The estimation of the expected signals at the far detector can be summarized thus:

$$N_{\rm ND}^{data}(\nu_\mu) = \Phi_{\rm ND}(\nu_\mu) \otimes \varepsilon_{\rm ND}(\nu_\mu) \otimes \sigma_{\rm ND}(\nu_\mu) \tag{4.6}$$

$$N_{\rm FD}^{expected}(\nu_\mu) = N_{\rm ND}^{data}(\nu_\mu) \otimes \frac{\Phi_{\rm FD}(\nu_\mu)}{\Phi_{\rm ND}(\nu_\mu)} \otimes P(\nu_\mu \to \nu_\mu) \otimes \frac{\varepsilon_{\rm FD}(\nu_\mu)}{\varepsilon_{\rm ND}(\nu_\mu)} \otimes \frac{\sigma_{\rm FD}(\nu_\mu)}{\sigma_{\rm ND}(\nu_\mu)} \tag{4.7}$$

$$
\begin{aligned}
N_{\mathrm{FD}}^{expected}(\nu_e) \;=\; & \underbrace{N_{\mathrm{ND}}^{data}(\nu_\mu) \otimes \frac{\Phi_{\mathrm{FD}}(\nu_\mu)}{\Phi_{\mathrm{ND}}(\nu_\mu)} \otimes P(\nu_\mu \to \nu_e) \otimes \frac{\varepsilon_{\mathrm{FD}}(\nu_e)}{\varepsilon_{\mathrm{ND}}(\nu_\mu)} \otimes \frac{\sigma_{\mathrm{FD}}(\nu_e)}{\sigma_{\mathrm{ND}}(\nu_\mu)}}_{\text{Expected signal events}} \\
& + \underbrace{N_{\mathrm{ND}}^{data}(\nu_e) \otimes \frac{\Phi_{\mathrm{FD}}(\nu_e)}{\Phi_{\mathrm{ND}}(\nu_e)} \otimes P(\nu_e \to \nu_e) \otimes \frac{\varepsilon_{\mathrm{FD}}(\nu_e)}{\varepsilon_{\mathrm{ND}}(\nu_e)} \otimes \frac{\sigma_{\mathrm{FD}}(\nu_e)}{\sigma_{\mathrm{ND}}(\nu_e)}}_{\text{Beam } \nu_{\mathrm{e}} \text{ events}} \\
& + \text{NC background extrapolated from } N_{\mathrm{ND}}^{data}(\nu_e) \\
& + \nu_\tau \text{ background extrapolated from } N_{\mathrm{ND}}^{data}(\nu_\mu)
\end{aligned}
\tag{4.8}
$$

Expected systematic uncertainties on the LBNE ν_e appearance and ν_μ signal samples in the three-flavor fit for LBNE (Table 4.2) are extrapolated from the current performance of the MINOS [143,154] and T2K [149] experiments. The dominant uncertainties on the current ν_e appearance analysis from MINOS and T2K and the expected corresponding uncertainties in LBNE are shown in Table 4.5. The categorization of the dominant experimental uncertainties in Table 4.5 are not always in exact correspondence since T2K and MINOS are very different experiments and deploy different analysis techniques. A detailed description of the expected LBNE performance on each of the dominant uncertainties follows.

Beam flux uncertainties: The LBNE high-resolution near detector is being designed with the goal of accurately measuring the unoscillated beam flux at the near site with a precision $\leq 2\%$ for both shape and absolute normalization. Table 4.6 summarizes the precision that can be achieved using different near detector analysis techniques, described in detail in Section 7.1, to measure the absolute normalization and shape of the different components of this flux. It is important to note that several of these techniques have already been used and *proven to work* in neutrino experiments such as MINOS [155] and NOMAD [156,157]. In particular, the inclusive neutrino charged current (CC) cross-section measurement in the MINOS near detector reported in [155] has already achieved a normalization uncertainty of $\sim 2\%$ in the range of $3 < E_\nu < 9$ GeV using the low-ν_0 method described in Section 7.1. The total systematic uncertainty on the NuMI neutrino flux determination by the MINOS near detector reported in [155] was $\sim 6\%$ and was limited by the detector performance. Recent independent studies on extraction of the neutrino flux using the low-ν_0 method [158] indicate that the technique can be reliably extended down to 1 GeV.

The LBNE near detector is being designed to significantly improve performance relative to the current generation of high-intensity neutrino detectors. A detailed beamline simulation will enable the extrapolation of the LBNE near detector flux measurements to the unoscillated far detector spectrum with high precision using techniques similar to those used by MINOS [159]. The near-to-far ν_μ unoscillated-spectrum extrapolation uncertainties already achieved by MINOS are $< 3\%$ in the MINOS (and also in the LBNE) appearance signal range of $1 < E_\nu < 8$GeV [160,159]. The MINOS extrapolation does not include any independent constraints on the hadron production spectrum from the proton target or information on the horn focusing performance from the muon flux measurements at the near site. The NuMI beamline — the design of which is very similar to

Table 4.5: The dominant systematic uncertainties on the ν_e appearance signal prediction in MINOS and T2K and a projection of the expected uncertainties in LBNE. For the MINOS uncertainties *absolute* refers to the total uncertainty and ν_e is the effect on the ν_e appearance signal only. The LBNE uncertainties are the total *expected* uncertainties on the ν_e appearance signal which include both correlated and uncorrelated uncertainties in the three-flavor fit.

Source of Uncertainty	**MINOS Absolute/ν_e**	**T2K ν_e**	**LBNE ν_e**	**Comments**
Beam Flux after N/F extrapolation	3%/0.3%	2.9%	2%	MINOS is normalization only. LBNE normalization and shape highly correlated between ν_μ/ν_e.
Detector effects				
Energy scale (ν_μ)	7%/3.5%	included above	(2%)	Included in LBNE ν_μ sample uncertainty only in three-flavor fit. MINOS dominated by hadronic scale.
Absolute energy scale (ν_e)	5.7%/2.7%	3.4% includes all FD effects	2%	Totally active LArTPC with calibration and test beam data lowers uncertainty.
Fiducial volume	2.4%/2.4%	1%	1%	Larger detectors = smaller uncertainty.
Neutrino interaction modeling				
Simulation includes: hadronization cross sections nuclear models	2.7%/2.7%	7.5%	$\sim 2\%$	Hadronization models are better constrained in the LBNE LArTPC. N/F cancellation larger in MINOS/LBNE. X-section uncertainties larger at T2K energies. Spectral analysis in LBNE provides extra constraint.
Total	**5.7%**	**8.8%**	**3.6 %**	**Uncorrelated ν_e uncertainty in full LBNE three-flavor fit = 1-2%.**

LBNE's — is expected to operate for more than a decade with improved flux measurements using the much more capable MINERνA detector [161] in both the low-energy and high-energy tunes. MINERνA is designed to measure the absolute NuMI flux with a precision of $\sim 5\%$ or better; data from MINERνA will be used to further improve the accuracy of the LBNE beamline simulation, reducing the uncertainties on the extrapolation of the flux. A new program of hadron production measurements at the NA61/SHINE [162] experiment will also reduce the near-to-far extrapolation uncertainties from the LBNE beamline simulation. The combination of LBNE near detector flux measurements and improved beamline simulation is expected to enable a prediction of the far detector ν_e appearance signal with a precision of $< 2\%$ total normalization and shape uncertainty. Since this uncertainty is highly correlated among the four data samples in the three-flavor fit, the final uncorrelated uncertainty on the ν_e signal sample will be significantly smaller.

Table 4.6: Precisions achievable from in situ ν_μ and ν_e flux measurements in the fine-grained, high-resolution ND with different techniques.

Technique	Flavor	Absolute normalization	Relative flux $\Phi(E_\nu)$	Near Detector requirements
NC Scattering $\boldsymbol{\nu_\mu e^- \to \nu_\mu e^-}$	ν_μ	2.5%	$\sim 5\%$	e ID θ_e Resolution e^-/e^+ Separation
Inverse muon decay $\boldsymbol{\nu_\mu e^- \to \mu^- \nu_e}$	ν_μ	3%		μ ID θ_μ Resolution 2-Track (μ+X) Resolution μ energy scale
CC QE $\boldsymbol{\nu_\mu n \to \mu^- p}$ $\boldsymbol{Q^2 \to 0}$	ν_μ	$3-5\%$	$5-10\%$	D target p Angular resolution p energy resolution Back-Subtraction
CC QE $\boldsymbol{\overline{\nu}_\mu p \to \mu^+ n}$ $\boldsymbol{Q^2 \to 0}$	$\overline{\nu}_\mu$	5%	10%	H target Back-Subtraction
Low-ν_0	ν_μ		2.0%	μ^- vs μ^+ E_μ-Scale Low-E_{Had} Resolution
Low-ν_0	$\overline{\nu}_\mu$		2.0%	μ^- vs μ^+ E_μ-Scale Low-E_{Had} Resolution
Low-ν_0	$\nu_e/\overline{\nu}_e$	1-3%	2.0%	e^-/e^+ Separation (K^0_L)
CC	ν_e/ν_μ	<1%	~2%	e^- ID & μ^- ID p_e/p_μ Resolution
CC	$\overline{\nu}_e/\overline{\nu}_\mu$	<1%	~2%	e^+ ID & μ^+ ID p_e/p_μ Resolution
Low-ν_0/CohPi	$\overline{\nu}_\mu/\nu_\mu$	~2%	~2%	μ^+ ID & μ^- ID p_μ Resolution E_{Had} Resolution

ν_μ energy-scale uncertainty: Both T2K and MINOS use the reconstructed ν_μ event spectrum in the near detector to predict the ν_e appearance signal at the far detector. Therefore the ν_μ energy-scale uncertainty in the near detector is propagated as an uncertainty on the ν_e appearance signal at the far detector. In MINOS — which has a high proportion of non-QE events — the ν_μ energy-scale uncertainty is dominated by uncertainty in the hadronic energy scale (7% for $E_\nu < 3$ GeV) [163] and the muon energy scale (2.5%). Utilization of the low-ν_0 method for energies less than 3 GeV in LBNE reduces the hadronic energy-scale contribution to the uncertainty in the ν_μ energy scale in the near detector. As discussed in Chapter 7, it is expected that both the muon and hadronic energy-scale uncertainties in the near detector will be $<1\%$, so far detector energy-scale uncertainties will

dominate the uncertainty in the ν_μ signal prediction. The high-resolution LArTPC far detector and an active program of hadron test-beam experiments planned for LBNE will reduce far detector hadronic energy-scale uncertainties, which also contribute to uncertainty in the energy scale of the far detector ν_μ signal used in the three-flavor analysis. Extrapolating from MINOS, the LBNE ν_μ energy-scale uncertainty is thus estimated to be $\sim 2\%$.

In MINOS, the 7% ν_μ energy-scale uncertainty resulted in a residual uncertainty of 3.5% on the ν_e signal prediction. In the LBNE full three-flavor analysis, this uncertainty is 100% correlated between the predicted ν_μ and ν_e signal samples; therefore a E_{ν_μ} energy-scale uncertainty of 2% is assigned to the ν_μ signal prediction in LBNE. The residual uncorrelated uncertainty on the ν_e signal prediction is considered to be negligible.

Absolute ν_e energy-scale uncertainties: In Figure 4.9, the MH and CP-violation sensitivity obtained using a rate-only, a shape-only and a rate+shape analysis of ν_e appearance is shown. This study demonstrates that a critical component of LBNE's oscillation sensitivity is an accurate measurement of the shape of the ν_e appearance signal. This measurement depends on the precision

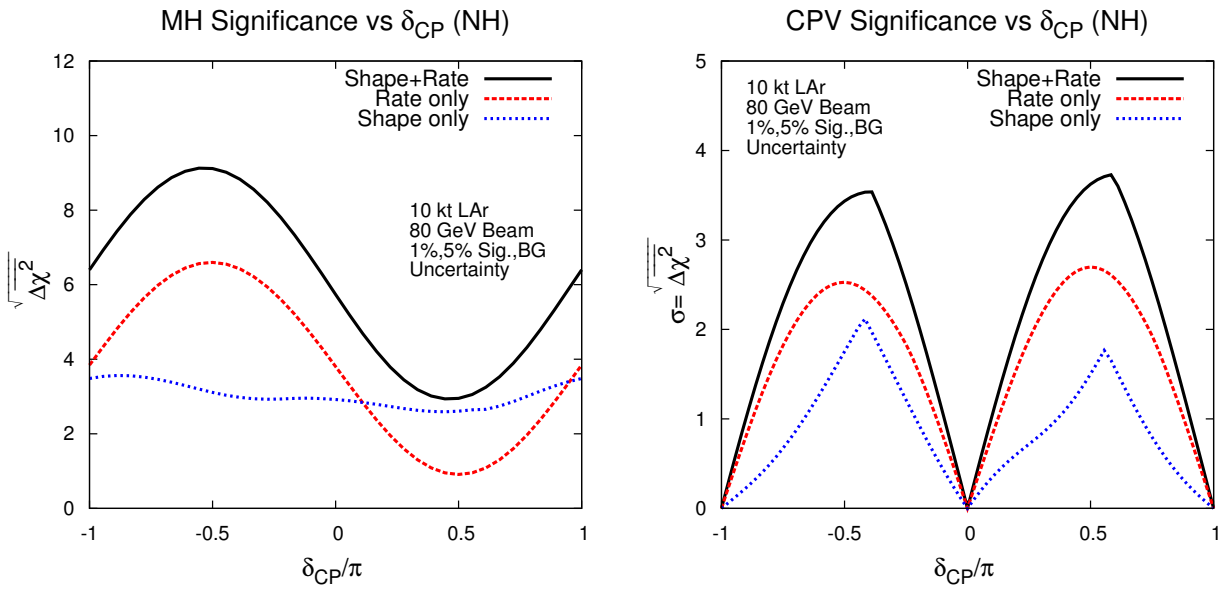

Figure 4.9: The mass hierarchy (left) and CP violation (right) sensitivities from shape, rate, and shape+rate. The sensitivity is for a 10-kt detector, 1.2-MW beam, 3+3 ($\nu + \overline{\nu}$) years, for true normal hierarchy.

with which the detector response to ν_e interactions is understood. The ν_e energy-scale uncertainty, which is not yet included in the current sensitivity calculation with the GLoBES framework, is therefore expected to be an important systematic uncertainty in the LBNE oscillation analysis.

The effect of ν_e energy-scale uncertainty on the ν_e signal normalization, determined by the precision of detector calibration, was 2.7% in MINOS and 3.4% in T2K, where the T2K uncertainty actually includes most far detector effects. LBNE's LArTPC detector technology is expected to

outperform both the MINOS sampling calorimeter and the T2K water Cherenkov detector in reconstruction of the ν_e interaction. For example, the proton produced from the ν_e-QE interaction — the interaction with potentially the best ν_e energy resolution — is clearly visible in a LArTPC [164], whereas it is often below Cherenkov threshold in T2K. An active program of test beam experiments with LArTPCs is currently being planned to address the detector response to electrons and hadrons. Results from the test beam experiments and the projected performance of the in situ calibration will enable LBNE to limit the detector energy-scale uncertainties below the level achieved by the current generation of experiments.

Hadronic energy is expected to contribute more than half of the total energy deposit for many ν_e and ν_μ interactions in LBNE. The hadronic energy scale does not depend on neutrino flavor; since it should be identical for ν_e and ν_μ interactions, this portion of the absolute energy-scale uncertainty is expected to largely cancel in the LBNE three-flavor analysis. This cancellation may be reduced to the extent that event-selection criteria vary the hadronic energy fraction among the samples.

Simulation uncertainties: The simulation uncertainties listed in Table 4.5 refer primarily to uncertainties in modeling neutrino interactions with the target nucleus in the near and far detectors. These uncertainties include ν_e and ν_μ cross-section uncertainties, uncertainties arising from the modeling of the structure of the target nucleus, modeling of final-state interactions within the nucleus, and hadronization model uncertainties arising from the break up of the target nucleus in higher-energy inelastic interactions. The deployment of identical nuclear targets in the MINOS (iron) and LBNE (argon) near and far detectors allows for a larger cancellation of the simulation uncertainties as compared to T2K, which used dissimilar target nuclei in its near detector (carbon) and far detector (oxygen). A high-resolution near detector such as that being designed for LBNE will enable further constraints on the hadronization models by resolving many of the individual particles produced in resonance and deep inelastic interactions, which represent $\sim$75% of LBNE neutrino interactions.

The MINOS ν_e appearance analysis achieved a 2.7% residual uncertainty from simulation after the near-to-far extrapolation. The MINOS simulation uncertainty is dominated by hadronization uncertainties, because cross-section uncertainties largely cancel between the identical nuclei in the near and far detectors. The T2K residual uncertainty after near-to-far extrapolation is 7%. Additionally, the T2K analysis includes more sources of cross-section uncertainties than MINOS and, at the lower T2K energies, larger differences in ν_μ/ν_e cross sections (2.9 %) persist after extrapolating the ν_μ spectrum in the near detector to the ν_e signal prediction in the far.

The LBNE near detector design is required to achieve a cancellation of near-to-far cross-section and hadronization-model uncertainties at the same level as MINOS or better. The ν_e appearance signal in LBNE peaks at 2.5 GeV; these higher energies will result in lower uncertainties from the cross-section effects considered by T2K. In addition, since cross-section variations impact the observed ν_e and ν_μ spectra differently when compared to oscillation effects, the fit to the wide-band spectrum in LBNE could constrain some of these uncertainties further. Therefore, it is expected that

LBNE could reduce the total ν_e appearance simulation uncertainties to a level of 2%. Preliminary results from the LBNE Fast MC simulation (described in Section A.3) indicate that many cross-section uncertainties cancel out when combining the ν_μ disappearance and ν_e appearance signal samples in a three-flavor fit, resulting in a much smaller uncorrelated uncertainty on the ν_e signal sample.

It is important to note that some $\nu/\overline{\nu}$ simulation uncertainties may not cancel out in the near-to-far extrapolation or in the combined fit; in particular, uncertainties due to nuclear models and intra-nuclear effects are different for $\nu/\overline{\nu}$ interactions. New models of intra-nuclear effects are being evaluated to determine the size of these irreducible residual uncertainties. Additionally, there are uncertainties at the level of 1-2% in the cross sections that will not cancel between ν_e and ν_μ [165]. In the absence of theoretical progress, these should also be considered irreducible.

Fiducial volume uncertainties: One of the dominant uncertainties in the MINOS ν_μ disappearance analysis — a high-precision oscillation analysis based on a detailed spectral shape — was the fiducial-volume uncertainty, which included near and far detector reconstruction uncertainties. The uncertainty on the fiducial volume of the MINOS far detector alone was 2.4%. T2K, with a much larger far detector (22.5 kt fiducial), was able to reduce this uncertainty to the 1% level. It is expected that LBNE will be able to achieve this level of uncertainty on the ν_e appearance signal. With the combination of all four signal samples ($\nu_\mu, \overline{\nu}_\mu, \nu_e, \overline{\nu}_e$) in a three-flavor fit, the ν_e uncorrelated portion of this uncertainty is expected to be smaller than 1%.

ν_e appearance background systematic uncertainties: The ν_e appearance normalization uncertainty is expected to be at least as good as the $\sim 5\%$ [143] achieved by the ν_e appearance search in the MINOS experiment, using the technique of predicting intrinsic-beam and neutral current (NC) background levels from near detector measurements. The LBNE far detector should be able to provide additional constraints on the background level by independently measuring NC and ν_τ background.

In Figure 4.10, the MH and CP-violation sensitivities as a function of exposure are evaluated using three different sets of assumptions regarding the uncorrelated ν_e signal/background normalization uncertainties: 1%/5% (the goal of the LBNE scientific program), 2%/5% and 5%/10%. The last is a conservative estimate of the uncertainties that can be achieved in LBNE without unoscillated neutrino beam measurements at the near site. The impact of signal and background normalization uncertainties on the MH sensitivity is small even at high exposures given the large $\nu/\overline{\nu}$ asymmetry at 1,300 km and the fact that much of the sensitivity to the MH comes from analysis of the spectral shapes (Figure 4.9). For CP violation, however, the impact of normalization uncertainties is significant at exposures ≥ 100 kt · MW · years.

Table 4.7 summarizes the LBNE exposures required to reach 3σ and 5σ sensitivity to CP violation for at least 50% of all possible values of $\delta_{\rm CP}$. The exposures vary depending on the assumptions made about the normalization uncertainties that can be achieved in LBNE. The normalization un-

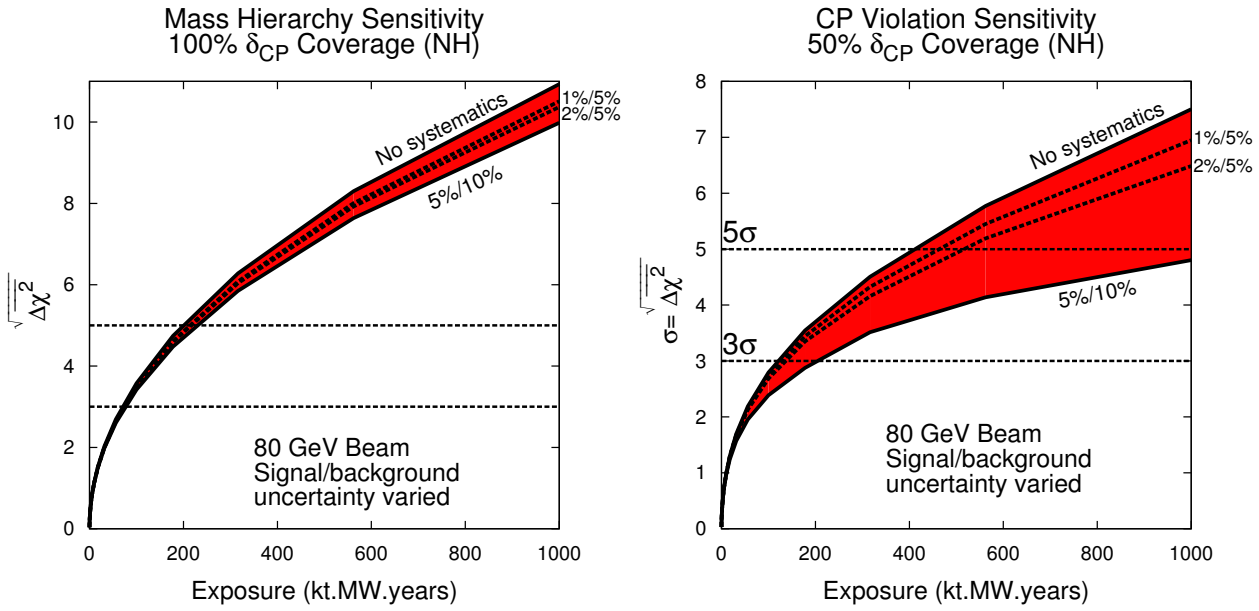

Figure 4.10: The mass hierarchy (left) and CP violation (right) sensitivities as a function of exposure in kt · year, for true normal hierarchy. The band represents the range of signal and background normalization errors.

Table 4.7: The exposures required to reach 3σ and 5σ sensitivity to CP violation for at least 50% of all possible values of $\delta_{\rm CP}$ as a function of systematic uncertainties assumed on the ν_e appearance signal. The uncertainties varied are the uncorrelated signal normalization uncertainty (Sig) and the background normalization uncertainty (Bkgd).

Systematic uncertainty	**CPV Sensitivity**		**Required Exposure**
	$\delta_{\rm CP}$ Fraction	**($\sqrt{\Delta\chi^2}$)**	
0 (statistical only)	50% $\delta_{\rm CP}$	3 σ	100 kt · MW · year
	50% $\delta_{\rm CP}$	5 σ	400 kt · MW · year
1%/5% (Sig/bkgd)	50% $\delta_{\rm CP}$	3 σ	100 kt · MW · year
	50% $\delta_{\rm CP}$	5 σ	450 kt · MW · year
2%/5% (Sig/bkgd)	50% $\delta_{\rm CP}$	3 σ	120 kt · MW · year
	50% $\delta_{\rm CP}$	5 σ	500 kt · MW · year
5%/10% (no near ν det.)	50% $\delta_{\rm CP}$	3 σ	200 kt · MW · year

certainty assumptions range from 1-2%/5% on signal/background to 5%/10%. The uncertainties listed in Table 4.7 and shown in the sensitivity figures pertain to the ν_e appearance signal and background normalization. In Figure 4.9 the sensitivities obtained from the rate only, shape only and rate+shape of the appearance spectrum are shown for a 10-kt detector with an 80-GeV beam. For CP violation (right), the rate information dominates the sensitivity, but the shape information enables the detector to exceed 3σ sensitivity for large CP violation. For the MH sensitivity, Figure 4.9 (left) demonstrates that the sensitivity in the least favorable range of $\delta_{\rm CP}$ values is dominated by the shape information. Further analysis has shown that it is the region of the second oscillation node

that is responsible for this effect. The shape of the signal in this region will enable LBNE to determine the sign of $\delta_{\rm CP}$, which is sufficient to break the degeneracy with MH effects and determine the correct sign of the mass ordering.

Figures 4.11, 4.12, and 4.13 show the variation in sensitivity to CP violation and MH when the true value of the oscillation parameters θ_{13}, θ_{23} and Δm^2_{31} are varied within the 3σ range allowed by the 2012 3ν global fit [54]. These sensitivities are calculated for six years with equal exposures in ν and $\overline{\nu}$ mode in a 1.2-MW beam for the case in which an upgraded 80-GeV beam and a near detector have both been implemented.

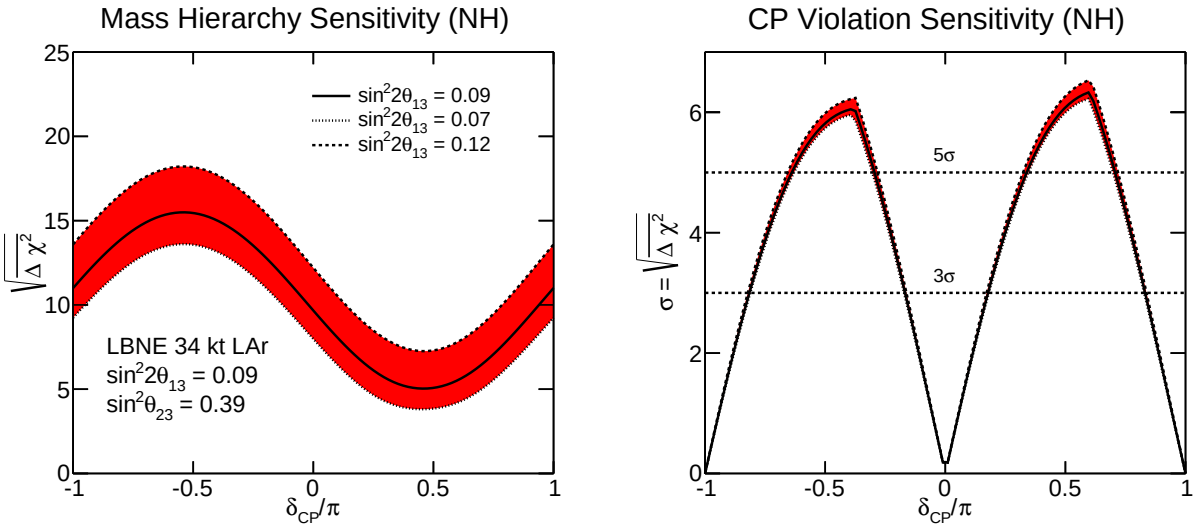

Figure 4.11: The significance with which the mass hierarchy (left) and CP violation, i.e., $\delta_{\rm CP} \neq 0$ or π, (right) can be determined by a typical LBNE experiment as a function of the value of $\delta_{\rm CP}$ for an allowed range of θ_{13} values and for normal hierarchy; assumes a 34-kt far detector.

In comparing Figures 4.11, 4.12 and 4.13, the dependence on the true value of θ_{23} is particularly striking. As $\sin^2\theta_{23}$ increases, the sensitivity to CP violation decreases because the CP asymmetry that LBNE measures is inversely proportional to $|\sin\theta_{23}|$ as demonstrated in Equation 2.20. For the same reason, as θ_{23} increases, the degeneracy between the CP and matter asymmetries is broken, which increases the LBNE sensitivity to neutrino MH. The explicit dependence of MH sensitivity on the value of $\sin^2\theta_{23}$ is shown in Figure 4.14. As this plot makes clear, LBNE resolves the MH with a significance of $\sqrt{\overline{\Delta\chi^2}} > 6$ for nearly all allowed values of $sin^2\theta_{23}$ and $\delta_{\rm CP}$.

4.3.3 Summary of CP-Violation and Mass Hierarchy Sensitivities

For the 10-kt LBNE, the statistical uncertainties are much larger than the systematic uncertainties. Combining the sensitivity from the 10-kt LBNE with expected knowledge from the NOνA and T2K experiments would allow LBNE to achieve a $\geq 4\sigma$ sensitivity for detecting CP violation for 30% of the allowed values of $\delta_{\rm CP}$ and a $\geq 3\sigma$ sensitivity for 50% of these values. It is clear that

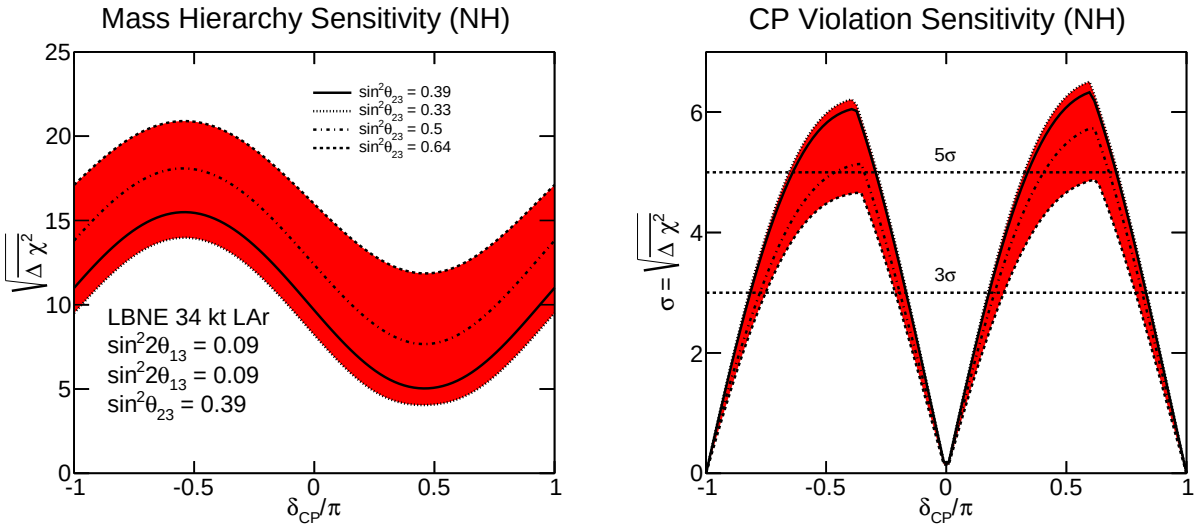

Figure 4.12: The significance with which the mass hierarchy (left) and CP violation, i.e., $\delta_{\rm CP} \neq 0$ or π, (right) can be determined by a typical LBNE experiment as a function of the value of $\delta_{\rm CP}$ for an allowed range of θ_{23} values and for normal hierarchy; assumes a 34-kt far detector.

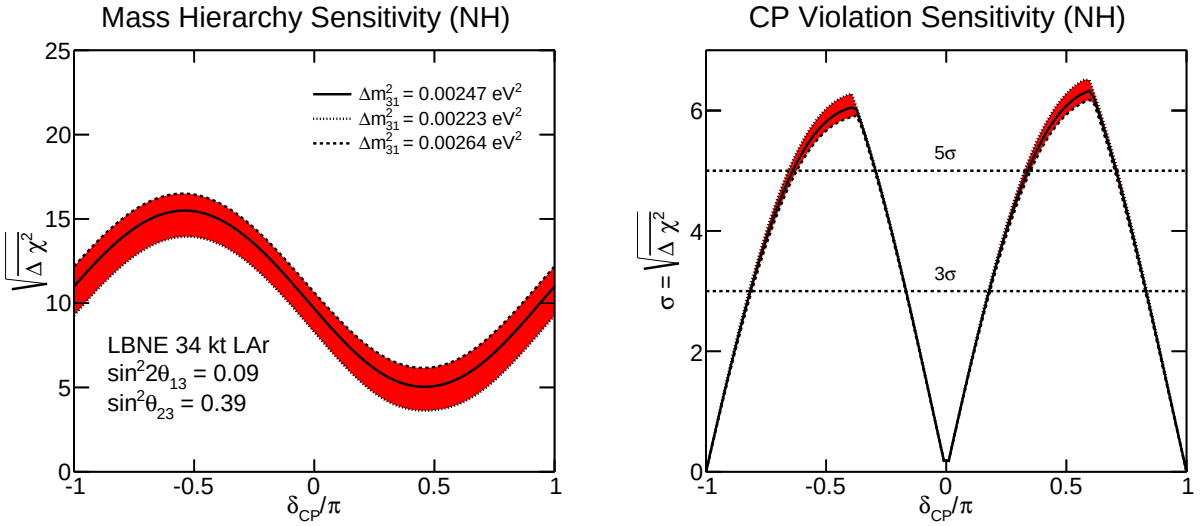

Figure 4.13: The significance with which the mass hierarchy (left) and CP violation, i.e., $\delta_{\rm CP} \neq 0$ or π, (right) can be determined by a typical LBNE experiment as a function of the value of $\delta_{\rm CP}$ for an allowed range of Δm^2_{31} values and for normal hierarchy; assumes a 34-kt far detector.

the 10-kt LBNE sensitivity would be the dominant contribution in the combined sensitivities and would therefore represent a significant advance in the search for leptonic CP violation over the current generation of experiments, particularly in the region where the CP and matter effects are degenerate.

The combination with T2K and NOνA would allow the MH to be determined with a *minimum* precision of $|\overline{\Delta\chi^2}| \geq 25$ over 60% $\delta_{\rm CP}$ values and $|\overline{\Delta\chi^2}| \geq 16$ for all possible values of $\delta_{\rm CP}$. Due to the low event statistics in these experiments, the combination with NOνA and T2K only helps

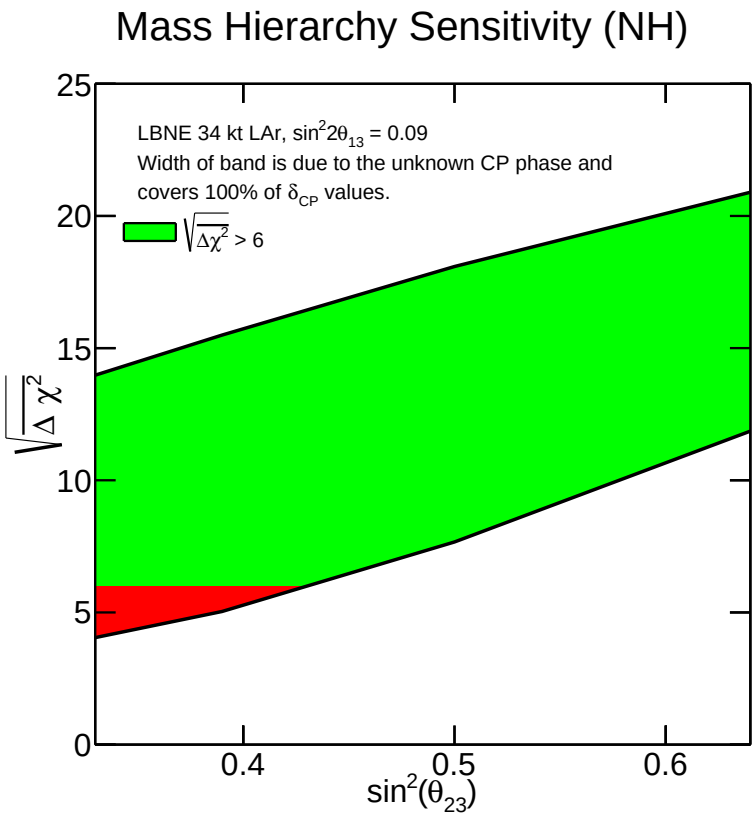

Figure 4.14: The significance with which the MH can be determined by a typical LBNE experiment as a function of the value of $\sin^2\theta_{23}$, for the 3σ allowed range of $\sin^2\theta_{23}$, for true normal hierarchy. The width of the band is due to the unknown value of $\delta_{\rm CP}$ and covers all possible values of $\delta_{\rm CP}$. The green region shows the parameter space for which $\sqrt{\Delta\chi^2} > 6$. Assumes a 34-kt far detector with 6 years of running in a 1.2 MW beam.

the sensitivity in the region of $\delta_{\rm CP} > 0$ (NH) or $\delta_{\rm CP} < 0$ (IH) where there are residual degeneracies between matter and CP-violating effects. As will be discussed in Section 4.6, the combination with atmospheric neutrino oscillation studies can also be used to improve the MH sensitivity in this region for the LBNE 10-kt configuration.

Assuming the normal hierarchy, the most recent global fit of experimental data for the three-neutrino paradigm favors a value of $\delta_{\rm CP}$ close to $-\pi/2$ with $\sin\delta_{\rm CP} < 0$ at a confidence level of $\sim 90\%$ [69] (Figure 4.15). LBNE alone with a 10-kt detector and six years of running would resolve with $\geq 3\sigma$ precision the question of whether CP is violated for the currently favored value of $\delta_{\rm CP}$. With a 34-kt detector running for six years, LBNE, alone will achieve a precision approaching 6σ.

Table 4.8 summarizes the MH and CP sensitivities that can be reached by a typical experiment with the LBNE 10-kt and 34-kt configurations assuming a running time of 3+3 ($\nu + \overline{\nu}$) years with a 1.2-MW beam under a variety of scenarios.

Table 4.8: The mass hierarchy and CP violation sensitivities that can be reached with a typical data set from the LBNE 10-kt and 34-kt configurations with a 1.2 MW beam, no near neutrino detector (ND) unless otherwise stated, and a run time of 3+3 $\nu + \overline{\nu}$ years under a variety of beam and systematic scenarios, for normal hierarchy. Note that the sensitivities for inverted hierarchy are similar but not identical. As discussed in the text, the significance of the MH determination should not be interpreted using Gaussian probabilities.

Scenario ($\sin^2\theta_{23} = 0.39$)	**MH sensitivity**		**CPV sensitivity**	
	δ_{CP} Fraction	**($\sqrt{\Delta\chi^2}$)**	**δ_{CP} Fraction**	**($\sqrt{\Delta\chi^2}$)**
LBNE 10 kt, CDR beam	50%	≥ 4	40%	$\geq 2\sigma$
	100%	≥ 2	-	-
LBNE 10 kt, 80-GeV upgraded beam	50%	≥ 5	23%	$\geq 3\sigma$
	100%	≥ 3	55%	$\geq 2\sigma$
LBNE 10 kt, 80-GeV beam, with ν ND	50%	≥ 5	33%	$\geq 3\sigma$
	100%	≥ 3	60%	$\geq 2\sigma$
+ NOνA (6 yrs), T2K (7.8×10^{21} POT)	75%	≥ 5	30%	$\geq 4\sigma$
	100%	≥ 4	50%	$\geq 3\sigma$
LBNE 34 kt , CDR beam	50%	≥ 7	20%	$\geq 4\sigma$
	100%	≥ 4	50%	$\geq 3\sigma$
LBNE 34 kt, 80-GeV upgraded beam	50%	≥ 8	15%	$\geq 5\sigma$
	100%	≥ 5	35%	$\geq 4\sigma$
LBNE 34 kt, 80-GeV beam, with ν ND	50%	≥ 9	35%	$\geq 5\sigma$
	100%	≥ 5	50%	$\geq 4\sigma$

4.3.4 CP-Violating and Mass Hierarchy Sensitivities with Increased Exposures

Figure 4.16 shows the minimum significance with which the MH can be resolved and CP violation determined by LBNE as a function of increased exposure in units of mass × beam power × time[§]. For this study, the LBNE beamline improvements discussed in Section 3.4 are used with $E_p = 80\,\text{GeV}$, and the signal and background normalization uncertainties are assumed to be 1% and 5%, respectively. Both ν_e and ν_μ appearance signals are used in a combined analysis. Due to the long baseline, the determination of the MH in LBNE to high precision does not require a large exposure; a sensitivity of $\sqrt{\Delta\chi^2} = 5$ for the worst case (NH, $\delta_{CP} = \pi/2$ or IH, $\delta_{CP} = -\pi/2$) requires an exposure of $\sim 200\,\text{kt}\cdot\text{MW}\cdot\text{years}$, but $\sqrt{\Delta\chi^2} = 5$ sensitivity can be reached for 50% of the allowed values of δ_{CP} with an exposure of less than $100\,\text{kt}\cdot\text{MW}\cdot\text{years}$. On the other hand, reaching discovery-level sensitivity ($\geq 5\sigma$) to leptonic CP violation for at least 50% of the possible values of δ_{CP} will require large exposures of $\approx 450\,\text{kt}\cdot\text{MW}\cdot\text{years}$. Figure 4.17 demonstrates the

[§]Time is denoted in years of running at Fermilab. One year of running at Fermilab corresponds to $\approx 1.7\times10^7$ seconds.

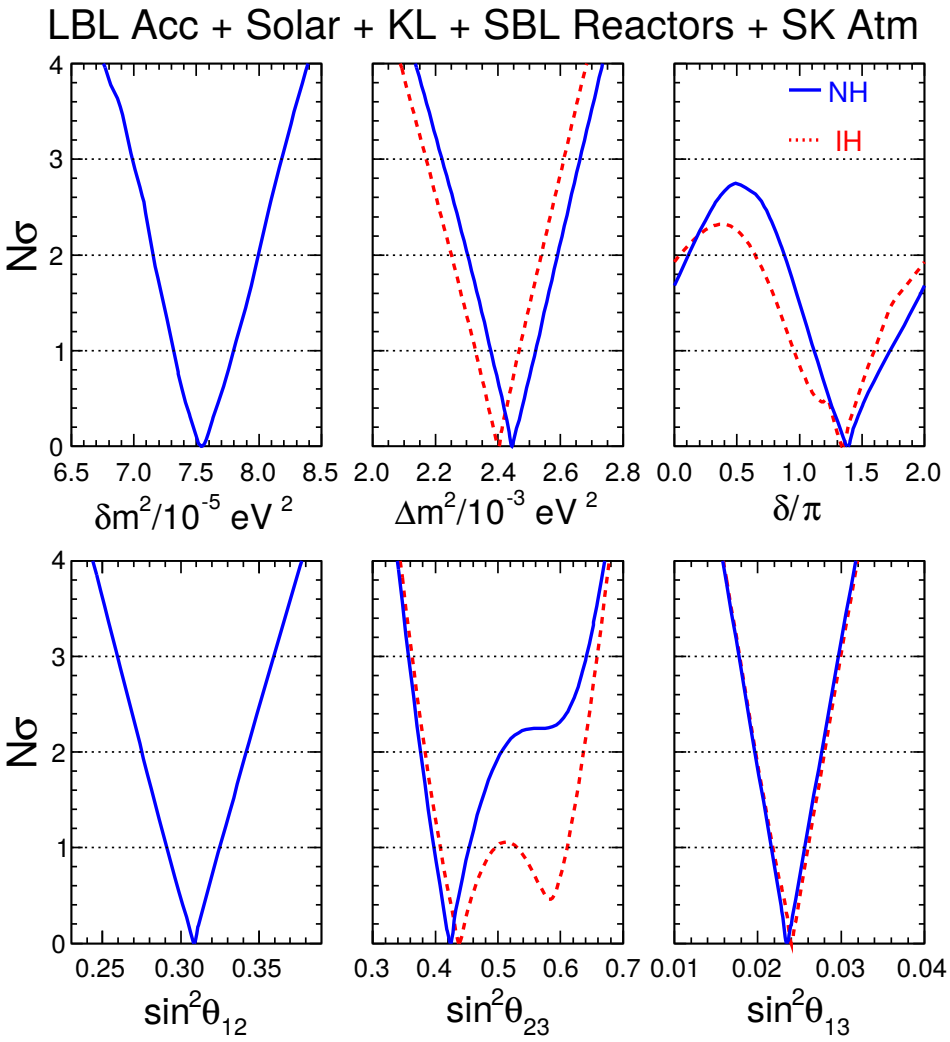

Figure 4.15: Results of the 2013 global analysis from Capozzi *et al.* shown as Nσ bounds on the six parameters governing three ν flavor oscillations. Blue (solid) and red (dashed) curves refer to NH and IH, respectively. Figure is from [69].

sensitivity to CP violation as a function of $\delta_{\rm CP}$ and exposure that can be achieved with various stages of the Fermilab Proton-Improvement-Plan (PIP-II and upgrades to PIP-II). In this study, the PIP-II upgrades are assumed to provide LBNE with 1.2 MW[¶] at 80 GeV, followed by further upgrades in which the booster is replaced with a linac that will provide 2.3 MW from the Main Injector (MI), also at 80 GeV. The study demonstrates that it is possible to reach 5σ sensitivity to CP violation over at least 40% of $\delta_{\rm CP}$ values running for a little over 10 years, starting with the PIP-II MI power and a LArTPC greater than 10 kt, and phasing in more detector mass. Other possible staging scenarios of detector mass and beam power are discussed in Chapter 9.

[¶]The assumed exposures are only accurate to the level of 15% due to incomplete knowledge of the PIP-II final design parameters and running conditions.

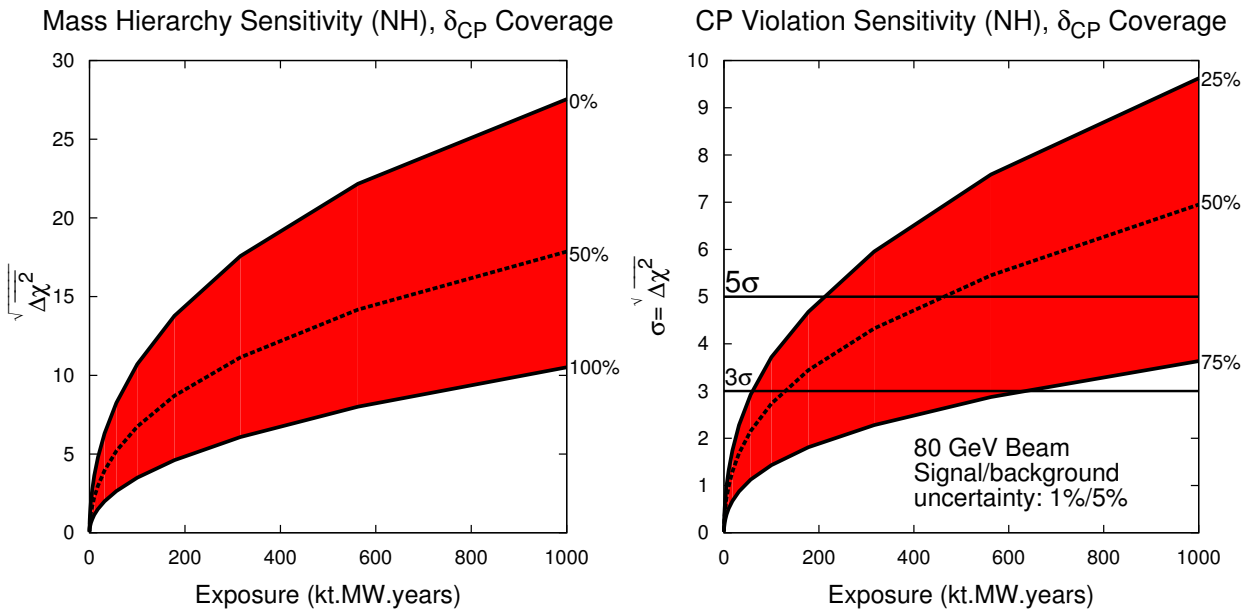

Figure 4.16: The minimum significance with which the mass hierarchy (left) and CP violation (right) can be resolved as a function of exposure in detector mass (kiloton) × beam power (MW) × time (years), for true NH. The red band represents the fraction of $\delta_{\rm CP}$ values for which the sensitivity can be achieved with at least the minimal significance on the y-axis.

Table 4.9: The CP violation sensitivities that can be reached by LBNE alone starting with the LBNE 10-kt configuration with a 1.2-MW beam and a run time of 3+3 ($\nu+\overline{\nu}$) years and phasing in additional far detector mass and beam power upgrades beyond the current PIP-II. In all cases, the sensitivities are calculated using the 80 GeV upgraded beam and 1%/5% signal/background normalization uncertainties, for true normal hierarchy. The sensitivity for each stage includes exposure from the previous stage(s) of the experiment.

Exposure	**Possible Scenario**	**CPV sensitivity**	
		$\delta_{\rm CP}$ Fraction	**($\sqrt{\Delta\chi^2}$)**
60 kt · years 1.2 MW beam	PIP-II, 10 kt, 6 years	60% $\delta_{\rm CP}$	$\geq 2\sigma$
		33% $\delta_{\rm CP}$	$\geq 3\sigma$
+ 200 kt · years 1.2 MW beam	PIP-II, 34 kt, 6 years	40% $\delta_{\rm CP}$	$\geq 5\sigma$
+ 200 kt · years 2.3 MW beam	Booster replaced, 34 kt, 6 years	60% $\delta_{\rm CP}$	$\geq 5\sigma$

4.4 Measurement of θ_{23} and Determination of the Octant

The value of $\sin^2 2\theta_{23}$ is measured to be > 0.95 at 90% CL using atmospheric neutrino oscillations [166]. This corresponds to a value of θ_{23} near 45°, but leaves an ambiguity as to whether the value of θ_{23} is in the lower octant (less than 45°), the upper octant (greater than 45°) or exactly 45°. The value of $\sin^2\theta_{23}$ from the 2013 global fit reported by [69] is $\sin^2\theta_{23} = 0.425^{+0.029}_{-0.027}(1\sigma)$ for normal hierarchy (NH), but as shown in Figure 4.15, the distribution of the χ^2 from the global fit has another local minimum — particularly if the MH is inverted — at $\sin^2\theta_{23} \approx 0.59$. A *maximal* mixing value of $\sin^2\theta_{23} = 0.5$ is therefore still allowed by the data and the octant is still largely

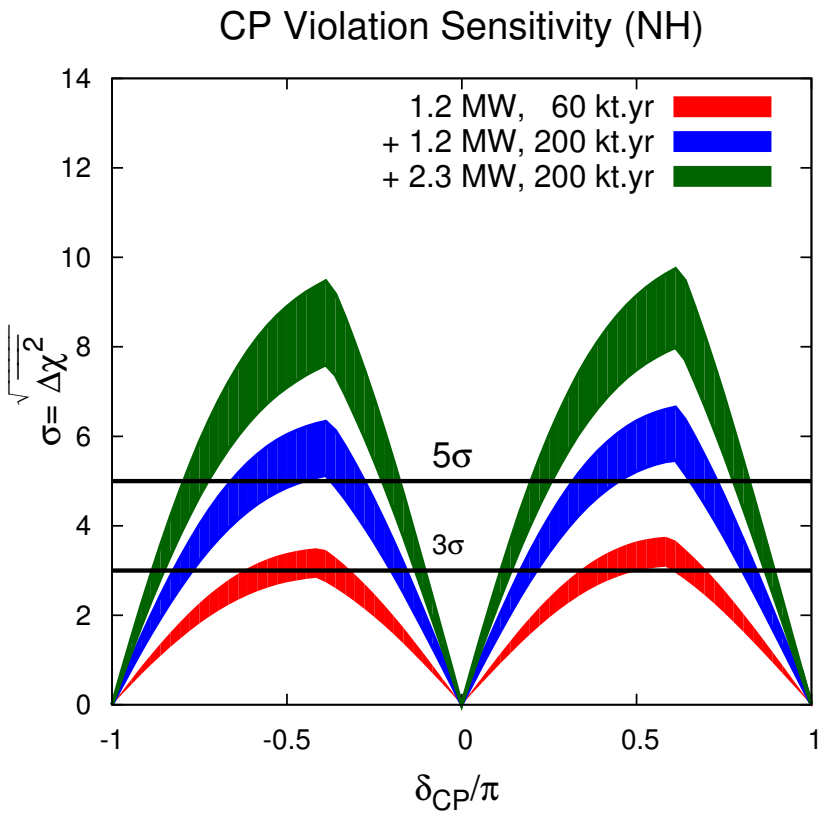

Figure 4.17: The significance with which CP violation — $\delta_{\rm CP} \neq 0$ or π — can be determined as a function of $\delta_{\rm CP}$. The different color curves represent possible exposures from different stages of PIP and detector mass upgrades as follows: 1.2 MW, 60 kt·years (red) + 1.2 MW, 200 kt·years (blue) + 2.3 MW, 200 kt·years (green). The sensitivity for each higher exposure is in addition to that from all lower exposures. The bands represent the range of sensitivities obtained from the improvements to the CDR beamline design.

undetermined. As discussed in Chapter 2, a value of θ_{23} exactly equal to 45° would indicate that ν_μ and ν_τ have equal contributions from ν_3, which could be evidence for a previously unknown symmetry. It is therefore important experimentally to determine the value of $\sin^2\theta_{23}$ with sufficient precision to determine the octant of θ_{23}.

The measurement of $\nu_\mu \rightarrow \nu_\mu$ oscillations is sensitive to $\sin^2 2\theta_{23}$, whereas the measurement of $\nu_\mu \rightarrow \nu_e$ oscillations is sensitive to $\sin^2\theta_{23}$. A combination of both ν_e appearance and ν_μ disappearance measurements can probe both maximal mixing and the θ_{23} octant. With the large statistics and rich spectral structure in a wide-band, long-baseline experiment such as LBNE (Figure 4.2), precision measurements of $\sin^2\theta_{23}$ can be significantly improved compared to existing experiments, particularly for values of θ_{23} near 45°. Figure 4.18 demonstrates the measurement precision of θ_{23} and Δm^2_{31} that can be achieved for different true values of these parameters by a 10-kt LBNE detector. The subdominant $\nu_\mu \rightarrow \nu_e$ appearance signal in a 10-kt detector is limited by statistical uncertainties.

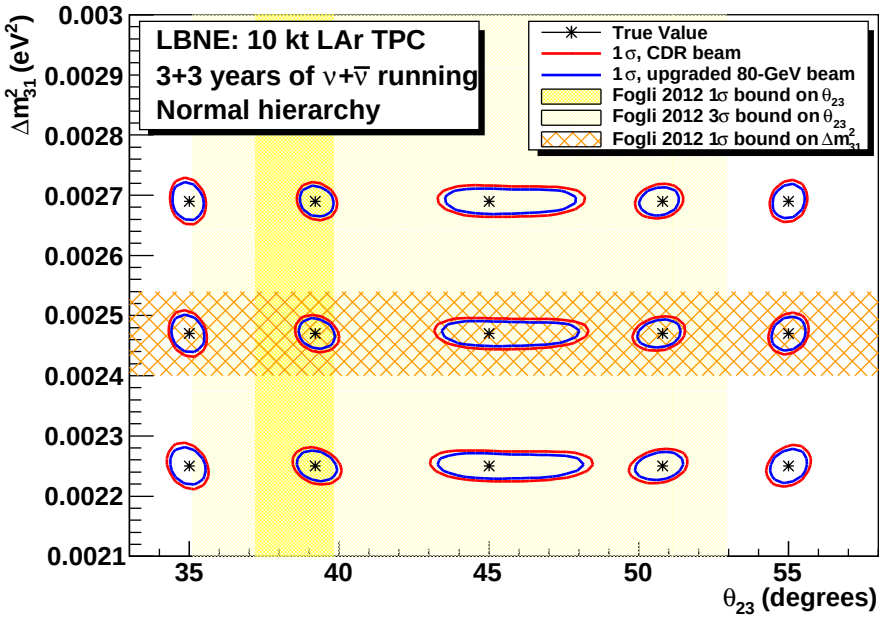

Figure 4.18: The precision with which a simultaneous measurement of θ_{23} and Δm^2_{31} can be determined with 10 kt and 3+3 years of $\nu + \overline{\nu}$ running in a 1.2-MW beam. The yellow bands represent the 1σ and 3σ allowed ranges of θ_{23} and the orange hatched region represents the 1σ allowed range of Δm^2_{31} from [54].

The significance with which a 10-kt LBNE detector can determine the θ_{23} octant is shown in the top plot of Figure 4.19. The $\Delta\chi^2$ metric is defined as:

$$\Delta\chi^2_{octant} \quad = \quad |\chi^2_{\theta_{23}^{test}>45^\circ} - \chi^2_{\theta_{23}^{test}<45^\circ}|, \tag{4.9}$$

where the value of θ_{23} in the *wrong* octant is constrained only to have a value within the *wrong* octant (i.e., it is not required to have the same value of $\sin^2 2\theta_{23}$ as the true value). The individual χ^2 values are given by Equation 4.4. As in the $\Delta\chi^2$ metrics for MH and CP violation, the χ^2 value for the *true* octant is identically zero in the absence of statistical fluctuations. If θ_{23} is within the 1σ bound of the global fit [54], an LBNE 10-kt detector alone will determine the octant with $> 3\sigma$ significance for all values of $\delta_{\rm CP}$. Figure 4.19 (bottom) demonstrates the increasing sensitivity to the θ_{23} octant for values closer to maximal ν_μ-ν_τ mixing that can be achieved with subsequent phases of LBNE coupled with upgrades in beam power from the Main Injector.

With sufficient exposure, LBNE can resolve the θ_{23} octant with $> 3\sigma$ significance even if θ_{23} is within a few degrees of 45°, the value at which the mixing between the ν_μ and ν_τ neutrino states is maximal.

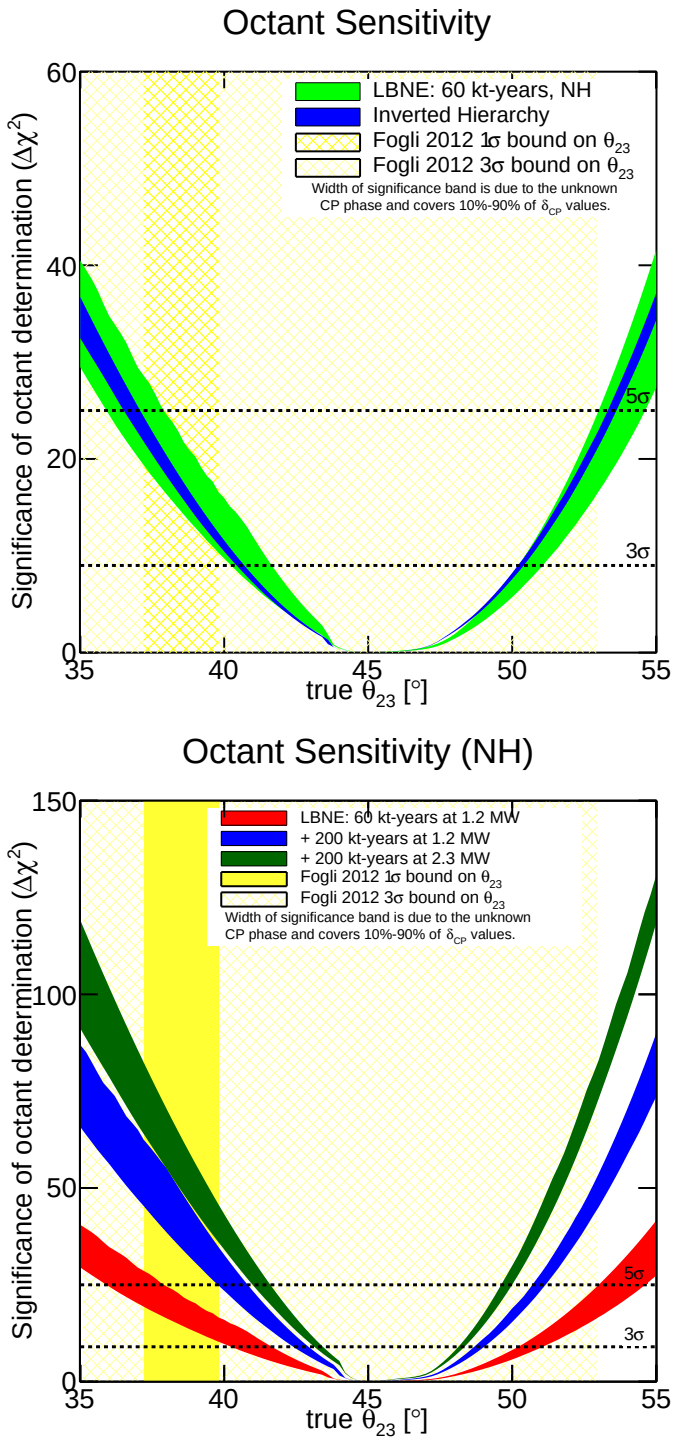

Figure 4.19: Top: significance with which LBNE can resolve the θ_{23} octant degeneracy for 3+3 years of ν+$\overline{\nu}$ running at 1.2 MW with a 10-kt detector. The bands are for normal (green) and inverted (blue) hierarchy. The widths of the bands correspond to the fraction of $\delta_{\rm CP}$ values covered at this significance or higher, ranging from 10% to 90%. The yellow bands represent the 1σ and 3σ allowed ranges of θ_{23} from [54]. Bottom: significance with which LBNE can resolve the θ_{23} octant degeneracy (normal hierarchy) for equal ν+$\overline{\nu}$ running with increased exposure. The colored bands represent increasing exposures as follows: 1.2 MW, 60 kt·year (red) + 1.2 MW, 200 kt·years (blue) + 2.3 MW, 200 kt·years (green). The sensitivity for each higher exposure is in addition to that from all lower exposures.

4.5 Precision Measurements of the Oscillation Parameters in the Three-Flavor Model

The rich oscillation structure that can be observed by LBNE and the excellent particle identification capability of the detector will enable precision measurement in a single experiment of all the mixing parameters governing ν_1-ν_3 and ν_2-ν_3 mixing. As discussed in Chapter 2, theoretical models probing quark-lepton universality predict specific values of the mixing angles and the relations between them. The mixing angle θ_{13} is expected to be measured accurately in reactor experiments by the end of the decade with a precision that will be limited by systematics. The systematic uncertainty on the value of $\sin^2 2\theta_{13}$ from the Daya Bay reactor neutrino experiment, which has the lowest systematics, is currently $\sim 4\%$ [142].

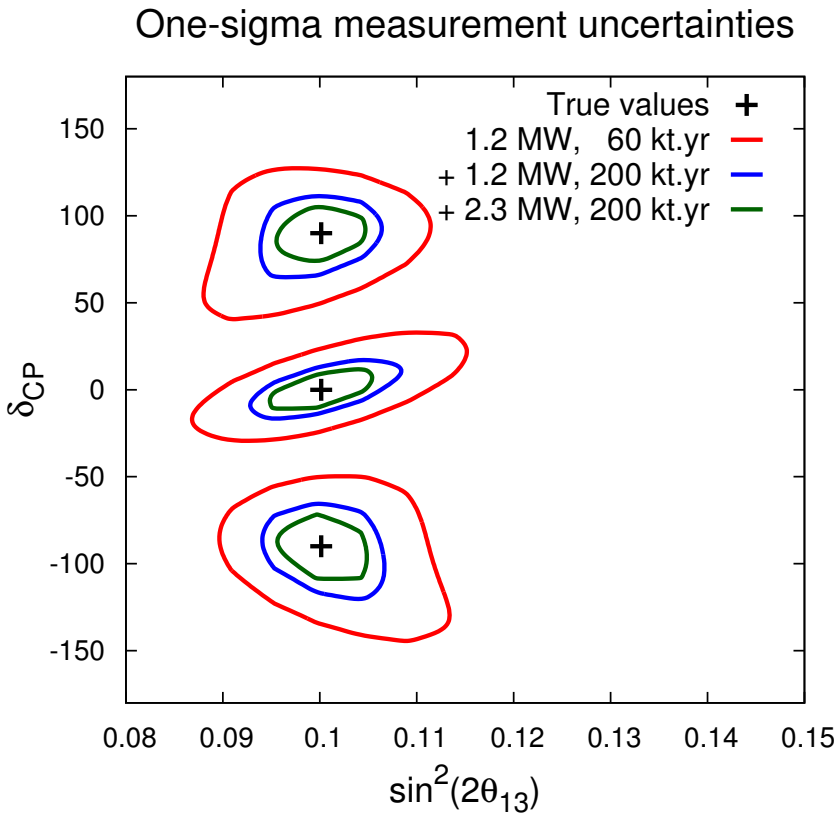

Figure 4.20: Measurement of $\delta_{\rm CP}$ and θ_{13} in LBNE with different exposures, for true normal hierarchy (NH). The different color curves represent one-sigma contours for three possible exposures from different stages of PIP and detector mass upgrades as follows: 1.2 MW, 60 kt·year (red), 1.2 MW, 200 kt·years (blue) + 2.3 MW, 200 kt·years (green). The sensitivity for each higher exposure is in addition to that from all lower exposures.

While the constraint on θ_{13} from the reactor experiments will be important in the early stages of LBNE for determining CP violation, measuring $\delta_{\rm CP}$ and determining the θ_{23} octant, LBNE

itself will eventually be able to measure θ_{13} independently with a precision on par with the final precision expected from the reactor experiments. Whereas the reactor experiments measure θ_{13} using $\overline{\nu}_e$ disappearance, LBNE will measure it through ν_e and $\overline{\nu}_e$ appearance, thus providing an independent constraint on the three-flavor mixing matrix. Figure 4.20 demonstrates the precision with which LBNE can measure $\delta_{\rm CP}$ and θ_{13} simultaneously, with no external constraints on θ_{13}, as a function of increased exposure, for three different exposures. Both appearance and disappearance modes are included in the fit using the upgraded 80-GeV beam. Signal/background normalization uncertainties of 1%/5% are assumed.

Figure 4.21 shows the expected 1σ resolution on different three-flavor oscillation parameters as a function of exposure in kt · year in a 1.2-MW beam with LBNE alone and LBNE in combination with the expected performance from T2K and NOνA. It should be noted that LBNE alone could reach a precision on $\sin^2 2\theta_{13}$ of 0.005 with an exposure of $\sim$300 kt · MW · years. LBNE can also significantly improve the resolution on Δm^2_{32} beyond what the combination of NOνA and T2K can achieve, reaching a precision of 1×10^{-5} eV^2 with an exposure of $\sim$300 kt · MW · years. The precision on Δm^2_{32} will ultimately depend on tight control of energy-scale systematics. Initial studies of the systematics reveal that the measurement of ν_μ disappearance in LBNE over a full oscillation interval, with two oscillation peaks and two valleys (Figure 4.2), reduces the dependency of the Δm^2_{23} measurement on the energy-scale systematics, which limited the measurement precision in MINOS [163].

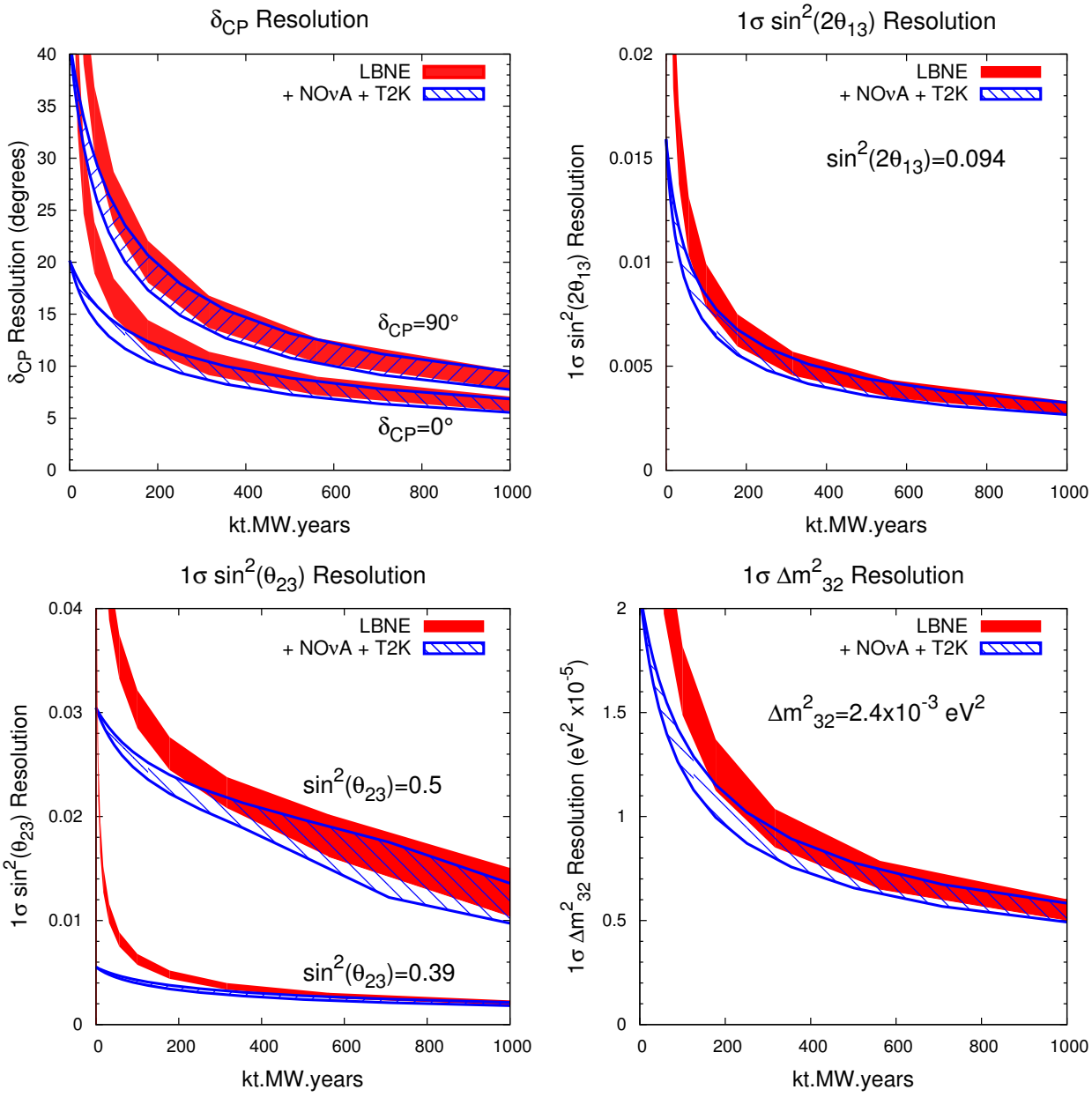

Figure 4.21: The expected 1σ resolution on different three-flavor oscillation parameters as a function of exposure in kt · MW · years, for true NH. The red curve indicates the precision that could be obtained from LBNE alone, and the blue curve represents the combined precision from LBNE and the T2K and NOνA experiments. The width of the bands represents the range of performance with the beam improvements under consideration.

4.6 Oscillation Studies Using Atmospheric Neutrinos

Atmospheric neutrinos are unique among sources used to study oscillations: the flux contains neutrinos and antineutrinos of all flavors, matter effects play a significant role, both Δm^2 values contribute, and the oscillation phenomenology occurs over several orders of magnitude each in energy (Figure 2.8) and path length. These characteristics make atmospheric neutrinos ideal for the study of oscillations (in principle sensitive to all of the remaining unmeasured quantities in the PMNS matrix) and provide a laboratory in which to search for exotic phenomena for which the dependence of the flavor-transition and survival probabilities on energy and path length can be defined. The large LBNE LArTPC far detector, placed at sufficient depth to shield against cosmic-ray background, provides a unique opportunity to study atmospheric neutrino interactions with excellent energy and path-length resolutions.

LBNE has obtained far detector physics sensitivities based on information from atmospheric neutrinos by using a Fast MC and a three-flavor analysis framework developed for the MINOS experiment [167]. Four-vector-level events are generated using the GENIE neutrino event generator [133]. For atmospheric neutrinos the Bartol [168] flux calculation for the Soudan, MN site was used, and for beam neutrinos the 80-GeV, 1.2-MW beamline design described in Section 3.4 was used. In this section, unless otherwise specified, the oscillation parameters are as specified in Table 4.10.

Table 4.10: Oscillation parameters used in the atmospheric-neutrino analysis.

Parameter	Value
$\Delta m^2 = 1/2(\Delta m^2_{32} + \Delta m^2_{31})$ (NH)	$+2.40 \times 10^{-3}$ eV^2
$\sin^2\theta_{23}$	0.40
Δm^2_{21}	7.54×10^{-5} eV^2
$\sin^2\theta_{12}$	0.307
$\sin^2\theta_{13}$	0.0242
δ_{CP}	0

The expected interaction rates in 100 kt · year are shown in Table 4.11. All interactions occur on argon and are distributed uniformly throughout a toy detector geometry consisting of two modules, each 14.0 m high, 23.3 m wide, and 45.4 m long. For this study, events with interaction vertices outside the detector volume (e.g., events that produce upward-going stopping or through-going muons) have not been considered. Cosmogenic background has not been studied in detail, but since atmospheric neutrinos are somewhat more tolerant of background than proton decay, a depth that is sufficient for a proton decay search is expected to also be suitable for studies of atmospheric

neutrinos. Given the detector's 4,850-ft depth, a veto should not be necessary and the full fiducial mass of the detector should be usable.

Table 4.11: Expected atmospheric ν interaction rates in a LArTPC with an exposure of 100 kt · years for the Bartol flux and GENIE argon cross sections (no oscillations).

Flavor	CC	NC	Total
ν_μ	10,069	4,240	14,309
$\overline{\nu}_\mu$	2,701	1,895	4,596
ν_e	5,754	2,098	7,852
$\overline{\nu}_e$	1,230	782	2,012
Total:	**19,754**	**9,015**	**28,769**

A Fast MC runs on the produced four-vectors, placing events into containment and flavor categories. Containment is evaluated by tracking leptons through the liquid argon detector box geometry and classifying events as either fully contained (FC) or partially contained (PC). A detection threshold of 50 MeV is assumed for all particles. Flavor determination, in which events are placed into electron-like or muon-like categories, is based on properties of the primary and secondary particles above detection threshold. Electrons are assumed to be correctly identified with 90% probability and other electromagnetic particles (e.g., π^0, γ) are misidentified as electrons 5% of the time. Muons are identified with 100% probability and charged pions are misidentified as muons 1% of the time. Events in which neither of the two leading particles is identified as a muon or electron are placed into an *NC-like* category. With these assumptions, the purities of the flavor-tagged samples are 97.8% for the FC electron-like sample, 99.7% for the FC muon-like sample, and 99.6% for the PC muon-like sample. The NC-like category is not used in this analysis, but would be useful for ν_τ appearance studies. The energy and direction of the event are then assigned by separately smearing these quantities of the leptonic and hadronic systems, where the width of the Gaussian

Table 4.12: Detector performance assumptions for the atmospheric neutrino and the combined atmospheric+beam neutrino analyses.

Particle	Resolution
Angular Resolutions	
Electron	1°
Muon	1°
Hadronic System	10°
Energy Resolutions	
Stopping Muon	3%
Exiting Muon	15%
Electron	$1\%/\sqrt{E(GeV)} \oplus 1\%$
Hadronic System	$30\%/\sqrt{E(GeV)}$

resolution functions for each flavor/containment category are given in Table 4.12. Detector performance assumptions are taken both from the LBNE CDR [29] and from published results from the ICARUS experiment [139,169,170,171]. Including oscillations, the expected number of events in 100 kt · year is summarized in Table 4.13.

Table 4.13: Atmospheric-neutrino event rates including oscillations in 100 kt · year with a LArTPC, fully or partially contained in the detector fiducial volume.

Sample	Event rate
fully contained electron-like sample	4,015
fully contained muon-like sample	5,958
partially contained muon-like sample	1,963

Figure 4.22 shows the expected L/E distribution for *high-resolution* muon-like events from a 350 kt · year exposure; the latest data from Super-Kamiokande are shown for comparison. LBNE defines high-resolution events similarly to Super-Kamiokande, i.e., either by excluding a region of low-energy events or events pointing toward the horizon where the baseline resolution is poor. The data provide excellent resolution of the first two oscillation nodes, even when taking into account the expected statistical uncertainty.

In performing oscillation fits, the data in each flavor/containment category are binned in energy and zenith angle. Figure 4.23 shows the zenith angle distributions for several ranges of reconstructed energy, where oscillation features are clearly evident.

The power to resolve the mass hierarchy (MH) with atmospheric neutrinos comes primarily from the MSW enhancement of few-GeV neutrinos at large zenith angles. This enhancement occurs for neutrinos in the normal hierarchy and antineutrinos in the inverted hierarchy. Figure 4.24 shows zenith angle distributions of events in the relevant energy range for each of the three flavor/containment categories. Small differences are evident in comparing the NH and IH predictions.

Since the resonance peak occurs for neutrinos in the NH and antineutrinos in the IH, the MH sensitivity can be greatly enhanced if neutrino and antineutrino events can be separated. The LBNE detector will not be magnetized; however, its high-resolution imaging offers possibilities for tagging features of events that provide statistical discrimination between neutrinos and antineutrinos. For the sensitivity calculations that follow, two such tags are included: a proton tag and a decay-electron tag. For low-multiplicity events, protons occur preferentially in neutrino interactions; protons are tagged with 100% efficiency if their kinetic energy is greater than 50 MeV. Decay electrons are assumed to be 100% identifiable and are assumed to occur 100% of the time for μ^+ and 25% of the time for μ^-, based on the $\mu^\pm$ capture probability on ^{40}Ar.

In the oscillation analysis, 18 nuisance parameters are included, with detector performance parameters correlated between beam and atmospheric data. In all cases, $\sin^2\theta_{12}$, $\Delta m^2 = 1/2(\Delta m^2_{32} + \Delta m^2_{31})$, and Δm^2_{21} are taken to be fixed at the values given in Table 4.10. The fits then range over

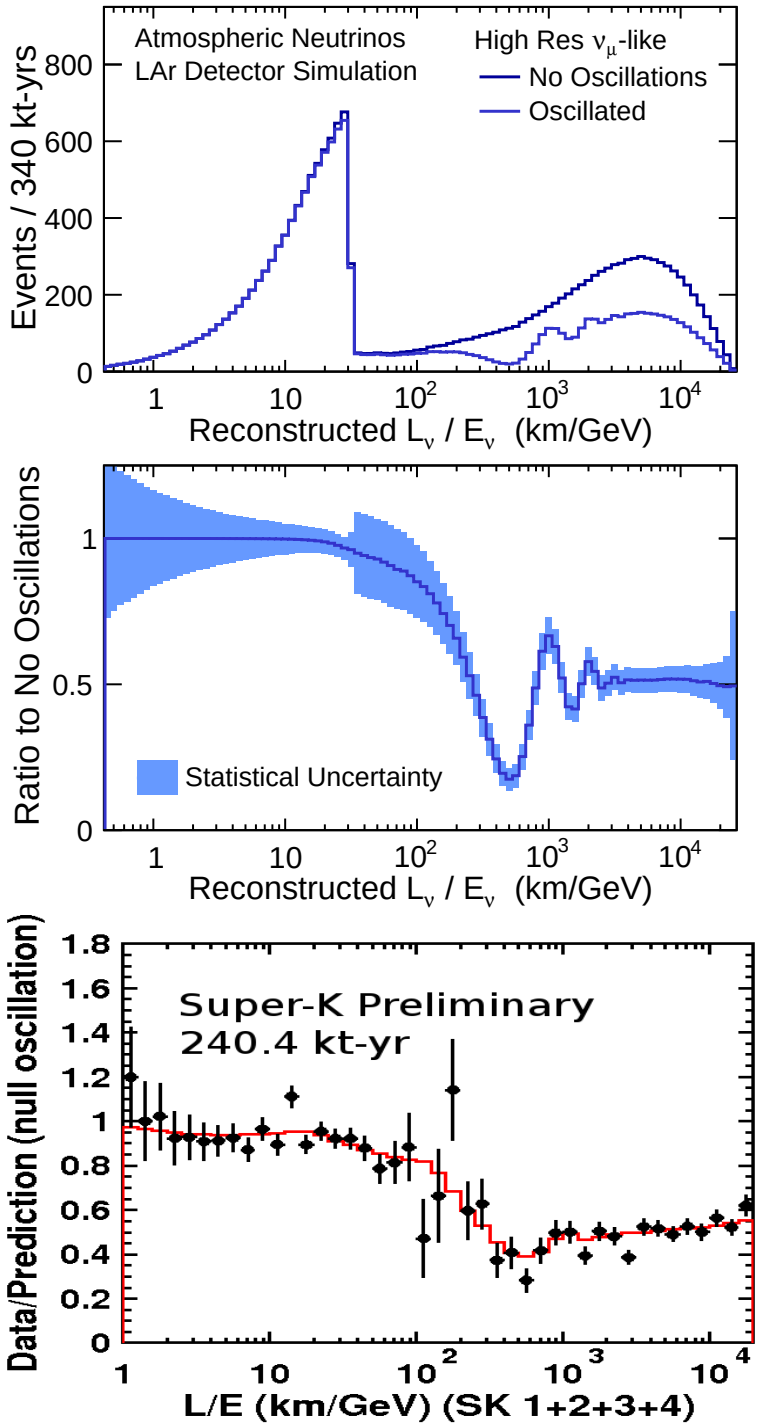

Figure 4.22: Reconstructed L/E distribution of *high-resolution* μ-like atmospheric neutrino events in LBNE with a 340 kt·MW·year exposure with and without oscillations (top); the ratio of the two, with the shaded band indicating the size of the statistical uncertainty (center); the ratio of observed data over the null oscillation prediction from the Super-Kamiokande detector with 240.4 kt · years of exposure (bottom).

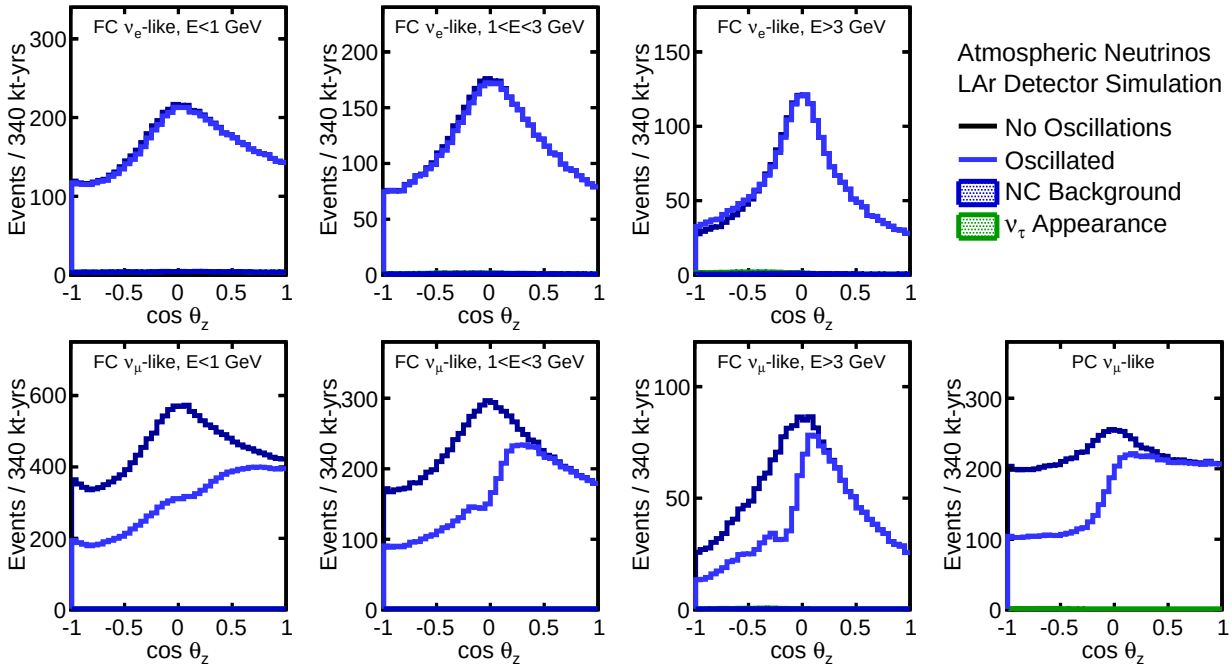

Figure 4.23: Reconstructed zenith angle distributions in several ranges of energy for the FC e-like, FC μ-like, and PC μ-like samples. The small contributions from NC background and ν_τ are also shown.

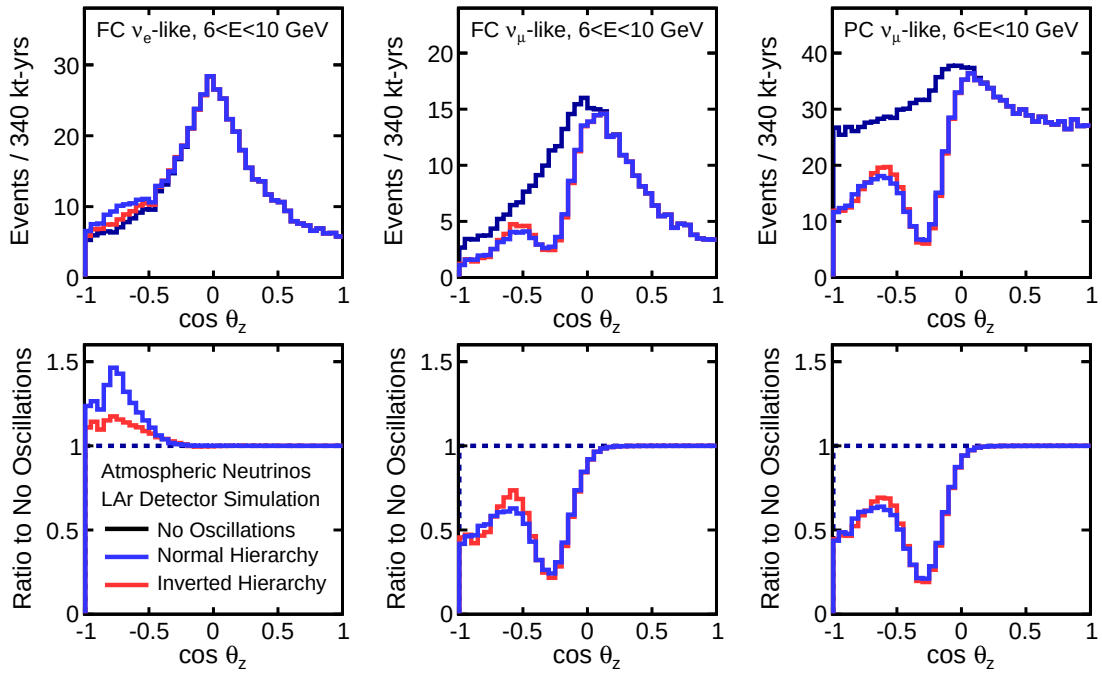

Figure 4.24: Reconstructed zenith angle distributions for 6 to 10-GeV events in the different FC and PC samples. Top plots show the expected distributions for no oscillations (black), oscillations with normal (blue), and inverted (red) hierarchy. Bottom plots show the ratio of the normal and inverted expectations to the no-oscillation distributions for each category.

θ_{23}, θ_{13}, $\delta_{\rm CP}$, and the MH. A 2% constraint is assumed on the value of θ_{13}; this value is chosen to reflect the expected ultimate precision of the current generation of reactor-neutrino experiments. The systematic errors included in this analysis are given in Table 4.14.

Table 4.14: Systematic errors included in the atmospheric and beam+atmospheric neutrino analysis. The beam values assume the existence of a near detector (ND). Atmospheric spectrum ratios include the combined effect of flux and detector uncertainties (e.g., the up/down flux uncertainty as well as the uncertainty on the detector performance for the up/down ratio). The atmospheric spectrum shape uncertainty functions are applied separately for $\nu_\mu, \nu_e, \overline{\nu}_\mu, \overline{\nu}_e$.

	Atmospheric	Beam (Assumes ND)
Normalization	Overall (15%)	μ-like (5%) e-like (1%)
NC Background	e-like (10%)	μ-like (10%) e-like (5%)
Spectrum Ratios	up/down (2%) ν_e/ν_μ (2%) $\overline{\nu}_\mu/\nu_\mu$ (5%) $\overline{\nu}_e/\nu_e$ (5%)	
Spectrum Shape	$f(E < E_0) = 1 + \alpha(E - E_0)/E_0$ $f(E > E_0) = 1 + \alpha \log(E/E_0)$ where σ_α=5%	
Energy Scales (Correlated)	Muons (stopping 1%, exiting 5%) Electrons (1%) Hadronic System (5%)	

For the determination of the MH, the $\overline{\Delta\chi^2}$ value is calculated between the best-fit points in the NH and IH where, at each, the nuisance parameters have been marginalized. The sensitivity in the plots that follow is given as $\sqrt{\overline{\Delta\chi^2}}$. Figure 4.25 shows the MH sensitivity from a 340-kt · year exposure of atmospheric neutrino data alone. For all values of the MH and $\delta_{\rm CP}$, the MH can be determined at $\sqrt{\overline{\Delta\chi^2}} > 3$. The resolution depends significantly on the true value of θ_{23}; the sensitivity for three θ_{23} values is shown. The sensitivity depends relatively weakly on the true hierarchy and the true value of $\delta_{\rm CP}$. This is in sharp contrast to the MH sensitivity of the beam, which has a strong dependence on the true value of $\delta_{\rm CP}$. Figure 4.26 shows the MH sensitivity as a function of the fiducial exposure. Over this range of fiducial exposures, the sensitivity goes essentially as the square root of the exposure, indicating that the measurement is not systematics-limited. Figure 4.27 shows the octant and CPV sensitivity from a 340-kt · year exposure of atmospheric neutrino data alone. For the determination of the octant of θ_{23}, the $\overline{\Delta\chi^2}$ value is calculated between the best-fit points in the lower ($\theta_{23} < 45°$) and higher ($\theta_{23} > 45°$) octants, where at each, the nuisance parameters have been marginalized. The discontinuities in the slopes of the octant sensitivity plot are real features, indicating points at which the best fit moves from one hierarchy to the other. For the detection of CP violation, the $\overline{\Delta\chi^2}$ exclusion is similarly computed for $\delta_{\rm CP} = (0, \pi)$.

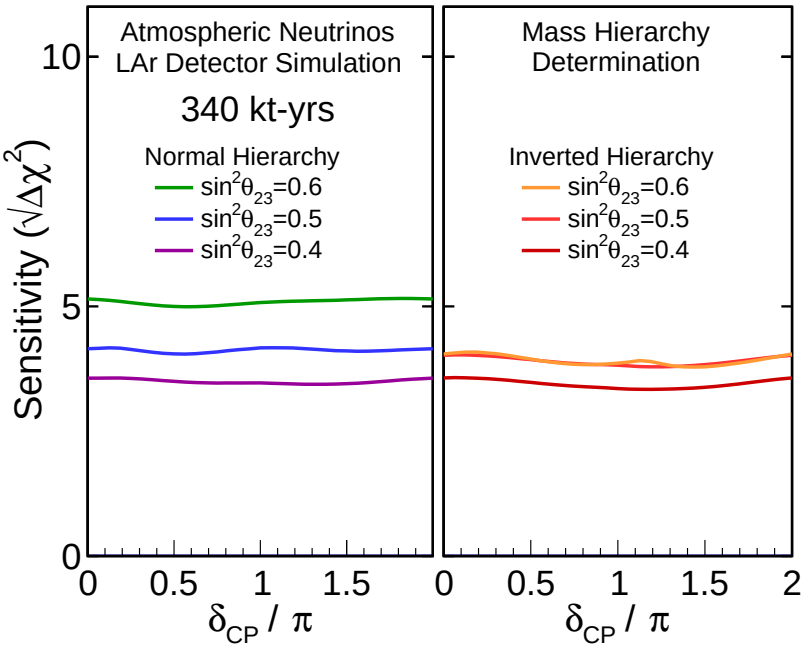

Figure 4.25: Sensitivity of 340 kt · years of atmospheric neutrino data to MH as a function of δ_{CP} for true normal (left) and inverted (right) hierarchy and different assumed values of $\sin^2\theta_{23}$.

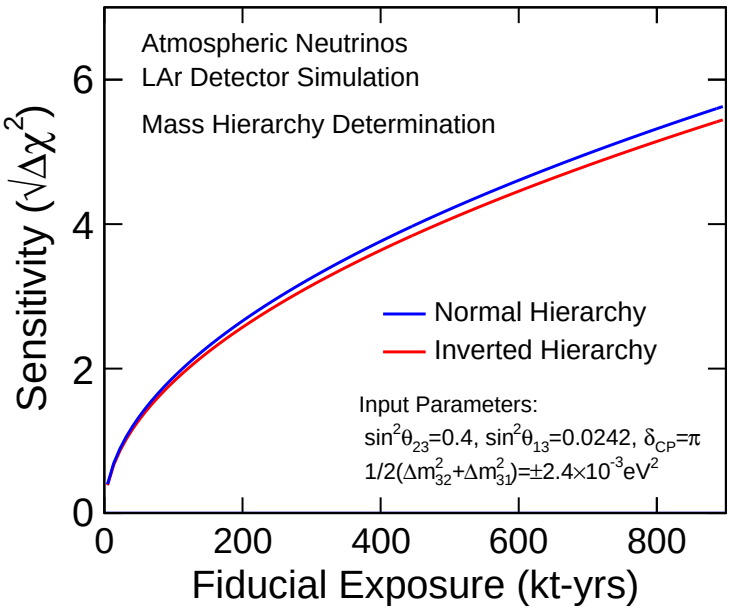

Figure 4.26: Sensitivity to mass hierarchy using atmospheric neutrinos as a function of fiducial exposure in a liquid argon detector.

Figure 4.28 shows the combined sensitivity to beam and atmospheric neutrinos for determination of the MH. This assumes a 10-year run with equal amounts of neutrino and antineutrino running in a 1.2-MW beam.

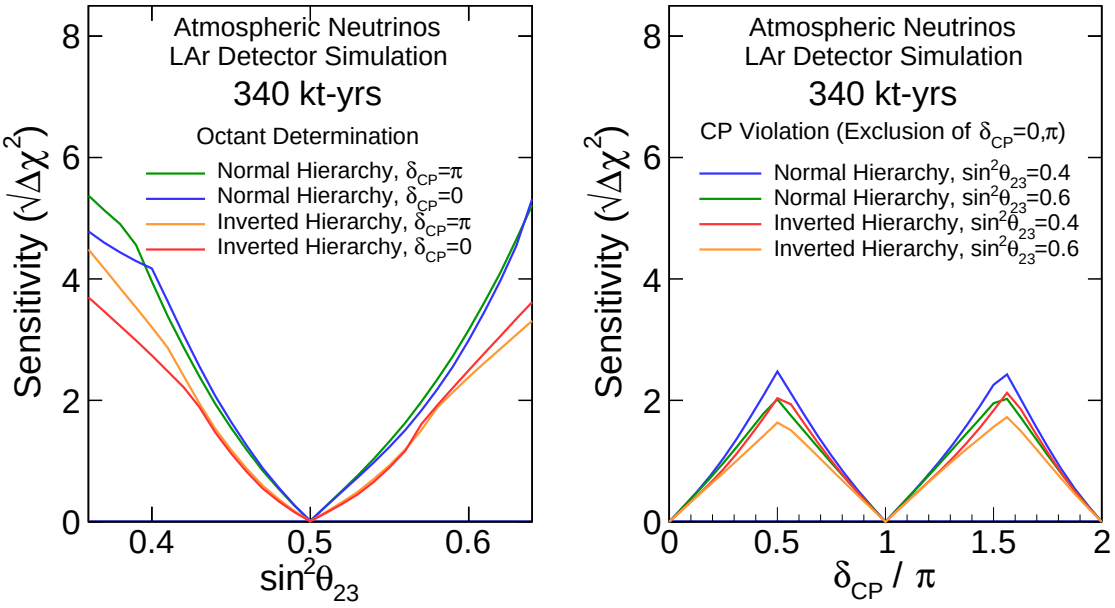

Figure 4.27: Sensitivity to θ_{23} octant (left) and CPV (right) using atmospheric neutrinos.

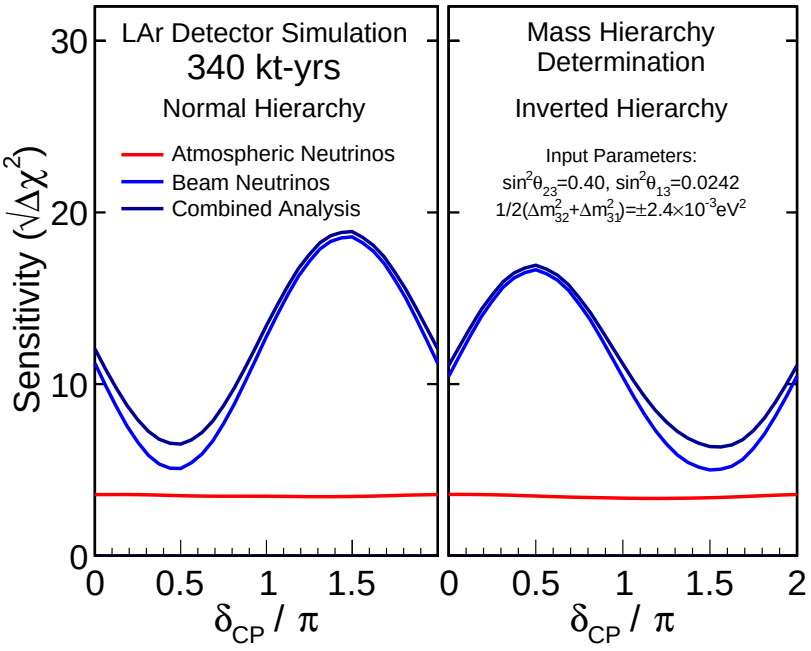

Figure 4.28: Sensitivity to mass hierarchy using atmospheric neutrinos combined with beam neutrinos with an exposure of 340 kt · year in a 1.2-MW beam for normal (left) and inverted (right) hierarchy.

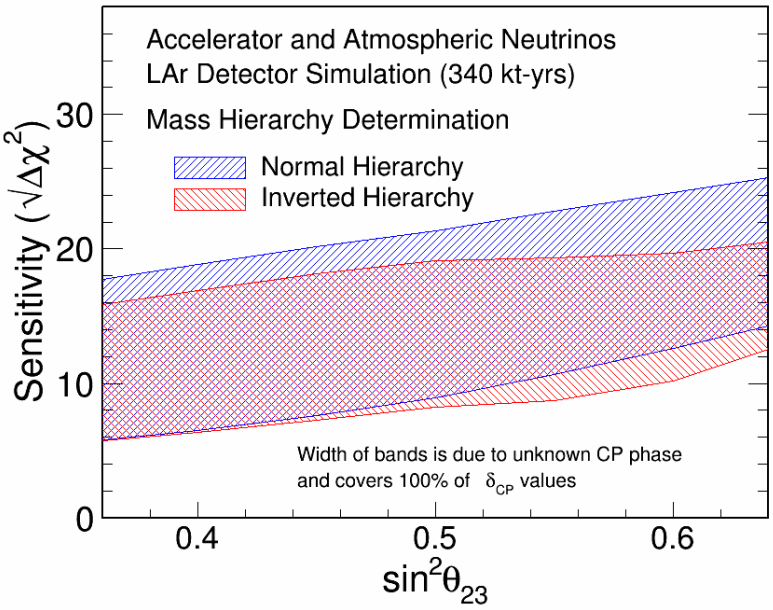

Figure 4.29: Sensitivity to mass hierarchy using atmospheric neutrinos combined with beam neutrinos as a function of the true value of $\sin^2\theta_{23}$, for true normal (blue) and inverted (red) hierarchy. The width of the band is due to the unknown value of $\delta_{\rm CP}$ and covers all possible values of $\delta_{\rm CP}$. Assumes an exposure of 340 kt · year in a 1.2-MW beam.

In the region of $\delta_{\rm CP}$ where the LBNE neutrino-beam-only analysis is least sensitive to the mass hierarchy, atmospheric neutrinos measured in the same experiment offer comparable sensitivity. The combined beam and atmospheric neutrino sensitivity to the mass hierarchy is $|\sqrt{\Delta\chi^2}| > 6$ for all values of $\delta_{\rm CP}$ ($\sin^2\theta_{23} = 0.4$) in a 34-kt detector, assuming a 1.2-MW beam running for ten years. It is important to note that the combined sensitivity is better than the sum of the separate $\Delta\chi^2$ values, as the atmospheric data help to remove degeneracies in the beam data.

Figure 4.29 shows the combined sensitivity to beam and atmospheric neutrinos for determination of MH as a function of the true value of $\sin^2\theta_{23}$, for the same 340-kt · year exposure in a 1.2-MW beam. This can be compared to Figure 4.14 in Section 4.3.3, which shows the same sensitivity using only beam neutrinos.

Figure 4.30 shows the combined sensitivity to beam and atmospheric neutrinos for the θ_{23} octant determination and CPV. The role played by atmospheric data in resolving beam-neutrino degeneracies is also clear from considering the combined and beam-only sensitivities in these plots.

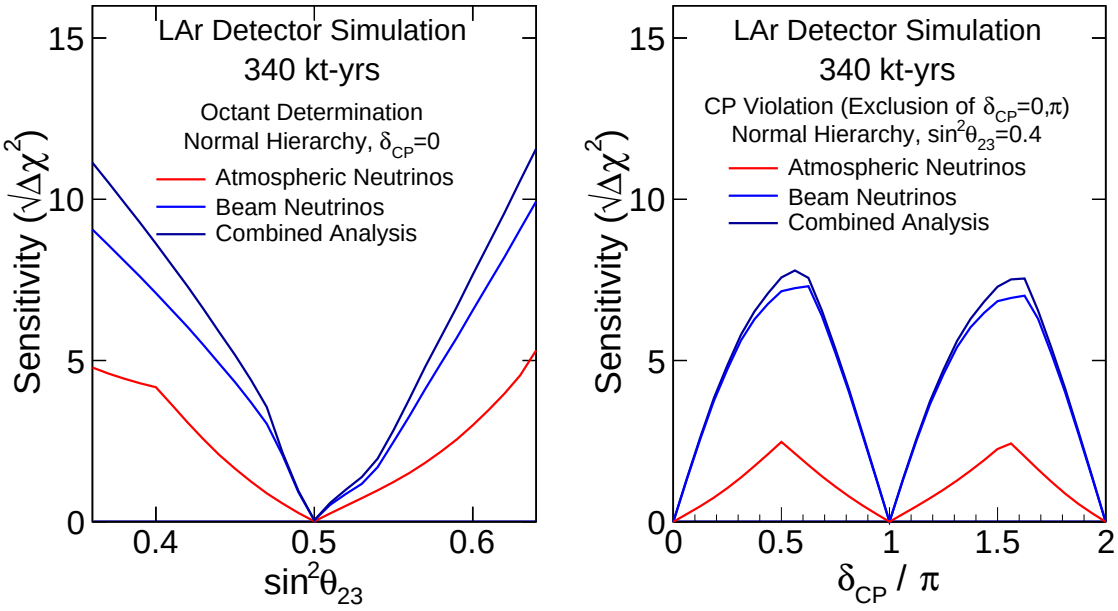

Figure 4.30: Sensitivity to θ_{23} octant (left) and CPV (right) using atmospheric neutrinos combined with beam neutrinos with an exposure of 340 kt · year in a 1.2-MW beam.

4.7 Searches for Physics Beyond the Standard Three-Flavor Neutrino Oscillation Model

Due to the very small masses and large mixing of neutrinos, their oscillations over a long distance act as an exquisitely precise interferometer with high sensitivity to very small perturbations caused by new physics phenomena, such as:

- nonstandard interactions in matter that manifest in long-baseline oscillations as deviations from the three-flavor mixing model
- new long-distance potentials arising from discrete symmetries that manifest as small perturbations on neutrino and antineutrino oscillations over a long baseline
- sterile neutrino states that mix with the three known active neutrino states
- large compactified extra dimensions from String Theory models that manifest through mixing between the Kaluza-Klein states and the three active neutrino states

Full exploitation of LBNE's sensitivity to such new phenomena will require higher-precision predictions of the unoscillated neutrino flux at the far detector and large exposures.

This section explores the potential of the full-scope LBNE design to pursue physics beyond the three-flavor neutrino oscillation model.

4.7.1 Search for Nonstandard Interactions

Neutral current (NC) nonstandard interactions (NSI) can be understood as nonstandard matter effects that are visible only in a far detector at a sufficiently long baseline. They can be parameterized as new contributions to the MSW matrix in the neutrino-propagation Hamiltonian:

$$H = U \begin{pmatrix} 0 & & \\ & \Delta m^2_{21}/2E & \\ & & \Delta m^2_{31}/2E \end{pmatrix} U^\dagger + \tilde{V}_{\rm MSW}\,, \tag{4.10}$$

with

$$\tilde{V}_{\rm MSW} = \sqrt{2} G_F N_e \begin{pmatrix} 1+\epsilon^m_{ee} & \epsilon^m_{e\mu} & \epsilon^m_{e\tau} \\ \epsilon^{m*}_{e\mu} & \epsilon^m_{\mu\mu} & \epsilon^m_{\mu\tau} \\ \epsilon^{m*}_{e\tau} & \epsilon^{m*}_{\mu\tau} & \epsilon^m_{\tau\tau} \end{pmatrix} \tag{4.11}$$

Here, U is the leptonic mixing matrix, and the ϵ-parameters give the magnitude of the NSI relative to standard weak interactions. For new physics scales of a few hundred GeV, a value of $|\epsilon| \lesssim 0.01$ is expected [172,173,174]. LBNE's 1,300-km baseline provides an advantage in the detection of NSI relative to existing beam-based experiments with shorter baselines. Only atmospheric-neutrino experiments have longer baselines, but the sensitivity of these experiments to NSI is limited by systematic effects.

To assess the sensitivity of LBNE to NC NSI, the NSI discovery reach is defined in the following way: the expected event spectra are simulated using GLoBeS, assuming *true* values for the NSI parameters, and a fit is then attempted assuming no NSI. If the fit is incompatible with the simulated data at a given confidence level, the chosen *true* values of the NSI parameters are considered to be within the experimental discovery reach. In Figure 4.31, the NSI discovery reach of LBNE is shown; only one of the $\epsilon^m_{\alpha\beta}$ parameters at a time is taken to be non-negligible.

4.7.2 Search for Long-Range Interactions

The small scale of neutrino-mass differences implies that minute differences in the interactions of neutrinos and antineutrinos with currently unknown particles or forces may be detected through perturbations to the time evolution of the flavor eigenstates. The longer the experimental baseline, the higher the sensitivity to a new long-distance potential acting on neutrinos. For example, some of the models for such long-range interactions (LRI) as described in [175] (Figure 4.32) could contain discrete symmetries that stabilize the proton and give rise to a dark-matter candidate particle, thus providing new connections between neutrino, proton decay and dark matter experiments. The

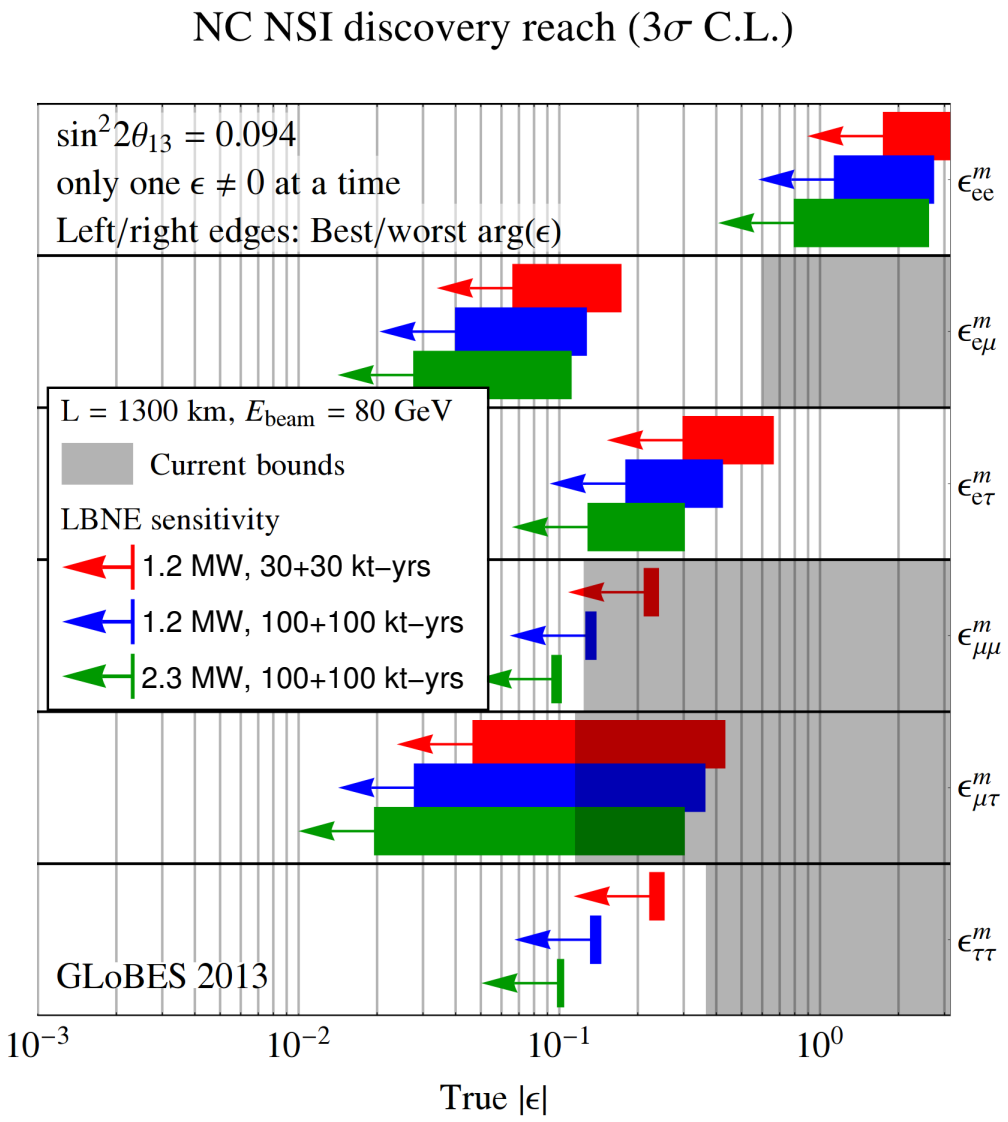

Figure 4.31: Nonstandard interaction discovery reach in LBNE with increasing exposure: 1.2 MW, 60 kt·years (red) + 1.2 MW, 200 kt · year (blue) + 2.3 MW, 200 kt · year (green). The left and right edges of the error bars correspond to the most favorable and the most unfavorable values for the complex phase of the respective NSI parameters. The gray shaded regions indicate the current model-independent limits on the different parameters at 3σ [172,173]. For this study the value of $\sin^2 2\theta_{13}$ was assumed to be 0.09. Figure courtesy of Joachim Kopp.

longer baseline of LBNE improves the sensitivity to LRI beyond that possible with the current generation of long-baseline neutrino experiments. The sensitivity will be determined by the amount of $\nu_\mu/\overline{\nu}_\mu$-CC statistics accumulated and the accuracy with which the unoscillated and oscillated ν_μ spectra can be determined.

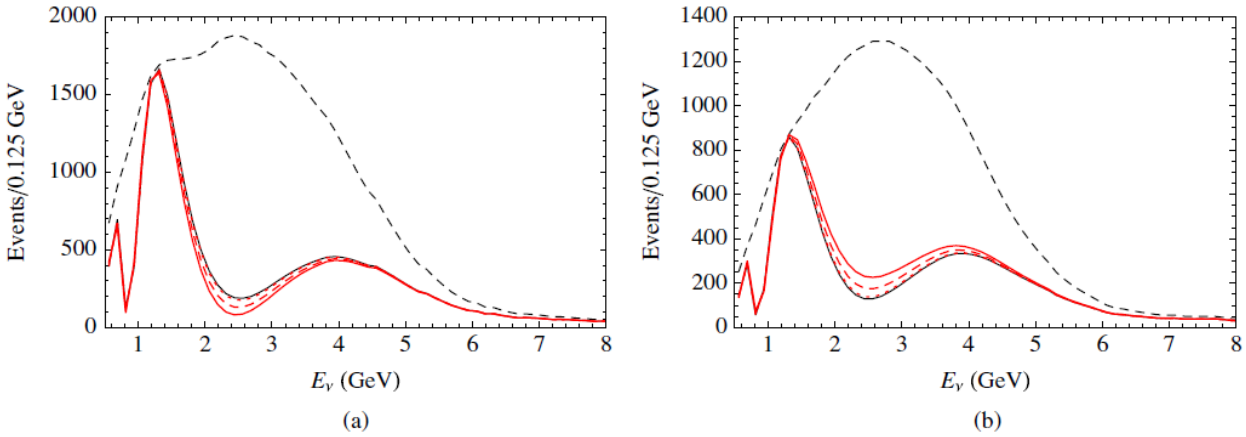

Figure 4.32: Long-range interactions in LBNE. The number of (a) neutrino and (b) antineutrino events versus E_ν, in a long-baseline experiment with a 1,300-km baseline. The unoscillated case (top black dashed curves) and the case of no new physics (thin black solid curves) are displayed, as well as the cases with $\alpha' = (1.0, 0.5, \text{and } 0.1) \times 10^{-52}$, corresponding to red solid, dashed, and dotted curves, respectively. α' is the *fine structure constant* of such interactions, which is constrained to be $\alpha' \leq 10^{-47}$ [175].

4.7.3 Search for Mixing between Active and Sterile Neutrinos

Searches for evidence of active-sterile neutrino mixing at LBNE can be conducted by examining the NC event rate at the far detector and comparing it to a precise estimate of the expected rate extrapolated from ν_μ flux measurements from the near detector and from beam and detector simulations. Observed deficits in the NC rate could be evidence for mixing between the active neutrino states and unknown sterile neutrino states. The most recent such search in a long-baseline experiment was conducted by the MINOS experiment [176].

LBNE will provide a unique opportunity to revisit this search with higher precision over a large range of neutrino energies and a longer baseline. The expected rate of NC interactions with visible energy > 0.5 GeV in a 10-kt detector over three years is approximately 2,000 events (Table 4.1) in the low-energy beam tune and 3,000 events in the medium-energy beam tune. The NC identification efficiency is high, with a low rate of ν_μ-CC background misidentification as shown in Table 4.2. The high-resolution LArTPC far detector will enable a coarse measurement of the incoming neutrino energy in a NC interaction by using the event topology and correcting for the missing energy of the invisible neutrino. This will greatly improve the sensitivity of LBNE to active-sterile mixing as compared to current long-baseline experiments such as MINOS+ since both the energy spectrum and the rate of NC interactions can be measured at both near and far detectors. Studies are currently underway to quantify LBNE's sensitivity to active-sterile mixing.

4.7.4 Search for Large Extra Dimensions

Several theoretical models propose that right-handed neutrinos propagate in large compactified extra dimensions, whereas the standard left-handed neutrinos are confined to the four-dimensional brane [177]. Mixing between the right-handed *Kaluza-Klein* modes and the standard neutrinos would change the mixing patterns predicted by the three-flavor model. The effects could manifest, for example, as distortions in the disappearance spectrum of ν_μ. The rich oscillation structure visible in LBNE, measured with its high-resolution detector using both beam and atmospheric oscillations, could provide further opportunities to probe for this type of new physics. Studies are underway to understand the limits that LBNE could impose relative to current limits and those expected from other experiments.

4.8 Comparison of LBNE Sensitivities to other Proposed Experiments

With tight control of systematics, LBNE will reach 5σ sensitivity to CP violation for a large fraction of $\delta_{\rm CP}$ values. LBNE delivers the best resolution of the value of $\delta_{\rm CP}$ with the lowest combination of power-on-target and far detector mass when compared to other future proposed neutrino oscillation experiments (Figure 4.33).

In Figure 4.33, the CP-violation sensitivity of LBNE is compared to that of other proposed neutrino oscillation experiments from an *independent study* with updated LBNE input based on [178]. The dashed black curve labeled "2020" is the expected sensitivity from the current generation of experiments that could be achieved by 2020. "LBNE-Full" represents a 34-kt LArTPC running in a 1.2-MW beam for 3 (ν) +3 ($\overline{\nu}$) years. "LBNE-PX" is LBNE staged with PIP-II and further upgraded beams with power up to 2.0 MW as shown in Figure 4.17. "T2HK" is a 560-kt (fiducial mass) water Cherenkov detector running in a 1.66-MW beam for 1.5 (ν) + 3.5 ($\overline{\nu}$) years [179]. "LBNO_{100}" is a 100-kt LArTPC at a baseline of 2,300 km running in a 0.8-MW beam from CERN for 5 (ν) + 5 ($\overline{\nu}$) years [180]. "IDS-NF" is the Neutrino Factory with a neutrino beam generated from muon decays in a 10-GeV muon storage ring produced from a 4-MW, 8-GeV Project X proton beam coupled with 100-kt magnetized iron detectors at a baseline of 2,000 km for 10 ($\nu + \overline{\nu}$) simultaneously) [181]. LBNE can reach 5σ sensitivity to CP violation for a large fraction of $\delta_{\rm CP}$ values with the lowest combination of power-on-target and far detector mass when compared to current and future proposed neutrino oscillation experiments.

Alone, LBNE can potentially reach a precision on $\delta_{\rm CP}$ between roughly 6° and 10°, i.e., close to the 4° CKM precision on $\delta_{\rm CP}^{\rm CKM}$ — but an exposure of $\sim$700 kt $\cdot$ MW $\cdot$ years is needed. Nevertheless, as shown in Figure 4.34, wide-band, long-baseline experiments such as LBNE (and LBNO) can

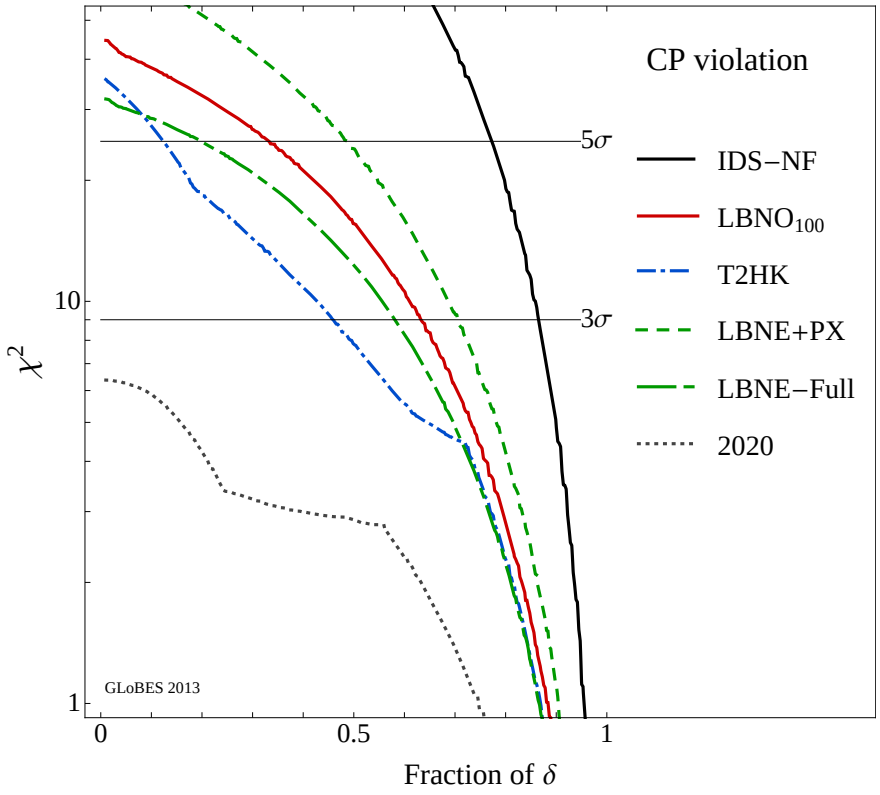

Figure 4.33: The minimal CP-violation sensitivity for a given fraction of $\delta_{\rm CP}$ values for different proposed neutrino oscillation experiments. The exposure and baseline of each experiment is described in the text. Figure is based on the studies detailed in [178].

achieve nearly CKM precision on $\delta_{\rm CP}$ with much less exposure than is required for existing experiments such as NOνA, T2K and proposed short-baseline, off-axis experiments such as T2HK. With the exception of the NuMAX sensitivity, which is taken from [182], the resolutions in the colored bands in Figure 4.34 are calculated independently by LBNE using GLoBES and found to be in good agreement with the values reported by the experiments themselves (T2HK [183], NOνA [38], LBNO [184]).

It is important to note that the precision on $\delta_{\rm CP}$ in the off-axis experiments shown in Figure 4.34 assumes the mass hierarchy (MH) is resolved. If the MH is unknown, the resolution of T2K, NOνA and T2HK will be much poorer than indicated. LBNE does not require external information on the MH to reach the precisions described in this section. Only a neutrino factory can possibly outperform a wide-band, long-baseline experiment — but not by much — for equivalent power, target mass and years of running. To achieve this precision, however, LBNE will need to tightly control the systematic uncertainties on the ν_e appearance signal. Its high-resolution near detector will enable it to reach this level of precision, as described in Section 3.5.

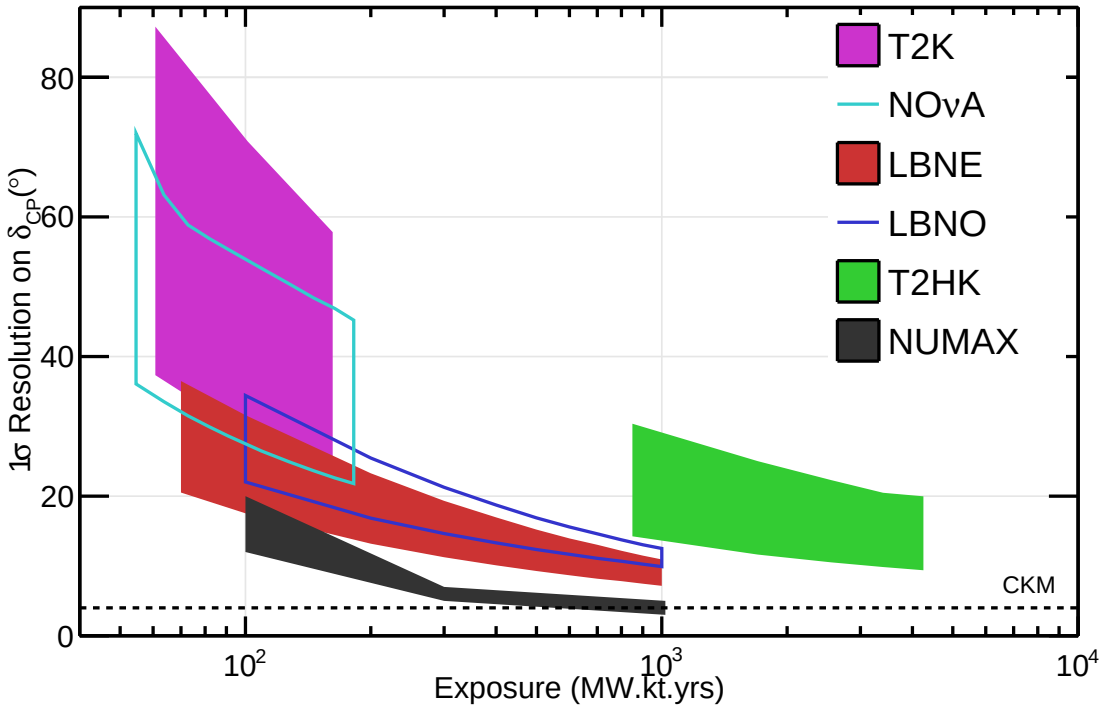

Figure 4.34: The 1σ resolution on $\delta_{\rm CP}$ that can be achieved by existing and proposed beamline neutrino oscillation experiments as a function of exposure in terms of mass $\times$ beam power $\times$ years of running. The band represents the variation in the resolution as a function of $\delta_{\rm CP}$ with the lower edge representing the best resolution and the upper edge the worst. The bands start and stop at particular milestones. For example, the LBNE band starts with the resolutions achieved by the 10-kt LBNE and ends with the full-scope LBNE running with the 2.3-MW upgrades beyond PIP-II. With the exception of the NuMAX sensitivity, which is taken from [182], the resolutions in the colored bands are calculated independently by LBNE using GLoBES. The dashed line denotes the 4° resolution point which is the resolution of $\delta_{\rm CP}^{\rm CKM}$ from the 2011 global fits.

An independent study comparing LBNE's sensitivity to the mass ordering to that of current and future proposed experiments highlights its potential [151]. The study uses frequentist methods of hypothesis testing to define sensitivities. The validity of the approach is tested using toy MC simulations of the various experiments. The comparison of expected MH sensitivities for a variety of current and proposed experiments using different approaches with reasonable estimates as to the start time of the different experiments is summarized in Figure 4.35.

Future upgrades to the Fermilab accelerator complex — in particular the prospect of high-power, low-energy proton beams such as the 3-MW, 8-GeV beam originally proposed as Stage 4 of Project X — could open up further unique opportunities for LBNE to probe CP violation using on-axis, low-energy beams specifically directed at the second oscillation maximum where CP effects dominate the asymmetries [185]. Such high-power, low-energy beams could even enable studies in ν_1-ν_2 mixing in very long-baseline experiments.

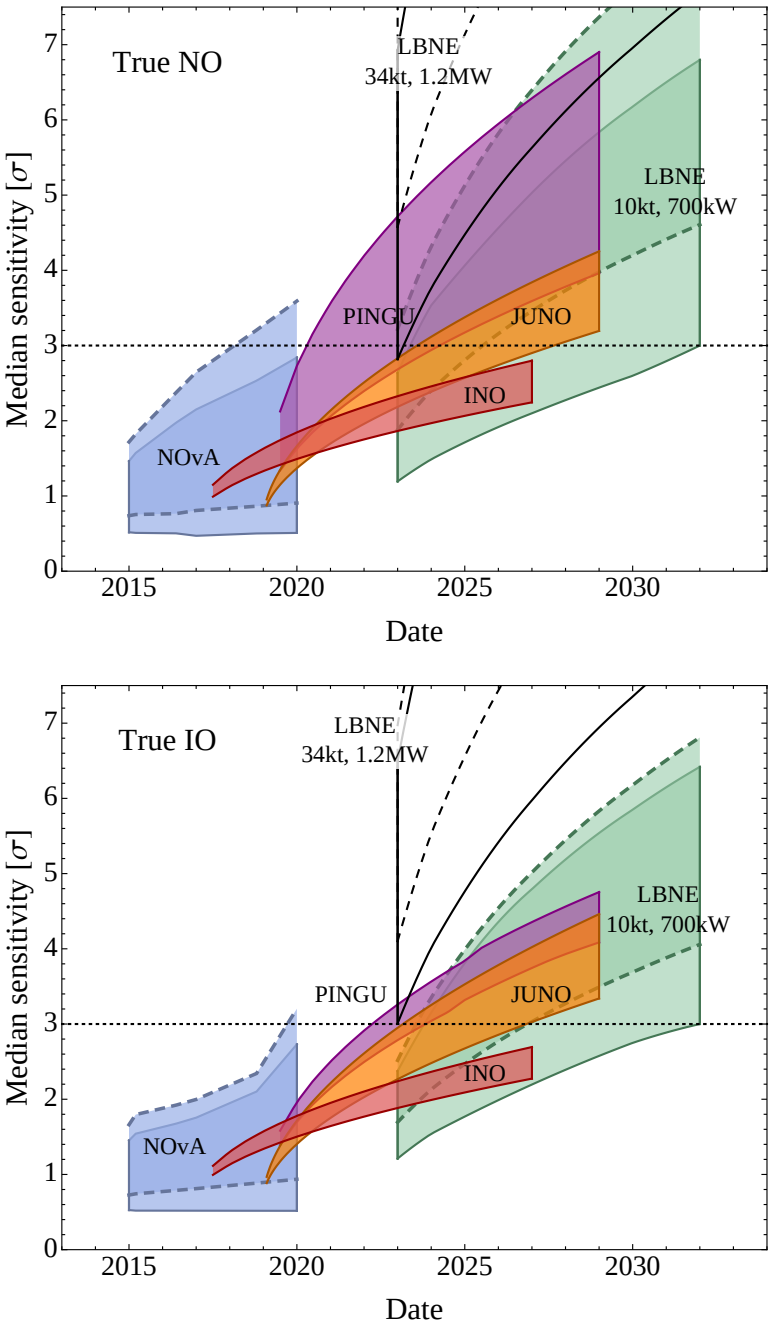

Figure 4.35: The top (bottom) figure shows the median sensitivity in number of sigmas for rejecting the inverted (normal) hierarchy if the normal (inverted) hierarchy is true for different facilities as a function of the date. The width of the bands corresponds to different true values of the CP phase $\delta_{\rm CP}$ for NOνA and LBNE, different true values of θ_{23} between 40° and 50° for INO and PINGU, and energy resolution between $3\%/\sqrt{E\ (\mathrm{MeV})}$ and $3.5\%/\sqrt{E\ (\mathrm{MeV})}$ for JUNO. For the long-baseline experiments, the bands with solid (dashed) contours correspond to a true value for θ_{23} of 40° (50°). In all cases, octant degeneracies are fully considered. This figure is from the analysis presented in [151], however, for the plots shown here, the beam power for the full-scope, 34-kt LBNE has been changed to 1.2 MW to reflect the Fermilab PIP-II upgrade plan.

Chapter 5 Nucleon Decay Motivated by Grand Unified Theories

Baryon number conservation is an unexplained symmetry in the Universe with deep connections to both cosmology and particle physics. As one of the conditions underlying the observed matter-antimatter asymmetry of the Universe, baryon number *should* be violated. Nucleon decay, which is a manifestation of baryon number violation, is a hallmark of many Grand Unified Theories (GUTs), theories that connect quarks and leptons in ways not envisioned by the Standard Model. Observation of proton or bound-neutron decay would provide a clear experimental signature of baryon number violation.

Predicted rates for nucleon decay based on GUTs are uncertain but cover a range directly accessible with the next generation of large underground detectors. LBNE, configured with its massive, deep-underground LArTPC far detector, offers unique opportunities for the discovery of nucleon decay, with sensitivity to key decay channels an order of magnitude beyond that of the current generation of experiments.

5.1 LBNE and the Current Experimental Context

Current limits on nucleon decay via numerous channels are dominated by Super–Kamiokande (SK) [186], for which the most recently reported preliminary results are based on an overall exposure of 260 kt · year. Although the SK search has so far not observed nucleon decay, it has established strict limits (90% CL) on the partial lifetimes for decay modes of particular interest to GUT models such as $\tau/B(p \to e^+\pi^0) > 1.3 \times 10^{34}$ year and $\tau/B(p \to K^+\overline{\nu}) > 0.59 \times 10^{34}$ year [40]. These are significant limits on theoretical models that constrain model builders and set a high threshold for the next-generation detectors such as LBNE and Hyper-Kamiokande (Hyper-K). After more than ten years of exposure, the SK limits will improve only slowly. A much more massive detector such as Hyper-K — which will have a 560-kt fiducial mass — is required to make a significant (order-of-magnitude) improvement using the water Cherenkov technique.

The uniqueness of proton decay signatures in a LArTPC and the potential for reconstructing them with redundant information has long been recognized as a key strength of this technology. A LArTPC can reconstruct all final-state charged particles and make an accurate assessment of particle type, distinguishing between muons, pions, kaons and protons. Electromagnetic showers are readily measured, and those that originate from photons generated by π^0 decay can be distinguished to a significant degree from those that originate from ν_e charged-current (CC) interactions. Kiloton-per-kiloton, LArTPC technology is expected to outperform water Cherenkov in both detection efficiency and atmospheric-neutrino background rejection for most nucleon decay modes,

although intranuclear effects, which can smear out some of the proton decay signal, are smaller for oxygen and nonexistent for hydrogen.

When mass and cost are taken into account, water Cherenkov technology is optimum for the $p \to e^+\pi^0$ final-state topology, where the signal efficiency is roughly 40% and the background rate is two events per Mt · year. The efficiency estimate for this mode [187] for a LArTPC is 45% with one event per Mt · year — not a significant enough improvement in efficiency to overcome the penalty of the higher cost per kiloton for liquid argon.

For the $p \to K^+\overline{\nu}$ channel, on the other hand, the LArTPC technology is superior based on the same criteria. In a LArTPC, the K^+ track is reconstructed and identified as a charged kaon. The efficiency for the $K^+\overline{\nu}$ mode in a LArTPC is estimated to be as high as 97.5% with a background rate of one event per Mt · year. In water Cherenkov detectors the efficiency for this mode is roughly 19% for a low-background search, with a background rate of four events per Mt · year. Based on these numbers and a ten-year exposure, LBNE's 34-kt LArTPC and the 560-kt Hyper-K WCD have comparable sensitivity (at 90% CL), but the estimated LArTPC background of 0.3 events is dramatically better than the 22 estimated for Hyper-K (assuming no further improvement in analysis technique past that currently executed for SK [40]).

5.2 Signatures for Nucleon Decay in Liquid Argon

The LBNE LArTPC's superior detection efficiencies for decay modes that produce kaons will outweigh its relatively low mass compared with multi-hundred-kiloton water Cherenkov detectors. Because the LArTPC can reconstruct protons that are below Cherenkov threshold, it can reject many atmospheric-neutrino background topologies by vetoing on the presence of a recoil proton. Due to its excellent spatial resolution, it also performs better for event topologies with displaced vertices, such as $p \to K^+\overline{\nu}$ (for multi-particle K^+ decay topologies) and $p \to K^0\mu^+$. The latter mode is preferred in some SUSY GUTs.

For modes with no electron in the final state, the same displaced vertex performance that underpins long-baseline neutrino oscillation measurements allows the rejection of CC interactions of atmospheric ν_e's. As will be stressed for the key mode of $p \to K^+\overline{\nu}$ described in detail below, the capability to reconstruct the charged kaon with the proper range and dE/dx profile allows for a high-efficiency, background-free analysis. In general, these criteria favor all modes with a kaon, charged or neutral, in the final state. Conversely, the efficiency for decay modes to a lepton plus light meson will be limited by intranuclear reactions that plague liquid argon to a greater extent than they do ^{16}O in a water Cherenkov detector.

An extensive survey [187] of nucleon decay efficiency and background rates for large LArTPCs

with various depth/overburden conditions, published in 2007, provides the starting point for the assessment of LBNE's capabilities. Table 5.1 lists selected modes where LArTPC technology exhibits a significant performance advantage (per kiloton) over the water Cherenkov technology. The remainder of this chapter focuses on the capabilities of LBNE for the $p \to K^+\overline{\nu}$ channel, as the most promising from theoretical and experimental considerations. Much of the discussion that follows can be applied to cover the other channels with kaons listed in the table.

Table 5.1: Efficiencies and background rates (events per Mt · year) for nucleon decay channels of interest for a large underground LArTPC [187], and comparison with water Cherenkov detector capabilities. The entries for the water Cherenkov capabilities are based on experience with the Super–Kamiokande detector [40].

Decay Mode	Water Cherenkov		Liquid Argon TPC	
	Efficiency	Background	Efficiency	Background
$p \to K^+\overline{\nu}$	19%	4	97%	1
$p \to K^0\mu^+$	10%	8	47%	< 2
$p \to K^+\mu^-\pi^+$			97%	1
$n \to K^+e^-$	10%	3	96%	< 2
$n \to e^+\pi^-$	19%	2	44%	0.8

The key signature for $p \to K^+\overline{\nu}$ is the presence of an isolated charged kaon (which would also be monochromatic for the case of free protons, with p =340 MeV). Unlike the case of $p \to e^+\pi^0$, where the maximum detection efficiency is limited to 40–45% because of inelastic intranuclear scattering of the π^0, the kaon in $p \to K^+\overline{\nu}$ emerges intact (because the kaon momentum is below threshold for inelastic reactions) from the nuclear environment of the decaying proton $\sim 97\%$ of the time. Nuclear effects come into play in other ways, however: the kaon momentum is smeared by the proton's Fermi motion and shifted downward by re-scattering [188]. The kaon emerging from this process is below Cherenkov threshold, therefore a water detector would need to detect it after it stops, via its decay products. Not all K decay modes are reconstructable, however, and even for those that are, insufficient information exists to determine the initial K momentum. Still, water detectors can reconstruct significant hadronic channels such as $K^+ \to \pi^+\pi^0$ decay, and the 6-MeV gamma from de-excitation of O^{16} provides an added signature to help with the $K^+ \to \mu^+\nu$ channel. The overall detection efficiency in SK [40] thus approaches 20%.

In LArTPC detectors, the K^+ can be tracked, its momentum measured by range, and its identity positively resolved via detailed analysis of its energy-loss profile. Additionally, all decay modes can be cleanly reconstructed and identified, including those with neutrinos, since the decaying proton is essentially at rest. With this level of detail, it is possible for a single event to provide overwhelming evidence for the appearance of an isolated kaon of the right momentum originating from a point within the fiducial volume. The strength of this signature is clear from cosmogenic-induced kaons observed by the ICARUS Collaboration in the cosmic-ray (CR) test run of half of the T600 detector, performed at a surface installation in Pavia [189] and in high-energy neutrino

interactions with the full T600 in the recent CNGS (CERN Neutrinos to Gran Sasso) run [190]. Figure 5.1 shows a sample event from the CNGS run in which the kaon is observed as a progressively heavily-ionizing track that crosses into the active liquid argon volume, stops, and decays to $\mu\nu$, producing a muon track that also stops and decays such that the Michel-electron track is also visible. The 3D reconstruction of the event is shown in Figure 5.2.

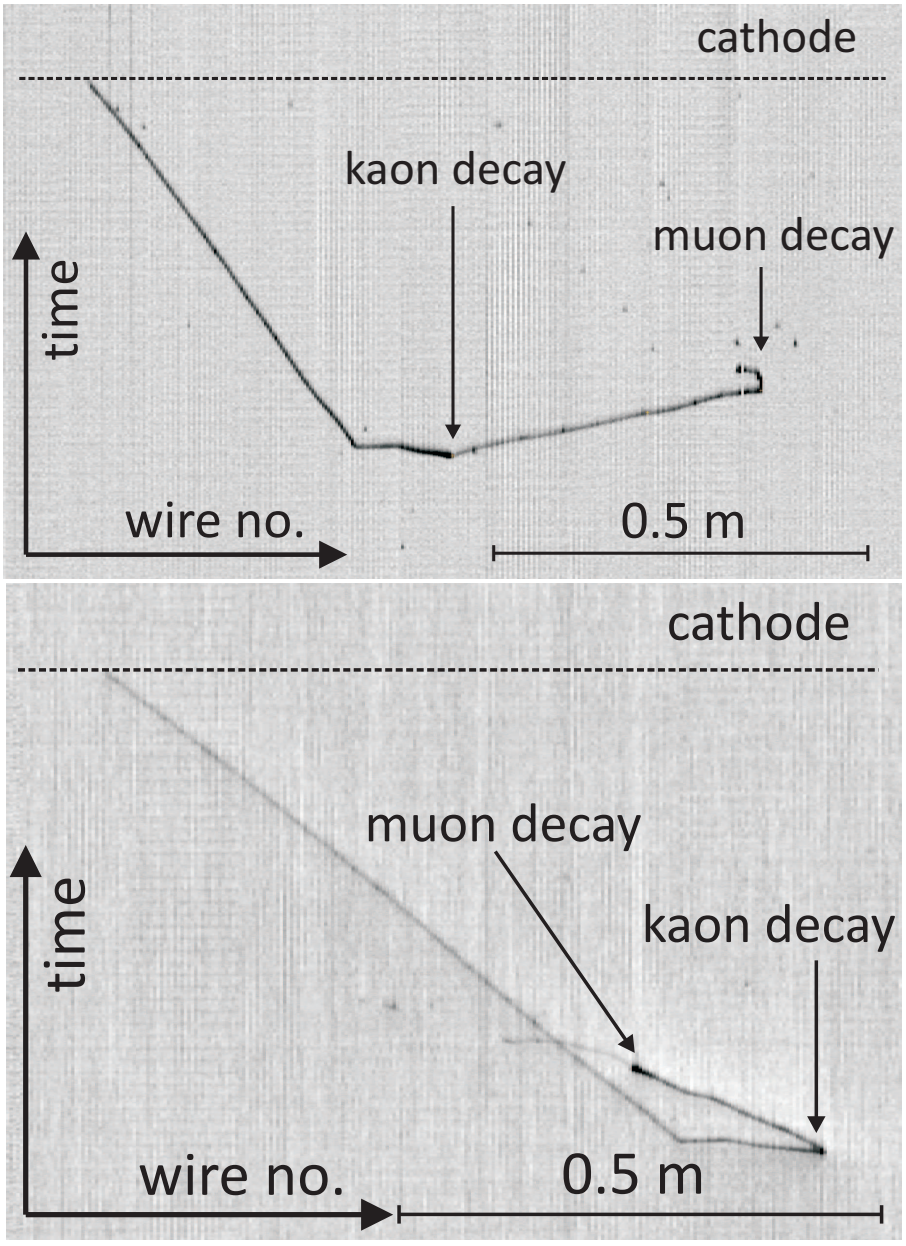

Figure 5.1: Event display for a decaying kaon candidate $K \to \mu\nu_\mu$ $\mu \to e\nu_e\nu_\mu$ in the ICARUS T600 detector observed in the CNGS data (K: 90 cm, 325 MeV; μ : 54 cm, 147 MeV; e : 13 cm, 27 MeV). The top figure shows the signal on the collection plane, and the bottom figure shows the signal on the second induction plane [190].

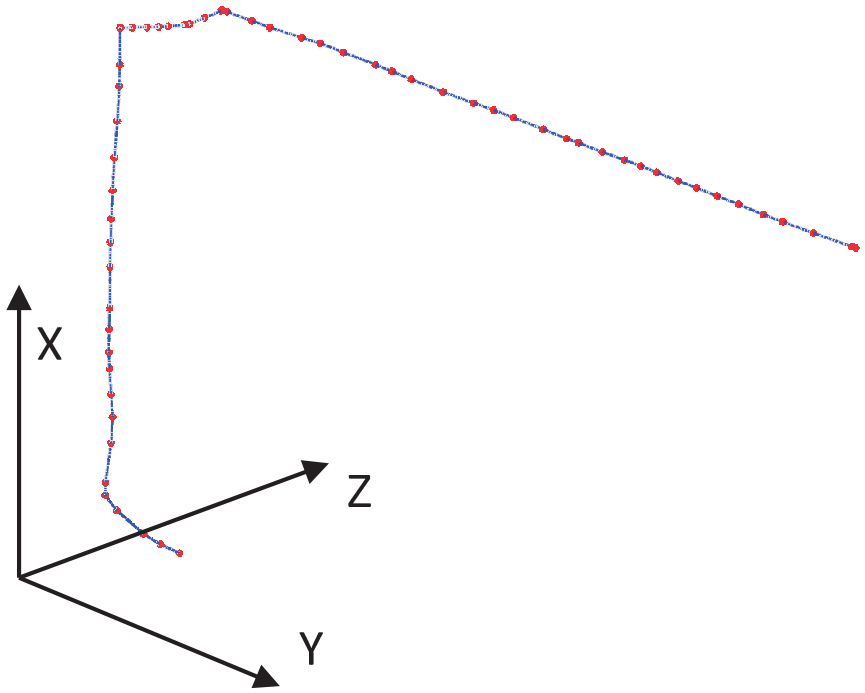

Figure 5.2: 3D reconstruction of the decaying kaon event observed in the ICARUS T600 detector and shown in Figure 5.1.

If it can be demonstrated that background processes mimicking this signature can be rejected at the appropriate level, a single $p \to K^+\overline{\nu}$ candidate could constitute evidence for proton decay.

5.3 Background Levels and Rejection Capabilities

This section discusses the key background processes and their signatures, focusing on the $p \to K^+\overline{\nu}$ channel as the benchmark mode*. The two potential sources of background are cosmic-ray muons and atmospheric neutrinos, described separately below.

5.3.1 Cosmic-Ray Muon Backgrounds

Cosmic-ray (CR) muons contribute background signals when they penetrate the detector. Hence, the self-shielding feature of the LArTPC and the depth of the site are important assets for controlling the rate of signals that can mimic a proton decay event. Additionally, the energy deposition associated with spallation products is well below the hundreds-of-MeV range for depositions from proton decay final-state particles.

The most pernicious CR-muon background in liquid argon for proton decay with kaon final states

*Much of this discussion applies equally well to other nucleon decay modes involving charged or neutral kaons.

thus comes from particular pathological processes. Specifically, CR muons that produce kaons via photonuclear interactions in the rock near the detector or in the liquid argon itself but outside the active volume are capable of producing signatures that mimic $p \rightarrow K^+\overline{\nu}$ and other modes with kaons. CR-induced kaon backgrounds as a function of depth have been studied for liquid argon [187,191,192].

In particular, at the 4,850-ft level, the vertical rock overburden will be approximately 4-km water equivalent, at which depth the muon rate through a 34-kt LArTPC will be approximately 0.1 s^{-1}. This is low enough that a veto on the detection of a muon in the liquid argon volume can be applied with negligible loss of live-time. Specifically, assuming a maximum drift time of 2 ms, the probability of a muon passing through the detector in time with any candidate event (i.e., a candidate for proton decay or other signal of interest) will be 2×10^{-4}. Thus, any candidate event that coincides in time with a large energy deposition from a muon or muon-induced cascade can be rejected with a negligible signal efficiency loss of 0.02%. Only background from events associated with CR muons in which the muon itself does not cross the active region of the detector remain to be considered.

One class of such backgrounds involves production of a charged kaon outside the active volume, which then enters the active region. Assuming unambiguous determination of the drift time (via the scintillation-photon detection system and other cues such as detailed analysis of the dE/dx profile of the kaon candidate), it will be possible to identify and reject such entering kaons with high efficiency. It should be noted that, through studies of CR muons that interact within the active volume of the detector, backgrounds of this type can be well characterized with data from the detector itself.

A potentially less tractable background for the decay mode $p^+ \rightarrow K^+\overline{\nu}$ occurs when a neutral particle (e.g., a K^0_L) originating in a muon-induced cascade outside the detector propagates into the detector volume and undergoes a charge-exchange reaction in the fiducial volume. To further understand the possible rate for this background at LBNE, simulations of CR muons and their secondaries at depth have been run. The rate of positive kaons produced inside the 34-kt detector by a neutral particle entering from outside (and with no muon inside) has been found to be 0.9 events per year before any other selection criteria are applied. Further studies included the following additional selection criteria:

1. No muon is in the detector active volume.

2. The K^+ candidate is produced inside the liquid argon active volume at a distance from the wall greater than 10 cm.

3. The energy deposition from the K^+ and its descendants (excluding decay products) is less than 150 MeV.

4. The total energy deposition from the K^+, its descendants and decay products is less than 1 GeV.

5. Energy deposition from other particles in the muon-induced cascade (i.e., excluding the energy deposition from the positive kaon, its descendants and decay products) is less than 100 MeV.

No event survived the additional selection criteria, resulting in an upper bound on the rate of this type of background event of 0.07 events per year in a 34-kt LArTPC, equivalent to two events per Mt · year. A key factor contributing to the rejection of CR backgrounds to this level is that although a large number of K^+'s generated by cosmic rays deposit an energy similar to that expected from proton decay, the energy depositions from K^+'s are not the only ones recorded for these events. Other particles from the CR-muon interaction tend also to enter the detector and deposit additional visible energy, making the rejection of background events simpler than would be expected assuming only the appearance of a kaon in the detector.

In addition to the impact of an active veto system for detectors at various depths, the studies of [187] also consider impacts of progressively restrictive fiducial volume cuts. Together, these and the above studies demonstrate that proton decay searches in the LBNE LArTPC at the 4,850-ft level can be made immune to CR-muon backgrounds, without the requirement of an external active veto system. To the extent that there are uncertainties on the rate of kaon production in CR-muon interactions, one has flexibility to suppress background from this source further by application of modest fiducial volume cuts.

5.3.2 Background from Atmospheric-Neutrino Interactions

Unlike the case of CR-muon backgrounds, the contamination of a nucleon decay candidate set due to interactions of atmospheric neutrinos cannot be directly controlled by changing the depth or fiducial volume definition of the LBNE detector. Furthermore the atmospheric-neutrino flux is naturally concentrated around the energy range relevant for proton decay. In the analysis of [187], a single simulated neutral-current (NC) event survived the requirement of having an isolated single kaon with no additional tracks or π^0's, and total deposited energy below 800 MeV. This event is responsible for the estimated background rate of 1.0 per Mt · year.

While this rate is acceptable for LBNE, it is natural to ask to what extent simulations are capable of providing reliable estimates for such rare processes. What if the actual rate for single-kaon atmospheric-neutrino events is higher by a factor of ten or more? Is that even conceivable? To set the scale, it is useful to recall that the atmospheric-neutrino sample size in LBNE is expected to be of order 10^5 per Mt · year of exposure (Table 4.11). Hence, "rare-but-not-negligible" in this context denotes a process that occurs at a level of no less than 10^{-6}.

Super–Kamiokande has given considerable attention to atmospheric-neutrino backgrounds in its nucleon decay searches (e.g., [193]). In the SK analyses, data obtained with relaxed cuts have been studied to validate the atmospheric-neutrino flux and interaction models employed. Consequently, the atmospheric-neutrino backgrounds for nucleon decay searches are well established at the level required for the water Cherenkov detector approach to this physics.

For the case of LBNE, however, with a different detector technology, and with a goal of being sufficiently background-free to enable a discovery based on observation of a single candidate event, one would like to go further to understand at a detailed level what the rates for the specific background processes are. The first question to ask is what are the physical processes that could produce the exact signature of a $p \to K^+\overline{\nu}$ event? Some possibilities are discussed below.

Strange particle production in $\Delta S = 0$ processes: An identified source of background events for SK [193] involves associated production of a pair of strange hadrons, nominally in the strong decay of a nucleonic resonance excited via an inelastic NC neutrino-nucleon interaction. This could be in the form of a kaon accompanying a Λ baryon. Again, conservation of strangeness holds that the baryon cannot be absorbed, and thus a weak decay of the strange quark is guaranteed. For water Cherenkov detectors the strange baryon is produced with a small enough momentum that its decay products are typically below Cherenkov threshold. For a liquid argon detector, these final state particles should be detectable, leaving distinctive signatures that can be reconstructed. Thus in principle, this source of background can be suppressed with appropriate event reconstruction and analysis tools. To understand this prospect in quantitative terms, the range of kinematic distributions are currently under investigation.

It is possible to imagine yet more contrived scenarios, for example where the meson produced is a K^0_L that escapes detection, while a charged kaon (K^- in this case) results from the decay of an excited Λ or Σ baryon produced in association. However, one would expect such processes to be even more rare than those described above. Thus if the rates for (say) the $K^+\Lambda$ production channel described above can be constrained as being sufficiently small, it can be argued that the more contrived scenarios can be ignored.

Strange particle production in $\Delta S = 1$ processes: A potentially challenging source of background is production of a single charged kaon (in this case a K^-) in a $\Delta S = 1$ process. In the simplest case, one could think of it as the Cabibbo-suppressed version of single π production in a CC antineutrino interaction. In contrast to the $\Delta S = 0$ processes described above, no strange baryon is produced in association, and so there are no other hadrons to detect. (Similarly, one could imagine the kaon originating in the decay of a strange baryon resonance produced in a Cabibbo-suppressed neutrino interaction, accompanied by a neutron that goes undetected.) On the other hand, such processes can only occur in CC interactions, and thus a charged lepton will accompany the kaon. This therefore constitutes a background only for cases where the charged lepton is missed, which should be rare. The combination of probabilities associated with (1) Cabibbo-suppression, (2) single hadron production, and (3) circumstances causing the charged lepton to be missed, lead to an

overall suppression of this source of background. Thus it should be possible to rule it out as a source of concern for LBNE on the basis of these features alone.

Misidentification of pions in atmospheric neutrino events: While misidentification of leading pions as kaons in atmospheric-neutrino scattering events is a potential problem, it can be argued that the rate for such misidentification events can be controlled. Key signatures for the kaon are found in the distinctive residual-range dependence of its energy deposition near the end of its trajectory (nominally 14 cm) as well as in the explicit reconstruction of its decay products. Similarly, tails in the measurement of dE/dx would be a concern if they led a pion track to mimic a kaon, however the momentum (30 MeV) and hence range of the muon produced in the decay of a stopping pion would not match that of the corresponding muon (236 MeV) in a $K^+ \rightarrow \mu^+\nu$ decay. Thus, it should be possible to control this background experimentally.

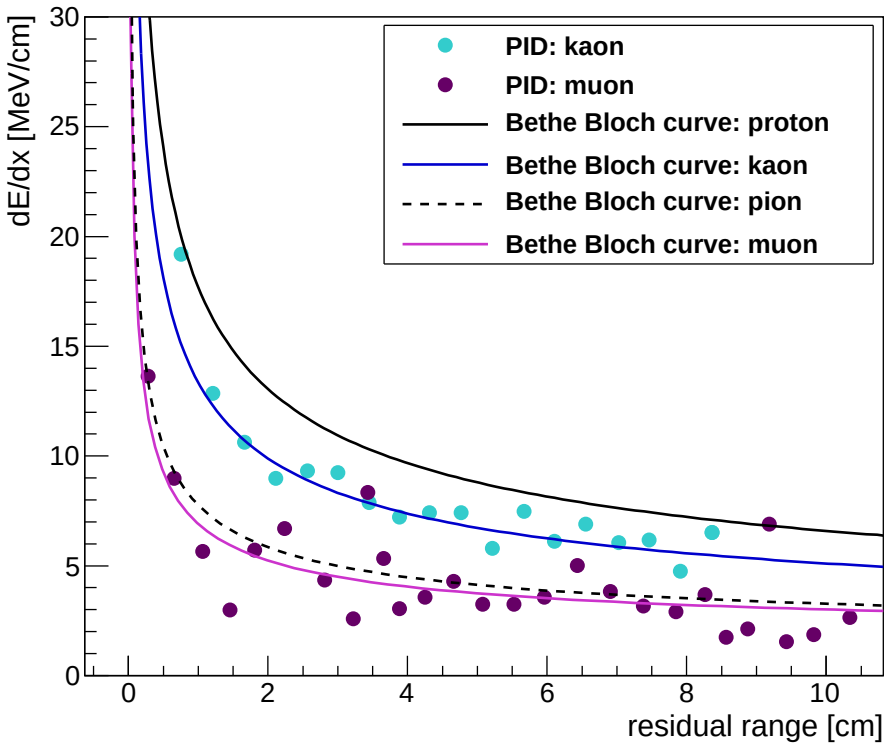

Figure 5.3: Measurements of dE/dx versus residual range for signals associated with the kaon track in Figure 5.1 (cyan points) and the decay muon (magenta points). Overlaid are the expected dE/dx profiles for the two particle identities [190].

One variant of this background source occurs for the case where the pion decays in flight. Two experimental handles on this background can be immediately identified. First is the deviation from the expected dE/dx profile for a kaon, which will be more dramatic than in the case of the stopping pion. Second is the correlation of the direction of the decay muon with that of the pion, which is absent in the decay of a particle at rest. Assessment of the cumulative impact of event rejection

based on these features is under study. However, the decaying kaon observed in the ICARUS CNGS run displayed in Figure 5.1 can be used to give a sense of the π/K discrimination possible in a LArTPC via dE/dx. In Figure 5.3, the measurements of dE/dx versus residual range for the anode wires registering signals from the kaon and muon tracks in this event are plotted against the expected dE/dx profiles [190]. The data from the kaon track (cyan points) agree very well with the expected dE/dx profile (blue curve) and are quite distinguishable from the expected pion profile (dashed curve).

Event reconstruction pathologies: While consideration of rare event topologies in atmospheric-neutrino interactions is important, it will be equally important to understand ways in which more typical events might be misreconstructed so as to mimic nucleon decay processes. For example, a quasi-elastic ν_μ-CC interaction will produce a muon and a recoil proton from a common vertex. However, it may be possible to interpret the vertex as the kink associated with the decay of a stopping kaon, where the proton track is confused with a kaon traveling in the opposite direction. Tools are still under development to be able to understand the degree to which this possibility poses a potential background. Naively, the dE/dx profile of the proton as a function of residual range will not match the time-reversed version of this for a kaon, and distributions of kinematic quantities will be distinct. Additionally, such a background will only affect the portion of the $p \to K^+\overline{\nu}$ analysis focused on $K^+ \to \mu^+\nu$; other K^+ decays will be immune to this pathology.

The point of this example is to illustrate that although the exquisite performance characteristics of the LArTPC technique enables unambiguous identification of nucleon decay signatures, an extensive program of detailed analysis will be required to fully exploit these capabilities.

Conclusions on atmospheric-neutrino backgrounds: The above examples suggest that it will be possible to demonstrate the desired level of suppression of atmospheric-neutrino background without undue reliance on simulations via a combination of arguments based on existing experimental data (from SK proton decay searches, as well as data from various sources on exclusive and inclusive neutrino-interaction processes that yield rare topologies), physics considerations, and detailed analysis of anticipated detector response. For the latter, ongoing LBNE event-reconstruction efforts will play a role with simulated atmospheric-neutrino samples. Additionally, useful input is expected to come in over the short/intermediate term from analyses of LArTPC data from ArgoNeuT, MicroBooNE and the proposed LArIAT. Finally, while the state of neutrino flux and interaction models is already quite advanced, vigorous theoretical work is ongoing to improve these further, exploiting existing data from neutrino and electron-scattering experiments. In particular, kaon production in neutrino interactions in relevant energy ranges is receiving renewed attention [194].

5.4 Summary of Expected Sensitivity to Key Nucleon Decay Modes

Based on the expected signal efficiency and the upper limit on the background rates estimated in Section 5.3, the expected limit on the proton lifetime as a function of running time in LBNE for $p \to K^+\overline{\nu}$ is shown in Figure 5.4.

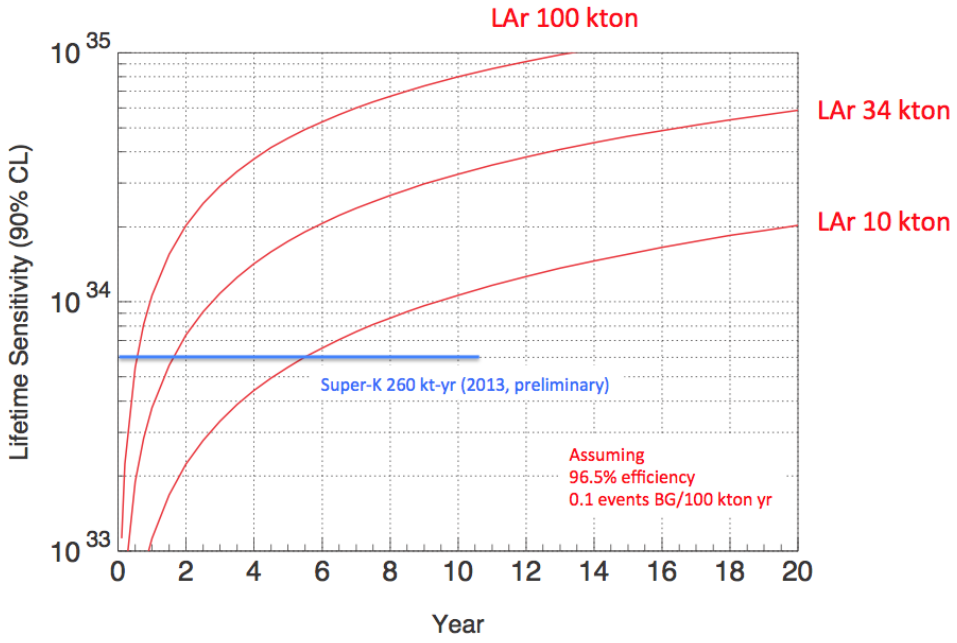

Figure 5.4: Proton decay lifetime limit for $p \to K^+\overline{\nu}$ as a function of time for underground LArTPCs of fiducial masses 10, 34 and 100 kt. For comparison, the current limit from SK is also shown. The limits are at 90% C.L., calculated for a Poisson process including background, assuming that the detected events equal the expected background.

Figure 5.4 demonstrates that to improve the current limits on the $p \to \overline{\nu}K^+$, set by Super–Kamiokande, significantly beyond that experiment's sensitivity, a LArTPC detector of at least 10 kt, installed deep underground, is needed. A 34-kt detector will improve the current limits by an order of magnitude after running for two decades. Clearly a larger detector mass would improve the limits even more in that span of time.

While the background rates are thought to be no higher than those assumed in generating the above sensitivity projections, it is possible to estimate the impact of higher rates. For $p \to K^+\overline{\nu}$, Table 5.2 shows a comparison of the 90% CL lower bounds on proton lifetime for an exposure of 340 kt · year assuming the nominal 1.0 per Mt · year background rate with the corresponding bounds for a rate that is ten times higher, as well as for a fully background-free experiment. While a factor of ten

increase in the background would hurt the sensitivity, useful limits can still be obtained. As stated above, however, there is good reason to believe such a case is highly unlikely.

Table 5.2: The impact of different assumed background rates on the expected 90% CL lower bound for the partial proton lifetime for the $p \to K^+\overline{\nu}$ channel, for a 34-kt detector operating for ten years. The expected background rate is one event per Mt · year. Systematic uncertainties are not included in these evaluations.

Background Rate	Expected Partial Lifetime Limit
0 events/Mt · year	3.8×10^{34} years
1 events/Mt · year	3.3×10^{34} years
10 events/Mt · year	2.0×10^{34} years

Sensitivities have been computed for some of the other decay channels listed in Table 5.1. The limits that could be obtained from an LBNE 34-kt detector in ten years of running as compared to other proposed future experiments and theoretical expectations are shown in Figure 5.5.

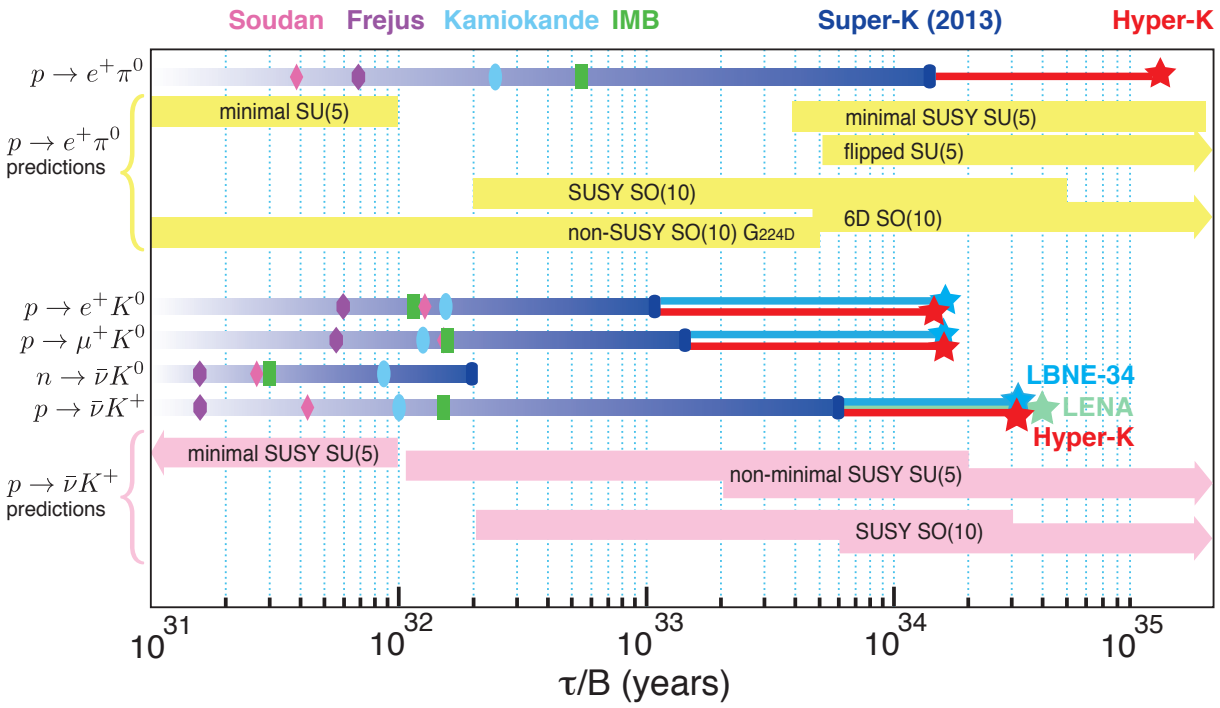

Figure 5.5: Proton decay lifetime limits that can be achieved by the LBNE 34-kt detector compared to other proposed future experiments. The limits are at 90% C.L., calculated for a Poisson process including background, assuming that the detected events equal the expected background.

Chapter 6 Core-Collapse Supernova Neutrinos

Neutrinos emitted in the first few seconds of a core-collapse supernova carry with them the potential for great insight into the mechanisms behind some of the most spectacular events that have played key roles in the evolution of the Universe. Collection and analysis of this high-statistics neutrino signal from a supernova within our galaxy would provide a rare opportunity to witness the energy and flavor development of the burst as a function of time. This would in turn shed light on the astrophysics of the collapse as well as on neutrino properties.

6.1 The Neutrino Signal and Astrophysical Phenomena

A core-collapse supernova* occurs when a massive star reaches the end of its life, and stellar burning can no longer support the star's weight. This catastrophic collapse results in a compact remnant such as a neutron star, or possibly a black hole, depending on the mass of the progenitor. The infall is followed by a *bounce* when sufficiently high core density is reached, and in some unknown (but nonzero) fraction of cases, the shock wave formed after the bounce results in a bright explosion [195]. The explosion energy represents only a small fraction of the enormous total gravitational binding energy of the resulting compact remnant, however — thanks to the neutrinos' weak coupling, which allows them to escape — within a few tens of seconds almost all of the energy is emitted in the form of neutrinos in the tens-of-MeV range. In spite of their weak coupling, the neutrinos are copious enough to (very likely) play a significant role in the explosion.

Neutrinos from the celebrated SN1987A core collapse [103,104] in the Large Magellanic Cloud outside the Milky Way were observed; however, the statistics were sparse and a great many questions remain. A high-statistics observation of a neutrino burst from a nearby supernova would be possible with the current generation of detectors. Such an observation would shed light on the nature of the astrophysical event, as well as on the nature of neutrinos themselves. Sensitivity to the different flavor components of the flux is highly desirable.

The core-collapse neutrino signal starts with a short, sharp *neutronization* burst primarily composed of ν_e (originating from $p + e^- \rightarrow n + \nu_e$, as protons and electrons get squeezed together), and is followed by an *accretion* phase lasting some hundreds of milliseconds, as matter falls onto the collapsed core. The later *cooling* phase over $\sim$10 seconds represents the main part of the signal, over which the proto-neutron star sheds its gravitational binding energy. The neutrino flavor con-

Supernova always refers to a *core-collapse supernova* in this chapter unless stated otherwise.

tent and spectra change throughout these phases, and the supernova's temperature evolution can be followed with the neutrino signal. Some fairly generic supernova signal features are illustrated in Figure 6.1, based on [196] and reproduced from [197].

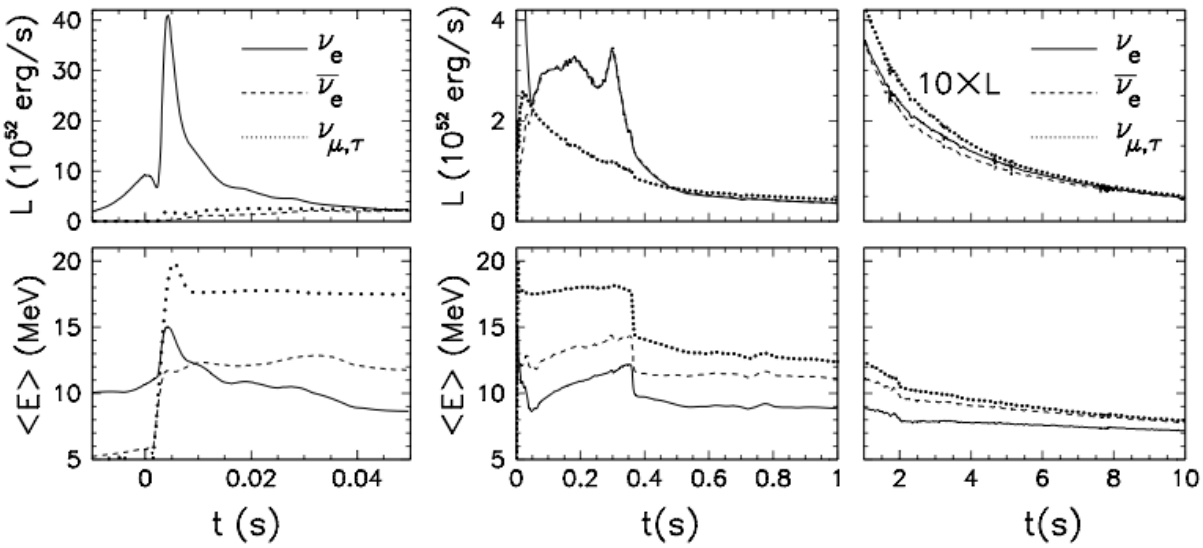

Figure 6.1: Expected core-collapse neutrino signal from the *Basel* model [196], for a 10.8 $M_\odot$ progenitor. The left plots show the very early signal, including the neutronization burst; the middle plots show the accretion phase, and the right plots show the cooling phase. Luminosities as a function of time are shown across the top plots. The bottom plots show average energy as a function of time for the ν_e, $\overline{\nu}_e$ and $\nu_{\mu,\tau}$ flavor components of the flux (fluxes for ν_μ, $\overline{\nu}_\mu$, ν_τ, and $\overline{\nu}_\tau$ should be identical). Figure courtesy of [197].

The supernova-neutrino spectrum at a given moment in time is expected to be well described by a parameterization [198,199] given by:

$$\phi(E_\nu) = \mathcal{N}\left(\frac{E_\nu}{\langle E_\nu\rangle}\right)^{\alpha} \exp\left[-\left(\alpha+1\right)\frac{E_\nu}{\langle E_\nu\rangle}\right] , \tag{6.1}$$

where E_ν is the neutrino energy, $\langle E_\nu\rangle$ is the mean neutrino energy, α is a *pinching parameter*, and $\mathcal{N}$ is a normalization constant. Large α corresponds to a more pinched spectrum (suppressed high-energy tail). This parameterization is referred to as a *pinched-thermal* form. The different ν_e, $\overline{\nu}_e$ and ν_x, $x = \mu, \tau$ flavors are expected to have different average energy and α parameters and to evolve differently in time.

A wide variety of astrophysical phenomena affect the flavor-energy-time evolution of the spectrum, including neutrino oscillation effects that are determined by the mass hierarchy (MH) and *collective* effects due to neutrino-neutrino interactions. A voluminous literature exists exploring these collective phenomena, e.g., [200,201,202,203,204,205,206,207,208].

A number of astrophysical phenomena associated with supernovae are expected to be observable in the supernova-neutrino signal, providing a remarkable window into the event, for example:

- The initial burst, primarily composed of ν_e and called the *neutronization* or *breakout* burst, represents only a small component of the total signal. However, oscillation effects can manifest in an observable manner in this burst, and flavor transformations can be modified by the *halo* of neutrinos generated in the supernova envelope by scattering [209].
- The formation of a black hole would cause a sharp signal cutoff (e.g., [210,211]).
- Shock wave effects (e.g., [212]) would cause a time-dependent change in flavor and spectral composition as the shock wave propagates.
- The standing accretion shock instability (SASI) [213,214], a *sloshing* mode predicted by 3D neutrino-hydrodynamics simulations of supernova cores, would give an oscillatory flavor-dependent modulation of the flux.
- Turbulence effects [215,216] would also cause flavor-dependent spectral modification as a function of time.

This list is far from comprehensive. Furthermore, signatures of *collective* effects and signatures that depend on the MH will make an impact on many of the above signals (examples will be presented in Section 6.2). Certain phenomena are even postulated to indicate beyond-the-Standard-Model physics [217] such as axions, extra dimensions and an anomalous neutrino magnetic moment; non-observation of these effects, conversely, would enable constraints on these phenomena.

The supernova-neutrino burst signal is prompt with respect to the electromagnetic signal and therefore can be exploited to provide an early warning to astronomers [116,117]. Additionally, a LArTPC signal [218] is expected to provide some pointing information, primarily from elastic scattering on electrons.

Even non-observation of a burst, or non-observation of a ν_e component of a burst in the presence of supernovae (or other astrophysical events) observed in electromagnetic or gravitational wave channels, would still provide valuable information about the nature of the sources. Moreover, a long-timescale, sensitive search yielding no bursts will also provide limits on the rate of core-collapse supernovae.

6.2 Expected Signal and Detection in Liquid Argon

As discussed in Section 2.4, liquid argon is known to exhibit a singular sensitivity to the ν_e component of a supernova-neutrino burst. This feature is especially important, as it will make LBNE a unique source in the global effort to combine data from a variety of detectors with different flavor sensitivities to obtain a complete picture of the physics of the burst.

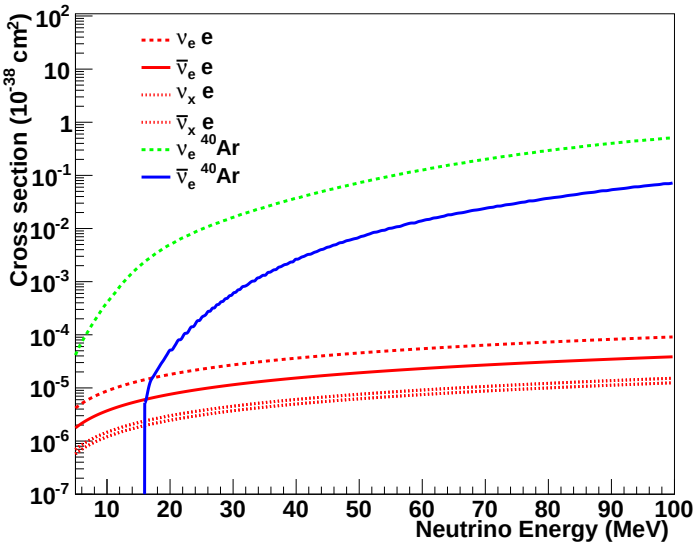

Figure 6.2: Cross sections for supernova-relevant interactions in argon.

The predicted event rate from a supernova-neutrino burst may be calculated by folding expected neutrino differential energy spectra in with cross sections for the relevant channels, and with detector response. For event rate estimates in liquid argon, a detection threshold of 5 MeV is assumed. The photon-detection system of the LBNE far detector, coupled with charge collection and simple pattern recognition, is expected to provide a highly efficient trigger. Most LBNE supernova physics sensitivity studies so far have been done using parameterized detector responses from [139] implemented in the SNOwGLoBES software package [219]. SNOwGLoBES takes as input fluxes, cross sections (Figure 6.2), *smearing matrices* (that incorporate both interaction product spectra and detector response) and post-smearing efficiencies. The energy resolution used is

$$\frac{\sigma}{E\ (\mathrm{MeV})} = \frac{11\%}{\sqrt{E\ \mathrm{MeV}}} + 2\% \tag{6.2}$$

Work is currently underway using the full Geant4 simulation [132] framework and the LArSoft software package [220] to characterize low-energy response for realistic LBNE detector configurations. Preliminary studies of the detector response with the full simulation are summarized in Section A.1.2 and are found to be consistent with the parameterized response implemented in SNOwGLoBES.

Table 6.1 shows rates calculated with SNOwGLoBES for the dominant interactions in argon for the *Livermore* model [221], and the *GKVM* model [222]. Figure 6.3 shows the expected observed differential event spectra for these fluxes. Clearly, the ν_e flavor dominates.

Table 6.1: Event rates for different supernova models in 34 kt of liquid argon for a core collapse at 10 kpc, for ν_e and $\overline{\nu}_e$ charged-current channels and elastic scattering (ES) on electrons. Event rates will simply scale by active detector mass and inverse square of supernova distance.

Channel	Events *Livermore* model	Events *GKVM* model
$\nu_e + {}^{40}\mathrm{Ar} \rightarrow e^- + {}^{40}\mathrm{K}^*$	2308	2848
$\overline{\nu}_e + {}^{40}\mathrm{Ar} \rightarrow e^+ + {}^{40}\mathrm{Cl}^*$	194	134
$\nu_x + e^- \rightarrow \nu_x + e^-$	296	178
Total	**2794**	**3160**

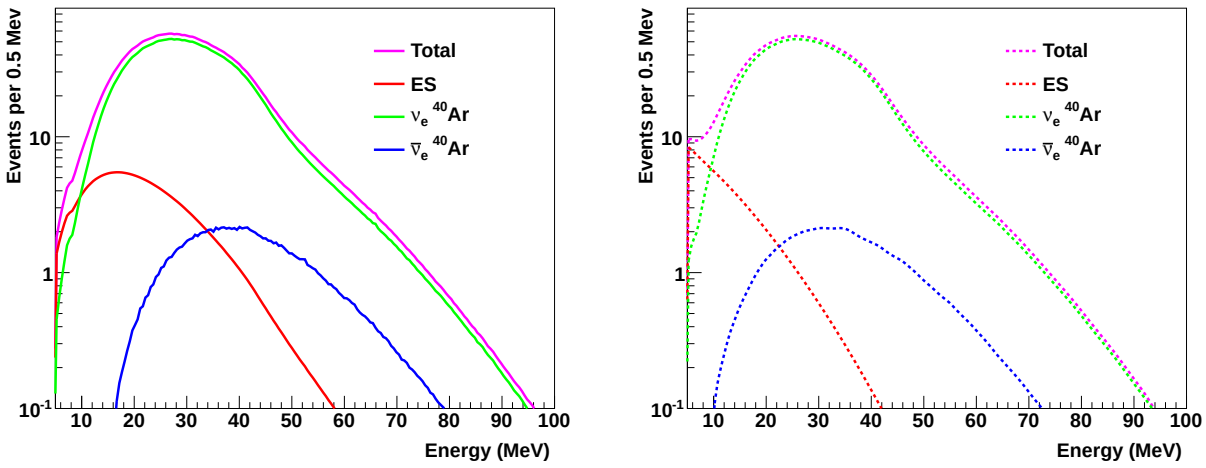

Figure 6.3: Supernova-neutrino event rates in 34 kt of argon for a core collapse at 10 kpc, for the GKVM model [222] (events per 0.5 MeV), showing three relevant interaction channels. Left: interaction rates as a function of true neutrino energy. Right: *smeared* rates as a function of detected energy, assuming resolution from [139].

Figure 6.4 gives another example of an expected burst signal, for which a calculation with detailed time dependence of the spectra is available [223] out to nine seconds post-bounce. This model has relatively low luminosity but a robust neutronization burst. Note that the relative fraction of neutronization-burst events is quite high.

In Figure 6.5, different oscillation hypotheses have been applied to *Duan* fluxes [208]. The Duan flux represents only a single late time slice of the supernova-neutrino burst and not the full flux; MH information will be encoded in the time evolution of the signal, as well. The figure illustrates, if only anecdotally, potential MH signatures.

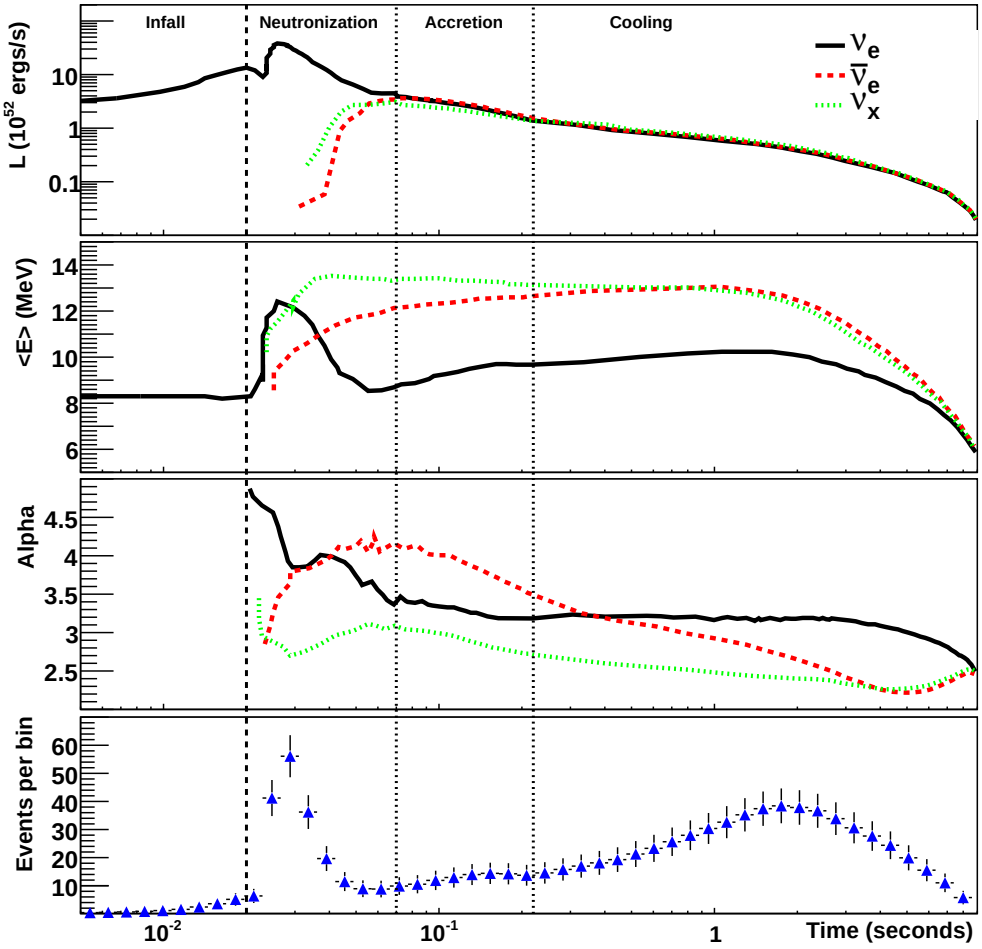

Figure 6.4: Expected time-dependent signal for a specific flux model for an electron-capture supernova [223] at 10 kpc. The top plot shows the luminosity, the second plot shows average neutrino energy, and the third plot shows the α (pinching) parameter. The fourth (bottom) plot shows the total number of events (mostly ν_e) expected in 34 kt of liquid argon, calculated using SNoWGLoBES. Note the logarithmic binning in time; the plot shows the number of events expected in the given bin and the error bars are statistical. The vertical dashed line at 0.02 seconds indicates the time of core bounce, and the vertical lines indicate different eras in the supernova evolution. The leftmost time interval indicates the infall period. The next interval, from core bounce to 50 ms, is the neutronization burst era, in which the flux is composed primarily of ν_e. The next period, from 50 to 200 ms, is the accretion period. The final era, from 0.2 to 9 seconds, is the proto-neutron-star cooling period.

Another potential MH signature is shown in Figure 6.6, for which a clear time-dependent shock-wave-related feature is visible for the normal MH case.

Figure 6.7 shows yet another example of a preliminary study showing how one might track supernova temperature as a function of time with the ν_e signal in liquid argon. Here, a fit is made to the pinched-thermal form of Equation 6.1. Not only can the internal temperature of the supernova be effectively measured, but the time evolution is observably different for the different hierarchies.

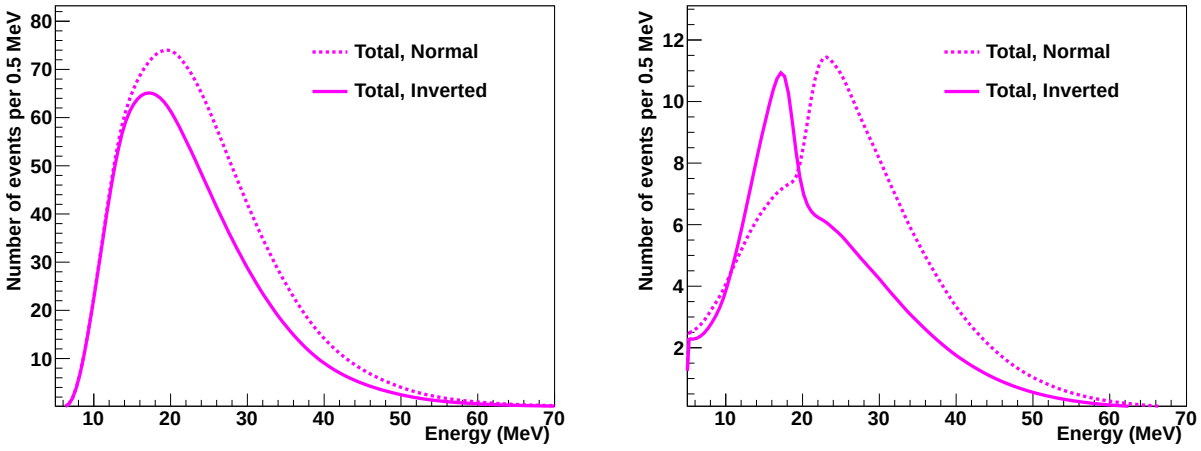

Figure 6.5: Comparison of total event rates for normal and inverted MH, for a specific flux example, for a 100-kt water Cherenkov detector (left) and for a 34-kt LArTPC (right) configuration, in events per 0.5 MeV. There are distinctive features in liquid argon for different neutrino mass hierarchies for this supernova model [224].

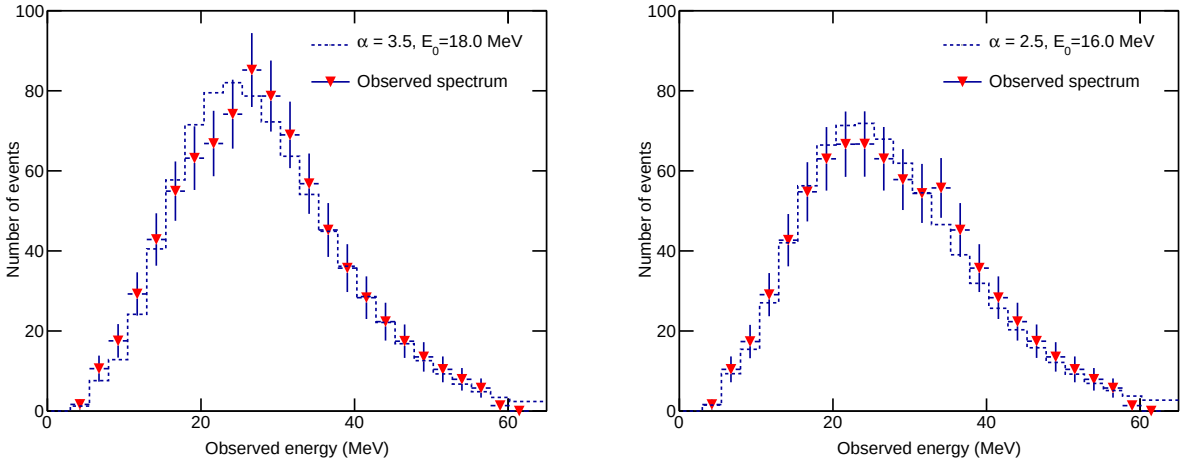

Figure 6.6: Observed ν_e spectra in 34 kt of liquid argon for a 10-kpc core collapse, representing about one second of integration time each at one-second intervals during the supernova cooling phase. The dashed line represents the best fit to a parameterized pinched-thermal spectrum. Clear *non-thermal* features in the spectrum that change with time are visible, on the left at around 20 MeV and on the right at around 35 MeV. Error bars are statistical. These features are present *only* for the normal MH.

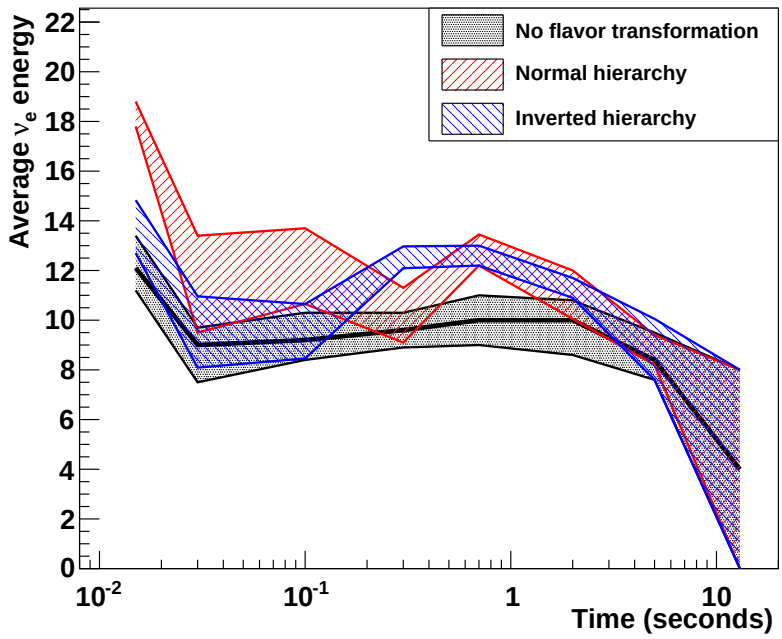

Figure 6.7: Average ν_e energy from fit to SNOwGLoBES-smeared, pinched-thermal spectrum as a function of time (34 kt at 10 kpc), for a flux model based on [225] and including collective oscillations, for two different MH assumptions. The bands represent 1σ error bars from the fit. The solid black line is the truth $\langle E_\nu \rangle$ for the unoscillated spectrum. Clearly, meaningful information can be gleaned by tracking ν_e spectra as a function of time.

6.3 Low-Energy Backgrounds

6.3.1 Cosmic Rays

Due to their low energy, supernova-neutrino events are subject to background from cosmic rays, although the nature of the signal — a short-timescale burst — is such that the background from these muons and their associated Michel electrons can in principle be well known, easily distinguished and subtracted. Preliminary studies [226] suggest that the shielding provided by the 4,850-ft depth available at the Sanford Underground Research Facility is acceptable.

6.3.2 Local Radiation Sources

It is possible that radioactive decays will directly overlap with the energy spectrum created by supernova-neutrino events in LBNE. It is also possible for an ensemble of radioactive-decay events in and around higher-energy particle interactions (e.g., from beam neutrinos) to obscure the edges of electromagnetic showers from highly scattering particles such as electrons and pions; this would appear as the radiological equivalent of dark noise in a digital image, and could potentially intro-

duce a systematic uncertainty in the energy calculated for events, even at much higher energy than the decays themselves. It is therefore very important to calculate the radioactive-decay backgrounds in the LBNE far detector with sufficient accuracy to properly account for their presence, either as direct backgrounds or as systematic effects in energy calculations. To this end, LBNE collaborators are in the process of creating a physics-driven, radioactive-background budget and associated event generator for low-energy background events in the far detector.

The radioactive-background budget will have many components, each of which will fall into one of two categories:

1. intrinsic radioactive contamination in the argon or support materials, or
2. cosmogenic radioactivity produced in situ from cosmic-ray showers interacting with the argon or the support materials.

The former is dependent on the detector materials, and is therefore independent of far detector depth. The latter is strongly coupled to the cosmic-ray flux and spectrum. A preliminary estimate [227] of the cosmogenic radioactivity from beta emitters produced from cosmic-ray interactions with argon in the LBNE far detector at the 4,850 ft level of the Sanford Underground Research Facility is shown in Figure 6.8. Both of these background categories add to the direct energy depositions from cosmic rays themselves and associated showers.

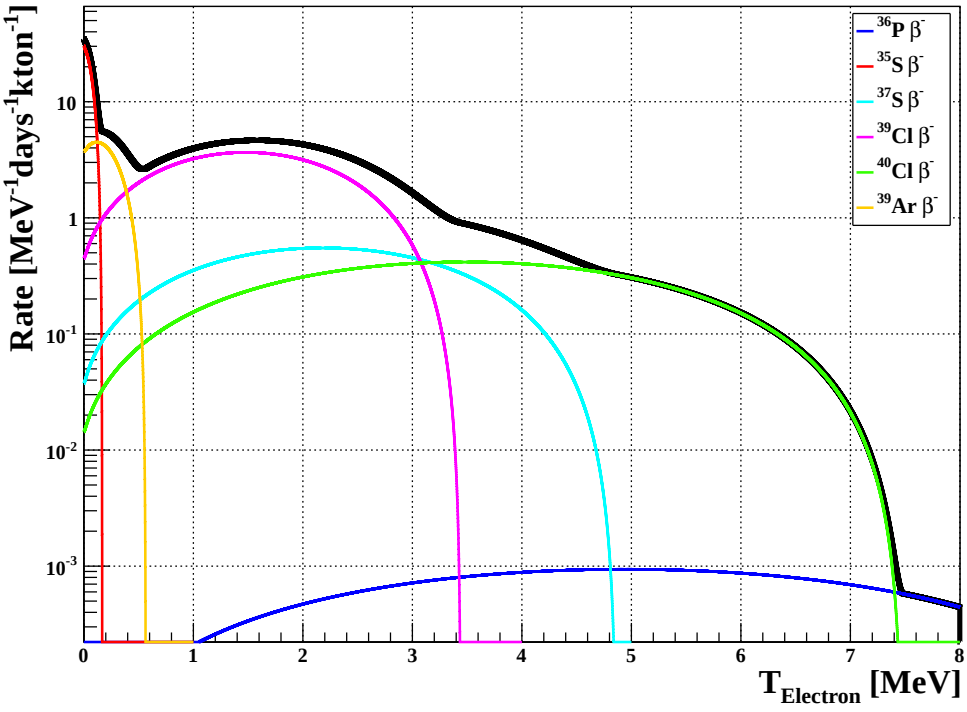

Figure 6.8: Cosmogenic background rates in the LBNE LArTPC as a function of the decay beta kinetic energy calculated at the 4,850-ft level of the Sanford Underground Research Facility.

6.3.3 Intrinsic Radioactive Background Mitigation

Intrinsic backgrounds in the far detector come from the radioactive material that is prevalent in the detector materials (both active and instrumentation/support materials and the cryostat itself), in the cavern walls and in the dust [228]. The isotopes of primary interest are "the usual suspects" in experiments where radioactive backgrounds must be controlled: ^{232}Th and ^{238}U (and their associated decay chains), ^{40}K, and ^{60}Co. In addition, ^{39}Ar will contribute a significant component, since it is present in natural argon harvested from the atmosphere at the level of approximately 1 Bq/kg. In consequence, a 10-kt far detector filled with $^{\mathrm{nat.}}$Ar will experience a rate from ^{39}Ar of approximately 10 MHz across the whole detector. The beta decay spectrum from ^{39}Ar is thankfully quite low in energy (Q_β = 0.565 MeV), so it will not interfere directly with the supernova signal, but it may contribute to the *dark noise* effect. Furthermore, the product of the average beta energy with this rate indicates the level at which the background due to introduction of power into the detector becomes a problem. This radioactive power from ^{39}Ar is approximately:

$$P_{Rad} \sim 0.25 \text{ MeV} \times 10 \text{ MHz} = 2.5 \times 10^6 \text{ MeV/s}. \tag{6.3}$$

Because this category of background can come from the cavern walls, the concrete cavern lining, the cryostat materials or the materials that compose the submersed instrumentation, it is important to know which type of radioactive decay is produced by each isotope as well as the total energy it releases. For instance, an alpha decay from an isotope in the U or Th decay chain will deposit its full energy into the detector if it occurs in the active region of the detector, but will deposit no energy if it occurs inside of some macroscopically thick piece of support material because of its very short range ($\lesssim$1 μm) in most solids. This requires different accounting for energy depositions from intrinsic radioactive contamination measured in different locations (or groups of locations). This is clearly a tractable problem, but one which must be handled with care and forethought.

Since a large body of work has been compiled on the control of radiological background in previous experiments that have encountered similar conditions, much of the work in this area will be cited from these experiments (e.g., DARKSIDE [229], EXO [230], ICARUS, BOREXINO, KamLAND and Super–Kamiokande). Work remains, however, on understanding the background particular to the LBNE far detector location/depth (e.g., radon levels and dust activity, for instance), and on integrating existing and new work into the LBNE simulation, reconstruction and analysis framework.

6.4 Summary of Core-Collapse Supernova Sensitivities

LBNE, with its high-resolution LArTPC far detector, is uniquely sensitive to the ν_e component of the neutrino flux from a core-collapse supernova within our galaxy. The ν_e component of the neutrino flux dominates the initial neutronization burst of the supernova. Preliminary studies indicate that such a supernova at a distance of 10 kpc would produce $\sim$3,000 events in a 34-kt LArTPC. The time dependence of the signal will allow differentiation between different neutrino-driven core-collapse dynamical models, and will exhibit a discernible dependence on the neutrino mass hierarchy.

A low energy threshold of $\sim$ 5 MeV will enable the detector to extract the rich information available from the ν_e supernova flux. LBNE's photon detection system is being designed to provide a high-efficiency trigger for supernova events. Careful design and quality control of the detector materials will minimize low-energy background from radiological contaminants.

Chapter 7 Precision Measurements with a High-Intensity Neutrino Beam

The LBNE near neutrino detector provides scientific value beyond its essential role of calibrating beam and neutrino interaction properties for the long-baseline physics program described in Chapter 4. By virtue of the theoretically clean, purely weak leptonic processes involved, neutrino beams have historically served as unique probes for new physics in their interactions with matter. The high intensity and broad energy range of the LBNE beam will open the door for a highly capable near detector to perform its own diverse program of incisive investigations.

The reduction of systematic uncertainties for the neutrino oscillation program requires excellent resolution in the reconstruction of neutrino events. Combined with the unprecedented neutrino fluxes available — which will allow the collection of $\mathcal{O}(10^8)$ inclusive neutrino charged current (CC) interactions for 10^{22} protons-on-target (POT) just downstream of the beamline — the near detector (ND) will significantly enhance the LBNE long-baseline oscillation program and produce a range of short-baseline neutrino scattering physics measurements. The combined statistics and resolution expected in the ND will allow precise tests of fundamental interactions resulting in a better understanding of the structure of matter.

Table 7.1 lists the expected number of beam-neutrino interactions per ton of detector at the LBNE ND site, located 459 m downstream from the target.

This chapter presents a short description of some of the studies that can be performed with LBNE's fine-grained near neutrino detector and gives a flavor of the outstanding physics potential. A more detailed and complete discussion of the ND physics potential can be found in [129].

Appendix B describes neutrino scattering kinematics and includes definitions of the kinematic variables used in this chapter.

7.1 Precision Measurements with Long-Baseline Oscillations

From the studies of uncertainties and the impact of the spectral shape presented in Section 4.3.2, it is evident that to fully realize the goals of the full LBNE scientific program — in particular, sensitivity to CP violation and the precision measurement of the three-flavor oscillation parameters — it is necessary to characterize the expected unoscillated neutrino flux with high precision. In addition to the precise determination of the neutrino flux, shape and flavor composition, the char-

Table 7.1: Estimated interaction rates in the neutrino (second column) and antineutrino (third column) beams per ton of detector (water) for 1×10^{20} POT at 459 m assuming neutrino cross-section predictions from NUANCE [231] and a 120-GeV proton beam using the CDR reference design. Processes are defined at the initial neutrino interaction vertex and thus do not include final-state effects. These estimates do not include detector efficiencies or acceptance [232,233].

Production mode	ν_μ Events	$\overline{\nu}_\mu$ Events
CC QE ($\nu_\mu n \to \mu^- p$)	50,100	26,300
NC elastic ($\nu_\mu N \to \nu_\mu N$)	18,800	8,980
CC resonant π^+ ($\nu_\mu N \to \mu^- N \pi^+$)	67,800	0
CC resonant π^- ($\overline{\nu}_\mu N \to \mu^+ N \pi^-$)	0	20,760
CC resonant π^0 ($\nu_\mu n \to \mu^- p \pi^0$)	16,200	6,700
NC resonant π^0 ($\nu_\mu N \to \nu_\mu N \pi^0$)	16,300	7,130
NC resonant π^+ ($\nu_\mu p \to \nu_\mu n \pi^+$)	6,930	3,200
NC resonant π^- ($\nu_\mu n \to \nu_\mu p \pi^-$)	5,980	2,570
CC DIS ($\nu_\mu N \to \mu^- X$ or $\overline{\nu}_\mu N \to \mu^+ X, W > 2$)	66,800	13,470
NC DIS ($\nu_\mu N \to \nu_\mu X$ or $\overline{\nu}_\mu N \to \overline{\nu}_\mu X, W > 2$)	24,100	5,560
NC coherent π^0 ($\nu_\mu A \to \nu_\mu A \pi^0$ or $\overline{\nu}_\mu A \to \overline{\nu}_\mu A \pi^0$)	2,040	1,530
CC coherent π^+ ($\nu_\mu A \to \mu^- A \pi^+$)	3,920	0
CC coherent π^- ($\overline{\nu}_\mu A \to \mu^+ A \pi^-$)	0	2,900
NC resonant radiative decay ($N^* \to N\gamma$)	110	50
NC elastic electron ($\nu_\mu e^- \to \nu_\mu e^-$ or $\overline{\nu}_\mu e^- \to \overline{\nu_\mu} e^-$)	30	17
Inverse Muon Decay ($\nu_\mu e \to \mu^- \nu_e$)	12	0
Other	42,600	15,800
Total CC (rounded)	**236,000**	**81,000**
Total NC+CC (rounded)	**322,000**	**115,000**

acterization of different neutrino interactions and interaction cross sections on a liquid argon target is necessary to estimate physics backgrounds to the oscillation measurements. The high-resolution near tracking detector described in Section 3.5 can measure the unoscillated flux normalization, shape and flavor to a few percent using systematically independent techniques that are discussed in the following sections.

7.1.1 Determination of the Relative Neutrino and Antineutrino Flux

The most promising method of determining the shape of the ν_μ and $\overline{\nu}_\mu$ flux is by measuring CC events with low hadronic-energy deposition (low-ν) where ν is the total energy of the hadrons that are produced after a neutrino interaction, $E_\nu - E_\mu$. It is important to note that not all the hadrons escape the remnant nucleus, and intranuclear effects will smear the visible energy of the hadronic system. A method of relative flux determination known as low-ν_0 — where ν_0 is a given value of visible hadronic energy in the interaction that is selected to minimize the fraction of the total interaction energy carried by the hadronic system — is well developed [234]. The method follows

from the general expression of the ν-nucleon differential cross section:

$$\mathcal{N}(\nu < \nu_0) \simeq C\Phi(E_\nu)\nu_0 \left[\mathcal{A} + \left(\frac{\nu_0}{E_\nu}\right)\mathcal{B} + \left(\frac{\nu_0}{E_\nu}\right)^2 \mathcal{C} + \mathcal{O}\left(\frac{\nu_0}{E_\nu}\right)^3\right], \tag{7.1}$$

where the coefficients are $\mathcal{A} = \mathcal{F}_2, \mathcal{B} = (\mathcal{F}_2 \pm \mathcal{F}_3)/2, \mathcal{C} = (\mathcal{F}_2 \mp \mathcal{F}_3)/6$, and $\mathcal{F}_i = \int_0^1 \int_0^{\nu_0} F_i(x) dx d\nu$ is the integral of structure function $F_i(x)$. The dynamics of neutrino-nucleon scattering implies that the number of events in a given energy bin with hadronic energy $E_{\text{had}} < \nu_0$ is proportional to the (anti)neutrino flux in that energy bin up to corrections $\mathcal{O}(\nu_0/E_\nu)$ and $\mathcal{O}(\nu_0/E_\nu)^2$. The number $\mathcal{N}(\nu < \nu_0)$ is therefore proportional to the flux up to correction factors of the order $\mathcal{O}(\nu_0/E_\nu)$ or smaller, which are not significant for small values of ν_0 at energies $\geq \nu_0$. The coefficients $\mathcal{A}$, $\mathcal{B}$ and $\mathcal{C}$ are determined for each energy bin and neutrino flavor within the ND data.

LBNE's primary interest is the relative flux determination, i.e., the neutrino flux in one energy bin relative to that in another; variations in the coefficients do not affect the relative flux. The prescription for the relative flux determination is simple: count the number of neutrino CC events below a certain small value of hadronic energy (ν_0). The observed number of events, up to the correction of the order $\mathcal{O}(\nu_0/E_\nu)$ due to the finite ν_0 in each total visible energy bin, is proportional to the relative flux. The smaller the factor ν_0/E_ν is, the smaller is the correction. Furthermore, the energy of events passing the low-ν_0 cut is dominated by the corresponding lepton energy.

It is apparent from the above discussion that this method of relative flux determination is not very sensitive to nucleon structure, QCD corrections or types of neutrino interactions such as scaling or nonscaling. With the excellent granularity and resolution foreseen in the low-density magnetized tracker, it will be possible to use a value of ν_0 ~0.5 GeV or lower, thus allowing flux predictions down to E_ν ~0.5 GeV. A preliminary analysis with the high-resolution tracker achieved a precision $\leq 2\%$ on the relative ν_μ flux with the low-ν_0 method in the energy region $1 \leq E_\nu \leq 30$ GeV in the fit with $\nu_0 < 0.5$ GeV. Similar uncertainties are expected for the $\overline{\nu}_\mu$ component (the dominant one) in the antineutrino beam mode (negative focusing).

7.1.2 Determination of the Flavor Content of the Beam: $\nu_\mu, \overline{\nu}_\mu, \nu_e, \overline{\nu}_e$

The empirical parameterization of the pion and kaon neutrino parents produced from the proton target, determined from the low-ν_0 flux at the ND, allows prediction of the ν_μ and $\overline{\nu}_\mu$ flux at the far detector location. This parameterization provides a measure of the $\pi^+/K^+/\mu^+(\pi^-/K^-/\mu^-)$ distributions of neutrino parents of the beam observed in the ND. Additionally, with the capability to identify $\overline{\nu}_e$ CC interactions, it is possible to directly extract the elusive K^0_L content of the beam. Therefore, an accurate measurement of the $\nu_\mu, \overline{\nu}_\mu$ and $\overline{\nu}_e$ CC interactions provides a prediction of the ν_e content of the beam, which is an irreducible background for the ν_e appearance search in the far detector:

$$\nu_e \equiv \mu^+(\pi^+ \to \nu_\mu) \oplus K^+(K^+ \to \nu_\mu) \oplus K^0_L \quad (7.2)$$

$$\overline{\nu}_e \equiv \mu^-(\pi^- \to \overline{\nu}_\mu) \oplus K^-(K^- \to \overline{\nu}_\mu) \oplus K^0_L \quad (7.3)$$

The μ component is well constrained from $\nu_\mu(\overline{\nu}_\mu)$ CC data at low energy, while the $K^\pm$ component is only partially constrained by the $\nu_\mu(\overline{\nu}_\mu)$ CC data at high energy and requires external hadro-production measurements of $K^\pm/\pi^\pm$ ratios at low energy from hadro-production experiments such as MIPP [235] and NA61 [162]. Finally, the K^0_L component can be constrained by the $\overline{\nu}_e$ CC data and by external dedicated measurements at hadron-production experiments. In the energy range $1(5) \leq E_\nu \leq 5(15)$ GeV, the approximate relative contributions to the ν_e spectrum are 85% (55%) from μ^+, 10% (30%) from K^+ and 3% (15%) from K^0_L.

Based on the NOMAD experience, a precision of $\leq 0.1\%$ on the flux ratio ν_e/ν_μ is expected at high energies. Taking into account the projected precision of the ν_μ flux discussed in Section 7.1.1, this translates into an absolute prediction for the ν_e flux at the level of 2%.

Finally, the fine-grained ND can directly identify ν_e CC interactions from the LBNE beam. The relevance of this measurement is twofold:

1. It provides an independent validation for the flux predictions obtained from the low-ν_0 method.
2. It can further constrain the uncertainty on the knowledge of the absolute ν_e flux.

7.1.3 Constraining the Unoscillated ν Spectral Shape with the QE Interaction

In any long-baseline neutrino oscillation program, including LBNE, the quasi-elastic (QE) interactions are special. First, the QE cross section is substantial at lower energies [236]. Second, because of the simple topology (a μ^- and a proton), the visible interaction energy provides, to first order, a close approximation to the neutrino energy (E_ν). In the context of a fine-grained tracker, a precise measurement of QE will impose direct constraints on nuclear effects related to both the primary and final-state interaction (FSI) dynamics (Section 7.6), which can affect the overall neutrino energy scale and, thus, the entire oscillation program. To this end, the key to reconstructing a high-quality sample of ν_μ QE interactions is the two-track topology where both final-state particles are visible: μ^- and p. A high-resolution ND can efficiently identify the recoil proton and measure its momentum vector as well as dE/dx. Preliminary studies indicate that in a fine-grained tracking detector the efficiency (purity) for the proton reconstruction in QE events is 52% (82%). A comparison between the neutrino energy reconstructed from the muon momentum through the QE kinematics (assuming a free target nucleon) with the visible neutrino energy measured as the sum of μ and p energies is sensitive to both nuclear effects and FSI. Furthermore, comparing the two-track sample

(μ and p) with the single-track sample (in which only μ is reconstructed) empirically constrains the rate of FSI.

7.1.4 Low-Energy Absolute Flux: Neutrino-Electron NC Scattering

Neutrino neutral current (NC) interaction with the atomic electron in the target, $\nu_\mu e^- \rightarrow \nu_\mu e^-$, provides an elegant measure of the absolute flux. The total cross section for NC elastic scattering off electrons is given by [237]:

$$\sigma(\nu_l e \rightarrow \nu_l e) = \frac{G_\mu^2 m_e E_\nu}{2\pi}\left[1 - 4\sin^2\theta_W + \frac{16}{3}\sin^4\theta_W\right], \quad (7.4)$$

$$\sigma(\overline{\nu}_l e \rightarrow \overline{\nu}_l e) = \frac{G_\mu^2 m_e E_\nu}{2\pi}\left[\frac{1}{3} - \frac{4}{3}\sin^2\theta_W + \frac{16}{3}\sin^4\theta_W\right], \quad (7.5)$$

where θ_W is the weak mixing angle (WMA). For the currently known value of $\sin^2\theta_W \simeq 0.23$, the above cross sections are very small: $\sim 10^{-42}(E_\nu/\mathrm{GeV})$ cm^2. The NC elastic scattering off electrons can be used to determine the absolute flux normalization since the cross section only depends on the knowledge of $\sin^2\theta_W$. Within the Standard Model, the value of $\sin^2\theta_W$ at the average momentum transfer expected at LBNE, $Q \sim 0.07$ GeV, can be extrapolated down from the LEP/SLC* measurements with a precision of $\leq 1\%$. The $\nu_\mu e^- \rightarrow \nu_\mu e^-$ will produce a single e^- collinear with the ν-beam (≤ 40 mrad). The background, dominated by the asymmetric conversion of a photon in an ordinary ν-nucleon NC event, will produce e^- and e^+ in equal measure with much broader angular distribution. A preliminary analysis of the expected elastic scattering signal in the high-resolution tracking ND shows that the scattering signal can be selected with an efficiency of about 60% with a small background contaminant. The measurement will be dominated by the statistical error. The determination of the absolute flux of the LBNE neutrinos is estimated to reach a precision of $\simeq 2.5\%$ for $E_\nu \leq 10$ GeV. The measurement of NC elastic scattering off electrons can only provide the integral of all neutrino flavors.

7.1.5 High-Energy Absolute Flux: Neutrino-Electron CC Scattering

The ν_μ-e^- CC interaction, $\nu_\mu + e^- \rightarrow \mu^- + \nu_e$ (*inverse muon decay* or *IMD*), offers an elegant way to determine the absolute flux. Given the energy threshold needed for this process, IMD requires $E_\nu \geq 10.8$ GeV. The high-resolution ND in the LBNE neutrino beam will observe $\geq$ 2,000 IMD events in three years. The reconstruction efficiency of the single, energetic forward μ^- will be $\geq$ 98%; the angular resolution of the IMD μ is $\leq$ 1 mrad. The background, primarily from the ν_μ-QE interactions, can be precisely constrained using control samples. In particular, the systematic limitations of the CCFR ([238,239]) and the CHARM-II [240] IMD measurements can be

*LEP was the Large Electron-Positron Collider at CERN that operated from 1989 to 2000 and provided a detailed study of the electroweak interaction.

substantially alleviated in LBNE with the proposed ND design. A preliminary analysis indicates that the absolute flux can be determined with an accuracy of $\approx 3\%$ for $E_\nu \geq 11$ GeV (average $E_\nu \approx$25 GeV).

7.1.6 Low-Energy Absolute Flux: QE in Water and Heavy-Water Targets

Another independent method to extract the absolute flux is through the QE-CC scattering ($\nu_\mu n(p) \rightarrow \mu^- p(n)$) on deuterium at low Q^2. Neglecting terms in $(m_\mu/M_n)^2$ at $Q^2 = 0$, the QE cross section is independent of neutrino energy for $(2E_\nu M_n)^{1/2} > m_\mu$:

$$\frac{d\sigma}{dQ^2} \mid Q^2 = 0 \mid = \frac{G_\mu^2 \cos^2\theta_c}{2\pi}\left[F_1^2(0) + G_A^2(0)\right] = 2.08 \times 10^{-38}\ \mathrm{cm}^2\mathrm{GeV}^{-2}, \tag{7.6}$$

which is determined by neutron β decay and has a theoretical uncertainty $< 1\%$. The flux can be extracted experimentally by measuring low Q^2 QE interactions (≤ 0.05 GeV) and extrapolating the result to the limit of $Q^2 = 0$. The measurement requires a deuterium (or hydrogen for antineutrino) target to minimize the smearing due to Fermi motion and other nuclear effects. This requirement can only be achieved by using both H_2O and D_2O targets embedded in the fine-grained tracker and extracting the events produced in deuterium by statistical subtraction of the larger oxygen component. The experimental resolution on the muon and proton momentum and angle is crucial. Dominant uncertainties of the method are related to the extrapolation to $Q^2 = 0$, to the theoretical cross section on deuterium, to the experimental resolution and to the statistical subtraction. Sensitivity studies and the experimental requirements are under study.

7.1.7 Neutral Pions, Photons and $\pi^\pm$ in NC and CC Events

The principal background to the ν_e and $\overline{\nu}_e$ appearance comes from the NC events where a photon from the π^0 decay produces a signature similar to that produced by ν_e-induced electron; the second source of background is due to π^0's from ν_μ CC where the μ^- evades identification — typically at high y_{Bj}. Since the energy spectra of NC and CC interactions are different, it is critical for the ND to measure π^0's in NC and CC interactions in the full kinematic phase space.

The proposed ND is designed to measure π^0's with high accuracy in three topologies:

1. Both photons convert in the tracker ($\simeq$25%).

2. One photon converts in the tracker and the other in the calorimeter ($\simeq$50%).

3. Both photons convert in the calorimeter; the first two topologies afford the best resolution because the tracker provides precise γ-direction measurement.

The π^0 reconstruction efficiency in the proposed fine-grained tracker is expected to be $\geq$75% if photons that reach the ECAL are included. By contrasting the π^0 mass in the tracker versus in the calorimeter, the relative efficiencies of photon reconstruction will be well constrained.

Finally, the $\pi^{\pm}$ track momentum and dE/dx information will be measured by the tracker. An in situ determination of the charged pions in the $\nu_\mu/\overline{\nu}_\mu$ CC events — with μID and without μID — and in the ν NC events is crucial to constrain the systematic error associated with the $\nu_\mu(\overline{\nu}_\mu)$ disappearance, especially at low E_ν.

7.1.8 Signal and Background Predictions for the Far Detector

In order to achieve reliable predictions for signal and backgrounds in the far detector, near detector measurements — including (anti)neutrino fluxes, nuclear cross sections and detector smearing — must be unfolded and extrapolated to the far detector location. The geometry of the beam and detectors (point source versus extended source) as well as the expected neutrino oscillations imply differences in the (anti)neutrino fluxes in the near and far detectors. These differences, in turn, will result in increased sensitivity of the long-baseline analysis to cross-section uncertainties, in particular between neutrinos and antineutrinos and for exclusive background topologies. Furthermore, the much higher event rates at the near site and the smaller detector size (i.e., reduced containment) make it virtually impossible to achieve identical measurement conditions in both the near and far detectors. However, as discussed in Sections 7.1.1 to 7.1.7, the energy, angular and space resolution of the low-density ND are key factors in reducing the systematic uncertainties achievable on the event predictions for the far detector; the ND can offer a precise *in situ* measurement of the absolute flux of all flavor components of the beam, $\nu_\mu, \nu_e, \bar{\nu}_\mu, \bar{\nu}_e$, resulting in constraints on the parent $\pi^{\pm}/K^{\pm}/\mu^{\pm}$ distributions. In addition, measurements of momenta and energies of final-state particles produced in (anti)neutrino interactions will allow a detailed study of exclusive topologies affecting the signal and background rates in the far detector. All of these measurements will be used to cross-check and fine-tune the simulation programs needed for the actual extrapolation from the near to the far detector.

It is important to note that several of these techniques have already been used and *proven to work* in neutrino experiments such as MINOS [155] and NOMAD [156,157,241]. The higher segmentation and resolution in the LBNE ND with respect to past experiments will increase the available information about the (anti)neutrino event topologies, allowing further reduction of systematic uncertainties both in the ND measurements and in the Monte Carlo extrapolation.

For a more detailed discussion of the impact of ND measurements on the long-baseline oscillation analysis see Section 4.3.2.

7.2 Electroweak Precision Measurements

Neutrinos and antineutrinos are the most effective probes for investigating electroweak physics. Interest in a precise determination of the weak mixing angle ($\sin^2\theta_W$) at LBNE energies via neutrino scattering is twofold: (1) it provides a direct measurement of neutrino couplings to the Z boson and (2) it probes a different scale of momentum transfer than LEP did by virtue of not being at the Z boson mass peak.

The weak mixing angle can be extracted experimentally from three main NC physics processes:

1. deep inelastic scattering off quarks inside nucleons: $\nu N \to \nu X$
2. elastic scattering off electrons: $\nu e^- \to \nu e^-$
3. elastic scattering off protons: $\nu p \to \nu p$

Figure 7.1 shows the Feynman diagrams corresponding to the three processes.

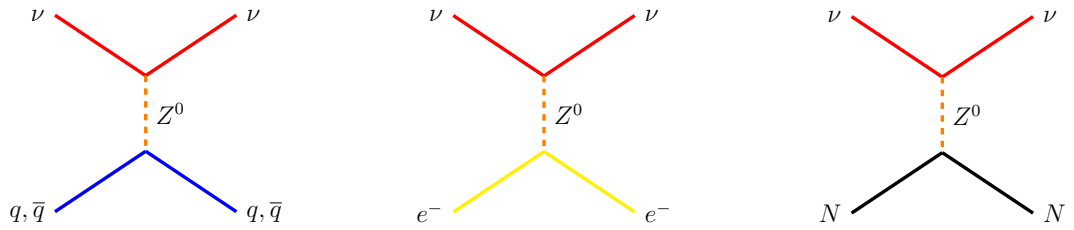

Figure 7.1: Feynman diagrams for the three main neutral current processes that can be used to extract $\sin^2\theta_W$ with the LBNE near detector. From left, deep inelastic scattering off quarks, elastic scattering off electrons and elastic scattering off nucleons.

7.2.1 Deep Inelastic Scattering

The most precise measurement of $\sin^2\theta_W$ in neutrino deep inelastic scattering (DIS) comes from the NuTeV experiment, which reported a value that is 3σ from the Standard Model [242]. The LBNE ND can perform a similar analysis in the DIS channel by measuring the ratio of NC and CC interactions induced by neutrinos:

$$\mathcal{R}^\nu \equiv \frac{\sigma^\nu_{\rm NC}}{\sigma^\nu_{\rm CC}} \simeq \rho^2 \left(\frac{1}{2} - \sin^2\theta_W + \frac{5}{9}(1+r)\sin^4\theta_W\right). \tag{7.7}$$

Here ρ is the relative coupling strength of the neutral-to-charged current interactions ($\rho = 1$ at tree-level in the Standard Model) and r is the ratio of antineutrino to neutrino cross section ($r \sim 0.5$).

The absolute sensitivity of $\mathcal{R}^\nu$ to $\sin^2\theta_W$ is 0.7, which implies that a measurement of $\mathcal{R}^\nu$ to 1% precision would in turn provide a 1.4% precision on $\sin^2\theta_W$. This technique was used by the CDHS [243], CHARM [244] and CCFR [245] experiments. In contrast to the NuTeV experiment, the antineutrino interactions cannot be used for this analysis at LBNE due to the large number of ν_μ DIS interactions in the $\overline{\nu}_\mu$ beam compared to the $\overline{\nu}_\mu$ DIS interactions.

The measurement of $\sin^2\theta_W$ from DIS interactions can only be performed with a low-density magnetized tracker since an accurate reconstruction of the NC event kinematics and of the ν CC interactions are crucial for keeping the systematic uncertainties on the event selection under control. The analysis selects events in the ND after imposing a cut on the visible hadronic energy of $E_{\rm had} > 5$ GeV (the CHARM analysis had $E_{\rm had} > 4$ GeV). With an exposure of 5×10^{21} POT in the 120-GeV beam using the CDR reference design, about 7.7×10^6 CC events and 2.4×10^6 NC events are expected, giving a statistical precision of 0.074% on $\mathcal{R}^\nu$ and 0.1% on $\sin^2\theta_W$ (Table 7.2).

Table 7.2: Comparison of uncertainties on the $\mathcal{R}^\nu$ measurement between NuTeV and LBNE with a 5 t fiducial mass after an exposure of 5×10^{21} POT (5 year) with the CDR reference 120-GeV beam. The corresponding relative uncertainties on $\sin^2\theta_W$ must be multiplied by a factor of 1.4, giving for LBNE a projected overall precision of 0.35%.

Source of uncertainty	$\delta R^\nu / R^\nu$		Comments
	NuTeV	LBNE	
Data statistics	0.00176	0.00074	
Monte Carlo statistics	0.00015		
Total Statistics	*0.00176*	*0.00074*	
$\nu_e, \overline{\nu}_e$ flux ($\sim$ 1.7%)	0.00064	0.00010	e^-/e^+ identification
Energy measurement	0.00038	0.00040	
Shower length model	0.00054	n.a.	
Counter efficiency, noise	0.00036	n.a.	
Interaction vertex	0.00056	n.a.	
$\overline{\nu}_\mu$ flux	n.a.	0.00070	Large $\bar{\nu}$ contamination
Kinematic selection	n.a.	0.00060	Kinematic identification of NC
Experimental systematics	*0.00112*	*0.00102*	
d,s$\rightarrow$c, s-sea	0.00227	0.00140	Based on existing knowledge
Charm sea	0.00013	n.a.	
$r = \sigma^{\overline{\nu}}/\sigma^\nu$	0.00018	n.a.	
Radiative corrections	0.00013	0.00013	
Non-isoscalar target	0.00010	N.A.	
Higher twists	0.00031	0.00070	Lower Q^2 values
R_L (F_2, F_T, xF_3)	0.00115	0.00140	Lower Q^2 values
Nuclear correction		0.00020	
Model systematics	*0.00258*	*0.00212*	
Total	**0.00332**	**0.00247**	

The use of a low-density magnetized tracker can substantially reduce systematic uncertainties compared to a massive calorimeter. Table 7.2 shows a comparison of the different uncertainties on the measured $\mathcal{R}^{\nu}$ between NuTeV and LBNE. While NuTeV measured both $\mathcal{R}^{\nu}$ and $\mathcal{R}^{\overline{\nu}}$, the largest experimental uncertainty in the measurement of $\mathcal{R}^{\nu}$ is related to the subtraction of the ν_e CC contamination from the NC sample. Since the low-density tracker at LBNE can efficiently reconstruct the electron tracks, the ν_e CC interactions can be identified on an event-by-event basis, reducing the corresponding uncertainty to a negligible level. Similarly, uncertainties related to the location of the interaction vertex, noise, counter efficiency and so on are removed by the higher resolution and by changing the analysis selection. The experimental selection at LBNE will be dominated by two uncertainties: the knowledge of the $\overline{\nu}_{\mu}$ flux and the kinematic selection of NC interactions. The former is relevant due to the larger NC/CC ratio for antineutrinos. The total experimental systematic uncertainty on $\sin^2\theta_W$ is expected to be about 0.14%.

The measurement of $\mathcal{R}^{\nu}$ will be dominated by theoretical systematic uncertainties on the structure functions of the target nucleons. The estimate of these uncertainties for LBNE is based upon the extensive work performed for the NOMAD analysis and includes a Next-to-Next-Leading-Order (NNLO) QCD calculation of structure functions (NLO for charm production) [246,247,248], parton distribution functions (PDFs) extracted from dedicated low-Q global fits, high-twist contributions [246], electroweak corrections [249] and nuclear corrections [250,251,252]. The charm quark production in CC, which has been the dominant source of uncertainty in all past determinations of $\sin^2\theta_W$ from νN DIS, is reduced to about 4% of the total ν_{μ} CC DIS for $E_{\rm had} > 5$ GeV with the low-energy beam spectrum at LBNE. This number translates into a systematic uncertainty of 0.14% on $\mathcal{R}^{\nu}$ (Table 7.2), assuming the current knowledge of the charm production cross section. It is worth noting that the recent measurement of charm dimuon production by the NOMAD experiment allowed a reduction of the uncertainty on the strange sea distribution to $\sim 3\%$ and on the charm quark mass m_c to ~ 75 MeV [241]. The lower neutrino energies available at LBNE reduce the accessible Q^2 values with respect to NuTeV, increasing in turn the effect of non-perturbative contributions (high twists) and R_L. The corresponding uncertainties are reduced by the recent studies of low-Q structure functions and by improved modeling with respect to the NuTeV analysis (NNLO vs. LO). The total model systematic uncertainty on $\sin^2\theta_W$ is expected to be about 0.21% with the reference beam configuration. The corresponding total uncertainty on the value of $\sin^2\theta_W$ extracted from νN DIS is 0.35%.

Most of the model uncertainties will be constrained by dedicated in situ measurements using the large CC samples and employing improvements in theory that will have evolved over the course of the experiment. The low-density tracker will collect about 350,000 neutrino-induced inclusive charm events in a five-year run with the 120-GeV 1.2-MW beam. The precise reconstruction of charged tracks will allow measurement of exclusive decay modes of charmed hadrons (e.g., D^{*+}) and measurement of charm fragmentation and production parameters. The average semileptonic branching ratio B_{μ} is of order 5% with the low-energy LBNE beam, and the low-density ND will be able to reconstruct both the $\mu\mu$ and μe decay channels. Currently, the most precise sample of 15,400

dimuon events has been collected by the NOMAD experiment. Finally, precision measurements of CC structure functions in the LBNE ND would further reduce the uncertainties on PDFs and on high-twist contributions.

The precision that can be achieved from νN DIS interactions is limited by both the event rates and the energy spectrum of the standard beam configuration. The high-statistics beam exposure with the low-energy default beam-running configuration (described in Chapter 3) combined with a dedicated run with the high-energy beam option would increase the statistics by more than a factor of ten. This major step forward would not only reduce the statistical uncertainty to a negligible level, but would provide large control samples and precision auxiliary measurements to reduce the systematic uncertainties on structure functions. The two dominant systematic uncertainties, charm production in CC interactions and low Q^2 structure functions, are essentially defined by the available data at present. Overall, the use of a high-energy beam with upgraded intensity can potentially improve the precision achievable on $\sin^2\theta_W$ from νN DIS to better than 0.2%.

7.2.2 Elastic Scattering

A second independent measurement of $\sin^2\theta_W$ can be obtained from NC $\nu_\mu e$ elastic scattering. This channel has lower systematic uncertainties since it does not depend on knowledge of the structure of nuclei, but it has limited statistics due to its very low cross section. The value of $\sin^2\theta_W$ can be extracted from the ratio of interactions [237] as follows:

$$\mathcal{R}_{\nu e}(Q^2) \equiv \frac{\sigma(\overline{\nu}_\mu e \to \overline{\nu}_\mu e)}{\sigma(\nu_\mu e \to \nu_\mu e)}(Q^2) \simeq \frac{1 - 4\sin^2\theta_W + 16\sin^4\theta_W}{3 - 12\sin^2\theta_W + 16\sin^4\theta_W}, \tag{7.8}$$

in which systematic uncertainties related to the selection and the electron identification cancel out. The absolute sensitivity of this ratio to $\sin^2\theta_W$ is 1.79, which implies that a measurement of $\mathcal{R}_{\nu e}$ to 1% precision would provide a measurement of $\sin^2\theta_W$ to 0.65% precision.

The best measurement of NC elastic scattering off electrons was performed by CHARM II, which observed 2677$\pm$82 ν and 2752$\pm$88 $\overline{\nu}$ events [253]. The CHARM II analysis was characterized by a sizable uncertainty related to the extrapolation of the background into the signal region.

The event selection for NC elastic scattering is described in Section 7.1.4. Since the NC elastic scattering off electrons is also used for the absolute flux normalization, the WMA analysis can be performed only with the low-density, magnetized tracker in conjunction with a large liquid argon detector. In the case of the flux normalization measurement, the total reconstructed statistics is limited to about 4,500 (2,800) $\nu(\bar{\nu})$ events. These numbers do not allow a competitive determination of $\sin^2\theta_W$ by using the magnetized tracker alone. However, a 100-t liquid argon detector in the ND would be expected to collect about 90,000 (60,000) reconstructed $\nu(\overline{\nu})$ events with the standard beam, and an additional factor of two with an upgraded 2.3-MW beam.

A combined analysis of both detectors can achieve the optimal sensitivity: the fine-grained tracker

is used to reduce systematic uncertainties (measurement of backgrounds and calibration), while the liquid argon detector provides the statistics required for a competitive measurement. Overall, the use of the complementary liquid argon detector can provide a statistical accuracy on $\sin^2\theta_W$ of about 0.3%. However, the extraction of the WMA is dominated by the systematic uncertainty on the $\overline{\nu}_\mu/\nu_\mu$ flux ratio in Equation (7.8). This uncertainty has been evaluated with the low-ν_0 method for the flux extraction and a systematic uncertainty of about 1% was obtained on the ratio of the $\overline{\nu}_\mu/\nu_\mu$ flux integrals. An improved precision on this quantity could be achieved from a measurement of the ratios π^-/π^+ and ρ^-/ρ^+ from coherent production in the fine-grained tracker. Due to the excellent angular and momentum resolution and to large cancellations of systematic uncertainties, preliminary studies indicate that an overall precision of about 0.3% can be achieved on the $\overline{\nu}_\mu/\nu_\mu$ flux ratio using coherent production.

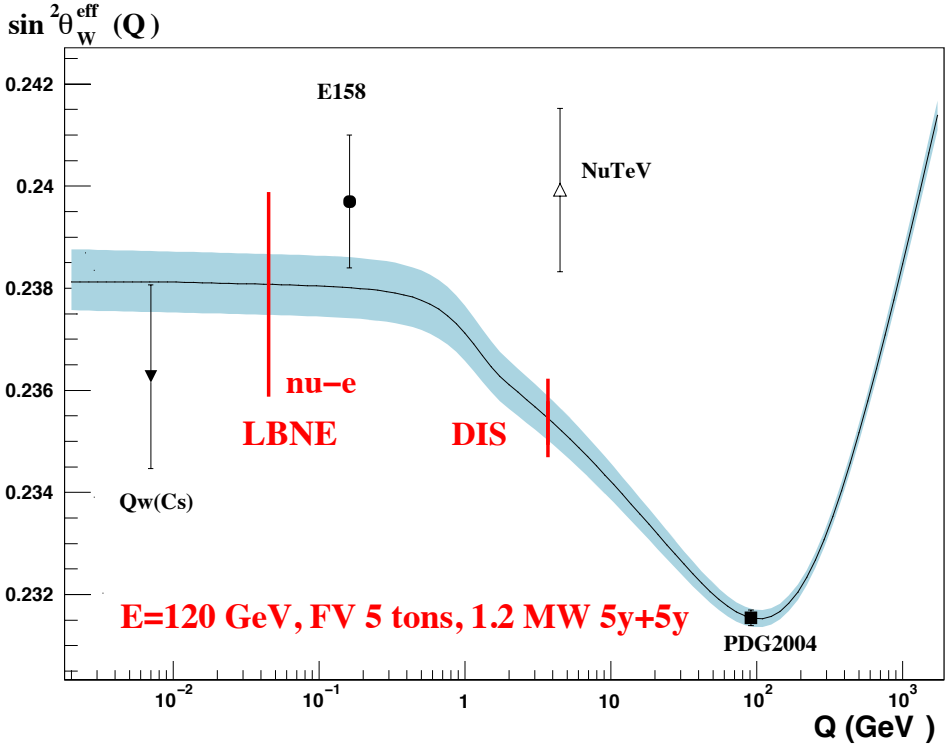

Figure 7.2: Expected sensitivity to the measurement of $\sin^2\theta_W$ from the LBNE ND with the reference 1.2-MW beam and an exposure of 5×10^{21} POT with a neutrino beam (five years) and 5×10^{21} POT with an antineutrino beam (five years). The curve shows the Standard Model prediction as a function of the momentum scale [254]. Previous measurements from Atomic Parity Violation [255,256], Moeller scattering (E158 [257]), ν DIS (NuTeV [242]) and the combined Z pole measurements (LEP/SLC) [256] are also shown for comparison. The use of a high-energy beam tune can reduce the LBNE uncertainties by almost a factor of two.

Together, the DIS and the NC elastic scattering channels involve substantially different scales of momentum transfer, providing a tool to test the running of $\sin^2\theta_W$ in a single experiment. To this end, the study of NC elastic scattering off protons can provide additional information since

it occurs at a momentum scale that is intermediate between the two other processes. Figure 7.2 summarizes the target sensitivity from the LBNE ND, compared with existing measurements as a function of the momentum scale.

In the near future, another precision measurement of $\sin^2\theta_W$ is expected from the $Q_{\rm weak}$ experiment [258] at Jefferson Laboratory. From the measurement of parity-violating asymmetry in elastic electron-proton scattering, the $Q_{\rm weak}$ experiment should achieve a precision of 0.3% on $\sin^2\theta_W$ at $Q^2 = 0.026$ GeV^2. It should be noted that the $Q_{\rm weak}$ measurement is complementary to those from neutrino scattering given the different scale of momentum transfer and the fact that neutrino measurements are the only direct probe of the Z coupling to neutrinos. With the 12-GeV upgrade of Jefferson Laboratory, the Q_{weak} experiment [259] could potentially reach precisions on the order of 0.2-0.1 %.

7.3 Observation of the Nucleon's Strangeness Content

The strange-quark content of the proton and its contribution to the proton spin remain enigmatic [260]. The question is whether the strange quarks contribute substantially to the vector and axial-vector currents of the nucleon. A large observed value of the strange-quark contribution to the nucleon spin (axial current), Δs, would enhance our understanding of the proton structure.

The spin structure of the nucleon also affects the couplings of axions and supersymmetric particles to dark matter.

7.3.1 Strange Form Factors of Nucleons

The strange quark *vector* elastic form factors[†] of the nucleon have been measured to high precision in parity-violating electron scattering (PVES) at Jefferson Lab, Mainz and elsewhere. A recent global analysis [261] of PVES data finds a strange magnetic moment $\mu_s = 0.37 \pm 0.79$ (in units of the nucleon magneton), so that the strange quark contribution to proton magnetic moment is less than 10%. For the strange electric charge radius parameter, ρ_s, one finds a very small value, $\rho_s = -0.03 \pm 0.63$ GeV^{-2}, consistent with zero. Both results are consistent with theoretical expectations based on lattice QCD and phenomenology [262].

In contrast, the strange *axial vector* form factors are poorly determined. A global study of PVES

[†]Nucleon form factors describe the scattering amplitudes off different partons in a nucleon. They are usually given as a function of Q^2 the momentum transfer to the nucleon from the scattering lepton (since the structure of the nucleon looks different depending on the energy of the probe).

data [261] finds $\widetilde{G}_A^N(Q^2) = \widetilde{g}_A^N \left(1 + Q^2/M_A^2\right)^2$, where $M_A = 1.026$ GeV is the axial dipole mass, with the effective proton and neutron axial charges $\widetilde{g}_A^p = -0.80 \pm 1.68$ and $\widetilde{g}_A^n = 1.65 \pm 2.62$.

The strange quark axial form factor at $Q^2 = 0$ is related to the *spin* carried by strange quarks, Δs. Currently the world data on the spin-dependent g_1 structure function constrain Δs to be ≈ -0.055 at a scale $Q^2 = 1$ GeV^2, with a significant fraction coming from the region $x < 0.001$.

An independent extraction of Δs, which does not rely on the difficult measurements of the g_1 structure function at very small values of the Bjorken variable x, can be obtained from (anti)neutrino NC elastic scattering off protons (Figure 7.3). Indeed, this process provides the most direct measurement of Δs. The differential cross section for NC-elastic and CC-QE scattering of (anti)neutrinos from protons can be written as:

$$\frac{d\sigma}{dQ^2} = \frac{G_\mu^2}{2\pi}\frac{Q^2}{E_\nu^2}\left(A \pm BW + CW^2\right); \quad W = 4E_\nu/M_p - Q^2/M_p^2, \tag{7.9}$$

where the positive (negative) sign is for neutrino (antineutrino) scattering and the coefficients A, B, and C contain the vector and axial form factors as follows:

$$\begin{aligned} A &= \frac{1}{4}\left[G_1^2(1+\tau) - \left(F_1^2 - \tau F_2^2\right)(1-\tau) + 4\tau F_1 F_2\right] \\ B &= -\frac{1}{4}G_1\left(F_1 + F_2\right) \\ C &= \frac{1}{16}\frac{M_p^2}{Q^2}\left(G_1^2 + F_1^2 + \tau F_2^2\right) \end{aligned}$$

The axial-vector form factor, G_1, for NC scattering can be written as the sum of the known axial form factor G_A plus a strange form factor G_A^s:

$$G_1 = \left[-\frac{G_A}{2} + \frac{G_A^s}{2}\right], \tag{7.10}$$

while the NC vector form factors can be written as:

$$F_{1,2} = \left[\left(\frac{1}{2} - \sin^2\theta_W\right)\left(F_{1,2}^p - F_{1,2}^n\right) - \sin^2\theta_W\left(F_{1,2}^p + F_{1,2}^n\right) - \frac{1}{2}F_{1,2}^s\right], \tag{7.11}$$

where $F_1^{p(n)}$ is the Dirac form factor of the proton (neutron), $F_2^{p(n)}$ is the corresponding Pauli form factor, and $F_{1,2}^s$ are the strange-vector form factors. These latter form factors are expected to be small from the PVES measurements summarized above. In the limit $Q^2 \to 0$, the differential cross section is proportional to the square of the axial-vector form factor $d\sigma/dQ^2 \propto G_1^2$ and $G_A^s \to \Delta s$. The value of Δs can therefore be extracted experimentally by extrapolating the NC differential cross section to $Q^2 = 0$.

7.3.2 Extraction of the Strange Form Factors

Previous neutrino scattering experiments have been limited by the statistics and by the systematic uncertainties on background subtraction. One of the earliest measurements available comes from the analysis of 951 NC νp and 776 NC $\overline{\nu} p$ collected by the experiment BNL E734 [263,264,265]. There are also more recent results with high statistics from MiniBooNE where a measurement of Δs was carried out using neutrino NC elastic scattering with 94,531 νN events [266]. The MiniBooNE measurement was limited by the inability to distinguish the proton and neutron from νN scattering. The LBNE neutrino beam will be sufficiently intense that a measurement of NC elastic scattering on protons in the fine-grained ND can provide a definitive statement on the contribution of the strange sea to either the axial or vector form factor.

Systematic uncertainties can be reduced by measuring the NC/CC ratios for both neutrinos and antineutrinos as a function of Q^2:

$$\mathcal{R}_{\nu p}(Q^2) \equiv \frac{\sigma(\nu_\mu p \to \nu_\mu p)}{\sigma(\nu_\mu n \to \mu^- p)}(Q^2); \qquad \mathcal{R}_{\overline{\nu} p}(Q^2) \equiv \frac{\sigma(\overline{\nu}_\mu p \to \overline{\nu}_\mu p)}{\sigma(\overline{\nu}_\mu p \to \mu^+ n)}(Q^2), \tag{7.12}$$

Figure 7.3 shows the absolute sensitivity of both ratios to Δs for different values of Q^2. The sensitivity for $Q^2 \sim 0.25$ GeV^2 is about 1.2 for neutrinos and 1.9 for antineutrinos, which implies that a measurement of $\mathcal{R}_{\nu p}$ and $\mathcal{R}_{\overline{\nu} p}$ of 1% precision would enable the extraction of Δs with an uncertainty of 0.8% and 0.5%, respectively.

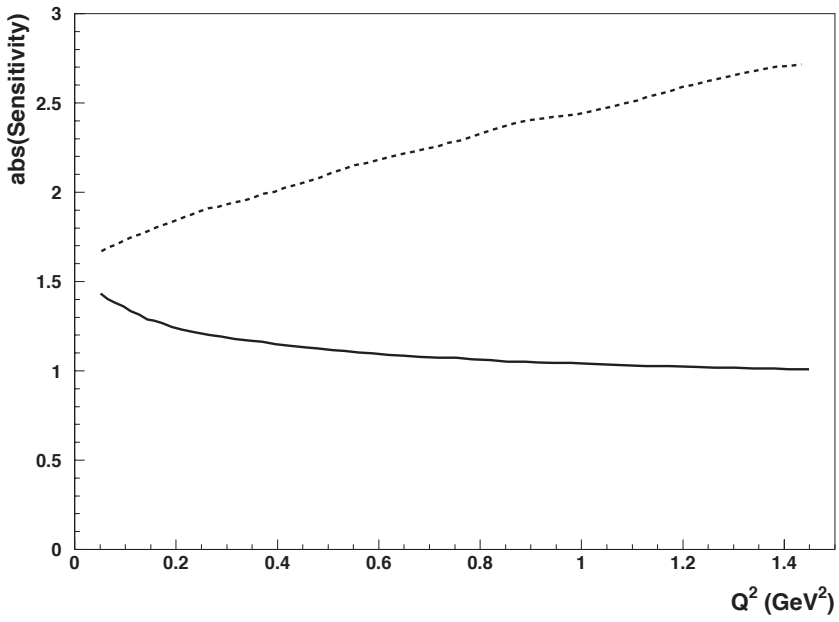

Figure 7.3: Sensitivity (magnitude) of the ratios $\mathcal{R}_{\nu p}$ (solid) and $\mathcal{R}_{\overline{\nu} p}$ (dashed) to a variation of the strange contribution to the spin of the nucleon, Δs, as a function of Q^2. Values greater than one imply that the relative uncertainty on Δs is smaller than that of the corresponding ratio (see text).

The design of the tracker includes several different nuclear targets. Therefore, most of the neutrino scattering is from nucleons embedded in a nucleus, requiring nuclear effects to be taken into account. Fortunately, in the ratio of NC/CC, the nuclear corrections are expected to largely cancel out. The Δs analysis requires a good proton reconstruction efficiency as well as high resolution on both the proton angle and energy. To this end, the low-density tracker can increase the range of the protons inside the ND, allowing the reconstruction of proton tracks down to $Q^2 \sim 0.07$ GeV^2. This capability will reduce the uncertainties in the extrapolation of the form factors to the limit $Q^2 \to 0$.

Table 7.3 summarizes the expected proton range for the low-density ($\rho \sim 0.1\,\mathrm{g\,cm^{-3}}$) straw-tube tracker (STT) in the ND tracking detector design described in Section 3.5. About $2.0(1.2) \times 10^6$ $\nu p(\overline{\nu} p)$ events are expected after the selection cuts in the low-density tracker, yielding a statistical precision on the order of 0.1%.

Table 7.3: Expected proton range for the low-density ($\rho \sim 0.1\,\mathrm{g\,cm^{-3}}$) tracker. The first column gives the proton kinetic energy and the last column the proton momentum. The Q^2 value producing T_p is calculated assuming the struck nucleon is initially at rest.

T_p MeV	Q^2 GeV$^2/c^2$	Range STT cm	P_p GeV/c
20	0.038	4.2	0.195
40	0.075	14.5	0.277
60	0.113	30.3	0.341
80	0.150	50.8	0.395
100	0.188	75.7	0.445

The determination of Δs in the STT utilizes analysis techniques performed by the FINeSSE Collaboration [267] and used by the SciBooNE experiment. In particular, based on the latter, LBNE expects a purity of about 50%, with background contributions of 20% from neutrons produced outside of the detector, 10% νn events and 10% NC pion backgrounds. The dominant systematic uncertainty will be related to the background subtraction. The low-energy beam spectrum at LBNE provides the best sensitivity for this measurement since the external background from neutron-induced proton recoils will be reduced by the strongly suppressed high-energy tail. The low-density magnetized tracker is expected to increase the purity by reducing the neutron background and the NC pion background. The outside neutron background, it should be noted, can be determined using the $n \to p + \pi^-$ process in the STT. The sensitivity analysis is still in progress, however LBNE is confident of achieving a precision on Δs of about 0.02–0.03.

7.4 Nucleon Structure and QCD Studies

Precision measurements of (anti)neutrino differential cross sections in the LBNE near detector will provide additional constraints on several key nucleon structure functions that are complementary to results from electron scattering experiments.

In addition, these measurements would directly improve LBNE's oscillation measurements by providing accurate simulation of neutrino interactions in the far detector and offer an estimate of all background processes that are dependent upon the angular distribution of the outgoing particles in the far detector. Furthermore, certain QCD analyses — i.e., global fits used for extraction of parton distribution functions (PDFs) via the differential cross sections measured in ND data — would constrain the systematic error in precision electroweak measurements. This would apply not only in neutrino physics but also in hadron collider measurements.

7.4.1 Determination of the F_3 Structure Function and GLS Sum Rule

For quantitative studies of inclusive deep-inelastic lepton-nucleon scattering, it is vital to have precise measurements of the F_3 structure functions as input into global PDF fits. Because it depends on weak axial quark charges, the F_3 structure function can only be measured with neutrino and antineutrino beams and is unique in its ability to differentiate between the quark and antiquark content of the nucleon. On a proton target, for instance, the neutrino and antineutrino F_3 structure functions (at leading order in α_s) are given by

$$xF_3^{\nu p}(x) = 2x\left(d(x) - \overline{u}(x) + s(x) + \cdots\right), \tag{7.13}$$

$$xF_3^{\overline{\nu} p}(x) = 2x\left(u(x) - \overline{d}(x) - \overline{s}(x) + \cdots\right), \tag{7.14}$$

$$xF_3^{\nu n}(x) = 2x\left(u(x) - \overline{d}(x) + s(x) + \cdots\right), \tag{7.15}$$

$$xF_3^{\overline{\nu} n}(x) = 2x\left(d(x) - \overline{u}(x) - \overline{s}(x) + \cdots\right). \tag{7.16}$$

where $u_v = u - \bar{u}$ and $d_v = d - \bar{d}$ are the valence sea quark distributions. Under the assumption of a symmetric strange sea, i.e., $s(x) = \bar{s}(x)$, the above expressions show that a measurement of the average $xF_3 = (xF_3^{\nu N} + xF_3^{\bar{\nu} N})/2$ for neutrino and antineutrino interactions on isoscalar targets provides a direct determination of the valence quark distributions in the proton. This measurement is complementary to the measurement of Drell-Yan production at colliders, which is essentially proportional to the sea quark distributions.

The first step in the structure function analysis is the measurement of the differential cross section:

$$\frac{1}{E_\nu}\frac{d\sigma^2}{dxdQ^2} = \frac{N(x,Q^2,E_\nu)}{N(E_\nu)}\frac{\sigma_{\rm tot}/E_\nu}{dxdQ^2} \tag{7.17}$$

where $N(x,Q^2,E_\nu)$ is the number of events in each (x,Q^2,E_ν) bin and $N(E_\nu)$ is the number of events in each E_ν bin integrated over x and Q^2. The average xF_3 structure function can be extracted by taking the difference between neutrino and antineutrino differential cross sections:

$$\frac{1}{E_\nu}\frac{d^2\sigma^\nu}{dxdQ^2} - \frac{1}{E_\nu}\frac{d^2\sigma^{\bar\nu}}{dxdQ^2} = 2\left[y\left(1-\frac{y}{2}\right)\frac{y}{Q^2}\right]xF_3 \tag{7.18}$$

where xF_3 denotes the sum for neutrino and antineutrino interactions.

The determination of the xF_3 structure functions will, in turn, allow a precision measurement of the Gross-Llewellyn-Smith (GLS) QCD sum rule:

$$\begin{aligned} S_{\rm GLS}(Q^2) &= \frac{1}{2}\int_0^1 \frac{1}{x}\left[xF_3^{\nu N} + xF_3^{\bar\nu N}\right]dx \\ &= 3\left[1-\frac{\alpha_s(Q^2)}{\pi} - a(n_f)\left(\frac{\alpha_s(Q^2)}{\pi}\right)^2 - b(n_f)\left(\frac{\alpha_s(Q^2)}{\pi}\right)^3\right] + \Delta{\rm HT} \end{aligned} \tag{7.19}$$

where α_s is the strong coupling constant, n_f is the number of quark flavors, a and b are known functions of n_f, and the quantity ΔHT represents higher-twist contributions. The equation above can be inverted to determine $\alpha_s(Q^2)$ from the GLS sum rule. The most precise determination of the GLS sum rule was obtained by the CCFR experiment on an iron target [268] $S_{\rm GLS}(Q^2 = 3\ GeV^2) = 2.50 \pm 0.018 \pm 0.078$. The high-resolution ND combined with the unprecedented statistics would substantially reduce the systematic uncertainty on the low-x extrapolation of the xF_3 structure functions entering the GLS integral. In addition, the presence of different nuclear targets, as well as the availability of a target with free protons will allow investigation of isovector and nuclear corrections, and adding a tool to test isospin (charge) symmetry (Section 7.5).

7.4.2 Determination of the Longitudinal Structure Function $F_L(x,Q^2)$

The structure function F_L is directly related to the gluon distribution $G(x,Q^2)$ of the nucleon, as can be seen from the Altarelli-Martinelli relation:

$$F_L(x,Q^2) = \frac{\alpha_s(Q^2)}{\pi}\left[\frac{4}{3}\int_x^1\frac{dy}{y}\left(\frac{x}{y}\right)^2 F_2(x,Q^2) + n_f\int_x^1\frac{dy}{y}\left(\frac{x}{y}\right)^2\left(1-\frac{x}{y}\right)G(y,Q^2)\right] \tag{7.20}$$

where n_f is the number of parton flavors. In the leading order approximation the longitudinal structure function F_L is zero, while at higher orders a nonzero $F_L(x,Q^2)$ is originated as a consequence of the violation of the Callan-Gross relation:

$$F_L(x,Q^2) = \left(1+\frac{4M^2x^2}{Q^2}\right)F_2(x,Q^2) - 2xF_1(x,Q^2) \tag{7.21}$$

where $2xF_1 = F_T$ is the transverse structure function. A measurement of $R = F_L/F_T$ is therefore both a test of perturbative QCD at large x and a clean probe of the gluon density at small x where the quark contribution is small. A poor knowledge of R, especially at small x, results in uncertainties in the structure functions extracted from deep inelastic scattering cross sections, and in turn, in electroweak measurements. It is instructive to compare the low-Q^2 behavior of R for charged-lepton versus neutrino scattering. In both cases CVC implies that $F_T \propto Q^2$ as $Q^2 \to 0$. However, while $F_L \propto Q^4$ for the electromagnetic current, for the weak current F_L is dominated by the finite PCAC (partial conservation of the axial current) contribution [251]. The behavior of R at $Q^2 \ll 1$ GeV^2 is therefore very different for charged-lepton and neutrino scattering. A new precision measurement of the Q^2 dependence of R with (anti)neutrino data would also clarify the size of the high-twist contributions to F_L and R, which reflect the strength of multi-parton correlations (qq and qg).

The ratio of longitudinal to transverse structure functions can be measured from the y dependence of the deep inelastic scattering data. Fits to the following function:

$$F(x, Q^2, \epsilon) = \frac{\pi(1-\epsilon)}{y^2 G_F^2 M E_\nu}\left[\frac{d^2\sigma^\nu}{dxdy} + \frac{d^2\sigma^{\bar{\nu}}}{dxdy}\right] = 2xF_1(x, Q^2)\left[1 + \epsilon R(x, Q^2)\right] \tag{7.22}$$

have been used by CCFR and NuTeV to determine $R = \sigma_L/\sigma_T$. In this equation $\epsilon \simeq 2(1-y)/(1+(1-y)^2)$ is the polarization of the virtual W boson. This equation assumes $xF_3^\nu = xF_3^{\bar{\nu}}$, and a correction must be applied if this is not the case. The values of R are extracted from linear fits to F versus ϵ at fixed x and Q^2 bins.

7.4.3 Determination of F_2^n and the d/u Ratio of Quark Distribution Functions

Because of the larger electric charge on the u quark than on the d, the electromagnetic proton F_2 structure function data provide strong constraints on the u-quark distribution, but are relatively insensitive to the d-quark distribution. To constrain the d-quark distribution a precise knowledge of the corresponding F_2^n structure functions of free neutrons is required, which in current practice is extracted from inclusive deuterium F_2 data. At large values of x ($x > 0.5$) the nuclear corrections in deuterium become large and, more importantly, strongly model-dependent, leading to large uncertainties on the resulting d-quark distribution. Using the isospin relation $F_2^{\bar{\nu}p} = F_2^{\nu n}$ and $F_2^{\nu p} = F_2^{\bar{\nu} n}$ it is possible to obtain a direct determination of $F_2^{\nu n}$ and $F_2^{\bar{\nu} n}$ with neutrino and antineutrino scattering off a target with free protons. This determination is free from model uncertainties related to nuclear targets. The extraction of $F_2^{\nu n}$ and $F_2^{\bar{\nu} n}$ will allow a precise extraction on the d-quark distribution at large x. Existing neutrino data on hydrogen have relatively large errors and do not extend beyond $x \sim 0.5$ [269,270].

The $F_2^{\bar{\nu}p}$ and $F_2^{\nu p}$ structure functions can be obtained from interactions on a target with free protons after subtracting the contributions from xF_3 and R. These latter can either be modeled within global PDF fits or taken from the other two measurements described above. As discussed in Section 7.5

the LBNE ND can achieve competitive measurements of $F_2^{\bar{\nu}p}$ and $F_2^{\nu p}$ with an increase of statistics of three orders of magnitude with respect to the existing hydrogen data [269,270].

7.4.4 Measurement of Nucleon Structure Functions

At present neutrino scattering measurements of cross sections have considerably larger uncertainties than those of the electromagnetic inclusive cross sections. The measurement of the differential cross sections [236] is dominated by three uncertainties: (1) muon energy scale, (2) hadron energy scale, and (3) knowledge of the input (anti)neutrino flux. Table 7.4 shows a comparison of past and present experiments and the corresponding uncertainties on the energy scales. The most precise measurements are from the CCFR, NuTeV and NOMAD experiments, which are limited to a statistics of about 10^6 neutrino events.

Table 7.4: Summary of past experiments performing structure function measurements. The expected numbers in the LBNE near detector for a five-year run with the 1.2-MW 120-GeV reference beam (5×10^{21} POT) are also given for comparison.

Experiment	Mass	ν_μ CC Stat.	Target	E_ν (GeV)	ΔE_μ	ΔE_{H}
CDHS [271]	750 t	10^7	p,Fe	20-200	2.0%	2.5%
BEBC [272,273]	various	5.7×10^4	p,D,Ne	10-200		
CCFR [274,275]	690 t	1.0×10^6	Fe	30-360	1.0%	1.0%
NuTeV [276]	690 t	1.3×10^6	Fe	30-360	0.7%	0.43%
CHORUS [277]	100 t	3.6×10^6	Pb	10-200	2.5%	5.0%
NOMAD [156]	2.7 t	1.3×10^6	C	5-200	0.2%	0.5%
[241]	18 t	1.2×10^7	Fe	5-200	0.2%	0.6%
MINOS ND [155]	980 t	3.6×10^6	Fe	3-50	2-4%	5.6%
LBNE ND	5 t	5.9×10^7	$(C_3H_6)_n$	0.5-30	$< 0.2\%$	$< 0.5\%$

The MINERνA [161] experiment is expected to provide new structure function measurements on a number of nuclear targets including He, C, Fe and Pb in the near future. Since the structure function measurement mainly involves DIS events, the MINERνA measurement will achieve a competitive statistics after the completion of the new run with the medium-energy beam. MINERνA will focus on a measurement of the ratio of different nuclear targets to measure nuclear corrections in (anti)neutrino interactions. It must be noted that the MINERνA experiment relies on the MINOS ND for muon identification. The corresponding uncertainty on the muon-energy scale (Table 7.4) is substantially larger than that in other modern experiments, e.g., NuTeV and NOMAD, thus limiting the potential of absolute structure function measurements. Furthermore, the muon-energy scale is also the dominant source of uncertainty in the determination of the (anti)neutrino fluxes with the low-ν method. Therefore, the flux uncertainties in MINERνA are expected to be larger than in NOMAD and NuTeV.

Given its reference beam design and 1.2-MW proton-beam power, LBNE expects to collect about 2.3×10^7 neutrino DIS events and about 4.4×10^6 antineutrino DIS events in the ND. These numbers correspond to an improvement by more than one order of magnitude with respect to the most precise past experiments, e.g., NuTeV [276] and NOMAD [156,241]. With these high-statistics samples, LBNE will be able to significantly reduce the gap between the uncertainties on the weak and electromagnetic structure functions. A possible high-energy run with the upgraded 2.3-MW beam would offer a further increase by more than a factor of ten in statistics.

In addition to the large data samples, the use of a high-resolution, low-density spectrometer allows LBNE to reduce systematic uncertainties with respect to previous measurements. The LBNE ND is expected to achieve precisions better than 0.2% and 0.5% on the muon- and hadron-energy scales, respectively. These numbers are based on the results achieved by the NOMAD experiment (Table 7.4), which had much lower statistics and poorer resolution than is expected in the LBNE ND. The calibration of the momentum and energy scales will be performed with the large sample of reconstructed $K^0_S \rightarrow \pi\pi$, $\Lambda \rightarrow p\pi$, and $\pi^0 \rightarrow \gamma\gamma$ decays. In addition, the overall hadronic energy scale can be calibrated by exploiting the well-known structure of the Bjorken y distribution in (anti)neutrino DIS interactions [156,278]. The relative fluxes as a function of energy can be extracted to a precision of about 2% with the low-ν method, due to the small uncertainty on the muon-energy scale. The world average absolute normalization of the differential cross sections $\sigma_{\rm tot}/E$, is known to 2.1% precision [55]. However, with the 1.2-MW beam available from the PIP-II upgrades, it will be possible to improve the absolute normalization using ν-e NC elastic scattering events, coherent meson production, etc. An overall precision of 1-2% would make (anti)neutrino measurements comparable to or better than the complementary measurements from charged-lepton DIS.

On the time scale of LBNE, comparable measurements from (anti)neutrino experiments are not expected, primarily due to the low energy of competing beamlines (J-PARC neutrino beamline in Japan [279]) or to the poorer resolution of the detectors used (MINERνA [161] , T2K [134], NOνA [126]). The experimental program most likely to compete with the LBNE ND measurements is the 12-GeV upgrade at Jefferson Laboratory (JLab) [280]. However, it must be emphasized that the use of electron beams at JLab makes this program *complementary* to LBNE's. In particular, the three topics discussed above are specific to the (anti)neutrino interactions.

Several planned experiments at JLab with the energy-upgraded 12-GeV beam will measure the d/u ratio from D targets up to $x \sim 0.85$, using different methods to minimize the nuclear corrections. The LBNE measurement will be competitive with the proposed JLab 12-GeV experiments, since the large statistics expected will allow a precise determination of $F_2^{\nu n}$ and $F_2^{\bar{\nu} n}$ up to $x \sim 0.85$. Furthermore, the use of a weak probe coupled with a wide-band beam will provide a broader Q^2 range than in JLab experiments, thus allowing a separation of higher twist and other sub-leading effects in $1/Q^2$.

7.5 Tests of Isospin Physics and Sum-Rules

One of the most compelling physics topics accessible to LBNE's high-resolution near detector is the isospin physics using neutrino and antineutrino interactions. This physics involves the Adler sum rule and tests isospin (charge) symmetry in nucleons and nuclei.

The Adler sum rule relates the integrated difference of the antineutrino and neutrino F_2 structure functions to the isospin of the target:

$$\mathcal{S}_A(Q^2) = \int_0^1 dx \left[F_2^{\overline{\nu}}(x,Q^2) - F_2^{\nu}(x,Q^2)\right]/(2x) = 2\,I_z, \tag{7.23}$$

where the integration is performed over the entire kinematic range of the Bjorken variable x and I_z is the projection of the target isospin vector on the quantization axis (z axis). For the proton $\mathcal{S}_A^p = 1$ and for the neutron $\mathcal{S}_A^n = -1$.

In the quark-parton model the Adler sum is the difference between the number of valence u and d quarks of the target. The Adler sum rule survives the strong-interaction effects because of the conserved vector current (CVC) and provides an exact relation to test the local current commutator algebra of the weak hadronic current. In the derivation of the Adler sum rule the effects of both non-conservation of the axial current and heavy-quark production are neglected.

Experimental tests of the Adler sum rule require the use of a hydrogen target to avoid nuclear corrections to the bound nucleons inside the nuclei. The structure functions $F_2^{\overline{\nu}}$ and F_2^{ν} have to be determined from the corresponding differential cross sections and must be extrapolated to small x values in order to evaluate the integral. The test performed in bubble chambers by the BEBC Collaboration — the only test available — is limited by the modest statistics; it used about 9,000 $\overline{\nu}$ and 5,000 ν events collected on hydrogen [273].

The LBNE program can provide the first high-precision test of the Adler sum rule. To this end, the use of the high-energy beam tune shown in Figure 3.19, although not essential, would increase the sensitivity, allowing attainment of higher Q^2 values. Since the use of a liquid H_2 bubble chamber is excluded in the ND hall due to safety concerns, the (anti)neutrino interactions off a hydrogen target can only be extracted with a subtraction method from the composite materials of the ND targets. Using this technique to determine the position resolution in the location of the primary vertex is crucial to reducing systematic uncertainties. For this reason, a precision test of the Adler sum rule is best performed with the low-density magnetized ND.

A combination of two different targets — the polypropylene $(C_3H_6)_n$ foils placed in front of the STT modules and pure carbon foils — are used in the low-density, magnetized ND to provide a fiducial hydrogen mass of about 1 t. With the LBNE fluxes from the standard exposure, $5.0(1.5) \times 10^6 \pm 13(6.6) \times 10^3(sub.)$ $\nu(\overline{\nu})$ CC events (where the quoted uncertainty is dominated by the

statistical subtraction procedure) would be collected on the hydrogen target. The level of precision that can be achieved is sufficient to open up the possibility of making new discoveries in the quark and hadron structure of the proton. No other comparable measurement is expected on the timescale of LBNE.

7.6 Studies of (Anti)Neutrino-Nucleus Interactions

An integral part of the physics program envisioned for the LBNE ND involves detailed measurements of (anti)neutrino interactions in a variety of nuclear targets. The LBNE ND offers substantially larger statistics coupled with a much higher resolution and, in turn, lower systematic uncertainties with respect to past experiments (Table 7.4) or ongoing and future ones (MINERνA [161], T2K [134], NOνA [126]). The most important nuclear target is of course the argon target, which matches the LBNE far detector. The ND standard target is polypropylene $(C_3H_6)_n$, largely provided by the mass of the STT radiators. An additional proposed ND target is argon gas in pressurized aluminum tubes with sufficient mass to provide $\simeq$10 times the ν_μCC and NC statistics as expected in the LBNE far detector. Equally important nuclear targets are carbon (graphite), which is essential in order to get (anti)neutrino interactions on free protons through a statistical subtraction procedure from the main polypropylene target (Section 7.5), and calcium. In particular, this latter target has the same atomic weight ($A = 40$) as argon but is isoscalar. One additional nuclear target is iron, which is used in the proposed India-based Neutrino Observatory (INO) [281]. The modularity of the STT provides for successive measurements using thin nuclear targets (thickness $< 0.1X_0$), while the excellent angular and space resolution allows a clean separation of events originating in different target materials. Placing an arrangement of different nuclear targets upstream of the detector provides the desired nuclear samples in (anti)neutrino interactions. For example, a single 7-mm-thick calcium layer at the upstream end of the detector will provide about 3.1×10^5 ν_μCC interactions in one year.

Potential ND studies in nuclear effects include the following:

- nuclear modifications of form factors
- nuclear modifications of structure functions
- mechanisms for nuclear effects in coherent and incoherent regimes
- a dependence of exclusive and semi-exclusive processes
- effect of final-state interactions
- effect of short-range correlations
- two-body currents

The study of nuclear effects in (anti)neutrino interactions off nuclei is directly relevant for the long-baseline oscillation studies. The use of heavy nuclei like argon in the LBNE far detector requires a measurement of nuclear cross sections on the same targets in the ND in order to reduce signal and background uncertainties in the oscillation analyses. Cross-section measurements obtained from other experiments using different nuclei are not optimal; in addition to the different p/n ratio in argon compared to iron or carbon where measurements from other experiments exist, nuclear modifications of cross sections can differ from 5% to 15% between carbon and argon for example, while the difference in the final-state interactions could be larger. Additionally, nuclear modifications can introduce a substantial smearing of the kinematic variables reconstructed from the observed final-state particles. Detailed measurements of the dependence on the atomic number A of different exclusive processes are then required in order to understand the absolute energy scale of neutrino event interactions and to reduce the corresponding systematic uncertainties on the oscillation parameters.

It is worth noting that the availability of a free-proton target through statistical subtraction of the $(C_3H_6)_n$ and carbon targets (Section 7.5) will allow for the first time a direct model-independent measurement of nuclear effects — including both the primary and final-state interactions — on the argon target relevant for the far detector oscillation analysis.

Furthermore, an important question in nuclear physics is how the structure of a nucleon is modified when said nucleon is inside the medium of a heavy nucleus as compared to a free nucleon like the proton in a hydrogen nucleus. Studies of the ratio of structure functions of nuclei to those of free nucleons (or in practice, the deuteron) reveal nontrivial deviations from unity as a function of x and Q^2. These have been well explored in charged-lepton scattering experiments, but little empirical information exists from neutrino scattering. Measurements of structure using neutrino scattering are complementary to those in charged-lepton scattering.

Another reason to investigate the nuclear-medium modifications of neutrino structure functions is that most neutrino scattering experiments are performed on nuclear targets, from which information on the free nucleon is inferred by performing a correction for the nuclear effects. In practice this often means applying the same nuclear correction as for the electromagnetic structure functions, which introduces an inherent model-dependence in the result. In particular, significant differences between photon-induced and weak-boson-induced nuclear structure functions are predicted, especially at low Q^2 and low x, which have not been tested. A striking example is offered by the ratio R of the longitudinal-to-transverse structure functions [251]. While the electromagnetic ratio tends to zero in the photoproduction limit, $Q^2 \to 0$, by current conservation, the ratio for neutrino structure functions is predicted to be *finite* in this limit. Thus, significant discovery potential exists in the study of neutrino scattering from nuclei.

The comparison of argon and calcium targets ($^{40}_{18}$Ar and $^{40}_{20}$Ca) in the LBNE ND would be particularly interesting. Since most nuclear effects depend on the atomic weight A, inclusive properties of (anti)neutrino interactions are expected to be the same for these two targets [251,282,283,284].

This fact would allow the use of both targets to model signal and backgrounds in the LBNE far detector (argon target), as well as to compare LBNE results for nuclear effects on argon with the extensive data on calcium from charged lepton DIS. In addition, a high-precision measurement of (anti)neutrino interactions in both argon and calcium opens the possibility for studying a potential flavor and isovector dependence of nuclear effects and to further test the isospin (charge symmetry) in nuclei (Section 7.5). Evidence for any of these effects would constitute important discoveries.

Finally, the extraction of (anti)neutrino interactions on deuterium from the statistical subtraction of H_2O from D_2O, which is required to measure the fluxes (Section 7.1), would allow the first direct measurement of nuclear effects in deuterium. This measurement can be achieved since the structure function of a free isoscalar nucleon is given by the average of neutrino and antineutrino structure functions on hydrogen ($F_2^{\nu n} = F_2^{\bar{\nu}p}$). A precise determination of nuclear modifications of structure functions in deuterium would play a crucial role in reducing systematic uncertainties from the global PDF fits.

7.7 Search for Heavy Neutrinos

The most economical way to handle the problems of neutrino masses, dark matter and the Baryon Asymmetry of the Universe in a unified way may be to add to the Standard Model (SM) three Majorana singlet fermions with masses roughly on the order of the masses of known quarks and leptons using the seesaw mechanism [67]. The appealing feature of this theory (called the νMSM for *Neutrino Minimal SM*) [285] is that every left-handed fermion has a right-handed counterpart, leading to a consistent way of treating quarks and leptons.

The most efficient mechanism proposed for producing these heavy sterile singlet states experimentally is through weak decays of heavy mesons and baryons, as can be seen from the left-hand diagram in Figure 7.4, showing some examples of relevant two- and three-body decays [286]. These heavy mesons can be produced by energetic protons scattering off the LBNE neutrino production target and the heavy singlet neutrinos from their decays detected in the near detector.

The lightest of the three new singlet fermions in the νMSM, is expected to have a mass from 1 keV to 50 keV [287] and could play the role of the dark matter particle [288]. The two other neutral fermions are responsible for giving mass to ordinary neutrinos via the seesaw mechanism at the *electroweak scale* and for creation of the Baryon Asymmetry of the Universe (BAU; for a review see [287]). The masses of these particles and their coupling to ordinary leptons are constrained by particle physics experiments and cosmology [286,289]. They should be almost degenerate, thus nearly forming Dirac fermions (this is dictated by the requirement of successful baryogenesis). Different considerations indicate that their mass should be in the region of $\mathcal{O}(1)$ GeV [290].

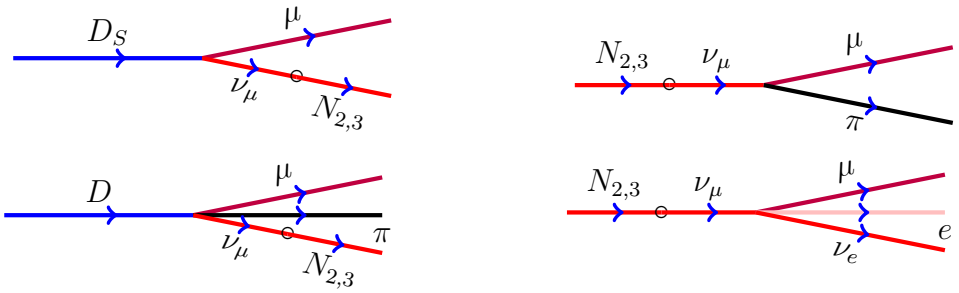

Figure 7.4: Left: Feynman diagrams of meson decays producing heavy sterile neutrinos. Right: Feynman diagrams of sterile-neutrino decays.

The mixing angle, U^2, between the singlet fermions and the three active-neutrino states must be small [285,291] — otherwise the large mixing would have led to equilibration of these particles in the early Universe above the electroweak temperatures, and, therefore, to erasing of the BAU — explaining why these new particles have not been seen previously.

Several experiments have conducted searches for heavy neutrinos, for example BEBC [292], CHARM [293], NuTeV [294] and the CERN PS191 experiment [295,296] (see also a discussion of different experiments in [289]). In the search for heavy neutrinos, the strength of the LBNE ND, compared to earlier experiments, lies in reconstructing the exclusive decay modes, including electronic, hadronic and muonic. Furthermore, the detector offers a means to constrain and measure the backgrounds using control samples.

In case of the LBNE experiment the relevant heavy mesons are charmed. With a typical lifetime (in the rest frame) of about 10^{-10} s, these mesons mostly decay before further interaction, yielding the sterile-neutrino flux. Since these sterile neutrinos are very weakly interacting they can cover quite a large distance before decay, significantly exceeding the distance of roughly 500 m from the target to the ND. The ND can search for decays of neutrinos into SM particles due to mixing with active neutrinos, provided a sufficiently long instrumented decay region is available. Two examples of the interesting decay modes are presented on the right panel of Figure 7.4. More examples can be found in [286].

An estimate of sterile-neutrino events that can be observed in the LBNE ND, N_{signal}^{LBNE}, is obtained by comparing the relevant parameters of the LBNE and CHARM experiments. The number of events grows linearly with the number of protons on target, the number of produced charmed mesons, the detector length (decay region) and the detector area. In particular, this latter linear increase is valid if the angular spread of the neutrino flux, which is on the order of $N_m M_D / E_{beam}$, is larger than the angle at which the ND is seen from the target. Here N_m is the multiplicity of the produced hadrons, and the above condition is valid for both LBNE and CHARM. The number of events decreases linearly when the energy increases, since this increases the lifetime, reducing the decay probability within the detector. Finally, the number of mesons decreases quadratically with

the distance between the target and the detector.

The considerations above imply that a search for νMSM sterile neutrinos in the LBNE ND can be competitive after only five years of running with the reference beam, corresponding to an overall integrated exposure of about 5×10^{21} POT with a proton energy of 120 GeV. The use of a low-density, high-resolution spectrometer in the ND substantially reduces backgrounds and allows the detection of both leptonic and hadronic decay modes. Assuming a fiducial length of the magnetized tracker of 7 m as decay region, the ratio between the signal event to be observed in the LBNE ND and those in the CHARM experiment can be estimated to be more than a factor of 50 after only four years of running. Since both production and decay rates are proportional to the square of the neutrino mixing angles, the corresponding improvement in the square of the neutrino mixing angle U^2 will be about a factor of seven with respect to the CHARM experiment. Figure 7.5 shows the projected LBNE sensitivity in the (U^2, M) plane. At lower values of the mass of the heavy neutrinos, additional constraints can be obtained for kaons by comparing the LBNE and PS191 experiments, as shown in Figure 7.5.

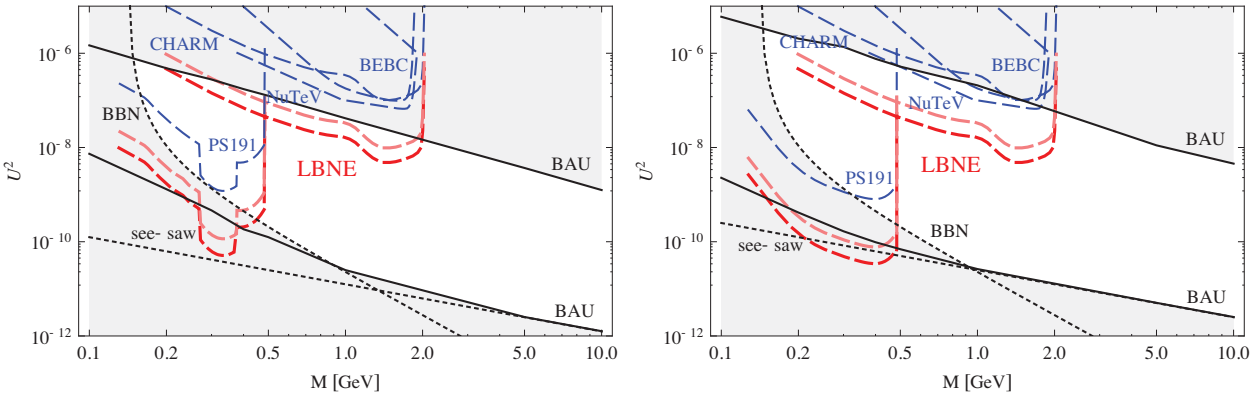

Figure 7.5: Upper limits on U^2, the mixing angle between heavy sterile neutrinos and the light active states, coming from the Baryon Asymmetry of the Universe (solid lines), from the seesaw mechanism (dotted line) and from the Big Bang nucleosynthesis (dotted line). The regions corresponding to different experimental searches are outlined by blue dashed lines. Left panel: normal hierarchy; right panel: inverted hierarchy (adopted from [297]). Pink and red curves indicate the expected sensitivity of the LBNE near detector with an exposure of 5×10^{21} POT (~ 5 years) with the 1.2-MW reference beam at 120 GeV for detector lengths of 7 m and 30 m , respectively (see text for details).

It must be noted that exploitation of the complete 5 + 5 years (ν + $\overline{\nu}$) years of data taking would further improve the number of expected events by a factor of two, since it scales linearly with the number of protons on target. With the beam upgrade to 2.3-MW, this improvement would become a factor of four with respect to the initial five year run and the 1.2 MW beam.

A better sensitivity to νMSM can be achieved by instrumenting the upstream region of the ND hall (e.g., with the liquid argon detector and some minimal tracking device upstream). The fiducial volume of the new detector will need to be empty (material-free) or fully sensitive in order to suppress background events. The geometry of the ND hall would allow a maximal decay length of

about 30 m. The sensitivity of this configuration can be estimated by rescaling the expected limits on the neutrino mixing angle U^2. The expected number of signal events with a total decay length of $\sim$ 30 m exceeds by about 200 (800) times the number of events in CHARM after a five (5 +5) year run with the standard (upgraded) beam. In turn, this implies an improvement by a factor of 15 (28) in the sensitivity to U^2 with respect to the CHARM experiment.

If the magnetic moment of the sterile neutrinos is sizeable, the dominant decay channel would be a radiative electromagnetic decay into $\gamma\nu$, which has also been proposed as a possible explanation for the observed MiniBooNE low-energy excess [148]. This possibility, in turn, requires a detector capable of identifying and reconstructing single photon events. The low-density ND in LBNE can achieve an excellent sensitivity to this type of search as demonstrated by a similar analysis in NOMAD [298].

7.8 Search for High Δm^2 Neutrino Oscillations

The evidence for neutrino oscillations obtained from atmospheric, long-baseline accelerator, solar and long-baseline reactor data from different experiments consistently indicates two different scales, with Δm^2_{32} $\sim$2.4 $\times$ 10^{-3} eV^2 defining the atmospheric oscillations (also long-baseline accelerator and short-baseline reactor scales) and Δm^2_{21} $\sim$7.9 $\times$ 10^{-5} eV^2 defining the solar oscillations (and long-baseline reactor oscillations). The only way to accommodate oscillations with relatively high Δm^2 at the eV^2 scale as suggested by the results from the LSND experiment [299] is therefore to add one or more sterile neutrinos to the conventional three light neutrinos.

Recently, the MiniBooNE experiment reported that its antineutrino data might be consistent with the LSND $\overline{\nu}_\mu \to \overline{\nu}_e$ oscillation with $\Delta m^2 \sim$ eV^2 [300]. Contrary to the antineutrino data, the neutrino data seem to exclude high Δm^2 oscillations, possibly indicating a different behavior between neutrinos and antineutrinos.

Models with five (3+2) or six (3+3) neutrinos can potentially explain the MiniBooNE results. In addition to the cluster of the three neutrino mass states (accounting for *solar* and *atmospheric* mass splitting), two (or three) states at the eV scale are added, with a small admixture of ν_e and ν_μ to account for the LSND signal. One distinct prediction from such models is a significant probability for $\overline{\nu}_\mu$ disappearance into sterile neutrinos, on the order of 10%, in addition to the small probability for $\overline{\nu}_e$ appearance.

Given a roughly 500-m baseline and a low-energy beam, the LBNE ND can reach the same value $L/E_\nu \sim 1$ as MiniBooNE and LSND. The large fluxes and the availability of fine-grained detectors make the LBNE program well suited to search for active-sterile neutrino oscillations beyond the three-flavor model with Δm^2 at the eV^2 scale.

Due to the potential differences between neutrinos and antineutrinos, four possibilities have to be considered in the analysis: ν_μ disappearance, $\overline{\nu}_\mu$ disappearance, ν_e appearance and $\overline{\nu}_e$ appearance. As discussed in Section 7.1, the search for high Δm^2 oscillations has to be performed simultaneously with the in situ determination of the fluxes.

To this end, an independent prediction of the ν_e and $\overline{\nu}_e$ fluxes starting from the measured ν_μ and $\overline{\nu}_\mu$ CC distributions are required since the ν_e and $\overline{\nu}_e$ CC distributions could be distorted by the appearance signal. The low-ν_0 method can provide such predictions if external measurements for the K^0_L component are available from hadro-production experiments (Section 7.1).

The study will implement an iterative procedure:

1. extraction of the fluxes from ν_μ and $\overline{\nu}_\mu$ CC distributions assuming no oscillations are present
2. comparison with data and determination of oscillation parameters (if any)
3. new flux extraction after subtraction of the oscillation effect
4. iteration until convergence

The analysis has to be performed separately for neutrinos and antineutrinos due to potential CP or CPT violation, according to MiniBooNE/LSND data. The ratio of ν_e CC events to ν_μ CC events will be measured:

$$\mathcal{R}_{e\mu}(L/E) \equiv \frac{\#\ of\ \nu_e N \to e^- X}{\#\ of\ \nu_\mu N \to \mu^- X}(L/E); \qquad \overline{\mathcal{R}}_{e\mu}(L/E) \equiv \frac{\#\ of\ \overline{\nu}_e N \to e^+ X}{\#\ of\ \overline{\nu}_\mu N \to \mu^+ X}(L/E) \quad (7.24)$$

This is then compared with the predictions obtained from the low-ν_0 method. Deviations of $\mathcal{R}_{e\mu}$ or $\overline{\mathcal{R}}_{e\mu}$ from the expectations as a function of L/E would provide evidence for oscillations. This procedure only provides a relative measurement of $\nu_e(\overline{\nu}_e)$ versus $\nu_\mu(\overline{\nu}_\mu)$; since the fluxes are extracted from the observed ν_μ and $\overline{\nu}_\mu$ CC distributions, an analysis of the $\mathcal{R}_{e\mu}(\overline{\mathcal{R}}_{e\mu})$ ratio cannot distinguish between $\nu_\mu(\overline{\nu}_\mu)$ disappearance and $\nu_e(\overline{\nu}_e)$ appearance.

The process of NC elastic scattering off protons (Section 7.3) can provide the complementary measurement needed to disentangle the two hypotheses of $\nu_\mu(\overline{\nu}_\mu)$ disappearance into sterile neutrinos and $\nu_e(\overline{\nu}_e)$ appearance. In order to cancel systematic uncertainties, the NC/CC ratio with respect to QE scattering will be measured:

$$\mathcal{R}_{NC}(L/E) \equiv \frac{\#\ of\ \nu p \to \nu p}{\#\ of\ \nu_\mu n \to \mu^- p}(L/E); \qquad \overline{\mathcal{R}}_{NC}(L/E) \equiv \frac{\#\ of\ \overline{\nu} p \to \overline{\nu} p}{\#\ of\ \overline{\nu}_\mu p \to \mu^+ n}(L/E) \quad (7.25)$$

It is possible to reconstruct the neutrino energy from the proton angle and momentum under the assumption that the nuclear smearing effects are small enough to neglect (the same for the neutrino CC sample). In the oscillation analysis, only the *relative* distortions of the ratio $\mathcal{R}_{NC}(\overline{\mathcal{R}}_{NC})$ as a

function of L/E are of interest, not their absolute values. For $Q^2 > 0.2$ GeV^2 the relative shape of the total cross sections is not very sensitive to the details of the form factors. To improve the energy resolution, it is possible to use neutrino interaction events originating from the deuterium inside the D_2O target embedded into the fine-grained tracker. These events have better energy resolution due to the smaller nuclear smearing effects in D_2O.

An improved oscillation analysis is based on a simultaneous fit to both $\mathcal{R}_{e\mu}(\overline{\mathcal{R}}_{e\mu})$ and $\mathcal{R}_{NC}(\overline{\mathcal{R}}_{NC})$. The first ratio provides a measurement of the oscillation parameters while the latter constrains the $\nu_e(\overline{\nu}_e)$ appearance versus the $\nu_\mu(\overline{\nu}_\mu)$ disappearance. This analysis imposes two main requirements on the ND:

- e^+/e^- separation to provide an unambiguous check of the different behavior between neutrinos and antineutrinos suggested by MiniBooNE
- accurate reconstruction of proton momentum and angle

Validation of the unfolding of the high Δm^2 oscillations from the in situ extraction of the $\nu(\overline{\nu})$ flux would also require changes to the beam conditions, since the ND cannot be easily moved. This would require a short run with a high-energy beam and the capability to change or switch off the beam focusing system.

7.9 Light (sub-GeV) Dark Matter Searches

According to the latest cosmological and astrophysical measurements, nearly eighty percent of the matter in the Universe is in the form of cold, non-baryonic dark matter (DM) [301,302]. The search to find evidence of the particle (or particles) that make up DM, however, has so far turned up empty. Direct detection experiments and indirect measurements at the LHC, however, are starting to severely constrain the parameter space of Weakly-Interacting Massive Particles (WIMPs), one of the leading candidates for DM. The lack of evidence for WIMPs at these experiments has forced many in the theory community to reconsider.

Some theories consider an alternative possibility to the WIMP paradigm in which the DM mass is much lighter than the electroweak scale (e.g., below the GeV level). In order to satisfy constraints on the relic density of DM, these theories require that DM particles be accompanied by light *mediator* particles that would have allowed for efficient DM annihilation in the early Universe. In the simplest form of these theories an extra U(1) gauge field mixes with the SM U(1) gauge field, but with an additional kinetic term. This mixing term provides a *portal* from the dark sector to the charged particles of the SM. In this model, the mediators are called *dark photons* and are denoted by V.

Recently, a great deal of interest has been paid to the possibility of studying models of light (sub-GeV) Dark Matter at low-energy, fixed-target experiments [303,304,305,306]. High-flux neutrino beam experiments — such as LBNE — have been shown to potentially provide coverage of DM+mediator parameter space that cannot be covered by either direct detection or collider experiments.

Upon striking the target, the proton beam can produce the dark photons either directly through $pp(pn) \rightarrow V$ as in the left-hand diagram of Figure 7.6 or indirectly through the production of a π^0 or a η meson which then promptly decays into a SM photon and a dark photon as in the center diagram in the figure. For the case where $m_V > 2m_{DM}$, the dark photons will quickly decay into a pair of DM particles.

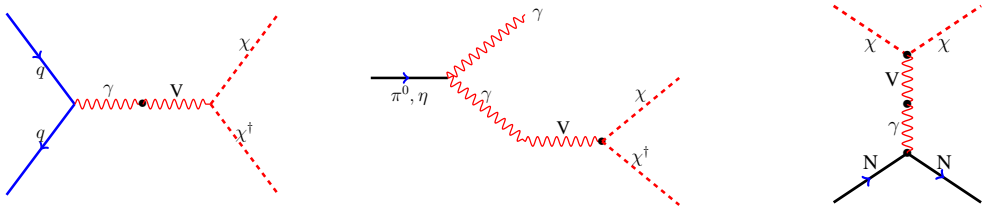

Figure 7.6: On the left is shown the direct production of a dark photon, while, in the center, the dark photon is produced via the decay of a neutral pion or eta meson. In both cases, the dark photon promptly decays into a pair of DM particles. Right: Tree-level scattering of a DM particle off of nuclei. Analogous interactions with electrons in the detector are also possible.

The LBNE ND together with the high-intensity beam will provide an excellent setup for making this measurement. The relativistic DM particles from the beam will travel along with the neutrinos to the detector where they can be detected through NC-like interactions either with electrons or nucleons, as shown in the right-hand diagram of Figure 7.6. Since the signature of a DM event looks similar to that of a neutrino event, the neutrino beam provides the major source of background for the DM signal.

Several ways have been proposed to suppress neutrino backgrounds using the unique characteristics of the DM beam. Since DM will travel much more slowly than the much lighter neutrinos, DM events in the ND will arrive out of time with the beam pulse. In addition, since the electrons struck by DM will be in a much more forward direction compared to neutrino interactions, the angle of these electrons may be used to reduce backgrounds, taking advantage of the ND's fine angular resolution.

Finally, a special run can be devised to turn off the focusing horn to significantly reduce the charged particle flux that will produce neutrinos. Figure 7.7 shows the expected sensitivity of the MiniBooNE DM search using this technique [306]. With a wider-band, higher-energy, more intense

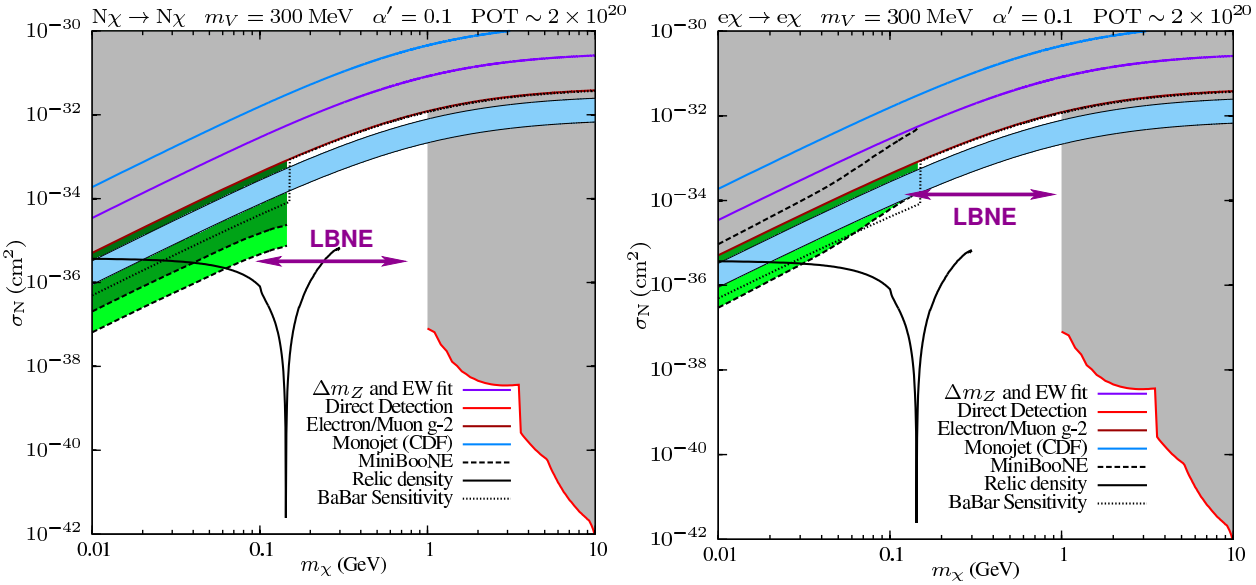

Figure 7.7: Regions of nucleon-WIMP scattering cross section (corresponding to dark matter in the lab moving with $v = 10^{-3}c$). The plot uses $m_V = 300$ MeV and $\alpha' = 0.1$. Constraints are shown from different experiments. The left plot shows the exclusion regions expected from MiniBooNE given 1-10 (light green), 10-1000 (green), and more than 1000 (dark green) elastic scattering events off nucleons. The right panel shows the same for elastic scattering off electrons. The magenta arrows indicate the region where LBNE can extend the MiniBooNE sensitivity. Figure is based on studies in [306].

beam, LBNE is expected to not only cover the MiniBooNE sensitivity region with higher statistics, but will also extend the sensitivity to cover the region between MiniBooNE and the direct DM searches. If the LBNE ND were a LArTPC and the entire detector volume active, the effective number of DM events detected would be much higher when compared to a MINOS-like detector of the same mass. Much more thorough studies must be conducted to obtain reliable sensitivities. This requires an integration of theoretical predictions into a simulation package for the detector.

Chapter 8 Additional Far Detector Physics Opportunities

The deep underground location of LBNE's LArTPC far detector will expand the range of science opportunities it can pursue to potentially include observation of solar and other low-energy neutrinos, dark matter, magnetic monopoles and nucleon-antinucleon transitions.

8.1 Solar Neutrinos

In the early 20^{th} century, Arthur Stanley Eddington suggested that nuclear reactions of protons fuel energy production in the Sun. After the discovery of the neutron, Hans Bethe [307] proposed that the first stage of these nuclear reactions involves the weak interaction: a β decay of a proton into a neutron, a positron and a neutrino accompanied by the fusion of that neutron with another proton to form deuterium. This proton-proton (pp) reaction $p+p \rightarrow {}^{1}_{1}\text{H}+e^{+}+\nu_e$ is the origin of most solar neutrinos (called pp neutrinos). In 0.2% of the cases deuterium is produced by the corresponding three-body reaction $p+e^{-}+p \rightarrow {}^{1}_{1}\text{H}+\nu_e$ (called pep) which produces monoenergetic solar neutrinos at 1.4 MeV. The pp reaction is the starting point of a chain of nuclear reactions which converts four protons into a ${}^{4}_{2}\text{He}$ nucleus, two positrons and two neutrinos. This reaction chain, shown in Figure 8.1, produces 98% of the energy from the Sun. In addition to pp and pep, neutrinos are produced by the reactions ${}^{7}_{4}\text{Be}+e^{-} \rightarrow {}^{7}_{3}\text{Li}+\nu_e$ (^{7}Be neutrinos) and ${}^{3}_{2}\text{He}+p \rightarrow {}^{4}_{2}\text{He}+e^{+}+\nu_e$ (*hep* neutrinos) as well as the β decay ${}^{8}_{5}\text{B} \rightarrow {}^{8}_{4}\text{Be}+e^{+}+\nu_e \rightarrow {}^{4}_{2}\text{He}+{}^{4}_{2}\text{He}+e^{+}+\nu_e$ (^{8}B neutrinos). Carl-Friedrich von Weizsäcker [308] complemented the pp-chain with a cyclical reaction chain dubbed *CNO cycle* after the principal elements involved (shown in the top right illustration of Figure 8.1). Although theorized to be responsible for only 2% of energy production in the Sun, the CNO cycle plays the dominant role in the energy production of stars heavier than 1.3 solar masses.

The expected spectra of neutrinos from the pp reaction chain [309] are shown as solid curves in the bottom diagram of Figure 8.1. Neutrinos from the CNO cycle are shown as dashed blue curves.

The chief motivation of Raymond Davis to build his pioneering solar-neutrino detector in the Homestake mine was the experimental verification of stellar energy production by the observation of the neutrinos from these nuclear processes. While he succeeded in carrying out the first measurements of solar neutrinos — and shared the 2002 Nobel Prize in physics for the results — the measured flux [120] fell short of solar model calculations: the *solar-neutrino problem*. Data from the Super–Kamiokande (SK) and SNO [310,311] experiments eventually explained this mystery 30 years later as due to flavor transformation. However, intriguing questions in solar-neutrino physics remain. Some unknowns, such as the fraction of energy production via the CNO cycle in

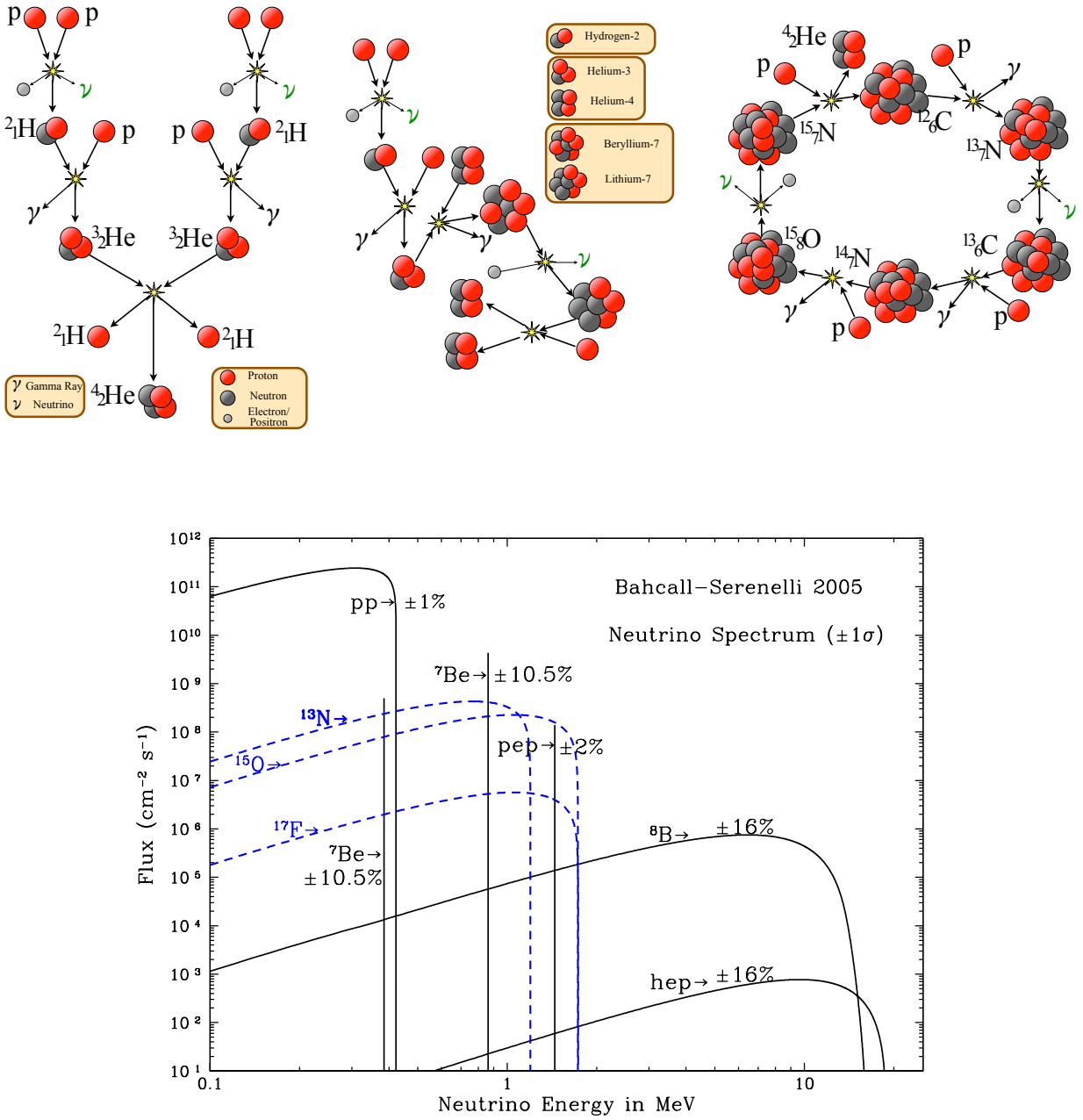

Figure 8.1: Top: the proton-proton and CNO reaction chain in the Sun. Bottom: solar-neutrino fluxes from [309].

the Sun, flux variation due to helio-seismological modes that reach the solar core, or long-term stability of the solar core temperature, are astrophysical in nature. Others directly impact particle physics. Can the MSW model explain the amount of flavor transformation as a function of energy, or are nonstandard neutrino interactions required? Do solar neutrinos and reactor antineutrinos oscillate with the same parameters? Experimental data expected in the immediate future (e.g., further

data from Borexino [312] and SK as well as SNO+ [313]) will address some questions, but the high-statistics measurements necessary to further constrain alternatives to the standard oscillation scenario may need to wait for a more capable experiment such as LBNE.

Detection of solar and other low-energy neutrinos is challenging in a LArTPC because of high intrinsic detection energy thresholds for the charged-current (CC) interaction on argon (>5 MeV). To be competitive, this physics requires either a very low visible-energy threshold (∼1 MeV) or a very large mass (50 kt). However, compared with other technologies, a LArTPC offers a large cross section and unique signatures from de-excitation photons. Aggressive R&D efforts in low-energy triggering and control of background from radioactive elements may make detection in LBNE possible, and a large detector mass would make the pursuit of these measurements worthwhile.

The solar-neutrino physics potential of a large LArTPC depends primarily on its energy threshold and depth. The energy threshold is not only determined by the ability to pick up a low-energy electron, but also by the light collection of the photon-triggering system as well as background suppression. Only at a deep underground location will it have a reasonable chance of detecting solar neutrinos. In any detector of this kind, the decay of the naturally occurring ^{39}Ar produces β's with a 567-keV endpoint and an expected rate of 10 MHz per 10 kt of liquid argon. This limits the fundamental reach of LBNE to neutrino interactions with visible energies above 1 MeV. Possible signatures of solar neutrinos in LBNE are:

Elastic scattering of ^{8}B neutrinos with electrons: This signature would only reproduce the SK data; SK has already accumulated large statistics (>60,000 solar-neutrino events). An energy threshold of about 1 MeV (lower than the SK threshold which is currently 3.5 MeV [314]) would be required for a more interesting measurement of *pep* (defined in Figure 8.1) and CNO fluxes. Such solar-neutrino interactions are difficult to detect, as only low-energy single electrons (and neutrinos) are produced.

Charged-current interactions with argon: The signature for this interaction is:

$$\nu_e + {}^{40}\mathrm{Ar} \rightarrow {}^{40}\mathrm{K}^{*} + e^{-} \tag{8.1}$$

This signal is more interesting experimentally, as there is a signature of de-excitation photons and the visible energy is directly correlated with the neutrino energy; however, the reaction has an energy threshold of 5 MeV.

Cosmic-muon and fast-neutrino interactions with the ^{40}Ar nucleus (which are rather complex compared to interactions on ^{16}O or ^{12}C) are likely to generate many long-lived spallation products that could limit the detection threshold for low-energy neutrinos. Studies of the spallation background

in the LBNE LArTPC are underway. The production rate of ^{40}Cl, a beta emitter with an endpoint of 7.48 MeV that is a dominant source of background at energies above 5 MeV, is shown in Figure 8.2 as a function of depth. The cosmogenic background rates as a function of beta kinetic energy from several other beta emitters at the 4,850-ft level of Sanford Underground Research Facility are shown in Figure 6.8.

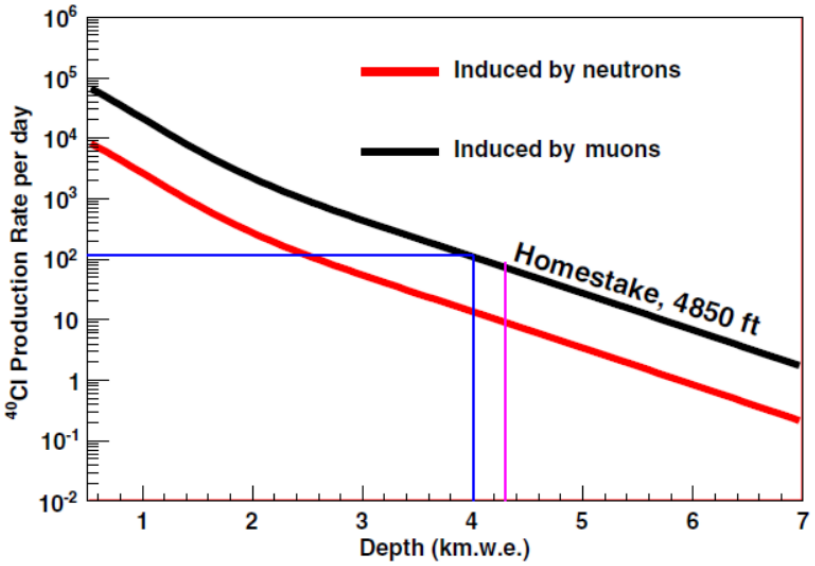

Figure 8.2: ^{40}Cl production rates in a 10-kt detector produced by (n,p) reaction as a function of depth.

In Table 8.1 the solar-neutrino event rate in a 34-kt LArTPC is shown, assuming a 4.5-MeV neutrino energy threshold and 31% ν_e.

Table 8.1: Solar-neutrino event rates in a 34-kt LArTPC assuming a 4.5-MeV neutrino energy threshold and an electron-flavor survival probability $P_{ee} = 31\%$.

Transition	Rate (evts/day)
Fermi	31
Gamow-Teller	88

The ICARUS Collaboration has reported a 10-MeV threshold [315]. Assuming the detector itself has low enough radioactivity levels, this threshold level would enable a large enough detector to measure the electron flavor component of the solar ^{8}B neutrino flux with high statistical accuracy. It could thereby further test the MSW flavor transformation curve (Figure 8.3) with higher statistical precision and potentially better energy resolution.

In addition to these solar matter effects, solar neutrinos also probe terrestrial matter effects with the variation of the ν_e flavor observed with solar zenith angle while the Sun is below the horizon — the *day/night effect*. A sizable effect is predicted only for the highest solar-neutrino energies, so while

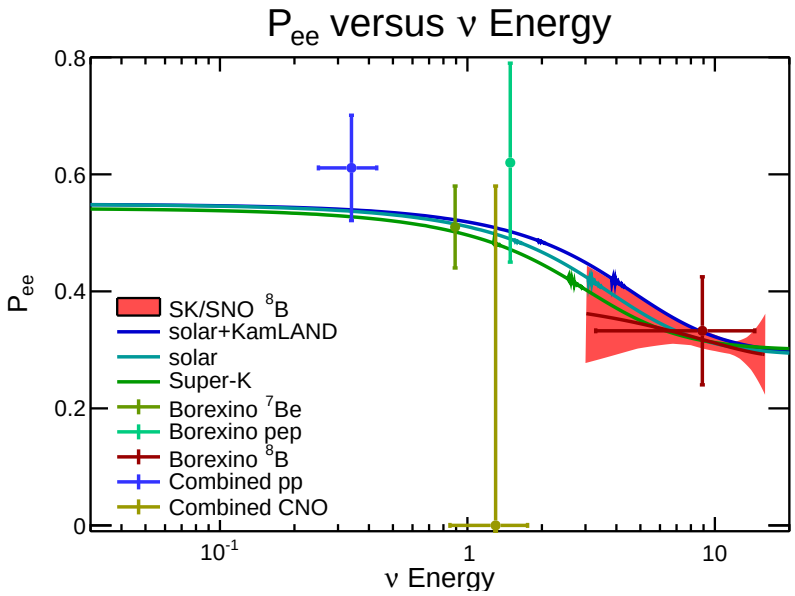

Figure 8.3: Measurements of the solar MSW transition. The red band combines SK and SNO ^{8}B data [75], the green measurements of ^{7}Be and pep are from Borexino [312,316] and the red error bar is Borexino's ^{8}B measurement [317]. The blue *pp* point and the yellow error bar (CNO) combine all solar data. MSW resonance curves for three different parameters are overlaid.

the comparatively high energy threshold is a handicap for testing the solar MSW resonance curve, it has a smaller impact on the high-statistics test of terrestrial matter effects. Recently, indication of the existence of the terrestrial matter effects were reported [76]. Measurements of this effect currently give the best constraints on the solar mass (Δm^2_{21}) splitting (Figure 8.4) using neutrinos rather than antineutrinos [318].

The comparison of ν disappearance to $\overline{\nu}$ disappearance tests CPT invariance. For good sensitivity to either solar-neutrino measurement, a liquid argon far detector of at least 34 kt is required.

8.2 Indirect Searches for WIMP Dark Matter

If the true nature of Dark Matter (DM) involves a weakly-interacting massive particle (WIMP) with a mass on the order of 1 GeV, an experiment could look for anomalous signals in astrophysical data from the annihilation (or decay) of DM into Standard Model particles, e.g., neutrinos [319]. Neutrinos produced by DM decay are expected to come from such distant objects as the galactic center, the center of the Sun or even from the Earth.

As our solar system moves through the DM halo, WIMPs interact with the nuclei of celestial bodies and become trapped in a body's gravitational well. Over time, the WIMPs accumulate near the core of the body, enhancing the possibility of annihilation. The high-energy neutrinos ($E \sim m_{\mathrm{WIMP}}$) from these annihilations can free-stream through the astrophysical body and emerge

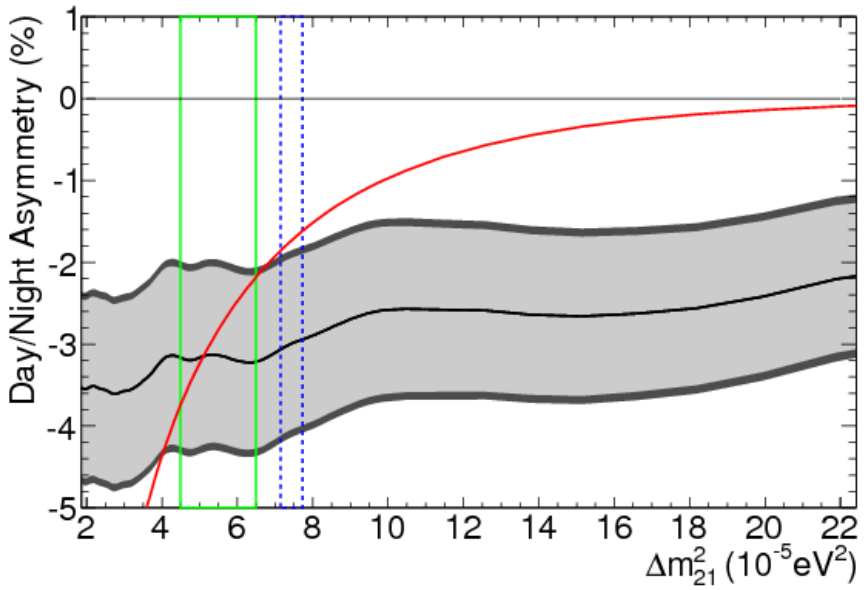

Figure 8.4: Dependence of the measured day/night asymmetry (fitted day/night amplitude times the expected day/night asymmetry in red) on Δm^2_{21}, for $\sin^2\theta_{12} = 0.314$ and $\sin^2\theta_{13} = 0.025$. The 1σ statistical uncertainties from the recent measurements by SK are given by the light grey band. The additional dark grey width to the band shows the inclusion of the systematic uncertainties. Overlaid are the 1σ allowed ranges from the solar global fit (solid green) and the KamLAND experiment (dashed blue). Figure is from [76].

roughly unaffected, although oscillation and matter effects can slightly alter the energy spectrum. Neutrinos produced via the nuclear-fusion processes in the Sun have energies close to 1 MeV, much lower than likely DM-decay neutrino energies.

The LBNE far detector's large mass and directional tracking capabilities will enable it to act as a *neutrino telescope* and search for neutrino signals produced by annihilations of dark matter particles in the Sun and/or the core of the Earth. Detection of high-energy neutrinos coming exclusively from the Sun's direction, for example, would provide clear evidence of dark matter annihilation [320].

IMB [321], IceCube [322] and SK, all water Cherenkov-based detectors, have searched for signals of DM annihilations coming from these sources, so far with negative results. A LArTPC can provide much better angular resolution than can water Cherenkov detectors, therefore providing better separation of the directional solar WIMP signal from the atmospheric-neutrino background. More thorough studies [323] are needed to determine whether LBNE could provide a competitive detection of dark matter.

8.3 Supernova Relic Neutrinos

Galactic supernovae are relatively rare, occurring somewhere between one and four times a century (Chapter 6). In the Universe at large, however, thousands of neutrino-producing explosions occur every hour. The resulting neutrinos — in fact most of the neutrinos emitted by all the supernovae since the onset of stellar formation — suffuse the Universe. Known both as *supernova relic neutrinos (SRN)* and as the *diffuse supernova-neutrino background (DSNB)*, their energies are in the few-to-30-MeV range. SRN have not yet been observed, but an observation would greatly enhance our understanding of supernova-neutrino emission and the overall core-collapse rate.

A liquid argon detector such as LBNE's far detector is sensitive to the ν_e component of the diffuse relic supernova-neutrino flux, whereas water Cherenkov and scintillator detectors are sensitive to the $\overline{\nu}_e$ component. However, backgrounds in liquid argon are as yet unknown, and a huge exposure ($>$500 kt $\cdot$ years) would likely be required for observation. Given a detector of the scale required to achieve these exposures (50 kt to 100 kt) together with tight control of backgrounds, LBNE — in the long term — could play a unique and complementary role in the physics of relic neutrinos.

In the current LBNE design, the irreducible background from solar neutrinos will limit the search for these relic neutrinos to an energy threshold greater than 18 MeV. Similarly, a search for relic antineutrinos is limited by the reactor-antineutrino background to a threshold greater than $\sim$10 MeV. The lower threshold and the smaller average ν_e energy relative to that for $\overline{\nu}_e$ (Figure 8.5) leads to the need for a larger detector mass.

A small but dedicated industry devotes itself to trying to predict the flux of these relic supernova neutrinos here on Earth [324,325,326,327,328,329,330,331]. Examples of two different predicted SRN spectra are shown in Figure 8.5, along with some of the key physics backgrounds from other neutrino sources.

In the LBNE LArTPC, relic supernova electron neutrinos would be detected primarily via the CC process as described by Equation 8.1. The electron track should be accompanied by evidence of ionization from the de-excitation of the potassium, e.g., shorter tracks sharing a common vertex; this is expected to help reduce backgrounds, but a detailed study has not yet been undertaken. In water Cherenkov and scintillator detectors, it is the $\overline{\nu}_e$ SRN flux that is detected through the process of inverse-beta decay. Unlike inverse-beta decay, for which the cross section is known to the several-percent level in the energy range of interest [332,333], the cross section for neutrino interactions on argon is uncertain at the 20% level [334,335,336]. Another limitation is that the solar *hep* neutrinos (defined in Figure 8.1), which have an endpoint at 18.8 MeV, will determine the lower bound of the SRN search window ($\sim$ 16 MeV). The upper bound is determined by the atmospheric ν_e flux as shown in Figure 8.5 and is around 40 MeV. Although the LArTPC provides

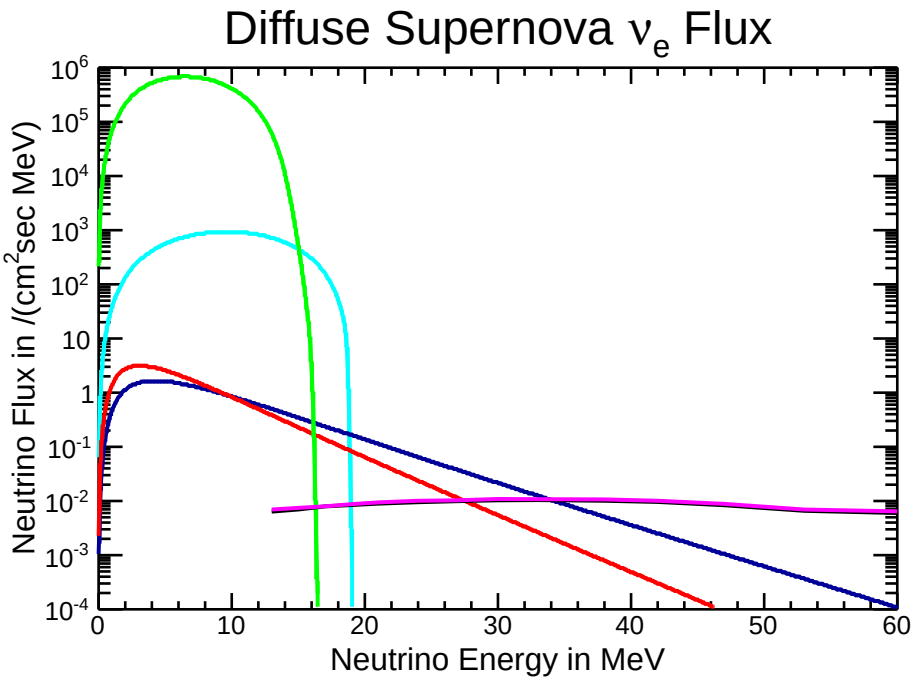

Figure 8.5: Predicted relic supernova ν_e spectra from two different models (red and blue) and some key neutrino backgrounds: ^{8}B solar ν_e (green), hep solar ν_e (cyan) and atmospheric ν_e (magenta).

a unique sensitivity to the ν_e component of the SRN flux, early studies indicate that due to this lower bound of ∼16 MeV, LBNE would need a huge mass of liquid argon — of order 100 kt — to get more than 4σ evidence for the diffuse supernova flux in five years [337]. The expected number of relic supernova neutrinos, N_{SRN}, that could be observed in a 100-kt LArTPC detector in five years [337] assuming normal hierarchy is:

$$N_{\mathrm{SRN}} = 57 \pm 12, \quad 16\,\mathrm{MeV} \leq E_e \leq 40\,\mathrm{MeV}, \tag{8.2}$$

where E_e is the energy of the electron from the CC interaction as shown in Equation 8.1. The estimate of the SRN rate in Equation 8.2 has a weak dependence on the value of $\sin^2\theta_{13}$. The above calculation is valid for values of $\sin^2\theta_{13} > 10^{-3}$. The main challenge for detection of such a low rate of relic neutrinos in a LArTPC is understanding how much of the large spallation background from cosmic-ray interactions with the heavy argon nucleus (some of which are shown in Figure 6.8) leaks into the SRN search window.

8.4 GUT Monopoles

Searches for massive, slow-moving magnetic monopoles produced in the early Universe continue to be of pressing interest. Magnetic monopoles left over from the Big Bang are predicted by Grand Unified Theories, but to date have not been observed. Because of the very large masses set by the

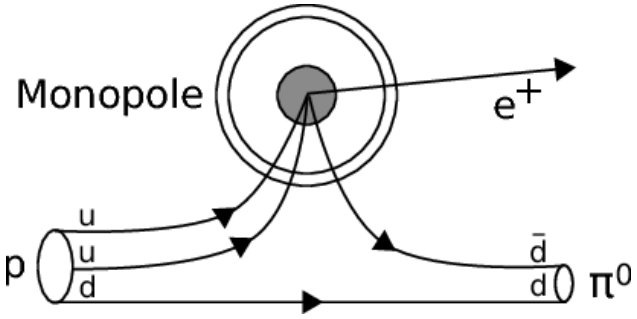

Figure 8.6: Illustration of a proton decay into a positron and a neutral pion catalyzed by a GUT monopole from [341].

GUT scale, these monopoles are normally non-relativistic, however searches for relativistic and ultra-relativistic monopoles are also of interest.

Relativistic monopoles are expected to be heavily ionizing, and hence best suited for detection in the large-area, neutrino-telescope Cherenkov detectors deployed in natural bodies of water or ice (e.g., [338,339]). With its much smaller active area, LBNE will most likely not be competitive in searches for fast monopoles.

Massive GUT monopoles are postulated to catalyze nucleon decay (Figure 8.6). It is possible that large underground detectors could detect this type of signal from transiting monopoles [340,341] via a signature consisting of multiple proton decays concurrent with the monopole's passage through the detector. Proton decay catalyzed by magnetic monopoles may be easier to observe in a LArTPC due to its superior imaging capability as compared to Cherenkov detectors, namely its high detection efficiency for a wider variety of proton decay modes, and its low energy thresholds. Whether these features are sufficient to overcome the limitation of smaller detector area relative to the very large neutrino telescopes has yet to be studied.

It should also be possible for LBNE to detect slow-moving monopoles via time-of-flight measurements, thereby eliminating reliance on the assumption of a proton-decay catalysis signature. The most stringent limits from direct searches for GUT monopoles with velocities in the range $4 \times 10^{-5} < \beta < 1$ have been obtained by the MACRO experiment [342], which has excluded fluxes at the level of $1.4 \times 10^{-16}\,\mathrm{cm^{-2}\,s^{-1}\,sr^{-1}}$. These limits probe the flux region just beyond that excluded by the existence of the galactic magnetic field (as characterized in variants of the Parker Bound).

The LBNE LArTPC far detector provides an opportunity to extend the reach of direct searches for slow monopoles, thanks to excellent timing and ionization measurement capabilities. Quantitative studies of sensitivity have yet to be carried out, but it is likely that the full-scope LBNE far detector will exceed the 10,000 m · sr isotropic-flux acceptance of MACRO.

8.5 Neutron-Antineutron Oscillations ($\Delta B = 2$)

Some Grand Unified Theories suggest the existence of double baryon-number-violating transitions that change nucleons into antinucleons [343]. The nucleon-antinucleon annihilation resulting from such a transition would provide an unmistakable signal in the LBNE LArTPC.

The imaging properties of the detector — superior to those of water detectors — would enable observation of nucleon annihilation final states in which the signal is broadened by the mix of charged and neutral hadrons. This signal could, however, be suppressed in a LArTPC if the neutron-to-antineutron transition rate is suppressed for bound neutrons due to interactions with the other nucleons.

8.6 Geo and Reactor $\overline{\nu}_e$'s

Electron antineutrinos ($\overline{\nu}_e$'s) produced by radioactive decays of the uranium, thorium and potassium present in the Earth are referred to as *geo-antineutrinos*. Decays of these three elements are currently understood to be the dominant source of the heat that causes mantle convection, the fundamental geological process that regulates the thermal evolution of the planet and shapes its surface. Detection of these geo-antineutrinos near the Earth's surface can provide direct information about the deep-Earth uranium and thorium content.

Geo-antineutrino energies are typically below 3.5 MeV. Reactor antineutrinos are somewhat more energetic, up to 8 MeV.

In a LArTPC, electron antineutrinos can in principle be detected by argon inverse-beta decay, represented by

$$\overline{\nu}_e + {}^{40}\mathrm{Ar} \rightarrow {}^{40}\mathrm{Cl}^* + e^+. \tag{8.3}$$

However, the threshold for this reaction is about 8.5 MeV, leading to the conclusion that an ^{40}Ar detector cannot use this method to detect either geo-antineutrinos or reactor antineutrinos.

Interaction via elastic scattering with electrons, another potential avenue, presents other obstacles. Not only are the recoil electrons from this interaction produced at very low energies, but solar neutrinos scatter off electrons and form an irreducible background roughly a thousand times larger than the geo-antineutrino signal. Although LBNE's location far away from any nuclear reactors leaves only a small reactor-antineutrino background and is thus favorable for geo-antineutrino detection, another detector technology (e.g., liquid scintillator) would be required to do so.

Chapter 9 Summary and Conclusion

The preceding chapters of this document describe the design of the Long-Baseline Neutrino Experiment, its technical capabilities, and the breadth of physics topics at the forefront of particle and astrophysics the experiment can address. This chapter concludes the document with several discussions that look forward in time, specifically:

- a consideration of how the design and construction of the LBNE experiment might unfold from this point on for a general class of staging scenarios,
- a summary of the grand vision for the science of LBNE and its potential for transformative discovery,
- a summary of the compelling reasons — such as LBNE's current advanced state of technical development and planning, and its alignment with the national High Energy Physics (HEP) program — for which *LBNE represents the world's best chance for addressing this science on a reasonable timescale*,
- comments on the broader impacts of LBNE, including the overarching benefits to the field of HEP, both within and beyond the U.S. program.

9.1 LBNE Staging Scenarios and Timeline

With DOE CD-1 ("Alternate Selection and Cost Range") approval in hand, the LBNE Project is working toward its technical design specifications, including detailed costs and schedule, in preparation for CD-2 ("Performance Baseline"). It should be noted that the Project already has fully developed schedules for both the CD-1 scope (10-kt far detector on the surface at the Sanford Underground Research Facility, no near neutrino detector), and for the full-scope (34-kt far detector located deep underground and near neutrino detector) for the scenario of funding solely from DOE. Partnerships with non-DOE groups are being sought to enable the construction of LBNE with a near neutrino detector and an underground far detector mass greater than 10 kt in the first phase.

Section 1.2.3 described the substantial progress that has been achieved so far toward making LBNE a fully international project. While the specific form and timing of contributions from new partners are not yet known, there are several plausible scenarios in which the Project can be implemented to accommodate non-DOE contributions. A review of the DOE project milestones, indicating where flexibility and potential for incorporating non-DOE contributions exist, provides a starting point.

DOE-funded projects are subject to several *critical decision (CD)* milestones as shown in Figure 9.1 and explained in DOE Order O 413.3B [344]. At CD-2 the first-phase LBNE Project will

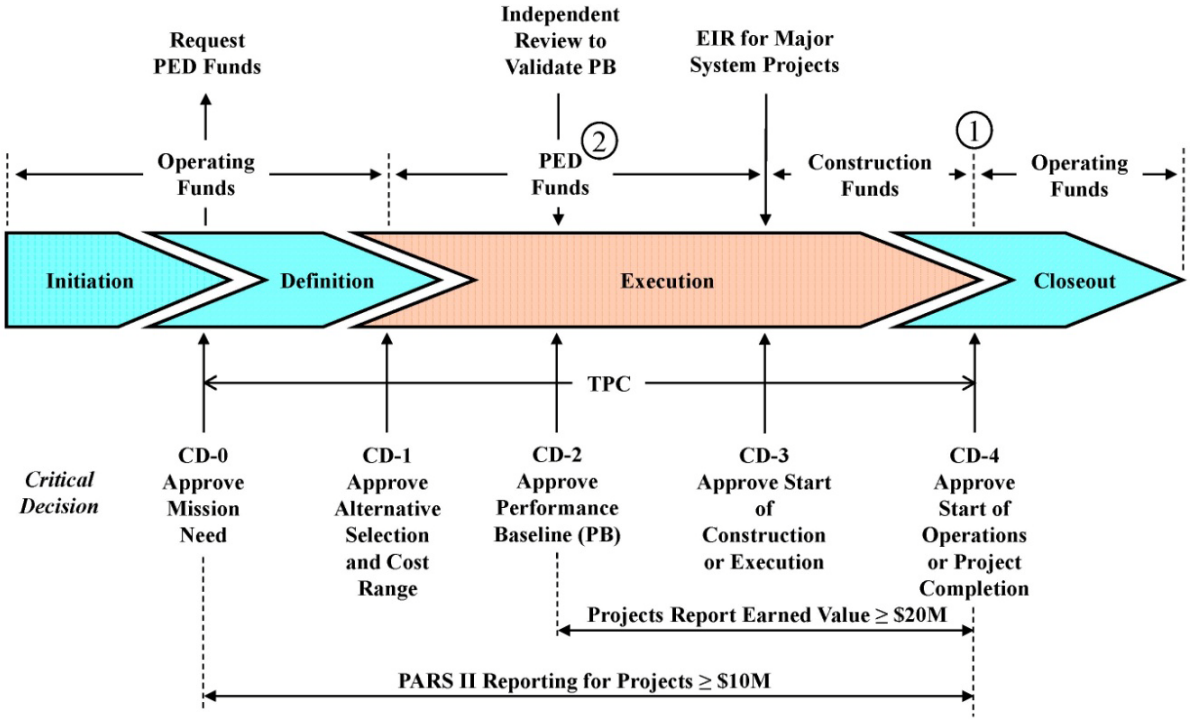

Figure 9.1: Typical DOE Acquisition Management System for line item capital asset projects [344].

be baselined. Currently, the timescale for CD-2 is projected to be toward the end of FY 2016, although the DOE has indicated flexibility in the project approval process specifically to allow for incorporation of scope changes enabled by additional partners. For example, it has been suggested that the design and construction approval for different portions of the Project can be approved at different times to facilitate proper integration of international partners. It is also expected that CD-3a approval (start of construction/execution) may take place for some parts of the Project before CD-2, thereby authorizing expenditures for long-leadtime components and construction activities, such as the advanced site preparation at Fermilab for the new beamline. The CD-4 milestone (completion of the construction project and transition to experiment operations) is currently projected for 2025. However, it is expected that commissioning and operations for LBNE will have started approximately a year before CD-4, which is considered the formal termination of the construction project.

The actual timeframe for achieving LBNE science goals will depend on the manner in which a complex sequence of developments takes place, including the actions of partners as well as

implementation of the milestones above for the DOE-funded elements of the Project. Various scenarios for incorporating contributions from new partners/sources of funding have been identified [345].

Using the current understanding of DOE funding profiles, we outline one plausible long-term timeline that integrates evolution of LBNE detector mass with development of the Fermilab accelerator complex (i.e., PIP-II) and contributions from non-DOE partners. Implicit in this timeline is an assumption that agreements with new partners be put in place on a timescale of three years (by 2017). In this scenario, the milestones that bear on the physics are as follows:

1. LBNE begins operation in 2025 with a 1.2-MW beam and a 15-kt far detector. (In such a scenario, a significant fraction of the far detector mass might be provided in the form of a standalone LArTPC module developed, funded, and constructed by international partners.)
2. Data are recorded for five years, for a net exposure of 90 kt · MW · year.
3. In 2030, the LBNE far detector mass is increased to 34 kt, and proton beam power is increased to 2.3 MW.
4. By 2035, after five years of additional running, a net exposure of 490 kt · MW · year is attained.

Physics considerations will dictate the desired extent of operation of LBNE beyond 2035.

This very coarse timeline is indicative of the degree of flexibility available for the staging of various elements of LBNE. For example, near detector construction (and the corresponding funding) could be undertaken by partners outside the U.S., on a timescale driven by the constraints they face, and could be completed somewhat earlier or later than the far detector or beamline.

With this timeline as a guide, the discussion of LBNE physics milestones can be anchored by plausible construction scenarios.

9.2 Science Impact

While considering the practical challenges implicit in the discussion in Section 9.1 for the realization of LBNE, it is important to reiterate the compelling science motivation in broad terms.

The discovery that neutrinos have mass constitutes the only palpable evidence *within the body of particle physics data* that the Standard Model of electroweak and strong interactions does not describe all observed phenomena. In the Standard Model, the simple Higgs mechanism — now confirmed with the observation of the Higgs boson — is responsible for quark as well as lepton masses, mixing and CP violation. Puzzling features such as the extremely small masses of neutrinos compared to other fermions and the large extent of mixing in the lepton sector relative to the quark sector, suggest that new physics not included in the current Standard Model is needed to connect the two sectors. These discoveries have moved the study of neutrino properties to the forefront of experimental and theoretical particle physics as a crucial tool for understanding the fundamental nature and underlying symmetries of the physical world.

The measurement of the neutrino mass hierarchy and search for CP violation in LBNE will further clarify the pattern of mixing and mass ordering in the lepton sector and its relation to the patterns in the quark sector. The impact of exposures of $90\,\mathrm{kt}\cdot\mathrm{MW}\cdot\mathrm{year}$ (2030) and $490\,\mathrm{kt}\cdot\mathrm{MW}\cdot\mathrm{year}$ (2035) for Mass Hierarchy and CP-violation signatures is easily extracted from Figure 4.16. Should CP be violated through neutrino mixing effects, the typical signal in LBNE establishing this would have a significance of at least three (2030) and five standard deviations (2035), respectively for 50% of δ_{CP} values (and greater than three standard deviations for nearly 75% of δ_{CP} by 2035). In such a scenario, the mass hierarchy can be resolved with a sensitivity for a typical experiment of $\sqrt{\overline{\Delta\chi^2}} \geq 6$ for 50% (100%) of δ_{CP} by 2030 (2035).

If CP is violated maximally with a CP phase of $\delta_{\mathrm{CP}} \sim -\pi/2$ as hinted at by global analyses of recent data [69], the significance would be in excess of 7σ. This opportunity to establish the paradigm of leptonic CP violation is highly compelling, particularly in light of the implications for leptogenesis as an explanation for the Baryon Asymmetry of the Universe (BAU). With tight control of systematic uncertainties, additional data taking beyond 2035 would provide an opportunity to strengthen a marginally significant signal should δ_{CP} take a less favorable value.

Similarly, the typical LBNE data set will provide evidence for a particular mass ordering by 2030 in the scenario described in Section 9.1, and will exclude the incorrect hypothesis at a high degree of confidence by 2035, over the full range of possible values for δ_{CP}, θ_{23} and the mass ordering itself. In addition to the implications for models of neutrino mass and mixing directly following from this measurement, such a result could take on even greater importance. Should LBNE exclude the normal hierarchy hypothesis, the predicted rate for neutrinoless double-beta decay would then

be high enough so as to be accessible to the next generation of experiments [346]. A positive result from these experiments would provide unambiguous — and exciting — evidence that neutrinos are Majorana particles*, and that the empirical law of lepton number conservation — a law lacking deeper theoretical explanation — is not exact. Such a discovery would indicate that there may be heavier sterile right-handed neutrinos that mix with ordinary neutrinos, giving rise to the tiny observed neutrino masses as proposed by the seesaw mechanism [67]. On the other hand, a rejection of the normal neutrino mass hierarchy by LBNE coupled with a null result from the next generation of neutrinoless double-beta decay experiments would lead to the conclusion that neutrinos are purely Dirac particles. This would be a profound and astonishing realization, since it is extremely difficult theoretically to explain the tiny masses of Dirac neutrinos. High-precision neutrino oscillation measurements carried out by LBNE beyond 2035 may provide evidence for Majorana neutrino mass effects that are outside of the ordinary Higgs mechanism or for new interactions that differentiate the various neutrino species.

Within the program of underground physics, LBNE's most exciting milestones would correspond to observations of rare events. By 2035, LBNE will have been live for galactic supernova neutrino bursts for ten years in the above scenario. Such an event would provide a spectacular data set that would likely be studied for years and even decades to follow.

For proton decay, the net exposure obtained by 2035 in the above scenario also provides a compelling opportunity. A partial lifetime for $p \rightarrow K^{+}\overline{\nu}$ of 1×10^{34} years, beyond the current limit from Super-Kamiokande by roughly a factor of two, would correspond to six candidate events in LBNE by 2035, with 0.25 background events expected. Running for seven more years would double this sample. (Similarly, one should not ignore the corresponding value of an LBNE construction scenario that has a larger detector mass operating from the start, in 2025). With careful study of backgrounds, it may also be possible to suppress them further and/or relax fiducial cuts to gain further in sensitivity.

Finally, the proposed high-resolution near detector, operating in the high-intensity LBNE neutrino beam, will not only constrain the systematic errors that affect the oscillation physics but will also conduct precise and comprehensive measurements of neutrino interactions — from cross sections to electroweak constants.

9.3 Uniqueness of Opportunity

Considering the time and overall effort taken to reach the current state of development of LBNE, it will be challenging for alternative programs of similarly ambitious scope to begin operation before 2025, particularly in light of the current constrained budget conditions in HEP. It should be noted that similar-cost alternatives for the first phase of LBNE utilizing the existing NuMI beam

*A Majorana particle is an elementary particle that is also its own antiparticle

were considered during the reconfiguration exercise in 2012 [25]. The panel concluded that none of these alternatives presented a path toward an experiment capable of a CP-violation signal of 5σ. Furthermore, a large water Cherenkov far detector option for LBNE was carefully considered prior to selection of the LArTPC technology [347]. While both detector options are capable of satisfying the scientific requirements, the LArTPC was judged to have a better potential for scientific performance while also presenting the attraction of an advanced technological approach.

In the broader context of planned experimental programs with overlapping aims for portions of the LBNE science scope, it must be recognized that progress will be made toward some of these during the period before LBNE operations commence. For example, indications for a preferred neutrino mass ordering may emerge from currently running experiments and/or from dedicated initiatives that can be realized on a shorter timescale. Global fits will continue to be done to capitalize, to the extent possible, on the rich phenomenology of neutrino oscillation physics where disparate effects are intertwined. At the same time, each experimental arena will be subject to its own set of systematic uncertainties and limitations.

It is in this sense that the power of LBNE is especially compelling. LBNE will on its own be able to measure the full suite of neutrino mixing parameters, and with redundancy in some cases. To use the MH example just given, it is notable that LBNE will have sensitivity both with beam and atmospheric neutrinos. Control of the relative $\nu_\mu/\overline{\nu}_\mu$ content of the beam as well as the neutrino energy spectrum itself, provides additional handles and cross-checks absent in other approaches.

9.4 Broader Impacts

9.4.1 Intensity Frontier Leadership

The U.S. HEP community faces serious challenges to maintain its vibrancy in the coming decades. As is currently the case with the LHC, the next-generation energy frontier facility is likely to be sited outside the U.S. It is critical that the U.S. host facilities aimed at pursuing science at the HEP scientific frontiers (Figure 3.1), the lack of which could result in erosion of expertise in key technical and scientific sectors (such as accelerator and beam physics).

LBNE represents a world-class U.S.-based effort to address the science of neutrinos with technologically advanced experimental techniques. By anchoring the U.S. Intensity Frontier program [348], LBNE provides a platform around which to grow and sustain core infrastructure for the community. Development of the Fermilab accelerator systems, in particular, will not only advance progress toward achieving the science goals of LBNE, it will also greatly expand the capability of Fermilab to host other key experimental programs at the Intensity Frontier.

9.4.2 Inspirational Project for a New Generation

Attracting young scientists to the field demands a future that is rich with ground-breaking scientific opportunities. LBNE provides such a future, both in the technical development efforts required and its physics reach. The unparalleled potential of LBNE to address fundamental questions about the nature of our Universe by making high-precision, unambiguous measurements with the ambitious technologies it incorporates will attract the best and brightest scientists of the next generation to the U.S. HEP effort.

A young scientist excited by these prospects can already participate in current experiments — some of which use medium-scale LArTPCs — and make contributions to leading-edge R&D activities that provide important preparation for LBNE, both scientifically and technically.

9.5 Concluding Remarks

Understanding the fundamental nature of fermion flavor, the existence of CP violation in the lepton sector and how this relates to the Baryon Asymmetry of the Universe; knowing whether proton decay occurs and how; and elucidating the dynamics of supernova explosions all stand among the grand scientific questions of our times. The bold approach adopted for LBNE provides the most rapid and cost-effective means of addressing these questions. With the support of the global HEP community, the vision articulated in this document can be realized in a way that maintains the level of excitement for particle physics and the inspirational impact it has in the U.S. and worldwide.

Appendix A LBNE Detector Simulation and Reconstruction

A 10-kt or larger LArTPC far detector fulfills the high-mass requirement for LBNE and provides excellent particle identification with high signal-selection efficiency ($\geq$ 80%) over a wide range of energies. The far detector is described in detail in the LBNE Conceptual Design Report Volume 1 [29] and briefly in Section 3.6 of this document. This appendix summarizes the status of the LBNE LArTPC simulation and reconstruction efforts and their expected performance.

A.1 Far Detector Simulation

A.1.1 Tools and Methods

In the full simulation of the far detector, neutrino interactions are simulated with Geant4 [132] using the LArSoft [220] package. LArSoft is being developed to provide an integrated, experiment-agnostic set of software tools to perform simulation, data reconstruction and analysis for LArTPC neutrino experiments. Individual experiments provide experiment-specific components including a detector geometry description and analysis code, and they contribute to the LArSoft software development itself.

LArSoft is based on *art* [349], an event-processing framework developed and supported by the Fermilab Scientific Computing Division. *Art* is designed to be shared by multiple experiments and is currently used by several intensity frontier experiments, including NOνA, Mu2e, MicroBooNE [350] and ArgoNeuT [351]. The last two have liquid argon TPC-based detectors and thus share many simulation and reconstruction requirements with LBNE. Reconstruction algorithms developed in LArSoft for the ArgoNeuT and MicroBooNE experiments can readily benefit LBNE. Examples of neutrino beam interactions in a LArTPC obtained from the LArSoft package using the MicroBooNE detector geometry are shown in Figure A.1.

The LBNE far detector geometries currently available in LArSoft are the LBNE 10-kt surface detector and the 34-kt underground detector. Also included is geometry for a 35-t prototype that LBNE has constructed at Fermilab*. The LBNE far detector geometry description is generated in a flexible way that allows the simulation of various detector design parameters such as the wire spacing and angles, drift distances, and materials. The photon-detector models are based on the design that uses acrylic bars coated with wavelength-shifting tetraphenyl butadiene (TPB), read out with silicon photomultiplier tubes (SiPMs).

Geant4 is used to simulate particles traveling through the active and inactive detector volumes

*One of the goals of the 35-t prototype is to test key elements of the TPC module design for the 10-kt and 34-kt detectors including the wrapped wire planes and drift distances.

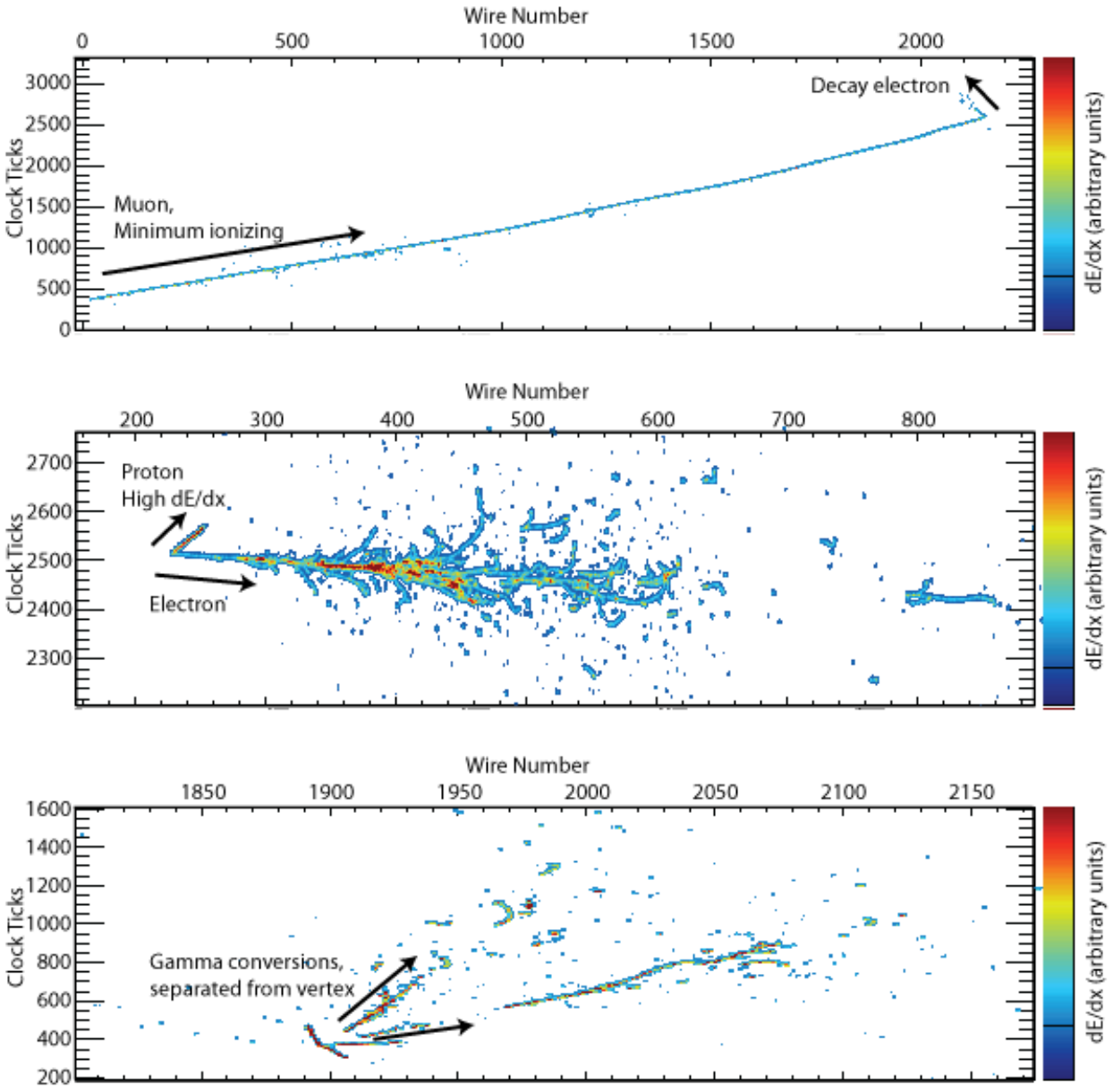

Figure A.1: Examples of neutrino beam interactions in a LArTPC obtained from a Geant4 simulation [220]. A ν_μ-CC interaction with a stopped μ followed by a decay Michel electron (top), a ν_e-CCQE interaction with a single electron and a proton (middle), and an NC interaction which produced a π^0 that then decayed into two γ's with separate conversion vertices (bottom).

and the surrounding materials such as the cryostat and rock. The tens of thousands of photons and electrons produced (by the ionization of the argon) per MeV deposited are simulated using a parameterization rather than a full Geant4 Monte Carlo, as tracking them individually would be prohibitive. The drifting electrons are modeled as many small clouds of charge that diffuse as they travel toward the collection wires. The response of the channels to the drifting electrons is parameterized as a function of drift time, with a separate response function for collection and induction wires. The signals on the induction-plane wires result from induced currents and are thus bipolar as a function of time as charge drifts past the wires, while the signals on the collection-plane wires are unipolar. The response functions include the expected response of the electronics. Noise is simulated using a spectrum measured in the ArgoNeuT detector. The decays of ^{39}Ar are included, but some work is required to make them more realistic.

For the 10-kt far detector, a 1.5-ms readout of the TPC signals at 2 MHz gives a simulated data volume of just under 2 GB per event. If the readout is extended to include the beam window, then in order to collect charge deposited by cosmic rays (which would otherwise be partially contained), a greater data volume will be required. To reduce the data volume and speed up the calculation, long strings of consecutive ADC counts below a settable threshold are suppressed in the readout. Huffman coding of the remaining data is included in the digitization [352].

The photon-detection system likewise requires a full Monte Carlo simulation. Photons propagating from the TPC to the acrylic bars have been fully simulated using Geant4, and their probabilities of striking each bar (as a function of the emission location and the position along the bar at which the photon strikes) have been computed. Smooth parameterizations of these functions are currently used in the simulation to compute the average number of photons expected to strike a bar (as a function of position along it). Given the current design of the optical detectors, approximately 2-3% of VUV (vacuum ultraviolet) photons produced uniformly in the fiducial detector volume strike the bars. This low number is largely due to the small fraction of the total area in contact with the argon that is represented by the bars, and the low reflectivity of the stainless steel cathode planes, the field cage and the CuBe wires.

A second function is used to parameterize the attenuation of light within the bar as a function of position along the bar. The total response of a SiPM to light produced in the detector is the product of the number of photons produced, the probability of the photons to survive propagation, the interaction with the wavelength shifter (commonly called *downconversion*), the attenuation in the bar, and the detection efficiency of the SiPM. This product is used as the mean of a Poisson distribution from which the number of photoelectrons is randomly drawn to simulate the measurement of the SiPM. Measured waveforms for cold SiPMs are used in simulating the digitized response. Measurements in prototype dewars will be used to normalize the yield for signals in the SiPMs as a function of the incident location of the VUV photon on the bar. The NEST [353] model, which describes the conversion of ionization energy into both electrons and photons in an anticorrelated manner, and which has been shown to model a large range of data from noble liquid detectors, is

currently being incorporated into the LBNE detector simulation.

A variety of event generators are available for use in the simulation. Neutrino hard-scattering interactions and subsequent nuclear breakup are simulated using GENIE [133], though the use of other generators is possible. Cosmic rays are simulated with CRY [354]. Single particles can be generated one at a time, and general text-file interfaces are available allowing arbitrary generators to be used without linking them with LArSoft.

Currently, samples of single electrons, muons, charged and neutral pions, protons and tau leptons have been generated and simulated using the 10-kt surface geometry and the 35-ton geometry, though without photon-detector simulation. These samples are being used to develop reconstruction algorithms.

Planned improvements to the simulation include creating an interface to a calibration database, updating the response functions with measured responses from MicroBooNE, which uses an electronics design very similar to that of LBNE, simulating the effects of space-charge buildup in the drift volume, and creating more detailed maps of the drift in the gaps between the APAs and the charge that is deposited between the wire planes.

A.1.2 Low-Energy Neutrino-Response Studies with LArSoft

Work is currently underway using the LArSoft simulation package to characterize low-energy response for realistic LBNE detector configurations. Figure A.2 shows a sample 20-MeV event in the LBNE 35-t prototype geometry simulated with LArSoft. So far, most studies have been done with the MicroBooNE geometry, with the results expected to be generally applicable to the larger LBNE detector. For a preliminary understanding of achievable energy resolution, isotropic and uniform monoenergetic electrons with energies of 5-50 MeV (which should approximate the ν_e-CC electron products) were simulated and reconstructed with the LArSoft package. The charge of reconstructed hits on the collection plane was used to reconstruct the energy of the primary electrons. (Induction-plane charge as well as track-length-based reconstruction were also considered, but with inferior results). Figure A.3 shows the results. A correction to compensate for loss of electrons during drift, $Q_{collection} = Q_{production} \times e^{-T_{\rm drift}/T_{\rm electron}}$ (where T_{drift} is the drift time of the ionization electrons, and $T_{electron}$ is the electron lifetime), using Monte Carlo truth to evaluate $T_{\rm drift}$, improved resolution significantly. This study indicated that photon time information will be valuable for low-energy event reconstruction. Some of the resolution was determined to be due to imperfect hit-finding by the nominal reconstruction software. A tuned hit-finding algorithm did somewhat better (Figure A.3), and further improvements for reconstruction algorithms optimized for low-energy events are expected.

Also under study is the potential for tagging ν_e-CC absorption events ($\nu_e + {}^{40}\mathrm{Ar} \rightarrow e^- + {}^{40}\mathrm{K}^*$) using the cascade of de-excitation γ rays, which should serve the dual purposes of rejecting background and isolating the CC component of the signal.

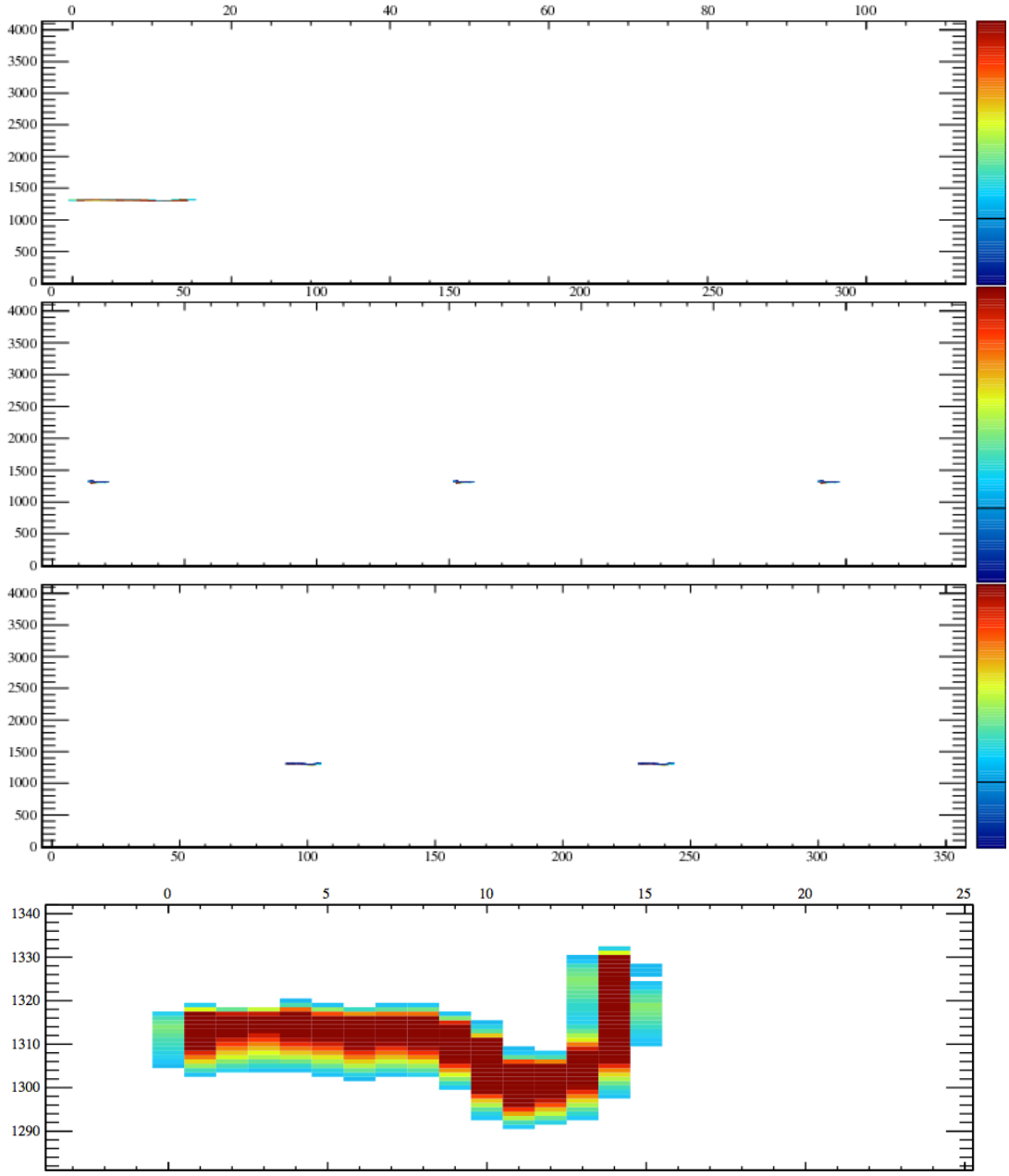

Figure A.2: Raw event display of a simulated 20-MeV event in the LBNE 35-t prototype; the top panel shows the collection plane, and the lower two panels show the induction planes (with multiple images due to wire wrapping). The bottom panel shows a zoom of the collection plane image.

A.2 Far Detector Reconstruction

The first stage of reconstruction of TPC data is unpacking and deconvoluting the electronics and field response of the wire planes. The deconvolution function includes a noise filter that currently is parameterized with ArgoNeuT's noise, but will be tuned for the eventual noise observed in the

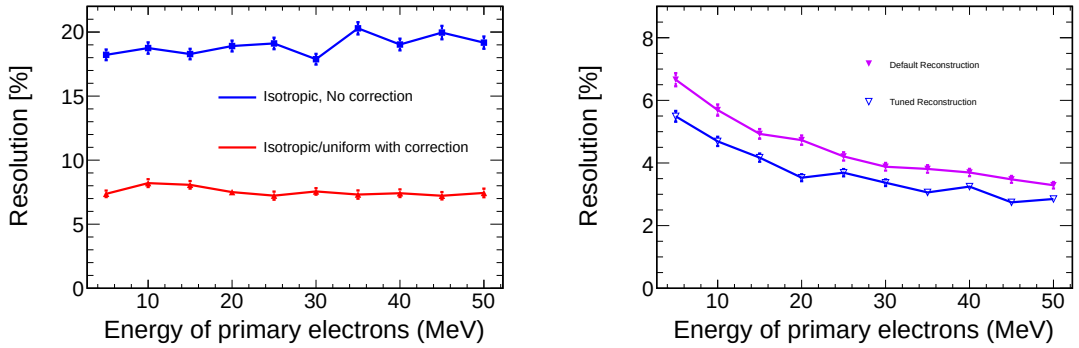

Figure A.3: Left: Comparison of energy resolution (defined as σ/E, where σ is the spread of the collection-plane-charge-based event energy E for a monoenergetic electron), with and without electron-lifetime correction, as a function of electron energy. The blue curve is the energy resolution of isotropic and uniform electrons without electron-lifetime correction. The red curve is the energy resolution with electron-lifetime correction based on MC truth. Right: Comparison of energy resolution before and after tuning the reconstruction algorithm (for fixed position/direction electron events).

LBNE detector. The deconvolution makes sharp, unipolar pulses from the bipolar induction-plane signals and also sharpens the response to collection-plane signals. Hits are then identified in the deconvoluted signals by fitting Gaussian functions, allowing for sums of several overlapping hits in each cluster. In LBNE, because of the large quantity of channels in the far detector, any inefficiency in CPU and memory is magnified. Improvements in the memory-usage efficiency relative to the ArgoNeuT and MicroBooNE implementations have been realized by rearrangement of the processing order and limiting the storage of the intermediate uncompressed raw data and the deconvoluted waveforms.

After signal deconvolution, line-finding and clustering based on a Hough transform in two dimensions is done using an algorithm called *fuzzy clustering* [355]. This clustering is performed separately on data from each induction plane. Since the hit data on LArTPCs are inherently 2D — wire number and arrival time of the charge — the location of the initial ionization point has a 2D ambiguity if the deposition time is unknown. For beam events, the t_0 is known, and thus only a 1D ambiguity remains; this 1D ambiguity is broken by angling the induction-plane wires relative to the collection-plane wires, in order to measure the y location of the hits for which t (thus x) and z are known. For (non-beam) cosmic-ray signals which arrive uniformly in time, the photon system provides t_0. After clustering, 3D track-fitting is performed using a Kalman filter [356]. Dedicated algorithms have been developed to optimize electromagnetic shower reconstruction and energy resolution.

LBNE poses a unique challenge for reconstruction because the induction-plane wires wrap around the edges of the APA frames. This introduces discrete ambiguities that are not present in other LArTPC designs. Whereas a hit on a collection-plane wire identifies uniquely the side of the APA from which it came, this is not known for a hit on an induction-plane wire. The angles between

the U and V plane wires are slightly different from 45° and from each other in order to break the ambiguities. A combinatoric issue arises, however, if many hits arrive on different wires at nearly the same time, for instance when a track, or even a track segment, propagates in a plane parallel to the wire planes (i.e., at constant drift distance). Showers will also contain many hits on different wires that arrive at similar times. Hits that arrive at different times can be clustered separately in the Z, U, and V views without ambiguity, while hits that arrive at similar times must be associated using a topological pattern-recognition technique. LBNE is developing a version of the fuzzy clustering tool for use as a pattern-recognition step to allow association of Z, U and V hits, a step that is needed to assign the correct y position to a track segment or portion of a cluster. This process is called *disambiguation* of the induction hits. Misassignment can affect particle-ID performance and reconstructed-energy resolution because fully contained tracks may appear partially contained and vice versa. After disambiguation has been performed, standard track, vertex and cluster reconstruction algorithms are applied.

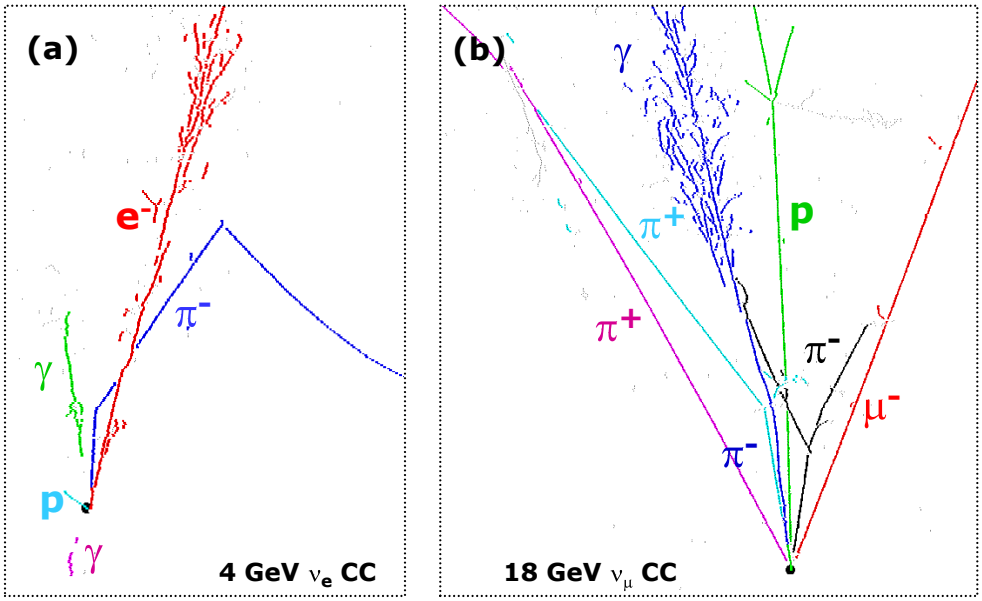

Figure A.4: PANDORA's 2D clusterings of hits created by the particles in two CC neutrino interactions in liquid argon. Panel (a) shows a 4-GeV ν_e interaction, and panel (b) shows an 18-GeV ν_μ interaction. The colors indicate the clusters into which PANDORA has divided the hits, and the particle labels are from the MC truth.

A promising suite of algorithms for event reconstruction is provided by the PANDORA toolkit [357], which provides a framework for reconstruction algorithms and visualization tools. Currently it is being used to develop pattern-recognition algorithms and to reconstruct primary vertices. PANDORA's pattern-recognition algorithm merges hits based on proximity and pointing to form 2D clusters. Vertices are then identified from the clusters that best connect to the same event. Clusters that best correspond to particles emitted from the primary vertex are identified in 2D. These

particle candidates are then used to seed 3D reconstructed particles, and a 3D primary vertex is identified. Examples of PANDORA's 2D clustering are shown in Figure A.4 for two simulated CC neutrino-scattering events. Figure A.5 shows the primary vertex spatial resolution in 3D with well-contained simulated beam-neutrino events, using the nominal LBNE spectrum and MicroBooNE geometry.

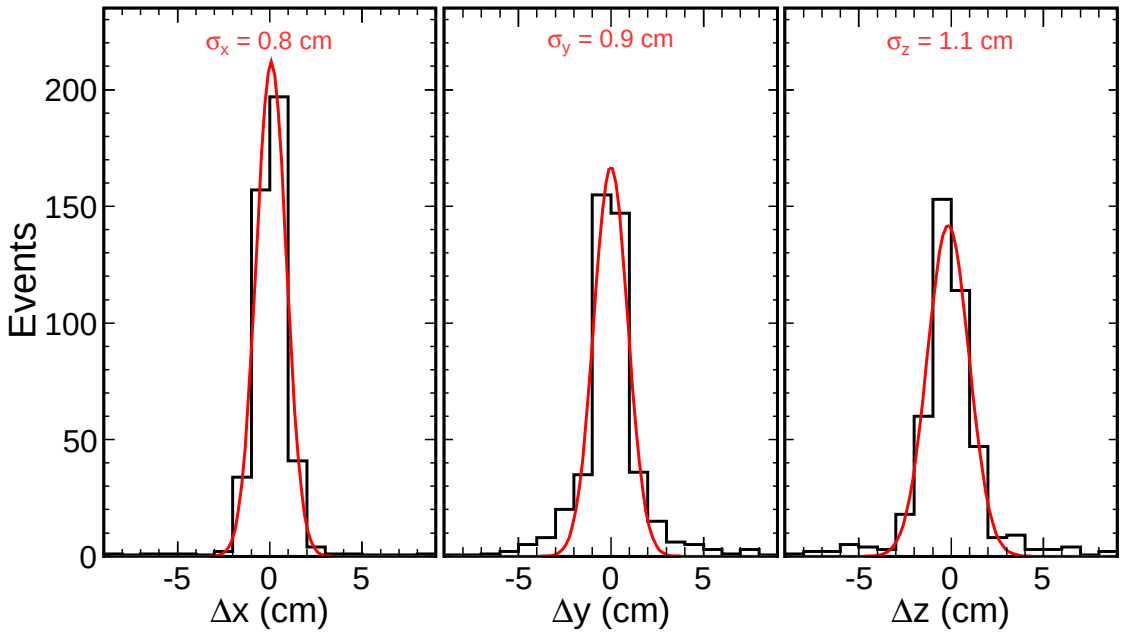

Figure A.5: Distributions of the residuals between the reconstructed and the Monte Carlo true locations of primary vertices in neutrino interactions in the MicroBooNE geometry using the LBNE beam spectrum. The x axis is oriented along the drift field, the y axis is parallel to the collection-plane wires, and the z axis points along the beam direction.

A.3 Fast Monte Carlo

The LBNE full Monte Carlo (MC) simulation will use a Geant4 simulation of the beamline to estimate the neutrino flux, a neutrino interaction generator (e.g., GENIE), and detailed detector simulation that mimics the real detector output for data events. Both data and MC will have the same reconstruction algorithms applied to produce quantities that will be used to analyze the data. The full MC detector simulation and reconstruction algorithms are still under development. Due to their detailed nature, these algorithms are CPU-intensive and time-consuming to run.

In parallel, a Fast Monte Carlo simulation has been developed and is available for use in place of the full MC to explore long-baseline physics analysis topics. A preliminary version of the Fast MC is currently available. Results from the latest detector simulations and advancements in reconstruction algorithms are actively being incorporated to improve the physics models and detector

parameterization. Because the Fast MC replaces CPU-intensive portions of the full MC simulation with a fast parameterized model, it offers a quick, dynamic alternative which is useful for trying out new ideas before implementing them in the full MC. This usefulness is expected to remain even after the full MC simulation is mature.

To accurately approximate a full MC simulation, the Fast MC combines the Geant4 LBNE beamline flux predictions, the GENIE event interaction generator, and a parameterized detector response that is used to simulate the measured (reconstructed) energy and momentum of each final-state particle. The simulated energy deposition of the particles in each interaction is then used to calculate reconstructed kinematic quantities (e.g., the neutrino energy), and classify the type of neutrino interaction, including backgrounds and misidentified interactions.

The Fast MC is designed primarily to perform detailed sensitivity studies that allow for the propagation of realistic systematic uncertainties. It incorporates effects due to choices of models and their uncertainties and design decisions and tolerances. The neutrino flux predictions, the neutrino-interaction cross-section models, and the uncertainties related to these are also incorporated. The parameterized detector response is informed by Geant4 simulations of particle trajectories in liquid argon, by studies of detector response simulation in MicroBooNE [350], results reported by the ICARUS Collaboration, and by the expected LBNE detector geometry. The realistic parameterization of reconstructed energy and angle resolution, missing energy, and detector and particle identification acceptances provide a simulation that respects the physics and kinematics of the interaction and allows for propagation of model changes to final-state reconstructed quantities.

Future efforts will allow for propagation of uncertainties in detector effects and of detector design choices. It should be noted that the same GENIE files generated for the Fast MC can be used as inputs for the full detector simulation and the results of the two simulations can be compared both on an event-by-event basis and in aggregate. Studies of this nature can be used to tune the Fast MC and to cross-check the full simulations.

In the current configuration of the Fast MC, GENIE generates interactions on ^{40}Ar nuclei with neutrinos selected from the energy spectra predicted by the Collaboration's Geant4 flux simulations (described in Section 3.4). For each interaction simulated in GENIE, a record of the interaction process, its initial kinematics, and the identity and four-momenta of the final-state particles is produced. The parameterized detector response applies spatial and energy/momentum smearing to each of the final-state particles based on the particle properties and encoded detector-response parameters. Detection thresholds are applied to determine if a final-state particle will deposit energy in the detector and if that energy deposition will allow for particle identification. The detector responses for neutrons and charged pions account for a variety of possible outcomes that describe the way these particles deposit energy in the detector. Neutral pions are decayed into two photons. Their conversion distance from the point of decay determines the starting position of the resulting electromagnetic showers. This distance is chosen from an exponential distribution with a characteristic length based on the radiation length of photons in liquid argon. Tau leptons are also decayed

by the Fast MC and their decay products are dealt with appropriately. The spatial extent of tracks and showers in liquid argon is simulated in Geant4 and encoded as a probability distribution function (PDF) or parameterization. Combined with vertex placement in a fiducial volume, the fraction of particle energy and/or track length visible in the detector is determined.

Once the Fast MC reconstructs the kinematics of the event (E_ν, E_{had}, Q^2, x, y, and so on), based on the smeared four-vectors of particles that are above detection threshold, it searches interaction final-state particle lists for lepton candidates to be used in event classification algorithms. The resulting classifications are used to isolate samples for the ν_e appearance and the ν_μ disappearance analyses which are in turn used to build energy spectra on an event-by-event basis.

Currently the classification algorithm categorizes each event as either ν_e-CC, ν_μ-CC, or NC. Events with a candidate muon are classified as ν_μ-CC. Events without a candidate muon, but with a candidate electron/positron are classified as ν_e-CC. Events without a candidate muon or a candidate electron/positron are classified as NC. A ν_τ-CC classification, which would identify ν_τ candidates is under development.

A muon candidate is defined as a MIP-like track that is greater than 2.0 m long, and is not consistent with the behavior of a charged pion. Charged pions will often *shower*, depositing a relatively large amount of energy in the detector at the end of its track, as compared to a muon. There are several situations in which a pion topology will be indistinguishable from a muon: (1) the pion stops at the end of its range without interacting, (2) the kinetic energy of the pion is sufficiently small when is showers, (3) the pion is absorbed cleanly by a nucleus with no hadronic debris, (4) the pion decays in flight, and (5) the track exists the detector. The 2.0-m cut was chosen because the probability of (1) or (2) is very small for pion tracks above this threshold.

An additional selection probability is enforced for low-energy tracks to simulate acceptance losses due to increased difficulty in particle identification for short tracks, especially in high-multiplicity events. (The falling edge of the selection probability is well below the energy required to generate a 2.0-m track, minimizing the effect of this criterion.)

An electron candidate is defined as the highest-momentum electromagnetic (EM) shower in an event that is not consistent with a photon. An EM shower is identified as a photon (1) if it converts 2.0 cm or more from the event vertex, (2) if it can be matched with another EM shower in the events to reconstruct the π^0 mass (135 ± 40 MeV), or (3) if dE/dx information from the first several planes of the track is more photon-like than e$\pm$-like. The latter is determined on a probabilistic basis as a function of EM-shower energy and hadronic-shower multiplicity. Signal and background efficiencies from the dE/dx e/γ discriminant are based on MicroBooNE simulations. Cut values are tuned to preserve 95% of the signal across all neutrino energies. As with muon candidates a low-energy selection probability is enforced to account for acceptance losses at low EM-shower energies, especially in high-multiplicity events. For the electron candidates this selection probability is tuned to agree with hand scan studies.

An event with no muon candidate and no electron candidate is assumed to be an NC interaction. Preliminary studies evaluating the use of transverse-momentum imbalance to identify ν_τ-CC interaction candidates have shown promising results for identifying NC candidates as well, and are likely to be included in the near future.

Currently no attempt is made to identify tau lepton candidates in order to isolate a ν_τ-CC sample. A preliminary algorithm to remove $\tau \to \mu + \nu + \nu$ and $\tau \to e + \nu + \nu$ backgrounds has recently been incorporated in the Fast MC. This algorithm may also prove useful for isolating a sample of ν_τ-CC interactions, in which the tau decays to a lepton. Development of an algorithm to identify taus that decay to hadrons is under discussion.

All of the selection criteria can easily be updated to reflect improved simulations or new understanding of particle-identification capabilities and analysis sample acceptances. Changes can also be made to investigate alternate analysis techniques, or more conservative or optimistic assumptions on signal acceptance and/or background-rejection rates. Furthermore, the information required to simulate effects related to particle identification is available in the Fast MC files and users are encouraged to construct and evaluate their own selection criteria.

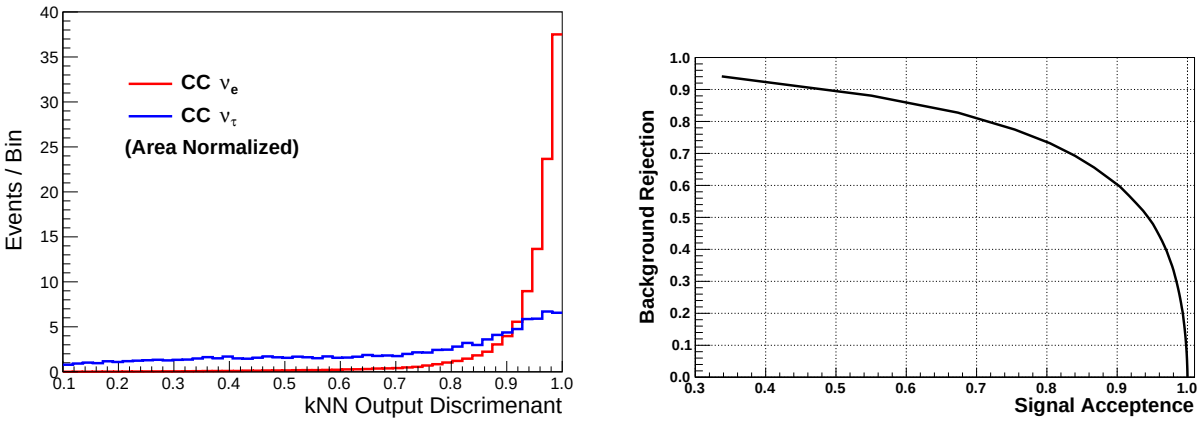

Figure A.6: The output discriminant of a kNN (left) created to remove ν_τ-CC-induced backgrounds from the $\nu_\mu \to \nu_e$ oscillation analysis sample. Signal events (red) tend toward high values, while the ν_τ-CC-induced background events (blue) are more evenly distributed. The fraction of ν_τ-CC-induced backgrounds removed from the $\nu_\mu \to \nu_e$ appearance candidate sample as a function of the corresponding signal efficiency (right). The curve is generated by varying the cut value on the kNN discriminant.

A preliminary algorithm for removing ν_τ-CC-induced backgrounds from from the ν_μ-CC and the ν_e-CC samples has been developed. It employs a k-Nearest Neighbor (kNN) machine-learning technique as implemented in the ROOT TMVA package. The inputs to the kNN are (1) the sum of the transverse momentum with respect to the incoming neutrino direction, (2) the reconstructed energy of the incoming neutrino, and (3) the reconstructed energy of the resulting hadronic shower. Figure A.6 (right) shows the distribution of the output discriminant for true ν_e-CC signal events, and for true ν_τ-CC-induced backgrounds. The algorithm is still being optimized but initial results are promising.

As can be seen in Figure A.6 (left), cuts on the discriminant that preserve 90% of the signal remove roughly 60% of the ν_τ-CC-induced background in the ν_e-CC sample. Similar results are expected for the ν_τ-CC-induced background in the ν_μ-CC sample.

A similar approach is being studied to isolate the ν_τ-CC sample for the ν_τ-CC appearance analysis. Current efforts are focused on identifying a set of reconstructed quantities that separate ν_τ-CC interactions from potential backgrounds. For leptonic decay channels the quantities used in the above kNN are prime candidates. Attempts to reconstruct a ρ mass from tracks originating at the vertex are expected to help to isolate hadronic τ decays. The parameterized pion response will allow for selection of high-energy charged pions produced in hadronic τ decays.

Figures A.7 and A.8 show the Fast MC reconstructed energy spectra of the signal and background for the ν_e appearance and the ν_μ disappearance samples, respectively. As an example of the cross-section and nuclear-effect systematics that can be studied, the black histograms and the bottom insert in each plot show the variation of the spectrum for each event type induced by changing the value of CC M_A^{res} by +1σ (+15%, 2014 GENIE official uncertainty). CC M_A^{res} is the axial mass parameter appearing in the axial form factor describing resonance production interactions in GENIE. This particular example demonstrates a spectral distortion that is not a simple normalization and is different for signal and for background. The effect of varying CC M_A^{res} on the $\nu_\mu \to \nu_e$ analysis sample exhibits a strong correlation with the changes induced in the $\nu_\mu \to \nu_\mu$ analysis sample.

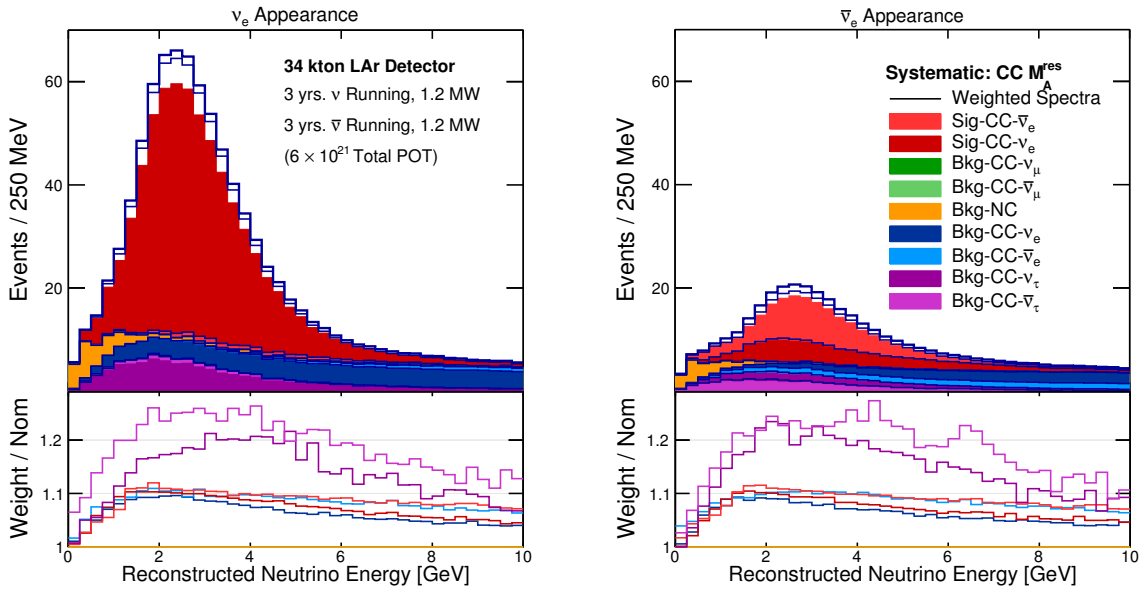

Figure A.7: The reconstructed energy distributions for the signals and backgrounds in the ν_e- (left) and $\overline{\nu}_e$ appearance (right) samples, as predicted by the Fast MC. The black histograms and bottom insert in each plot shows, for each event type, the variation in the spectrum that is induced by changing the value of CC M_A^{res} by +15%.

The left-hand plots of Figures A.9 and A.10 show the acceptance (efficiency) of the signal and the background for the Fast MC ν_e appearance and ν_μ disappearance selections, respectively. The

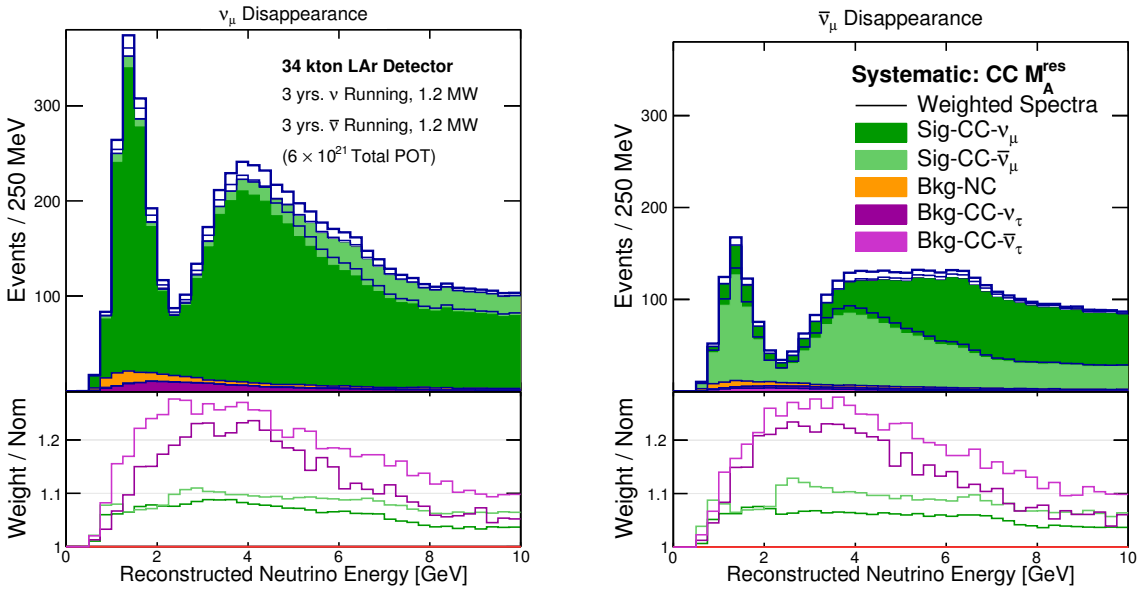

Figure A.8: The reconstructed energy distributions for the signals and backgrounds in the ν_μ (left) and $\overline{\nu}_\mu$ disappearance (right) samples, as predicted by the Fast MC. The black histograms and bottom insert in each plot shows, for each event type, the variation in the spectrum that is induced by changing the value of CC M_A^{res} by +15%.

effects of the low-energy selection probabilities induce the observed low-energy fall off in the ν_e appearance sample. On the other hand, the 2.0-m track length requirement is mainly responsible for the low-energy behavior in the ν_μ disappearance sample. The corresponding plots on the right-hand side show the relative fraction (purity) of the signal and each background sample for the Fast MC ν_e appearance and ν_μ disappearance selections. The increased wrong-sign contamination is evident in the $\overline{\nu}$ beam samples as compared to the ν beam samples. No attempt has been made to reduce the ν_τ background in these plots.

The output of the Fast MC is a file containing the information one would expect from a full MC simulation. There are truth level quantities that describe the generated event, and reconstructed quantities that are calculated from simulated observables. The latter mimic the information that is expected to be available from reconstructing data or full simulation and can be used in designing analyses aimed at measuring physics parameters. Analyses based on the simulated reconstruction produce event samples that can be used to estimate the sensitivity of LBNE to physics model parameters, specifically the parameters of the PMNS matrix, as a function of a variety of input parameters. Currently these studies are done using the GLoBES [130] software package. However, instead of constructing the event-rate spectra as a function of true neutrino energy from predictions of the flux and neutrino-interaction cross sections, they are built event-by-event from the Fast MC. Similarly, smearing functions that give the distribution of measured (reconstructed) neutrino energies as a function of the true neutrino energy are built event-by-event from the Fast MC, rather than estimated from external sources.

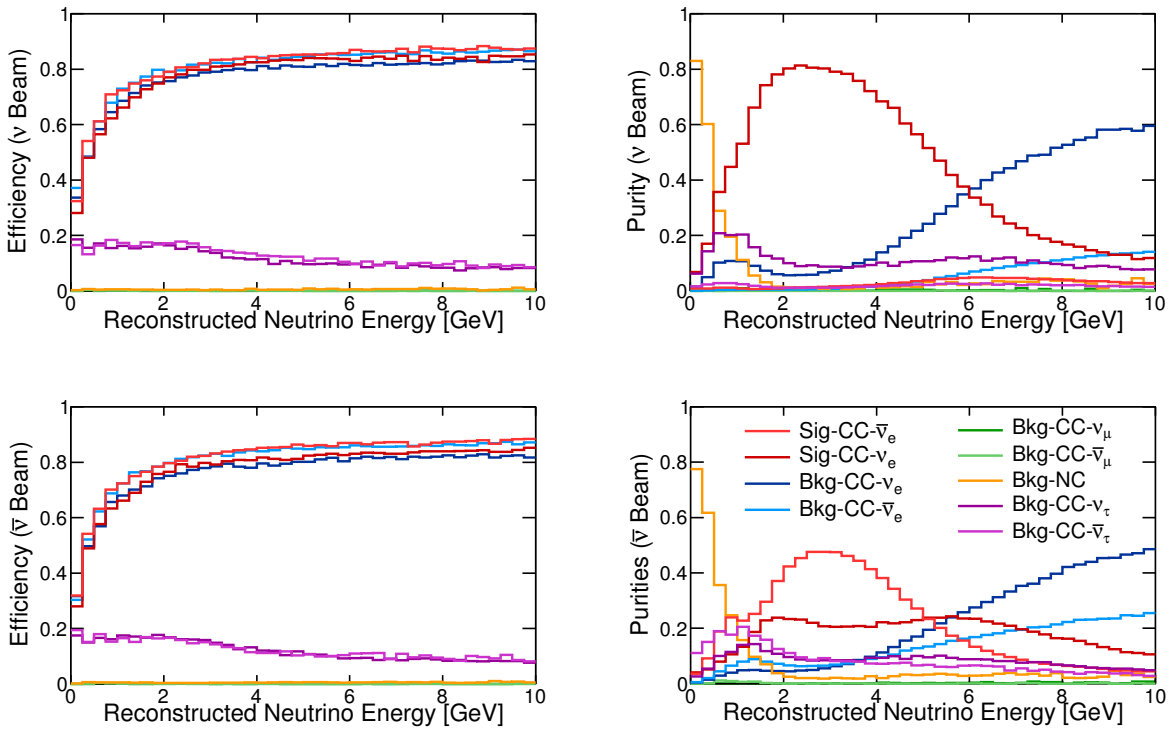

Figure A.9: The expected efficiencies and purities of selecting ν_e appearance events in a LArTPC, obtained from the Fast MC.

In addition to the usual GLoBES inputs the Fast MC can provide systematic uncertainty response functions, which encode the expected changes to the energy spectra when input model parameters are varied within their uncertainties. These response functions, along with an augmented version of GLoBES, can be used to propagate realistic systematic uncertainties in sensitivity studies.

The systematic uncertainty response functions are calculated from weights stored in the Fast MC output files. Each weight corresponds to the probability of producing the event with an alternate physics model relative to the model used. Currently the Fast MC generates weights for parameters in interaction models that can be reweighted in GENIE as well as a variety of parameters related to the neutrino flux. The flux parameters come in three varieties related to: changes to the beamline design, tolerances in the beamline design, and uncertainties in the physics models used in the simulations. The latter two contribute to systematic uncertainties while the first can be used to evaluate the impact of design optimizations.

Propagation of systematic uncertainties through LBNE sensitivity studies using the Fast MC will require inclusion of new algorithms and improvements to existing reweighting algorithms. This includes (1) the introduction of new models into GENIE, (2) adding to and improving the reweighting functions currently in GENIE, (3) constructing flux files that correspond to the changes in the three aforementioned categories, (4) implementing a system for reweighting individual events based on

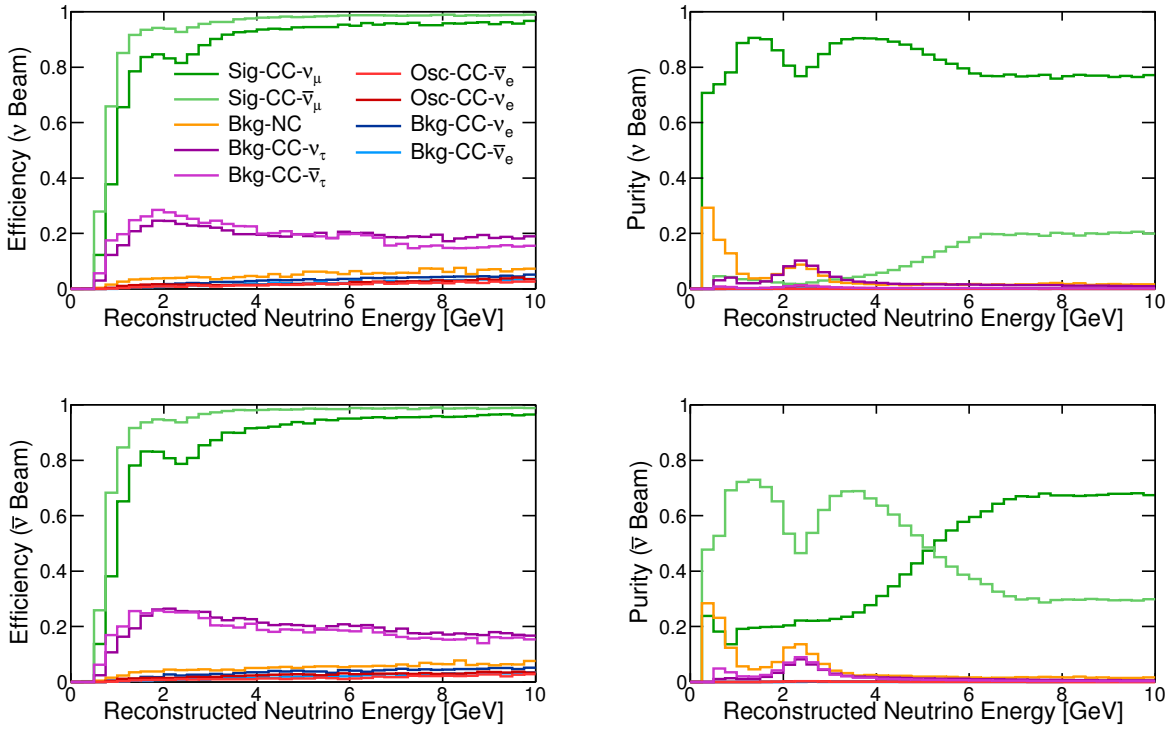

Figure A.10: The expected efficiencies and purities of selecting ν_μ disappearance events in a LArTPC obtained from the Fast MC.

changes to the models of hadronization from proton-target interactions, and (5) introducing detector parameterizations representing alternate detector designs, detector design tolerances, and model choices used in detector simulations.

The current focus of Fast MC studies is estimation of the effect of model uncertainties on sensitivity projections. This includes several steps, the first of which is to look at the changes in the analysis sample spectra induced by propagating individual systematic uncertainties. These studies are benchmarked by calculating the χ^2 between the nominal and altered spectra. In the second step, sensitivities are calculated for combined fits of the four main analysis samples ($\nu_\mu/\overline{\nu}_\mu$ disappearance, $\nu_e/\overline{\nu}_e$ appearance). These studies must be done carefully to allow for realistic constraints of systematic uncertainties across analysis samples within GLoBES. Input covariance matrices can also be used to enforce external constraints on the relations between sources of systematic uncertainty. The results of these studies will inform the investigators as to which model uncertainties cause significant degradation of the sensitivities and therefore must be constrained by other methods. Methods to constrain these parameters will be sought from currently running experiments, proposed intermediate experiments, and from the LBNE beam monitoring and the LBNE near detector. Estimates of these constraints can then be propagated to sensitivity calculations to estimate the degree to which they mitigate the decline in sensitivity.

Current studies focus on propagating uncertainties in flux and GENIE model parameters via reweighting techniques. A example study shown in Figure A.11 illustrates the effect of including the uncertainty on CC M_A^{res} in the calculation of sensitivity to CP violation. The sensitivity studies are performed for (1) a fit to the ν_e appearance sample (three years of ν-beam running), (2) a combined fit of the ν_e appearance sample and the $\overline{\nu}_e$ appearance sample (three years of ν-beam plus three years of $\overline{\nu}$-beam running), and (3) a combined fit of the $\nu_e/\overline{\nu}_e$ appearance samples along with the corresponding $\nu_\mu/\overline{\nu}_\mu$ disappearance samples. All three studies are done in two ways: with no allowance for non-oscillation parameter systematic variation, and with allowed 15% (width gaussian PDF) variations in CC M_A^{res}.

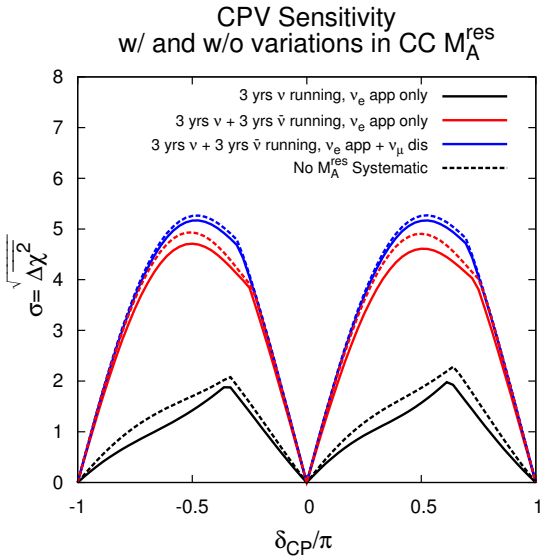

Figure A.11: The sensitivity to CP violation calculated using the energy spectra generated by the Fast MC. The sensitivities were generated with (solid) and without (dashed) allowed variations in the CC M_A^{res} resonance production model parameter in GENIE. The allowed variation degrades the sensitivity, however combined fits of multiple analysis samples provide additional constraints and reduce the impact.

As Figure A.11 shows, the inclusion of allowed variations in CC M_A^{res} degrades the sensitivity. However, combined fits of multiple analysis samples provide additional constraints and reduce the impact. The effect of these sample-to-sample constraints is dependent on the sample statistics, and the curves in Figure A.11 include the statistical limitations on sample-to-sample constraints from a six-year (three years ν + three years $\overline{\nu}$ running) exposure. However, the software also allows for the inclusion of other possible limitations on sample-to-sample constraints related to the relative lack of experimental constraints on cross-section ratios (i.e., $\sigma_{\nu_e}/\sigma_{\nu_\mu}$, $\sigma_{\nu_\tau}/\sigma_{\nu_\mu}$, and $\sigma_{\overline{\nu}}/\sigma_{\nu}$), as well as theoretical considerations.

The preliminary Fast MC spectra shown in Figures A.7 and A.8 were generated with a different beam configuration than the ones shown in Figures 4.2 and 4.3. Consequently, the sensitivities to CPV shown in Figure A.11 cannot be directly compared to the corresponding figures in Section 4.2.

However, both the Fast MC and the methods discussed in Section 4.2 have been used to generate comparable spectra and to perform a series of sensitivity studies. The two methods are consistent, except regarding known differences between the two simulations, e.g., the inclusion of ν_τ-CC-induced backgrounds. These differences are well understood, as are their impact on oscillation parameter sensitivities.

Eventually the Fast MC seeks to incorporate near detector and atmospheric-neutrino analyses and directly perform combined fits with the long-baseline neutrino analysis samples. These studies will provide the most accurate estimate of the ultimate sensitivity of LBNE, and provide a template for future data analysis procedures.

A.4 Simulation of Cosmic-Ray Background for a 10-kt Surface Detector

A preliminary study of the background events expected from cosmic rays in the 10-kt far detector installed near the surface at the Sanford Underground Research Facility is detailed in [226]. The study simulated cosmic-ray interactions in the far detector and focused on cosmic-ray induced events from neutrons and muons that mimic electron-neutrino interactions in the detector. These include electromagnetic cascades from knock-on electrons, muon bremsstrahlung, and hadronic cascades with electromagnetic components from photons and π^0's. The background from decays of neutral hadrons into electrons such as $K^0_L \to \pi e \nu$ were also studied. The energy of the cascades was required to be > 0.1 GeV.

These initial studies indicate that a combination of simple kinematic and beam timing cuts will help to significantly reduce the cosmic-ray background event rate in this far detector configuration. In particular:

1. Only electromagnetic cascades with energies greater than 0.25 GeV are considered background. For the neutrino oscillation sensitivity calculations, only neutrino energies ≥ 0.5 GeV are considered.

2. $e^\pm$ background candidates are tracked back to the parent muon; the distance between the muon track and the point-of-closest-approach (PoCA) to the muon track is required to be > 10 cm.

3. The vertex of the $e^\pm$ shower is required to be within the fiducial volume of the detector (defined as 30 cm from the edge of the active detector volume).

4. The $e^\pm$ cascade is required to be within a cone around the beam direction (determined from the angular distribution of the beam signal $e^\pm$ and the incoming neutrino beam).

5. It is assumed that EM showers initiated by γ's and $\pi^0 \to \gamma\gamma$ can be effectively distinguished from primary electron interactions using particle ID techniques such as dE/dX.

6. Events are timed with a precision of $\leq$1 µs using the photon-detection system, which limits background to events occurring within the 10 µs of the beam spill.

The result of applying these selection criteria to the electromagnetic showers initiated by cosmic rays is summarized in Table A.1 and Figure A.12. The background rates given in Table A.1 include the recalculation for the cosmic flux at 1,500 m above sea level, which was not included in the previous study [226] (and is not included in Figure A.12). In the table, the initial background event rate is calculated for one calendar year assuming a 1.4-ms drift time per beam pulse, a beam pulse every 1.33 seconds and 2×10^7 s/year of running. The expected event rate/yr after various selection criteria is applied from left to right in the table. The rates in all columns except the last are given for a time window of 1.4 ms, corresponding to the maximum electron drift time. The last column shows the rate reduction assuming an efficient photon-detection system. The first three rows show events with a muon in the detector where a PoCA cut (column 3) can be applied. The row labeled 'Missing μ' shows events without a muon in the detector; as there is no muon track, a PoCA cut can not be applied. The detector is assumed to be on the surface with three meters of rock overburden.

Table A.1: Cosmic-ray-induced background (at 1,500 m above sea level) to the beam ν_e-CC signal in the 10-kt detector.

Processes	**$E_e > 0.25$ GeV**	**PoCA > 10 cm and D > 30 cm**	**Beam angle**	**e/γ PID**	**Beam timing**
$\pi^0 \to \gamma \to e^\pm$	2.2×10^6	9.7×10^4	4.8×10^4	1.7×10^3	12
$\mu \to \gamma \to e^\pm$	7.1×10^6	12	0	0	< 0.003
Ext $\gamma \to e^\pm$	1.9×10^6	660	340	13	0.1
$\pi^0, K^0 \to e^\pm$	1.4×10^6	810	240	240	1.7
Missing μ	1.3×10^6	1.8×10^3	580	20	0.1
Atm n	2.9×10^6	1.6×10^4	6.5×10^2	240	1.7
Total	**1.1×10^7**	**1.2×10^5**	**5.6×10^4**	**2.2×10^3**	**16**

The dominant background is from $\pi^0 \to \gamma \to e^\pm$, which contributes 12 out of the 16 total events per year and comes from π^0's originating in cosmic showers. The study does not yet include specific π^0 reconstruction, only individual e/γ separation. More sophisticated reconstruction techniques should further reduce the π^0 background. The studies indicate that application of these selection criteria coupled with a more detailed background event reconstruction can potentially reduce the background from cosmic rays to a few events per year — mostly in the energy region < 1 GeV.

In Figure A.12, black-filled circles show events before any cuts are applied. The other point icons represent successively applied cuts in the order listed below and in the figure's legend:

1. Blue squares: PoCA to the muon track greater than 30 cm
2. Red triangles: angle with respect to the beam such that 99% of signal events are retained
3. Green triangles: application of energy-dependent e/γ discrimination
4. Magenta open circles: application of efficient photon detection, this allows the reduction of the time window from a maximum drift time of 1.4 ms down to a beam spill of 10 µs

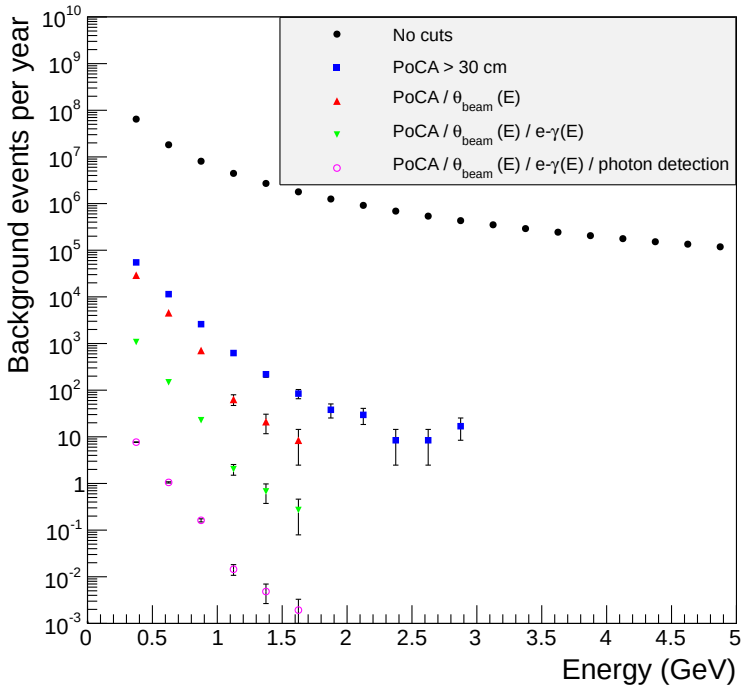

Figure A.12: Energy spectra of muon-induced background events for successively applied background rejection cuts. Simulations have been done for a muon spectrum at sea level. Correction for an altitude of 1,500 m above sea level has not been applied to the data.

Appendix B Neutrino-Nucleon Scattering Kinematics

The following explanation of neutrino-nucleon scattering kinematics is adapted from [358]:

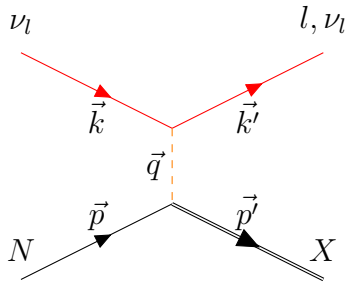

Figure B.1: A schematic diagram of a neutrino-nucleon scattering process

The expression $\nu_l + N \longrightarrow l, \nu_l + X$ describes the scattering of a neutrino, ν_l off a nucleon, N as shown in Figure B.1. This interaction proceeds through the exchange of a $W^{\pm}$ or Z^0 boson, depending on whether it is a CC or NC interaction, respectively. For the case of neutrino scattering, the incoming lepton is a neutrino and the outgoing lepton is either a neutrino (NC) or a charged lepton, l (CC). X denotes the resultant hadronic system.

The nucleon mass, M, is neglected where appropriate; the lepton mass is neglected throughout. The following kinematic variables describe the momenta and energies involved in the scattering process:

- $\vec{k}, \vec{k'}$ are the four-momenta of the incoming and outgoing lepton.
- $\vec{p}$ is the initial four-momentum of the nucleon.
- E_ν is the energy of the incoming neutrino.
- E_N is the energy of the nucleon.

The Lorentz invariants are the following:

- The squared ν+N collision energy is $s = (|\vec{p} + \vec{k}|)^2 = 4E_N E_\nu$.
- The squared momentum transfer to the lepton $Q^2 = -q^2 = -(|\vec{k} - \vec{k'}|)^2$ is equal to the virtuality of the exchanged boson. Large values of Q^2 provide a hard scale to the process, which allows resolution of quarks and gluons in the nucleon.

- The Bjorken variable $x_{Bj} = Q^2/(2\vec{p}\cdot\vec{q})$ is often simply denoted by x. It determines the momentum fraction of the parton (quark or gluon) on which the boson scatters. Note that $0 < x < 1$ for ν+N collisions.
- The inelasticity $y = (\vec{q}\cdot\vec{p})/(\vec{k}\cdot\vec{p})$ is limited to values $0 < y < 1$ and determines in particular the polarization of the virtual boson. In the lab frame, the energy of the scattered lepton is $E_l = E_\nu(1-y) + Q^2/(4E_\nu)$; detection of the scattered lepton thus typically requires a cut on $y < y_{max}$.

These invariants are related by $Q^2 = xys$. The available phase space is often represented in the plane of x and Q^2. For a given ν+N collision energy, lines of constant y are then lines with a slope of 45 degrees in a double logarithmic $x - Q^2$ plot.

Two additional important variables are:

- The squared invariant mass of the produced hadronic system (X) is denoted by $W^2 = (|\vec{p}+\vec{q}|)^2 = Q^2(1-1/x)$. Deep-inelastic scattering (DIS) is characterized by the Bjorken limit, where Q^2 and W^2 become large at a fixed value of x. Note: for a given Q^2, small x corresponds to a high W, Z - N collision energy.
- The energy lost by the lepton (i.e., the energy carried away by the virtual boson) in the nucleon rest frame, is denoted $\nu = \vec{q}\cdot\vec{p}/M = ys/(2M)$.

For scattering on a nucleus of atomic number A, the nucleon momentum $\vec{p}$ would be replaced by $\vec{P}/A$ in the definitions, where $\vec{P}$ is the momentum of the nucleus. Note that the Bjorken variable is then in the range $0 < x < A$.

Acknowledgments

This report is the result of an initial collaboration-wide effort to prepare a whitepaper for the APS Division of Particles and Fields Community Summer Study 2013 [1]. The paper has evolved into LBNE's formal science document due to the hard work of many LBNE Collaboration and Project members. We thank those colleagues who made significant contributions and provided excellent feedback on drafts of this document. The following is a nonexhaustive list of LBNE collaborators who made major contributions to this document. A major contribution is defined as $\geq$ a section and/or a study reported in a figure prepared for this document.

Contribution	LBNE Collaborator(s)
Overall editing	***Anne Heavey, Mary Bishai, Jon Urheim, Brett Viren, Maury Goodman***
Technical/Figures	Brett Viren
Original content	*Bob Wilson (Editor of the 2010 Interim Physics Report)*
General Guidance	Milind Diwan, Bob Wilson, Jim Strait, Sam Zeller, Bill Louis, Hank Sobel, Josh Klein, Nick Samios
Major Contributors by Chapter. A * indicates the chapter editor(s)	
Chapter 1	Jon Urheim*, Jim Strait, Bob Wilson
Chapter 2	Mary Bishai*, Elizabeth Worcester*, Jon Urheim, Kate Scholberg, Ed Kearns, Bill Marciano, Xin Qian.
Chapter 3	Mary Bishai*, Jim Strait, Elaine McCluskey, Kevin Lesko, Jim Stewart, Vaia Papadimitriou, Kevin Yarritu, Bill Louis
Chapter 4	Elizabeth Worcester*, Mary Bishai*, Matt Bass, Andy Blake, Xin Qian, Jon Urheim, Lisa Whitehead
Chapter 5	Ed Kearns*, Jon Urheim*, Vitaly Kudryavtsev
Chapter 6	Kate Scholberg*, Vic Gehman, Alex Friedland
Chapter 7	Roberto Petti*, Sanjib Mishra, Jaehoon Yu, Richard Van de Water
Chapter 8	Michael Smy*, Mary Bishai*, Jaehoon Yu
Chapter 9	Jon Urheim*, Jim Strait
Appendix A	Dan Cherdack*, Tom Junk*, Andy Blake, Vitaly Kudryavtsev, Zepeng Li, Kate Scholberg
Appendix B	Mary Bishai*, Roberto Petti

We would also like to express our gratitude to the following non-LBNE collaborators who supplied us with invaluable information: **Elke Aschenauer (Brookhaven Lab)**, the main editor of the Electron Ion Collider (EIC) whitepaper [358] which inspired the look and style of this document; **Joachim Kopp (Max-Planck Institute, Heidelberg)** for his study of LBNE's sensitivity

to Non-Standard Interactions summarized in Section 4.7.1; **Pilar Coloma (Virginia Tech)** for her studies comparing LBNE's sensitivities to other proposed neutrino experiments shown in Figures 4.33 and 4.35; **Patrick Huber (Virginia Tech)** for a long and fruitful collaborative effort, and his critical role in developing the case for a very long-baseline neutrino oscillation experiment over the past decade; **JJ Cherry (LANL)** and **Huaiyu Duan (U. of New Mexico)** for major input on the supernova studies shown in Chapter 6; **Dmitry Gorbunov (Institute for Nuclear Research, Moscow)** for his studies on LBNE sensitivities to νMSM heavy neutrinos shown in Figure 7.5; **Diana Brandonisio (Fermilab VMS)**, our graphic designer for her gorgeous cover design and invaluable design advice.

And last, but most importantly, our effusive thanks to **Anne Heavey** (AKA the **FIXME** monster) — our devoted general editor — for her dogged insistence on clarity and quality, her hard work well above and beyond the call of duty, and for being such an absolute pleasure to work with.

This work was supported in part by the U.S. Department of Energy (DOE), the National Science Foundation (NSF), the Sanford Underground Research Facility and the South Dakota Science and Technology Authority (SDSTA); the Brazilian Federal Agency for the Support and Evaluation of Graduate Education (CAPES), the Sao Paulo Research Foundation (FAPESP) and the National Council for Scientific and Technological Development (CNPq); the UK Science and Technology Facilities Council (STFC); the Italian government's Istituto Nazionale di Fisica Nucleare (INFN); the Indian Department of Atomic Energy (DAE) and the Department of Science and Technology (DST), Ministry of Science and Technology.

References

1. "APS Division of Particles and Fields Community Summer Study 2013," 2013. http://www.snowmass2013.org. Cited in Sections 1.1 (pg.4), 1.2.1 (pg.6), and B (pg.235).
2. M. Diwan and C. Jung, "Next generation nucleon decay and neutrino detector. Proceedings, Workshop, NNN99, Stony Brook, USA, September 23-25, 1999," 2000. Cited in Section 1.2 (pg.5).
3. W. J. Marciano, "Extra long baseline neutrino oscillations and CP violation," BNL-HET-01-31, arXiv:hep-ph/0108181 [hep-ph], 2001. Cited in Section 1.2 (pg.5).
4. R. Shrock, "Neutrinos and implications for physics beyond the standard model. Proceedings, Conference, Stony Brook, USA, October 11-13, 2002," 2003. Cited in Section 1.2 (pg.5).
5. M. Diwan, W. Marciano, W. Weng, D. Beavis, M. Brennan, *et al.*, "Report of the BNL neutrino working group: Very long baseline neutrino oscillation experiment for precise determination of oscillation parameters and search for nu mu –> nu e appearance and CP violation," BNL-69395, arXiv:hep-ex/0211001 [hep-ex], 2002. Cited in Section 1.2 (pg.5).
6. M. Diwan, D. Beavis, M.-C. Chen, J. Gallardo, S. Kahn, *et al.*, "Very long baseline neutrino oscillation experiments for precise measurements of mixing parameters and CP violating effects," *Phys.Rev.* **D68** (2003) 012002, arXiv:hep-ph/0303081 [hep-ph]. Cited in Section 1.2 (pg.5).
7. W. Weng, M. Diwan, D. Raparia, J. Alessi, D. Barton, *et al.*, "The AGS-Based Super Neutrino Beam Facility Conceptual Design Report," BNL-73210-2004-IR, 2004. Cited in Section 1.2 (pg.5).
8. M. Diwan, S. H. Kettell, L. Littenberg, W. Marciano, Z. Parsa, *et al.*, "Proposal for an Experimental Program in Neutrino Physics and Proton Decay in the Homestake Laboratory," BNL-76798-2006-IR, arXiv:hep-ex/0608023 [hep-ex], 2006. Cited in Section 1.2 (pg.5).
9. V. Barger, M. Bishai, D. Bogert, C. Bromberg, A. Curioni, *et al.*, "Report of the US long baseline neutrino experiment study," FERMILAB-0801-AD-E, BNL-77973-2007-IR, arXiv:0705.4396 [hep-ph], 2007. Cited in Section 1.2 (pg.5).
10. N. R. C. Neutrino Facilities Assessment Committee, *Neutrinos and Beyond: New Windows on Nature*. The National Academies Press, 2003. ISBN 0-309-08716-3. Cited in Section 1.2 (pg.5).
11. Interagency Working Group on the Physics of the Universe. National Science and Technology Council Committee on Science, "A 21^{st} Century Frontier of Discovery: The Physics of the Universe, a Strategic Plan for Federal Research at the Intersection of Physics

and Astronomy.". February, 2004. http://pcos.gsfc.nasa.gov/docs/Physics_of_the_Universe.pdf. Cited in Section 1.2 (pg.5).

12. N. R. C. Committee on Elementary Particle Physics in the 21st Century, *Revealing the Hidden Nature of Space and Time: Charting the Course for Elementary Particle Physics*. The National Academies Press, 2006. ISBN 0-309-66039-4. Cited in Section 1.2 (pg.5).
13. Neutrino Scientific Assessment Group, "Recommendations to the Department of Energy and the National Science Foundation on a Future U.S. Program in Neutrino Oscillations. Report to the Nuclear Science Advisory Committee and the High Energy Physics Advisory Board.". July, 2007. http://science.energy.gov/~/media/hep/pdf/files/pdfs/nusagfinalreportjuly13_2007.pdf. Cited in Section 1.2 (pg.5).
14. Particle Physics Project Prioritization Panel, "U.S. Particle Physics: Scientific opportunities, a plan for the next ten years.". May, 2008. http://science.energy.gov/~/media/hep/pdf/files/pdfs/p5_report_06022008.pdf. Cited in Sections 1.2 (pg.5), 3.1 (pg.46), and 3.2 (pg.48).
15. Ad Hoc Committee to Assess the Science Proposed for a Deep Underground Science and Engineering Laboratory (DUSEL); National Research Council, *An Assessment of the Deep Underground Science and Engineering Laboratory*. The National Academies Press, 2012. ISBN 978-0-309-21723-1. Cited in Section 1.2 (pg.5).
16. HEPAP Facilities Subpanel, "Major High Energy Physics Facilities 2014-2024. Input to the prioritization of proposed scientific user facilities for the Office of Science.". March, 2013. http://science.energy.gov/~/media/hep/hepap/pdf/Reports/HEPAP_facilities_letter_report.pdf. Cited in Section 1.2 (pg.5).
17. CERN Council, "The European Strategy for Particle Physics, Update 2013.". CERN-Council-S/106, May, 2013. http://council.web.cern.ch/council/en/EuropeanStrategy/esc-e-106.pdf. Cited in Sections 1.2 (pg.5) and 1.2.3 (pg.7).
18. DOE Office of Science, Office of High Energy Physics, "Mission Need Statement for a Long-Baseline Neutrino Experiment (LBNE)," DOE, LBNE-doc-6259, 2009. Cited in Sections 1.2.1 (pg.6) and 3.1 (pg.47).
19. A. S. Kronfeld, R. S. Tschirhart, U. Al-Binni, W. Altmannshofer, C. Ankenbrandt, *et al.*, "Project X: Physics Opportunities," FERMILAB-TM-2557, BNL-101116-2013-BC-81834, JLAB-ACP-13-1725, UASLP-IF-13-001, SLAC-R-1029, ANL-PHY-13-2, PNNL-22523, LBNL-6334E, arXiv:1306.5009 [hep-ex], 2013. Cited in Section 1.2.1 (pg.6).
20. A. de Gouvea *et al.*, **Intensity Frontier Neutrino Working Group** , "Neutrinos," FERMILAB-CONF-13-479-E, arXiv:1310.4340 [hep-ex], 2013. Cited in Sections 1.2.1 (pg.6) and 2.2 (pg.23).
21. K. Babu, E. Kearns, U. Al-Binni, S. Banerjee, D. Baxter, *et al.*, "Baryon Number Violation," arXiv:1311.5285 [hep-ph], 2013. Cited in Section 1.2.1 (pg.6).
22. Derwent, P. and others, "Proton Improvement Plan II," Project X-doc-1232, November, 2013. Cited in Sections 1.2.1 (pg.6), 3.2 (pg.51), and 3.4 (pg.63).

23. S. Holmes, R. Alber, B. Chase, K. Gollwitzer, D. Johnson, *et al.*, "Project X: Accelerator Reference Design," FERMILAB-TM-2557, BNL-101116-2013-BC-81834, JLAB-ACP-13-1725, PNNL-22523, SLAC-R-1020, UASLP-IF-13-001, arXiv:1306.5022 [physics.acc-ph], 2013. Cited in Sections 1.2.1 (pg.6), 3.2 (pg.51), and 4.2.1 (pg.88).
24. "Final Report, Director's Independent Conceptual Design and CD-1 Readiness Review of the LBNE Project," LBNE-doc-5788, March, 2012. Cited in Sections 1.2.2 (pg.7), 3.6 (pg.76), and 3.6.2 (pg.79).
25. Y. K. Kim *et al.*, "LBNE Reconfiguration: Steering Committee Report," 2012. http://www.fnal.gov/directorate/lbne_reconfiguration/index.shtml. Cited in Sections 1.2.2 (pg.7), 1.3 (pg.9), 4.2.1 (pg.86), and 9.3 (pg.210).
26. "Department of Energy Review Committee Report on the Technical, Cost, Schedule, and Management Review of the Long Baseline Neutrino Experiment (LBNE)," October, 2012. http://www.fnal.gov/directorate/OPMO/Projects/LBNE/DOERev/2012/10_30/1210_LBNE_rpt.pdf. Cited in Section 1.2.2 (pg.7).
27. "Independent Cost Review Closeout for the Long Baseline Neutrino Experiment (LBNE) Project," LBNE-doc-6522, November, 2012. Cited in Section 1.2.2 (pg.7).
28. "Critical Decision 1 Approve Alternative Selection and Cost Range of the Long Baseline Neutrino Experiment (LBNE) Project," LBNE-doc-6681, December, 2012. Cited in Section 1.2.2 (pg.7).
29. **LBNE Project Management Team** , "LBNE Conceptual Design Report, Volume 1: The LBNE Project," LBNE-doc-5235, 2012. Cited in Sections 1.2.2 (pg.7), 4.2.2 (pg.88), 4.3 (pg.92), 4.3 (pg.95), 4.6 (pg.124), and A (pg.213).
30. **LBNE Project Management Team** , "LBNE Conceptual Design Report, Volume 2: The Beamline at the Near Site," LBNE-doc-4317, 2012. Cited in Sections 1.2.2 (pg.7), 3.4 (pg.63), and 4.3 (pg.93).
31. **LBNE Project Management Team** , "LBNE Conceptual Design Report, Volume 3: Detectors at the Near Site," LBNE-doc-4724, 2012. Cited in Sections 1.2.2 (pg.7) and 3.5 (pg.73).
32. **LBNE Project Management Team** , "LBNE Conceptual Design Report, Volume 4: The Liquid Argon Detector at the Far Site," LBNE-doc-4892, 2012. Cited in Sections 1.2.2 (pg.7) and 3.6.1 (pg.77).
33. **LBNE Project Management Team** , "LBNE Conceptual Design Report, Volume 5: Conventional Facilities at the Near Site (MI-10 Shallow)," LBNE-doc-4623, 2012. Cited in Section 1.2.2 (pg.7).
34. **LBNE Project Management Team** , "LBNE Conceptual Design Report, Volume 6: Conventional Facilities at the Far Site," LBNE-doc-5017, 2012. Cited in Section 1.2.2 (pg.7).
35. R. J. Wilson, "Long-Baseline Neutrino Experiment, presentation, November 2013," 2013. https://indico.fnal.gov/getFile.py/access?contribId=25&sessionId=7&resId=0&materialId=slides&confId=7485. Cited in Section 1.2.3 (pg.8).

36. Marx-Reichanadter Committee, "Department of Energy Office of Science Review of Options for Underground Science.". June, 2011. http://science.energy.gov/~/media/np/pdf/review_of_underground_science_report_final.pdf. Cited in Section 1.3 (pg.9).
37. Grannis, P. and Green, D. and Nishikawa, K. and Robertson, H. and Sadoulet, B. and Wark, D., "The LBNE Science Capability Review," LBNE-doc-5333, December, 2011. Cited in Section 1.3 (pg.9).
38. M. Messier, **NOvA Collaboration** , "Extending the NOvA Physics Program," FERMILAB-CONF-13-308-E, arXiv:1308.0106 [hep-ex], 2013. Cited in Sections 1.3.1 (pg.10) and 4.8 (pg.136).
39. P. Huber and J. Kopp, "Two experiments for the price of one? – The role of the second oscillation maximum in long baseline neutrino experiments," *JHEP* **1103** (2011) 013, arXiv:1010.3706 [hep-ph]. Cited in Section 1.3.1 (pg.13).
40. E. Kearns, "Future Experiments for Proton Decay. Presentation at ISOUPS (International Symposium: Opportunities in Underground Physics for Snowmass), Asilomar, May 2013," 2013. Cited in Sections 1.3.2 (pg.13), 5.1 (pg.139), 5.1 (pg.140), and 5.2 (pg.141).
41. J. Strait, "Physics Research Goals After Reconfiguration," LBNE-doc-3056, 2011. Cited in Section 2.1 (pg.18).
42. R. Mohapatra, S. Antusch, K. Babu, G. Barenboim, M.-C. Chen, *et al.*, "Theory of neutrinos: A White paper," *Rept.Prog.Phys.* **70** (2007) 1757–1867, arXiv:hep-ph/0510213 [hep-ph]. Cited in Sections 2.2 (pg.21) and 2.2 (pg.23).
43. G. Aad *et al.*, **ATLAS Collaboration** , "Observation of a new particle in the search for the Standard Model Higgs boson with the ATLAS detector at the LHC," *Phys.Lett.* **B716** (2012) 1–29, arXiv:1207.7214 [hep-ex]. Cited in Section 2.2 (pg.21).
44. S. Chatrchyan *et al.*, **CMS Collaboration** , "Observation of a new boson at a mass of 125 GeV with the CMS experiment at the LHC," *Phys.Lett.* **B716** (2012) 30–61, arXiv:1207.7235 [hep-ex]. Cited in Section 2.2 (pg.21).
45. DNP/DPF/DAP/DPB Joint Study on the Future of Neutrino Physics, "The Neutrino Matrix.". November, 2004. http://www.aps.org/policy/reports/multidivisional/neutrino/upload/main.pdf. Cited in Section 2.2 (pg.22).
46. F. An *et al.*, **Daya Bay Collaboration** , "Improved Measurement of Electron Antineutrino Disappearance at Daya Bay," *Chin. Phys.* **C37** (2013) 011001, arXiv:1210.6327 [hep-ex]. Cited in Section 2.2 (pg.22).
47. A. Aguilar-Arevalo *et al.*, **LSND Collaboration** , "Evidence for neutrino oscillations from the observation of anti-neutrino(electron) appearance in a anti-neutrino(muon) beam," *Phys.Rev.* **D64** (2001) 112007, arXiv:hep-ex/0104049 [hep-ex]. Cited in Section 2.2 (pg.23).
48. A. Aguilar-Arevalo *et al.*, **MiniBooNE Collaboration** , "A Search for electron neutrino appearance at the $\Delta m^2 \sim 1\text{eV}^2$ scale," *Phys.Rev.Lett.* **98** (2007) 231801, arXiv:0704.1500 [hep-ex]. Cited in Section 2.2 (pg.23).

49. A. Aguilar-Arevalo *et al.*, **MiniBooNE Collaboration** , "Improved Search for $\overline{\nu_\mu} \to \overline{\nu_e}$ Oscillations in the MiniBooNE Experiment," *Phys.Rev.Lett.* **110** no. 16, (2013) 161801, arXiv:1207.4809 [hep-ex]. Cited in Section 2.2 (pg.23).
50. G. Mention, M. Fechner, T. Lasserre, T. Mueller, D. Lhuillier, *et al.*, "The Reactor Antineutrino Anomaly," *Phys.Rev.* **D83** (2011) 073006, arXiv:1101.2755 [hep-ex]. Cited in Section 2.2 (pg.23).
51. S. F. King, A. Merle, S. Morisi, Y. Shimizu, and M. Tanimoto, "Neutrino Mass and Mixing: from Theory to Experiment," arXiv:1402.4271 [hep-ph], 2014. Cited in Section 2.2 (pg.23).
52. P. Harrison, D. Perkins, and W. Scott, "Tri-bimaximal mixing and the neutrino oscillation data," *Phys.Lett.* **B530** (2002) 167, arXiv:hep-ph/0202074 [hep-ph]. Cited in Section $*$ (pg.23).
53. C. H. Albright and M.-C. Chen, "Model Predictions for Neutrino Oscillation Parameters," *Phys.Rev.* **D74** (2006) 113006, arXiv:hep-ph/0608137 [hep-ph]. Cited in Section 2.2 (pg.23).
54. G. Fogli, E. Lisi, A. Marrone, D. Montanino, A. Palazzo, *et al.*, "Global analysis of neutrino masses, mixings and phases: entering the era of leptonic CP violation searches," *Phys.Rev.* **D86** (2012) 013012, arXiv:1205.5254 [hep-ph]. Cited in Sections † (pg.24), 2.2.1 (pg.25), 4.3 (pg.92), 4.3 (pg.93), 4.3.2 (pg.110), and 4.4 (pg.117).
55. J. Beringer *et al.*, **Particle Data Group** , "Review of Particle Physics (RPP)," *Phys.Rev.* **D86** (2012) 010001. Cited in Sections 2.2.1 (pg.25), 2.2.2 (pg.27), and 7.4.4 (pg.183).
56. C. Jarlskog, "A Basis Independent Formulation of the Connection Between Quark Mass Matrices, CP Violation and Experiment," *Z.Phys.* **C29** (1985) 491–497. Cited in Section 2.2.1 (pg.24).
57. A. Meroni, S. Petcov, and M. Spinrath, "A SUSY SU(5)xT' Unified Model of Flavour with large θ_{13}," *Phys.Rev.* **D86** (2012) 113003, arXiv:1205.5241 [hep-ph]. Cited in Section 2.2.1 (pg.25).
58. G.-J. Ding, S. F. King, and A. J. Stuart, "Generalised CP and A_4 Family Symmetry," *JHEP* **1312** (2013) 006, arXiv:1307.4212. Cited in Section 2.2.1 (pg.25).
59. C. Luhn, "Trimaximal TM_1 neutrino mixing in S_4 with spontaneous CP violation," *Nucl.Phys.* **B875** (2013) 80–100, arXiv:1306.2358 [hep-ph]. Cited in Sections 2.2.1 (pg.25) and 2.2.6 (pg.35).
60. G.-J. Ding and Y.-L. Zhou, "Predicting Lepton Flavor Mixing from $\Delta(48)$ and Generalized CP Symmetries," arXiv:1312.5222 [hep-ph], 2013. Cited in Section 2.2.1 (pg.25).
61. S. Antusch, S. F. King, and M. Spinrath, "Spontaneous CP violation in $A_4 \times SU(5)$ with Constrained Sequential Dominance 2," *Phys.Rev.* **D87** no. 9, (2013) 096018, arXiv:1301.6764 [hep-ph]. Cited in Section 2.2.1 (pg.25).
62. S. F. King, "A model of quark and lepton mixing," *JHEP* **1401** (2014) 119, arXiv:1311.3295 [hep-ph]. Cited in Section 2.2.1 (pg.25).
63. E. Kolb and M. Turner, *The Early Universe*. Westview Press, 1994. ISBN 978-0201626742. Cited in Section 2.2.1 (pg.25).

64. S. Weinberg, *Cosmology*. Oxford University Press, USA, first ed., April, 2008. ISBN 978-0198526827. Cited in Section 2.2.1 (pg.25).
65. G. Steigman, "Primordial Nucleosynthesis in the Precision Cosmology Era," *Ann.Rev.Nucl.Part.Sci.* **57** (2007) 463–491, arXiv:0712.1100 [astro-ph]. Cited in Section 2.2.1 (pg.25).
66. M. Fukugita and T. Yanagida, "Baryogenesis Without Grand Unification," *Phys.Lett.* **B174** (1986) 45. Cited in Section 2.2.1 (pg.25).
67. T. Yanagida, "Horizontal Symmetry and Masses of Neutrinos," *Prog.Theor.Phys.* **64** (1980) 1103. Cited in Sections 2.2.1 (pg.25), 7.7 (pg.187), and 9.2 (pg.209).
68. S. Pascoli, S. Petcov, and A. Riotto, "Leptogenesis and Low Energy CP Violation in Neutrino Physics," *Nucl.Phys.* **B774** (2007) 1–52, arXiv:hep-ph/0611338 [hep-ph]. Cited in Section 2.2.1 (pg.26).
69. F. Capozzi, G. Fogli, E. Lisi, A. Marrone, D. Montanino, *et al.*, "Status of three-neutrino oscillation parameters, circa 2013," arXiv:1312.2878 [hep-ph], 2013. Cited in Sections 2.2.1 (pg.26), 4.3.1 (pg.99), 4.3.3 (pg.112), 4.4 (pg.115), and 9.2 (pg.208).
70. P. Adamson *et al.*, **MINOS Collaboration** , "Search for the disappearance of muon antineutrinos in the NuMI neutrino beam," *Phys.Rev.* **D84** (2011) 071103, arXiv:1108.1509 [hep-ex]. Cited in Section 2.2.2 (pg.26).
71. S. Mikheev and A. Y. Smirnov, "Resonance Amplification of Oscillations in Matter and Spectroscopy of Solar Neutrinos," *Sov.J.Nucl.Phys.* **42** (1985) 913–917. Cited in Section 2.2.2 (pg.27).
72. L. Wolfenstein, "Neutrino Oscillations in Matter," *Phys.Rev.* **D17** (1978) 2369–2374. Cited in Section 2.2.2 (pg.27).
73. G. Bellini *et al.*, **Borexino Collaboration** , "Measurement of the solar 8B neutrino rate with a liquid scintillator target and 3 MeV energy threshold in the Borexino detector," *Phys.Rev.* **D82** (2010) 033006, arXiv:0808.2868 [astro-ph]. Cited in Section 2.2.2 (pg.27).
74. G. Bellini, J. Benziger, D. Bick, S. Bonetti, G. Bonfini, *et al.*, "Precision measurement of the 7Be solar neutrino interaction rate in Borexino," *Phys.Rev.Lett.* **107** (2011) 141302, arXiv:1104.1816 [hep-ex]. Cited in Section 2.2.2 (pg.27).
75. B. Aharmim *et al.*, **SNO Collaboration** , "Combined Analysis of all Three Phases of Solar Neutrino Data from the Sudbury Neutrino Observatory," *Phys.Rev.* **C88** (2013) 025501, arXiv:1109.0763 [nucl-ex]. Cited in Section 2.2.2 (pg.27).
76. A. Renshaw *et al.*, **Super-Kamiokande Collaboration** , "First Indication of Terrestrial Matter Effects on Solar Neutrino Oscillation," arXiv:1312.5176 [hep-ex], 2013. Cited in Sections 2.2.2 (pg.27) and 8.1 (pg.199).
77. M. Freund, "Analytic approximations for three neutrino oscillation parameters and probabilities in matter," *Phys.Rev.* **D64** (2001) 053003, arXiv:hep-ph/0103300 [hep-ph]. Cited in Section 2.2.2 (pg.27).

78. W. Marciano and Z. Parsa, "Intense neutrino beams and leptonic CP violation," *Nucl.Phys.Proc.Suppl.* **221** (2011) 166–172, arXiv:hep-ph/0610258 [hep-ph]. Cited in Section 2.2.2 (pg.30).
79. B. Viren, "libnuosc++ - A library for calculating 3 neutrino oscillation probabilities.." https://github.com/brettviren/nuosc. Cited in Section 2.2.3 (pg.30).
80. A. M. Dziewonski and D. L. Anderson, "Preliminary reference Earth model," *Phys. Earth Plan. Int.* **25** (1981) 297. Cited in Section 2.2.3 (pg.30).
81. J. Appel *et al.*, "Physics Working Group Report to the LBNE Reconfiguration Steering Committee," 2012. http://www.fnal.gov/directorate/lbne_reconfiguration/files/LBNE-Reconfiguration-PhysicsWG-Report-August2012.pdf. Cited in Section 2.2.5 (pg.35).
82. R. Brun, F. Bruyant, M. Maire, A. McPherson, and P. Zanarini, "GEANT3," CERN-DD-EE-84-1, 1987. Cited in Section 2.2.5 (pg.33).
83. M. Bass *et al.*, **LBNE Collaboration** , "Baseline optimization for the measurement of CP violation and mass hierarchy in a long-baseline neutrino oscillation experiment," FERMILAB-PUB-13-506-E, arXiv:1311.0212 [hep-ex], 2013. Cited in Sections 2.2.5 (pg.35) and 3.1 (pg.47).
84. M. Raidal, "Relation between the neutrino and quark mixing angles and grand unification," *Phys.Rev.Lett.* **93** (2004) 161801, arXiv:hep-ph/0404046 [hep-ph]. Cited in Section 2.2.6 (pg.35).
85. H. Minakata and A. Y. Smirnov, "Neutrino mixing and quark-lepton complementarity," *Phys.Rev.* **D70** (2004) 073009, arXiv:hep-ph/0405088 [hep-ph]. Cited in Section 2.2.6 (pg.35).
86. A. Y. Smirnov, "Neutrino mass, mixing and discrete symmetries," *J.Phys.Conf.Ser.* **447** (2013) 012004, arXiv:1305.4827 [hep-ph]. Cited in Section 2.2.6 (pg.35).
87. J. Harada, "Non-maximal θ_{23}, large θ_{13} and tri-bimaximal θ_{12} via quark-lepton complementarity at next-to-leading order," *Europhys.Lett.* **103** (2013) 21001, arXiv:1304.4526 [hep-ph]. Cited in Section 2.2.6 (pg.35).
88. B. Hu, "Trimaximal-Cabibbo neutrino mixing: A parametrization in terms of deviations from tribimaximal mixing," *Phys.Rev.* **D87** no. 5, (2013) 053011, arXiv:1212.4079 [hep-ph]. Cited in Section 2.2.6 (pg.35).
89. P. Ramond, "Fundamental Physics Underground. Presentation at ISOUPS (International Symposium: Opportunities in Underground Physics for Snowmass), Asilomar, May 2013," 2013. Cited in Section 2.2.6 (pg.35).
90. S. Antusch, C. Biggio, E. Fernandez-Martinez, M. Gavela, and J. Lopez-Pavon, "Unitarity of the Leptonic Mixing Matrix," *JHEP* **0610** (2006) 084, arXiv:hep-ph/0607020 [hep-ph]. Cited in Section 2.2.6 (pg.35).
91. X. Qian, C. Zhang, M. Diwan, and P. Vogel, "Unitarity Tests of the Neutrino Mixing Matrix," arXiv:1308.5700 [hep-ex], 2013. Cited in Sections 2.2.6 (pg.35) and 2.2.6 (pg.36).

92. J. C. Pati and A. Salam, "Is Baryon Number Conserved?," *Phys.Rev.Lett.* **31** (1973) 661–664. Cited in Section 2.3.1 (pg.38).
93. H. Georgi and S. Glashow, "Unity of All Elementary Particle Forces," *Phys.Rev.Lett.* **32** (1974) 438–441. Cited in Section 2.3.1 (pg.38).
94. S. Dimopoulos, S. Raby, and F. Wilczek, "Proton Decay in Supersymmetric Models," *Phys.Lett.* **B112** (1982) 133. Cited in Section 2.3.1 (pg.38).
95. P. Langacker, "Grand Unified Theories and Proton Decay," *Phys.Rept.* **72** (1981) 185. Cited in Section 2.3.1 (pg.38).
96. W. de Boer, "Grand unified theories and supersymmetry in particle physics and cosmology," *Prog.Part.Nucl.Phys.* **33** (1994) 201–302, arXiv:hep-ph/9402266 [hep-ph]. Cited in Section 2.3.1 (pg.38).
97. P. Nath and P. Fileviez Perez, "Proton stability in grand unified theories, in strings and in branes," *Phys.Rept.* **441** (2007) 191–317, arXiv:hep-ph/0601023 [hep-ph]. Cited in Section 2.3.1 (pg.38).
98. S. Raby, T. Walker, K. Babu, H. Baer, A. Balantekin, *et al.*, "DUSEL Theory White Paper," SLAC-PUB-14734, FERMILAB-PUB-08-680-T, arXiv:0810.4551 [hep-ph], 2008. Cited in Section 2.3.1 (pg.38).
99. G. Senjanovic, "Proton decay and grand unification," *AIP Conf.Proc.* **1200** (2010) 131–141, arXiv:0912.5375 [hep-ph]. Cited in Section 2.3.1 (pg.38).
100. T. Li, D. V. Nanopoulos, and J. W. Walker, "Elements of F-ast Proton Decay," *Nucl.Phys.* **B846** (2011) 43–99, arXiv:1003.2570 [hep-ph]. Cited in Section 2.3.1 (pg.38).
101. E. Noether, "Invariant Variation Problems," *Gott.Nachr.* **1918** (1918) 235–257, arXiv:physics/0503066 [physics]. Cited in Section 2.3.1 (pg.39).
102. H. Nishino *et al.*, **Super-Kamiokande Collaboration** , "Search for Nucleon Decay into Charged Anti-lepton plus Meson in Super-Kamiokande I and II," *Phys.Rev.* **D85** (2012) 112001, arXiv:1203.4030 [hep-ex]. Cited in Section 2.3.2 (pg.40).
103. R. Bionta, G. Blewitt, C. Bratton, D. Casper, A. Ciocio, *et al.*, "Observation of a Neutrino Burst in Coincidence with Supernova SN 1987a in the Large Magellanic Cloud," *Phys.Rev.Lett.* **58** (1987) 1494. Cited in Sections 2.4 (pg.42) and 6.1 (pg.151).
104. K. Hirata *et al.*, **KAMIOKANDE-II Collaboration** , "Observation of a Neutrino Burst from the Supernova SN 1987a," *Phys.Rev.Lett.* **58** (1987) 1490–1493. Cited in Sections 2.4 (pg.42) and 6.1 (pg.151).
105. E. Alekseev, L. Alekseeva, V. Volchenko, and I. Krivosheina, "Possible Detection of a Neutrino Signal on 23 February 1987 at the Baksan Underground Scintillation Telescope of the Institute of Nuclear Research," *JETP Lett.* **45** (1987) 589–592. Cited in Section 2.4 (pg.42).
106. K. Scholberg, "Supernova neutrino detection," *Nucl.Phys.Proc.Suppl.* **221** (2011) 248–253, arXiv:astro-ph/0701081 [astro-ph]. Cited in Sections 2.4 (pg.42) and 2.4 (pg.44).
107. A. Dighe, "Physics potential of future supernova neutrino observations," *J.Phys.Conf.Ser.* **136** (2008) 022041, arXiv:0809.2977 [hep-ph]. Cited in Section 2.4 (pg.42).

108. G. A. Tammann, W. Loeffler, and A. Schroder, "The Galactic supernova rate," *Astrophys. J. Suppl.* **92** (1994) 487–493. Cited in Section 2.4 (pg.42).
109. E. Cappellaro, R. Evans, and M. Turatto, "A new determination of supernova rates and a comparison with indicators for galactic star formation," *Astron.Astrophys.* **351** (1999) 459, arXiv:astro-ph/9904225 [astro-ph]. Cited in Section 2.4 (pg.42).
110. G. Pagliaroli, F. Vissani, E. Coccia, and W. Fulgione, "Neutrinos from Supernovae as a Trigger for Gravitational Wave Search," *Phys. Rev. Lett.* **103** (2009) 031102, arXiv:0903.1191 [hep-ph]. Cited in Section 2.4 (pg.43).
111. C. Ott, E. O'Connor, S. Gossan, E. Abdikamalov, U. Gamma, *et al.*, "Core-Collapse Supernovae, Neutrinos, and Gravitational Waves," *Nucl.Phys.Proc.Suppl.* **235-236** (2013) 381–387, arXiv:1212.4250 [astro-ph.HE]. Cited in Section 2.4 (pg.43).
112. A. Mirizzi, G. Raffelt, and P. Serpico, "Earth matter effects in supernova neutrinos: Optimal detector locations," *JCAP* **0605** (2006) 012, arXiv:astro-ph/0604300 [astro-ph]. Cited in Sections 2.4 (pg.43) and 2.4 (pg.44).
113. S. Choubey, B. Dasgupta, A. Dighe, and A. Mirizzi, "Signatures of collective and matter effects on supernova neutrinos at large detectors," arXiv:1008.0308 [hep-ph], 2010. Cited in Section 2.4 (pg.43).
114. G. G. Raffelt, "Astrophysical axion bounds: An Update," arXiv:astro-ph/9707268 [astro-ph], 1997. Cited in Section 2.4 (pg.43).
115. S. Hannestad and G. Raffelt, "New supernova limit on large extra dimensions," *Phys.Rev.Lett.* **87** (2001) 051301, arXiv:hep-ph/0103201 [hep-ph]. Cited in Section 2.4 (pg.43).
116. P. Antonioli *et al.*, "Snews: The supernova early warning system," *New J. Phys.* **6** (2004) 114, astro-ph/0406214. Cited in Sections 2.4 (pg.44) and 6.1 (pg.153).
117. K. Scholberg, "The SuperNova Early Warning System," *Astron. Nachr.* **329** (2008) 337–339, arXiv:0803.0531 [astro-ph]. Cited in Sections 2.4 (pg.44) and 6.1 (pg.153).
118. K. Scholberg, "Future supernova neutrino detectors," *J.Phys.Conf.Ser.* **203** (2010) 012079. Cited in Section 2.4 (pg.44).
119. "Sanford Underground Research Facility." http://www.sanfordlab.org. Cited in Section 3.3 (pg.54).
120. B. Cleveland, T. Daily, R. Davis Jr., J. R. Distel, K. Lande, *et al.*, "Measurement of the solar electron neutrino flux with the Homestake chlorine detector," *Astrophys.J.* **496** (1998) 505–526. Cited in Sections 3.3 (pg.54) and 8.1 (pg.195).
121. F. Gray, C. Ruybal, J. Totushek, D.-M. Mei, K. Thomas, *et al.*, "Cosmic Ray Muon Flux at the Sanford Underground Laboratory at Homestake," *Nucl.Instrum.Meth.* **A638** (2011) 63–66, arXiv:1007.1921 [nucl-ex]. Cited in Section 3.3 (pg.58).
122. W. Roggenthen and A. Smith, "U, Th, K contents of materials associated with the Homestake DUSEL site, Lead, South Dakota," *Private Communication* . Cited in Section 3.3 (pg.59).

123. D. Akerib *et al.*, **LUX Collaboration** , "First results from the LUX dark matter experiment at the Sanford Underground Research Facility," arXiv:1310.8214 [astro-ph.CO], 2013. Cited in Section 3.3 (pg.59).
124. M. Bishai and Y. Lu, "Conceptual Designs for a Wide-Band Low-Energy Neutrino Beam Target," LBNE-doc-3151, November, 2010.
125. B. Lundberg, "A beginner guide to horn design and history of LBNE horn design," LBNE-doc-8398, November, 2014.
126. D. Ayres *et al.*, **NOvA Collaboration** , "The NOvA Technical Design Report," FERMILAB-DESIGN-2007-01, 2007. http://lss.fnal.gov/archive/design/fermilab-design-2007-01.pdf. Cited in Sections 3.4 (pg.63), 4.2.1 (pg.88), 7.4.4 (pg.183), and 7.6 (pg.185).
127. E. Worcester, "Potential Sensitivity Improvements with 10 kT LBNE," LBNE-doc-6599, 2012. Cited in Section 3.4 (pg.69).
128. S. Mishra, R. Petti, and C. Rosenfeld, "A High Resolution Neutrino Experiment in a Magnetic Field for Project-X at Fermilab," *PoS* **NUFACT08** (2008) 069, arXiv:0812.4527 [hep-ex]. Cited in Section 3.5 (pg.71).
129. B. Choudhary *et al.*, **Indian Institutions and Fermilab Collaboration** , "LBNE-India Detailed Project Report (DPR) submitted to DAE, India," LBNE-doc-6704, 2012. Cited in Sections 3.5 (pg.73), 3.5 (pg.74), and 7 (pg.163).
130. P. Huber, M. Lindner, and W. Winter, "Simulation of long-baseline neutrino oscillation experiments with GLoBES (General Long Baseline Experiment Simulator)," *Comput.Phys.Commun.* **167** (2005) 195, arXiv:hep-ph/0407333 [hep-ph]. Cited in Sections 4.2 (pg.85), 4.2.1 (pg.86), 4.2.2 (pg.88), and A.3 (pg.225).
131. P. Huber, J. Kopp, M. Lindner, M. Rolinec, and W. Winter, "New features in the simulation of neutrino oscillation experiments with GLoBES 3.0: General Long Baseline Experiment Simulator," *Comput.Phys.Commun.* **177** (2007) 432–438, arXiv:hep-ph/0701187 [hep-ph]. Cited in Sections 4.2 (pg.85) and 4.2.2 (pg.88).
132. S. Agostinelli *et al.*, **GEANT4** , "GEANT4: A simulation toolkit," *Nucl. Instrum. Meth.* **A506** (2003) 250–303. Cited in Sections 4.2.1 (pg.85), 6.2 (pg.154), and A.1.1 (pg.213).
133. C. Andreopoulos, **GENIE Collaboration** , "The GENIE neutrino Monte Carlo generator," *Acta Phys.Polon.* **B40** (2009) 2461–2475. Cited in Sections 4.2.1 (pg.88), 4.6 (pg.122), and A.1.1 (pg.216).
134. K. Abe *et al.*, **T2K Collaboration** , "The T2K Experiment," *Nucl.Instrum.Meth.* **A659** (2011) 106–135, arXiv:1106.1238 [physics.ins-det]. Cited in Sections 4.2.1 (pg.88), 7.4.4 (pg.183), and 7.6 (pg.185).
135. **NuMI-MINOS** . http://www-numi.fnal.gov/. Cited in Section 4.2.1 (pg.88).
136. A. Rubbia, "LAGUNA-LBNO: Design of an underground neutrino observatory coupled to long baseline neutrino beams from CERN," *J.Phys.Conf.Ser.* **408** (2013) 012006. Cited in Section 4.2.1 (pg.88).

137. J.-P. Delahaye, C. Ankenbrandt, A. Bogacz, S. Brice, A. Bross, *et al.*, "Enabling Intensity and Energy Frontier Science with a Muon Accelerator Facility in the U.S.: A White Paper Submitted to the 2013 U.S. Community Summer Study of the Division of Particles and Fields of the American Physical Society," FERMILAB-CONF-13-307-APC, arXiv:1308.0494 [physics.acc-ph], 2013. Cited in Section 4.2.1 (pg.88).
138. A. Longhin, "Optimization of neutrino beams for underground sites in Europe," arXiv:1206.4294 [physics.ins-det], 2012. Cited in Section 4.2.1 (pg.88).
139. S. Amoruso *et al.*, **ICARUS Collaboration** , "Measurement of the mu decay spectrum with the ICARUS liquid argon TPC," *Eur.Phys.J.* **C33** (2004) 233–241, arXiv:hep-ex/0311040 [hep-ex]. Cited in Sections 4.2.2 (pg.88), 4.6 (pg.124), and 6.2 (pg.154).
140. T2K Collaboration, "A Proposal for a Detector 2km Away from the T2K Neutrino Source.". 2005. http://www.phy.duke.edu/~cwalter/nusag-members/2km-proposal-05-05-30.pdf. Cited in Section 4.2.2 (pg.88).
141. A. Ankowski *et al.*, **ICARUS Collaboration** , "Measurement of through-going particle momentum by means of multiple scattering with the ICARUS T600 TPC," *Eur.Phys.J.* **C48** (2006) 667–676, arXiv:hep-ex/0606006 [hep-ex]. Cited in Section 4.2.2 (pg.88).
142. F. An *et al.*, **Daya Bay Collaboration** , "Spectral measurement of electron antineutrino oscillation amplitude and frequency at Daya Bay," arXiv:1310.6732 [hep-ex], 2013. Cited in Sections 4.3 (pg.93) and 4.5 (pg.119).
143. P. Adamson *et al.*, **MINOS Collaboration** , "Electron neutrino and antineutrino appearance in the full MINOS data sample," *Phys.Rev.Lett.* **110** no. 17, (2013) 171801, arXiv:1301.4581 [hep-ex]. Cited in Sections 4.3 (pg.93), 4.3.2 (pg.103), and 4.3.2 (pg.108).
144. M. J. Murtagh, **E734 Collaboration** , "A Search for muon-neutrino to electron-neutrino oscillations using the E734 detector," BNL-39667, 1987.
145. R. Seto, "BNL E776: A Search for neutrino oscillations," *AIP Conf.Proc.* **176** (1988) 957–963.
146. L. Borodovsky, C. Chi, Y. Ho, N. Kondakis, W.-Y. Lee, *et al.*, "Search for muon-neutrino oscillations muon-neutrino to electron-neutrino (anti-muon-neutrino to anti-electron-neutrino in a wide band neutrino beam," *Phys.Rev.Lett.* **68** (1992) 274–277.
147. P. Astier *et al.*, **NOMAD Collaboration** , "Search for nu(mu) –> nu(e) oscillations in the NOMAD experiment," *Phys.Lett.* **B570** (2003) 19–31, arXiv:hep-ex/0306037 [hep-ex].
148. A. Aguilar-Arevalo *et al.*, **MiniBooNE Collaboration** , "Unexplained Excess of Electron-Like Events From a 1-GeV Neutrino Beam," *Phys.Rev.Lett.* **102** (2009) 101802, arXiv:0812.2243 [hep-ex]. Cited in Section 7.7 (pg.190).
149. K. Abe *et al.*, **T2K Collaboration** , "Observation of Electron Neutrino Appearance in a Muon Neutrino Beam," arXiv:1311.4750 [hep-ex], 2013. Cited in Section 4.3.2 (pg.103).

150. X. Qian, A. Tan, W. Wang, J. Ling, R. McKeown, *et al.*, "Statistical Evaluation of Experimental Determinations of Neutrino Mass Hierarchy," *Phys.Rev.* **D86** (2012) 113011, arXiv:1210.3651 [hep-ph]. Cited in Sections 4.3.1 (pg.96), 4.3.1 (pg.97), 4.3.1 (pg.99), and 4.3.1 (pg.100).
151. M. Blennow, P. Coloma, P. Huber, and T. Schwetz, "Quantifying the sensitivity of oscillation experiments to the neutrino mass ordering," arXiv:1311.1822 [hep-ph], 2013. Cited in Sections 4.3.1 (pg.97), 4.3.1 (pg.98), 4.3.1 (pg.99), 4.3.1 (pg.100), and 4.8 (pg.137).
152. R. Cousins, "Private communication," 2013. Cited in Section 4.3.1 (pg.99).
153. R. Cousins, J. Mumford, J. Tucker, and V. Valuev, "Spin discrimination of new heavy resonances at the LHC," *JHEP* **0511** (2005) 046. Cited in Section 4.3.1 (pg.99).
154. P. Adamson *et al.*, **MINOS Collaboration** , "Improved search for muon-neutrino to electron-neutrino oscillations in MINOS," *Phys.Rev.Lett.* **107** (2011) 181802, arXiv:1108.0015 [hep-ex]. Cited in Section 4.3.2 (pg.103).
155. P. Adamson *et al.*, **MINOS Collaboration** , "Neutrino and Antineutrino Inclusive Charged-current Cross Section Measurements with the MINOS Near Detector," *Phys.Rev.* **D81** (2010) 072002, arXiv:0910.2201 [hep-ex]. Cited in Sections 4.3.2 (pg.103) and 7.1.8 (pg.169).
156. Q. Wu *et al.*, **NOMAD Collaboration** , "A Precise measurement of the muon neutrino-nucleon inclusive charged current cross-section off an isoscalar target in the energy range 2.5 < E(nu) < 40-GeV by NOMAD," *Phys.Lett.* **B660** (2008) 19–25, arXiv:0711.1183 [hep-ex]. Cited in Sections 4.3.2 (pg.103), 7.1.8 (pg.169), and 7.4.4 (pg.183).
157. V. Lyubushkin *et al.*, **NOMAD Collaboration** , "A Study of quasi-elastic muon neutrino and antineutrino scattering in the NOMAD experiment," *Eur.Phys.J.* **C63** (2009) 355–381, arXiv:0812.4543 [hep-ex]. Cited in Sections 4.3.2 (pg.103) and 7.1.8 (pg.169).
158. A. Bodek, U. Sarica, K. Kuzmin, and V. Naumov, "Extraction of Neutrino Flux with the Low ν Method at MiniBooNE Energies," *AIP Conf.Proc.* **1560** (2013) 193–197, arXiv:1207.1247 [hep-ex]. Cited in Section 4.3.2 (pg.103).
159. P. Adamson *et al.*, **MINOS Collaboration** , "A Study of Muon Neutrino Disappearance Using the Fermilab Main Injector Neutrino Beam," *Phys.Rev.* **D77** (2008) 072002, arXiv:0711.0769 [hep-ex]. Cited in Section 4.3.2 (pg.103).
160. M. Bishai, "Determining the Neutrino Flux from Accelerator Neutrino Beams," *Nucl.Phys.Proc.Suppl.* **229-232** (2012) 210–214. Cited in Section 4.3.2 (pg.103).
161. B. Osmanov, **MINERvA Collaboration** , "MINERvA Detector: Description and Performance," arXiv:1109.2855 [physics.ins-det], 2011. Cited in Sections 4.3.2 (pg.104), 7.4.4 (pg.182), 7.4.4 (pg.183), and 7.6 (pg.185).
162. A. Korzenev, **NA61/SHINE** , "Hadron production measurement from NA61/SHINE," arXiv:1311.5719 [nucl-ex], 2013. Cited in Sections 4.3.2 (pg.104) and 7.1.2 (pg.166).

163. P. Adamson *et al.*, **MINOS Collaboration** , "Measurement of the neutrino mass splitting and flavor mixing by MINOS," *Phys.Rev.Lett.* **106** (2011) 181801, arXiv:1103.0340 [hep-ex]. Cited in Sections 4.3.2 (pg.105) and 4.5 (pg.120).
164. T. Yang, **ArgoNeuT Collaboration** , "New Results from ArgoNeuT," FERMILAB-CONF-13-510-E, arXiv:1311.2096 [hep-ex], 2013. Cited in Section 4.3.2 (pg.107).
165. M. Day and K. S. McFarland, "Differences in Quasi-Elastic Cross-Sections of Muon and Electron Neutrinos," *Phys.Rev.* **D86** (2012) 053003, arXiv:1206.6745 [hep-ph]. Cited in Section 4.3.2 (pg.108).
166. K. Abe *et al.*, **Super-Kamiokande Collaboration** , "Search for Differences in Oscillation Parameters for Atmospheric Neutrinos and Antineutrinos at Super-Kamiokande," *Phys.Rev.Lett.* **107** (2011) 241801, arXiv:1109.1621 [hep-ex]. Cited in Section 4.4 (pg.115).
167. P. Adamson *et al.*, **MINOS Collaboration** , "Measurement of Neutrino and Antineutrino Oscillations Using Beam and Atmospheric Data in MINOS," *Phys.Rev.Lett.* **110** (2013) 251801, arXiv:1304.6335 [hep-ex]. Cited in Section 4.6 (pg.122).
168. V. Agrawal, T. Gaisser, P. Lipari, and T. Stanev, "Atmospheric neutrino flux above 1-GeV," *Phys.Rev.* **D53** (1996) 1314–1323, arXiv:hep-ph/9509423 [hep-ph]. Cited in Section 4.6 (pg.122).
169. A. Ankowski *et al.*, "Energy reconstruction of electromagnetic showers from pi0 decays with the icarus t600 liquid argon tpc," *Acta Physica Polonica B* **41** no. 1, (2010) 103, arXiv:0812.2373 [hep-ex]. Cited in Section 4.6 (pg.124).
170. F. Arneodo *et al.*, **The ICARUS-Milano Collaboration** , "Performance of a liquid argon time projection chamber exposed to the cern west area neutrino facility neutrino beam," *Phys. Rev. D* **74** (Dec, 2006) 112001. http://link.aps.org/doi/10.1103/PhysRevD.74.112001. Cited in Section 4.6 (pg.124).
171. C. Rubbia *et al.*, "Underground operation of the ICARUS T600 LAr-TPC: first results," *JINST* **6** (2011) P07011, arXiv:1106.0975 [hep-ex]. Cited in Section 4.6 (pg.124).
172. S. Davidson, C. Pena-Garay, N. Rius, and A. Santamaria, "Present and future bounds on nonstandard neutrino interactions," *JHEP* **0303** (2003) 011, arXiv:hep-ph/0302093 [hep-ph]. Cited in Section 4.7.1 (pg.132).
173. M. Gonzalez-Garcia and M. Maltoni, "Phenomenology with Massive Neutrinos," *Phys.Rept.* **460** (2008) 1–129, arXiv:0704.1800 [hep-ph]. Cited in Section 4.7.1 (pg.132).
174. C. Biggio, M. Blennow, and E. Fernandez-Martinez, "General bounds on non-standard neutrino interactions," *JHEP* **0908** (2009) 090, arXiv:0907.0097 [hep-ph]. Cited in Section 4.7.1 (pg.132).
175. H. Davoudiasl, H.-S. Lee, and W. J. Marciano, "Long-Range Lepton Flavor Interactions and Neutrino Oscillations," *Phys.Rev.* **D84** (2011) 013009, arXiv:1102.5352 [hep-ph]. Cited in Section 4.7.2 (pg.132).

176. P. Adamson *et al.*, **MINOS Collaboration** , "Search for sterile neutrino mixing in the MINOS long baseline experiment," *Phys.Rev.* **D81** (2010) 052004, arXiv:1001.0336 [hep-ex]. Cited in Section 4.7.3 (pg.134).
177. P. Machado, H. Nunokawa, F. P. d. Santos, and R. Z. Funchal, "Large Extra Dimensions and Neutrino Oscillations," arXiv:1110.1465 [hep-ph], 2011. Cited in Section 4.7.4 (pg.135).
178. P. Coloma, P. Huber, J. Kopp, and W. Winter, "Systematic uncertainties in long-baseline neutrino oscillations for large θ_{13}," *Phys.Rev.* **D87** no. 3, (2013) 033004, arXiv:1209.5973 [hep-ph]. Cited in Section 4.8 (pg.135).
179. K. Abe, T. Abe, H. Aihara, Y. Fukuda, Y. Hayato, *et al.*, "Letter of Intent: The Hyper-Kamiokande Experiment — Detector Design and Physics Potential —," arXiv:1109.3262 [hep-ex], 2011. Cited in Section 4.8 (pg.135).
180. A. Stahl, C. Wiebusch, A. Guler, M. Kamiscioglu, R. Sever, *et al.*, "Expression of Interest for a very long baseline neutrino oscillation experiment (LBNO)," CERN-SPSC-2012-021, SPSC-EOI-007, 2012. Cited in Section 4.8 (pg.135).
181. M. Apollonio, A. Bross, J. Kopp, and K. Long, **IDS-NF Collaboration** , "The International Design Study for the Neutrino Factory," *Nucl.Phys.Proc.Suppl.* **229-232** (2012) 515. Cited in Section 4.8 (pg.135).
182. E. Christensen, P. Coloma, and P. Huber, "Physics Performance of a Low-Luminosity Low Energy Neutrino Factory," arXiv:1301.7727 [hep-ph], 2013. Cited in Section 4.8 (pg.136).
183. E. Kearns *et al.*, **Hyper-Kamiokande Working Group** , "Hyper-Kamiokande Physics Opportunities," arXiv:1309.0184 [hep-ex], 2013. Cited in Section 4.8 (pg.136).
184. S. Agarwalla *et al.*, **LAGUNA-LBNO Collaboration** , "The mass-hierarchy and CP-violation discovery reach of the LBNO long-baseline neutrino experiment," arXiv:1312.6520 [hep-ph], 2013. Cited in Section 4.8 (pg.136).
185. M. Bishai, M. Diwan, S. Kettell, J. Stewart, B. Viren, *et al.*, "Precision Neutrino Oscillation Measurements using Simultaneous High-Power, Low-Energy Project-X Beams," BNL-101234-2013-CP, FERMILAB-FN-0962, arXiv:1307.0807 [hep-ex], 2013. Cited in Section 4.8 (pg.137).
186. J. L. Raaf, **Super-Kamiokande Collaboration** , "Recent Nucleon Decay Results from Super-Kamiokande," *Nucl.Phys.Proc.Suppl.* **229-232** (2012) 559. Cited in Section 5.1 (pg.139).
187. A. Bueno, Z. Dai, Y. Ge, M. Laffranchi, A. Melgarejo, *et al.*, "Nucleon decay searches with large liquid argon TPC detectors at shallow depths: Atmospheric neutrinos and cosmogenic backgrounds," *JHEP* **0704** (2007) 041, arXiv:hep-ph/0701101 [hep-ph]. Cited in Sections 5.1 (pg.140), 5.2 (pg.140), 5.3.1 (pg.144), 5.3.1 (pg.145), and 5.3.2 (pg.145).
188. D. Stefan and A. M. Ankowski, "Nuclear effects in proton decay," *Acta Phys.Polon.* **B40** (2009) 671–674, arXiv:0811.1892 [nucl-th]. Cited in Section 5.2 (pg.141).
189. S. Amerio *et al.*, **ICARUS Collaboration** , "Design, construction and tests of the ICARUS T600 detector," *Nucl.Instrum.Meth.* **A527** (2004) 329–410. Cited in Section 5.2 (pg.141).

190. M. Antonello, B. Baibussinov, P. Benetti, E. Calligarich, N. Canci, *et al.*, "Precise 3D track reconstruction algorithm for the ICARUS T600 liquid argon time projection chamber detector," *Adv.High Energy Phys.* **2013** (2013) 260820, arXiv:1210.5089 [physics.ins-det]. Cited in Sections 5.2 (pg.142) and 5.3.2 (pg.148).
191. A. Bernstein, M. Bishai, E. Blucher, D. B. Cline, M. V. Diwan, *et al.*, "Report on the Depth Requirements for a Massive Detector at Homestake," FERMILAB-TM-2424-E, BNL-81896-2008-IR, LBNL-1348E, arXiv:0907.4183 [hep-ex], 2009. Cited in Section 5.3.1 (pg.144).
192. V. Kudryavtsev *et al.*, "Cosmic rays and cosmogenics. report to the lbne collaboration.," LBNE-doc-5904, 2012. Cited in Section 5.3.1 (pg.144).
193. K. Kobayashi *et al.*, **Super-Kamiokande Collaboration** , "Search for nucleon decay via modes favored by supersymmetric grand unification models in Super-Kamiokande-I," *Phys.Rev.* **D72** (2005) 052007, arXiv:hep-ex/0502026 [hep-ex]. Cited in Section 5.3.2 (pg.146).
194. H. Gallagher, "Private communication.". Cited in Section 5.3.2 (pg.148).
195. H.-T. Janka, "Explosion Mechanisms of Core-Collapse Supernovae," *Ann.Rev.Nucl.Part.Sci.* **62** (2012) 407–451, arXiv:1206.2503 [astro-ph.SR]. Cited in Section 6.1 (pg.151).
196. T. Fischer, S. Whitehouse, A. Mezzacappa, F.-K. Thielemann, and M. Liebendorfer, "Protoneutron star evolution and the neutrino driven wind in general relativistic neutrino radiation hydrodynamics simulations," *Astron.Astrophys.* **517** (2010) A80, arXiv:0908.1871 [astro-ph.HE]. Cited in Section 6.1 (pg.152).
197. M. Wurm *et al.*, **LENA Collaboration** , "The next-generation liquid-scintillator neutrino observatory LENA," *Astropart.Phys.* **35** (2012) 685–732, arXiv:1104.5620 [astro-ph.IM]. Cited in Section 6.1 (pg.152).
198. H. Minakata, H. Nunokawa, R. Tomas, and J. W. Valle, "Parameter Degeneracy in Flavor-Dependent Reconstruction of Supernova Neutrino Fluxes," *JCAP* **0812** (2008) 006, arXiv:0802.1489 [hep-ph]. Cited in Section 6.1 (pg.152).
199. I. Tamborra, B. Muller, L. Hudepohl, H.-T. Janka, and G. Raffelt, "High-resolution supernova neutrino spectra represented by a simple fit," *Phys.Rev.* **D86** (2012) 125031, arXiv:1211.3920 [astro-ph.SR]. Cited in Section 6.1 (pg.152).
200. H. Duan, G. M. Fuller, and Y.-Z. Qian, "Collective neutrino flavor transformation in supernovae," *Phys.Rev.* **D74** (2006) 123004, arXiv:astro-ph/0511275 [astro-ph]. Cited in Section 6.1 (pg.152).
201. G. L. Fogli, E. Lisi, A. Marrone, and A. Mirizzi, "Collective neutrino flavor transitions in supernovae and the role of trajectory averaging," *JCAP* **0712** (2007) 010, arXiv:0707.1998 [hep-ph]. Cited in Section 6.1 (pg.152).
202. G. G. Raffelt and A. Y. Smirnov, "Self-induced spectral splits in supernova neutrino fluxes," *Phys.Rev.* **D76** (2007) 081301, arXiv:0705.1830 [hep-ph]. Cited in Section 6.1 (pg.152).

203. G. G. Raffelt and A. Y. Smirnov, "Adiabaticity and spectral splits in collective neutrino transformations," *Phys.Rev.* **D76** (2007) 125008, arXiv:0709.4641 [hep-ph]. Cited in Section 6.1 (pg.152).
204. A. Esteban-Pretel, A. Mirizzi, S. Pastor, R. Tomas, G. Raffelt, *et al.*, "Role of dense matter in collective supernova neutrino transformations," *Phys.Rev.* **D78** (2008) 085012, arXiv:0807.0659 [astro-ph]. Cited in Section 6.1 (pg.152).
205. H. Duan and J. P. Kneller, "Neutrino flavour transformation in supernovae," *J.Phys.G* **G36** (2009) 113201, arXiv:0904.0974 [astro-ph.HE]. Cited in Section 6.1 (pg.152).
206. B. Dasgupta, A. Dighe, G. G. Raffelt, and A. Y. Smirnov, "Multiple Spectral Splits of Supernova Neutrinos," *Phys.Rev.Lett.* **103** (2009) 051105, arXiv:0904.3542 [hep-ph]. Cited in Section 6.1 (pg.152).
207. H. Duan, G. M. Fuller, and Y.-Z. Qian, "Collective Neutrino Oscillations," *Ann.Rev.Nucl.Part.Sci.* **60** (2010) 569–594, arXiv:1001.2799 [hep-ph]. Cited in Section 6.1 (pg.152).
208. H. Duan and A. Friedland, "Self-induced suppression of collective neutrino oscillations in a supernova," *Phys.Rev.Lett.* **106** (2011) 091101, arXiv:1006.2359 [hep-ph]. Cited in Sections 6.1 (pg.152) and 6.2 (pg.155).
209. J. F. Cherry, J. Carlson, A. Friedland, G. M. Fuller, and A. Vlasenko, "Halo Modification of a Supernova Neutronization Neutrino Burst," *Phys.Rev.* **D87** (2013) 085037, arXiv:1302.1159 [astro-ph.HE]. Cited in Section 6.1 (pg.153).
210. J. F. Beacom, R. Boyd, and A. Mezzacappa, "Black hole formation in core collapse supernovae and time-of-flight measurements of the neutrino masses," *Phys.Rev.* **D63** (2001) 073011, arXiv:astro-ph/0010398 [astro-ph]. Cited in Section 6.1 (pg.153).
211. T. Fischer, S. C. Whitehouse, A. Mezzacappa, F. K. Thielemann, and M. Liebendorfer, "The neutrino signal from protoneutron star accretion and black hole formation," arXiv:0809.5129 [astro-ph], 2008. Cited in Section 6.1 (pg.153).
212. R. C. Schirato and G. M. Fuller, "Connection between supernova shocks, flavor transformation, and the neutrino signal," LA-UR-02-3068, arXiv:astro-ph/0205390 [astro-ph], 2002. Cited in Section 6.1 (pg.153).
213. F. Hanke, A. Marek, B. Muller, and H.-T. Janka, "Is Strong SASI Activity the Key to Successful Neutrino-Driven Supernova Explosions?," *Astrophys.J.* **755** (2012) 138, arXiv:1108.4355 [astro-ph.SR]. Cited in Section 6.1 (pg.153).
214. F. Hanke, B. Mueller, A. Wongwathanarat, A. Marek, and H.-T. Janka, "SASI Activity in Three-Dimensional Neutrino-Hydrodynamics Simulations of Supernova Cores," *Astrophys.J.* **770** (2013) 66, arXiv:1303.6269 [astro-ph.SR]. Cited in Section 6.1 (pg.153).
215. A. Friedland and A. Gruzinov, "Neutrino signatures of supernova turbulence," LA-UR-06-2202, arXiv:astro-ph/0607244 [astro-ph], 2006. Cited in Section 6.1 (pg.153).

216. T. Lund and J. P. Kneller, "Combining collective, MSW, and turbulence effects in supernova neutrino flavor evolution," arXiv:1304.6372 [astro-ph.HE], 2013. Cited in Section 6.1 (pg.153).
217. G. G. Raffelt, "Particle Physics from Stars," *Ann. Rev. Nucl. Part. Sci.* **49** (1999) 163–216, arXiv:hep-ph/9903472. Cited in Section 6.1 (pg.153).
218. A. Bueno, I. Gil Botella, and A. Rubbia, "Supernova neutrino detection in a liquid argon TPC," ICARUS-TM-03-02, arXiv:hep-ph/0307222 [hep-ph], 2003. Cited in Section 6.1 (pg.153).
219. K. Scholberg *et al.*, "SNOwGLoBES: SuperNova Observatories with GLoBES." http://www.phy.duke.edu/~schol/snowglobes. Cited in Section 6.2 (pg.154).
220. E. D. Church, "LArSoft: A Software Package for Liquid Argon Time Projection Drift Chambers," arXiv:1311.6774 [physics.ins-det], 2013. Cited in Sections 6.2 (pg.154) and A.1.1 (pg.213).
221. T. Totani, K. Sato, H. E. Dalhed, and J. R. Wilson, "Future detection of supernova neutrino burst and explosion mechanism," *Astrophys. J.* **496** (1998) 216–225, arXiv:astro-ph/9710203. Cited in Section 6.2 (pg.155).
222. J. Gava, J. Kneller, C. Volpe, and G. C. McLaughlin, "A dynamical collective calculation of supernova neutrino signals," *Phys. Rev. Lett.* **103** (2009) 071101, arXiv:0902.0317 [hep-ph]. Cited in Section 6.2 (pg.155).
223. L. Hudepohl, B. Muller, H.-T. Janka, A. Marek, and G. Raffelt, "Neutrino Signal of Electron-Capture Supernovae from Core Collapse to Cooling," *Phys.Rev.Lett.* **104** (2010) 251101, arXiv:0912.0260 [astro-ph.SR]. Cited in Section 6.2 (pg.155).
224. A. Cherry, A. Friedland, and H. Duan, "Private communication.".
225. M. T. Keil, G. G. Raffelt, and H.-T. Janka, "Monte Carlo study of supernova neutrino spectra formation," *Astrophys.J.* **590** (2003) 971–991, arXiv:astro-ph/0208035 [astro-ph].
226. E. Church *et al.*, "Muon-induced background for beam neutrinos at the surface," LBNE-doc-6232, October, 2012. Cited in Sections 6.3.1 (pg.158), A.4 (pg.229), and A.4 (pg.230).
227. Gehman, V. and Kadel, R, "Calculation of intrinsic and cosmogenic backgrounds in the LBNE far detector for use in detection of supernova neutrinos," LBNE-doc-8419, January, 2014. Cited in Section 6.3.2 (pg.159).
228. J. H. Harley *et al.*, "Report No. 094 - Exposure of the Population in the United States and Canada from Natural Background Radiation," *National Council on Radiation Protection and Measurements* (2014) . http://www.ncrppublications.org/Reports/094. Cited in Section 6.3.3 (pg.160).
229. L. Grandi, "Darkside-50: performance and results from the first atmospheric argon run," February, 2014. UCLA's 11th Symposium on Sources and Detection of Dark Matter and Dark Energy in the Universe. Cited in Section 6.3.3 (pg.160).

230. D. Leonard, P. Grinberg, P. Weber, E. Baussan, Z. Djurcic, *et al.*, "Systematic study of trace radioactive impurities in candidate construction materials for EXO-200," *Nucl.Instrum.Meth.* **A591** (2008) 490–509, arXiv:0709.4524 [physics.ins-det]. Cited in Section 6.3.3 (pg.160).
231. D. Casper, "The Nuance neutrino physics simulation, and the future," *Nucl.Phys.Proc.Suppl.* **112** (2002) 161–170, arXiv:hep-ph/0208030 [hep-ph].
232. G. Zeller, "Nuclear Effects in Water vs. Argon," LBNE-doc-740, 2010.
233. G. Zeller, "Expected Event Rates in the LBNE Near Detector," LBNE-doc-783, 2010.
234. S.R.Mishra, Apr, 1990. Review talk presented at Workshop on Hadron Structure Functions and Parton Distributions, Fermilab. Cited in Section 7.1.1 (pg.164).
235. R. Raja, "The Main injector particle production experiment (MIPP) at Fermilab," *Nucl.Instrum.Meth.* **A553** (2005) 225–230, arXiv:hep-ex/0501005 [hep-ex]. Cited in Section 7.1.2 (pg.166).
236. J. Formaggio and G. Zeller, "From eV to EeV: Neutrino Cross Sections Across Energy Scales," *Rev.Mod.Phys.* **84** (2012) 1307, arXiv:1305.7513 [hep-ex]. Cited in Sections 7.1.3 (pg.166) and 7.4.4 (pg.182).
237. W. J. Marciano and Z. Parsa, "Neutrino-Electron Scattering Theory," *J. Phys.* **G29** (2003) 2629–2645, arXiv:hep-ph/0403168. Cited in Sections 7.1.4 (pg.167) and 7.2.2 (pg.173).
238. S. Mishra, K. Bachmann, R. Bernstein, R. Blair, C. Foudas, *et al.*, "Measurement of Inverse Muon Decay $\nu_\mu + e \to \mu^- + \nu_e$ at Fermilab Tevatron Energies 15-GeV - 600-GeV," *Phys.Rev.Lett.* **63** (1989) 132–135. Cited in Section 7.1.5 (pg.167).
239. S. Mishra, K. Bachmann, R. Blair, C. Foudas, B. King, *et al.*, "Inverse Muon Decay, $\nu_\mu e \to \mu^- \nu_e$, at the Fermilab Tevatron," *Phys.Lett.* **B252** (1990) 170–176. Cited in Section 7.1.5 (pg.167).
240. P. Vilain *et al.*, **CHARM-II Collaboration** , "A Precise measurement of the cross-section of the inverse muon decay muon-neutrino + e- –> mu- + electron-neutrino," *Phys.Lett.* **B364** (1995) 121–126. Cited in Section 7.1.5 (pg.167).
241. O. Samoylov *et al.*, **NOMAD** , "A Precision Measurement of Charm Dimuon Production in Neutrino Interactions from the NOMAD Experiment," *Nucl.Phys.* **B876** (2013) 339–375, arXiv:1308.4750 [hep-ex]. Cited in Sections 7.1.8 (pg.169), 7.2.1 (pg.172), and 7.4.4 (pg.183).
242. G. Zeller *et al.*, **NuTeV Collaboration** , "A Precise determination of electroweak parameters in neutrino nucleon scattering," *Phys.Rev.Lett.* **88** (2002) 091802, arXiv:hep-ex/0110059 [hep-ex]. Cited in Section 7.2.1 (pg.170).
243. H. Abramowicz, R. Belusevic, A. Blondel, H. Blumer, P. Bockmann, *et al.*, **CDHS Collaboration** , "A Precision Measurement of sin**2theta(W) from Semileptonic Neutrino Scattering," *Phys.Rev.Lett.* **57** (1986) 298. Cited in Section 7.2.1 (pg.171).
244. J. Allaby *et al.*, **CHARM Collaboration** , "A Precise Determination of the Electroweak Mixing Angle from Semileptonic Neutrino Scattering," *Z.Phys.* **C36** (1987) 611. Cited in Section 7.2.1 (pg.171).

245. P. Reutens, F. Merritt, D. MacFarlane, R. Messner, D. Novikoff, *et al.*, **CCFR Collaboration** , "Measurement of $\sin^2\theta_W$ and ρ in Deep Inelastic Neutrino - Nucleon Scattering," *Phys.Lett.* **B152** (1985) 404–410. Cited in Section 7.2.1 (pg.171).
246. S. Alekhin, S. A. Kulagin, and R. Petti, "Modeling lepton-nucleon inelastic scattering from high to low momentum transfer," *AIP Conf.Proc.* **967** (2007) 215–224, arXiv:0710.0124 [hep-ph]. Cited in Section 7.2.1 (pg.172).
247. S. Alekhin, S. A. Kulagin, and R. Petti, "Update of the global fit of PDFs including the low-Q DIS data," arXiv:0810.4893 [hep-ph], 2008. Cited in Section 7.2.1 (pg.172).
248. S. Alekhin, S. A. Kulagin, and R. Petti, "Determination of Strange Sea Distributions from Neutrino-Nucleon Deep Inelastic Scattering," *Phys.Lett.* **B675** (2009) 433–440, arXiv:0812.4448 [hep-ph]. Cited in Section 7.2.1 (pg.172).
249. A. Arbuzov, D. Y. Bardin, and L. Kalinovskaya, "Radiative corrections to neutrino deep inelastic scattering revisited," *JHEP* **0506** (2005) 078, arXiv:hep-ph/0407203 [hep-ph]. Cited in Section 7.2.1 (pg.172).
250. S. A. Kulagin and R. Petti, "Global study of nuclear structure functions," *Nucl.Phys.* **A765** (2006) 126–187, arXiv:hep-ph/0412425 [hep-ph]. Cited in Section 7.2.1 (pg.172).
251. S. A. Kulagin and R. Petti, "Neutrino inelastic scattering off nuclei," *Phys.Rev.* **D76** (2007) 094023, arXiv:hep-ph/0703033 [HEP-PH]. Cited in Sections 7.2.1 (pg.172), 7.4.2 (pg.181), and 7.6 (pg.186).
252. S. Kulagin and R. Petti, "Structure functions for light nuclei," *Phys.Rev.* **C82** (2010) 054614, arXiv:1004.3062 [hep-ph]. Cited in Section 7.2.1 (pg.172).
253. P. Vilain *et al.*, **CHARM-II Collaboration** , "Precision measurement of electroweak parameters from the scattering of muon-neutrinos on electrons," *Phys.Lett.* **B335** (1994) 246–252. Cited in Section 7.2.2 (pg.173).
254. A. Czarnecki and W. J. Marciano, "Polarized Moller scattering asymmetries," *Int.J.Mod.Phys.* **A15** (2000) 2365–2376, arXiv:hep-ph/0003049 [hep-ph].
255. S. Bennett and C. Wieman, "Erratum: Measurement of the 6s –> 7s Transition Polarizability in Atomic Cesium and an Improved Test of the Standard Model [Phys. Rev. Lett. 82, 2484 (1999)]," *Phys.Rev.Lett.* **82** (1999) 4153–4153.
256. W. Yao *et al.*, **Particle Data Group** , "Review of Particle Physics," *J.Phys.* **G33** (2006) 1–1232.
257. P. Anthony *et al.*, **SLAC E158 Collaboration** , "Precision measurement of the weak mixing angle in Moller scattering," *Phys.Rev.Lett.* **95** (2005) 081601, arXiv:hep-ex/0504049 [hep-ex].
258. J. H. Lee, "The Qweak: Precision measurement of the proton's weak charge by parity violating experiment," *Few Body Syst.* **54** (2013) 129–134. Cited in Section 7.2.2 (pg.175).
259. Nuruzzaman, "Q-weak: First Direct Measurement of the Weak Charge of the Proton," arXiv:1312.6009 [nucl-ex], 2013. Cited in Section 7.2.2 (pg.175).
260. R. Jaffe and A. Manohar, "The G(1) Problem: Fact and Fantasy on the Spin of the Proton," *Nucl.Phys.* **B337** (1990) 509–546. Cited in Section 7.3 (pg.175).

261. R. D. Young, J. Roche, R. D. Carlini, and A. W. Thomas, "Extracting nucleon strange and anapole form factors from world data," *Phys.Rev.Lett.* **97** (2006) 102002, arXiv:nucl-ex/0604010 [nucl-ex]. Cited in Sections 7.3.1 (pg.175) and 7.3.1 (pg.176).
262. D. B. Leinweber, S. Boinepalli, I. Cloet, A. W. Thomas, A. G. Williams, *et al.*, "Precise determination of the strangeness magnetic moment of the nucleon," *Phys.Rev.Lett.* **94** (2005) 212001, arXiv:hep-lat/0406002 [hep-lat]. Cited in Section 7.3.1 (pg.175).
263. L. Ahrens, S. Aronson, P. Connolly, B. Gibbard, M. Murtagh, *et al.*, "Measurement of Neutrino - Proton and anti-neutrino - Proton Elastic Scattering," *Phys.Rev.* **D35** (1987) 785. Cited in Section 7.3.2 (pg.177).
264. G. Garvey, W. Louis, and D. White, "Determination of proton strange form-factors from neutrino p elastic scattering," *Phys.Rev.* **C48** (1993) 761–765. Cited in Section 7.3.2 (pg.177).
265. W. Alberico, M. Barbaro, S. M. Bilenky, J. Caballero, C. Giunti, *et al.*, "Strange form-factors of the proton: A New analysis of the neutrino (anti-neutrino) data of the BNL-734 experiment," *Nucl.Phys.* **A651** (1999) 277–286, arXiv:hep-ph/9812388 [hep-ph]. Cited in Section 7.3.2 (pg.177).
266. A. Aguilar-Arevalo *et al.*, **MiniBooNE Collaboration** , "Measurement of the Neutrino Neutral-Current Elastic Differential Cross Section on Mineral Oil at $E_\nu \sim 1$ GeV," *Phys.Rev.* **D82** (2010) 092005, arXiv:1007.4730 [hep-ex]. Cited in Section 7.3.2 (pg.177).
267. L. Bugel *et al.*, **FINeSSE Collaboration** , "A Proposal for a near detector experiment on the booster neutrino beamline: FINeSSE: Fermilab intense neutrino scattering scintillator experiment," FERMILAB-PROPOSAL-0937, arXiv:hep-ex/0402007 [hep-ex], 2004. Cited in Section 7.3.2 (pg.178).
268. W. Leung, P. Quintas, S. Mishra, F. Sciulli, C. Arroyo, *et al.*, "A Measurement of the Gross-Llewellyn-Smith sum rule from the CCFR x(F3) structure function," *Phys.Lett.* **B317** (1993) 655–659. Cited in Section 7.4.1 (pg.180).
269. A. Bodek and A. Simon, "What Do Electron and Neutrino Experiments Tell Us About Nuclear Effects in the Deuteron," *Z.Phys.* **C29** (1985) 231. Cited in Sections 7.4.3 (pg.181) and 7.4.3 (pg.182).
270. G. Jones *et al.*, **Birmingham-CERN-Imperial Coll.-MPI(Munich)-Oxford-University Coll. Collaboration** , "A Measurement of the Proton Structure Functions From Neutrino Hydrogen and Anti-neutrino Hydrogen Charged Current Interactions," *Z.Phys.* **C44** (1989) 379–384. Cited in Sections 7.4.3 (pg.181) and 7.4.3 (pg.182).
271. J. Berge, H. Burkhardt, F. Dydak, R. Hagelberg, M. Krasny, *et al.*, "A Measurement of Differential Cross-Sections and Nucleon Structure Functions in Charged Current Neutrino Interactions on Iron," *Z.Phys.* **C49** (1991) 187–224.
272. D. Allasia *et al.*, **WA25 Collaboration** , "Measurement of the Neutron and Proton Structure Functions From Neutrino and Anti-neutrinos Scattering in Deuterium," *Phys.Lett.* **B135** (1984) 231.

273. D. Allasia, C. Angelini, A. Baldini, L. Bertanza, A. Bigi, *et al.*, "Q**2 Dependence of the Proton and Neutron Structure Functions from Neutrino and anti-neutrinos Scattering in Deuterium," *Z.Phys.* **C28** (1985) 321. Cited in Section 7.5 (pg.184).
274. U.-K. Yang *et al.*, **CCFR/NuTeV Collaboration** , "Measurements of F_2 and $xF_3^{\nu} - xF_3^{\bar{\nu}}$ from CCFR ν_μ−Fe and $\bar{\nu}_\mu$−Fe data in a physics model independent way," *Phys.Rev.Lett.* **86** (2001) 2742–2745, arXiv:hep-ex/0009041 [hep-ex].
275. U.-K. Yang *et al.*, **CCFR/NuTeV Collaboration** , "Extraction of R = sigma(L) / sigma(T) from CCFR Fe-neutrino(muon) and Fe-anti-neutrino(muon) differential cross-sections," *Phys.Rev.Lett.* **87** (2001) 251802, arXiv:hep-ex/0104040 [hep-ex].
276. M. Tzanov *et al.*, **NuTeV Collaboration** , "Precise measurement of neutrino and anti-neutrino differential cross sections," *Phys.Rev.* **D74** (2006) 012008, arXiv:hep-ex/0509010 [hep-ex]. Cited in Section 7.4.4 (pg.183).
277. G. Onengut *et al.*, **CHORUS Collaboration** , "Measurement of nucleon structure functions in neutrino scattering," *Phys.Lett.* **B632** (2006) 65–75.
278. R. Petti and O. Samoylov, "Charm dimuon production in neutrino-nucleon interactions in the NOMAD experiment," *Phys.Part.Nucl.Lett.* **8** (2011) 755–761. Cited in Section 7.4.4 (pg.183).
279. T. Sekiguchi, "Neutrino facility and neutrino physics in J-PARC," *PTEP* **2012** (2012) 02B005. Cited in Section 7.4.4 (pg.183).
280. J. Dudek, R. Ent, R. Essig, K. Kumar, C. Meyer, *et al.*, "Physics Opportunities with the 12 GeV Upgrade at Jefferson Lab," *Eur.Phys.J.* **A48** (2012) 187, arXiv:1208.1244 [hep-ex]. Cited in Section 7.4.4 (pg.183).
281. N. Mondal, "India-Based Neutrino Observatory (INO)," *Eur.Phys.J.Plus* **127** (2012) 106. Cited in Section 7.6 (pg.185).
282. A. Butkevich, "Quasi-elastic neutrino charged-current scattering off medium-heavy nuclei: 40Ca and 40Ar," *Phys.Rev.* **C85** (2012) 065501, arXiv:1204.3160 [nucl-th]. Cited in Section 7.6 (pg.186).
283. A. Butkevich and S. A. Kulagin, "Quasi-elastic neutrino charged-current scattering cross sections on oxygen," *Phys.Rev.* **C76** (2007) 045502, arXiv:0705.1051 [nucl-th]. Cited in Section 7.6 (pg.186).
284. A. M. Ankowski and J. T. Sobczyk, "Construction of spectral functions for medium-mass nuclei," *Phys.Rev.* **C77** (2008) 044311, arXiv:0711.2031 [nucl-th]. Cited in Section 7.6 (pg.186).
285. T. Asaka and M. Shaposhnikov, "The nuMSM, dark matter and baryon asymmetry of the universe," *Phys.Lett.* **B620** (2005) 17–26, arXiv:hep-ph/0505013 [hep-ph]. Cited in Sections 7.7 (pg.187) and 7.7 (pg.188).
286. D. Gorbunov and M. Shaposhnikov, "How to find neutral leptons of the νMSM?," *JHEP* **0710** (2007) 015, arXiv:0705.1729 [hep-ph]. Cited in Sections 7.7 (pg.187) and 7.7 (pg.188).

287. A. Boyarsky, O. Ruchayskiy, and M. Shaposhnikov, "The Role of sterile neutrinos in cosmology and astrophysics," *Ann.Rev.Nucl.Part.Sci.* **59** (2009) 191–214, arXiv:0901.0011 [hep-ph]. Cited in Section 7.7 (pg.187).
288. S. Dodelson and L. M. Widrow, "Sterile-neutrinos as dark matter," *Phys.Rev.Lett.* **72** (1994) 17–20, arXiv:hep-ph/9303287 [hep-ph]. Cited in Section 7.7 (pg.187).
289. A. Atre, T. Han, S. Pascoli, and B. Zhang, "The Search for Heavy Majorana Neutrinos," *JHEP* **0905** (2009) 030, arXiv:0901.3589 [hep-ph]. Cited in Sections 7.7 (pg.187) and 7.7 (pg.188).
290. M. Shaposhnikov, "The nuMSM, leptonic asymmetries, and properties of singlet fermions," *JHEP* **0808** (2008) 008, arXiv:0804.4542 [hep-ph]. Cited in Section 7.7 (pg.187).
291. E. K. Akhmedov, V. Rubakov, and A. Y. Smirnov, "Baryogenesis via neutrino oscillations," *Phys.Rev.Lett.* **81** (1998) 1359–1362, arXiv:hep-ph/9803255 [hep-ph]. Cited in Section 7.7 (pg.188).
292. A. M. Cooper-Sarkar *et al.*, **WA66 Collaboration** , "Search for Heavy Neutrino Decays in the BEBC Beam Dump Experiment," *Phys.Lett.* **B160** (1985) 207. Cited in Section 7.7 (pg.188).
293. F. Bergsma *et al.*, **CHARM Collaboration** , "A Search for Decays of Heavy Neutrinos in the Mass Range 0.5-GeV to 2.8-GeV," *Phys.Lett.* **B166** (1986) 473. Cited in Section 7.7 (pg.188).
294. A. Vaitaitis *et al.*, **NuTeV Collaboration, E815 Collaboration** , "Search for Neutral Heavy Leptons in a High-Energy Neutrino Beam," *Phys.Rev.Lett.* **83** (1999) 4943–4946, arXiv:hep-ex/9908011 [hep-ex]. Cited in Section 7.7 (pg.188).
295. G. Bernardi, G. Carugno, J. Chauveau, F. Dicarlo, M. Dris, *et al.*, "Search for Neutrino Decay," *Phys.Lett.* **B166** (1986) 479. Cited in Section 7.7 (pg.188).
296. G. Bernardi, G. Carugno, J. Chauveau, F. Dicarlo, M. Dris, *et al.*, "Further Limits on Heavy Neutrino Couplings," *Phys.Lett.* **B203** (1988) 332. Cited in Section 7.7 (pg.188).
297. L. Canetti and M. Shaposhnikov, "Baryon Asymmetry of the Universe in the NuMSM," *JCAP* **1009** (2010) 001, arXiv:1006.0133 [hep-ph].
298. C. Kullenberg *et al.*, **NOMAD Collaboration** , "A Search for Single Photon Events in Neutrino Interactions in NOMAD," *Phys.Lett.* **B706** (2012) 268–275, arXiv:1111.3713 [hep-ex]. Cited in Section 7.7 (pg.190).
299. C. Volpe, N. Auerbach, G. Colo, T. Suzuki, and N. Van Giai, "Neutrino C-12 reactions and the LSND and KARMEN experiments on neutrino oscillations," *Phys. Atom. Nucl.* **64** (2001) 1165–1168. Cited in Section 7.8 (pg.190).
300. M. Maltoni and T. Schwetz, "Sterile neutrino oscillations after first MiniBooNE results," *Phys.Rev.* **D76** (2007) 093005, arXiv:0705.0107 [hep-ph]. Cited in Section 7.8 (pg.190).
301. P. Ade *et al.*, **Planck Collaboration** , "Planck 2013 results. XVI. Cosmological parameters," arXiv:1303.5076 [astro-ph.CO], 2013. Cited in Section 7.9 (pg.192).

302. C. Bennett *et al.*, **WMAP** , "Nine-Year Wilkinson Microwave Anisotropy Probe (WMAP) Observations: Final Maps and Results," *Astrophys.J.Suppl.* **208** (2013) 20, arXiv:1212.5225 [astro-ph.CO]. Cited in Section 7.9 (pg.192).
303. B. Batell, M. Pospelov, and A. Ritz, "Exploring Portals to a Hidden Sector Through Fixed Targets," *Phys.Rev.* **D80** (2009) 095024, arXiv:0906.5614 [hep-ph]. Cited in Section 7.9 (pg.193).
304. P. deNiverville, M. Pospelov, and A. Ritz, "Observing a light dark matter beam with neutrino experiments," *Phys.Rev.* **D84** (2011) 075020, arXiv:1107.4580 [hep-ph]. Cited in Section 7.9 (pg.193).
305. P. deNiverville, D. McKeen, and A. Ritz, "Signatures of sub-GeV dark matter beams at neutrino experiments," *Phys.Rev.* **D86** (2012) 035022, arXiv:1205.3499 [hep-ph]. Cited in Section 7.9 (pg.193).
306. R. Dharmapalan *et al.*, **MiniBooNE Collaboration** , "Low Mass WIMP Searches with a Neutrino Experiment: A Proposal for Further MiniBooNE Running," FERMILAB-PROPOSAL-1032, arXiv:1211.2258 [hep-ex], 2012. Cited in Section 7.9 (pg.193).
307. H. Bethe, "Energy production in stars," *Phys.Rev.* **55** (1939) 434–456. Cited in Section 8.1 (pg.195).
308. C. Weizsäcker, "Über Elementumwandlungen im Innern der Sterne II," *Physik.Z.* **39** (1938) 633–646. Cited in Section 8.1 (pg.195).
309. J. N. Bahcall, A. M. Serenelli, and S. Basu, "New solar opacities, abundances, helioseismology, and neutrino fluxes," *Astrophys.J.* **621** (2005) L85–L88, arXiv:astro-ph/0412440 [astro-ph]. Cited in Section 8.1 (pg.195).
310. S. Fukuda *et al.*, **Super-Kamiokande Collaboration** , "Solar B-8 and hep neutrino measurements from 1258 days of Super-Kamiokande data," *Phys.Rev.Lett.* **86** (2001) 5651–5655, arXiv:hep-ex/0103032 [hep-ex]. Cited in Section 8.1 (pg.195).
311. Q. Ahmad *et al.*, **SNO Collaboration** , "Measurement of the rate of nu/e + d -> p + p + e- interactions produced by B-8 solar neutrinos at the Sudbury Neutrino Observatory," *Phys.Rev.Lett.* **87** (2001) 071301, arXiv:nucl-ex/0106015 [nucl-ex]. Cited in Section 8.1 (pg.195).
312. G. Bellini, J. Benziger, D. Bick, S. Bonetti, G. Bonfini, *et al.*, "Precision measurement of the 7Be solar neutrino interaction rate in Borexino," *Phys.Rev.Lett.* **107** (2011) 141302, arXiv:1104.1816 [hep-ex]. Cited in Section 8.1 (pg.197).
313. C. Kraus, **SNO+ Collaboration** , "SNO with liquid scintillator: SNO+," *Prog. Part. Nucl. Phys.* **57** (2006) 150–152. Cited in Section 8.1 (pg.197).
314. H. Sekiya, **Super-Kamiokande Collaboration** , "Solar neutrino analysis of Super-Kamiokande," arXiv:1307.3686, 2013. Cited in Section 8.1 (pg.197).
315. A. Guglielmi, **ICARUS Collaboration** , "Status and early events from ICARUS T600," *Nucl.Phys* **B (Proc. Suppl.) 229-232** (2012) 342–346. Cited in Section 8.1 (pg.198).
316. G. Bellini *et al.*, **Borexino Collaboration** , "First evidence of pep solar neutrinos by direct detection in Borexino," *Phys.Rev.Lett.* **108** (2012) 051302, arXiv:1110.3230 [hep-ex].

317. G. Bellini *et al.*, **Borexino Collaboration** , "Measurement of the solar 8B neutrino rate with a liquid scintillator target and 3 MeV energy threshold in the Borexino detector," *Phys.Rev.* **D82** (2010) 033006, arXiv:0808.2868 [astro-ph].
318. A. Gando *et al.*, **KamLAND Collaboration** , "Reactor On-Off Antineutrino Measurement with KamLAND," arXiv:1303.4667 [hep-ex], 2013. Cited in Section 8.1 (pg.199).
319. J. Silk, K. A. Olive, and M. Srednicki, "The Photino, the Sun and High-Energy Neutrinos," *Phys.Rev.Lett.* **55** (1985) 257–259. Cited in Section 8.2 (pg.199).
320. M. Cirelli, N. Fornengo, T. Montaruli, I. A. Sokalski, A. Strumia, *et al.*, "Spectra of neutrinos from dark matter annihilations," *Nucl.Phys.* **B727** (2005) 99–138, arXiv:hep-ph/0506298 [hep-ph]. Cited in Section 8.2 (pg.200).
321. J. LoSecco, J. Van der Velde, R. Bionta, G. Blewitt, C. Bratton, *et al.*, "Limits on the Flux of Energetic Neutrinos from the Sun," *Phys.Lett.* **B188** (1987) 388. Cited in Section 8.2 (pg.200).
322. M. Aartsen *et al.*, **IceCube Collaboration** , "Search for dark matter annihilations in the Sun with the 79-string IceCube detector," *Phys.Rev.Lett.* **110** (2013) 131302, arXiv:1212.4097 [astro-ph.HE]. Cited in Section 8.2 (pg.200).
323. M. Blennow, M. Carrigan, and E. F. Martinez, "Probing the Dark Matter mass and nature with neutrinos," *JCAP* **1306** (2013) 038, arXiv:1303.4530 [hep-ph]. Cited in Section 8.2 (pg.200).
324. T. Totani, K. Sato, and Y. Yoshii, "Spectrum of the supernova relic neutrino background and evolution of galaxies," *Astrophys.J.* **460** (1996) 303–312, arXiv:astro-ph/9509130 [astro-ph]. Cited in Section 8.3 (pg.201).
325. K. Sato, T. Totani, and Y. Yoshii, "Spectrum of the supernova relic neutrino background and evolution of galaxies," 1997. Cited in Section 8.3 (pg.201).
326. D. Hartmann and S. Woosley, "The cosmic supernova neutrino background," *Astropart.Phys.* **7** (1997) 137–146. Cited in Section 8.3 (pg.201).
327. R. Malaney, "Evolution of the cosmic gas and the relic supernova neutrino background," *Astropart.Phys.* **7** (1997) 125–136, arXiv:astro-ph/9612012 [astro-ph]. Cited in Section 8.3 (pg.201).
328. M. Kaplinghat, G. Steigman, and T. Walker, "The Supernova relic neutrino background," *Phys.Rev.* **D62** (2000) 043001, arXiv:astro-ph/9912391 [astro-ph]. Cited in Section 8.3 (pg.201).
329. S. Ando, J. F. Beacom, and H. Yuksel, "Detection of neutrinos from supernovae in nearby galaxies," *Phys.Rev.Lett.* **95** (2005) 171101, arXiv:astro-ph/0503321 [astro-ph]. Cited in Section 8.3 (pg.201).
330. C. Lunardini, "Testing neutrino spectra formation in collapsing stars with the diffuse supernova neutrino flux," *Phys.Rev.* **D75** (2007) 073022, arXiv:astro-ph/0612701 [astro-ph]. Cited in Section 8.3 (pg.201).
331. M. Fukugita and M. Kawasaki, "Constraints on the star formation rate from supernova relic neutrino observations," *Mon.Not.Roy.Astron.Soc.* **340** (2003) L7, arXiv:astro-ph/0204376 [astro-ph]. Cited in Section 8.3 (pg.201).

332. P. Vogel and J. F. Beacom, "Angular distribution of neutron inverse beta decay, anti-neutrino(e) + p —> e+ + n," *Phys.Rev.* **D60** (1999) 053003, arXiv:hep-ph/9903554 [hep-ph]. Cited in Section 8.3 (pg.201).
333. A. Strumia and F. Vissani, "Precise quasielastic neutrino nucleon cross section," *Phys. Lett.* **B564** (2003) 42–54, arXiv:astro-ph/0302055. Cited in Section 8.3 (pg.201).
334. W. E. Ormand, P. M. Pizzochero, P. F. Bortignon, and R. A. Broglia, "Neutrino capture cross-sections for Ar-40 and Beta decay of Ti-40," *Phys. Lett.* **B345** (1995) 343–350, arXiv:nucl-th/9405007. Cited in Section 8.3 (pg.201).
335. E. Kolbe, K. Langanke, G. Martinez-Pinedo, and P. Vogel, "Neutrino nucleus reactions and nuclear structure," *J. Phys.* **G29** (2003) 2569–2596, arXiv:nucl-th/0311022. Cited in Section 8.3 (pg.201).
336. M. Sajjad Athar and S. K. Singh, "nu/e (anti-nu/e) - Ar-40 absorption cross sections for supernova neutrinos," *Phys. Lett.* **B591** (2004) 69–75. Cited in Section 8.3 (pg.201).
337. A. Cocco, A. Ereditato, G. Fiorillo, G. Mangano, and V. Pettorino, "Supernova relic neutrinos in liquid argon detectors," *JCAP* **0412** (2004) 002, arXiv:hep-ph/0408031 [hep-ph]. Cited in Section 8.3 (pg.202).
338. R. Abbasi *et al.*, **IceCube Collaboration** , "Search for Relativistic Magnetic Monopoles with IceCube," *Phys.Rev.* **D87** (2013) 022001, arXiv:1208.4861 [astro-ph.HE]. Cited in Section 8.4 (pg.203).
339. M. Aartsen *et al.*, **IceCube Collaboration** , "The IceCube Neutrino Observatory Part IV: Searches for Dark Matter and Exotic Particles," arXiv:1309.7007 [astro-ph.HE], 2013. Cited in Section 8.4 (pg.203).
340. K. Ueno *et al.*, **Super-Kamiokande Collaboration** , "Search for GUT Monopoles at Super-Kamiokande," *Astropart.Phys.* **36** (2012) 131–136, arXiv:1203.0940 [hep-ex]. Cited in Section 8.4 (pg.203).
341. M. Aartsen *et al.*, **IceCube Collaboration** , "Search for non-relativistic Magnetic Monopoles with IceCube," arXiv:1402.3460 [astro-ph.CO], 2014. Cited in Section 8.4 (pg.203).
342. M. Ambrosio *et al.*, **MACRO Collaboration** , "Final results of magnetic monopole searches with the MACRO experiment," *Eur.Phys.J.* **C25** (2002) 511–522, arXiv:hep-ex/0207020 [hep-ex]. Cited in Section 8.4 (pg.203).
343. R. Mohapatra, "Neutron-Anti-Neutron Oscillation: Theory and Phenomenology," *J.Phys.* **G36** (2009) 104006, arXiv:0902.0834 [hep-ph]. Cited in Section 8.5 (pg.204).
344. The United States Department of Energy, "Program and Project Management for the Acquisition of Capital Assets," DOE, DOE O 413.3B, November, 2010. Cited in Section 9.1 (pg.206).
345. J. Strait, R. Wilson, and V. Papadimitriou, "LBNE Presentations to P5," LBNE-doc-8694, November, 2013. Cited in Section 9.1 (pg.207).
346. S. Bilenky and C. Giunti, "Neutrinoless double-beta decay: A brief review," *Mod.Phys.Lett.* **A27** (2012) 1230015, arXiv:1203.5250 [hep-ph]. Cited in Section 9.2 (pg.209).

347. **LBNE Project Management Team** , "LBNE Conceptual Design Report: The LBNE Water Cherenkov Detector," LBNE-doc-5118, 2012. Cited in Section 9.3 (pg.210).
348. J. Hewett, H. Weerts, K. Babu, J. Butler, B. Casey, *et al.*, "Planning the Future of U.S. Particle Physics (Snowmass 2013): Chapter 2: Intensity Frontier," FERMILAB-CONF-14-019-CH02, arXiv:1401.6077 [hep-ex], 2014. Cited in Section 9.4.1 (pg.210).
349. C. Green, J. Kowalkowski, M. Paterno, M. Fischler, L. Garren, *et al.*, "The art framework," *J.Phys.Conf.Ser.* **396** (2012) 022020. Cited in Section A.1.1 (pg.213).
350. T. Katori, **MicroBooNE Collaboration** , "MicroBooNE, A Liquid Argon Time Projection Chamber (LArTPC) Neutrino Experiment," *AIP Conf.Proc.* **1405** (2011) 250–255, arXiv:1107.5112 [hep-ex]. Cited in Sections A.1.1 (pg.213) and A.3 (pg.221).
351. M. Soderberg, **ArgoNeuT Collaboration** , "ArgoNeuT: A Liquid Argon Time Projection Chamber Test in the NuMI Beamline," FERMILAB-CONF-09-516-E, arXiv:0910.3433 [physics.ins-det], 2009. Cited in Section A.1.1 (pg.213).
352. D.Huffman, "A Method for the Construction of Minimum-Redundancy Codes," in *Proceedings of the IRE*. 1952. Cited in Section A.1.1 (pg.215).
353. M. Szydagis, N. Barry, K. Kazkaz, J. Mock, D. Stolp, *et al.*, "NEST: A Comprehensive Model for Scintillation Yield in Liquid Xenon," *JINST* **6** (2011) P10002, arXiv:1106.1613 [physics.ins-det]. Cited in Section A.1.1 (pg.215).
354. C. Hagman, D. Lange, J. Verbeke, and D. Wright, "Cosmic-ray Shower Library (CRY)," Lawrence Livermore National Laboratory, UCRL-TM-229453, March, 2012. http://nuclear.llnl.gov/simulation/doc_cry_v1.7/cry.pdf. Cited in Section A.1.1 (pg.216).
355. R. P. Sandhir, S. Muhuri, and T. Nayak, "Dynamic Fuzzy c-Means (dFCM) Clustering and its Application to Calorimetric Data Reconstruction in High Energy Physics," *Nucl.Instrum.Meth.* **A681** (2012) 34–43, arXiv:1204.3459 [nucl-ex]. Cited in Section A.2 (pg.218).
356. R. E. Kalman, "A new approach to linear filtering and prediction problems," *Transactions of the ASME–Journal of Basic Engineering* **82** no. Series D, (1960) 35–45. Cited in Section A.2 (pg.218).
357. J. Marshall and M. Thomson, "The Pandora software development kit for particle flow calorimetry," *J.Phys.Conf.Ser.* **396** (2012) 022034. Cited in Section A.2 (pg.219).
358. A. Accardi, J. Albacete, M. Anselmino, N. Armesto, E. Aschenauer, *et al.*, "Electron Ion Collider: The Next QCD Frontier - Understanding the glue that binds us all," BNL-98815-2012-JA, JLAB-PHY-12-1652, arXiv:1212.1701 [nucl-ex], 2012. Cited in Sections B (pg.233) and B (pg.235).

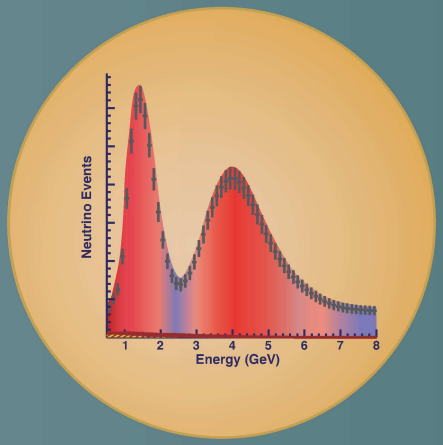

Through precise studies of neutrino flavor oscillations enabled by an intense, optimized beam and advanced detectors, LBNE aims to shed light on the mystery of the matter-antimatter asymmetry in the Universe.

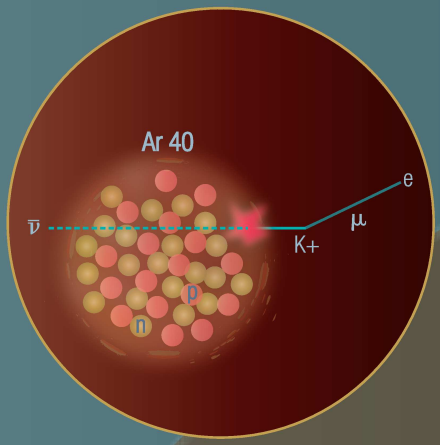

With the world's largest cryogenic particle detector deep underground, LBNE will probe the stability of matter and its relation to the Grand Unification of forces.

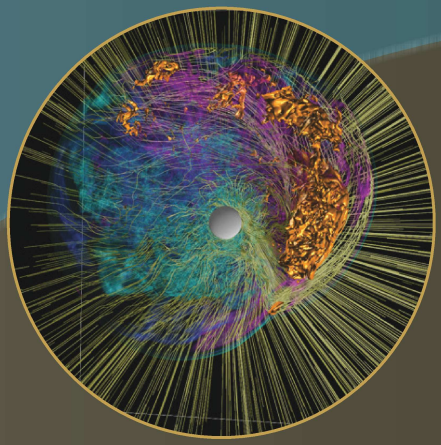

LBNE's observation of thousands of neutrinos from a core-collapse supernova in the Milky Way would allow us to peer inside a newly-formed neutron star and potentially witness the birth of a black hole.

U.S. DEPARTMENT OF ENERGY | Office of Science

Sanford Underground Research Facility

Fermilab